

MASARYK UNIVERSITY

Faculty of Science
Department of Chemistry

Experimental and theoretical study of phase diagrams

Habilitation thesis

Ondřej Zobač
Brno 2025

Bibliographic record

Author Ondřej Zobač
Institute of Physics of Materials, The Czech Academy
of Sciences

Title of Thesis: Experimental and theoretical study of phase diagrams
Habilitation Field: Physical chemistry
Year: 2025
Number of Pages: 220
Keywords: phase diagrams, thermodynamic equilibria, scanning
electron microscopy, X-ray diffraction, differential
thermal analysis, differential scanning calorimetry,
CALPHAD, thermodynamic modelling

Bibliografický záznam

Autor: Ondřej Zobač
Ústav fyziky materiálů, Akademie věd České republiky

Název práce: Experimentální a teoretická studie fázových diagramů

Obor habilitačního řízení: Fyzikální chemie

Rok: 2025

Počet stran: 220

Klíčová slova: fázové diagramy, termodynamické rovnováhy, skenovací elektronová mikroskopie, rentgenová difrakční analýza, diferenční termická analýza, diferenční skenovací kalorimetrie, CALPHAD, termodynamické modelování

Table of content

Table of content	4
Commentary to habilitation thesis	5
Komentář k habilitační práci	7
Declaration	9
Acknowledgements	10
Abbreviations	11
Introduction	12
1 Systems studied	13
2 Experimental investigation of phase diagrams	14
2.1 Results and discussion	15
3 CALPHAD approach	22
3.1 Third-generation data of pure elements	25
3.2 Results and discussion	28
4 Conclusion.....	34
5 References	36
5.1 Author's publications	36
5.2 Further references.....	37
6 Papers.....	41

Commentary to habilitation thesis

This habilitation thesis documents the most important research results of the applicant after obtaining a doctoral (Ph.D.) degree. The main research activities and results described here are related to the experimental and theoretical investigations of various systems, where the phase equilibria are unknown or where discrepancies occur in the literature.

The applicant is an author of thirty-three papers (fifteen of them as a first author) and five chapters in monography (two of them as a first author). Twelve papers [P1-P12] are included and commented on in this habilitation thesis. Out of these twelve scientific papers in journals with impact factor, the applicant is the first author of nine and the corresponding author of ten. This habilitation thesis divides topics into two chapters: "Experimental investigation of phase diagrams" and "CALPHAD approach".

The first chapter, "Experimental investigation of phase diagrams", describes the construction process of experimental phase diagrams and demonstrates them on selected technological perspective systems [P1, P3, P4, P7, P9, P10]. Despite the significant shift in the use of theoretical approaches calculating the thermodynamic stability of individual phases using ab initio methods, experimental work in the field of phase equilibria is still irreplaceable. Moreover, these two approaches are not opposed to each other but can be suitably complementary and supportive, as for example, in the experimental observation of the non-stoichiometricity of the ternary phase in the Al-Ge-Mg system, which was later supported by ab initio calculations in combination with phonon spectra (see commentary to paper P10). Experimental work is mainly targeted at systems where there are discrepancies between earlier works or in areas that have not been studied with sufficient accuracy. The importance of the targeted experimental work can be demonstrated on the paper on the Al-Cu system [P1], which has gained more than a hundred citations in five years. In this paper, we have newly described, among others, the region of transition between γ' and δ phases and metastable congruent melting of the θ phase.

The second chapter, "CALPHAD approach", summarises the core concepts and innovations of the semiempirical thermodynamic CALPHAD (Calculation of PHase Diagram) approach [1998Sau] and the author's main contributions in this field [P2, P5, P6, P8, P11, P12]. This approach uses a basic amount of input data and the sequential modelling of thermodynamic properties to provide robust, consistent and reliable sets of thermodynamic parameters describing binary and higher systems. With a reliable and sufficient set of experimental data available, it is possible to model such a system with high precision. It is important to have experimental or/and ab initio data of both the thermodynamic properties of individual phases (e.g. heat capacities, enthalpies of formation or mixing, activities) and phase equilibria (e.g. temperatures of phase transformations, chemical compositions and amounts of phases).

The thermodynamic descriptions of binary and ternary systems are then merged into large databases for various material types (e.g. for durals [P2, P5, P11, P12] or thermoelectrics

[P6, P8]). These databases have great application potential, especially in the development, production and heat treatment of metal alloys.

By default, the CALPHAD method uses polynomial mathematical models to describe the Gibbs energy. These polynomial functions are mostly defined above room temperature only. In the last decade, intensive work has been done on a new approach (so-called third-generation modelling) based on a physical background using Einstein's heat capacity model for the solid phase and the so-called two-state model for the liquid phase of pure elements. The physically based theoretical approach of solid phase allows defining a description of unaries over the whole temperature range from 0 K to high temperature above the melting temperature. A two-state model for the liquid phase provides a sound basis for extrapolating the heat capacity to temperatures below the melting point. A description of the thermodynamic properties of the liquid phase below the melting point is required to describe undercooled liquids and metallic glasses. An important part of the transition to the so-called third-generation models is the possibility to use the values of the interaction parameters developed earlier for the second generation. This approach is described in more detail in a paper dealing with the Al-Zn binary system [P2] and in a follow-up paper describing an extension for ternary system Al-Si-Zn [P12]. The third-generation issue is jointly addressed by an international working group led by Prof. Malin Selleby (KTH Royal Institute of Technology, Stockholm), of which the author of this thesis is a member.

The author's contributions to the results published in the selected twelve papers included in this habilitation thesis are summarised in chapter 5.1 "Author's publications" of this thesis. The author's contribution is divided into the following topics: scientific work (experimental and theoretical work), supervision of students, manuscript writing and research motivation.

Komentář k habilitační práci

Tato habilitační práce dokumentuje nejdůležitější výsledky výzkumu uchazeče po získání doktorského titulu (Ph.D.). Hlavní výzkumné aktivity a výsledky zde popsané se týkají experimentálního a teoretického zkoumání různých slitin, u nichž nejsou známy fázové rovnováhy nebo se v literatuře vyskytují rozpory.

Uchazeč je autorem třiceti tří článků (z toho patnácti jako první autor) a pěti kapitol v monografii (z toho dvou jako první autor). Dvanáct prací [P1-P12] je zahrnuto a komentováno v této habilitační práci. Z těchto dvanácti vědeckých prací v časopisech s impakt faktorem je uchazeč prvním autorem devíti a korespondujícím autorem deseti z nich. Tato habilitační práce je tematicky rozdělena do dvou kapitol: „Experimentální popis fázových diagramů“ a „Metoda CALPHAD“.

První kapitola „Experimentální popis fázových diagramů“ popisuje postup konstrukce experimentálních fázových diagramů a demonstruje je na vybraných technologicky perspektivních systémech [P1, P3, P4, P7, P9, P10]. I přes výrazný posun ve využívání teoretických přístupů schopných predikovat termodynamickou stabilitu jednotlivých fází metodami ab initio je experimentální práce v oblasti fázových rovnováh stále nezastupitelná. Tyto dva přístupy navíc nestojí proti sobě, ale mohou se vhodně doplňovat a podporovat, jako například při experimentálním pozorování nestechiometričnosti ternární fáze v systému Al-Ge-Mg, které bylo později podpořeno ab initio výpočty v kombinaci s fononovými spektry (viz komentář k článku P10). Experimentální práce jsou zaměřeny především na systémy, kde existují rozpory mezi dřívějšími pracemi nebo v oblastech, které nebyly dostatečně přesně prozkoumány. Význam cílené experimentální práce lze demonstrovat na článku o systému Al-Cu [P1], který za pět let získal více než sto citací. V této práci jsme mimo jiné nově popsali oblast přechodu mezi fázemi γ' a δ a metastabilní kongruentní tání fáze θ .

Druhá kapitola „Metoda CALPHAD“ shrnuje základní koncepty a inovace semiempirického termodynamického přístupu CALPHAD (Calculation of PHase Diagram) [1998Sau] a hlavní příspěvky autora v této oblasti [P2, P5, P6, P8, P11, P12]. Tento přístup využívá základní množství vstupních údajů a postupné modelování termodynamických vlastností k získání robustních, konzistentních a spolehlivých souborů termodynamických parametrů popisujících binární a vyšší systémy. Pokud je k dispozici spolehlivý a dostatečný soubor experimentálních dat, je možné takový systém modelovat s vysokou přesností. Je důležité mít k dispozici experimentální a/nebo ab initio údaje jak o termodynamických vlastnostech jednotlivých fází (např. tepelné kapacity, tvorné nebo směšovací entalpie, aktivity), tak o fázových rovnováhách (např. teploty fázových přeměn, chemické složení a množství fází).

Termodynamické popisy binárních a ternárních systémů jsou pak sloučeny do rozsáhlých databází pro různé typy materiálů (např. pro duraly [P2, P5, P11, P12] nebo termoelektrika [P6, P8]). Tyto databáze mají velký aplikační potenciál, zejména při vývoji, výrobě a tepelném zpracování kovových slitin.

Ve výchozím nastavení používá metoda CALPHAD k popisu Gibbsovy energie polynomické matematické modely. Tyto polynomiální funkce jsou většinou definovány pouze nad pokojovou teplotou. V posledním desetiletí se intenzivně pracuje na novém přístupu (tzv. třetí generace) založeném na fyzikálním pozadí s využitím Einsteinova modelu tepelné kapacity pro pevnou fázi a tzv. modelu dvou stavů pro kapalnou fázi čistých prvků. Fyzikálně založený teoretický přístup pro pevnou fázi umožňuje definovat popis čistých prvků v celém teplotním rozsahu od 0 K až po vysoké teploty nad teplotou tání. Model dvou stavů pro kapalnou fázi poskytuje spolehlivý základ pro extrapolaci tepelné kapacity na teploty pod bodem tání. Popis termodynamických vlastností kapalně fáze pod bodem tání je nutný pro popis podchlazených kapalin a kovových skel. Důležitou součástí přechodu k modelům tzv. třetí generace je možnost použít hodnoty interakčních parametrů vyvinuté dříve pro druhou generaci. Tento přístup je podrobněji popsán v článku zabývajícím se binárním systémem Al-Zn [P2] a v navazujícím článku popisujícím rozšíření pro ternární systém Al-Si-Zn [P12]. Problematikou třetí generace se společně zabývá mezinárodní pracovní skupina vedená Prof. Malin Selleby (Královský technologický institut KTH, Stockholm), jejímž členem je i autor této práce.

Autorův podíl na výsledcích publikovaných ve vybraných jedenácti pracích obsažených v této habilitační práci je shrnut v kapitole 5.1 „Author's publications“ této práce. Autorův podíl je rozdělen do následujících témat: vědecká práce (experimentální a teoretická práce), vedení studentů, psaní rukopisů a motivace k výzkumu.

Declaration

I hereby confirm that I have written the habilitation thesis independently, that I have not used other sources than the ones mentioned and that I have not submitted the habilitation thesis elsewhere.

In Brno, January 2025

.....

Ondřej Zobač

Acknowledgements

During my scientific career, from a student to a scientist, I have been lucky enough to work with many great scientists and collaborators. I would especially like to thank our group leader Dr. Aleš Kroupa from the Institute of Physics of Materials of the Czech Academy of Sciences who accepted me into his team after graduation and helped me to get postdoctoral positions, Dr. Martin Friák from the Institute of Physics of Materials of the Czech Academy of Sciences and Assoc. prof. Jana Pavlů from the Department of Chemistry of Masaryk University, with whom I collaborate in the field of linking ab initio calculations and the CALPHAD approach, and Prof. Klaus Richter from Universität Wien in Austria, where I spent two years as a postdoctoral fellow and with whom I continue intensive collaboration in the field of experimental phase diagrams and structural XRD characteristics. Many thanks are also due to my wonderful colleagues, former and current students and last but not least to my family and friends.

Abbreviations

BCC	body-centred cubic
CALPHAD	calculation of phase diagrams
DSC	differential scanning calorimetry
DTA	differential thermal analysis
EDX	energy-dispersive X-ray spectrometry
FCC	face-centred cubic
HCP	hexagonal close-packed
SEM	scanning electron microscope
TA	thermal analysis
XRD	X-ray diffraction
WDX	wavelength dispersive X-ray spectrometry

Introduction

The idea of equilibrium phase diagrams dates back to the second half of the 19th century to J. W. Gibbs and his study of thermodynamics and phase equilibria. A phase diagram is a graphical representation of the state of a system in thermodynamic equilibrium as a function of selected state variables. Phase diagrams are directly related to the rules of thermodynamics and thermodynamic quantities. They differ from property diagrams, because they carry a different type of information. Each point in a phase diagram has its own meaning and carries some information about phase equilibria.

The equilibrium phase diagram is an essential source of information for the design of new materials. Detailed knowledge of the coexistence and stability of phases in stable or metastable equilibrium significantly rationalises the development of material research.

For the **experimental phase diagram investigation**, a combination of dynamic and static analytical methods can be used. The overall and phase chemical composition is measured by scanning electron microscopy with an energy/wave dispersive X-ray spectroscopy detector (SEM-EDX/WDX) or transmission electron microscopy (sTEM-EDX) in specific cases. Identification of phase structure is done by powder X-ray diffraction (XRD) or electron diffraction analysis in TEM. Temperatures of phase transitions are evaluated by methods of thermal analysis - differential scanning calorimetry (DSC) or differential thermal analysis (DTA).

Phase diagrams can be predicted by a semiempirical thermodynamic method known as **a CALPHAD approach** (CALculation of the PHase Diagram) [1998Sau]. This approach is based on the sequential modelling of multicomponent systems, starting from the simplest - modelling the temperature dependence of the Gibbs energy of the pure elements, followed by modelling more complex binary and ternary systems, which include solid solutions and intermetallic phases. The robust theoretical description of simpler (binary and ternary) systems consequently allows us to predict the behaviour of complex multicomponent systems by extrapolation without additional model parameters. The knowledge of the Gibbs energy dependence on composition, temperature and pressure for all phases which might occur in the system (stable and even metastable) is crucial. Unfortunately, this information is usually experimentally inaccessible for metastable phases. The lack of experimental data can be compensated by first-principles calculations, which, based on quantum mechanics, can determine thermodynamic quantities such as enthalpy of formation even for metastable or unstable phases at temperature $T = 0$ K. Using phonon spectra modelling, the calculations can be extended to the high-temperature region and used to calculate e.g. the specific heat capacity for a given phase.

Over the last decade, an international collaborative activity has started towards the development of a new generation of data for the pure elements [2017Vre, 2018Jia, 2019Big] based on the conclusions of a series of workshops held at Schloß Ringberg [1995Agr, 1995Cha, 1995Sun]. This progress is motivated by the suggestion that the thermodynamic functions for elements should be described by models accounting for different physical phenomena rather than simple mathematical polynomials.

1 Systems studied

Since this work is devoted to the experimental and theoretical studies of phase diagrams, a characterisation and list of the systems studied are given in this chapter.

The first group of studied materials are aluminium-based alloys, namely the binary systems Al-Cu [P1, P6] and Al-Zn [P2] and ternary systems Al-Cu-Zn [P3], Al-Cu-Si [P4], Al-Si-Zn [12] and Al-Ge-Mg [P10]. Dural alloys based on the Al-Cu system are of great technological importance, e.g. for producing castings for automotive engine components. Heat-treated alloys can achieve superior mechanical properties for aircraft and other high-strength applications. Specifically, Al-Cu-Si alloys are of interest for automotive and aerospace technology applications due to their quality and lightweight. Their corrosion resistance is superior to that of Al-Cu alloys, and their strength is better than that of Al-Si alloys [2005Pan]. Alloys in the Al-Cu-Zn system, on the other hand, have been intensively studied for shape-memory properties of the β BCC_A2 phase in these alloys [2013Gom, 2015Gom].

The second group of materials is selenium-based alloys, namely binary system Ni-Se [P7] and ternary systems Ag-Se-Sn [P8], Pb-Se-Sn [P9] and Ni-Se-Sn [P12], which are promising as a basis of future advanced materials for photovoltaics, superconductors, thermoelectrics, etc. Among others, for example, SnSe₂ is well known for its interesting thermophysical [2012He], transport [2017Din] and thermoelectric properties [2018Zou] and NiSe continuously attracts attention for its structural, electronic, thermal and transport properties [2019Goe].

2 Experimental investigation of phase diagrams

Sample preparation is crucial for the study of experimental phase diagrams because even the best analytical methods cannot extract relevant information from a poorly prepared sample. Alloy samples can be prepared from pure elements or so-called mother-alloys. For the synthesis of alloys, it is necessary to select elements of sufficient purity (usually at least 99.99 %) and to protect them against the influence of the external atmosphere, especially oxidation, both during casting and further processing. Alloying can occur in an arc-melting furnace or in an evacuated quartz glass ampoule in a conventional furnace. The alloy must be shaken or inverted to ensure the highest possible homogeneity of the sample. The microstructure of the alloyed samples (so-called as-cast state) should be analysed for subsequent comparison with the microstructure of the annealed samples. The resulting alloys are annealed in evacuated quartz glass ampoules for a long time. In the case of elements that interact with the quartz glass or are highly reactive, it is advisable to place them in a corundum crucible to avoid direct contact of the sample with the wall of the quartz ampoule. The annealing is completed by dropping the sample vial into ice-cold water, where the vial must be broken immediately below the surface. In the case of water-reactive samples, quenching in liquid nitrogen is used. Metallographic grinding and sample polishing are necessary to prepare the surface for microscopic observation. Reactive samples need to be ground and polished under an anhydrous coolant such as ethanol or isopropanol to avoid surface oxidation of the sample.

A combination of static and dynamic analytical methods is used to characterise the phase equilibrium. The overall and phase composition is usually measured by SEM. The overall chemical composition is measured over as large area of the sample as possible. It is useful to compare it with the nominal composition obtained from pure metal weights. In this way, it can be determined whether there is a change in composition during synthesis, e.g. by evaporation of a high vapour-tensile element. The chemical composition of the phases is measured pointwise, in the middle of the grain, to avoid the interaction of the irradiated volume with the matrix or the adjacent grain. Phases that have decomposed to a fine-grained structure during quenching (typically liquid) are measured as an area scan to record the chemical composition of the phase before the decomposition.

The crystallographic structure of the coexisting phases can be confirmed by powder XRD methods. For this analysis, a fine powder must be prepared from the alloy. For brittle materials, the powder can be prepared using a friction pan and a pestle (steel or agate). If the alloy is too hard, the powder can be prepared using a diamond file. However, the resulting powder needs to be annealed briefly at an annealing temperature to release the stresses in the material created by the use of the file. Alloys that are ductile or malleable can be analysed using the metallographically prepared surface, where the grains are expected to be randomly oriented and in sufficient quantity for XRD measurements. It is advisable to perform a Rietveld analysis for the evaluation of XRD patterns to allow a comparison of the observed composition of the individual phases with the results of the SEM-EDX chemical analysis, although a qualitative assessment would theoretically be sufficient for the identification of stable phases. In the case of binary phases with a solubility of a third element, a change of the lattice parameters induced by the third element-impurity introduction should be considered.

2.1 Results and Discussion

Although the Al-Cu [P1] system and its alloys are widely used industrially and have been studied for a long time, due to their complexity, they have not been reliably described experimentally over the whole range of concentrations and temperatures. Figure 1 shows the gradual evolution of the Al-Cu phase diagram as different authors refined the phase equilibria over time [1978Kau, 1985Mur, 2011Pon, P1]. It can be seen that the gradual development of knowledge about the behaviour of the Al-Cu binary system and led to the discovery of the very complex behaviour of the stable phases. According to [P1], there are a total of twelve individual phases in the Al-Cu system that interact with each other in different ways. Although Ponweiser et al. [2011Pon] experimentally described the phase diagram of Al-Cu over the whole range of concentrations and temperatures, they still did not resolve some unanswered questions, especially in the central region of the diagram, e.g. regarding the stability and interactions of the δ phase.

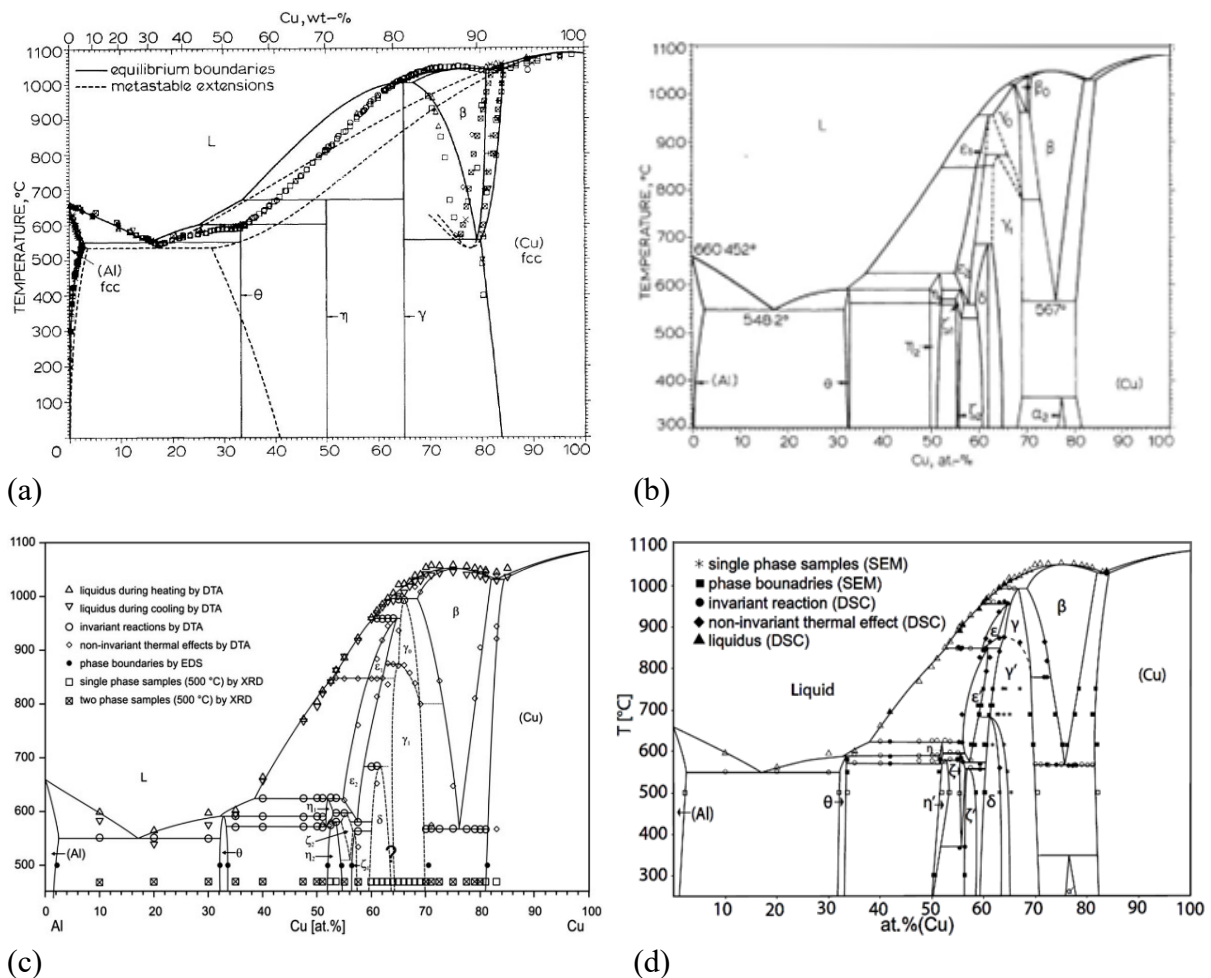


Figure 1: Binary phase diagram of the Al-Cu system: a) Kaufmann [1978Kau]; b) Murray [1985Mur]; c) Ponweiser [2011Pon]; d) Zobač [P1] with superimposed new experimental data from Zobač [P1] and from Ponweiser [2011Pon].

In light of the previously stated information, forty samples were prepared and long-term annealed at eight different temperatures to study the Al-Cu phase diagram. Another ten samples were used to study the metastable equilibrium of the theta phase transition. A total of thirty samples were studied by thermal analysis using DTA and DSC. The obtained results are presented in Ref. [P1] and can be summarised as follows. It was found that the theta phase decomposes peritectically upon heating, although the metastable equilibrium corresponds to congruent melting. The zeta phase was determined stable in the 373 °C - 597 °C temperature range. The two-phase field region $\gamma' + \delta$ was newly determined. The temperature of the second-order $\gamma \leftrightarrow \gamma'$ transition was determined to be 779.6 °C (see Figure 2).

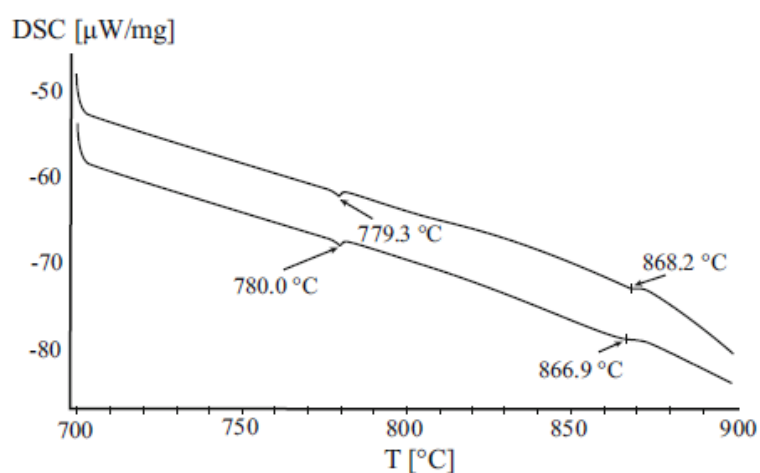


Figure 2: Second and third DSC heating curves of Al-71.8Cu (at. %) sample. Measured signals correspond to the higher ordered phase transition $\gamma \leftrightarrow \gamma'$ and to transition $\beta \leftrightarrow \gamma + \beta$. A heating rate $1 \text{ } ^\circ\text{C min}^{-1}$, under the inert atmosphere 5N Ar flowing 50 ml min^{-1} was selected.

Although the phase diagram of the Al-Cu system has been intensively studied in the past, these new findings have been widely accepted by the scientific community, as evidenced by the high number of citations in materials science journals. This demonstrates the timeliness and usefulness of the detailed study of phase equilibria, even in simple, presumably well-known systems.

Subsequently, the Al-Cu-Zn ternary phase diagram was studied at four temperatures (400 °C, 550 °C, 700 °C and 820 °C) [P3], where a total of 119 samples were analysed. Here, the mutual interactions of the $\gamma + \gamma'$ phases were studied over the entire concentration and temperature range: the two-phase field was found at temperatures of 400 °C and below, with a second-order transition at higher temperatures. The interaction between $\gamma + \gamma'$ phases has been extensively studied in the past [1998Lia, 2015Lia] and various alternatives have been proposed due to the high potential of these brass phases. Finally, our work has provided an experimental evidence for the existence of two-phase regions at lower temperatures as well as second-order transitions at higher temperatures. The isothermal section of the Al-Cu-Zn ternary phase

diagram at 400 °C is shown in Figure 3a and the isopleth passing through the $\gamma + \gamma'$ two-phase region is shown in Figure 3b.

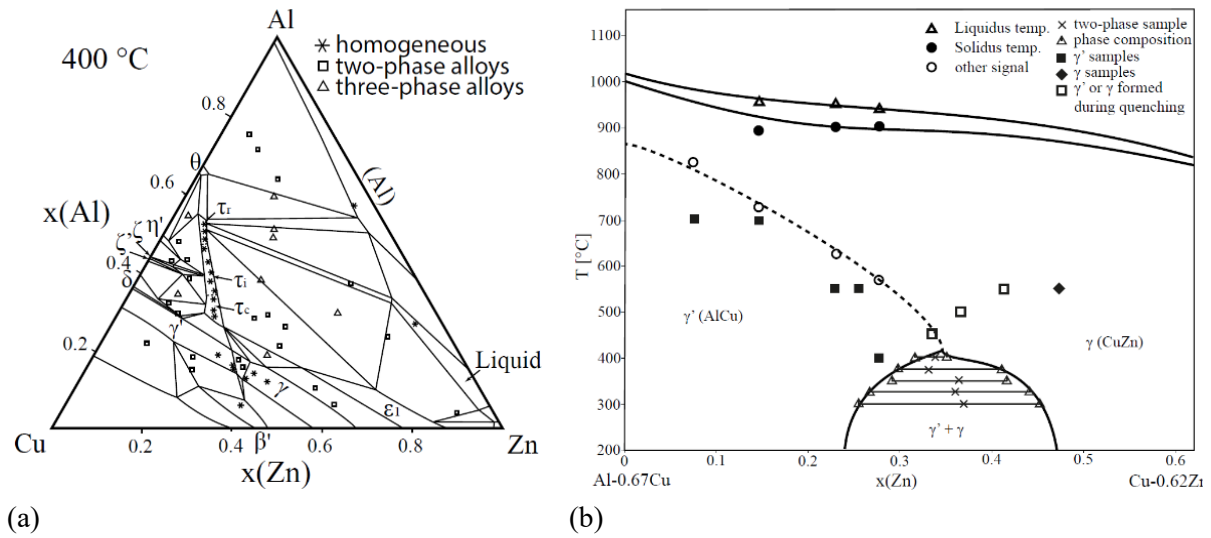


Figure 3: Experimental phase diagram of the system Al-Cu-Zn: a) isothermal section at 400 °C [P3]; b) isopleths going through the two-phase field $\gamma + \gamma'$ [P3].

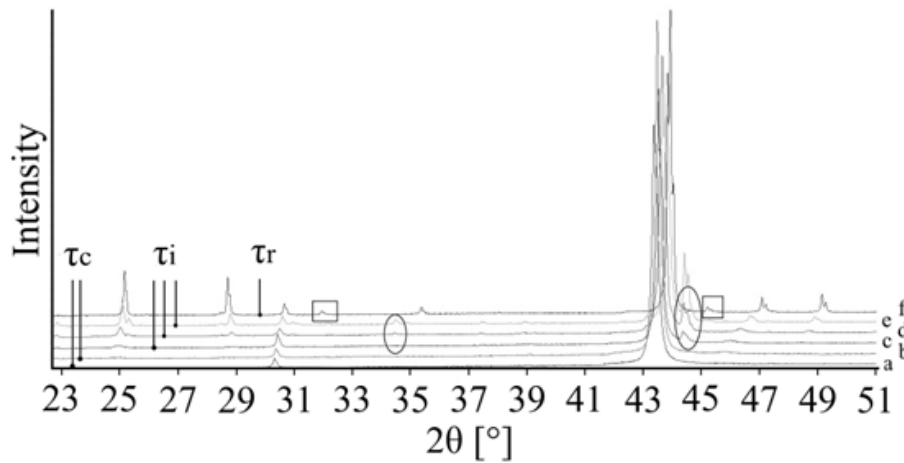


Figure 4: Central part of XRD pattern of selected Al-Cu-Zn alloys containing ternary phase τ . Rectangles indicate specific peaks of the rhombohedral τ_r phase; ellipses denote peaks identifying the incommensurate phase τ_i . Overall compositions of the samples are following: a) 28.9Al-Cu-21.7Zn (τ_c); b) 32.8Al-Cu-19.4Zn (τ_c); c) 35.0Al-Cu-18.9Zn (τ_i); d) 39.9Al-Cu-15.5Zn (τ_i); e) 45.4Al-Cu-11.0Zn (τ_i); f) 48.4Al-Cu-9.9Zn (τ_r). Compositions are given in at. %.

Furthermore, three structural modifications of the ternary phase τ at 400 °C were found in the Al-Cu-Zn system [P3]: a cubic CsCl-type structure (τ_c), a derived rhombohedral structure (τ_r) and an apparently incommensurate modulation structure (τ_i), in the region in between the

τ_c and τ_r . These findings were confirmed by the careful analysis of the specific XRD patterns (see Figure 4).

In total, four isothermal sections of the phase diagram of the Al-Cu-Zn system were constructed in whole concentration ranges at temperatures of 400 °C, 550 °C, 700 °C and 820 °C.

The ternary system **Al-Cu-Si** [P4] contains one ternary phase τ at 700 °C with an unclear structure, according to Ponweiser [2012Pon]. The aim of my work was to clarify the structure and stability of the proposed ternary phase and to describe the Al-Cu-Si phase diagram in a larger temperature range. Hence, two isothermal sections of the ternary Al-Cu-Si phase diagram at 600 °C and 800 °C and one isopleth led through the proposed stability region of the ternary phase τ were studied. Over sixty samples were long-term annealed, and six samples were analysed using thermal analysis. Figure 5a shows the Cu-rich part of the isothermal section at 800 °C; the rest of the section is quite elementary because all the binary phases are in equilibrium with silicon with very small mutual solubility. Figure 6 is a micrograph of the sample 7.0Al-Si-79.3Cu (at. %) consisting of phases κ and δ .

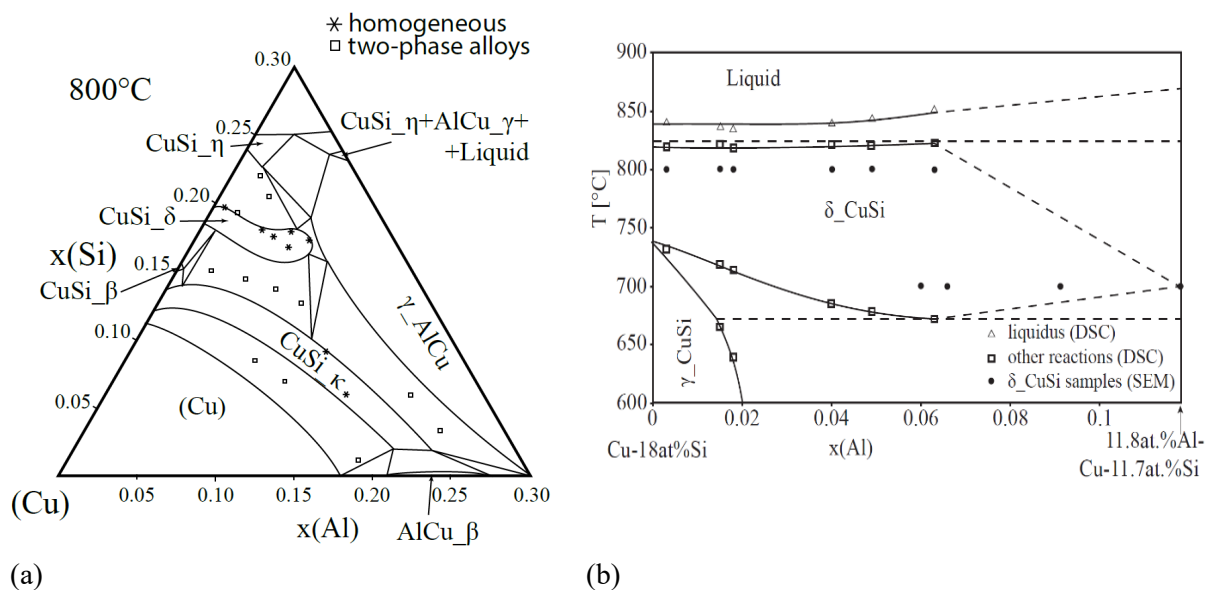


Figure 5: Experimental phase diagram of the Al-Cu-Si system: a) copper-rich part of the isothermal section at 800 °C; b) isopleth through the one phase region of δ phase superimposed with experimental data [P4].

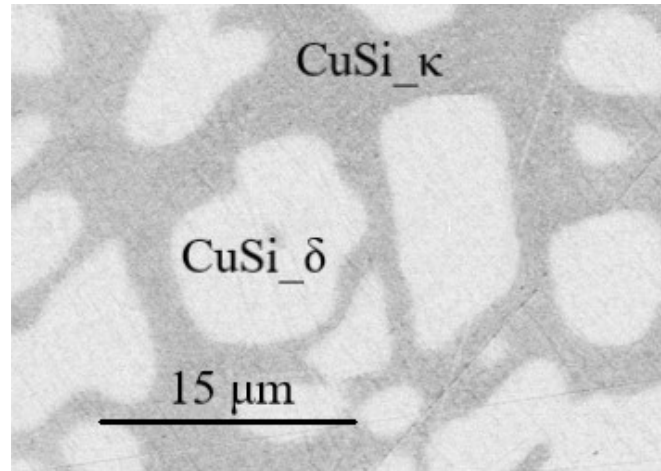


Figure 6: A micrograph of sample 7.0Al-Si-79.3Cu (at. %) consisting of phases CuSi_κ and CuSi_δ.

The main objective concerning the stability of the ternary phase τ was solved based on the results of the thermal analysis. It was found that the ternary phase stable at 700 °C proposed by Ponweiser is, in fact, a pseudo-ternary δ phase, which is stable at higher temperatures in the Cu-Si binary phase diagram, and stabilised by aluminium at lower temperatures (see Figure 5b). The high solubility of the third element in the CuSi_κ and AlCu_γ binary phases was observed.

The phase equilibria and phase diagram of the ternary **Al-Ge-Mg** system [P10] were experimentally studied at temperatures of 250 °C, 300 °C, 400 °C and 450 °C because no experimental data about the isothermal sections was published before. The obtained results were based on a study of twenty-eight samples. Significant solubility of the binary intermetallic phase GeMg₂ was observed (see Figure 7a) in contrast to its stoichiometricity reported in the literature [1971Rao, 2010Yan]. The ternary phase τ (Al₂Ge₂Mg) proposed by Pukas in the structural study [2012Puk] was found to be thermodynamically stable at all the temperatures studied. The microstructure of the sample with the stable phase τ is given in Figure 7b. Nevertheless, the chemical composition of the τ phase was 36Al-Ge-28Mg (at. %), which does not correspond to the published stoichiometricity of Al₂Ge₂Mg proposed by Pukas [2012Puk]. The stability of the off-stoichiometric phase (Al₇Ge₈Mg₅) was later studied by ab initio methods by Friak et al. [2024Fri]. Considering static lattices, both the stoichiometric Al₂Ge₂Mg τ phase and its non-stoichiometric Al₇Ge₈Mg₅ variant were found mechanically and dynamically stable. Further, the static-lattice stoichiometric Al₂Ge₂Mg τ phase is predicted to be thermodynamically more stable than the non-stoichiometric case. When making the thermodynamic assessment more realistic by including phonons, the free energies of formation containing phonon contributions show that the non-stoichiometric Al₇Ge₈Mg₅ is thermodynamically more stable than the stoichiometric Al₂Ge₂Mg τ phase, even at 0 K (see Figure 7c). Figure 7d compares 20-atom calculated supercells Al₂Ge₂Mg (upper) and Al₇Ge₈Mg₅ (lower).

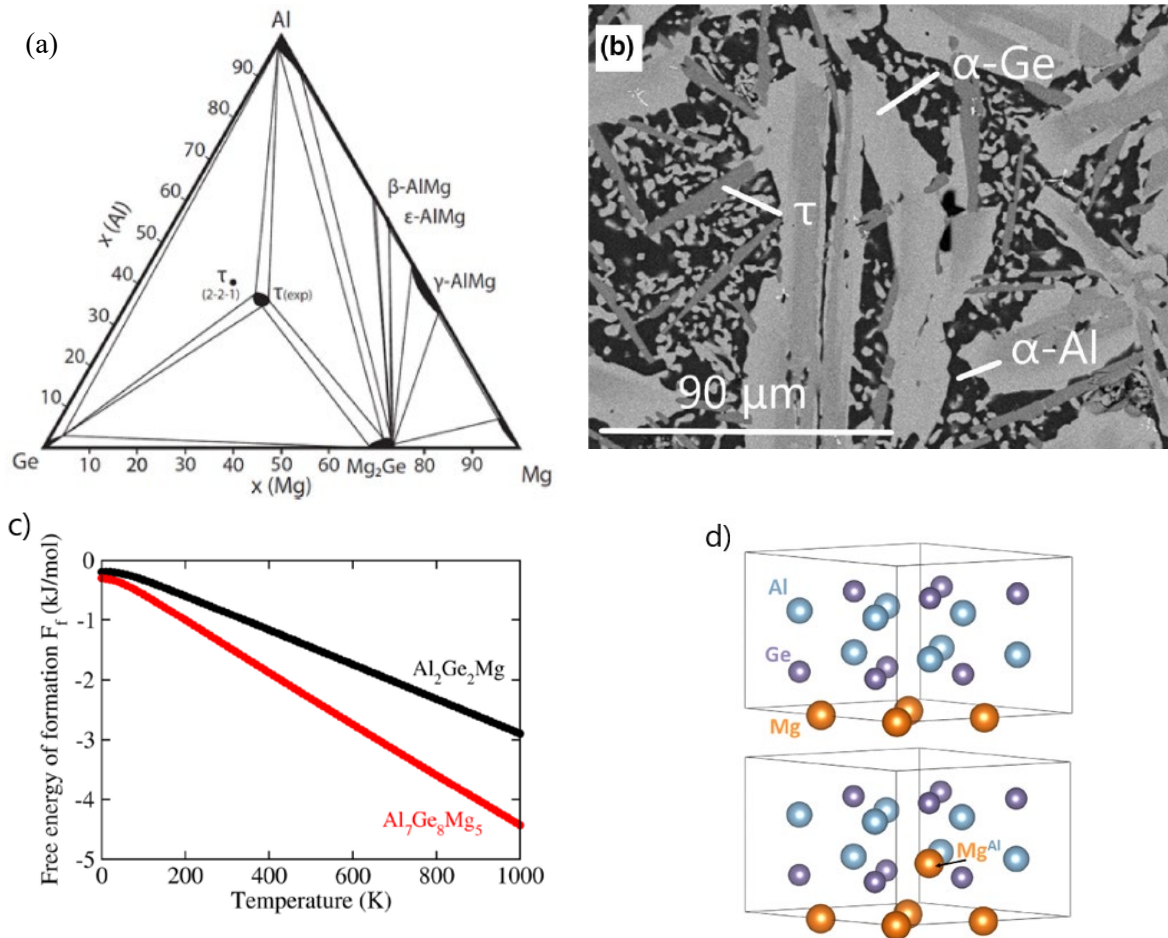


Figure 7: Characteristics of the Al-Ge-Mg system and its phases: a) isothermal section of ternary phase diagram at 250 °C; b) microstructure of the sample 63.9Al-32.9Ge-Mg (at. %) consisting of germanium, aluminium and ternary phase τ ; c) calculated temperature dependence of formation free energy of $\text{Al}_2\text{Ge}_2\text{Mg}$ and $\text{Al}_7\text{Ge}_8\text{Mg}_5$; d) schematic visualisation of 20-atom calculated supercells (upper $\text{Al}_2\text{Ge}_2\text{Mg}$ τ , lower $\text{Al}_7\text{Ge}_8\text{Mg}_5$).

The **Ag-Se-Sn** system [P8] has recently been studied [2020Ram], but some of its complex phase equilibria have not been well described. Therefore, thirty-four samples were studied to investigate the phase equilibria at temperatures of 250 °C, 400 °C and 550 °C. The ternary Ag-Se-Sn system contains two ternary phases, $\text{Ag}_8\text{Se}_6\text{Sn}$ and AgSe_2Sn . It was found that the ternary phase $\text{Ag}_8\text{Se}_6\text{Sn}$ is characterised by a huge solubility of Se in its structure at 250 °C, although it is almost stoichiometric at 550 °C (compare Figures 8a and 8b). In contrast to the recently published isothermal section [2020Ram], an intermediate liquid region was found at 550 °C. This result agrees well with previously published liquid surface and vertical liquid sections in the works of Yusibov et al. [2018Yus] and Ollitrault-Fitchet et al. [1988Oll].

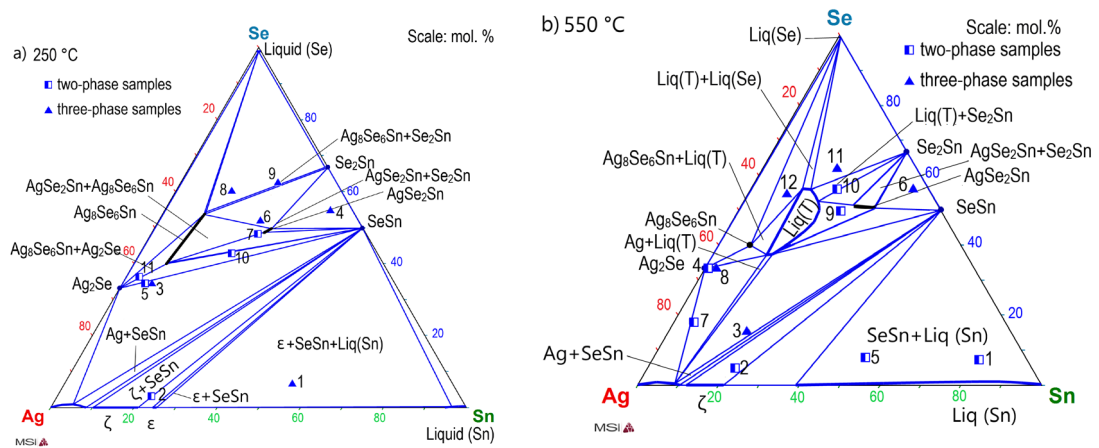


Figure 8: Isothermal section of ternary phase diagram Ag-Se-Sn at a) 250 °C and b) 550 °C with noticeable difference in solubility of ternary phase $\text{Ag}_3\text{Se}_6\text{Sn}$ and the intermediate liquid phase.

In the ternary system **Ni-Se-Sn** [P12], three ternary phases, $\text{Ni}_{5.62}\text{SnSe}_2$, Ni_3SnSe and NiSeSn , are known from the literature [2004Bar, 2021Mus]. To acquire more information, three isothermal sections of ternary phase diagram Ni-Se-Sn have been studied at temperatures 527 °C, 727 °C and 827 °C based on detailed analyses of twenty-seven long-term annealed samples. Isothermal section of phase diagram Ni-Se-Sn is shown on Fig 9a. Only $\text{Ni}_{5.62}\text{SnSe}_2$ ternary phase was stable up to 727 °C with small solubility around the ideal stoichiometric composition. Metastable binary phase Ni_3Se_4 was found to be stable as a pseudoternary phase at 527 °C (see micrograph on Fig. 9b), probably stabilised by a small amount of tin. This finding reasonably corresponds with the literature [1960Hil]. The remaining two ternary phases, Ni_3SnSe and NiSeSn , might be stable at lower temperatures or are metastable.

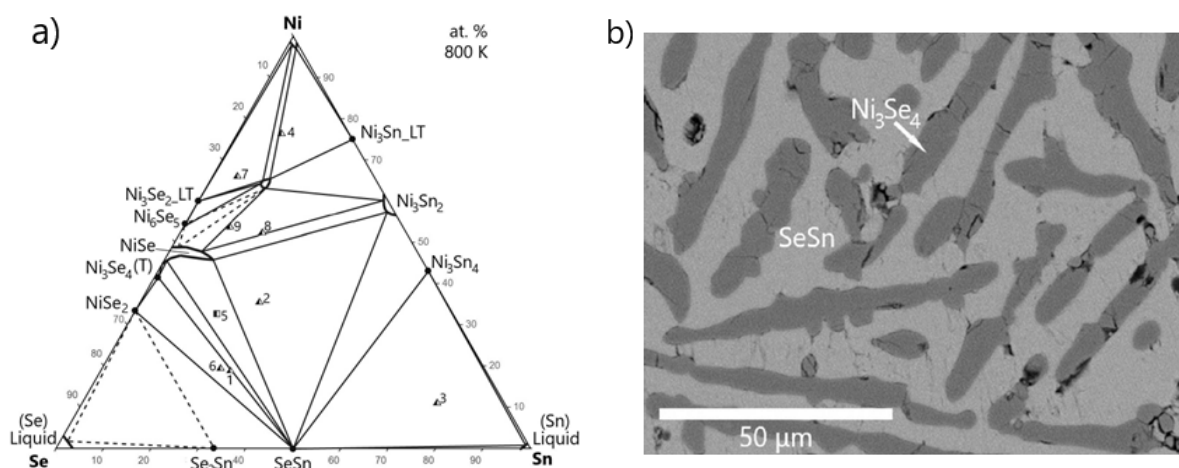


Figure 9: Characteristics of the Ni-Se-Sn system: a) isothermal section of phase diagram at 727 °C; b) microstructure of the sample with overall composition 19.1Ni-53.8Se-Sn (at. %) in BSE mode.

3 CALPHAD approach

Detailed knowledge of the coexistence and stability of phases in stable or metastable equilibrium significantly rationalises the development of material research. Equilibrium phase diagrams are also important in other fields of science and engineering, e.g. for the prediction of material properties. Phase diagrams can either be investigated experimentally or predicted by a theoretical semiempirical method known as the CALPHAD method [1998Sau]. Unfortunately, the experimental data are often sparse and difficult and expensive to obtain for the complex and in-practice-significant systems; therefore, the semiempirical CALPHAD modelling significantly contributes to the description of phase equilibria.

The main feature of the CALPHAD approach is the combination of experimental observations and theoretical modelling. Experimental thermodynamic and phase data are used to optimise the model parameters describing the Gibbs energy of phases as a function of pressure, temperature and composition. Using this approach, one can find the phase composition at thermodynamic equilibrium corresponding to the minimum total Gibbs energy of a closed system at constant temperature and pressure. The calculations are usually performed using specific software (most commonly Pandat [2009Cao], ThermoCalc [2002And] and FactSage [2002Bal]), which searches for the thermodynamic equilibrium of the system through the Gibbs energy constrained minimisation for a given temperature, pressure and overall composition. The Gibbs energies are considered relative to the standard element reference (SER) states, which means relative to the Gibbs energies of the phases of the pure elements stable at $p = 101\,325$ Pa and $T = 298$ K. The data for the pure elements are provided in the unary SGTE database [1991Din].

Solution phases

The molar Gibbs energy of a liquid (and solid solution) G_m^φ can generally be defined as the sum of several contributions:

$$\sum_{i=1}^n x_i \cdot {}^0G_{m,i}^\varphi + RT \cdot \sum_{i=1}^n x_i \cdot \ln(x_i) + {}^E G_m^\varphi + {}^{mag} G_m^\varphi + {}^P G_m^\varphi, \quad (1)$$

where the first term is the molar reference Gibbs energy ${}^{ref} G_m^\varphi$, which consists of the weighted sum of the Gibbs energies of the i components in the crystallographic structure identical to the phase φ with respect to the chosen reference state. Here, x_i is the molar fraction of component i and the temperature dependence of the Gibbs energy of pure component i in phase φ , ${}^0G_{m,i}^\varphi$, can be expressed by a polynomial [1]:

$$G_{m,i}^\varphi = a + b \cdot T + c \cdot T \ln(T) + \sum n \cdot d_i \cdot T^{n-1}, \quad (2)$$

where a , b , c and d_i are adjustable coefficients, n is a set of integers (usually 2, 3 and -1) and T is the temperature.

The second term in equation (1) is the contribution to the Gibbs energy from the ideal mixing of the components on the crystal lattice or in the liquid $^{id}G_m^\varphi$, where n is the number of components.

The third term, the excess molar Gibbs energy $^E G_m^\varphi$, describes the effect of the non-ideal behaviour of the system on the thermodynamic properties of the phase and is given by the Redlich-Kister formalism [1998Sau, 2004Luk]:

$$^E G_m^\varphi = \sum_{\substack{i,j=1 \\ i \neq j}}^n x_i \cdot x_j \cdot \sum_{z=0}^m {}^z L(x_i - x_j)^z, \quad (3)$$

where ${}^z L$ are temperature-dependent interaction parameters describing the interaction between components i and j . Their temperature dependence is defined as:

$${}^z L(T) = a + b \cdot T + c \cdot T \ln(T) \quad (4)$$

The fourth term $^{mag} G_m^\varphi$ describes the magnetic contribution of the φ phase and the fifth term $^p G_m^\varphi$ is the pressure contribution. The pressure contribution is only relevant for very high pressures or when a gaseous phase is present in the reaction

Usually, the phases with the face-centred cubic A1 (FCC_A1), body-centred cubic A2 (BCC_A2), and hexagonal close-packed A3 (HCP_A3) are modelled as solid solutions, which can be considered as a substitution phase of the solid solution with one sublattice. However, it is more convenient to model these phases as an interstitial solid solution using two sublattices $(M)_1(X,Va)_n$. Here, the first sublattice is occupied by metal atoms and the second by interstitial X atoms (such as carbon, nitrogen) or vacancies Va. This model is generally used to remain consistent with assessments of systems containing these phases with interstitials. In systems without interstitial atoms, the second sublattice contains only vacancies and the model behaves like the substitution model described above.

Intermetallic phases

The Compound Energy Formalism (CEF) was used to model intermetallics. The molar reference Gibbs energy (analogous to the first term in equation (1) for the two-sublattice model is given as:

$$^{ref} G_m^\varphi = \sum_{i,j} {}^1 y_i \cdot {}^2 y_j \cdot {}^0 G_{i,j}, \quad (5)$$

where the terms ${}^p y_i$ are the site fractions of the individual components i and j in sublattice p . The term ${}^0 G_{i,j}$ describes the Gibbs energy of the so-called "end-member" $i:j$. The end-members are structures with all possible exclusive occupancies of the sublattices by the available components. Hence, a pure element can occur even in a crystallographic structure φ if both sublattices are occupied by him. Usually, only a few end-members of a compound exist, but data on the Gibbs energy of all of them are necessary for theoretical modelling.

The ideal mixing term ${}^{id}G_m^\varphi$ in the two-sublattice model is given by the equation:

$${}^{id}G_m^\varphi = \sum_{p=1}^2 f_p \cdot \sum_{i=1}^n {}^p y_i \cdot \ln ({}^p y_i), \quad (6)$$

where f_p is the stoichiometric coefficient for sublattice p and the second sum describes the effect of the ideal mixing within the sublattice p , similar to equation (1).

The simplest model for the description of the contribution of the excess Gibbs energy for the two-sublattice model is defined as:

$$G_E^\varphi = \sum_{k=1}^n y_k^2 \cdot \sum_{i,j=1}^n y_i^1 \cdot y_j^1 \cdot L_{i,j;k} + \sum_{k=1}^n y_k^1 \cdot \sum_{i,j=1}^n y_i^2 \cdot y_j^2 \cdot L_{k;i,j} \quad (7)$$

where

$$L_{(i,j;k)} = \sum_z {}^z L_{(i,j;k)} \cdot (y_i - y_j)^z \quad (8)$$

Here, the $L_{i,j;k}$ and ${}^z L_{i,j;k}$ parameters describe the mutual interaction of constituents i and j in the first sublattice, when the second sublattice is fully occupied by constituent k . Moreover, this description can be extended to any number of sublattices.

The temperature dependence of the Gibbs energy of the pure constituent i in pure-constituent type formalism is expressed by equation (2). This expression is usually required for a given phase to cover the whole temperature range of interest. The whole temperature range can be described by multiple polynomials, but they must be continuously connected at the transition point. From such expression of Gibbs energy, the other molar thermodynamic functions such as entropy S , enthalpy H and heat capacity C_p can be evaluated as follows [1991Din]:

$$S_m^\varphi = -b - c - c \cdot \ln(T) - \sum n \cdot d_i \cdot T^{n-1}, \quad (9)$$

$$H_m^\varphi = a - c \cdot T - \sum (n - 1) \cdot d_i \cdot T^n, \quad (10)$$

$$C_{p,m}^\varphi = -c \cdot T - \sum n \cdot (n - 1) \cdot d_i \cdot T^{n-1}. \quad (11)$$

The variable coefficients of equation (11) describing the temperature dependence of the heat capacity of a given phase can be fitted to the experimental data and subsequently converted to the database in the form of Gibbs energy (equation 2). The parameters "a" and "b·T" remain optimisable to achieve agreement with the experimental phase diagram.

Thermodynamic databases

The results of the theoretical modelling of phase diagrams and thermodynamic quantities strongly depend on the quality of the data available for the system under study and their appropriate implementation in thermodynamic parameter databases. Even the most advanced software is unusable without reliable and consistent datasets. The Gibbs energy description used for each phase in the thermodynamic database must be unique and based on the same assumptions, conditions and models. The reason for this is consistency in the description of the individual phases when creating larger databases for complex systems, so that individual phase interactions can be modelled correctly. The polynomial describing the dependence of the Gibbs energy on temperature, pressure and composition of each component must, therefore, be mutually compatible, including other contributions, such as those related to the magnetic properties of the phase. For phases with the same or similar structure, it is appropriate to use the same model and phase name for all systems (binary, ternary and higher) where the phase occurs.

Large databases of thermodynamic parameters describing many binary and higher systems are usually created for specific materials, such as steels, solders, HEA alloys, etc. These databases are nowadays mainly designed by software (such as ThermoCalc, Pandat or FactSage) developers and sold to their users or bundled with the software. Nevertheless, many industrial companies develop their own databases (e.g. the Fe-C-Al-Si-Mn database developed by the applicant for voestalpine company) or are developed within scientific teams in the context of applied research (e.g. the Ag-Se-Sn-Pb thermoelectric materials database or the Steel16 steel database, in the development of which the applicant participated).

3.1 Third-generation data of pure elements

As mentioned above, the standardised thermodynamic description of the unary (pure element) Gibbs energies is essential for calculating the phase diagram of the higher-order systems and the consistency of obtained thermodynamic datasets.

The commonly used SGTE [1991Din] pure element database is limited to temperatures above room temperature. Furthermore, for systems with elements with different melting temperatures, the occurrence of breaks in the heat capacity calculation is also a problem. These breaks arise from predicting the heat capacity using the Neumann-Kopp rule, which is based on the weighted average of the contributing elements. Using the Einstein or Debye model with correction for crystalline phases allows a description of unaries over the whole temperature range from 0 K to temperature above the melting temperature [1995Cha]. In addition, a two-state model for the liquid phase provides a sound basis for extrapolating its heat capacity to temperatures below the melting point [1995Agr, 2014Bec]. A description of the thermodynamic properties of the liquid phase below the melting point is required to describe undercooled liquids and glasses. The use of new approaches (such as describing solid phases down to 0 K temperature or liquid phase below melting temperature) has led to the emergence of the new, third generation of thermodynamic data.

It has to be noted that transfer to the third-generation data is connected with a huge amount of work because the new generation of the thermodynamic descriptions of data for the unaries requires the reassessment of all binaries and higher-order systems. As there has been an enormous time and financial investment in current SGTE data, the transfer to the third generation is not supported by the whole scientific community.

Crystalline phases

In the third-generation approach, a thermodynamic description of the thermodynamic properties of a crystalline solid phase could be based on either the Einstein or Debye models for the heat capacity modelling [1995Cha]. In line with the recommendations of the Ringberg workshops [1995Cha], the Einstein model was used to represent the thermodynamic properties of the crystalline phases with the addition of terms which represents the C_V to C_p correction, anharmonicity corrections and electronic contributions. The value of the Einstein temperature should be chosen so that the resulting fit gives a good representation of the heat capacity at the whole temperature range [2015Pav] and that it reproduces precisely the assessed value for S^{298} . At temperatures above the melting point, the heat capacity will be extrapolated smoothly to merge with the data for the liquid phase at very high temperatures.

For the description of the heat capacity C_p of a crystalline phase, the Einstein model yields the relation:

$$C_p = 3R \left(\frac{\theta_E}{T} \right)^2 \frac{e^{\theta_E/T}}{(e^{\theta_E/T} - 1)^2} \quad (13)$$

where R is the universal gas constant and θ_E is an Einstein temperature. The Gibbs energy and entropy can also be expressed by following equation:

$$G = E_0 + \frac{3}{2}R\theta_E + 3RT \ln \frac{(e^{\theta_E/T} - 1)}{e^{\theta_E/T}} \quad (14)$$

$$S = 3R \left[\frac{\theta_E/T}{(e^{\theta_E/T} - 1)} - \ln \frac{(e^{\theta_E/T} - 1)}{e^{\theta_E/T}} \right] \quad (15)$$

Liquid phase

In the third-generation data modelling, the liquid phase of elements is described using a two-state model [1995Agr, 2000Tol, 2014Bec]. This assumes that the liquid notionally contains two types of atoms mixing ideally. The first type of atoms is known as “solid-like” atoms with no translational degrees of freedom, the second type of atoms is called “liquid-like” atoms with translational motion. The “solid-like” atoms can represent a pure amorphous solid phase [2001Chen]. For a given temperature, “solid-like” and “liquid-like” atoms are in

equilibrium. As they can possess different energy states [2014Bec], the relative amounts of the "liquid-like" χ and "solid-like" atoms depend on their Gibbs energy difference ΔG_{diff} (see equation 14). The variable χ is an internal order parameter and at equilibrium, it has the value that minimises the Gibbs energy. The equilibrium value of χ is defined by the formula:

$$\chi = \frac{e^{-\Delta G_{\text{diff}}/RT}}{1 + e^{-\Delta G_{\text{diff}}/RT}}. \quad (16)$$

The Gibbs energy of the "solid-like" atoms should be approximated by the Einstein equation complemented by additional terms:

$$G = E_0 + \frac{3}{2}R\theta_E + 3RT \ln \frac{(e^{\theta_E/T} - 1)}{e^{\theta_E/T}} + A + aT^2 + bT^3 \quad (17)$$

Value of Einstein temperature θ_E could be taken as the same as for the crystalline phase. The parameters a and, possibly, b can be optimised.

The Gibbs energy of "liquid-like" atoms can be described as follows:

$$G_m^{liq} = G_m^{sol} - RT \ln[1 + e^{(-\Delta G_{\text{diff}}/RT)}] \quad (18)$$

where the difference relative to "solid-like" atoms is:

$$\Delta G_{\text{diff}} = G_m^{liq} - G_m^{sol} = B + CT + D T \ln T \dots \quad (19)$$

To derive the data for the liquid phase, the assessment of parameters A , a , b , B , C and D is required. Gibbs energy of the "solid-like" and the "liquid-like" atoms should be equivalent in special cases.

3.2 Results and discussion

The theoretical reassessment of the **Al-Cu** binary system [P5] was motivated by new findings on phase equilibria in the scientific literature [P1] and by Ponweiser [2011Pon]. For the γ phase, a four-sublattice model based on the crystallographic structure has been newly applied to be consistent with databases containing phases from the γ brass family, in contrast to the previous evaluation performed by Liang [2015Lia]. In our work [P5], the η , ζ , γ and δ phases were modelled as non-stoichiometric in agreement with the experimentally observed solubility [2011Pon, P5]. Agreement with the experimental findings was achieved for both the phase diagram [2011Pon, P5] (see Figure 10a) and thermodynamic properties such as mixing enthalpy, enthalpy of formation and activity (see Figure 10b).

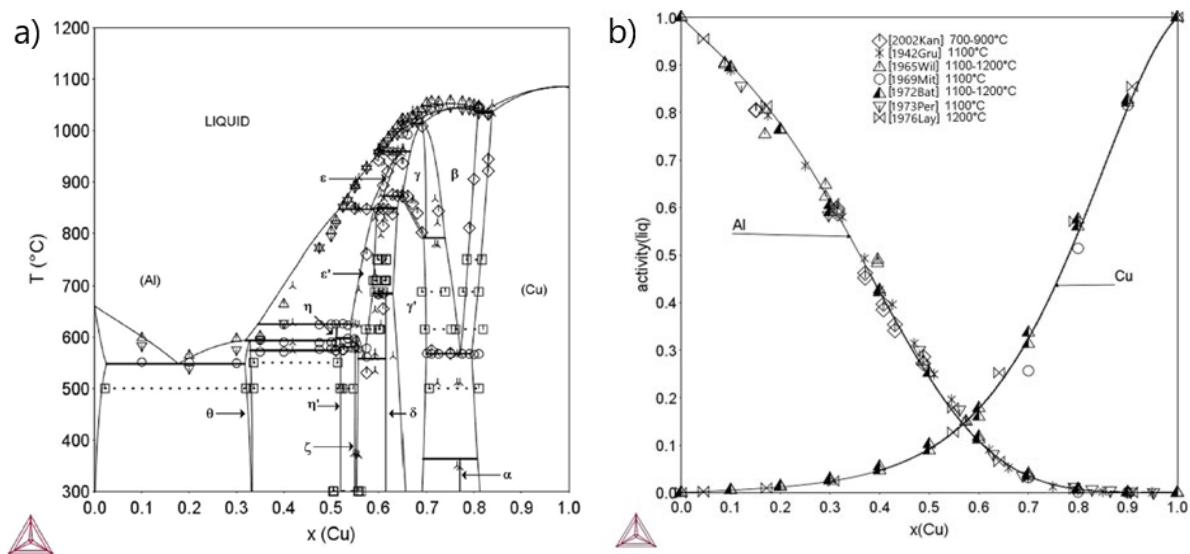


Figure 10: Characteristics of the Al-Cu system: a) theoretical phase diagram based on superimposed experimental data [P1, 2011Pon] (black three-pointed star - DSC, bold square - phase boundaries according to SEM/EDX measurements); b) calculated activities for liquid Al and Cu at 1100 °C compared with experimental data, the standard states are liquid for both Al and Cu [1942Gru, 1965Wil, 1969Mit, 1972Bat, 1973Per, 1976Lay].

The re-evaluation of the **Cu-Si** binary system using the CALPHAD method was carried out in the paper [P11], because the available experimental data indicate a non-negligible solubility of Al in all binary intermetallic phases of the Cu-Si system. Moreover, the purely stoichiometric models used so far are not entirely suitable for extension to the ternary system. In the re-evaluation of the Cu-Si system, excellent agreement with the experimental data of Sufryd et al. [2011Suf] and the previous theoretical work of Hallstedt et al. [2016Hal] was achieved.

Figure 11a shows the Cu-Si phase diagram with the established solubilities of aluminium in the η family phases structures with the superimposed experimental points from Sufryd et al [2011Suf]. The modelled mixing enthalpy of the liquid phase at 1008 °C is shown

in Figure 11b with comparison to experimental data of Iguchi [1977Igu], Castanet [1979Cas] and Batalin [1982Bat].

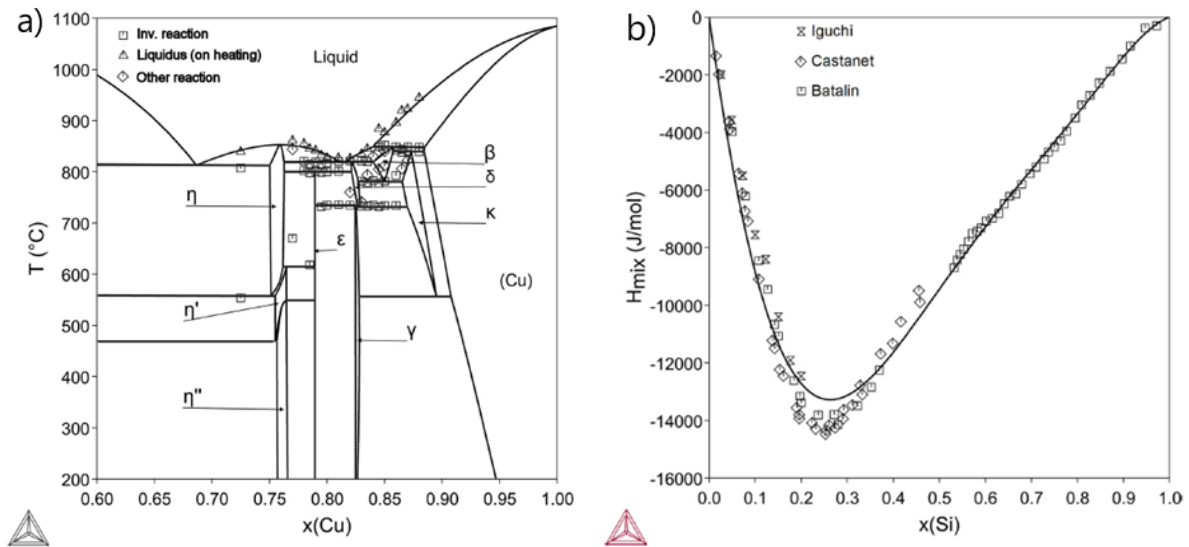


Figure 11: a) reassessed Cu-Si phase diagram compared with experimental data from DTA measurements from Sufryd et al.[2011Suf], b) mixing enthalpy of Cu-Si liquid phase at 1008 °C with superimposed experiments [1977Igu, 1979Cas, 1982Bat]

In this theoretical work, the ternary phase diagram of Al-Cu-Si was studied based on previous experimental data presented in this work (see Fig. 5) [P4] and data from the scientific literature [2009Ria, 2009He, 2012Pon]. To obtain a good agreement with the non-consistent experiments, the stability of the β (bcc) phase with complete solubility between the Al-Cu and Cu-Si binary systems was theoretically predicted at high temperatures (see Fig. 12a for the isothermal section at 800 C) which was in contradiction with the previously published experimental data (compare Fig. 5a). Based on this assumption, an experiment was proposed to confirm the stable structures at high temperatures by high-temperature XRD. The stability of the κ (hcp) phase was confirmed at 600°C (see Figure 13a), but at higher temperature of 800°C the β (bcc) phase was already found to be stable (see Figure 13b). This finding help to fully explain the discrepancies between the experimental isothermal sections [P4, 2011Pon] and the vertical sections [2011Pon] which was proposed based on thermal analysis methods (DTA/DSC), where the modelling achieved a very good match. Good agreement was also obtained for the mixing enthalpy of the liquid phase from literature [2000Wit].

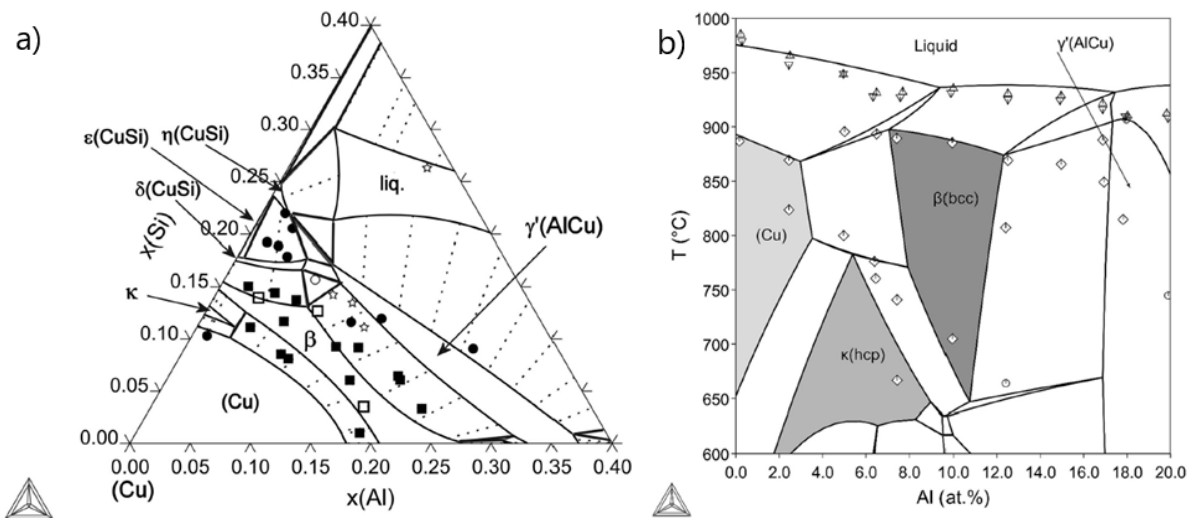


Figure 12: Reassessed isothermal section of ternary phase diagram Al-Cu-Si a) at 800°C with superimposed experimental data [P4] b) Cu-rich corner of the vertical section for 10at.% Si with comparison to DTA [2012Pon]

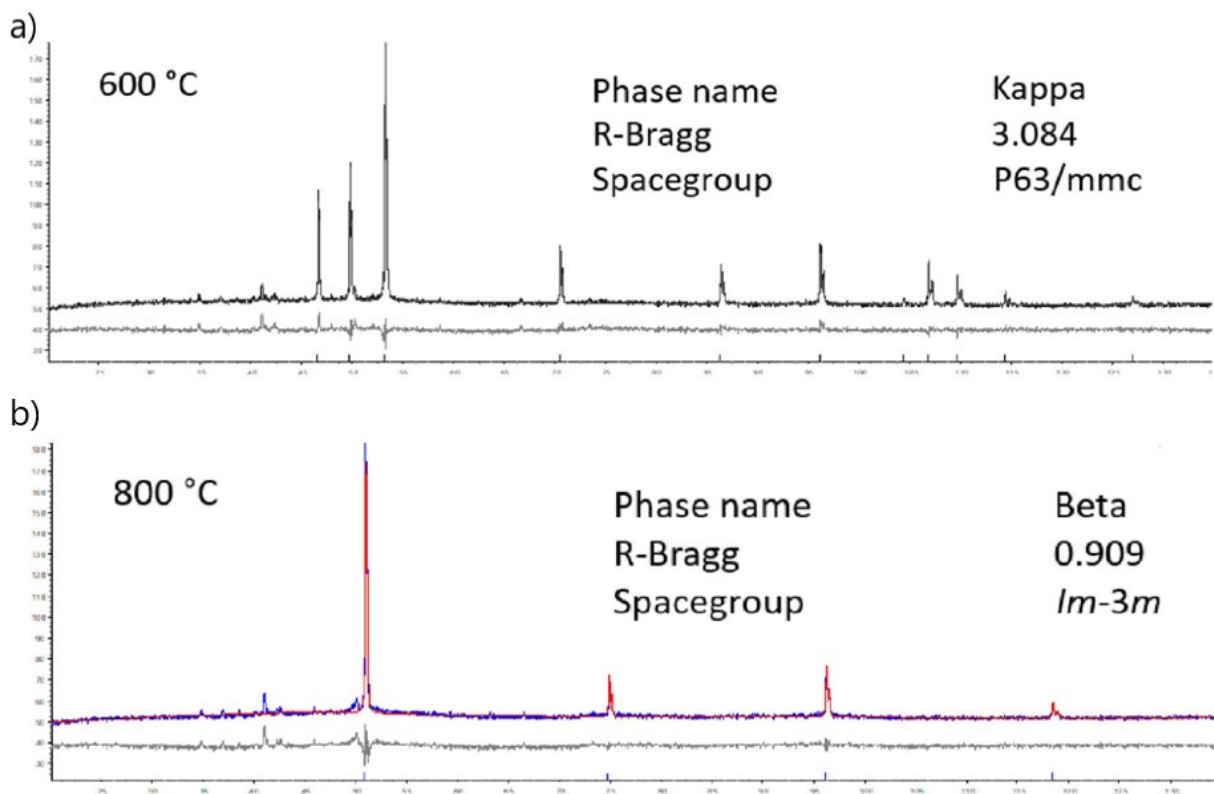


Figure 13: Reassessed isothermal section of ternary phase diagram Al-Cu-Si a) at 800°C with superimposed experimental data [P4] b) Cu-rich corner of the vertical section for 10at.% Si with comparison to DTA [2012Pon]

The first thermodynamic evaluation of the Ni-Se binary system [P6] was also achieved. The Ni-Se phase diagram consists of five intermetallic binary phases and exhibits a miscibility

gap in the Se-rich liquid phase. The experimental phase diagram was presented by Komarek et al. [1972Kom] and Lee [1991Lee]. In our work [P6], the thermodynamic modelling was mainly based on the experimental phase diagram [1972Kom], the enthalpy of formation of the NiSe phase at 25 °C [1972Gro], the mixing enthalpy of the NiSe phase at 1227 °C [1972Gro] and the heat capacity of the NiSe₂ phase [1975Gro]. The binary intermediate phases are modelled by a two-sublattice model and the liquid phase by an associate model with Ni₁Se₁ associates. The modelled phase diagram and the heat capacity of binary phase NiSe₂ are shown in Figures 14a and 14b, respectively.

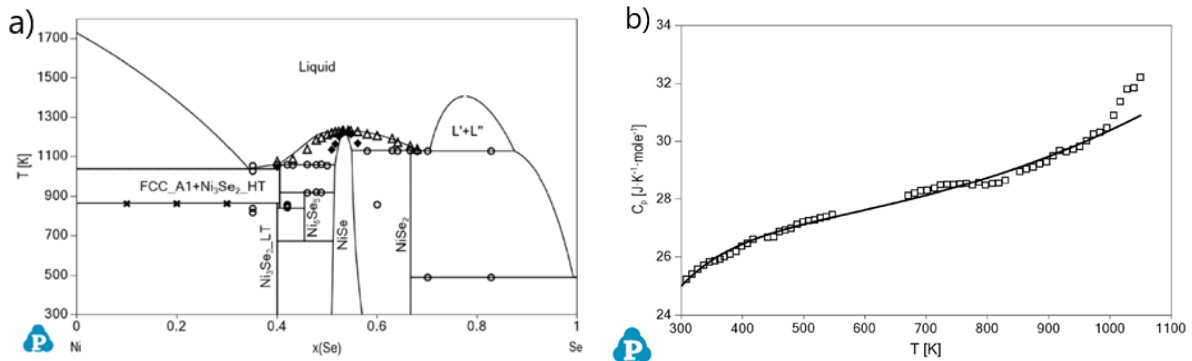


Figure 14: Characteristics of the Ni-Se system: a) phase diagram in comparison with experimental data from Komarek et al. [1972Kom] and Lee [1991Lee] (triangles: liquidus on heating, circles: invariant phase transitions measured by DTA, diamonds: additional thermal effect, crosses: temperature suggested by Lee [1991Lee]); b) calculated heat capacity of the NiSe₂ phase with experimental data by Grønvoid [1975Gro].

The CALPHAD-based assessment of the **Pb-Se-Sn** ternary system [P8] is based on recent experimental work by Chen et al. [2020Che]. Although the experimental results are rather sparse and not entirely consistent [1968Str, 1968Wol, 2020Chen], the calculated phase diagram reasonably agrees with the experimental sections at 350 °C and 500 °C proposed by Chen et al. [2020Che]. The liquid surface agrees reasonably well with the experimental liquid projection proposed by Saveliev et al. [1975Sav]. Figure 15a shows the isothermal section of the ternary phase diagram of Pb-Se-Sn at 500 °C with the experimental data by Chen et al. [2020Che] and Figure 15b shows the calculated liquid surface.

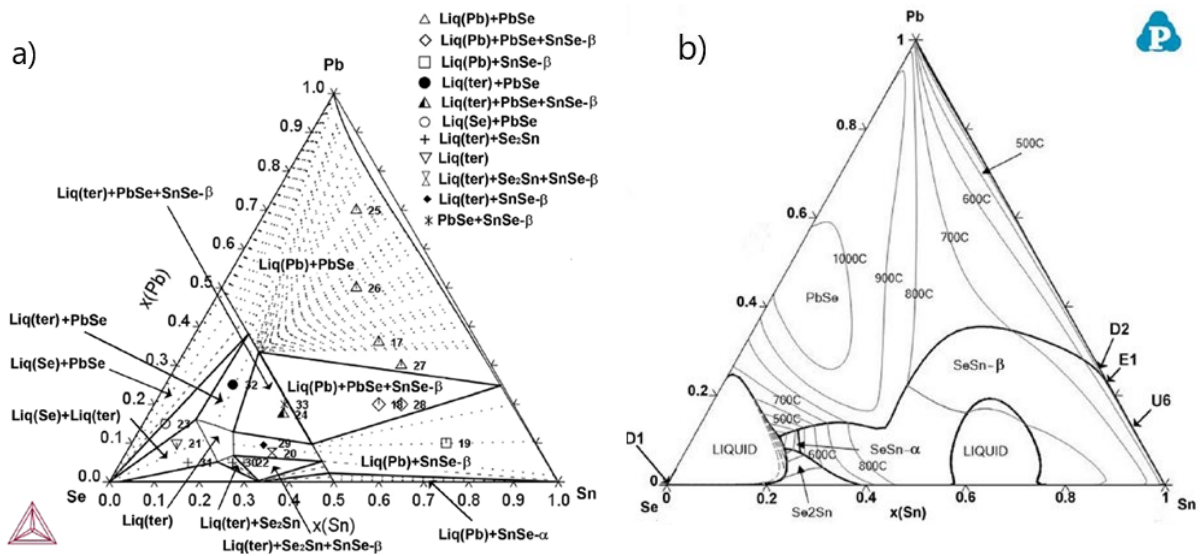


Figure 15: Characteristics of the Pb-Se-Sn system: a) isothermal section of phase diagram at 500 °C with superimposed experimental data from Chen et al. [2020Che]; b) predicted liquidus surface.

Binary system **Al-Zn** [P2] was reassessed using the third-generation data for pure elements (see Chapter 3.1 *Third-generation data of pure elements*). The Al-Zn phase diagram does not contain any binary phase, and the FCC_A1 phase shows a miscibility gap in solid solution (see Figure 16a). The derived phase diagram and thermodynamic properties are almost identical to the results of Mathon et al. [2000Mat] and agree very well with the experimental values. In this work, we mainly presented the concentration dependence of the thermodynamic properties for the solid and liquid phases and conversion of interaction parameters. The mixing enthalpy of the liquid phase is presented in Figure 16b.

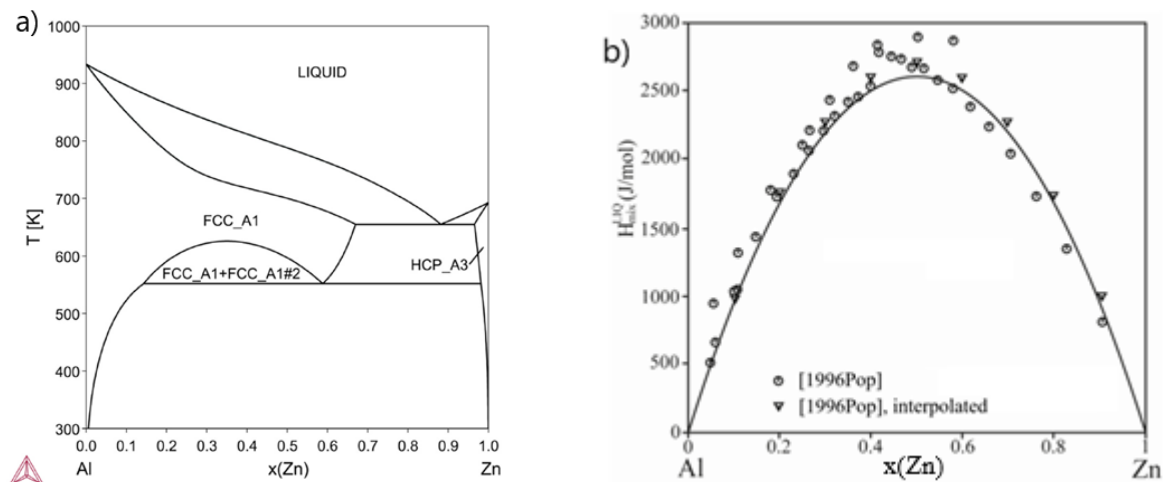


Figure 16: Characteristics of the Al-Zn system: a) theoretical phase diagram based on the third-generation database; b) mixing enthalpy of liquid phase with superimposed experimental data [1996Pop].

It turned out that a simple transformation of the entropy difference between two crystalline phases could be expressed by the ratio of two Einstein temperatures.

$$\Delta S = 3R \ln \left(\frac{\theta E^\beta}{\theta E^\alpha} \right) \quad (16)$$

Similarly, the dependence of the excess entropy of mixing on composition can be simply transformed into a change in the logarithm of the Einstein temperature.

$$S^{ex} = -3R x_A x_B (\ln \theta_0 + \ln \theta_1 (x_A - x_B) + \ln \theta_2 (x_A - x_B)^2 \dots) \quad (17)$$

The follow-up work was devoted to the theoretical description of the **Al-Si-Zn** ternary system [P12] based on the conversion equations derived in [P2]. In this way, a reassessment of the Al-Si and Si-Zn binary systems was carried out. After the above mentioned conversion, a very good agreement was achieved of the calculated results using the third generation with the original data based on SGTE [1996Jac] and experimental data respectively. The 3rd generation Al-Si, Al-Zn, and Si-Zn datasets were used for the description of ternary system Al-Si-Zn, where no interaction parameters are needed. The agreement with the experimental data is very good. Figure 17 a) shows the predicted isopleth of the system Al-Si-Zn at $x(\text{Si})=0.047$ with comparison to experimental data of Ibe [1996Ibe]. Figure 7b shows the mixing enthalpy of liquid phase at 1104°C with superimposed experimental data of Bros [1996Bro].

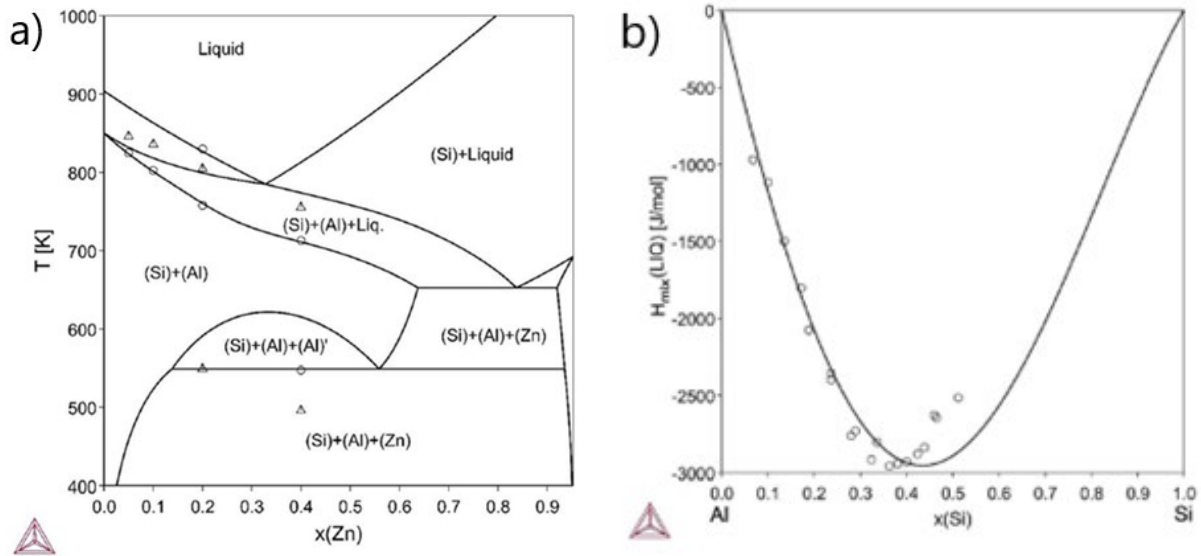


Figure 17: Prediction of the system Al-Si-Zn: a) vertical section at $x(\text{Si})=0.047$ based on the third-generation database with superimposed experimental data of Ibe [1996Ibe] b) mixing enthalpy of liquid phase at 1104°C with superimposed experimental data [1981Bro].

4 Conclusion

As mentioned above, studying the experimental equilibria of coexisting phases is crucial for understanding the behaviour of materials. In the present work, I focused on two classes of materials: aluminium-based and selenium-based.

The **experimental procedures** described here can be theoretically used for any combination of elements, but it is necessary to ensure the stability of the alloy, especially for easily oxidising elements. Using advanced methods of alloy synthesis, heat treatment and subsequent characterisation by a combination of static and dynamic analytical methods such as SEM-EDX, XRD, DTA and DSC, we can propose (i) the phase diagrams of alloys with different applications and (ii) the most suitable composition and heat treatment of new alloys with potential for practical use. The unique results obtained by combining some of the above-mentioned results are listed below.

The description of the θ phase of the system Al-Cu [P1] is an illustrative example of the combination of thermal analysis methods with phase analysis using a scanning electron microscope, where I discovered that the θ phase decomposes peritectically, although metastable equilibrium corresponds to the congruent melting. By the combination of DSC thermal analysis and XRD structural analysis, I newly determined phase equilibria $\gamma(\text{AlCu}) + \gamma(\text{CuZn})$ at low and high temperatures in system Al-Cu-Zn [P3]. Another example of the suitability of the combination of analytical methods is the description of structural modifications of the ternary τ phase family, where a transitional incommensurate phase τ_i between the cubic τ_c and the rhombohedral τ_r was discovered using detailed XRD analysis in combination with SEM microstructural analysis.

These experimental data, in combination with advanced theoretical approaches (such as **the semiempirical CALPHAD approach**), are appropriate for a more comprehensive understanding of material properties and thermodynamic behaviour. The subsequent CALPHAD thermodynamic modelling of phase diagrams deepens the possibilities of predicting alloy properties using thermodynamic quantities such as enthalpy, entropy, heat capacity, etc. It is very useful to complement thermodynamic modelling with the results of ab initio calculations at $T = 0$ K, in particular with the heats of formation of intermetallics and hypothetical unstable end-members or with the heat capacities of intermetallic compounds calculated even at higher temperatures using phonon spectra.

The suitability of using a combination of experimental results and CALPHAD thermodynamic modelling was shown in the description of the Ni-Se system [P6], where the knowledge of the specific heat capacity of the NiSe_2 phase and the mixing enthalpy of the NiSe phase enabled a very good thermodynamic description of the whole Ni-Se system. Another example of the complementarity of the CALPHAD method and experimental results is the theoretical study of the Al-Cu-Si system [P11] when, based on modelling of phase equations at higher temperatures, it was revealed by high-temperature XRD that the κ (hcp) phase is not stable at higher temperatures and that the β (bcc) phase is stable. The β (bcc) phase was found to be unquenchable, as low temperature XRD showed only the κ (hcp) phase even in samples annealed for long periods of time at 800°C .

The importance of ab initio calculations in conjunction with the experiments was illustrated by the discovery of the non-stoichiometricity of the ternary phase $\text{Al}_2\text{Ge}_2\text{Mg}$ [P10], where lower energy was calculated for the off-stoichiometric cell $\text{Al}_7\text{Ge}_8\text{Mg}_5$ even at higher temperatures due to the phonon contribution [2024Fri].

5 References

5.1 Author's publications

- [P1] **Zobač, O.**, Kroupa, A., Zemanová, A., Richter, K.W., *Experimental description of the Al-Cu binary phase diagram*, Metallurgical and Materials Transactions A: Physical Metallurgy and Materials Science, 2019, 50(8), pp. 3805-3815 doi: 10.1007/s11661-019-05286-x (IF 2.050)

Scientific work [%]	Supervision [%]	Manuscript [%]	Research direction [%]
80	0	80	100

- [P2] Dinsdale A., **Zobač O.**, Kroupa A., Khvan A., *Use of third generation data for the elements to model the thermodynamics of binary alloy systems: Part 1 - The critical assessment of data for the Al-Zn system*, CALPHAD, 2019, 65, pp. 86-92, doi: 10.1016/j.calphad.2019.02.007 (IF 1.947)

Scientific work [%]	Supervision [%]	Manuscript [%]	Research direction [%]
20	0	30	60

- [P3] **Zobač, O.**, Kroupa, A., Richter, K.W., *Experimental study of the Al-Cu-Zn ternary phase diagram*, Journal of Materials Science, 2020, 55(24), pp. 10796-10810, doi: 10.1007/s10853-020-04686-4 (IF 4.220)

Scientific work [%]	Supervision [%]	Manuscript [%]	Research direction [%]
80	0	90	100

- [P4] **Zobač, O.**, Kroupa, A., Richter, K.W., *Experimental isothermal sections of the ternary phase diagram Al-Cu-Si at 600 °C and 800 °C*, Journal of Materials Science, 2020, 55(31), pp. 15322-15333, doi: 10.1007/s10853-020-05077-5 (IF 4.220)

Scientific work [%]	Supervision [%]	Manuscript [%]	Research direction [%]
80	0	90	100

- [P5] Kroupa, A., **Zobač, O.**, Richter, K.W., *The thermodynamic reassessment of the binary Al-Cu system*, Journal of Materials Science, 2021, 56, pp. 3430-3443, doi: 10.1007/s10853-020-05423-7 (IF 4.682)

Scientific work [%]	Supervision [%]	Manuscript [%]	Research direction [%]
25	0	30	80

- [P6] **Zobač, O.**, Buchlovská, K., Pavlů, J., Kroupa, A., *A thermodynamic description of binary system nickel-selenium*, Journal of Phase Equilibria and Diffusion, 2021, 42(4), pp. 468-478, doi: 10.1007/s11669-021-00906-9 (IF 1.284)

Scientific work [%]	Supervision [%]	Manuscript [%]	Research direction [%]
50	80	70	80

- [P7] **Zobač, O.**, Richter, K.W., Kroupa, A., *Experimental phase diagram of the Ag-Se-Sn system at 250, 400 and 550 °C*, Journal of Phase Equilibria and Diffusion, 2022, 43, pp. 32-42, doi: 10.1007/s11669-022-00937-w (IF 1.4)

Scientific work [%]	Supervision [%]	Manuscript [%]	Research direction [%]
80	0	80	40

- [P8] **Zobač, O.**, Zemanová, A., Chen, S.W., Kroupa, A., *CALPHAD-type assessment of the Pb-Se-Sn system*, Journal of Phase Equilibria and Diffusion., 2022, 43, pp. 243-255, doi: 10.1007/s11669-022-00956-7 (IF 1.4)

Scientific work [%]	Supervision [%]	Manuscript [%]	Research direction [%]
40	0	60	40

- [P9] **Zobač, O.**, Karpíšková, L., Kroupa, A., *Experimental study of the ternary phase diagram Al-Ge-Mg*, Journal of Phase Equilibria and Diffusion, 2022, 44, pp. 127-136, doi: 10.1007/s11669-023-01025-3 (IF 1.4)

Scientific work [%]	Supervision [%]	Manuscript [%]	Research direction [%]
50	80	70	80

- [P10] **Zobač, O.**, Žižka, R., Roupčová, P., Kroupa, A., *Experimental study of the Ni-Se-Sn phase diagram isothermal sections at 800 K, 1000 K and 1100 K*, Journal of Phase Equilibria and Diffusion, 2023, 44, pp. 594-605, doi: 10.1007/s11669-023-01058-8. (IF 1.4)

Scientific work [%]	Supervision [%]	Manuscript [%]	Research direction [%]
50	100	80	80

- [P11] Kroupa A., **Zobač O.**, Zemanová A., Richter K.W., *CALPHAD-Type Reassessment of Cu-Si and Full Assessment of the Al-Cu-Si Systems*, Journal of Phase Equilibria and Diffusion, 2024, doi: 10.1007/s11669-024-01160-5. (IF 1.4)

Scientific work [%]	Supervision [%]	Manuscript [%]	Research direction [%]
30	50	40	80

- [P12] **Zobač O.**, Kroupa A., Dinsdale A., Use of third generation data for the pure elements to model the thermodynamics of binary alloy systems: Part 3 – The theoretical prediction of the Al–Si–Zn system, CALPHAD, 2024, 87, 102742. doi: 10.1007/s11669-024-01160-5. (IF 1.947)

Scientific work [%]	Supervision [%]	Manuscript [%]	Research direction [%]
30	0	40	80

5.2 Further references

- [1942Gru] G. Grube, P. Hantelmann, Z. Elektrochem. 48 (1942) 399-409.
 [1960Hil] J.H. Hiller, W. Wegener, Neues Jahrbuch für Mineralogie - Abhandlungen 94 (1960) 1147-1159.
 [1965Wil] T.C. Wilder, Trans. Met. Soc. AIME 233 (1965) 1202-1208.
 [1968Str] A.J. Strauss, Trans. Met. Soc. AIMIE 242 (1968) 354.
 [1968Wol] J.C. Wolley, O. Berollo, Mat. Res. Bull. 3 (1968) 445-450.
 [1969Mit] H. Mitani, H. Nagai, J. Jpn. Inst. Met. 33 (1969) 344-348.
 [1971Rao] Y.K. Rao, G.R. Belton, Metall. Trans., 2 (1971) 2215-2219.
 [1972Bat] G.I. Batalin, E.A. Beloborodova, V.N. Vasilev, Ukr. Khim. Zh. (Russ. Ed.) 38 (1972) 920-923.
 [1972Gro] F. Grønvold, Acta Chem. Scand. 26 (1972) 2085.
 [1972Kom] K.L. Komarek, K. Wessely, Monatsh. Chem. 103 (1972) 923.
 [1973Per] J. Perakis, C. Chatillon, A. Pattoret, C. R. Acad. Sci. C 276 (1973) 1513-1516.

- [1975Gro] F. Grønvold, *J. Chem. Thermodynamics* 7 (1975) 645.
- [1975Sav] V.P. Saveliev, E.M. Latypov, V.P. Zlomanov, *Zh. Neorg. Khimii* 20, (1975) 2006-2008.
- [1976Lay] D.I. Layner, L.M. Ostrovskaya, O.S. Serebryannikova, *Izv Akad Nauk SSSR Met* 15 (1976) 15-18.
- [1977Igu] Y. Iguchi, H. Shimoji, S. Ban-ya, and T. Fuwa, *Calorimetric Study of Heat of Mixing of Copper Alloys at 1120 °C*, *J. Iron Steel Inst. Jpn.*, 1977, 63, p 275-284.
- [1978Kau] L. Kaufman, H. Nesor, *CALPHAD* 2/4 (1978) 325-348.
- [1979Cas] R. Castanet, *J. Chem. Thermodyn.* 11 (1979) 787-791.
- [1981Bro] J.P. Bros, H. Eslami, P. Gaune, *Ber. Bunsenges, Phys. Chem.* 85 (1981) 333-336.
- [1982Bat] G.I. Batalin, V.S. Sudavtsova, *Inorg. Mater.* 18 (1982) 133-135.
- [1985Mur] J.L. Murray, *Int. Met. Rev.* 30 (1985) 211-234.
- [1988Oll] R. Ollitrault-Fitchet, J. Rivet, J. Flahaut, *J. Less-Common Met.* 138 (1988) 241-261.
- [1991Din] A.T. Dinsdale, *CALPHAD* 15 (1991) 317-425.
- [1991Lee] S.Y. Lee, P. Nash, in: "Phase Diagrams of Binary Nickel Alloys", P. Nash (ed.), ASM International, Materials Park, Ohio 1991.
- [1995Agr] J. Ågren, B. Cheynet, M.T. Clavaguera-Mora, K. Hack, J. Hertz, F. Sommer, U. Kattner, *CALPHAD* 19/4 (1995) 449-480.
- [1995Cha] M.W. Chase, I. Ansara, A.T. Dinsdale, G. Eriksson, G. Grimvall, L. Hoglund, H. Yokokawa, *CALPHAD* 19/4 (1995) 437-447.
- [1995Sun] B. Sundman, F. Aldinger, *CALPHAD* 19/4 (1995) 433-436.
- [1996Ibe] G. Ibe, S. Holtz, Noted in [1996Jac] as To Be Published.
- [1996Jac] M.H.G. Jacobs, P.J. Spencer, *Calphad* 20/3 (1996) 307-320.
- [1996Pop] S. Popovic, B. Grzeta, H. Loeffler, G. Wendrock, *Acta Crystallogr. A: Found. Crystallogr.* A52/C435 (1996) C435.
- [1998Lia] H. Liang, Y.A. Chang, *J. Phase Equilibria and Diffusion* 19 (1998) 25-37.
- [1998Sau] N. Saunders, Miodownik A.P., *CALPHAD (A Comprehensive Guide)*, Pergamon Press, Oxford, (1998).
- [2000Mat] M. Mathon, K. Jardet, E. Aragon, P. Satre, A. Sebaoun, *CALPHAD* 24/3 (2000) 253-284.
- [2000Tol] O. Tolochko, J. Agren, *J. Phase Equilibria and Diffusion*, 21/1 (2000) 19-24.
- [2002And] J.O. Andersson, T. Helander, L. Holund, P. Shi, B. Sundman, *CALPHAD* 26 (2002) 273-312.
- [2002Bal] C.W. Bale, P. Chartrand, S.A. Deckerov, G. Eriksson, K. Hack, R. Ben Mahfoud, J. Melançon, A.D. Pelton, S. Petersen, *CALPHAD* 62 (2002) 189-228.
- [2002Kan] D. Kanibolotsky, O. Bieloborodova, N. Kotova, V. Lisnyak, *J. Therm. Anal. Calorim.* 70 (2002) 975-983.
- [2004Bar] A.I. Baranov, A.A. Isaeva, L. Kloo, V.A. Kulbachinskii, R.A. Lunin, V.N. Nikiforov, B.A. Popovkin, *J. Solid State Chem.* 177 (2004) 3616-3625.
- [2000Wit] V.T. Witusiewicz, I. Arpshofen, H.-J. Seifert, F. Aldinger, *J. Alloys Compd.* 297 (2000), 176-184.
- [2004Luk] H.L. Lukas, S.G. Fries, B. Sundman, *Computational Thermodynamics: The Calphad Method*, Cambridge University Press, New York, 2004.
- [2005Pan] X.M. Pan, C. Lin, J.E. Morral, H.D. Brody, *J. Phase Equilibria and Diffusion* 26/3 (2005) 225-233.
- [2009Cao] W. Cao, S.L. Chen, F. Zhang, K. Wu, Y. Yang, Y.A. Chang, R. Schmid-Fetzer, W. A. Oates, *CALPHAD* 33 (2009) 328-342.
- [2010Yan] H Yan, Y. Du, L. Zhou, H. Xu, L. Zhang, S. Liu, *Int. J. Mat. Res.* 101 (2010) 1489-1496.
- [2011Pon] N. Ponweiser, C.L. Lengauer, K.W. Richter: *Intermetallics* 19 (2011) 1737-1746.

- [2011Suf] K. Sufryd, N. Ponweiser, P. Riani, K.W. Richter, and G. Cacciamani: *Intermetallics* 19 (2011) 1479-1488.
- [2012He] He X.C., Shen, H.L., *Physica B: Condensed Matter* 407 (2012) 1146-1152.
- [2012Pon] N. Ponweiser, K.W. Richter, *J. of Alloys and Compound* 512 (2012) 252-263
- [2012Puk] S. Pukas, L. Pylypchak, O. Matselko, P. Demchenko, R. Gladyshevskii, *Met. Alloys* 5(1/2) (2012) 59-65.
- [2013Gom] L. Gomidzelovic, I. Mihajlovic, A. Kostov, D. Zivkovic, *Hem. ind.* 67/1 (2013) 157-164.
- [2014Bec] C.A. Becker, J. Agren, M. Baricco, Q. Chen, A. Dectero, U. R. Kattner, J. H. Perepezko, G. R. Pottlacher, M. Selleby, *Phys. Status Solidi B*, 251/1 (2014) 33-52.
- [2015Big] S. Bigdeli, H. Mao, M. Selleby, *Phys. Status Solidi B* 252/10 (2015) 2199-2208.
- [2015Gom] L. Gomidzelovic, E. Pozega, A. Kostov, N. Vukovic, V. Krstic, D. Zivkovic, L. Balanovic, *Trans. Nonferrous Met. Soc. China*, 25 (2015) 2630-2636.
- [2015Lia] S.M. Liang, R. Schmid-Fetzer, *CALPHAD* 51 (2015) 252-260.
- [2015Pav] J. Pavlů, P. Řehák, J. Vřešťál, M. Šob, *CALPHAD* 51 (2015) 161-171.
- [2016Hal] B. Hallstedt, J. Gröbner, M. Hampl, R. Schmid-Fetzer, *Calphad* 53 (2016) 53 25-38.
- [2017Din] Y. Ding, B. Xiao, G. Tang, J. Hong., *J. Phys. Chem. C* 121 (2017) 225-236.
- [2017Vre] J. Vřešťál, J. Pavlů, U.D. Wdowik, M. Šob, *J. Min. Metall. Sect. B Metall.* 53/3 (2017) 239-247
- [2018Jia] Y. Jiang, S. Zomorodpoosh, I. Roslyakova, L. Zhang, *CALPHAD* 62 (2018) 109-118.
- [2018Yus] Y.A. Yusibov, I.D. Alverdiev, L.F. Mashadieva, D.M. Babanly, A.N. Mamedov, M.B. Babanly, *Zh. Neorg. Khim.* 63(12), (2018), 1607-1621.
- [2018Zou] D. Zou, C. Yu, Y. Li, Y. Ou, Y. Gao, *R. Soc. Open Sci.* 5 (2018) 171827.
- [2019Big] S. Bigdeli, M. Selleby, *CALPHAD* 64 (2019) 185-195.
- [2019Goe] P. Goel, M.K. Gupta, S.K. Mishra, *J. of Applied Physics* 125 (2019) 205106.
- [2020Che] S.-W. Chen, T.-Y. Huang, Y.-H. Hsu, A. Kroupa, *J. Electron. Mater.* 49/8 (2020) 4714-4729.
- [2020Ram] A. Ramakrishnan, S.W. Chen, Y. Hutabalian, *J. Alloys Compd.* 816 (2020) 152670.
- [2024Fri] M. Friák, O. Zobač, Z. Chlup, O. Fikar, P. Papež, M. Zelený, A. Kroupa, *Intermetallics* 169 (2024) 108294.
- [2024Zob] O. Zobač, A. Kroupa, A. Dinsdale, *CALPHAD* 87 (2024) 102742.

6 Papers

6.1 Paper 1

- [P1] **Zobač, O.**, Kroupa, A., Zemanová, A., Richter, K.W., *Experimental description of the Al-Cu binary phase diagram*, Metallurgical and Materials Transactions A: Physical Metallurgy and Materials Science, 2019, 50(8), pp. 3805-3815 doi: 10.1007/s11661-019-05286-x (IF 2.050)

Experimental Description of the Al-Cu Binary Phase Diagram



ONDREJ ZOBAC, ALES KROUPA, ADELA ZEMANOVA, and KLAUS W. RICHTER

The phase diagram of the Al-Cu binary system was reinvestigated experimentally. The current study was designed to contribute to a better description of those parts of the phase diagram which are disputed in the current scientific literature, and in addition, to study the phase equilibria at 300 °C. The melting behavior of the θ -phase was confirmed to be peritectic. A metastable congruent solidification of the θ -phase was observed from the microstructural examination of as-cast samples. The location of the liquidus curve in this region of the phase diagram was more accurately defined using DSC measurements taken at slow-heating rates (1 °C min⁻¹). The temperature stability of the ζ -phase was reevaluated and was found to lie in the range 373–597 °C. The phase boundaries of the $\gamma' + \varepsilon'$ two-phase field were experimentally defined. Difficulties in defining the γ'/δ transition were addressed by a combined EDX/XRD investigation of more than ten samples that had been annealed in the temperature range of 500 to 750 °C. The ($\gamma' + \delta$) two-phase field was postulated from XRD studies of quenched samples. The temperature of the ordering reaction $\gamma \leftrightarrow \gamma'$ within the $\gamma(\gamma') + \beta$ phase field was experimentally determined to be 779.6 °C. All other parts of the Al-Cu phase diagram studied here were found to be in very good agreement with the most recent previous descriptions.

<https://doi.org/10.1007/s11661-019-05286-x>
© The Author(s) 2019

I. INTRODUCTION AND LITERATURE REVIEW

A. Introduction

RELIABLE phase diagrams are essential for focused material development. The Al-Cu system, being the key binary system for many Al-based, Cu-based, and dural alloys, has been investigated intensively over recent decades owing to its importance to industry. The focus of most studies have been the Al-rich and Cu-rich parts of the phase diagram, respectively, which are used for interpreting microstructures of alloys that have been used in industrial applications. Knowledge of phase equilibria across the whole concentration range of a binary phase diagram is crucial for the extrapolation of material properties and thermodynamic modeling of higher order systems. Although the most recent

experimental phase diagram, that was published by Ponweiser *et al.*^[1] describes the whole concentration range, there are still some uncertainties and inconsistencies in the currently accepted version. Therefore, further experimental studies to clarify these points appear to be justified.

B. Literature Review

The Al-Cu phase diagram is characterized by many intermetallic phases with complex mutual relationships occurring in all regions of the phase diagram. The phase diagram has been studied by several authors, and several very comprehensive overviews have been published.^[2–5] In the following section, we briefly discuss the state of knowledge of the binary phase diagram. For a better illustration of key points, a comparison of the evaluated phase diagram published by Murray^[2] and that of Ponweiser *et al.*^[1] is shown in Figure 1. Figure 1(a) shows the whole concentration range of the phase diagram, whereas Figure 1(b) shows just the central region.

The maximum solubility of Cu in Al is equal to 2.5 at. pct at the eutectic temperature of 550 °C.^[2] The θ -phase (Al₂Cu) was described for the first time by Owen and Preston^[6] and also by Friauf.^[7] The phase was characterized using XRD (single-crystal rotational method), and a tetragonal symmetry was found. The crystal structure of the θ -phase was determined later by

ONDREJ ZOBAC is with the Department of Inorganic Chemistry - functional materials, University of Vienna, Währinger Straße 42, 1090 Vienna, Austria and also with the Institute of Physics of Materials, The Czech Academy of Sciences, Žitkova 22, 616 00 Brno, Czech Republic. Contact e-mail: ondrej.zobac@univie.ac.at ALES KROUPA and ADELA ZEMANOVA are with the Institute of Physics of Materials, The Czech Academy of Sciences. KLAUS W. RICHTER is with the Department of Inorganic Chemistry - functional materials, University of Vienna.

Manuscript submitted January 11, 2019.

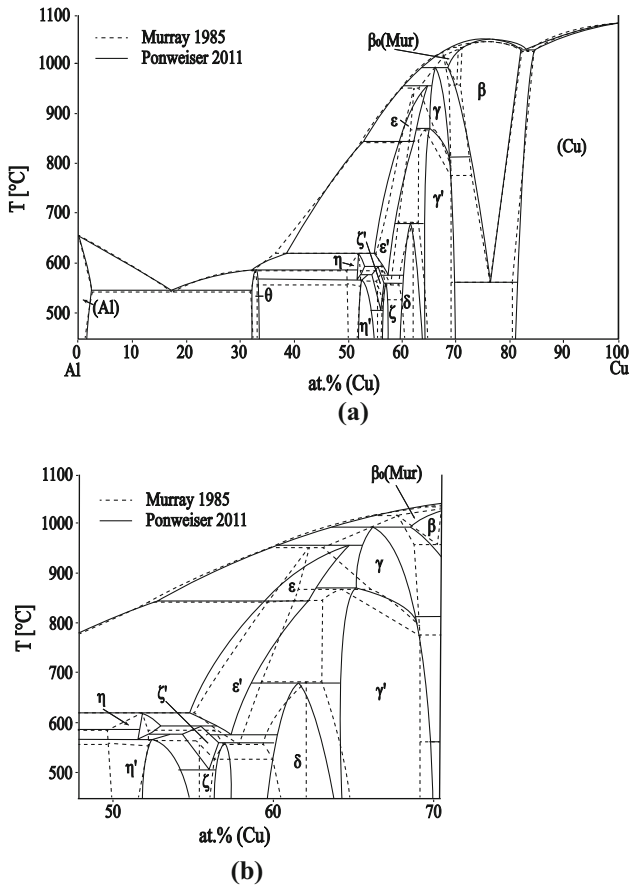


Fig. 1—Al-Cu phase diagrams adapted from Ref. [2] (dotted lines) and Ref. [1] (solid lines) (a) whole concentration range and (b) the central part of the phase diagram. Note that the labeling of the phases is consistent with Table 1.

Havinga^[8] as having an $I4/mcm$ space group. The melting behavior of the θ -phase has been described differently by different authors. In their experimental work, Histasune^[9] found that the solidification of the θ -phase involved the peritectic reaction (Liquid + $\eta \rightarrow \theta$), and this was accepted by Murray in their review of the system.^[2] On the other hand, Kulbush^[10] (cited by Murray) presented the θ -phase as a congruently melting compound. According to Murray,^[2] the θ -phase is stable up to 590 ± 1 °C. However, scatter in the experimental data for the liquidus and the invariant reactions close to the θ -phase does not allow the reaction type to be identified unambiguously. Goedecke and Sommer^[11] investigated the melting and solidification behavior of the θ -phase and proposed the formation of a metastable congruently melting Al_2Cu_m phase from undercooled liquid. Consequently, a metastable eutectic reaction $L \leftrightarrow \eta + \theta$ is observed on cooling and the stable peritectic reaction ($L + \eta \leftrightarrow \theta$) is only observed on the heating of annealed samples. The composition of this metastable θ -phase is enriched in Cu relative to the stable θ -phase. The homogeneity range of the (stable) θ -phase lies between 32 and 33.6 at. pct Cu at 500 °C^[1] and 32.1 to 32.6 at. pct Cu at the (Al)- θ eutectic temperature of 549 °C.^[11]

The low-temperature η' -phase ($\text{Al}_{48}\text{Cu}_{52}$) has a monoclinic structure (space group $C2/m$).^[12] Ponweiser *et al.*^[1] studied the homogeneity range of this phase by SEM-EDX and XRD, and found that the η' -phase extends from 51.9 at. pct Cu to 54.8 at. pct Cu at 500 °C. DSC analysis showed that the low-temperature η' -phase is stable below 580 °C. Ponweiser *et al.*^[1] supposed that the η' -phase is formed by a peritectoid reaction. This observation is in contrast with the previous experimental review; Murray^[2] suggested a second-order transition between η and η' . The structure of the high-temperature η -phase was not known for a long time. Recently, Ponweiser *et al.*^[1] determined the structure from high-temperature powder XRD data. The η -phase is orthorhombic (space group $Cmmm$), stable over the temperature range 574 °C to 625 °C and is also formed by peritectic reaction. The maximum homogeneity range is approximately 1 at. pct at 597 °C.

Two compositionally and crystallographically closely related phases, ζ and ζ' , are stable in the composition range 55 to 60 at. pct Cu. The structures of the ζ -family of phases, with the supposed low-temperature modification ζ' (Al_3Cu_4) and high-temperature modification ζ ($\text{Al}_3\text{Cu}_{4.8}$), are described in detail by Gulay and Harbrecht.^[13,14] The ζ' -phase is orthorhombic ($Fmm2$) and is stable below 579 °C, according to Gulay and Harbrecht.^[14] Ponweiser *et al.* suggested that the homogeneity range extends from 56 at. pct Cu and 57.5 at. pct Cu at 500 °C.^[1] The ζ' -phase is formed by a peritectoid reaction at 560.5 °C. The ζ -phase crystallizes with the space group $Imm2$. Between 400 and 500 °C it decomposes to the ζ' -phase and η -phase and it is still stable at 550 °C.^[13] Ponweiser *et al.* confirmed experimentally that the ζ -phase is stable below 597 °C and estimated that it decomposes eutectoidally at 507 °C.^[1]

According to Murray's review,^[2] the ε -family of phases exists over the same composition range as the ζ -phases at medium and high temperatures. The structure of the medium-temperature modification ε' was measured by high-temperature XRD by El-Boragy *et al.*^[12] They found that the ε' -phase has a filled NiAs-type structure with partial occupation of the 2d sites by Cu atoms. The crystal structure of the high-temperature ε -phase is still unknown. It is assumed to be cubic.^[2]

The situation in the composition range from 60 to 70 at. pct Cu is not clear and there are many contradictory data in the literature. Bradley^[15] proposed the existence of three different phases with cubic, monoclinic and rhombohedral crystal structures, respectively. Westman^[16] found that the δ -phase is trigonal rhombohedral and crystallizes with the space group $R3m$ and they supposed the existence of a third phase of unknown structure between the cubic and the rhombohedral compounds. Seshadri and Downie^[17] found five intermetallic phases in the Al-Cu phase diagram that are stable below 500 °C: θ , η' , ζ , the δ -phase and the γ' -phase. Murray^[2] accepted the experimental work of Funamizu^[18] in their review, which did not indicate any phase being present between the γ' -phase and δ -phase. Van Sande^[19] studied the Al-Cu phase diagram using

Table I. Stable Intermetallic Phases in Al-Cu Binary Phase Diagram

Phase Name [This Work]	Common Names	Pearson Symbol	Structure Type	T Range (°C)	Composition and Temperature Range [At. Pct Cu]		
					Min	Max	Ref.
(Al)	FCC_A1, Al	$cI2$	Al	≤ 660.5	0	2.48	2
				θ , Al ₂ Cu	$tI12$	Al ₂ Cu	≤ 591
η	η_1 , Eta HT	$oP16/ oC16$	n.a.	≤ 590.5	32	33.6	this work
				574–625			
η'	η_2 , Eta LT	$mC20$	Al-Cu	573.9-624.5	51.9	54.8	1
				≤ 581			
ζ	ζ_2 , Al ₃ Cu _{4-δ}	$Imm2$	Al ₃ Cu _{4-δ}	≤ 574.5	54.5	56.5	1
				507–597			
ζ'	ζ_1 , Al ₃ Cu ₄	$Fmm2$	Al ₃ Cu ₄	ca. 425 to min. 550	55	58	2
				min. 400 to 570			
ε	ε_1 , epsilon HT	cubic?	n.a.	373–597	56.3	57.4	1
				298–561			
ε'	ε_2 , epsilon LT	$hP4$	NiAs	min. 400 to 579	49.5	51.3	2
				530 to 590			
δ	δ , Al ₃ Cu ₈	$hR52$	Al ₄ Cu ₉ (r)	min. 300 to 560.5	59.5	64.5	1
				960 to 847			
γ	γ_0 , γ -CuZn, γ -brass	$cI52$	Cu ₅ Zn ₈	959 to 846	54.5	62.5	1
				847 to 578			
γ'	γ_1 , γ -AlCu, γ -D8 ₃	$cP52$	Al ₄ Cu ₉	846 to 568.5	60?	64?	1
				≤ 687			
β	β , BCC_A2	$cI2$	W	≤ 680	65	69	1
				993 to 800			
α'	α_2 , alpha_LT	n. a.	super structure based on TiAl ₃	991 to 779.6	65	70	1
				≤ 874			
(Cu)	FCC_A1, Cu	$cF4$	Cu	≤ 873.5	61.0	69.6	1
				1052 to 567			
				1052 to 566.7	76	79	21
				≤ 360			
				≤ 360			
				< 1083			

n.a. not available.

very slow-cooling experiments and confirmed the presence of a two-phase equilibrium between the γ' and δ -phases. Ponweiser *et al.*^[1] did not find any other equilibrium phase in this region but marked the whole composition area with a question mark because they were unable to clearly separate the two γ' and δ single phase regions using their combined EDX and Rietveld refinement results. The samples all appeared to be single phase in the EDX studies, but the transition from cubic to trigonal rhombohedral was unclear from the XRD results.

Murray^[2] concluded that there are two γ -phases; γ (low temperature) and γ' (high temperature). The transition temperature was investigated by thermal analysis (temperature range 780 °C to 873 °C) but could not be confirmed metallographically. Liu *et al.*^[3] studied the Cu-rich part of the phase diagram using several analytical methods (SEM-EDX, HT-XRD, DSC). They found that the γ -phase crystallizes with a CuZn γ -brass type structure. They did not find a two-phase region between the γ' - and γ -phases, so they proposed a second-order transition between the two. A

second-order type of phase transition was also confirmed experimentally by Ponweiser *et al.*^[1]

Dawson^[20] identified the β -phase with an $Im3m$ crystallographic structure, and proposed the existence of a high-temperature β_0 -phase. Murray^[2] assumed in their phase diagram evaluation that it is formed by a peritectic reaction from β and liquid at 1037 °C. The existence of the β_0 -phase in the equilibrium phase diagram has not been confirmed subsequently. Liu *et al.*^[3] showed a two-phase region between β (BCC_A2) and γ without any other phase occurring in that part of the diagram. Only one peak was found in their DSC measurements, which was interpreted as the solidus of the β -phase rather than the eutectoid reaction. According to,^[2] the β -phase decomposes by a eutectoid reaction to (Cu) solid solution and the γ' -phase at a temperature of approximately 560 °C to 575 °C, and melts congruently at 1049 °C. The temperature of the eutectoid reaction was determined later by Ponweiser *et al.*^[1] to be 567 °C using DTA investigations of several samples with differing compositions.

The α' phase, with a composition of 77.5 at. pct Cu, is stable below 363 °C. The α' phase has an ordered fcc long-period super lattice structure.^[21] The maximum solubility of Al in Cu is 18.5 at. pct at the eutectoid temperature of 566.7 °C.^[1]

The available information for all solid phases of the system is summarized in Table I. The abbreviated phase names in the form of Greek letters used in the text and phase diagrams are provided in the first column. Other common phase names used in the literature^[1,2,5] are shown in column 2. The Pearson symbol and structure type (columns 3 and 4) are generally accepted from the Materials Science International Team (MSIT) report.^[22] The maximum temperature and composition range of the stable phases according to different authors are presented in columns 4 to 6.

II. EXPERIMENTAL

The overall sample compositions were selected to address the unsolved questions in the experimental phase diagrams as mentioned above. The prepared samples were analyzed and characterized by different static or dynamic analytical methods (SEM-EDX, DSC, DTA; XRD).

A. Sample Preparation

Samples were prepared from pure elements of 5N purity. Any oxide present in the copper was reduced under flowing H₂ at 300 °C for 3 hours. Samples were prepared by arc melting on a water-cooled copper plate under a low-pressure Ar atmosphere using pure Zr as a getter. The alloys were remelted several times to improve the homogenization of the material. Long-term annealing of the samples was performed at selected temperatures on material sealed in evacuated quartz glass ampoules. A conventional tube furnace was used for the heat treatment. Samples were quenched into cold water from their annealing temperatures. Annealing times and temperatures were selected with the aim of obtaining states close to thermodynamic equilibrium. Annealing temperature, time, overall composition, coexisting phases and phase compositions of each sample are listed in Table II.

B. Experimental Phase Diagram Investigation

A combination of dynamic and static methods was used for investigation of the phase diagram. Phase equilibria investigations and chemical analysis of phase and overall compositions were performed using scanning electron microscopy combined with energy-dispersive X-ray spectroscopy (SEM-EDX), employing either a Zeiss Supra 55 VP instrument equipped with an energy-dispersive detector for quantitative analysis or a similarly equipped SEM JEOL JSM-6460. Overall and phase compositions are listed in Table II in columns 4, 6, 7.

Identification of phases present in the long-term annealed samples was achieved using X-ray powder diffraction. A Bruker D8 Diffractometer equipped with

a high-speed position sensitive (PSD) detector (Lynxeye) was used in the $\theta/2\theta$ reflection setting. Coexisting phases in the samples are listed in Table II, column 5.

Phase transition temperatures were measured using a high-temperature heat flow DSC (NETZSCH Pegasus 404 C). Alumina DSC crucibles with lids were used under a permanent Ar flow of 50 mL min⁻¹ and with heating and cooling rates of 10 °C min⁻¹. Slower heating and cooling rates (5 or 1 °C min⁻¹) were used in some special cases (see below). The calorimeter was calibrated using a set of pure metal standards having well-defined melting temperatures (Sn, Al, Zn, Cu, Ag, Au). Calibration was carried out under the same conditions as the experimental measurements. Three runs were performed for each sample; the thermal effects during the first heating run were not taken into account. It is assumed that optimal thermal contact between the sample and the bottom of the crucible is established only after the first heating. The temperature of the thermal effect used is thus the average value of the thermal effects of the 2nd and 3rd heating curves only. Small differences between the first and subsequent heating and cooling curves are caused by changes in the shape of the sample following initial melting. Melting the sample can result in an increase in the contact area between the sample and the crucible as the solidifying material takes the shape of the crucible wall. Thermal analysis results are listed in Table III.

III. RESULTS AND DISCUSSION

More than 50 samples have been studied across the whole concentration and temperature range of Al-Cu phase diagram. Combining the results from DSC, SEM-EDX and XRD allows a complete description of the phase diagram to be proposed; shown in Figure 2. The results are mostly in very good qualitative agreement with the phase diagram of Ponweiser *et al.*^[1] But the focus of the current study was on those parts of the phase diagram which have not been described satisfactorily previously.^[1] Furthermore, phase equilibria at 300 °C have been investigated.

A. Solidification of the θ -Phase

A calculated phase diagram of the Al-Cu system was published by Liang and Schmid-Fetzer^[5] where a semi-empirical CALPHAD-type assessment of the system was presented. The peritectic reaction $L + \eta \rightarrow \theta$ was modeled but it was found that the calculated liquidus line in the composition range 33 at. pct < x(Cu) < 45 at. pct did not agree well with the experimental results published by Ponweiser *et al.*^[1] A new CALPHAD-type assessment^[23] attempts to provide better agreement between calculation and experiment for the liquidus in the 33 at. pct < x(Cu) < 45 at. pct concentration range, but this required a change in the nature of the solidification behavior of the θ -phase from peritectic to congruent.

Congruent melting has been proposed previously,^[10,11] but Goedecke^[11] suggested that this reaction

Table II. Chemical Composition of the Long-Term Annealed Samples

T[°C]_No.	Annealing [h]	Nominal composition [x(Cu%)]	Overall composition [x(Cu%)]	Coexisting phases	Phase 1 [x(Cu%)]	Phase 2 [x(Cu%)]
300_1	1464	55	54.7 (3)	$\eta' + \zeta'$	50.4 (3)	55.7 (5)
300_2	1464	55.5	55.2 (5)	$\eta' + \zeta'$	50.6 (6)	56.2 (5)
500_1	625	55.5	55.6 (5)	$\eta' + \zeta$	55.6 (5)	not known
500_2	625	58.5	59.3 (5)	δ	59.3 (5)	—
500_3	625	63	63.1 (4)	δ/γ'	63.1 (4)	—
500_4	625	64	65.2 (4)	δ/γ'	65.2 (4)	—
540_3	720	34	34.7 (2)	$\theta + \eta'$	34.3 (1)	51.3 (2)
540_4	720	34.5	34.9 (3)	$\theta + \eta'$	34.4 (1)	51.3 (2)
550_1	625	42	41.9 (9)	$\theta + \eta'$	33.6 (4)	51.4 (4)
550_2	625	54.6	56.4 (4)	ζ	56.4 (4)	—
550_3	625	57	56.9 (4)	ζ'	56.9 (4)	—
550_4	625	63.6	64.7 (4)	δ/γ'	64.7 (4)	—
550_5	625	75	83.8 (4)	Cu	83.8 (4)	—
615_1	505	58.8	59.6 (5)	$\epsilon' + \delta$	58.2 (4)	60.4 (3)
615_2	505	63.3	64.1 (5)	δ/γ'	64.1 (5)	—
615_3	505	72.9	71.7 (3)	$\gamma' + \beta$	69.6 (3)	75.2 (8)
615_4	505	79.3	80.0 (5)	$\beta + \text{Cu}$	76.1 (7)	81.9 (6)
615_5	290	63.3	60.1 (1)	$\epsilon' + \delta$	57.3 (1)	60.2 (1)
615_6	290	62.5	63.9 (2)	δ/γ'	63.9 (2)	—
615_7	290	63	61.8 (2)	$\delta?$	61.8 (2)	—
688_2	410	79.7	79.2 (2)	$\beta + \text{Cu}$	77.6 (6)	81.0 (4)
688_3	410	72.2	71.8 (7)	$\gamma' + \beta$	69.0 (5)	73.9 (5)
688_4	410	61.5	63.9 (5)	δ/γ'	63.9 (5)	—
688_5	410	59.6	58.5 (8)	ϵ'	58.5 (8)	—
688_6	410	65	65.0 (4)	δ/γ'	65.0 (4)	—
688_7	410	62.7	60.3 (4)	$\epsilon' + \gamma'$	59.9 (5)	61.0 (4)
688_8	410	61.5	62.7 (2)	δ/γ'	62.7 (2)	—
688_9	410	62.7	62.9 (5)	δ/γ'	62.9 (5)	—
710_1	200	59.7	59.9 (1)	$\epsilon' + \gamma'$	59.5 (1)	61.5 (1)
710_2	200	60.7	60.1 (2)	$\epsilon' + \gamma'$	58.9 (2)	61.4 (1)
710_3	200	62	60.7 (5)	$\epsilon' + \gamma'$	59.4 (2)	61.7 (2)
750_1	300	66.6	64.2 (5)	δ/γ'	64.2 (5)	—
750_2	300	60.6	60.3 (5)	$\epsilon' + \gamma'$	59.7 (1)	61.6 (1)
750_3	300	80.4	80.3 (1)	$\beta + \text{Cu}$	78.5 (5)	81.7 (5)
750_4	300	60.5	61.2 (4)	$\epsilon' + \gamma'$	59.9 (2)	61.9 (2)
750_5	300	62.8	63.2 (6)	δ/γ'	63.2 (6)	—
750_6	300	72	74.3 (2)	β	74.3 (2)	—
750_7	300	71.6	74.3 (3)	β	74.3 (3)	—
750_8	300	60.6	67.1 (1)	γ'	67.1 (1)	—

was in fact metastable. Because of these disagreements, the concentration range between 31 and 40 at. pct Cu has been reinvestigated in the present work. The solidification behavior of the θ -phase was studied using samples that had been melted, homogenized and then quickly cooled in the arc furnace. Two sets of samples were prepared with compositions close to 33.3 at. pct Cu; a set with slightly higher and a set with slightly lower copper contents. The morphology of the as-cast samples was studied using SEM. A eutectic microstructure was observed in both sets of samples, but the morphology of the microstructures was different for each set of samples (see Figure 3(a) for the Al-rich side and Figure 3(b) for the Cu-rich sample) as would be expected for a congruent reaction.

In the second step, the melting behavior of the θ -phase was studied under conditions close to equilibrium and hence to the phase diagram for the

thermodynamically stable system. Several samples with nominal composition between 32% Cu and 40% Cu were long-term annealed at 540 °C or 582 °C. The temperatures of the phase transitions were measured by DSC using sample cooling and heating rates of 1, 5 and 10 °C min⁻¹, respectively. The data are presented in Figure 4, which also shows an enlarged portion of the phase diagram in the vicinity of the θ -phase. For all heating rates, both single phase samples containing the θ -phase, as well as samples exhibiting a two-phase morphology ($\theta + \eta'$), indicate an invariant reaction at 589 °C, which is the temperature of the peritectic reaction $L + \eta \leftrightarrow \theta$. There is no evidence of congruent melting in the long-term annealed samples.

Therefore, congruent melting of the θ -phase was confirmed to be a metastable reaction and the observed microstructures were found to be in very good agreement with the metastable version of the phase diagram

Table III. Summary of the temperature of phase transitions measured by DSC

T [°C]_No.	Nominal Comp. (at. pct Cu)	Thermal Effects (heating) (°C)						
		Liquidus	Invariant			Others		
DSC								
theta_1 ^a	35.3	602.9				538.8	597.2	
300_1	54.7	893.3	852.3	575.6		626.7	373.5	
300_2	55.2	902.7	586.6	574.7		851.7	625	373
300_3	55.9	908.1	623.8	577.6		850.1	692.2	370
300_4	77.1		566.8	511.1		347		
300_5	76.4		566.6	511.1		350		
300_6	77.4		566.8	510.9		350		
300_7	77.3		565.8	509.8		352		
400_1	77		565.2	510.1		350		
400_2	77.3		567.2	511.7		353		
400_3	74		567.2	510.3		345		
400_4	78		564.4	511.8		363		
500_1	55.6	894	614	585	574	846	372	
500_2	59.3	946	723.8	560.5		847.2	652.5	568.5
500_3	63.1	998.1	959.3	871.1	843.2	939.1	563.2	
540_1	77.1		566.1	510.2		349		
540_2	77.7		567.3	512		354		
550_1	41.9	699.9	627.9	590.4		573.9		
550_5	83.8	1042.5	1033.2					
615_3	72.3	1048.8	568.1	510.8				
615_3 ^b	72.3					820	777.8	
688_3 ^b	71.8					867	779	
688_6	65.1	1014.2	960.3			965.7	873.1	
750_8	67.1	1039.1				864.7		
DTA								
550_4	64.8	1018	956			1003	876	
615_2	64.1	1006	963			874		
710_1	59.9	967	682			960	845	
710_2	60.1	998	745	682		935	868	830
710_3	61.3	937				867.4	829.9	747.7
750_2	60.1	973	681			963	875	848

^aAs-cast sample.

^bHeating and cooling rate 1 °C min⁻¹.

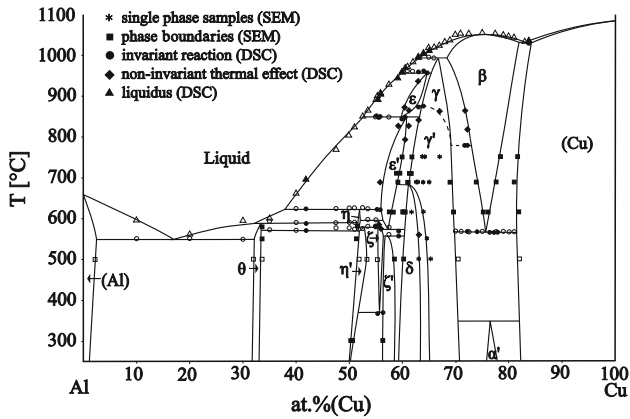


Fig. 2—Experimental Al-Cu phase diagram based on this work (filled symbols) and on data published in Ref. [1] (empty symbols).

published by Goedecke.^[11] The discrepancy between the calculated^[5] and experimental^[1] liquidus line in this region is probably due to the fact that the

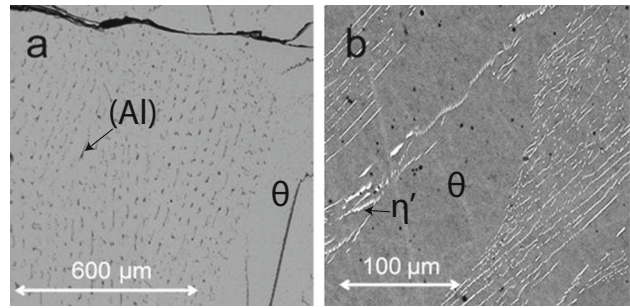


Fig. 3—Eutectic microstructures observed by using SEM with a BSE detector in the as cast samples with overall composition $x(\text{Cu}) = 32.4$ at. pct (a) and $x(\text{Cu}) = 33.9$ at. pct (b).

metastable reactions were observed during DSC studies of Ponweiser *et al.*^[1]

It is worth discussing the observed thermal effects associated with the liquidus that were seen at different heating rates in more detail. While the temperatures of the invariant reactions are independent of the heating

rate, the (monovariant) thermal effects associated with the liquidus strongly depend on the heating rate (Figure 4). This is due to the fact that the liquidus thermal effect is superimposed on the peak maximum associated with the invariant when the two temperatures are very close to one another. In such a case, the thermal effect of the liquidus can no longer be separated and evaluated from the DSC curves. At higher heating rates, the peak maximum from the invariant is shifted to higher temperatures. Consequently, the lowest heating rate ($1\text{ }^{\circ}\text{C min}^{-1}$) yields the best representation of the true liquidus temperature and the liquidus line was drawn accordingly in Figure 4.

The samples that were annealed at $540\text{ }^{\circ}\text{C}$, $550\text{ }^{\circ}\text{C}$, $582\text{ }^{\circ}\text{C}$ were studied to determine the location of the Cu-rich phase boundary of the θ -phase. The position of this phase boundary is temperature independent and lies at 33.5 at. pct Cu. The solubility limit of Cu in the η' -phase is 51.5 at. pct at $550\text{ }^{\circ}\text{C}$ and 51.8 at. pct at $582\text{ }^{\circ}\text{C}$. The X-ray powder diffraction pattern of the Al-41.9 at. pct Cu sample that was annealed at $550\text{ }^{\circ}\text{C}$ is shown in

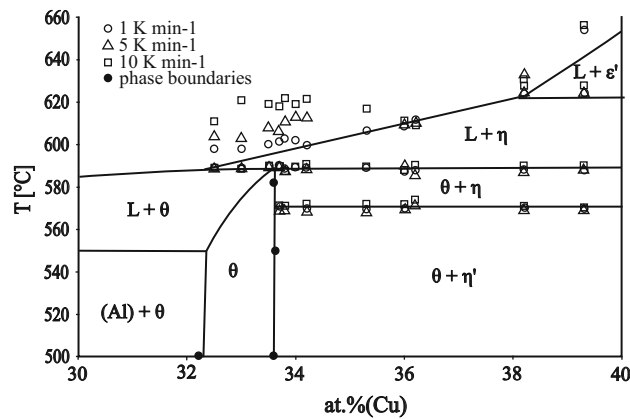


Fig. 4—Detail of the Al-Cu phase diagram around the θ -phase with superimposed experimental data.

Figure 5. Lattice parameters that were obtained by Rietveld refinement were $a = 12.1066(3)\text{ \AA}$, $b = 4.1024(1)\text{ \AA}$, $c = 6.9213(2)\text{ \AA}$ and $\beta = 54.994(2)^{\circ}$ for the η' -phase, and $a = 6.0603(1)\text{ \AA}$, $c = 4.8763(1)\text{ \AA}$ for the θ -phase, respectively.

B. The $\epsilon' + \gamma'$ Two-Phase Field

The phase boundaries in the high-temperature ($\epsilon' + \gamma'$) two-phase field have not been described satisfactorily in the literature. Several samples with nominal compositions close to Al-60Cu were long-term annealed at temperatures of $688\text{ }^{\circ}\text{C}$, $710\text{ }^{\circ}\text{C}$ and $750\text{ }^{\circ}\text{C}$ to determine these compositions. A selected micrograph, taken with an SEM in BSE mode, of the sample with the overall composition Al-60.1Cu that had been annealed at $710\text{ }^{\circ}\text{C}$, is shown in Figure 6. According to the present results, the ($\epsilon' + \gamma'$)/ γ' boundary is located between 61% Cu at $682.1\text{ }^{\circ}\text{C}$ and 63.3% Cu at $846\text{ }^{\circ}\text{C}$ (see Table IV, reactions number 7 and 9).

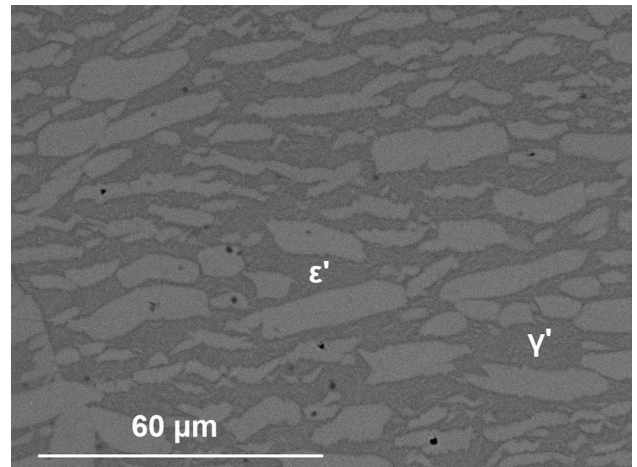


Fig. 6—Micrograph in BSE mode of the sample with the overall composition Al-60.1Cu annealed at $710\text{ }^{\circ}\text{C}$ ($\epsilon' + \gamma'$).

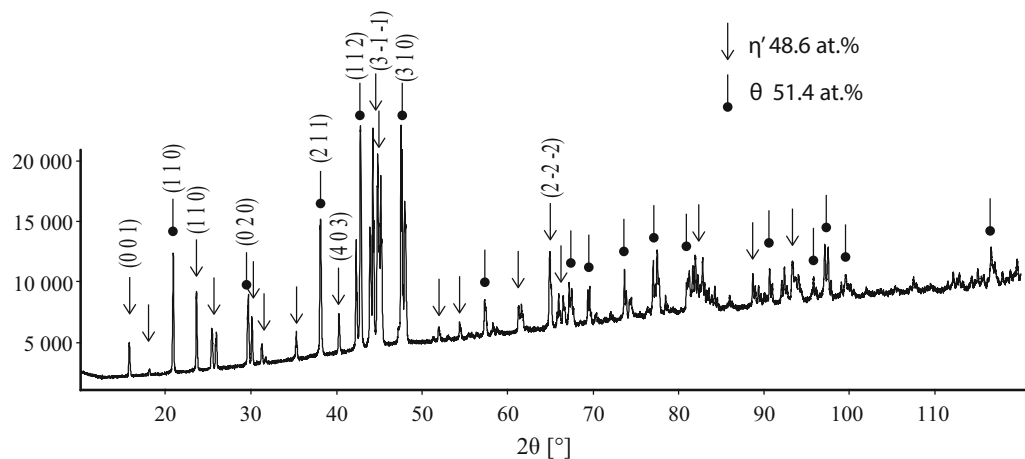


Fig. 5—XRD pattern of the alloy Al-41.9% Cu containing θ (Al-33.6 at. pct Cu) and η' (51.4 at. pct Cu). The numbers of phase percentage in the insert right was obtained by Rietveld refinement.

Table IV. Invariant Reactions in the Al-Cu System

No.	Reaction	T [°C]	Cu Content in Phases [At. Pct (Cu)]			Ref.
1.	congruent $L \leftrightarrow \beta$	1052	L 76	β 76		11
2.	eutectic $L \leftrightarrow (Cu) + \beta$	1035	L 83	(Cu) 84.5	β 82	11
3.	peritectic $L + \beta \leftrightarrow \gamma$	993 991	L 63 63	β 69 69	γ 65 65	11 this work
4.	peritectic $L + \gamma \leftrightarrow \varepsilon$	960 959	L 60 60	γ 65.5 65.5	ε 64.5 64.5	11 this work
5.	ordering $(\gamma, \gamma') \leftrightarrow (\gamma, \gamma') + \varepsilon$	874 873.5	γ 65 65	ε 62.5 62.3		this work
6.	catatectic $\varepsilon \leftrightarrow \varepsilon' + L$	847 846	ε 59.5 59.5	ε' 59.5 59.5	L 52.5 52.2	11 this work
7.	peritectoid $\varepsilon + \gamma' \leftrightarrow \varepsilon'$	847 84.6	ε 62.5 59.5	γ' 64.2 63.3	ε' 62.5 61.4	11 this work
8.	ordering $(\gamma, \gamma') \leftrightarrow (\gamma, \gamma') + \beta$	800 779.6	γ 69 69	β 73 73		11 this work
9.	peritectoid $\gamma' + \varepsilon' \leftrightarrow \delta$	684 682.1	γ' 63 61.1	ε' 58.5 58.5	δ 61.5 61	11 this work
10.	peritectic $L + \varepsilon' \leftrightarrow \eta$	625 624.5	L 38.5 38.5	ε' 52.0 52	η 54.5 55	11 this work
11.	peritectic $\eta + \varepsilon' \leftrightarrow \zeta$	597 597	η 53 52	ε' 56.5 55.5	ζ 55 56.5	11 this work
12.	peritectic $L + \eta \leftrightarrow \theta$	591 589	L 32.5 32.5	η 51.1 51.5	θ 33.5 33.5	11 this work
13.	peritectoid $\eta + \zeta \leftrightarrow \eta'$	581 580	η 52 52	ζ 54.5 55.5	η' 53.5 53.5	11 this work
14.	eutectoid $\varepsilon' \leftrightarrow \zeta + \delta$	578 575	ε' 57.4 57.3	ζ 56 56	δ 60 60	11 this work
15.	eutectoid $\eta \leftrightarrow \theta + \eta'$	574 573.9	θ 33 33.3	η 49.8 51.7	η' 49.8 52.3	11 this work
16.	eutectoid $\beta \leftrightarrow \gamma' + (Cu)$	567 566.7	β 76 75.4	γ' 70 69	(Cu) 81.5 81.5	11 this work
17.	peritectoid $\zeta + \delta \leftrightarrow \zeta'$	563 560.5	ζ 56.5 56.5	δ 60 60	ζ' 57 57	11 this work
18.	eutectic $L \leftrightarrow (Al) + \theta$	550	L 17	(Al) 2.5	θ 32	11
19.	eutectoid $\zeta \leftrightarrow \zeta' + \eta'$	373	ζ 55.6	ζ' 56.5	η' 52	this work
20.	peritectoid $\gamma' + (Cu) \leftrightarrow \alpha'$	350	γ' 70.5	(Cu) 82	α' 76.6	this work

Present results are compared to those of Ponweiser *et al.*^[11]

C. The γ' to δ Phase Transition

Most of the previous studies of this part of the Al-Cu system agree on the existence of two separate phase fields for the δ and γ' -phases. The γ' -phase is cubic and

crystallizes with the Al_4Cu_9 -type structure, while the δ -phase can be described by a rhombohedrally distorted superstructure of the Al_4Cu_9 type. However, the location of the phase boundaries separating the two different

phase fields have not been fixed reliably in any previous study. Ponweiser *et al.*^[1] investigated this region by analyzing (by SEM/EDX) a fine raster of samples that had been annealed at 450 °C and found that all were single phase. Powder XRD analyses revealed that compositions between 60 and 63 at. pct Cu contained the single δ -phase. At 64 at. pct Cu, the diffraction pattern could not be evaluated completely, but in samples with higher Cu-contents the cubic γ' -phase was found.

In the current study, several samples with different compositions were annealed at different temperatures to locate the boundaries of the $(\delta + \gamma')$ two-phase field. However, it was not possible to determine the phase boundaries of δ and γ' -phase fields by SEM-EDX measurement of the phase composition. The compositions of all grains in all samples were in agreement with the overall sample composition within the experimental error of the measurement. Thus, all samples were single phase based on EDX characterization, which is in complete agreement with.^[1] On the other hand, careful analysis of the X-ray powder patterns showed that only two of the samples could be refined completely with one single structural model: the single δ -phase was identified in the sample Al-61.8Cu (615_7) and the single γ' -phase in the sample Al-67.1Cu (750_8). These two samples are marked with a circled star in Figure 7. All other samples in the composition range $x(\text{Cu})=(62-67)$ have XRD patterns that were evaluated as a combination of both γ' and δ -phases even for a temperature higher than the presumed upper temperature limit of the δ -phase (682 °C). Samples give a diffraction pattern corresponding to either the δ or the γ' -phase but with small additional peaks which could not always be fitted well with the applied structural models.

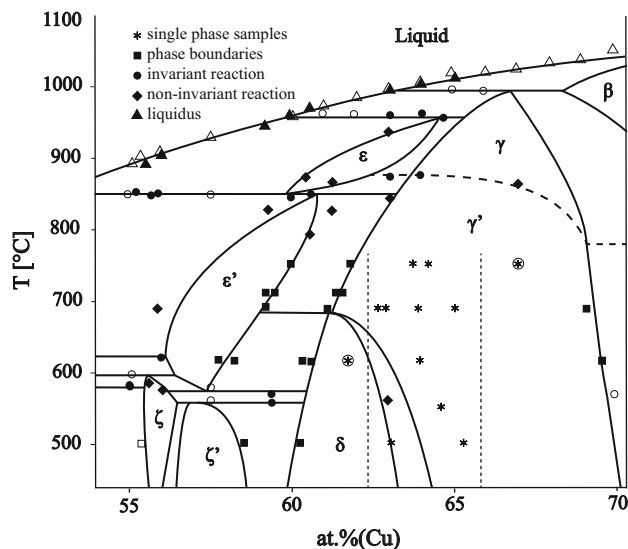


Fig. 7—Detail of the Al-Cu phase diagram in the δ/γ' region with superimposed experimental data.

The discrepancy between the SEM and XRD results may be explained by the fact that most of the samples investigated undergo the $\gamma' \rightarrow \delta$ phase transition during quenching. They were single phase γ' at the temperature of annealing but were forced to undergo a fast rhombohedral distortion during the quenching process. Such a transition is usually incomplete as the structure may distort locally, but diffusion is not fast enough to allow macroscopic phase separation. Thus, it is proposed that all samples located at compositions between the two dashed lines in Figure 7 were frozen in a state of structural transition between γ' and δ during the quenching process. The same is true for the sample at 64 at. pct Cu that had been annealed at 450 °C as reported in Reference 1. Using this hypothesis, it was possible to propose the location of the equilibrium two-phase field ($\gamma' + \delta$) as shown in Figures 2 and 7. It is strongly temperature dependent and shows a significant widening of the δ single phase field at lower temperatures.

D. High-Temperature Phase Transition Between γ' and γ

The γ -phase is formed by the peritectic reaction $L + \beta \leftrightarrow \gamma$ at 991 °C (Table IV, reaction 3). Ponweiser *et al.*^[1] defined the γ'/γ phase transition as second order because they did not observe any indication of an invariant reaction involving the γ and γ' -phases. This conclusion was based on DTA measurements and on earlier results that were published by Liu *et al.*^[3] The temperature stability of the γ' -phase has been described very well in the literature.^[1,3] The temperature of the $\gamma \leftrightarrow \gamma'$ second-order transition lies between 874 °C and 779 °C. The higher temperature, which corresponds to the transition $\gamma(\gamma') \leftrightarrow \gamma(\gamma') + \epsilon$, was established by,^[1] and this temperature was confirmed by the present DSC measurements (Table III samples 500_3, 550_4, 688_6).

The lower temperature, corresponding to the transition $\gamma(\gamma') \leftrightarrow \gamma(\gamma') + \beta$ (Table IV, reaction 8) results from DSC studies using heating and cooling rates of

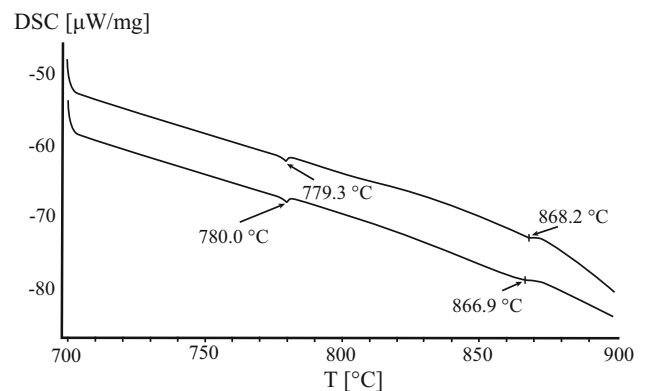


Fig. 8—DSC heating 2nd and 3rd curves of the Al-71.8 at. pct Cu sample. Signals correspond to the temperature of the ordering reaction $\gamma \leftrightarrow \gamma'$, (β) (779.6 °C) and to the phase transition $\beta \leftrightarrow \beta + \gamma$ (867.6 °C). Measurement conditions: inert atmosphere 5N Ar 50 mL min⁻¹, heating rate 1 °C min⁻¹.

1 °C min⁻¹ in this work. Figure 8 shows the corresponding DSC curves. The temperature of the ordering reaction $\gamma \leftrightarrow \gamma'$ at the phase boundary of the two-phase field is 779.6 °C.

E. Revised Complete Phase Diagram

By combining all of the experimental results listed in Tables II through IV it is possible to obtain a complete binary phase diagram of the Al-Cu system, which is presented in Figure 2, with details shown in Figures 4 and 7. It agrees well with the phase diagram published by Ponweiser *et al.*^[1] Liu *et al.*^[3] and Riani *et al.*^[24] but contains some additional clarification and improvement of areas which were not investigated in detail in the previous studies. The invariant reactions, together with the reaction temperatures and the compositions of the reacting phases are listed in Table IV. The proposed stable phase diagram should be used as a basis for further study, such as the effect of high pressures^[25] or strong magnetic fields^[26] on the Al-Cu binary phase diagram.

IV. CONCLUSION

Although literature relating to the Al-Cu phase diagram is numerous, some of the complex phase equilibria are not well defined. The current study was designed to contribute to a better understanding of those parts of the phase diagram that needed improvement and refinement, and also on the study of selected phase equilibria at 300 °C. This was achieved by a combination of standard methods: overall and phase compositions of samples were measured using SEM-EDX, the temperature of phase transitions by DSC or DTA and the crystal structures were identified by XRD.

The following main results were obtained in the study:

- The melting behavior of the θ -phase, which was uncertain owing to problems with modeling the liquidus curve in its vicinity by the CALPHAD approach, was confirmed to be peritectic in nature. A metastable congruent solidification of the θ -phase as proposed in Reference 11 was confirmed by microstructural analysis of the as-cast samples. The description of the liquidus curve in this region of the phase diagram was improved using slow-heating rates (1 °C min⁻¹) in the DSC studies.
- The temperature stability of the ζ -phase was reevaluated and was found to lie in the range 373 °C to 597 °C. The phase boundaries of the two-phase field $\gamma' + \varepsilon'$ were experimentally defined.
- The difficulties in defining the γ'/δ transition was addressed by a combined EDX/XRD investigation of more than ten samples that were annealed in the temperature range 500 °C to 750 °C. Although (similar to previous studies) it was not possible to determine the two-phase field between the γ' and δ phases directly, the shape of the ($\gamma' + \delta$) two-phase field could be postulated from the XRD studies of quenched samples.

- The temperature of the ordering reaction $\gamma \leftrightarrow \gamma'$, (β) was experimentally determined to be 779.6 °C.

All other parts of the Al-Cu phase diagram studied here were found to be in excellent agreement with the most recent previous descriptions.^[1,5]

ACKNOWLEDGMENTS

Open access funding provided by University of Vienna. This study was supported by the Austrian Science Fund (FWF) under the Lisa-Meitner Project M2293-N34. The authors thank Stephan Puchegger from the Department of Dynamic of Condensed Systems at the University of Vienna for the assistance with the SEM measurements.

OPEN ACCESS

This article is distributed under the terms of the Creative Commons Attribution 4.0 International License (<http://creativecommons.org/licenses/by/4.0/>), which permits unrestricted use, distribution, and reproduction in any medium, provided you give appropriate credit to the original author(s) and the source, provide a link to the Creative Commons license, and indicate if changes were made.

REFERENCES

1. N. Ponweiser, C.L. Lengauer, and K.W. Richter: *Intermetallics*, 2011, vol. 19, pp. 1737–46.
2. J.L. Murray: *Int. Met. Rev.*, 1985, vol. 30, pp. 211–34.
3. X.J. Liu, I. Ohnuma, R. Kainuma, and K. Ishida: *J. Alloy Compd.*, 1998, vol. 264, pp. 201–08.
4. V.T. Witusiewicz, U. Hecht, S.G. Fries, and S. Rex: *J. Alloy Compd.*, 2004, vol. 385, pp. 133–34.
5. S.M. Liang and R. Schmid-Fetzer: *CALPHAD*, 2015, vol. 51, pp. 252–60.
6. E.A. Owen and G.D. Preston: *Proc. Phys. Soc. Lond.*, 1924, vol. 36, pp. 14–49.
7. J.B. Friauf: *J. Am. Chem. Soc.*, 1927, vol. 49, pp. 3107–14.
8. E.E. Havinga: *J. Less-Common Met.*, 1972, vol. 27, pp. 187–93.
9. C. Hisatsune: *Mem. Coll. Eng., Kyoto Univ.*, 1934, vol. 8/2, pp. 74–91.
10. G.P. Kulbush: *J. Inst. Met.*, 1930, vol. 44, p. 485.
11. T. Goedecke and F. Sommer: *Z. Metall.*, 1996, vol. 87, pp. 581–86.
12. M. El-Boragy, R. Szepan, and K. Schubert: *J. Less-Common Met.*, 1972, vol. 29, pp. 133–40.
13. L.D. Gulay and B. Harbrecht: *Z. Anorg. Allg. Chem.*, 2003, vol. 629, pp. 463–66.
14. L.D. Gulay and B. Harbrecht: *J. Alloy Compd.*, 2004, vol. 367, pp. 103–08.
15. A.J. Bradley, H.J. Goldschmidt, and H. Lipson: *J. Inst. Met.*, 1938, vol. 63, pp. 149–62.
16. S. Westman: *Acta Chem. Scand.*, 1965, vol. 19, pp. 2369–72.
17. S.K. Seshadri and D.B. Downie: *Met. Sci.*, 1979, vol. 13, pp. 696–98.
18. Y. Funamizu and K. Watanabe: *Trans. Jpn. Inst. Met.*, 1971, vol. 12, pp. 147–52.
19. M. Van Sande, J. Van Landuyt, M. Avalos-Borja, G.T. Villaseñor, and S. Amelinckx: *Mater. Sci. Eng.*, 1980, vol. 46, pp. 197–73.
20. A.G. Dawson: *J. Inst. Met.*, 1937, vol. 61, pp. 197–204.

21. N. Kuwano, T. Doi, and T. Eguchi: *Trans. JIM*, 1977, vol. 18, pp. 807–15.
22. J. Gröbner: G. Effenberg Binary evaluations, MSI, Materials Science International Serviced GmbH, Stuttgart, 2004.
23. A. Kroupa: Institute of Physics of Materials, CAS, Brno. Czech Republic, unpublished research, 2019.
24. P. Riani, L. Arrighi, R. Marazza, D. Mazzone, G. Zanicchi, and R. Ferro: *J. Phase Equilib. Diff.*, 2004, vol. 25, pp. 22–52.
25. V.N. Danilenko, S.N. Sergeev, J.A. Baimova, G.F. Korznikova, K.S. Nazarov, R.K. Khisamov, A.M. Glezer, and R.R. Mulyukov: *Mater. Lett.*, 2019, vol. 236, pp. 51–55.
26. C.J. Li, R. Guo, S.Y. He, W.D. Xuan, X. Li, Y.B. Zhong, and Z.M. Ren: *J. Alloy Compd.*, 2019, vol. 776, pp. 353–56.

Publisher's Note Springer Nature remains neutral with regard to jurisdictional claims in published maps and institutional affiliations.

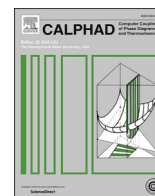
6.2 Paper 2

- [P2] Dinsdale A., **Zobač O.**, Kroupa A., Khvan A., *Use of third generation data for the elements to model the thermodynamics of binary alloy systems: Part 1 - The critical assessment of data for the Al-Zn system*, CALPHAD, 2019, 65, pp. 86-92, doi: 10.1016/j.calphad.2019.02.007 (IF 1.947)



Contents lists available at ScienceDirect

Calphad

journal homepage: <http://www.elsevier.com/locate/calphad>

Use of third generation data for the elements to model the thermodynamics of binary alloy systems: Part 1 – The critical assessment of data for the Al-Zn system

Alan Dinsdale^{a,*}, Ondrej Zobac^b, Ales Kroupa^c, Alexandra Khvan^d

^a Hampton Thermodynamics Limited, UK

^b Department of Inorganic Chemistry - Functional Materials, University of Vienna, Währinger Straße 42, 1090, Vienna, Austria

^c Institute of Physics of Materials, The Czech Academy of Sciences, Žitkova 22, 616 00, Brno, Czech Republic

^d Thermochemistry of Materials Scientific Research Centre, NUST MISIS, Leninskiy Prosp, 4, 119049, Moscow, Russia

ARTICLE INFO

Dedicated to Prof. Gerhard Inden in celebration of his 80th birthday

Keywords:

CALPHAD assessment

Al-Zn system

3rd generation unary data

Concentration dependence of the Einstein temperature

ABSTRACT

Over the last four years there has been a renewed interest in the development of new critically assessed data using physically based models. Nearly all work so far has been concerned with the critical assessment of data for the elements. This has involved the selection of Einstein or Debye temperatures for the stable crystalline phases and the liquid phase and associated parameters. However, until now, these data have not been extended in a comprehensive way to model the thermodynamic properties of binary, ternary and multicomponent systems. In this paper the way in which the parameters underlying these physical models vary with composition is explored. This includes a method to define the Einstein temperature for metastable phases of the elements and its relation to the so-called lattice stabilities used in the past, and the variation of the Einstein temperature with composition to account for the composition dependence of the excess entropy. This approach is demonstrated for the Al-Zn system which shows extensive regions of solid solution and complete miscibility in the liquid phase. Here Einstein temperatures are derived for Al in the HCP_ZN phase and Zn in the FCC_A1 phase together with parameters describing the variation of the Einstein temperature with composition for the HCP_ZN, FCC_A1 and liquid phases.

1. Introduction

There have been many developments recently in trying to explore the possibility of representing the thermodynamic properties of elements and binary alloy systems using physically based models. These have been developed based on the conclusions of a series of workshops held at Schloß Ringberg [1–3]. In the first Ringberg meeting the use of Debye and Einstein as a basis to represent the variation of the thermodynamic properties of crystalline phases with temperature was discussed, supplemented by additional contributions to take into account magnetic behaviour, anharmonicity, electronic effects and the conversion of heat capacity from constant volume to constant pressure. It was noted that the Einstein model is simpler to work with while the Debye model is capable of giving a more accurate description at very low temperatures. The approach has been used with some success for a number of elements [4–10]. A simplified approach had been applied by Refs. [11,12] using the Einstein model for the description of the thermodynamic behaviour

of pure elements below 298.15 K linked to the existing SGTE pure elements data.

There have been a limited number of attempts to use third generation data or similar to model the thermodynamic properties and phase diagrams of binary systems [13–17]. While the pure components and any intermetallic compounds were modelled using an Einstein or Debye model as a basis for the representation, none of the assessments attempted to express the variation of the Einstein or Debye temperature of the solution phases as a function of composition or to represent data for metastable phases of the pure components (lattice stabilities). This is one of the objects of this current paper.

1.1. Thermodynamic model for crystalline phases

According to the Einstein model the contribution to the heat capacity at constant volume from harmonic lattice vibrations is given by:

* Corresponding author.

E-mail address: alan@hamptonthermodynamics.co.uk (A. Dinsdale).

<https://doi.org/10.1016/j.calphad.2019.101723>

Received 13 September 2019; Received in revised form 28 November 2019; Accepted 15 December 2019

Available online 11 January 2020

0364-5916/© 2020 The Authors.

Published by Elsevier Ltd.

This is an open access article under the CC BY-NC-ND license

(<http://creativecommons.org/licenses/by-nc-nd/4.0/>).

$$C_v = 3R \left(\frac{\theta_E}{T} \right)^2 \frac{e^{\theta_E/T}}{(e^{\theta_E/T} - 1)^2} \quad (1)$$

where R ($\text{J}\cdot\text{mol}^{-1}\text{K}^{-1}$) is the gas constant, T (K) the temperature and θ_E (K) the Einstein temperature. It was recognised during the Ringberg meetings that the Einstein model did not give a good representation of the properties at very low temperatures; the more complicated Debye model would be significantly better in this region. However, in practice, the aspiration in the critical assessment of data is to obtain an exact representation of the thermodynamic properties eg. heat capacity at constant pressure and entropy, at 298.15 K and above, using a reliable model to provide an extrapolation of the Gibbs energy at temperatures down to 0 K. For temperatures above 298.15 K for nearly all elements the differences between the two models (Einstein or Debye) would be small. Additionally the Debye model would not provide a closed expression for the other thermodynamic properties such as the Gibbs energy, enthalpy or entropy, meaning that it would be considerably harder to use in practice.

Additional contributions, or correction terms, to the thermodynamic properties are necessary to account for magnetic contributions, anharmonicity, electronic effects and the conversion from C_v to C_p . With the exception of the magnetic contributions these can be represented satisfactorily by a power series in temperature.

In the absence of magnetic terms but with correction terms included, the expression for the heat capacity at constant pressure from the Einstein model becomes

$$C_p = 3R \left(\frac{\theta_E}{T} \right)^2 \frac{e^{\theta_E/T}}{(e^{\theta_E/T} - 1)^2} + aT + bT^2 + cT^3 + dT^4 \quad (2)$$

The Gibbs energy and the entropy can also be expressed as follows:

$$G = E_0 + \frac{3}{2}R\theta_E + 3RT \ln \frac{(e^{\theta_E/T} - 1)}{e^{\theta_E/T}} - \frac{a}{2}T^2 - \frac{b}{6}T^3 - \frac{c}{12}T^4 - \frac{d}{20}T^5 \quad (3)$$

$$S = 3R \left[\frac{\theta_E/T}{(e^{\theta_E/T} - 1)} - \ln \frac{(e^{\theta_E/T} - 1)}{e^{\theta_E/T}} \right] + aT + \frac{b}{2}T^2 + \frac{c}{3}T^3 + \frac{d}{4}T^4 \quad (4)$$

During the critical assessment of data the aim is to define the parameters a , b , c , d and θ_E to reproduce the known value for S_{298} and the heat capacity from 298.15 K to higher temperatures. It should be noted that the choice of terms in the correction function ensures that the entropy of each phase approaches zero at 0 K. It should also be emphasised that because the values for the heat capacity predicted by the Einstein model at very low temperatures are always too low relative to the experimental data, and the data need to be constrained to give exact values for the entropy at 298.15 K, the predicted value for the heat capacity at higher temperatures (eg. between 200 K and 300 K) will generally be higher than any experimental data.

At higher temperatures, eg. above the range where experimental data are available it is important to constrain any extrapolation to higher temperatures to prevent the entropy of the crystalline phase becoming higher than that of the liquid phase. The approach used currently was suggested by Chen and Sundman [5]. Here an extra temperature range is included for temperatures above the melting point with the general formula:

$$C_p = 3R \left(\frac{\theta_E}{T} \right)^2 \frac{e^{\theta_E/T}}{(e^{\theta_E/T} - 1)^2} + a' + b'T^{-6} + c'T^{-12} \quad (5)$$

The parameters a' , b' and c' are selected such that the heat capacity and its derivative are continuous at the melting point and merges with that of the liquid phase at some high temperature eg. 6000 K. However other approaches are under discussion [18].

1.2. Thermodynamic model for the liquid phase

The two-state model was adopted by the Ringberg workshops [1] as

providing the basis for future representation of the thermodynamic data for the liquid phase. According to this model the liquid can be thought of as consisting of two types of atoms existing in thermodynamic equilibrium, (a) *solid like atoms*, which would predominate at lower temperatures, and which would have similar thermodynamic properties to the stable crystalline phase and (b) *liquid like atoms*, which would tend to predominate at high temperatures, and be associated with more translational freedom. Other terms have been used to refer to these entities such as *translational* and *vibrational* atoms [10]. The advantage of this model is that it allows the liquid and amorphous phase to be modelled together over the whole temperature range without any artificial kink at the melting point. The two-state model was originally proposed by Agren [19].

The thermodynamic properties of the *liquid like* and *solid like atoms* could be presented separately. However, in practice, it is simpler to provide expressions for the Gibbs energy of the *solid like atoms* and, additionally, the difference between the Gibbs energy of the *liquid like atoms* and *solid like atoms*, ΔG_d . The total Gibbs energy of the liquid will be the sum of the Gibbs energies of the two types of atoms weighted by their relative proportions which will, of course, vary with temperature.

The Gibbs energy of the *solid like atoms* can be thought of as representing the amorphous solid and will therefore take a similar form to that for the crystalline phase.

$$G_{am} = E_0 + \frac{3}{2}R\theta_E + 3RT \ln \frac{(e^{\theta_E/T} - 1)}{e^{\theta_E/T}} + A + aT^2 + bT^3 \quad (6)$$

The Einstein temperature of the amorphous phase could be expected to be similar to that of the stable crystalline phase while fewer correction terms may be necessary.

The difference in Gibbs energy between the *liquid like* and *solid like atoms*, ΔG_d can be expressed as:

$$\Delta G_d = B + CT + DT \ln(T) \dots \quad (7)$$

For each temperature the *solid like* and *liquid like atoms* are in thermodynamic equilibrium and this results in a total Gibbs energy of the liquid phase of

$$G_{liq} = G_{am} - RT \ln \left[1 + \exp \left(- \frac{\Delta G_d}{RT} \right) \right] \quad (8)$$

The parameters θ_E , A , a , b , B , C and D may in principle be used in order to get best agreement with the experimental data. In practice the number of parameters used may be limited by the quantity of reliable experimental thermodynamic data available for the liquid phase.

2. Modelling of lattice stabilities using the Einstein model ie. differences in Gibbs energies between two phases of an element

One of the key pieces of information required in order to model phase diagrams and thermodynamic data for systems is the *so-called* lattice stability. By this we mean the difference in Gibbs energy between two phases of a given element. In principal this could be a constant value ie. independent of temperature, to reflect the difference in crystal structure and strength of bonds in the two phases. In practice, of course, the two phases would also have different Einstein temperatures leading to a difference in entropy between the two phases. It is worth exploring how this lattice stability concept can be adapted for use with the third generation data for the elements.

According to the traditional representation of thermodynamic properties

$$G^\beta = G^\alpha + A + BT \quad (9)$$

which gives a constant enthalpy difference of A between the two phases, α and β , and an entropy difference of $-B$.

Using the Einstein model without any correction terms the entropy S is given by

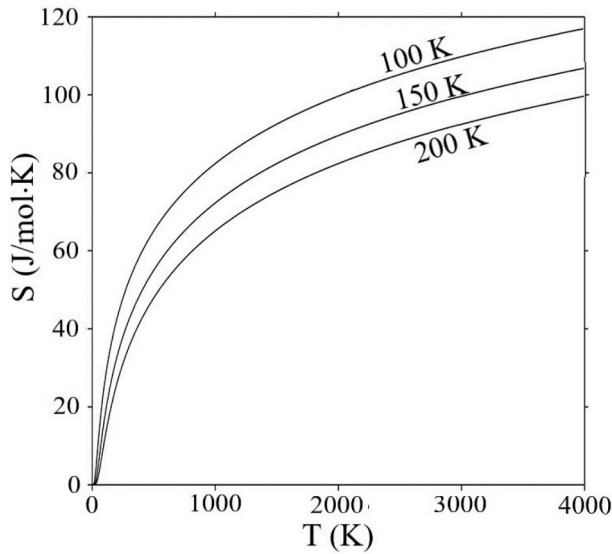


Fig. 1. Calculated entropy against temperature for different values of the Einstein temperature. As the temperatures increase, the curves become parallel.

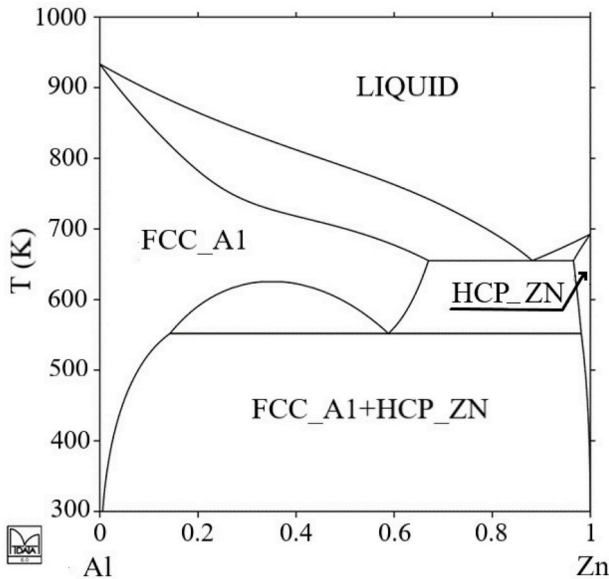


Fig. 2. Calculated phase diagram for the Al-Zn system using the critically assessed data of Mathon et al. [24].

$$S = 3R \left[\frac{\theta_E/T}{(e^{\theta_E/T} - 1)} - \ln \frac{(e^{\theta_E/T} - 1)}{e^{\theta_E/T}} \right] = 3R \left[\frac{\theta_E/T}{(e^{\theta_E/T} - 1)} - \ln(1 - e^{-\theta_E/T}) \right] \quad (10)$$

For high temperatures this can be simplified since

$$\frac{\theta_E/T}{(e^{\theta_E/T} - 1)} \rightarrow \frac{\theta_E/T}{1 + (\theta_E/T) + \frac{(\theta_E/T)^2}{2} + \frac{(\theta_E/T)^3}{6} + \dots - 1} \quad (11)$$

And this approaches a value of 1.
Furthermore at high temperatures

$$\ln(1 - e^{-\theta_E/T}) \rightarrow \ln \left(1 - 1 + \theta_E/T - \frac{(\theta_E/T)^2}{2} + \frac{(\theta_E/T)^3}{6} + \dots \right) \rightarrow \ln(\theta_E/T) \quad (12)$$

Therefore, at high temperatures the entropy, S , tends to approach

values defined by the following equation:

$$S = 3R (1 - \ln(\theta_E/T)) \quad (13)$$

The entropy difference between two phases, α and β , at high temperatures can now be expressed as:

$$\begin{aligned} S^\alpha - S^\beta &= 3R \left(1 - \ln\left(\frac{\theta_E^\alpha}{T}\right) \right) - 3R \left(1 - \ln\left(\frac{\theta_E^\beta}{T}\right) \right) \\ &= 3R \ln\left(\frac{\theta_E^\beta}{\theta_E^\alpha}\right) \end{aligned} \quad (14)$$

This means that the difference in entropy between the two phases will become constant at high temperatures. If we already have some knowledge of the entropy difference between two phases or we wish to retain the lattice stabilities used previously, this equation provides us with a way of estimating easily the Einstein temperature for a metastable phase.

The validity of equation (14) can be seen in Fig. 1 which shows the calculated entropy using different values of the Einstein temperature. At higher temperatures the entropy differences become constant.

3. Application of third generation unary data to binary systems

In the remainder of this paper we will focus on modelling the thermodynamic and phase diagram data for the Al-Zn system. The phase diagram for the system shows extensive solid solutions in both the FCC_A1 and HCP_ZN phases and complete mixing in the liquid phase. There is a miscibility gap in the fcc phase which provides an additional challenge in assessing the data for the system.

3.1. Review of published critical assessments of data

Various critical assessments of data for the Al-Zn system have been carried out using the CALPHAD approach [20–25]. The miscibility gap in the fcc solid solution has also been modelled [26] in the framework of the Bragg-Williams approximation combined with a simple Lennard-Jones type potential and reasonable agreement with the experiment was obtained. More recently [27] calculated the energies of mixing using first principle calculations giving results in good agreement with the CALPHAD assessments. The thermodynamic data recently critically assessed by Mathon et al. [24] were used in this work as being the most recent critical assessment using the Redlich-Kister model to represent the variation of thermodynamic properties with composition. They obtained excellent agreement with the bulk of the experimental data available. The phase diagram calculated using these data is shown in Fig. 2.

There is some small disagreement between the calculated miscibility gap in the fcc phase and the experimental data and a rather larger difference between the calculated enthalpies of mixing in the fcc phase and experimental data. The critical assessment of Wasiur-Rahman and Medraj [25] used the modified quasichemical model to represent the thermodynamic properties of the liquid phase. This added an extra level of complexity to the modelling of data for the system and was not considered further for this work.

3.2. Review of the experimental data for the Al-Zn system

The Al-Zn system has been studied intensively in the past because of its industrial importance. The phase diagram is dominated by complete mixing in the liquid phase and extensive ranges of solid solution in both the Al based fcc phase and the Zn based hcp phase. There is a single eutectic reaction in the system $\text{Liq} \rightarrow \text{FCC_A1} + \text{HCP_ZN}$ at 654 K (381 °C) with the relevant compositions $x_{\text{Zn}}^{\text{Liq}} = 0.887$, $x_{\text{Zn}}^{\text{FCC_A1}} = 0.670$ and $x_{\text{Zn}}^{\text{HCP_ZN}} = 0.972$ [28]. The thermodynamic behaviour of the FCC phase deviates positively from an ideal solution, resulting in the

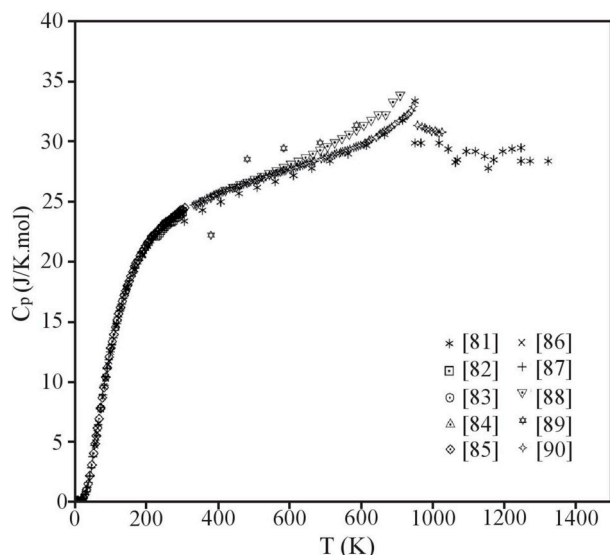


Fig. 3. Experimental heat capacity data for Al [81–90].

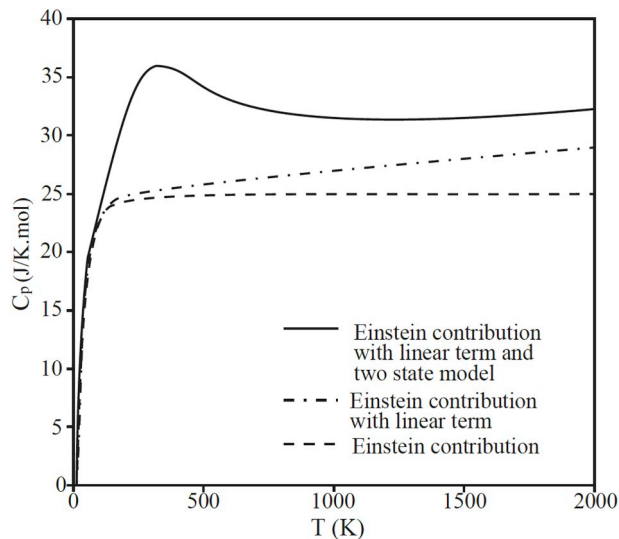


Fig. 4. Different contributions to the heat capacity of the liquid phase.

formation of a miscibility gap at low temperatures with a critical temperature of 624.7 K at $x_{\text{Zn}}^{\text{FCC,Al}} = 0.395$ [28,29].

The first critical review of experimental phase diagram information was carried out by Hansen and Anderko [29]. It was pointed out that phase boundaries and equilibria in this system published before 1932 were obsolete, apart from the liquidus lines. Hansen and Gayler [30], Ishihara [31], and Tanabe [32] expected to find evidence for a peritectic reaction but this was shown by Hansen and Anderko [29] to be incorrect. They identified an fcc miscibility gap which closes at 624.7 K. The results were extensively reviewed by Murray [28] and Okamoto [33,34] who also included consideration of newer experimental data. The liquidus surface has been determined by several authors [31,32,35–42]. The solidus curve in the (Al) solid solution region has been investigated by Refs. [30–32,37,40,41,43–52]. The solubility of Zn in (Al) has been measured by Refs. [29,53–56] and Schmid [57], who determined the lattice parameters by x-ray diffractometry. Resistometric measurements and metallographic investigations were carried out by Fink et al. [58] to determine the solubility up to 64.4 at% Zn. Further data concerning the phase boundaries in the (Al)–rich region have been published by Refs. [45,50,52,59–65]. Using several different experimental methods, the

solubility of Al in (Zn) has been determined by Refs. [31,32,53–56,66,67]. The spinodal curve within the fcc miscibility gap was determined by differential scanning calorimetry [68].

The experimental phase diagram in Massalski [69] is based on experimental phase boundaries reported in more than twenty of the above mentioned papers. It agrees very well with more recent observations of [70–72].

The thermodynamic properties of the system have also been measured by many authors. The thermodynamic activities in the liquid were measured e.g. by Balanovic et al. [73], who measured the thermodynamic properties calorimetrically at 1000 K using the Oelsen method. These results are in good agreement with older works [74,75]. Integral enthalpies of formation of solid alloys (FCC phase) have been determined at 643 K (370°C) by solution calorimetry in liquid Zn as a solvent by Wittig and Schoeffl [76]. Extensive calorimetric measurements were carried out by Debski et al. [77]. They measured the integral molar mixing enthalpy of Al–Zn liquid solutions by means of drop calorimetry at 957 K and 1001 K, and their results are in good agreement with those of Wittig and Schoeffl [76]. Debski et al. [77] also measured the integral mixing enthalpy by means of drop calorimetry and also evaluated the excess Gibbs energy of liquid phase at 1000 K, and the mixing entropy of the liquid phase at $T = 1000$ K. The excess entropy of formation of the fcc solid solution at 653 K were calculated from experimental data by Hultgren et al. [75]. The data of Debski et al. [77] are higher than those of Hultgren et al. [75], but similar to the data calculated by Miedema [78] who used a semi-empirical model for the estimation of the integral mixing enthalpy. The data for the entropy of mixing data derived by Debski et al. [77] are symmetrical with respect to the concentration and those evaluated by Hultgren et al. [75] are asymmetrical with the maximum for $x_{\text{Zn}} = 0.6$. Enthalpy of mixing and entropy of mixing have been measured by Hillard et al. [79] at 300°C and 380°C over the whole composition range.

4. Data for Al and Zn and the derivation of lattice stabilities

The data for the HCP_ZN and liquid phases of Zn have recently been assessed by Dinsdale and Khvan [80]. A value of 162.2 K was derived for the Einstein temperature for the HCP_ZN phase.

The data for FCC_Al Al, including the Einstein temperature, were based on those derived by Bigdeli [8] who assessed a value of 294.414 K for the Einstein temperature. It was felt that the assessment of Bigdeli for the liquid phase of Al did not correspond to the spirit of the two state model in that the *liquid like* atoms were not predicted to predominate at high temperatures. As a result new data were derived for the liquid phase above the melting point. Fig. 3 shows the experimental heat capacity data for crystalline and liquid phases. Most of the assessments of data for liquid Al assumed a constant heat capacity obtained from enthalpy drop measurements and the aim of the present assessment is to reproduce these data.

It is worth describing in some detail here the process of assessing the data for the liquid Al. The aim behind using the two state model for the liquid phase is to provide a dataset with some greater semblance of physical reality than could be achieved using a simple power series expression in temperature. As explained earlier the Gibbs energy using two state model has two contributions, (a) data for the *solid like* atoms represented as the amorphous state described using the extended Einstein equation:

$$G_{\text{am}} = E_0 + \frac{3}{2}R\theta_E + 3RT \ln \frac{(e^{\theta_E/T} - 1)}{e^{\theta_E/T}} + A + aT^2 + bT^3 \quad (15)$$

And data for the difference in Gibbs energy between the *liquid like* atoms and the *solid like* atoms:

$$\Delta G_d = B + CT + DT \ln(T) \dots \quad (16)$$

Because there are several parameters to be derived for the phase there is the possibility that many sets of parameters will give acceptable

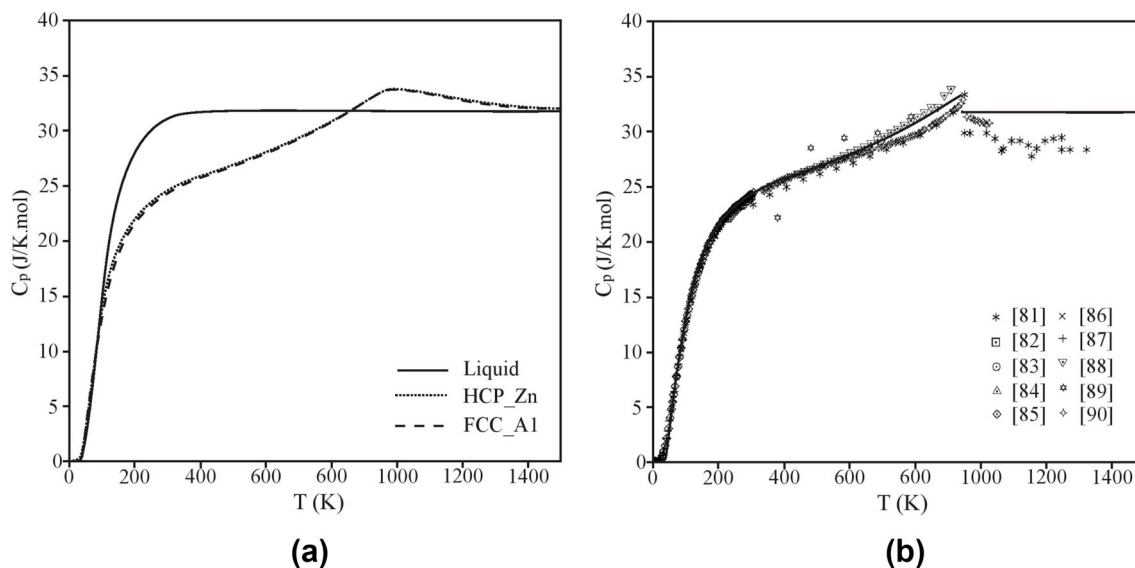


Fig. 5. a: Modelled heat capacity for the FCC_A1, HCP_ZN and liquid phases of Al. **5b:** Comparison of calculated heat capacity of Al using the new dataset and the experimental data.

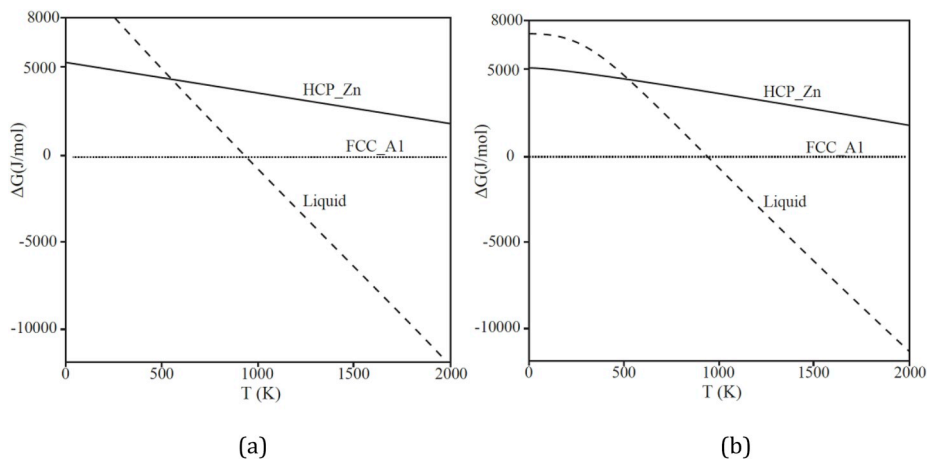


Fig. 6. Variation of the Gibbs energy of hcp and liquid phases of Al with temperature relative to FCC_A1 (a) using data from Ref. [91] (b) using the data derived in this paper.

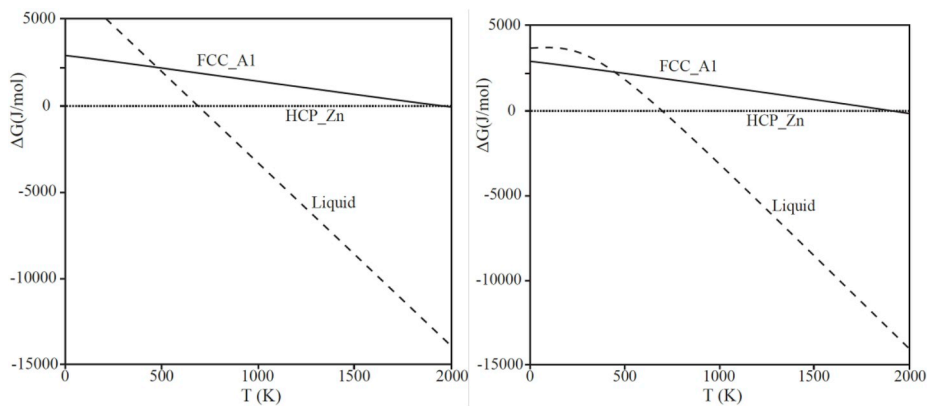


Fig. 7. Variation of the Gibbs energy of FCC_A1 and liquid phases of Zn with temperature relative to HCP_ZN (a) using data from Ref. [91] (b) using the data derived in this paper.

Table 1

The interaction parameters for the Al-Zn system according to Ref. [24].

L_0	$7298.94 + 0.47531 * T$
L_1	$6612.875 - 4.592 * T$
L_2	$-3097.93 + 3.30635 * T$

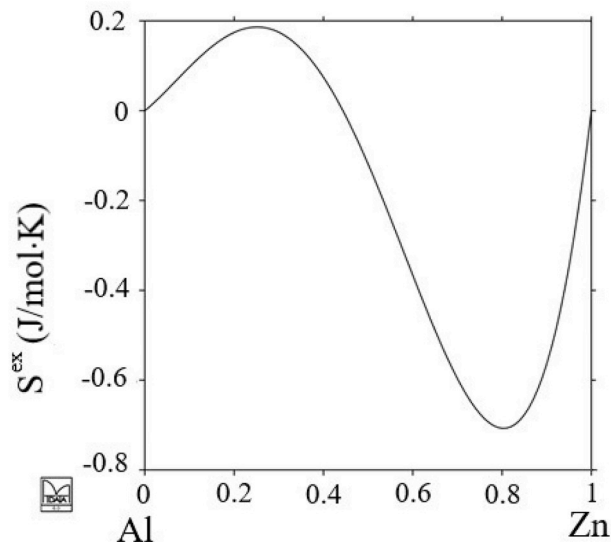


Fig. 8. Excess entropy of FCC_A1 phase in Al-Zn system from the assessment of Mathon et al. [24].

Table 2

The interaction parameters for the FCC_A1 phase in the Al-Zn system developed in the scope of this work.

L_0	7298.94
L_1	6612.875
L_2	-3097.93
$\ln \theta_0$	0.01905544
$\ln \theta_1$	-0.18409584
$\ln \theta_2$	0.13255341

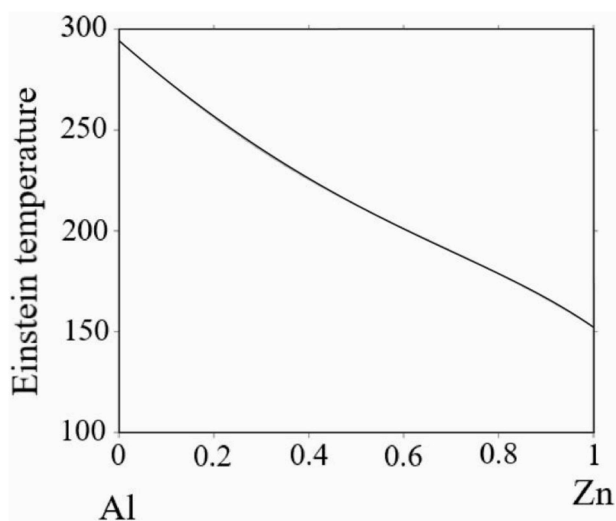


Fig. 9. Variation of the Einstein temperature of the FCC_A1 phase in the Al-Zn system with composition.

fits to the experimental data. Not all of them will be in accordance with the spirit of the two state model in ensuring the *liquid like* atoms predominate at high temperatures and the *solid like* atoms predominate at lower temperatures. This can be achieved by limiting the number of parameters used and ensuring that ΔG_d in equation (16) changes from positive to negative in the vicinity of the melting point of the element.

Fig. 4 shows the effect of the different contributions to the heat capacity of the liquid phase. The heat capacity of the amorphous phase is based on the Einstein contribution where the Einstein temperature may be assumed to be close to or even the same as that of the stable crystalline phase. If there is evidence of a temperature dependence (eg. the dash-dot curve in Fig. 4) of the liquid heat capacity at high temperatures this would best be incorporated into the correction term for the heat capacity of the *solid like* atoms eg. using parameters a and b in equation (15). The solid line curve in Fig. 4 represents the total modelled heat capacity. The maximum in this heat capacity is a consequence of the equilibrium between the *solid like* and *liquid like* atoms. Similar effects can be seen in changes in heat capacity arising from electronic excitations in gaseous species or bond breaking eg. associated with monomer to dimer equilibria. The difference between the solid curve and the dash-dot curve in Fig. 4 is best modelled by the D term in equation (16). Having defined the parameters θ_E , a, b and D in equations (15) and (16), the remaining parameters A, B and C can be optimised in order to give the required values for the entropy of the liquid phase at the melting point.

In the specific case of Al, the assessed constant heat capacity of the liquid phase is $31.75 \text{ J K}^{-1} \text{ mol}^{-1}$. Because the heat capacity is constant the parameters a and b in equation (15) can be set to 0. Parameter D represents the difference between $3R$, the Einstein contribution to the heat capacity, and the assessed liquid heat capacity ie. $D = -6.81347$.

Mathon et al. [24], in their assessment of data for the Al-Zn system, used the data for Al from Dinsdale [91]. In this work the lattice stability of HCP_ZN Al relative to FCC_A1 Al is (for simplification we omit the subscript E in the symbol for the Einstein temperature in following equations):

$$G_{Al}^{hcp-Zn} = G_{Al}^{fcc-A1} + 5481 - 1.8 T \quad (17)$$

According to the equation derived earlier

$$S^{fcc} - S^{hcp} = 3R \ln \left(\frac{\theta^{hcp-Zn}}{\theta^{fcc-A1}} \right) \quad (18)$$

and consequently

$$\theta^{hcp-Zn} = \theta^{fcc-A1} e^{((S^{fcc-A1} - S^{hcp-Zn})/3R)} \quad (19)$$

The additional contributions to the heat capacity for FCC_A1 Al were assumed to apply for HCP_ZN Al.

Fig. 5a and b shows the new modelled heat capacity for the FCC_A1, HCP_ZN and liquid phases of Al.

It is worth comparing the new Gibbs energy differences between the three phases with those used up until now for the critical assessment of data for Al systems. Fig. 6a shows the diagram from the SGTE recommended data [91] extrapolated down to 0 K while Fig. 6b shows the equivalent using the data derived in this paper. It is apparent that the curves are almost identical except for the low temperature region where, in the data derived in this paper, the curves become parallel as the entropy of each phase tends towards a value of zero.

The corresponding curves for the variation of the difference in Gibbs energy of the FCC_A1 and liquid phases of Zn relative to the stable HCP_ZN phase using the new description and the data from Ref. [91] are shown in Fig. 7. Again there are no significant differences between the curves.

The Einstein temperature of FCC_A1 Zn was derived in the same manner as described for HCP_ZN Al. The entropy contribution to the lattice stability for FCC_A1 Zn was converted into an Einstein temperature for the phase using equation (19). The additional contributions to

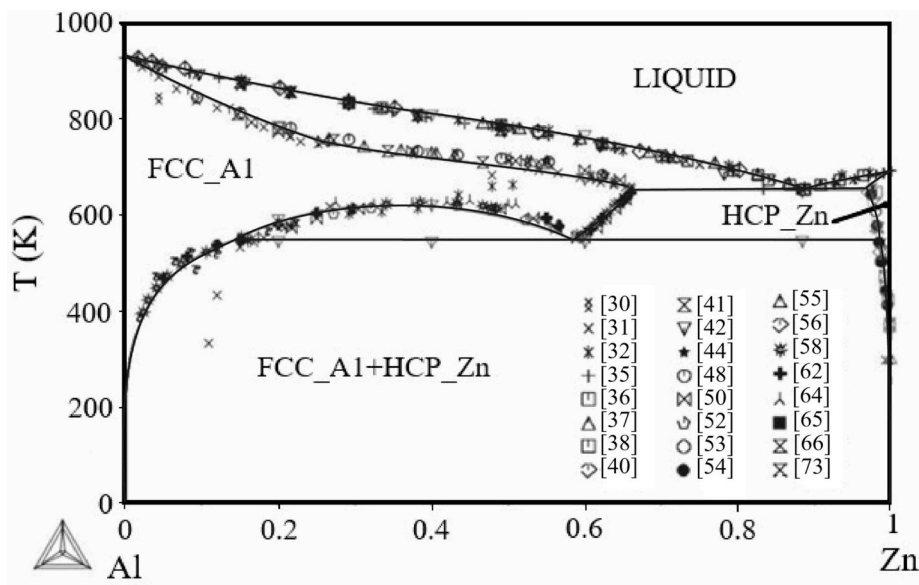


Fig. 10. Calculated phase diagram for the Al-Zn system using the coefficients derived in this paper with the experimental data superimposed.

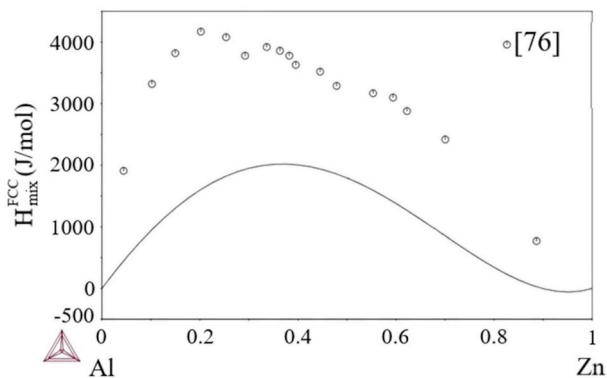


Fig. 11. Calculated enthalpies of mixing at 643 K in the FCC_Al phase of the Al-Zn system using the coefficients derived in this paper with the experimental data of Wittig and Schoeffl [76] superimposed.

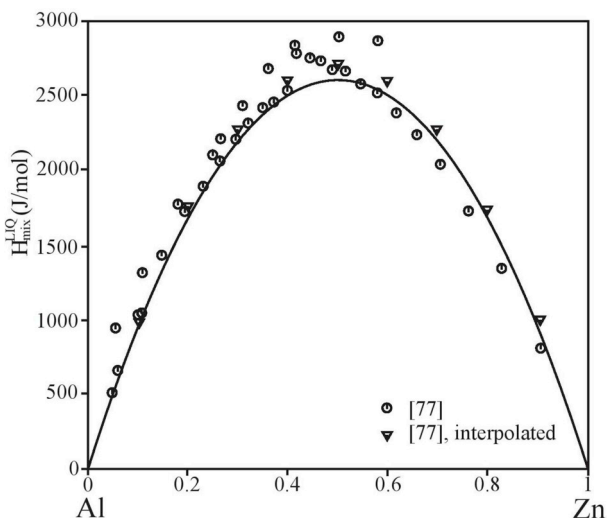


Fig. 12. Calculated enthalpies of mixing in the liquid phase of the Al-Zn system at 1000 K using the coefficients derived in this paper with the experimental data of Debski et al. [77] superimposed.

the heat capacity for HCP_ZN Zn were assumed to apply for FCC_Al Zn.

5. Composition dependence of the thermodynamic properties

While thermodynamic data for a number of elements have now been critically assessed using an extended Einstein model for the crystalline phases and a two state model for the liquid phase, considerably less effort has been devoted to the variation of the parameters for these models with composition. Few assessments of binary system have been published using these new models. Tolochko and Agren [4] assessed data for the Fe-B system but they were concerned mainly with the liquid phase and did not consider any variation of the Einstein temperature with composition for the crystalline phases. More recently Bigdeli and Selleby [13] assessed data for the Fe-Mn system using recently published data for the two pure elements. In this work the authors did not explicitly include any variation of the Einstein temperature with composition but did include temperature dependent parameters to express the variation of the excess Gibbs energy with composition. These imply that the non-configurational entropy of the solid solutions would not be zero at 0 K which does not seem to be consistent with the aspiration underlying the use of new physically based models.

In this paper we have attempted to extend the description of the thermodynamic properties of the elements into the Al-Zn binary in a logical and consistent manner such that there are no excess entropy terms *per se* i.e. any temperature dependence of the excess Gibbs energy of the fcc, liquid and hcp phases result from variations of the Einstein temperature with composition. This implies that there are no non-configurational contributions to the entropy of mixing of a solution phase at 0 K. This involves some extension of the equations developed earlier to derive the Einstein temperatures of metastable phases of the elements.

By definition the excess entropy for a solution phase between components A and B can be written as

$$S^{ex} = S - x_A S_A - x_B S_B - S^{id} \quad (20)$$

where S^{ex} is the excess entropy, S is the entropy of the solution phase, S_A and S_B are the entropies of the pure components, S^{id} the ideal entropy of mixing and x_A and x_B their mole fractions.

As shown earlier (equation (13)) the contribution to the entropy of a pure element at high temperatures using Einstein model can be simplified to:

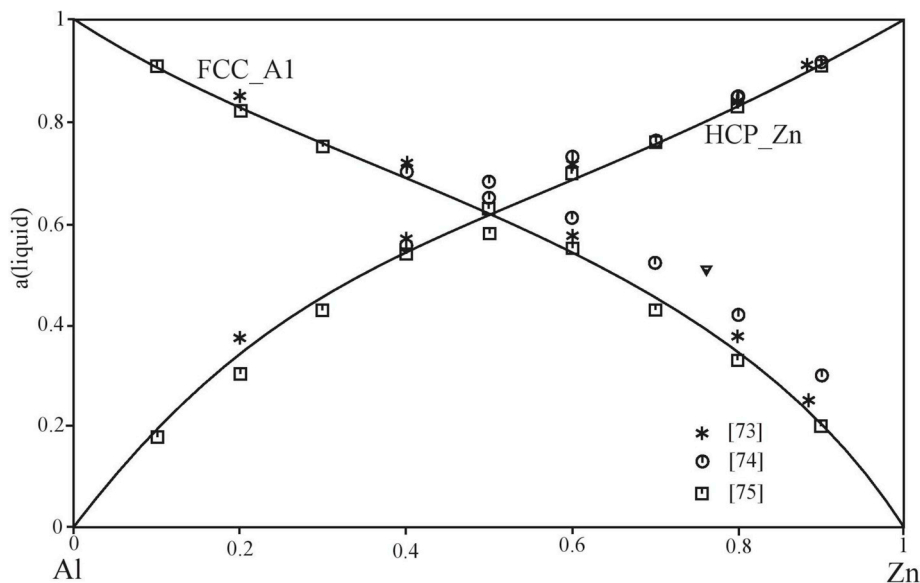


Fig. 13. Calculated activities in the liquid phase of the Al-Zn system at 1000 K using the coefficients derived in this paper with the experimental data of Balanovic et al. [73] and Yazawa [74] superimposed. Also included are the assessed values from Hultgren et al. [75].

$$S = 3R(1 - \ln(\theta/T)) \quad (21)$$

By combining equations (20) and (21) we obtain:

$$S^{ex} = 3R((1 - \ln(\theta_M/T)) - x_A[3R(1 - \ln(\theta_A/T))] - x_B[3R(1 - \ln(\theta_B/T))]) \quad (22)$$

where θ_M is the Einstein temperature appropriate for the composition x_A, x_B .

$$= 3R(1 - x_A - x_B) + 3R(\ln T - x_A \ln T - x_B \ln T) - 3R(\ln \theta_M - x_A \ln \theta_A - x_B \ln \theta_B) \quad (23)$$

On simplification this gives

$$S^{ex} = -3R(\ln \theta_M - x_A \ln \theta_A - x_B \ln \theta_B) \quad (24)$$

The mixing properties of a solution phase are commonly expressed in terms of a Redlich-Kister power series eg.

$$G^{ex} = x_A x_B (L_0 + L_1(x_A - x_B) + L_2(x_A - x_B)^2 + \dots) \quad (25)$$

$$S^{ex} = x_A x_B (S_0 + S_1(x_A - x_B) + S_2(x_A - x_B)^2 + \dots) \quad (26)$$

$\ln \theta^{ex}$ can also be expressed in terms of a Redlich Kister power series

$$\ln \theta^{ex} = x_A x_B (\ln \theta_0 + \ln \theta_1(x_A - x_B) + \ln \theta_2(x_A - x_B)^2 + \dots) \quad (27)$$

and $\ln \theta$ by

$$\ln \theta = x_A \ln \theta_A + x_B \ln \theta_B + x_A x_B (\ln \theta_0 + \ln \theta_1(x_A - x_B) + \ln \theta_2(x_A - x_B)^2 + \dots) \quad (28)$$

A comparison of equation (28) and equations (24) and (26) shows that the coefficients for the excess entropy, S_0, S_1, S_2 , etc can be related directly to the coefficients for the variation of $\ln \theta$ with composition.

eg.

$$\ln \theta_0 = -S_0/3R, \quad \ln \theta_1 = -S_1/3R, \quad \ln \theta_2 = -S_2/3R, \quad \text{etc.} \quad (29)$$

So, in the critical assessment of data for the Al-Zn system by Mathon et al. [24], the data for the fcc phase are in Table 1:

It is necessary to retain parameters to express the variation of the enthalpy of mixing (the first part of the parameters L_0, L_1 and L_2). The second part of the L_0, L_1 and L_2 parameters, expressing the temperature dependence, are transformed into parameters expressing the variation of

the Einstein temperature with composition.

The excess entropy calculated using these data is shown in Fig. 8. The effect is quite pronounced.

These coefficients can now be replaced by values shown in Table 2:

It is quite interesting to see the resulting variation of the Einstein temperature with composition. This is shown in Fig. 9. The Einstein temperatures for FCC_A1 Al and FCC_A1 Zn are, respectively, 294.414 K and 152.307 K. If there had been no excess entropy of mixing in the fcc phase the natural logarithm of the Einstein temperatures would have varied linearly with composition. This would have resulted in slightly nonlinear behaviour in the variation of the Einstein temperature itself. The variation in the Einstein temperature derived above gives a somewhat more pronounced effect as shown in Fig. 9.

6. Calculated phase diagram and thermodynamic properties

The data derived in the paper are essentially nearly identical in effect to the assessment of Mathon et al. [24]. The data for the crystalline elements and the solid solution phases should be almost exactly the same for the temperatures of interest. The data for the liquid phase, because they are now based on the two state model, could differ from the previous assessment. Therefore it is necessary to calculate the phase diagram and thermodynamic properties for the system to compare them with the available experimental data. Fig. 10 shows the calculated phase diagram which is very good agreement with almost all the experimental data. There is some slight discrepancy associated with the closure of the miscibility gap in the fcc phase. Fig. 11 shows the calculated enthalpies of mixing in the fcc phase. Here there is an obvious discrepancy between the assessed values and the experimental data of Wittig and Schoeffl [76]. As mentioned above, this discrepancy exists also for the original assessment of [24]. Fig. 12 shows the calculated enthalpies of mixing in the liquid phase with the experimental data of Debski et al. [77] superimposed. The agreement is very good. Finally in Fig. 13 is shown the calculated activities of the components in the liquid phase at 1000 K compared with the experimental data of Balanovic et al. [73] and Yazawa and Lee [74] and the assessed data of Hultgren et al. [75].

7. Conclusions

In this paper it was shown how the composition dependence of the thermodynamic properties for the liquid phase and solid solution phases

could be expressed simply using the more physically based 3rd generation models now under development. It was shown that a simple transformation of the entropy difference between two crystalline phases can be expressed in terms of a ratio of 2 E temperatures. Similarly the composition dependence of the excess entropy of mixing could be simply transformed into a variation of the log of the Einstein temperature. Using this approach thermodynamic and phase diagram data for the Al-Zn system were critically evaluated. An almost exact correspondence was found between the calculated results using the new models and data and, what we considered to be, the most reliable published assessment. Future work will explore this approach to systems where the component elements have significantly different melting points such as the Al-Si, Al-Sn and Si-Zn systems.

Data availability

Values of the processed database required to reproduce these findings are available as a supplementary material. Database in TDB format will be sent on request.

Declaration of competing interest

The authors are not aware of any conflict of interest in relation to this publication.

Acknowledgement

This study was supported by the Austrian Science Found (FWF) under the Lisa-Meitner project M2293-N34, the project of the Czech Science Foundation No 18-25660J, SGTE and the Ministry of Science and Higher Education of the Russian Federation in the framework of Increased Competitiveness Program of NUST « MISiS» (N^o K2-2019-003), implemented by a governmental decree dated 16th of March 2013, N 211. Collaboration within the 3rd generation unary project organized by the Department of Materials Science and Engineering at KTH Royal Institute of Technology, Stockholm, Sweden is gratefully acknowledged.

Appendix A. Supplementary data

Supplementary data to this article can be found online at <https://doi.org/10.1016/j.calphad.2019.101723>.

Appendix. Implementation of the Einstein model and the two state model in TDB files

The implementation of the new models within TDB files has not, to the knowledge of the authors, been documented, although the models have been implemented in ThermoCalc and PyCalphad. This appendix aims to provide some pointers.

Einstein Temperature

In the TDB file the Einstein temperature, or rather, the natural logarithm of the Einstein temperatures is entered through the parameter THETA.

Eg. PARAMETER THETA(FCC_A1,AL,VA; 0) 1 LN(294.414); 6000 N ! defines the Einstein temperature of pure Al in the fcc phase to be 294.414 K.

The composition dependence of the natural logarithm of the Einstein temperature is given in the same way.

PARAMETER THETA(FCC_A1,AL,ZN,VA; 0) 1 0.01905544; 6000 N !
PARAMETER THETA(FCC_A1,AL,ZN,VA; 1) 1-0.18409584; 6000 N !
PARAMETER THETA(FCC_A1,AL,ZN,VA; 2) 1 0.13255341; 6000 N !

The two state model for the Liquid phase

The two state model in the TDB file has two sets of parameters: PARAMETER G(LIQUID,AL; 0) or PARAMETER L(LIQUID,AL,ZN; 0). and.

PARAMETER GD(LIQUID,AL; 0) etc.

The G and L parameters can best be thought of in terms of the *solid like* atoms, while the GD parameters can be thought of as the difference in Gibbs energy between the *liquid like* atoms and the *solid like* atoms.

References

- [1] J. Ågren, B. Cheynet, M.T. Clavaguera-Mora, J. Hertz, F. Sommer, U. Kattner, Group 2: extrapolation of the heat capacity in liquid and amorphous phases, CALPHAD 19/4 (1995) 449–480.
- [2] M.W. Chase, I. Ansara, A.T. Dinsdale, G. Grimvall, L. Hoglund, H. Yokokawa, Group 1: heat capacity models for crystalline phases from 0 K to 6000 K, CALPHAD 19 (1995) 437.
- [3] B. Sundman, F. Aldinger, The Ringberg workshop 1995 on unary data for elements and other end-members of solutions, CALPHAD 19/4 (1995) 433–436.
- [4] O. Tolochko, J. Ågren, Thermodynamic properties of supercooled Fe-B liquids-A theoretical and experimental study, J. Phase Equilibria 21/1 (2000) 20–24.
- [5] Q. Chen, B. Sundman, Modeling of thermodynamic properties for BCC, FCC, liquid and amorphous iron, J. Phase Equilibria 22/6 (2001) 631–644.
- [6] C.A. Becker, J. Ågren, M. Baricco, Q. Chen, S.A. Deckerov, U.R. Kattner, J. H. Perepezko, G.R. Pottlacher, M. Selleby, Thermodynamic modelling of liquids: CALPHAD approaches and contributions from statistical physics, Phys. Status Solidi B 251/1 (2014) 33–52.
- [7] S. Bigdeli, H. Mao, M. Selleby, On the third-generation Calphad databases: an updated description of Mn, Phys. Status Solidi B 252/10 (2015) 2199–2208.
- [8] S. Bigdeli, PhD thesis, KTH Royal Institute of Technology, Stockholm Sweden 2017.
- [9] A.V. Khvan, A.T. Dinsdale, I.A. Uspenskaya, M. Zhilin, T. Babkina, A.M. Phiri, A thermodynamic description of data for pure Pb from 0 K using the expanded Einstein model for the solid and the two state model for the liquid phase, CALPHAD 60 (2018) 144–155.
- [10] A.V. Khvan, T. Babkina, A.T. Dinsdale, I.A. Uspenskaya, I.V. Fartushna, A. I. Druzhinina, A.B. Syzdykova, M.P. Belov, I.A. Abrikosov, Thermodynamic properties of tin: Part I Experimental investigation, ab-initio modelling of α -, β -phase and a thermodynamic description for pure metal in solid and liquid state from 0 K, CALPHAD 65 (2019) 50–72.
- [11] J. Vřešťál, J. Štof, J. Pavlů, Extension of SGTE data for pure elements to zero kelvin temperature-A case study, CALPHAD 37 (2012) 37–48.
- [12] J. Pavlů, P. Řehák, J. Vřešťál, M. Šob, Combined quantum-mechanical and calphad approach to description of heat capacity of pure elements below room temperature, CALPHAD 51 (2015) 161–171.
- [13] S. Bigdeli, M. Selleby, A thermodynamic assessment of the binary Fe-Mn system for the third generation of Calphad databases, CALPHAD 64 (2019) 185–195.
- [14] J. Vřešťál, J. Pavlů, U.D. Wdowik, M. Šob, Modelling of phase equilibria in the Hf-V system, J. Min. Metall. Sect. B Metall. 53/3 (2017) 239–247.
- [15] Y. Jiang, S. Zomorodpoosh, I. Roslyakova, L. Zhang, Thermodynamic re-assessment of binary Cr-Nb system down to 0 K, Calphad 62 (2018) 109–118.
- [16] Y. Jiang, S. Zomorodpoosh, I. Roslyakova, L. Zhang, Thermodynamic re-assessment of the binary Cr-Ta system down to 0 K, Int. J. Mater. Res. 110/9 (2019) 797–807.
- [17] M.H.G. Jacobs, R. Schmid-Fetzer, A.P. van den Berg, Phase diagrams, thermodynamic properties and sound velocities derived from a multiple Einstein method using vibrational densities of states: an application to MgO-SiO₂, Phys. Chem. Miner. 44 (2017) 43–62.
- [18] B. Sundman, U.R. Kattner, S. Bigdeli, Q. Chen, A.T. Dinsdale, B. Hallstedt, M. Hillert, A.V. Khvan, H. Mao, R. Otis, M. Selleby, J. Ågren, To Be Submitted for Publication, 2019 “A Method for Handling the Extrapolation of the Thermodynamic Properties of Solid Phases above Their Melting Temperature”.
- [19] J. Ågren, Thermodynamics of supercooled liquids and their glass transition, Phys. Chem. Liq. Intl J. 18/2 (1988) 123–139.
- [20] S. Mey, G. Effenberg, A thermodynamic evaluation of the aluminum-zinc system, Z. Metallkd. 77/7 (1986) 449–453.
- [21] S.L. Chen, Y.A. Chang, A thermodynamic analysis of the Al-Zn system and phase diagram calculation, CALPHAD 17/2 (1993) 113–124.
- [22] S. Mey, Reevaluation of the Al-Zn system, Z. Metallkd. 84/7 (1993) 451–455.
- [23] H. Adachi, K. Osamura, H. Okuda, Metastable phases in Al-Zn-Mg ternary based alloys, Nippon Kinzoku Gakkaiishi 63/6 (1999) 733–740.
- [24] M. Mathon, K. Jardet, E. Aragon, P. Satre, A. Sebaoun, Al-Ga-Zn system: reassessments of the three binary systems and discussion on possible estimations and on optimisation of the ternary system, CALPHAD 24/3 (2000) 253–284.
- [25] S. Wasiur-Rahman, M. Medraj, A thermodynamic description of the Al-Ca-Zn ternary system, CALPHAD 33/3 (2009) 584–598.
- [26] J. Holender, R. Kozubski, J. Soltys, Miscibility gap modelling in the alpha phase of Al-Zn, Z. Metallkd 78/12 (1987) 836–840.
- [27] E.A. Smirnova, P.A. Korzhavyi, Y.K. Vekilov, B. Johansson, I.A. Abrikosov, Electronic topological transitions and phase stability in the fcc Al-Zn alloys, Eur. Phys. J. B 30/1 (2002) 57–66.
- [28] J. Murray, The Al-Zn system, Bull. Alloy Phase Diagr. 4/1 (1983) 55–73.

- [29] M. Hansen, K. Anderko, *Constitution of Binary Alloys*, McGraw-Hill, New York, 1958.
- [30] D. Hanson, M.L. Gayler, Further study of the alloys of aluminium and zinc, *J. Inst. Med.* 27 (1922) 267–294.
- [31] T. Ishihara, On the Equilibrium Diagram of the Aluminum-Zinc System, vol.13, Science Reports of the Tohoku Imperial University, 1924, pp. 18–21.
- [32] T. Tanabe, Studies in the aluminium-zinc system, *J. Inst. Med.* 32 (1924) 415.
- [33] H. Okamoto, Comment on Al-Zn (Aluminum-Zinc), *J. Phase Equilibria* 15/1 (1994) 125–126.
- [34] H. Okamoto, Al-Zn (Aluminum-Zinc), *J. Phase Equilibria* 16/3 (1995) 281–282.
- [35] C.T. Heycock, F.H. Neville, The freezing points of alloys containing zinc and another metal, *J. Chem. Soc.* 71 (1897) 383–422.
- [36] M.L. Fuller, R.L. Wilcox, Phase changes during aging of zinc-alloy die castings, II changes in the solid solution of aluminum in zinc and their relation to dimensional changes, *T. Metall. Soc. AIME* 122 (1936) 231–243.
- [37] M.L.V. Gayler, M. Haughton, E.G. Sutherland, The constitution of aluminum-zinc alloys of high purity: the nature of the thermal change of 443 °C, *J. Inst. Med.* 63 (1938) 123–147.
- [38] E. Pelzel, H. Schneider, Contribution to the understanding of Zn alloys, *Z. Metallkd.* 35 (1943) 124–127.
- [39] G.V. Raynor, Annotated Equilibrium Diagram Series, 1944. No. 1, London: J. I. Met.
- [40] E. Butchers, W. Hume-Rothery, On the constitution of aluminium-magnesium-manganese-zinc alloys: the solidus, *J. Inst. Med.* 71 (1945) 291–311.
- [41] E. Pelzel, The positions of the liquidus and solidus curves in the Al-Zn system from 30 to 70 wt, % Al, *Z. Metallkd.* 40 (1949) 134–136.
- [42] I.S. Solet, H. W. St Clair, Liquidus Temperatures and Liquid Densities of Zinc-Aluminum Alloys, Bureau of Mines Report of Investigations, 1949, p. 4553.
- [43] W. Guertler, H. Krause, F. Voltz, Experiments on the Al-Zn system, *Metallwirtschaft* 18 (1939) 97–100.
- [44] T. Morinaga, On the equilibrium diagram of the aluminium-zinc system, *Nippon Kinzoku Gakkaishi* 3 (1939) 216–221.
- [45] E.C. Ellwood, An X-ray study of the constitution of aluminium-zinc alloys of high purity above 275 °C, *J. Inst. Med.* 66 (1940) 87–97.
- [46] E. Butchers, G.V. Raynor, W. Hume-Rothery, The constitution of magnesium-manganese-zinc-aluminum alloys in the range 0–5 percent manganese, 0–8 percent zinc. I. The liquidus, *J. Inst. Med.* 69 (1943) 209–228.
- [47] D.J. Strawbridge, W. Hume-Rothery, A.T. Little, The constitution of aluminium-copper-magnesium-zinc alloys at 460°C, *J. Inst. Med.* 74 (1948) 191–225.
- [48] E. Gebhardt, Zinc-Aluminum phase diagram, *Z. Metallkd.* 40 (1949) 463–464.
- [49] V.S. Lyashenko, Energy of formation and phase transitions of the alloys in the Al-Zn system, *Izv. Akad. Nauk SSSR, Otd. Khim. Nauk* (1951) 242.
- [50] E.C. Ellwood, The solid solutions of zinc in aluminium, *J. Inst. Med.* 80 (1951) 217–224.
- [51] J. Veró, Dilatometric determination of the solidus temperature A. *Acta Tech Hung* 2 (1951) 97.
- [52] A. Münster, K. Sagel, Miscibility gap and critical point of the aluminum-zinc system, *Z. Phys. Chem.* 7 (1956) 296–316.
- [53] W.M. Peirce, M.S. Palmerton, Studies on the constituent of binary zinc-based alloys, *T. Metall. Soc. AIME* 68 (1923) 767–795.
- [54] H. Auer, K.E. Mann, Magnetic investigation of zinc aluminum system, *Z. Metallkd.* 28/10 (1936) 323–326.
- [55] A. Burkhardt, Zinc alloys as a substitute material, *Z. Metallkd.* 28/10 (1936) 299–308.
- [56] K. Löhberg, X-ray determination of the solubility of aluminum and copper in zinc, *Z. Metallkd.* 32 (1940) 86.
- [57] E. Schmid, G. Wassermann, Gibt es eine Verbindungen Al Zn, *Metallwirtschaft* 11 (1932) 386.
- [58] W.L. Fink, L.A. Willey, Equilibrium relations in aluminum-zinc alloys of high purity—II, *T. Metall. Soc. AIME* 12 (1936) 244–260.
- [59] E.A. Owen, L. Pickup, X-ray study of aluminium-zinc alloys at elevated temperatures, *The London, Edinburgh, and Dublin Philos. Mag* 20 (135) (1935) 761–777.
- [60] I. Obinata, M. Hagiya, S. Itimura, X-ray study of the aluminium-zinc system, *Tetsu-To-Hagane* 22/8 (1936) 622–629.
- [61] H. Auer, K.E. Mann, *Gmelins Handbuch der anorganischen Chemie*, Verlag Chemie, Berlin, 1937. System No. 35A (5), 685.
- [62] G. Borelius, L.E. Larsson, Kinetics of precipitation in Al-Zn alloys, *Ark. Mat. Astr. Fys.* 35A/13 (1948) 1–14.
- [63] G. Borelius, Kinetics of precipitation in supercooled solid solutions, *T. Metall. Soc. AIME* 191 (1951) 477–484.
- [64] L.E. Larsson, Pre-precipitation and precipitation phenomena in the Al-Zn system, *Acta* 15 (1967) 35–44.
- [65] M. Simerka, P. Bartuska, The X-ray diffraction and electron microscopic investigation of stable and metastable equilibria in Al-rich Al-Zn alloys, *Czech. J. Phys.* B24 (1974) 553–559.
- [66] W. Hofmann, G. Fahrenhorst, Precipitation rates in high purity zinc-aluminum and zinc-copper alloys, *Z. Metallkd.* 42 (1950) 460–463.
- [67] A. Pasternak, The solid solubility of metals in lead and zinc, *Bull. Int. Acad. Polon. Sci. Sér. A* (1952) 177–192.
- [68] M. Vijayalakshmi, V. Seetharaman, V.S. Raghunathan, A rapid method for the determination of spinodal solvus applied to Al-Zn system, *Acta Metall.* 32/9 (1984) 1371–1380.
- [69] T.B. Massalski, *Binary Alloy Phase Diagrams*, 2nd edition, ASM International, Metals Park, Ohio, 1990.
- [70] H. Araki, Y. Minamoto, T. Yamane, K. Azuma, Y.S. Kang, Y. Miyamoto, Partial phase diagram of the aluminum-rich region of the Al-Zn system at 0.1 MPa and 2.1 GPa, *J. Mater. Sci. Lett.* 11/3 (1992) 181–183.
- [71] Y.S. Kang, H. Araki, Y. Minamoto, T. Yamane, S. Saji, K. Azuma, Y. Miyamoto, Phase diagram of Al-Zn system under high pressure, *Nippon Kinzoku Gakkaishi* 57/9 (1993) 990–997.
- [72] S. Popovic, B. Grzeta, H. Loeffler, G. Wendrock, Phase transitions in Al-Zn alloys, *Acta Crystallogr. A: Found. Crystallogr.* A52/C435 (1996) C435.
- [73] L. Balanovic, D. Zivkovic, D. Manasjjevic, D. Minic, V. Cosovic, N. Talijan, Calorimetric investigation of Al-Zn alloys using Oelsen method, *J. Therm. Anal. Calorim.* 118 (2014) 1287–1292.
- [74] A. Yazawa, Y.K. Lee, Thermodynamic studies of the liquid aluminum alloy systems, *T. Jpn. I. Met.* 11/6 (1970) 411–418.
- [75] R. Hultgren, P.D. Desai, D.T. Hawkins, M. Gleiser, K.K. Kelley, Selected Values of the Thermodynamic Properties of Binary Alloys, *Am. Soc. Met, Metals Park, Ohio*, 1973.
- [76] R.E. Wittig, L. Schoeffl, Heat of formation in the aluminum-zinc system at 330, 370, and 430 °C, *Z. Metallkd.* 51 (1960) 700–707.
- [77] A. Debski, W. Gasior, K. Szmit, Calorimetric measurements of liquid Al-Zn alloys, *Metall. Mater. Trans. A* 47A (2016) 4933–4940.
- [78] A.R. Miedema, The electronegativity parameter for transition metals: heat of formation and charge transfer in alloys, *J. Less Common. Met.* 32/1 (1973) 117–136.
- [79] J.E. Hilliard, B.L. Averbach, M. Cohen, Thermodynamic properties of solid aluminum-zinc alloys, *Acta Metall.* 2 (1954) 621–631.
- [80] A. Dinsdale, A. Khvan, A. Aristova, A New Generation of Data for the Elements: Critical Assessment of Data for Zn and Cd, Presented at CALPHAD XLIV, Book of abstract, Loano, Italy, May, p. 42.
- [81] U. Schmidt, O. Vollmer, R. Kohlhaas, Thermodynamische Analyse kalorimetrischer Messungen an Aluminium und Wolfram im Bereich hoher Temperaturen, *Z. Naturforschung* 25a (1970) 1258–1264.
- [82] D. C. Hopkins, PhD thesis, University of Illinois, 1962.
- [83] J.A. Kok, w.H. Keesom, Measurements of the atomic heat of aluminum from 1.1 to 20° K, *Physica* 4/9 (1937) 835–842.
- [84] W.T. Berg, Heat capacity of aluminium between 2.7 and 20 K, *Phys. Rev.* 167/3 (1968) 583–586.
- [85] W.F. Giauque, P.F. Meads, The heat capacities and entropies of aluminum and copper from 15 to 300° K, *J. Am. Chem. Soc.* 63 (1941) 1897–1901.
- [86] C.G. Maier, C.T. Anderson, The disposition of work energy applied to crystals, *J. Chem. Phys.* 2 (1934) 513–527, 1934.
- [87] D. B. Downie, J.F. Martin, An adiabatic calorimeter for heat-capacity measurements between 6 and 300 K. The molar heat capacity of aluminium, *J. Chem. Thermodyn.* 12 (1982) 779–786.
- [88] C.R. Brooks, R.E. Bingham, The specific heat of aluminum from 330 to 890 K and contributions from the formation of vacancies and anharmonic effects, *J. Phys. Chem. Solids* 29 (1968) 1553–1560.
- [89] E.L. Dosch, W.W. Wendlandt, The deltat therm dynamic adiabatic calorimeter: some applications, *Thermochimi, Acta* 1/2 (1970) 181–189.
- [90] W. Kramer, J. Nöling, Anomale spezifische Wärmen und Fehlordnung der Metalle Indium, Zinn, Blei, Zink, Antimon und Aluminium, *Acta Metall.* 20/12 (1972) 1353–1359.
- [91] A.T. Dinsdale, SGTE data for pure elements, *CALPHAD* 15/3 (1991) 317–425.

6.3 Paper 3

- [P3] **Zobač, O.**, Kroupa, A., Richter, K.W., *Experimental study of the Al-Cu-Zn ternary phase diagram*, Journal of Materials Science, 2020, 55(24), pp. 10796-10810, doi: 10.1007/s10853-020-04686-4 (IF 4.220)



Experimental study of the Al–Cu–Zn ternary phase diagram

Ondrej Zobac^{1,2,*} , Ales Kroupa², and Klaus W. Richter¹

¹Department of Inorganic Chemistry - Functional Materials, University of Vienna, Währinger Straße 42, 1090 Vienna, Austria

²Institute of Physics of Materials, The Czech Academy of Sciences, Žitkova 22, 616 00 Brno, Czech Republic

Received: 10 February 2020

Accepted: 15 April 2020

© The Author(s) 2020

ABSTRACT

The phase diagram of the Al–Cu–Zn ternary system was re-investigated experimentally. The current study was designed to contribute to a better description of those parts of the phase diagram, which are disputed in the current scientific literature. Mutual relations in the family of ternary intermetallic phases τ with cubic, rhombohedral and modulated structure at temperatures 400 °C and 550 °C were described. The phase relation between the γ and γ' phases was studied at different temperatures. A two-phase field between γ and γ' was observed below 400 °C, while the transition appears to be second order at higher temperatures. A vertical section between γ and γ' phases in Cu–Zn and Al–Cu and four isothermal sections at 400 °C, 550 °C, 700 °C and 820 °C, respectively, were constructed.

Introduction and literature review

The Al–Cu–Zn ternary system has been investigated intensively in the past because of its technical importance for developing of light-weight alloys. However, several areas of the phase diagram are still not well understood and discussed intensively. Our work is focused on several doubtful regions of the phase diagram, which have not yet been satisfactorily resolved in the scientific literature, and on the divergent results from the experimental and theoretical publications [1, 2]. Major topics were the extensions of the γ and γ' solid solution phases (with primitive and base-centered brass structures, respectively) and their mutual relation in the whole

concentration and temperature range. We also studied the crystal structure and homogeneity ranges of the reported ternary phases τ and τ' and constructed the isothermal sections of the phase diagram Al–Cu–Zn based on our new experimental results at 400 °C, 550 °C, 700 °C and 820 °C as well as the vertical section describing the mutual relation between γ and γ' phases.

Literature review

Detailed literature reviews of all binary subsystems are described in recent literature. The experimental description of the Al–Cu phase diagram is published in our previous work [3]. Liang et al. [4] published a

Address correspondence to E-mail: zobac@ipm.cz

theoretical modeling of the Al–Cu phase diagram based on CALPHAD approach.

The Al–Zn binary phase diagram was assessed by Murray [5] and reported by Massalski [6]. Dinsdale et al. [7] have done the most recent theoretical modeling of the Al–Zn phase diagram, using the third generation of unary data. Theoretical modeling using the commonly used SGTE unary database [8] was published by Mathon et al. [9].

The assessed Cu–Zn binary phase diagram was published by Miodownik [10]. Liang et al. [11] published the most recent theoretically modeled binary phase diagram Cu–Zn. Figure 1a–c show redrawn binary experimental phase diagrams of the relevant subsystems.

Ghosh et al. [1] published a review of the experimental studies on the Al–Cu–Zn phase diagram available up to the year 2002. The experimental ternary phase diagram Al–Cu–Zn provided in [1] can be generally accepted except for the disagreement in the proposed phase equilibria between the γ and γ' phases in comparison with the detailed analysis of existing experimental studies presented by Liang and Schmid-Fetzer [2]. These authors also published the most recent theoretical assessment based on this analysis in the same paper [2]. The main difference exists for mutual relation between the two closely related γ (Al_4Cu_9) and γ' (Cu_5Zn_8) phases and ternary τ and τ' phases which will be discussed later. Most of the original references from the years 1905–2002 evaluated in Ghosh et al. [1] are not duplicated here.

Liang and Chang [12] published an overall thermodynamic description based on the CALPHAD approach. Two isothermal sections at 500 °C and 700 °C and a liquidus projection were published in this paper. Only one ternary intermetallic compound τ (approx. formula $\text{Al}_3\text{Cu}_5\text{Zn}_2$) was theoretically modeled in this system by Liang and Chang [12]. Despite the fact that the experimentally established homogeneity range of the τ phase is highly temperature dependent, Liang and Schmid-Fetzer [2] modeled the τ phase as a linear phase with constant composition $x(\text{Zn}) = 0.10$. It was found earlier that the family of τ -phases appears in two modifications, cubic B2-type τ phase and a structurally related rhombohedral τ' phase [13]. The τ' phase was not included into Liang's [2, 12] thermodynamic description because the composition range and thermal stability had not yet been reasonably determined.

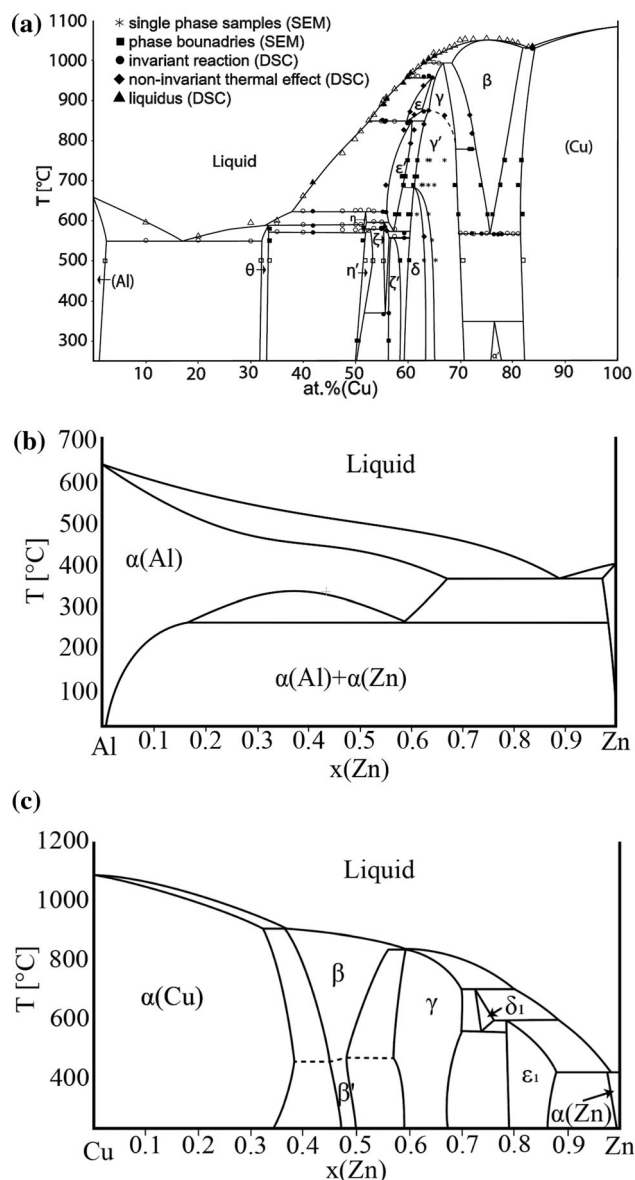


Figure 1 Binary phase diagram of subsystem. **a** Al–Cu [3], **b** Al–Zn [6], **c** Cu–Zn [6].

The continuous solid solutions were modeled between some binary intermetallic phases in this system. The β (BCC_A2) phase exists in both Al–Cu and Cu–Zn systems and the continuous solid solution was modeled in [12]. The situation is more complicated in the case of the family of γ -phases. The γ phase region forms continuous solid solution in all experimentally assessed isothermal sections from 350 °C to 700 °C [1], from the Al–Cu side, where the low temperature γ' (Al_4Cu_9) with the Pearson symbol $cP52$ exists in the binary Al–Cu system, to the Cu–Zn

side where the γ (Cu_5Zn_8) phase with the Pearson symbol *cI52* is stable.

The first results showing continuous γ phase region between Al–Cu and Cu–Zn binaries were presented by Bauer and Hansen [14]. They constructed several isothermal sections of Al–Cu–Zn ternary system in the Cu-rich corner in temperature range 410–800 °C. They proposed the continuous solid solution of the γ phase based on their experimental results. Koster and Moeller [13] constructed an isothermal section at 350 °C and confirmed the continuous solubility of the γ phase. Ashirimbetov et al. [15] reported two isothermal sections at 20 °C and 350 °C. The results showed the solid solubility of Al in γ at 20 °C and 350 °C are about 3.5 and 7.0 wt % (2.2 and 5.5 at.%), respectively, and solubility of Zn in γ' at the same temperatures about 30 wt %. They detected a wide two-phase region between γ and γ' at room temperature and 350 °C. They predicted that these two different γ phases might be miscible at higher temperatures where the high temperature modification of the γ phase exists in the Al–Cu system with the same crystal structure as in the Cu–Zn system. Also Liang and Schmid-Fetzer [2] did not accept the continuous solid solution between these crystallographically slightly different types of γ phases in their theoretical work. They described this decision in detail in the text of their paper. Nevertheless, they did not run any experimental study to confirm their conclusions.

With respect to previously mentioned result discrepancies, the aim of our study of the Al–Cu–Zn ternary system was to experimentally solve the question of solubilities between the γ' and γ phases and a detailed crystallography and compositional and temperature stability of τ and τ' phases.

The current available information for all solid phases of the system is summarized in Table 1. The abbreviated phase names in the form of Greek letters used in the text and phase diagrams are provided in the first column. Other common phase names used in the literature [1–3] are shown in column 2. The Pearson symbol and structure type (columns 3 and 4) are taken from the Materials Science International Team (MSIT) report [16]. Temperature stability of binary phases is taken from relevant phase diagrams [3, 6]. Temperature stability of ternary phase τ (in our text is equal to τ_c) from Ghosh et al. [1] and ternary phases τ_1 and τ_r (which corresponds to τ') is based on our new results.

Experimental

The overall compositions of experimental samples were selected in order to address the unsolved questions in the experimental phase diagrams as mentioned above. Furthermore, it was our aim to determine complete isothermal phase equilibria in four isothermal sections. The prepared samples were analyzed and characterized by different static and dynamic analytical methods (SEM–EDX, DTA, XRD).

Sample preparation

Samples were prepared from pure elements of 5 N purity. Any oxide presented in the copper was reduced by flowing of the H_2 gas at 300 °C for 3 h. The alloys were re-melted at 950 °C several times in evacuated quartz glass ampoules in order to improve the homogenization of the material. Long-term annealing of the samples was performed at selected temperatures on material sealed in evacuated quartz glass ampoules. To prevent reaction of liquid Al with the Si from material of quartz glass, the samples with high content of Al-rich liquid were placed inside the corundum crucibles. These crucibles with samples were sealed in evacuated quartz glass ampoules. A conventional muffle resistance furnace was used for the heat treatment. Samples were long-term annealed to achieve state close to the thermodynamic equilibrium. Annealing time was selected with respect to annealing temperature. For the annealing temperature closer to the melting temperature, shorter annealing time is sufficient. Annealing was terminated by quenching of the samples into cold water from their annealing temperatures, and sample was prepared for further investigations. Annealing times and temperatures are given in Table 2 together with experimental results.

Experimental phase diagram investigation

A combination of dynamic and static methods was used for the investigation of the phase diagram. Phase equilibria, microstructure and chemical analysis of phases and overall compositions were performed by using scanning electron microscopy combined with energy dispersive X-ray spectroscopy (SEM–EDX), employing either a Zeiss Supra 55 VP instrument equipped with an energy dispersive detector for quantitative analysis or a similarly

Table 1 Stable phases in Al–Cu–Zn ternary phase diagram and binary subsystems

Phase name [This work]	Common names	Pearson symbol	Structure prototype	T. range (°C)
α (Al)	FCC_Al, Al	<i>cF4</i>	Al	≤ 660.5
α (Cu)	FCC_Al, Cu	<i>cF4</i>	Cu	≤ 1083
α (Zn)	HCP_Zn, Zn	<i>hP2</i>	Mg	
θ	θ , Al ₂ Cu	<i>tI12</i>	Al ₂ Cu	≤ 590.5
η	η_1 _AlCu, Eta HT	<i>oP16/oC16</i>	n.a.	573.9–624.5
η'	η_2 _AlCu, Eta LT	<i>mC20</i>	AlCu	≤ 574.5
ζ	ζ_2 , Al ₃ Cu _{4-δ}	<i>Imm2</i>	Al ₃ Cu _{4-δ}	373–597
ζ'	ζ_1 , Al ₃ Cu ₄	<i>Fmm2</i>	Al ₃ Cu ₄	min. 300–560.5
ε	ε_1 _AlCu, epsilon HT	cubic?	n.a.	959–846
ε'	ε_2 _AlCu, epsilon LT	<i>hP4</i>	NiAs	846–568.5
δ	δ , Al ₅ Cu ₈	<i>hR52</i>	Al ₄ Cu ₉ (r)	≤ 680
γ	γ_0 , γ _CuZn, γ _brass	<i>cI52</i>	Cu ₅ Zn ₈	991–779.6
γ'	γ_1 , γ' _AlCu, γ' _D δ_3	<i>cP52</i>	Al ₄ Cu ₉	≤ 873.5
β	BCC_A2 (AlCu)	<i>cI2</i>	W	1052–566.7
α'	α_2 _AlCu, alpha_LT	n. a.	super structure based on TiAl ₃	≤ 360
β'	BCC_B2, CuZn	<i>cP2</i>	CsCl	≤ 468
δ_1	CuZn ₃	<i>hP3</i>	CuZn ₃	700–560
ε_1	CuZn ₄	<i>hP2</i>	Mg	≤ 598
τ_c	τ , Cu ₅ Zn ₂ Al ₃	<i>cP2</i>	CsCl	≤ 740
τ_i			Incommensurate τ phase	$\leq 550^*$
τ_r	τ'	<i>hR9</i>	superstructure of CsCl	$< 440^*$

*Based on constructed isothermal sections in this work

equipped SEM JEOL JSM-6460. Identification of phases present in the long-term annealed samples was achieved using X-ray powder diffraction. The Bruker D8 diffractometer equipped with a high-speed position sensitive (PSD) detector (Lynxeye) was used in the $\theta/2\theta$ reflection setting. Rietveld refinements of selected diffraction patterns were performed with the Topas software [17]. Annealing temperature of the sample, overall composition, coexisting phases and phase compositions of the concrete phases in the equilibrium are listed in Table 2. Annealing temperature and number of the sample are listed in column 1, and the annealing time is shown in column 2. Column 3 shows the overall composition measured by SEM–EDX area scans. Coexisting phases stable in the samples are listed in column 4; columns 5–7 show the composition of equilibrium phases existing in the samples measured by SEM–EDX in same order as the phases are mentioned in column 4.

Phase transition temperatures were measured using a high-temperature DTA (NETZSCH Pegasus 404 C) with samples placed in closed and evacuated quartz glass DTA ampoules. Closed ampoules were

used to limit uncontrolled Zn evaporation during the measurement and contamination of the inner parts of the instrument. The DTA was calibrated using a set of pure metal standards having well-defined melting temperatures (Sn, Al, Zn, Cu, Ag, Au). Calibration was carried out under the same conditions as the experimental measurements. Three heating and cooling runs were performed for each sample; the thermal effects during the first heating run were not taken into account. Thermal analysis results for four samples situated in the section $\gamma' - \gamma$ are listed in Table 3.

Results and discussion

By combining all experimental results listed in Tables 2 and 3, it was possible to draw complete isothermal sections of ternary phase diagram Al–Cu–Zn at 400 °C, 550 °C, 700 °C and 820 °C. These sections are presented in Fig. 2. The shape of the phase boundaries and phase fields not defined by our own samples was drawn based on information from

Table 2 Chemical composition of the long-term annealed representative sample

T [°C]_No.	Annealing time [h]	Overall composition (at. %)			Coexist. phases	Phase 1 (at. %)			Phase 2 (at. %)			Phase 3 (at. %)		
		Al	Cu	Zn		Al	Cu	Zn	Al	Cu	Zn	Al	Cu	Zn
300_1	700	14.3	48.8	36.9	$\gamma + \gamma'$	10.5	44.2	45.3	21.0	53.5	25.5	–	–	–
325_1	700	15.1	48.6	36.3	$\gamma + \gamma'$	11.0	45.1	43.9	20.1	53.2	26.7	–	–	–
350_1	700	14.9	48.2	36.9	$\gamma + \gamma'$	11.4	47.0	41.6	18.5	52.4	29.1	–	–	–
375_1	700	16.9	50.8	32.3	$\gamma + \gamma'$	12.2	46.7	41.1	17.8	52.4	29.8	–	–	–
400_1	648	21.0	39.0	40.0	$\tau_c + \varepsilon_1$	29.9	46.7	23.4	17.9	36.4	45.7	–	–	–
400_2	648	42.4	52.3	5.3	$\zeta + \eta'$	45.3	51.7	3.0	41.9	52.0	6.1	–	–	–
400_3	648	14.3	61.6	24.1	$\gamma' + \beta'$	22.2	61.7	16.1	10.9	61.8	27.3	–	–	–
400_4	648	53.6	42.5	3.9	$\eta' + \tau_r + \theta$	47.8	50.2	2.0	55.3	40.0	4.7	65.4	34.0	0.6
400_5	648	47.6	47.7	4.8	$\eta' + \tau_r$	46.59	49.61	3.80	53.1	41.0	5.9	–	–	–
400_6	648	26.1	34.8	39.1	$\tau_i + \varepsilon_1$	42.3	42.6	15.1	13.3	30.3	56.4	–	–	–
400_7	648	18.6	42.9	38.5	$\tau_c + \gamma + \varepsilon_1$	25.6	49.1	25.3	15.7	44.4	39.9	15.4	36.8	47.8
400_8	648	32.8	47.8	19.4	τ_c	32.8	47.8	19.4	–	–	–	–	–	–
400_9	648	37.4	46.0	16.6	τ_i	37.4	46.0	16.6	–	–	–	–	–	–
400_10	648	42.4	44.1	13.5	τ_i	42.4	44.1	13.5	–	–	–	–	–	–
400_11	625	48.4	41.7	9.9	τ_r	48.4	41.7	9.9	–	–	–	–	–	–
400_12	625	29.1	57.5	13.4	$\delta + \tau_c$	29.4	59.3	11.3	28.4	50.9	20.7	–	–	–
400_13	625	38.6	55.8	5.6	$\delta + \zeta'$	35.8	59.8	4.4	41.0	52.5	6.5	–	–	–
400_14	625	15.8	49.7	34.5	$\gamma + \gamma'$	15.8	49.2	35.0	17.4	51.0	31.6	–	–	–
400_15	625	13.8	48.2	38.0	γ	13.8	48.2	38.0	–	–	–	–	–	–
400_16	625	11.8	46.3	41.9	γ	11.8	46.3	41.9	–	–	–	–	–	–
400_17	612	16.4	51.6	32.0	γ'	16.4	51.6	32.0	–	–	–	–	–	–
400_18	612	42.9	48.3	8.8	$\eta' + \tau_r$	42.9	49.6	7.5	44.7	43.8	11.5	–	–	–
400_19	612	38.2	50.7	11.1	$\zeta' + \tau_i + \delta$	40.4	50.3	9.4	34.3	48.4	17.3	–	–	–
400_20	612	31.9	58.0	10.1	$\delta + \tau_c$	32.0	59.5	8.5	30.3	51.0	18.7	–	–	–
400_21	612	28.1	40.8	31.1	$\tau_i + \varepsilon_1$	35.6	46.1	18.3	13.4	32.0	54.6	–	–	–
400_22	612	9.8	36.6	53.6	$\gamma + \varepsilon_1$	9.5	40.2	50.4	10.5	32.4	57.0	–	–	–
400_23	612	5.7	55.3	39.0	β	5.7	55.3	39.0	–	–	–	–	–	–
400_24	612	37.5	14.8	47.7	$\tau_r + L$	51.1	40.2	8.7	35.0	8.6	56.4	–	–	–
400_25	660	29.4	21.8	48.8	$\tau_r + L + \varepsilon_1$	50.3	40.3	9.4	31.0	8.0	61.0	8.8	23.6	67.6
400_26	660	56.7	4.6	38.7	α (Al)	56.7	4.6	38.7	–	–	–	–	–	–
400_27	660	38.0	34.0	28.0	$\tau_r + \varepsilon_1 + L$	50.3	39.8	9.9	10.6	25.8	63.6	–	–	–
400_28	660	23.2	15.3	61.5	$\varepsilon_1 + L$	9.96	23.12	66.92	32.3	8.1	59.6	–	–	–
400_29	660	6.1	34.3	59.6	$\gamma + \varepsilon_1$	6.6	35.7	57.7	4.7	26.3	69.0	–	–	–
400_30	660	21.7	67.9	10.4	$\gamma' + \alpha$ (Cu)	25.7	64.7	9.6	12.3	74.2	13.5	–	–	–
400_31	660	18.0	59.8	22.2	$\gamma' + \beta$	20.3	59.6	20.1	10.7	59.1	30.2	–	–	–
400_32	660	14.4	52.1	33.5	γ'	14.4	52.1	33.5	–	–	–	–	–	–
400_33	660	17.0	50.2	32.8	$\gamma + \gamma'$	15.4	48.7	35.9	18.2	50.7	31.1	–	–	–
400_34	715	50.9	40.3	8.8	τ_r	50.9	40.3	8.8	–	–	–	–	–	–
400_35	715	74.8	18.8	6.4	$\theta + \alpha$ (Al)	65.7	32.5	1.8	85.2	2.1	12.7	–	–	–
400_36	715	69.2	19.2	11.6	$\theta + \alpha$ (Al)	65.7	31.7	2.6	78.8	3.1	18.1	–	–	–
400_37	715	26.6	6.3	67.1	L	26.5	6.3	67.2	–	–	–	–	–	–
400_38	715	18.6	53.7	27.7	γ'	18.6	53.7	27.7	–	–	–	–	–	–
400_39	715	63.8	18.0	18.2	$\theta + \alpha$ (Al)	65.8	31.5	2.7	60.3	4.1	35.4	–	–	–
400_40	715	28.8	37.8	33.4	$\tau_i + \varepsilon_1$	40.2	43.5	16.3	13.3	31.6	55.1	–	–	–
400_41	715	59.4	20.9	19.7	$\theta + \tau_r + \alpha$ (Al)	65.8	31.9	2.3	53.5	38.7	7.8	54.0	4.7	41.3
400_42	680	51.1	25.1	23.8	$\tau_r + \alpha$ (Al) + L	52.7	39.0	8.3	50.3	4.7	45.0	30.0	9.8	60.2
400_43	680	48.6	26.7	24.7	$\tau_r + \alpha$ (Al) + L	51.7	39.9	8.4	48.7	4.6	46.7	30.3	8.5	61.2
400_44	680	34.1	54.8	11.1	$\delta + \zeta' + \tau_c$	32.8	60.2	7.0	38.9	51.5	9.6	32.0	50.7	17.3

Table 2 continued

T [°C]_No.	Annealing time [h]	Overall composition (at. %)			Coexist. phases	Phase 1 (at. %)			Phase 2 (at. %)			Phase 3 (at. %)		
		Al	Cu	Zn		Al	Cu	Zn	Al	Cu	Zn	Al	Cu	Zn
400_45	680	3.5	8.3	88.2	$\varepsilon_1 + L$	1.7	15.1	83.2	4.6	3.1	92.3	–	–	–
400_46	680	30.4	49.0	20.6	τ_c	30.4	49.0	20.6				–	–	–
400_47	680	45.4	43.6	11.0	τ_i	45.4	43.6	11.0				–	–	–
400_48	680	39.9	44.6	15.5	τ_i	39.8	44.7	15.5				–	–	–
400_49	680	35.0	46.1	18.9	τ_i	35.0	46.1	18.9				–	–	–
400_50	680	28.9	49.4	21.7	τ_c	28.9	49.4	21.7				–	–	–
450_1	500	15.9	50.9	33.2	γ/γ'	15.9	50.1	34.0	16.2	50.5	33.3	–	–	–
500_1	500	16.0	49.3	34.7	γ/γ'	15.3	52.2	32.5				–	–	–
550_1	840	32.5	55.2	12.3	$\gamma' + \tau_c$	31.9	59.1	9.0	32.8	53.0	14.2	–	–	–
550_2	840	29.5	55.5	15.0	$\gamma' + \tau_c$	29.3	57.5	13.2	30.3	52.1	17.6	–	–	–
550_3	840	21.7	55.4	22.9	γ'	21.7	55.4	22.9				–	–	–
550_4	840	10.5	55.8	33.7	$\beta + \gamma'$	8.3	58.5	33.2	11.7	54.5	33.8	–	–	–
550_5	840	36.0	56.1	7.9	$\delta + \tau_i$	35.4	58.6	6.0	36.3	53.4	10.3	–	–	–
550_6	840	31.8	41.0	27.2	$\tau_c + L + \varepsilon_1$	33.9	46.7	19.4	43.4	30.9	25.7	26.1	42.5	31.4
550_7	840	5.9	39.8	54.3	γ	5.9	39.8	54.3	–	–	–	–	–	–
550_8	840	5.4	52.5	42.1	$\beta + \gamma'$	4.5	55.2	40.3	6.6	49.0	44.4	–	–	–
550_9	840	24.3	45.5	30.2	$\varepsilon_1 + \gamma$	24.3	45.5	30.2	–	–	–	–	–	–
550_10	840	4.5	65.3	30.2	$\alpha(\text{Cu}) + \beta$	4.1	67.0	28.9	6.2	62.3	31.5	–	–	–
550_11	840	22.6	47.4	30.0	$\tau_c + \gamma + \delta$	26.6	50.0	23.4	19.2	48.6	32.2	23.9	45.4	30.7
550_12	420	23.7	69.9	6.4	$\beta + \gamma'$	20.4	72.6	7.0	27.6	67.0	5.4	–	–	–
550_13	420	20.2	65.9	13.9	$\beta + \gamma'$	25.1	63.5	11.4	16.2	67.6	16.2	–	–	–
550_14	420	10.2	71.3	18.5	$\alpha(\text{Cu}) + \beta$	9.4	72.0	18.6	13.2	67.6	19.2	–	–	–
550_15	420	40.6	48.1	11.3	τ_i	40.6	48.1	11.3	–	–	–	–	–	–
550_16	420	35.1	48.4	16.5	τ_c	35.1	48.4	16.5	–	–	–	–	–	–
550_17	420	41.3	43.8	14.9	$\tau_i + L$	40.6	44.4	15.0	58.7	29.5	11.8	–	–	–
550_18	420	27.5	47.1	25.4	$\tau_c + \varepsilon_1$	29.6	49.9	20.5	26.7	46.4	26.9	–	–	–
550_19	420	30.3	34.4	35.3	$\varepsilon_1 + L$	25.3	42.5	32.2	36.9	23.7	39.4	–	–	–
550_20	420	41.6	47.8	10.6	τ_i	41.6	47.8	10.6	–	–	–	–	–	–
550_21	560	56.8	40.3	2.9	$\tau_r + \theta$	49.9	45.4	4.7	65.2	34.0	0.8	–	–	–
550_22	560	46.7	46.1	7.2	τ_i	46.7	46.1	7.2	–	–	–	–	–	–
550_23	560	37.4	51.9	10.7	τ_i	37.4	51.9	10.7	–	–	–	–	–	–
550_24	560	12.4	46.3	41.3	γ/γ'	12.4	46.3	41.3	–	–	–	–	–	–
550_25	560	9.5	50.1	40.4	γ	9.5	50.1	40.4	–	–	–	–	–	–
550_26	560	9.5	47.1	43.4	γ	9.4	47.2	43.4	–	–	–	–	–	–
550_27	560	24.7	73.9	1.4	$\alpha(\text{Cu}) + \gamma'$	18.3	80.3	1.4	28.9	69.8	1.3	–	–	–
550_28	560	53.3	39.2	7.5	$\tau_i + L$	47.1	45.5	7.4	62.5	29.6	7.9	–	–	–
550_29	635	25.8	32.3	41.9	$\varepsilon_1 + L$	21.9	39.2	38.9	31.9	19.2	48.9	–	–	–
550_30	635	25.2	49.4	25.4	$\tau_c + \gamma'$	28.2	49.8	22.0	22.7	49.1	28.2	–	–	–
550_31	635	6.2	31.5	62.3	$\varepsilon_1 + \gamma$	6.5	33.0	60.5	3.8	26.5	69.7	–	–	–
550_32	635	39.4	57.9	2.7	$\delta + \zeta'$	37.7	59.7	2.6	39.8	57.6	2.6	–	–	–
550_33	635	16.8	39.6	43.6	$\gamma + \delta_1$	16.6	41.2	42.2	17.1	39.2	43.7	–	–	–
550_34	635	42.6	54.5	2.9	ζ	42.6	54.5	2.9				–	–	–
550_35	635	16.4	40.3	43.3	$\gamma + \delta_1$	15.2	42.1	42.7	16.1	39.1	44.8	–	–	–
550_36	635	3.8	30.0	66.2	$\varepsilon_1 + \gamma$	4.2	34.9	60.9	3.9	30.7	65.4	–	–	–
550_37	635	11.6	36.1	52.3	$\varepsilon_1 + \gamma$	11.3	36.1	52.6	12.1	33.5	54.4	–	–	–
550_38	635	21.3	45.2	33.5	$\gamma + \delta + \varepsilon_1$	19.1	47.4	33.5	22.0	43.4	34.6	–	–	–
700_1	570	40.26	57.87	1.87	ε'	40.26	57.87	1.87				–	–	–
700_2	570	38.4	56.8	4.8	$\gamma' + \varepsilon'$	*	*	*	38.4	56.8	4.8	–	–	–

Table 2 continued

T [°C]_No.	Annealing time [h]	Overall composition (at. %)			Coexist. phases	Phase 1 (at. %)			Phase 2 (at. %)			Phase 3 (at. %)		
		Al	Cu	Zn		Al	Cu	Zn	Al	Cu	Zn	Al	Cu	Zn
700_3	570	33.3	59.1	7.6	<i>γ' + ε'</i>	33.3	59.1	7.6	*	*	*	–	–	–
700_4	570	32.8	56.8	10.4	<i>γ'</i>	32.8	56.8	10.4				–	–	–
700_5	570	30.4	56.9	12.7	<i>γ + τ_c</i>	29.7	59.5	10.8	30.8	56.3	12.9	–	–	–
700_6	570	27.9	57.5	14.6	<i>γ + τ_c</i>	27.7	57.7	14.6	*	*	*	–	–	–
700_7	570	24.4	55.7	19.9	<i>γ</i>	24.4	55.7	19.9				–	–	–
700_8	570	17.5	54.7	27.8	<i>γ</i>	17.5	54.7	27.8	–	–	–	–	–	–
700_9	450	35.5	58.4	6.1	<i>γ' + ε'</i>	34.4	59.9	5.7	35.6	58.3	6.1	–	–	–
700_10	450	33.6	56.1	10.3	<i>γ' + τ_c</i>	32.0	58.6	9.4	33.6	55.7	10.7	–	–	–
700_11	450	13.4	73.4	13.2	<i>α (Cu) + β</i>	12.9	73.6	13.5	16.0	70.5	13.5	–	–	–
700_12	450	12.5	57.1	30.4	<i>β + γ</i>	12.5	57.6	29.9	14.5	54.8	30.7	–	–	–
700_13	450	40.7	44.8	14.5	<i>τ_c + L</i>	34.3	51.5	14.2	45.3	39.7	15.0	–	–	–
700_14	480	33.7	43.4	22.9	<i>τ_c + L</i>	28.9	49.0	22.1	40.9	36.5	22.6	–	–	–
700_15	480	24.8	43.0	32.2	<i>ε_l + L</i>	24.6	42.8	32.6	33.3	28.7	38.0	–	–	–
700_16	480	16.3	35.2	48.5	<i>ε_l + L</i>	16.2	39.4	44.4	16.6	28.0	55.4	–	–	–
700_17	480	12.5	32.6	54.9	<i>ε_l + L</i>	13.0	35.6	51.4	12.6	22.3	65.1	–	–	–
700_18	480	8.1	28.2	63.7	<i>ε_l + L</i>	7.8	32.3	59.9	9.2	23.4	67.4	–	–	–
820_1	330	33.8	59.3	6.9	<i>γ' + ε</i>	32.9	60.8	6.3	34.2	59.0	6.8	–	–	–
820_2	330	19.6	61.1	19.3	<i>γ</i>	19.6	61.1	19.3	–	–	–	–	–	–
820_3	330	36.5	60.3	3.2	<i>γ' + ε'</i>	35.2	61.7	3.1	37.2	59.6	3.2	–	–	–
820_4	330	28.6	57.9	13.5	<i>γ + L</i>	27.7	59.1	13.2	29.4	54.9	15.7	–	–	–
820_5	330	24.8	52.6	22.6	<i>γ + L</i>	24.3	53.4	22.3	25.3	51.6	23.1	–	–	–
820_6	330	17.8	70.1	12.1	<i>β</i>	17.8	70.1	12.1	–	–	–	–	–	–
820_7	330	30.0	61.6	8.4	<i>γ</i>	30.0	61.6	8.4	–	–	–	–	–	–
820_8	330	24.8	71.0	4.2	<i>β + γ</i>	25.0	70.5	4.5	28.2	67.9	3.9	–	–	–
820_9	330	17.9	64.9	17.2	<i>β</i>	17.9	64.9	17.2	–	–	–	–	–	–
820_10	330	15.2	76.9	7.9	<i>α (Cu) + β</i>	14.0	77.9	8.1	17.2	74.5	8.3	–	–	–
820_11	330	30.8	57.0	12.2	<i>γ + L</i>	30.8	57.6	11.6	32.2	54.1	13.7	–	–	–
820_12	330	9.1	68.6	22.3	<i>α (Cu) + β</i>	7.7	70.6	21.7	9.4	66.4	24.2	–	–	–
820_13	330	4.7	53.4	41.9	<i>β</i>	4.7	53.4	41.9	–	–	–	–	–	–

Coexisting phases found by XRD are in italic font. Coexisting phases established from their compositions are in standard font. * composition has not been measured

Table 3 Temperature of phase transitions measured by DTA

T [°C]_No.	Nominal comp. (at.%)			Thermal effects (heating) (°C)			
	Al	Cu	Zn	Liquidus	Solidus	Transition $\gamma \leftrightarrow \gamma'$	other transitions
400_38	18.6	53.7	27.7	940.7	903.8	569.1	
550_3	21.7	55.4	22.9	952.2	903.6	622.2	270.2
700_6	27.9	57.5	14.6	955.0	892.0	727.8	
700_4	32.8	56.8	10.4	*	*	826.9	641.9

*Has not been measured

binary subsystems, phase rules and data published by Ghosh et al. [1].

Our results generally agree well with the older phase diagrams published by Ghosh et al. [1], and the theoretical phase diagram published by Liang et al. [2], but contains some additional clarification and improvement of areas, which were not investigated in detail in the previous studies.

Isothermal section at 400 °C

The isothermal section of phase diagram Al–Cu–Zn at 400 °C is shown in Fig. 2a. The ternary phase field τ exhibits a long line-shaped homogeneity range between the approximate compositions

Al₂₉Cu₄₉Zn₂₂ and Al₄₈Cu₄₂Zn₁₀. In this area, we found at least three structural modifications (cubic form τ_c , (presumably) incommensurate modification τ_i and rhombohedral τ_r). The structural details are described in detail in the following paragraph. The Zn-poor region of the isothermal section shows equilibria of the τ -phase family with various binary Al–Cu compounds (phases θ , η' , ζ , ζ' , δ). The Al–Cu binary compounds in this central region show limited solubility of Zn. The solubility of Zn in the θ -phase is about 1 at.%. The phases η' , ζ , ζ' show solubility of Zn about 5 at.% and δ phase about 10 at.%. γ' phase has highest solubility of Zn up to 35 at.% of Zn. Based on binary phase diagram Cu–Zn, the ordered phase β' is stable at 400 °C. Solubility of Al is up to 10%. The γ

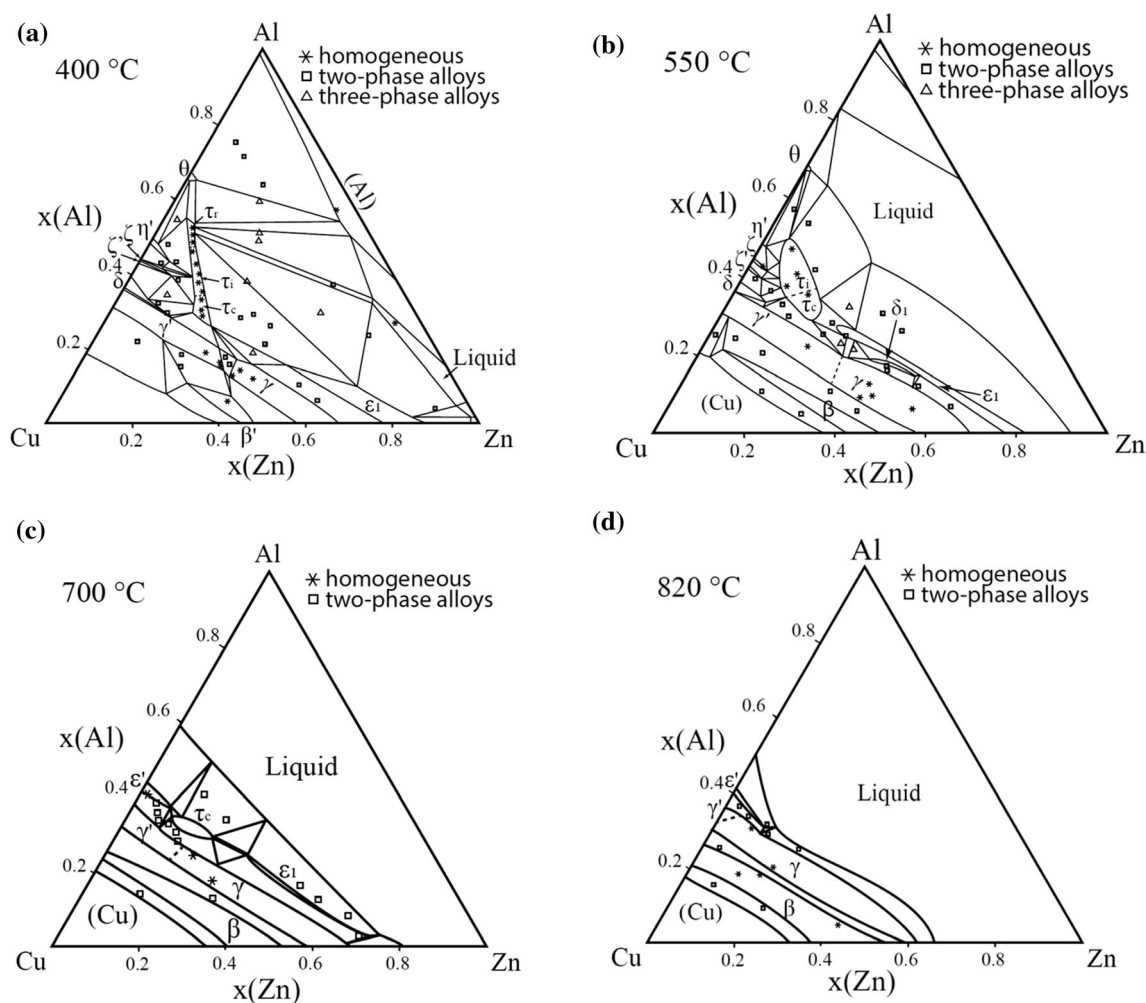


Figure 2 Isothermal sections of the Al–Cu–Zn experimental phase diagram at **a** 400 °C, **b** 550 °C, **c** 700 °C, **d** 820 °C. Overall compositions of selected samples are represented by several symbols. Stars represent the samples located in the single-phase field. Squares are the overall composition of the samples

containing two phases in equilibrium. Compositions of each phase and relevant tie lines are not shown as the figure would be very difficult to read. Triangles represent the overall composition of the samples containing three phases in equilibrium. Phase compositions are defined by the corner of the tie triangle.

phase and ε_1 phase have similar solubility of almost 20 at.% of Al. Figure 3 shows the microstructure of the two-phase sample $\varepsilon_1 + \tau_c$. The liquid phase is stable around the binary eutectic point in Al–Zn and extends toward the more Al-rich compositions in the ternary with a solubility for Cu up to 5 at.%. The solubility of Cu in α (Al) solid solution increases with increasing Zn content reaches up to 5 at.%. The microstructure of the α (Al) phase in the two-phase field α (Al) + θ is not homogeneous (Fig. 4) due to the fact that the annealed samples go through the miscibility gap of α (Al) phase, and it decomposed to two α (Al) phases according the Al–Zn binary phase diagram (Fig. 1b).

The τ -phase

As mentioned above, the composition area of the τ -phase is crystallographically complex. Originally, two different modifications of the phase were reported in the literature [18]: τ with CsCl-type structure and τ' with a closely related rhombohedral structure space group $R\bar{3}m$, Pearson symbol $hR30$. In the latter structure, six atomic sites are present, of which three being occupied by the Cs atoms and three by the Cl in specific sublattices of B2. Distortions from the ideal cubic coordination CN = 14 (8 + 6) are only small. Our detailed evaluation of the powder patterns of single-phase samples in the 400 °C isothermal section yielded the following results: The cubic B2 structure was found in samples situated at the Cu- and Zn-rich end of the homogeneity range (τ_c), while the rhombohedral structure was found at the opposite end of the homogeneity range (τ_r). The intermediate

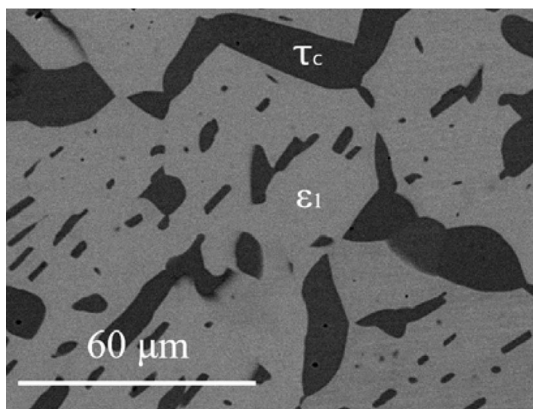


Figure 3 Microstructure of the sample 400_1 in BSE mode consist of ε_1 and τ_c phases.

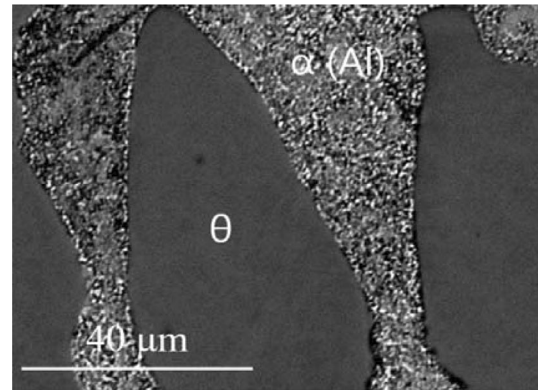


Figure 4 Microstructure of the sample 400_39 in BSE mode consist of θ and α (Al) phases.

composition range, here designated as (τ_i), could not be refined properly, although all samples were single phase according to SEM results. In this area, additional superstructure reflexes were observed which could not be indexed with any reasonable set of cell parameters. Position and intensity of superstructure reflexes varied continuously with the composition, but the number of observed superstructure reflexes increased with decreasing Cu content. This behavior leads to the conclusion that this intermediate area probably contains an incommensurately modulated crystal structure related to both, the B2 structure and its rhombohedral counterpart. It is not clear if the different phase regions τ_c , τ_i and τ_r are separated by two-phase fields, however, in spite of the large number of samples investigated in this area, it was not possible to identify any composition gap in the phases field. Consequently, the different areas are only separated by dashed lines in Fig. 2a. XRD patterns of some selected samples containing the family of τ phases are shown in comparison in Fig. 5.

Samples containing τ_c and τ_r were further investigated by Rietveld refinement in order to reveal the site occupations. For τ_c , a site occupation model allowing vacancies on the Cu site and Al/Zn substitution on the Al site yielded excellent agreement with the sample composition obtained by EDX measurements (Table 4). This defect mechanism is well in line with other nonstoichiometric B2 intermetallics like e.g., NiAl showing vacancies on the transition metal site [19].

The rhombohedral structure is much more complicated, so site occupation refinements were more demanding. Table 5 summarizes the refinement results for sample 400_34 in the single-phase region

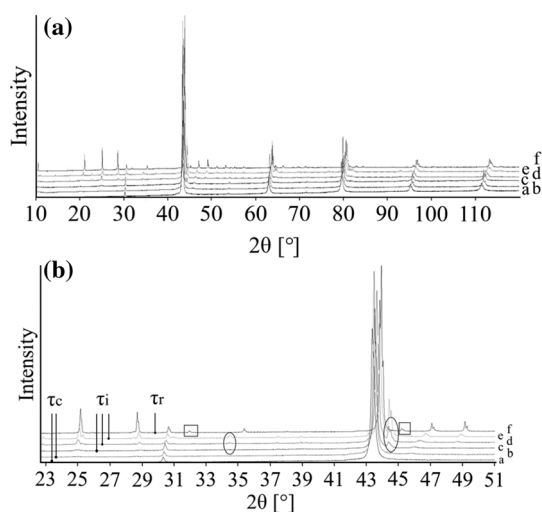


Figure 5 XRD patterns of the Al–Cu–Zn alloy containing τ phase. **a** whole measured range, **b** central part of the pattern. Specific peaks of τ_i phase are circled by ellipse. Specific peaks of τ_r phase are circled by square. Individual patterns were shifted on Y axis to better visualization. Overall compositions of the samples are following: *a*: 28.9 at.% Al–Cu–21.7 at.% Zn (τ_c); *b*: 32.8 at.% Al–Cu–19.4 at.% Zn (τ_c); *c*: 35.0 at.% Al–Cu–18.9 at.% Zn (τ_i); *d*: 39.9 at.% Al–Cu–15.5 at.% Zn (τ_i); *e* 45.4 at.% Al–Cu–11.0 at.% Zn (τ_i); *f* 48.4 at.% Al–Cu–9.9 at.% Zn (τ_r).

τ_r . Free refinement of Cu occupation factors yielded the two fully occupied positions Cu1 and Cu2, while the occupation of Cu3 is only 0.15. The position Al2 is fully occupied by Al, while the two positions Al1 and Al3 show partial substitution with Zn. The resulting calculated overall composition based on Rietveld refinement is in reasonable agreement with results from EDX concentration measurements; a second

Table 4 Comparison of phase compositions for τ_c and τ_r determined by Rietveld refinements and EDX

Sample	Phase	Method	at.% Al	at.% Cu	at.% Zn
400_13	τ_c	EDX	32.7	47.8	19.5
		Rietveld	29.9	48.5	21.6
400_46	τ_c	EDX	30.4	49.0	20.6
		Rietveld	31.6	49.0	19.4
400_86	τ_c	EDX	28.9	49.5	21.6
		Rietveld	28.8	49.5	21.7
400_11	τ_r	EDX	48.4	41.7	9.9
		Rietveld	54.2	40.0	5.8
400_34	τ_r	EDX	50.9	40.3	8.8
		Rietveld	54.9	39.8	5.3

sample in the τ_r region yielded comparable results (Table 4).

Isothermal section at 550 °C

The isothermal section of phase diagram Al–Cu–Zn at temperature 550 °C is shown in Fig. 2b. At this temperature, only τ_c and τ_i were identified—the rhombohedral structural modification was not observed. The pseudo-ternary phase δ_1 is found at 550 °C in equilibrium with γ (Fig. 6). Thus, the binary δ_1 phase in the Cu–Zn system is stabilized toward lower temperatures by the addition of Al. Binary Al–Cu compounds (phases θ , η' , ζ , ζ' , δ) from the central part of the binary phase diagram are in equilibrium with the τ -phase family with only limited solubility of Zn. This part of the phase diagram is quite complex and phase relations drawn in Fig. 2b are based on diagrams published by Ghosh et al. [1]. The θ -phase shows solubility of Zn about 1 at.%. The phases η' , ζ , ζ' , δ show solubility of Zn about 5 at.%. The γ' phase is stable up to 30 at.% of Zn. At this concentration, a second-order transition between the γ and γ' phases exists. Details of evaluation are discussed together with the vertical section in “The γ/γ' phase field” section. The disordered phase β is stable at 550 °C, and it shows high solubility of Al up to 20 at.%. ε_1 phase has very high solubility at almost 30 at.% of Al, close to the ternary τ_c . Figure 7 shows the microstructure of a sample in the two-phase field $\tau_c + \varepsilon_1$. The liquid phase is stable from Al–Zn binary phase diagram up to 30 at.% of Cu, and it is connected to the eutectic point of the Al–Cu system.

Isothermal section at 700 °C

The isothermal section of phase diagram Al–Cu–Zn at 700 °C is presented in Fig. 2c. At this temperature, the cubic modification of τ phase is the only remaining modification. Figure 8 shows a micrograph of the two-phase field $\tau_c + L$. The liquid phase is stable from Cu–80Zn to Al–40Cu and covers the whole Cu poor concentration range. Pseudo-ternary ε_1 was found stable between γ and the liquid phase. Phase ε' has a solubility up to 5 at.% of Zn close to the phase τ_c . The second-order transition between γ and γ' is found around 20 at.% Zn. The β phase exhibits a complete solubility from Al–Cu to Cu–Zn. Figure 9 shows β phase in equilibrium with γ phase.

Table 5 Crystallographic parameters for the phase τ_r in sample 400_34 obtained by Rietveld refinement

Space group $R\bar{3}m$, Pearson symbol $hR30$						
$a = 4.126569(18) \text{ \AA}$, $c = 25.19380(15) \text{ \AA}$						
Site	Wyckoff Pos.	x	y	z	Occupation	B_{eq}
Cu1	$3a$	1/3	2/3	1/8	Cu: 1.00(14)	0.878(30)
Cu2	$6c$	2/3	1/3	0.030544(50)	Cu: 1.00(14)	0.878(30)
Cu3	$6c$	0	0	0.10673(35)	Cu: 0.153(20)	0.878(30)
Al1	$6c$	1/3	2/3	0.06919(12)	Al: 0.90(11) Zn: 0.10(11)	0.678(94)
Al2	$6c$	2/3	1/3	0.132822(92)	Al: 1.000(94) Zn: 0.000(94)	0.678(94)
Al3	$3a$	0	0	0	Al: 0.76(13)	0.678(94)

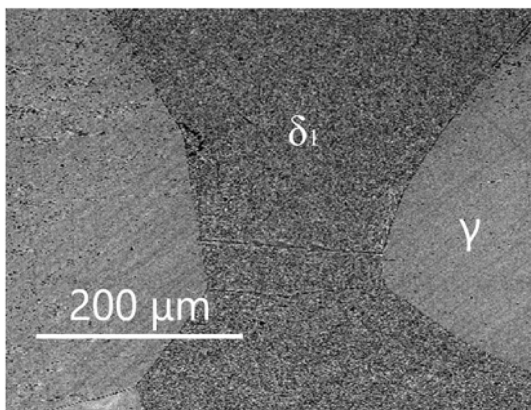


Figure 6 Microstructure of the sample 550_35 in BSE mode consists of γ and δ_1 phases.

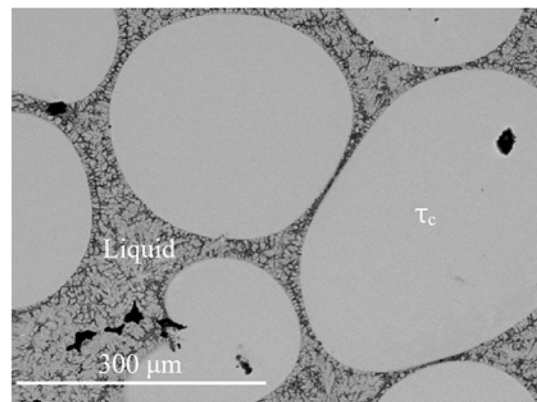


Figure 8 Microstructure of the sample 700_14 in BSE mode consists of liquid and τ_c phases.

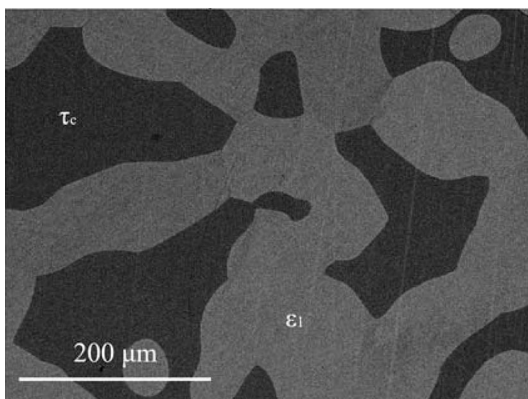


Figure 7 Microstructure of the sample 550_18 in BSE mode consists of ϵ_1 and τ_c phases.

Isothermal section at 820 °C

The isothermal section of phase diagram Al–Cu–Zn at 820 °C is presented in Fig. 2d. The temperature of 820 °C was chosen because at this temperature the γ phase is stable in Al–Cu as well as in the Cu–Zn

phase diagram. Figure 10 shows the microstructure of a $\gamma + L$ equilibrium. Full mutual solubility between the two binary γ phases has been expected and was confirmed. On Al-rich part of γ -family phase field was found γ' phase with very low solubility, this is in agreement with binary Al–Cu phase diagram.

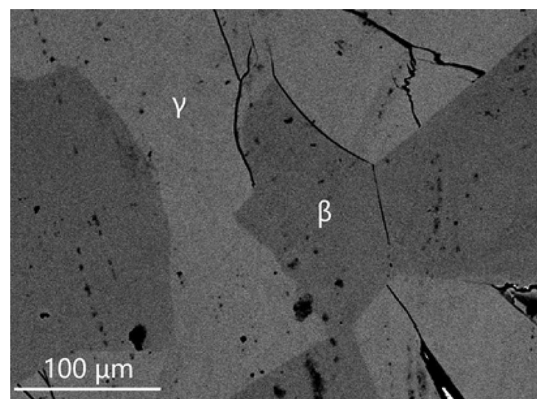


Figure 9 Microstructure of the sample 700_12 in BSE mode consists of β and γ phases.

We did not find any ternary or pseudo-ternary phase stable at 820 °C. The ε' phase shows solubility of Zn up to 15 at.%, and it is shown in equilibrium with γ' in Fig. 11.

The γ/γ' phase field

One of the major goals of the current study was to define the phase equilibrium relations between γ (cI52) and γ' (cP52). As mentioned in the previous sections, a small two-phase field $\gamma + \gamma'$ was found at 400 °C, while two different structures were identified in different samples at 550 °C and 700 °C (see detailed description below), but no two-phase field was found. In order to define the $\gamma + \gamma'$ two-phase field better, a set of additional samples with composition close to the 15 at.% Al-49 at.% Cu-Zn was prepared and long-term annealed at different temperatures at and below 400 °C. Samples annealed at the temperatures of 300 °C, 325 °C, 350 °C, 375 °C and 400 °C show well-crystallized and well-separated two phases $\gamma + \gamma'$ in equilibrium (see microstructure on Fig. 12a and XRD pattern Fig. 13a). In contrast to this, samples 15.9 at.% Al-50.9 at.% Cu-Zn annealed at 450 °C, 14.4 at.% Al-48.9 at.% Cu-Zn annealed at 500 °C and 12.4Al-46.3Cu-Zn annealed at 550 °C contained large grains in different orientation (see microstructure on Fig. 12b), but were found to be homogeneous in terms of composition. Their XRD patterns (see e.g., Fig. 13b) showed well-defined diffraction lines of the primitive structure of γ' in combination with a significant broadening of the basis of all lines fulfilling the reflection conditions for the base-centered structure. Consequently, it was possible to refine the pattern well by assuming an

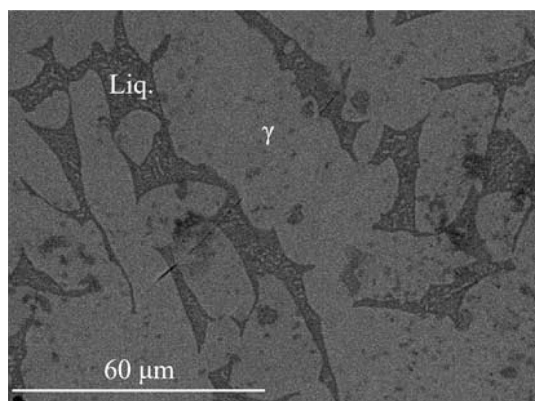


Figure 10 Microstructure of the sample 820_11 in BSE mode consists of liquid and γ phases.

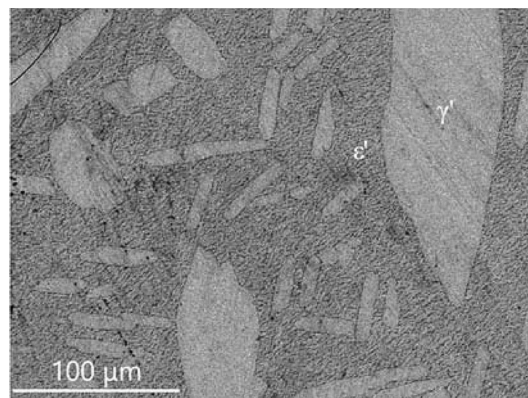


Figure 11 Microstructure of the sample 820_1 in BSE mode consists of ε' and γ' phases.

overlay of well-crystallized primitive γ' (refined crystalline domain size 212 nm) and base-centered γ of poor crystalline quality (refined crystalline domain size 24 nm). This leads to the conclusion that these samples were actually single phase at the temperature of annealing and partially transformed during quenching.

This conclusion was actually confirmed by plotting the results from all samples into a vertical section as shown in Fig. 14. The $\gamma' + \gamma$ two-phase samples are represented by the tie lines terminated by triangles with overall composition marked by cross symbol. The two-phase gap is getting smaller with increasing temperature and appears to close above 400 °C. Samples showing the characteristically broadened XRD pattern (open squares) are situated in the single-phase region but entered the two-phase field during quenching. Single-phase samples showing γ (diamond) or γ' (full squares) without specific broadening did not show the characteristic line broadening.

In order to confirm the proposed second-order transition line above approximately 440 °C shown as dashed line in Fig. 14, additional DTA experiments were performed on four samples situated in the respective composition area.

Measurements were performed under a permanent Ar flow of 50 ml min⁻¹ and with heating and cooling rates of 5 °C min⁻¹. Three runs were performed for each sample; the thermal effects during the first heating run were not taken into account. The temperature of the thermal effects used was thus the average value of the thermal effects of the second and third heating curves only. Small differences between the first and subsequent heating and cooling curves are caused by changes in the shape of the sample

Figure 12 Micrographs in BSE mode of **a** sample 350_1 with overall composition 14.9 at.% Al–48.2 at.% Cu–Zn that had been annealed at 350 °C containing well-crystallized phases $\gamma + \gamma'$ in equilibria, **b** sample 450_1 (15.9 at.% Al–50.9 at.% Cu–Zn) annealed at 450 °C without two-phase structure.

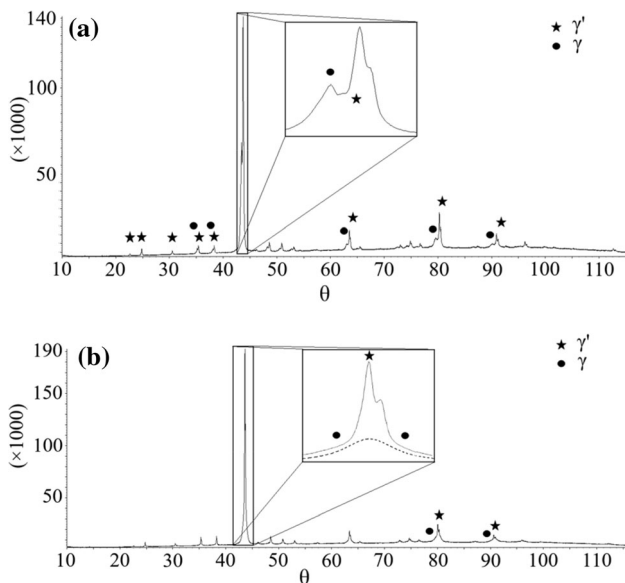
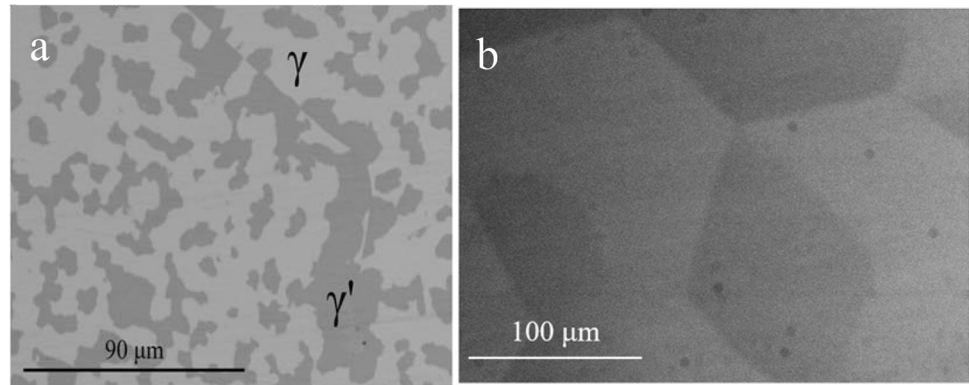


Figure 13 XRD pattern of the alloy Al–Cu–Zn containing. **a** well-crystallized phases γ and γ' in the sample 14.4 at.% Al–48.8 at.% Cu–Zn annealed at 300 °C (300_1) and **b** poorly crystallized phase γ in the sample 15.9 at.% Al–50.9 at.% Cu–Zn annealed at 450 (450_1).

following initial melting. Temperature of phase transition in solid phase was evaluated as an onset of peak, liquidus was evaluated as a minimum of peak. The results of the DTA third heating and cooling curves of the sample with composition 21.7 at.% Al–55.4 at.% Cu–Zn is presented in Fig. 15. Signals correspond to the temperature of the second-order reaction $\gamma \leftrightarrow \gamma'$ at 622.2 °C (open circles on Fig. 14), to solidus temperature at 903.8 °C (filled circles on Fig. 14) and to the liquidus temperature at 952.2 °C (triangles on Fig. 14). Composition of the samples was checked after DTA measurement to ascertain that the sample did not react with the SiO₂ material of the ampoules. Thermal analysis results are listed in

Table 3, and the transition temperatures for the $\gamma \leftrightarrow \gamma'$ transition are shown as open circles in Fig. 14.

The interpretation of the dashed line separating the γ and γ' phase fields as second-order reaction $\gamma \leftrightarrow \gamma'$ is well in line with the observed DTA effects. It also agrees with experimental results from binary phase diagram Al–Cu, where authors [3, 20] proposed a second-order transition between the primitive and base-centered structure there.

Conclusions

Although the literature related to the Al–Cu–Zn phase diagram is numerous, some of the complex phase equilibria were not well solved. The current study was designed to contribute to a better understanding of those parts of the phase diagram that needed improvement and refinement. The experimental studies were carried out at temperatures 400 °C, 550 °C, 700 °C and 820 °C, and some additional measurements were done also at additional temperatures in the $\gamma + \gamma'$ phase region. This was achieved by a combination of standard methods: overall and phase compositions of samples were measured using SEM–EDX, the temperatures of phase transitions by DTA measurements in evacuated quartz glass DTA ampoules. The crystal structures were identified by XRD.

The following main results were obtained in present study:

- Mutual relationships of $\gamma + \gamma'$ phases were studied in whole concentration and temperature range. Independent two-phase field of $\gamma + \gamma'$ was observed up to 400 °C. At higher temperature, the phase transition $\gamma \leftrightarrow \gamma'$ is proposed to be second order.

Figure 14 Vertical section of the ternary phase diagram Al–Cu–Zn between Al–0.67Cu and Cu–0.62Zn.

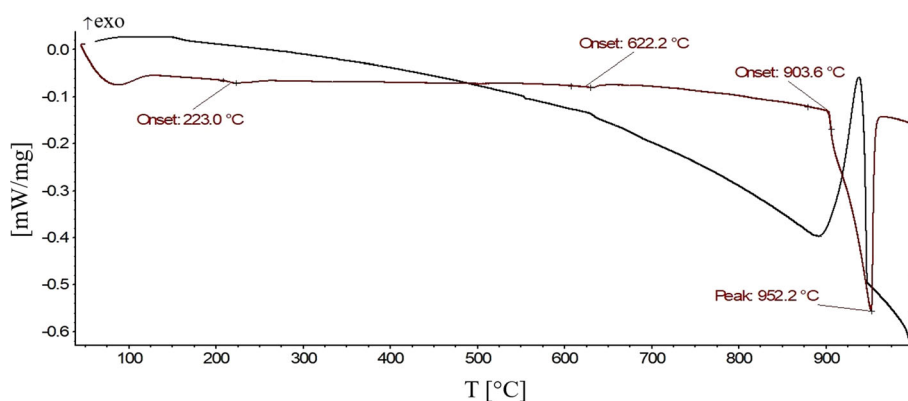
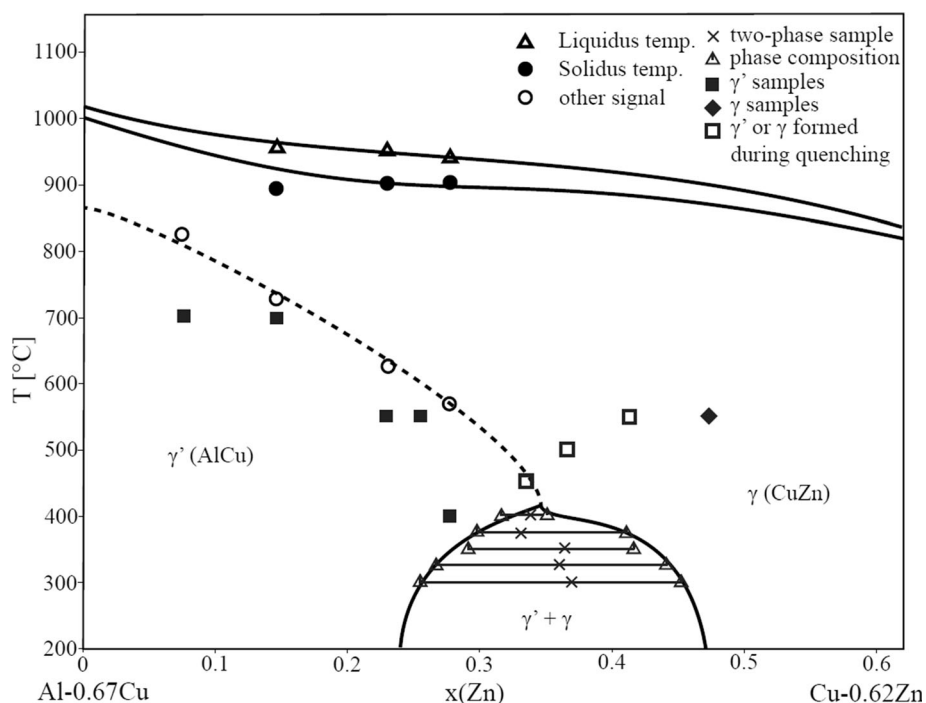


Figure 15 The third DTA heating and cooling curves of the 21.7 at.% Al–55.4 at.% Cu–Zn sample. Signals correspond to the temperature of the second-order reaction $\gamma \leftrightarrow \gamma'$ (632.4 °C) and to

- An isopleth between the binary phases γ and γ' was constructed
- For the ternary phase, at 400 °C we found strongly temperature-dependent one phase fields containing phases with cubic CsCl-type structure (τ_c) and a related rhombohedral structure type (τ_r), respectively, and an intermediate composition range with apparently incommensurate modulation (τ_i). The rhombohedral structure type (τ_r) was not found at 550 °C and above. At 700 °C we only found the cubic structure modification (τ_r)
- Isothermal sections at 400 °C, 550 °C, 700 °C and 820 °C were constructed

the liquidus temperature (952.2 °C). Measurement conditions: sample was placed in sealed evacuated quartz glass ampoule, inert atmosphere 5 N Ar 50 ml min⁻¹, heating rate 5 °C min⁻¹.

Acknowledgements

Open access funding provided by Austrian Science Fund (FWF). This study was funded by the Austrian Science Fund (FWF) under the Lise-Meitner project M2293-N34. The authors thank Stephan Puchegger from the Department of Dynamic of Condensed Systems at the University of Vienna for the assistance with the SEM measurements and Adela Zemanova from Institute of Physics of Materials, The Czech Academy of Sciences for assistance with some DTA measurement.

Author contribution

OZ: Investigation, Resources, Writing - Original Draft, Visualization, Project administration, Funding acquisition. AK: Conceptualization, Methodology, Writing - Review & Editing. KR: Methodology, Validation, Writing - Review & Editing, Supervision.

Compliance with ethical standards

Conflict of interest The authors declare that they have no conflict of interest.

Open Access This article is licensed under a Creative Commons Attribution 4.0 International License, which permits use, sharing, adaptation, distribution and reproduction in any medium or format, as long as you give appropriate credit to the original author(s) and the source, provide a link to the Creative Commons licence, and indicate if changes were made. The images or other third party material in this article are included in the article's Creative Commons licence, unless indicated otherwise in a credit line to the material. If material is not included in the article's Creative Commons licence and your intended use is not permitted by statutory regulation or exceeds the permitted use, you will need to obtain permission directly from the copyright holder. To view a copy of this licence, visit <http://creativecommons.org/licenses/by/4.0/>.

References

- [1] Ghosh G, van Humbeeck J, Perrot P (2004) Al–Cu–Zn ternary phase diagram evaluation, Ternary Evaluations, MSI, Materials Science. International Services GmbH, Stuttgart
- [2] Liang SM, Schmid-Fetzer R (2016) Thermodynamic assessment of the Al–Cu–Zn system, Part III: Al–Cu–Zn ternary system. CALPHAD 52:21–37
- [3] Zobac O, Kroupa A, Zemanova A, Richter KW (2019) Experimental description of the Al–Cu binary phase diagram. Met and Mat. Trans. A 50:3805–3815
- [4] Liang SM, Schmid-Fetzer R (2015) Thermodynamic assessment of the Al–Cu–Zn system, part II: Al–Cu binary system. CALPHAD 51:252–260
- [5] Murray JL (1983) The Al–Zn (Aluminum–Zinc) system. Bull Alloy Phase Diagrams 4(1):55–73
- [6] Massalski TB (1986) Binary alloy phase diagrams. ASM International, Metals Park, Ohio
- [7] Dinsdale AT, Zobac O, Kroupa A, Khvan A (2020) Use of third generation data for the elements to model the thermodynamics of binary alloy systems: Part 1—the critical assessment of data for the Al–Zn system. CALPHAD 68:101723
- [8] Dinsdale AT (1991) SGTE data for pure elements. CALPHAD 15(3):317–425
- [9] Mathon M, Jardet K, Aragon E, Satre P, Sebaoun A (2000) Al–Ga–Zn system: reassessments of the three binary systems and discussion on possible estimations and on optimisation of the ternary system. CALPHAD 24(3):253–284
- [10] A.P. Miodownik, Cu–Zn (copper–zinc), published in D.E. Laughlin, D.J. Chakrabarti, P. R. Subramanian: Phase diagrams of binary copper alloys, ASM International, Materials Park OH (1994) 87–496
- [11] Liang SM, Hsiao HM, Schmid-Fetzer R (2015) Thermodynamic assessment of the Al–Cu–Zn system, part I: Cu–Zn binary system. CALPHAD 51:224–232
- [12] Liang H, Chang YA (1998) A thermodynamic description for the Al–Cu–Zn System. J Phase Equilib 19:25–37
- [13] Koster W, Moeller K (1941) Zink-Kupfer-Aluminium-Legierungen. Z Metallkde 33:278–283
- [14] O. Bauer, M. Hansen, Der Einfluß vordritten Metallen auf die Konstitution der Messinglegierungen, IV. Der Einfluß von Aluminium, Z. Metallkde, 24 (1932) 73–78
- [15] Ashirimbetov ZA, Kandaurov NE, Kalina MM, Melikhov VD, Presnyakov AA (1973) Structure and properties of solid solutions of the γ -region of the Cu–Al–Zn system. Prikl. Teor. Fiz. 5:210–213
- [16] J. Gröbner, G. Effenberg Binary evaluations, MSI, Materials Science International Serviced GmbH, Stuttgart, 2004
- [17] Topas software, Version 4.2, Bruker, Karlsruhe (2009)
- [18] Murphy S (1975) The structure of the T' phase in the system Al–Cu–Zn. Met Sci 9:163–168
- [19] Taylor A, Doyle NJ (1972) Further studies on the nickel–aluminium system. I. β -NiAl and δ -Ni₂Al₃ phase fields. J Appl Cryst 5:201–209
- [20] Poweiser N, Lengauer ChL, Richter K (2011) Re-investigation of phase equilibria in the system Al–Cu and structural analysis of the high-temperature phase η -Al₁₁ – δ Cu. Intermetallics 19:1737–1746

Publisher's Note Springer Nature remains neutral with regard to jurisdictional claims in published maps and institutional affiliations.

6.4 Paper 4

- [P4] **Zobač, O.**, Kroupa, A., Richter, K.W., *Experimental isothermal sections of the ternary phase diagram Al-Cu-Si at 600 °C and 800 °C*, Journal of Materials Science, 2020, 55(31), pp. 15322-15333, doi: 10.1007/s10853-020-05077-5 (IF 4.220)



Experimental isothermal sections of the ternary phase diagram Al–Cu–Si at 600 °C and 800 °C

Ondrej Zbac^{1,2,*} , Ales Kroupa², and Klaus W. Richter¹

¹Department of Inorganic Chemistry, Functional Materials, University of Vienna, Währinger Straße 42, 1090 Vienna, Austria

²Institute of Physics of Materials, The Czech Academy of Sciences, Žitkova 22, 616 00 Brno, Czech Republic

Received: 29 April 2020

Accepted: 6 July 2020

© Springer Science+Business Media, LLC, part of Springer Nature 2020

ABSTRACT

The phase diagram of the Al–Cu–Si ternary system was investigated experimentally at the temperatures 600 °C and 800 °C. The current study was designed to contribute to a better understanding of the ternary phase diagram Al–Cu–Si at elevated temperatures, where some of the phase equilibria were only tentatively known. It was found that the ternary phase τ proposed earlier is actually an extended solid solution of Al in the CuSi_δ phase. At 700 °C, the phase CuSi_δ is stable as a pseudo ternary phase, and the existence of a significantly extended thermal stability range in the ternary was also confirmed by DSC measurements. In agreement with previous isothermal sections at other temperatures, a huge solubility of aluminum in CuSi_κ and negligible solubility of Si in AlCu_β was observed.

Introduction and literature review

The ternary system Al–Cu–Si has been heavily investigated over the last few decades due to its importance in industry. Al–Cu–Si alloys have growing importance for automotive and aerospace industry due to their low density and good materials properties. The ternary Al–Cu–Si alloys show better corrosion resistance than Al–Cu alloys and have higher strength than Al–Si alloys [1]. Knowledge of the complete ternary phase diagram is therefore crucial for the designing of the ternary alloys matching specific requirements. The Cu-rich corner of Al–Cu–Si phase diagram and the binary subsystems Cu–Si and especially Al–Cu are highly complex. Despite various studies of phase equilibria, the

ternary phase diagram is still not fully described. The current study was designed to contribute to the proper description of those parts of the phase diagram which are not solved in literature, or which have lead to conflicting results from different authors. A detailed literature review of existing phase diagram information on Al–Cu–Si and its binary subsystems is given below.

Al–Cu binary system

The Al–Cu phase diagram exhibits a wide range of intermetallic phases with complex mutual relationships in all regions of the phase diagram. It was studied by many authors and several very comprehensive overviews have been published [2–6]. The

Address correspondence to E-mail: zbac@ipm.cz

detailed literature review of experimental data is published in our previous work [6]. The binary phase diagram is shown in Fig. 1.

The maximal solid solution of the Cu in Al is equal to 2.5 at. % Cu at the eutectic temperature of 550 °C [2]. The crystal structure of the θ -phase was determined as having the space group $I4/mcm$ by Havinga [7]. Ponweiser et al. [4] studied the homogeneity ranges of the η -family of phases by SEM–EDX and XRD and found that the low-temperature η' -phase extends from 51.9 at.% Cu to 54.8 at.%. The orthorhombic η -phase is formed by peritectic reaction at 620 °C. Gulay and Harbrecht [8, 9] describe the structures of the ζ -family of phases with the supposed low temperature modification ζ' (Al₃Cu₄) and high temperature modification ζ (Al₃Cu₄- δ) in detail. The ε -family of phases exists over similar composition range as the ζ -phases at medium and high temperatures [2]. The γ' (AlCu γ -brass type structure) to δ transition was addressed by the combined EDX/XRD investigation and the shape of the ($\gamma' + \delta$) two-phase field was postulated from the XRD studies of quenched samples in our previous work [6].

Liu et al. [3] found that γ crystallizes with the CuZn γ -brass type structure and exhibits second-order transition reaction between γ' and γ . The β -phase decomposes by a eutectoid reaction to (Cu) solid solution and the γ' -phase at a temperature between 566.7 °C and it melts congruently at 1049 °C [4]. The α' phase, with a composition of 77.5 at.% Cu, is stable below 363 °C [10]. The maximal solubility of Al in Cu is 18.5 at.% at the eutectoid temperature of 566.7 °C [6].

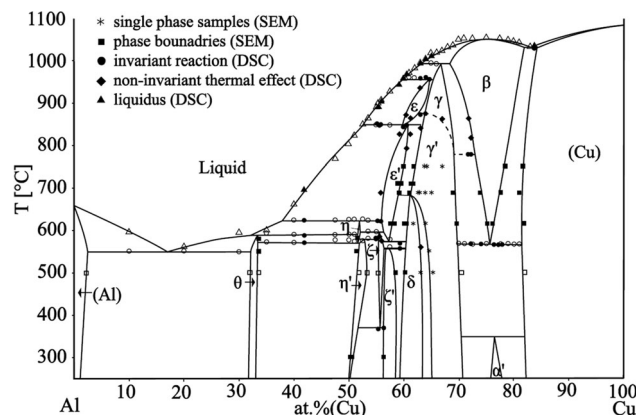


Figure 1 Experimental binary phase diagram of subsystem Al–Cu reprinted from our previous work [6].

Al–Si binary system

Murray and McAllister [11] presented the original theoretical assessment of the Al–Si phase diagram. Subsequently, the phase diagram of Al–Si system was re-adjusted using newer phase stability data and experimental results by Chakraborti and Lukas [12] and the resulting thermodynamic assessment was published in the scope of COST507 (cited in [13]). Al–Si is a simple eutectic system with two solid solution phases, FCC_A1 (Al) and diamond_A4 cubic (Si) (see Fig. 2). The composition of the eutectic point is Al–12.2 at.% Si and the eutectic temperature is 577 °C.

Cu–Si binary system

The Cu–Si system was investigated intensively in the last decades due to the possible development of new types of Li-ion batteries [14], applications in catalysis [15] and in microelectronic research [16].

Olesinski and Abbaschian [17] published a classical assessment of the Cu–Si phase diagram. Later, Sufryd et al. [18] published the most recent study of Cu-rich part of experimental phase diagram (Fig. 3).

Kaufman [19] computed the first simplified version of the phase diagram of the Cu–Si system. A more complex description of the Cu–Si phase diagram was obtained by Bühler and published in COST 507 database [20]. This assessment was later improved by Yan [21]. Hallstedt et al. [22] made a critical theoretical reassessment based on the most recently published experimental results.

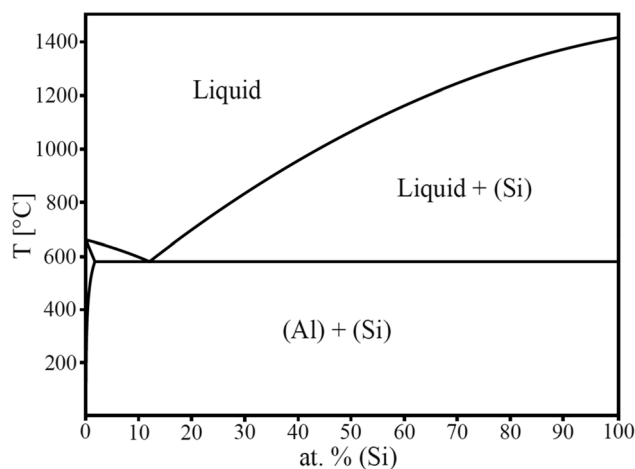


Figure 2 Redrawn theoretical phase diagram published in scope of COST507 [13].

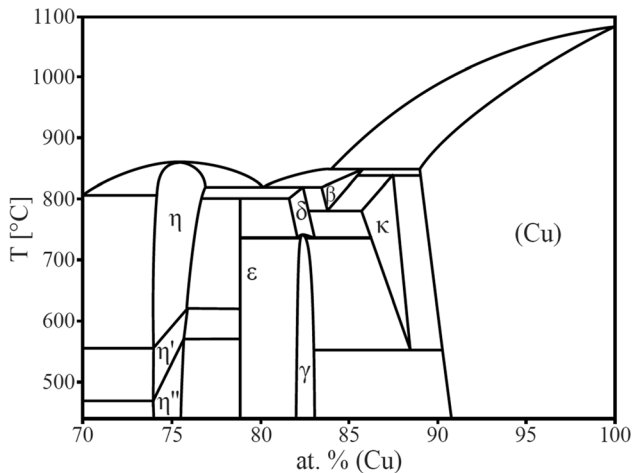


Figure 3 Section of the copper-rich part of the Cu–Si phase diagram [18].

All the binary intermetallic phases exist in the Cu-rich part of the phase diagram. The Cu_3Si family of phases consists of three different modifications with slightly different compositions stable over different temperature ranges. The high-temperature Cu_3Si modification is denoted as η , an intermediate-temperature as η' and low-temperature as η'' . The high-temperature η phase melts congruently at 859 °C. A first-order phase transformation is supposed between all Cu_3Si modifications, with two-phase fields existing between 558 °C and 620 °C for η and η' phases, and between 467–570 °C for η' and η'' phases. The Cu_3Si phases η and η' have a rhombohedral structure (R-3 m and R-3b, respectively). No exact information about the crystal structure of η'' exists, it was proposed to have an orthorhombic [23] or tetragonal symmetry [24].

The existence of the stoichiometric intermetallic phase $\text{Cu}_{15}\text{Si}_4$ (ϵ -phase) was widely discussed in the literature [25]. The assessment by Gierlotka [26] includes the ϵ phase, but some older works did not confirm the existence of this phase in the binary equilibrium phase diagram. The existence of this phase was firstly described by Arrhenius [27]. Experimental work [28, 29] based on diffusion-couple experiments did not confirm the existence of ϵ in the stable phase diagram. But later van Loo et al. [30] confirmed thermodynamic stability of ϵ phase by the diffusion-couple experiments. Sufryd et al. [18] proposed that the formation of ϵ is kinetically inhibited, but it is thermodynamically stable in Cu–Si system.

The γ -phase has cubic structure (β -Mn). According to [18], it is formed at approx. 736 °C by a congruent

transformation, but the extent of solubility of this phase has not yet been precisely determined. The high temperature phase δ decomposes eutectoidly at 734 and 735 °C, respectively [31]. Gierlotka modeled the γ -phase as stoichiometric being formed at 732 °C by peritectoid reaction $\delta + \kappa \rightarrow \gamma$ in his theoretical assessment [26].

The other three phases δ , β and κ are stable at high temperatures. The δ phase is formed by a peritectic reaction from β and liquid at 824 °C and decomposes at 710 °C. The β phase forms peritectically from FCC_A1 (Cu) and liquid at 852 °C and decomposes by eutectoid reaction at 785 °C. The β phase crystallizes in the cubic W-type structure. The κ phase (Mg-type structure) is formed by a peritectoid reaction from β and FCC_A1 (Cu) at 842 °C and decomposes at 552 °C [32].

Al–Cu–Si ternary system

The ternary system Al–Cu–Si was first studied by Matsuyama [33] and Hisatsune [34]. They described the phases present in the binaries and information on invariant ternary equilibria including the liquidus surface projection. Lukas and Lebrun [35], who included all relevant phase diagram information up to that year, carried out an assessment of the phase diagram information. They identified no ternary intermetallic phases at that time. A theoretical assessment of Pan et al. [1] focused on an optimization of the thermodynamic data of the Al-rich liquid phase. They computed a liquidus projection and vertical sections depicting the liquid–solid equilibria and compared these results with the experimental data. This work was included in the review paper by Raghavan [36]. Riani et al. [37] determined an isothermal section at 500 °C for the whole composition range, with special attention to Cu-rich alloys. Also He et al. [38] presented a thermodynamic assessment of the system, supplemented by new experimental results. Hallstedt et al. [22] published the most recent theoretical reassessment.

Ponwieser and Richter [39], who characterized isothermal phase equilibria at 500 °C and 700 °C and assessed the reaction sequences in the Cu-poor part of the ternary system did the most recent experimental study of the Al–Cu–Si system. A ternary high-temperature phase τ was found to exist in the 700 °C section. Cao et al. [40] studied the mobility of

elements in FCC_A1 alloys. A list of all phases present in the ternary system is given in Table 1.

Experimental

The overall compositions of experimental samples were selected in order to describe isothermal sections of Al–Cu–Si phase diagram at temperatures 600 °C and 800 °C. Our work focuses mainly on the Cu-rich part of the isothermal section, which is the most complex area. The prepared samples were analyzed and characterized by different static and dynamic analytical methods (SEM–EDX, DSC, XRD).

Sample preparation

Samples were prepared from pure elements of purity 5 N for Al and Cu and 6 N for Si. Any oxide present in the copper was reduced by keeping it in H₂ gas flow at 300 °C for 3 h. Samples were then arc melted on a water-cooled copper plate under a low-pressure Ar atmosphere using pure Zr as the getter. The alloys were re-melted several times in order to improve the homogenization of the material. Long-term annealing of the samples was performed at selected temperatures on material sealed in evacuated quartz glass ampoules. To prevent reaction of liquid Al with the SiO₂ from quartz glass, the samples with high content of Al-rich liquid were placed inside corundum

Table 1 Stable phases in Al–Cu–Si ternary system

Phase name (this work)	Common names	Pearson symbol	Structure prototype	T. range (°C)	Comments, references
α (Al)	FCC_A1, Al	<i>cF4</i>	Cu	≤ 660.5	
α (Cu)	FCC_A1, Cu	<i>cF4</i>	Cu	≤ 1083	
α (Si)	Diamond_A4, Si	<i>cF8</i>	Si	≤ 1413.9	
AlCu_θ	θ, Al ₂ Cu	<i>tI12</i>	Al ₂ Cu	≤ 590.5	[6]
AlCu_η	η ₁ , Eta HT	<i>oP16/oC16</i>	n.a.	573.9–624.5	[6]
AlCu_η'	η ₂ , Eta LT	<i>mC20</i>	AlCu	≤ 574.5	[6]
AlCu_ζ	ζ ₂ , Al ₃ Cu _{4–8}	<i>Imm2</i>	Al ₃ Cu _{4–8}	373–597	[6]
AlCu_ζ'	ζ ₁ , Al ₃ Cu ₄	<i>Fmm2</i>	Al ₃ Cu ₄	min. 300 – 560.5	[6]
AlCu_ε	ε ₁ , epsilon HT	cubic?	n.a.	959–846	[6]
AlCu_ε'	ε ₂ , epsilon LT	<i>hP4</i>	NiAs	846–568.5	[6]
AlCu_δ	δ, Al ₅ Cu ₈	<i>hR52</i>	Al ₄ Cu ₉ (r)	≤ 680	[6]
AlCu_γ	γ ₀ , γ-CuZn, γ_brass	<i>cI52</i>	Cu ₅ Zn ₈	991–779.6	[6]
AlCu_γ'	γ ₁ , γ-AlCu, γ_D8 ₃	<i>cP52</i>	Al ₄ Cu ₉	≤ 873.5	[6]
AlCu_β	BCC_A2	<i>cI2</i>	W	1052–566.7	Forms a continuous solution with CuSi_β [6]
AlCu_α'	α ₂ , alpha_LT	n.a.	Super structure based on TiAl ₃	≤ 360	[6]
CuSi_κ	Cu ₇ Si	<i>hP2</i>	Mg	552–842	[31]
CuSi_β	BCC_A2	<i>cI2</i>	W	785–852	Forms a continuous solution with AlCu_β [31]
CuSi_γ	Cu ₅ Si	<i>cP20</i>	β-Mn	≤ 729	[31]
CuSi_δ	Cu ₅ Si_HT	<i>t**</i>	**	711–824	[31]
CuSi_ε	Cu ₁₅ Si ₄	<i>cI76</i>	ε-CuSi	≤ 800	[25]
CuSi_η	Cu ₃ Si_HT	<i>hR*</i>	**	859–558	[23]
CuSi_η'	Cu ₃ Si_MT	<i>hR9</i>	η'-CuSi	620–467	[23]
CuSi_η''	Cu ₃ Si_LT	<i>oC*</i>	**	< 570	[31]

**Not known

crucibles. These crucibles with samples were sealed in evacuated quartz glass ampoules. A conventional tube furnace was used for the heat treatment. Samples were quenched into cold water from their annealing temperatures. Annealing times and temperatures were selected with the aim of obtaining states close to thermodynamic equilibrium.

Experimental phase diagram investigation

A combination of dynamic and static methods was used for investigation of the phase diagram. Phase equilibria, microstructure and chemical analysis of phases and overall compositions were performed by using scanning electron microscopy combined with energy dispersive X-ray spectroscopy (SEM–EDX), employing either a Zeiss Supra 55 VP instrument equipped with an energy dispersive detector for quantitative analysis or a similarly equipped SEM JEOL JSM-6460. Identification of phases present in the long-term annealed samples was achieved using X-ray powder diffraction. A Bruker D8 Diffractometer equipped with a high-speed position sensitive (PSD) detector (Lynxeye) was used in the $\theta/2\theta$ reflection setting. Rietveld refinements of selected diffraction patterns were performed with the Topas software [41]. Annealing temperature of the sample, overall composition, coexisting phases and phase compositions of the specific phases in equilibrium are listed in Table 2. Annealing temperature and number of the sample are listed in column 1 and the annealing time is shown in column 2. Column 3 shows the overall composition measured by SEM–EDX. Coexisting phases stable in the samples are listed in column 4; column 5–7 show the composition of equilibrium phases existing in the samples measured by SEM–EDX in same order as the phases are mentioned in column 4.

Phase transition temperatures were measured using a high-temperature DSC heat flow (NETZSCH Pegasus 404 C) in corundum crucibles with lid under the inert atmosphere of Ar 5 N with flow 50 ml min^{-1} . Heating and cooling rate was 10 K min^{-1} . The DSC was calibrated using a set of pure metal standards having well-defined melting temperatures (Sn, Bi, Al, Cu, Ag, Au). Calibration was carried out under the same conditions as the experimental measurements. Three heating and cooling runs were performed for each sample. Thermal analysis results are listed in Table 3.

Results and discussion

By combining experimental results listed in Table 2, it was possible to propose isothermal sections of ternary phase diagram Al–Cu–Si at 600 °C and 800 °C. The isothermal section at 700 °C is redrawn from Ponweiser and Richter [39] with some corrections. Overall compositions of selected samples are represented by several symbols in our phase diagrams. Stars represent the samples located in the single-phase field. Squares are the overall composition of the samples containing two phases in equilibrium. Compositions of each phase and relevant tie-lines are not shown as the figure would be very difficult to read. Triangles represent the overall composition of the samples containing three phases in equilibrium. Phase compositions are defined by the position of corners of the tie-triangle. The shape of the phase boundaries and phase fields not defined by our own samples were drawn based on information from binary subsystems and phase rules.

Isothermal sections at 600 °C

The isothermal section of phase diagram Al–Cu–Si at 600 °C is shown in Fig. 4. The phases CuSi_η/η' show solubility up to 2 at.% of Al, phases CuSi_γ and CuSi_ε (Fig. 5) have very limited solubility (up to 1 at.% Al). In contrast, the phase CuSi_κ (Fig. 6) has the highest Al solubility extending almost to the Al–Cu binary side of the ternary phase diagram Al–Cu–Si. The solubility of Al in α (Cu) solid solution reaches 20 at.%. The Al–Cu β phase exhibits very small solubility of Si. In the theoretically assessed phase diagram published by Hallstedt et al. [22], the AlCu_β phase dissolves up to 3 at.% Si. This was not confirmed experimentally—in this part of the phase diagram, the CuSi_κ phase is still stable according to our results. Also the phase AlCu_γ is very stable and shows solubility of Si up to 17 at.% Si. The phases AlCu_δ , AlCu_ε and AlCu_η have negligible solubility of Si. The liquid phase field extends continuously from Al–Cu part to the Al–Si part above the relevant eutectic points, in agreement with binary phase diagrams.

Isothermal sections at 700 °C

Figure 7 shows the redrawn isothermal section at 700 °C published by Ponweiser and Richter [39] with

Table 2 Chemical composition of the long-term annealed representative sample (measured by EDX)

T (°C) no.	Annealed time (h)	Overall composition (at.%)			Coexist. phases Phase 1 + 2 + 3	Phase 1 (at.%)			Phase 2 (at.%)			Phase 3 (at.%)		
		Al	Si	Cu		Al	Si	Cu	Al	Si	Cu	Al	Si	Cu
600_1	480	1.0	21.3	77.7	CuSi _ε + CuSi _η	0.6	22.4	77.0	1.9	23.0	75.1	–	–	–
600_2	480	1.3	19.2	79.5	CuSi _κ + CuSi _ε	6.5	11.3	82.2	1.0	21.4	77.6	–	–	–
600_3	480	4.1	17.4	78.5	CuSi _κ + AlCu _γ + CuSi _ε	10.6	10.7	78.7	8.9	14.4	76.7	1.5	21.5	77.0
600_4	480	4.8	17.6	77.6	AlCu _γ + CuSi _ε	8.5	14.7	76.8	1.4	21.2	77.4	–	–	–
600_5	480	7.5	17.1	75.4	AlCu _γ + CuSi _η	15.0	11.9	73.1	3.5	21.6	74.9	–	–	–
600_6	480	14.2	12.3	73.5	AlCu _γ + CuSi _η	15.2	11.2	73.6	3.1	21.7	75.2	–	–	–
600_7	480	1.6	14.8	83.6	CuSi _κ + CuSi _γ	3.5	12.9	83.6	1.2	17.7	81.1	–	–	–
600_8	480	4.6	14.0	81.4	CuSi _κ + CuSi _ε	6.4	11.1	82.5	0.8	22.0	77.2	–	–	–
600_9	480	6.2	13.4	80.4	CuSi _κ + CuSi _ε	8.1	11.2	80.7	1.2	21.0	77.8	–	–	–
600_10	480	8.6	12.0	79.4	AlCu _γ + CuSi _η	14.0	11.7	74.3	*	*	*	–	–	–
600_11	480	17.5	7.4	75.1	CuSi _κ + AlCu _γ	15.2	6.8	78.0	18.5	8.2	73.3	–	–	–
600_12	480	9.3	12.4	78.3	CuSi _κ + CuSi _ε	10.2	11.7	78.1	1.3	22.1	76.6	–	–	–
600_13	480	26.5	3.9	69.6	AlCu _γ	26.5	3.9	69.6	–	–	–	–	–	–
600_14	480	18.2	3.5	78.3	Cu + CuSi _κ	15.2	2.3	82.5	18.9	3.7	77.4	–	–	–
600_15	480	28.1	1.5	70.4	CuSi _κ + AlCu _γ	23.2	1.9	74.9	29.3	1.3	69.4	–	–	–
600_16	480	9.0	8.3	82.7	CuSi _κ	9.0	8.3	82.7	–	–	–	–	–	–
600_17	480	8.6	13.7	77.7	CuSi _κ + AlCu _γ	9.8	12.9	77.3	8.0	15.7	76.3	–	–	–
600_22	420	11.2	17.8	71.0	CuSi _η + AlCu _γ + Si	18.7	10.6	70.7	2.5	25.8	71.7	0.0	100.0	0.0
600_23	420	17.0	14.0	69.0	CuSi _η + AlCu _γ + Si	18.0	10.7	71.3	2.1	25.8	72.1	0.0	100.0	0.0
600_25	420	21.6	12.9	65.5	AlCu _γ + Si	23.7	6.7	69.6	0.0	100.0	0.0	–	–	–
600_26	420	19.5	1.3	79.2	Cu + CuSi _κ	17.9	1.2	80.9	20.9	1.6	77.5	–	–	–
600_27	420	5.9	18.6	75.5	CuSi _ε + CuSi _η + AlCu _γ	1.3	21.4	77.3	4.5	20.6	74.9	11.3	14.0	74.7
600_28	420	19.4	6.4	74.2	CuSi _κ + AlCu _γ	18.2	5.0	76.8	20.6	7.1	72.3	–	–	–
600_30	420	33.1	16.5	50.4	AlCu _δ + AlCu _ε + Si	39.8	0.3	59.9	41.8	0.2	58.0	0.0	100.0	0.0
600_31	420	54.0	4.4	41.6	AlCu _η + Liquid	46.7	0.0	53.3	61.0	9.1	29.9	–	–	–
600_32	420	59.1	7.0	33.9	AlCu _η + Liquid	46.3	0.1	53.6	60.7	8.4	30.9	–	–	–
600_33	420	15.7	8.1	76.2	CuSi _κ + AlCu _γ	14.0	8.1	77.9	17.3	9.0	73.7	–	–	–
600_34	420	12.2	8.9	78.9	CuSi _κ	12.2	8.9	78.9	–	–	–	–	–	–
600_35	420	9.4	36.9	53.7	CuSi _η + AlCu _γ + Si	2.4	25.5	72.1	18.6	10.5	70.9	0.0	100.0	0.0
600_36	420	7.4	7.8	84.8	CuSi _κ + Cu	7.5	7.5	85.0	7.4	9.5	83.1	–	–	–
600_38	420	3.8	11.3	84.9	CuSi _κ	3.8	11.3	84.9	–	–	–	–	–	–
600_39	420	10.5	6.5	83.0	Cu + CuSi _κ	11.0	6.6	82.4	*	*	*	–	–	–
600_40	420	10.8	15.2	74.0	CuSi _η + AlCu _γ	3.9	20.6	75.5	13.0	12.5	74.5	–	–	–
800_1	350	1.9	22.0	76.1	CuSi _δ + CuSi _η	3.2	18.4	78.4	1.7	22.5	75.8	–	–	–
800_2	350	1.8	19.2	79.0	CuSi _δ + CuSi _η	1.8	18.7	79.5	1.3	21.8	76.9	–	–	–
800_4	350	3.3	20.5	76.2	CuSi _δ + CuSi _η	5.2	17.5	77.3	2.0	22.2	75.8	–	–	–
800_6	350	14.9	11.9	73.2	AlCu _γ	14.9	11.9	73.2	–	–	–	–	–	–
800_7	350	2.4	15.0	82.6	CuSi _κ + CuSi _δ	2.3	13.9	83.8	2.1	17.5	80.4	–	–	–
800_8	350	4.8	14.4	80.8	CuSi _κ + CuSi _δ	5.1	13.3	81.6	4.2	16.2	79.6	–	–	–
800_9	350	7.0	13.7	79.3	CuSi _κ + CuSi _δ	8.0	11.5	80.5	6.1	15.7	78.2	–	–	–
800_10	350	9.2	12.6	78.2	CuSi _κ + CuSi _δ	10.1	10.5	79.4	8.1	14.4	77.5	–	–	–
800_13	350	22.6	3.3	74.1	CuSi _κ + AlCu _γ	22.0	2.8	75.2	23.7	3.7	72.6	–	–	–
800_20	350	15.3	6.0	78.7	CuSi _κ	15.3	6.0	78.7	–	–	–	–	–	–
800_26	370	18.6	1.0	80.4	Cu + CuSi _κ	17.3	0.8	81.9	20.2	2.1	77.7	–	–	–
800_28	370	19.4	6.0	74.6	CuSi _κ + AlCu _γ	18.4	5.1	76.5	20.8	6.8	72.4	–	–	–
800_34	370	12.5	9.2	78.3	CuSi _κ	12.5	9.2	78.3	–	–	–	–	–	–
800_40	370	11.7	14.3	74.0	AlCu _γ	11.7	14.3	74.0	–	–	–	–	–	–

Table 2 continued

T (°C) no.	Annealed time (h)	Overall composition (at.%)			Coexist. phases Phase 1 + 2 + 3	Phase 1 (at.%)			Phase 2 (at.%)			Phase 3 (at.%)		
		Al	Si	Cu		Al	Si	Cu	Al	Si	Cu	Al	Si	Cu
800_42	370	0.3	20.2	79.5	CuSi _δ	0.3	20.2	79.5	–	–	–	–	–	–
800_43	370	1.5	20.8	77.7	CuSi _δ	1.5	20.8	77.7	–	–	–	–	–	–
800_44	370	2.9	18.9	78.2	CuSi _δ + CuSi _η	2.3	19.4	78.3	2.0	21.6	76.4	–	–	–
800_45	370	4.9	17.7	77.4	CuSi _δ	4.9	17.7	77.4	–	–	–	–	–	–
800_46	370	4.0	18.1	77.9	CuSi _δ	4.0	18.1	77.9	–	–	–	–	–	–
800_47	370	5.9	17.9	76.2	CuSi _δ	5.9	17.9	76.2	–	–	–	–	–	–
800_48	370	6.0	18.3	75.7	CuSi _δ	6.0	18.3	75.7	–	–	–	–	–	–
800_49	370	6.3	16.8	76.9	CuSi _δ	6.3	16.8	76.9	–	–	–	–	–	–

*Not measured

Table 3 Temperature of equilibrium phase transitions measured by DSC visualized in Fig. 14

T (°C) no.	Nominal comp. (at.%)			Thermal effects (heating) (°C)			
	Al	Si	Cu	Liquidus	Solidus	Other effects	Non-equilibrium
800_42	0.3	20.2	79.4	840	819	731	359; 796
800_43	1.5	20.8	77.7	836	821	665; 718	387; 780
800_2	1.8	19.3	79.0	834	818	639; 714	390; 783
800_46	4.0	18.1	77.9	839	821	685	591
800_45	4.9	17.7	77.4	843	819	678	–
800_49	6.3	16.8	76.9	850	822	672	–

Overall composition of sample lies in line between binary points Cu-18 at.% Si and Cu-35 at.% Al

necessary improvements stemming from our new experimental results. Phase AlCu_β, which is still stable in binary phase diagram Al–Cu at this temperature was added to the isothermal section, and the relevant two- and three-phase fields are included in the figure. The ternary phase τ proposed by Ponweiser and Richter [39] is re-interpreted to be the pseudo-ternary CuSi_δ phase field which is stabilized to lower temperatures by Al substitution. This interpretation is based on our experimental findings at 800 °C discussed in “Isothermal sections at 800 °C and The CuSi_δ phase field” sections. The three-phase field (CuSi_δ + CuSi_ε + Al–Cu_γ), missing in [39] was also added.

Isothermal sections at 800 °C

Experimental isothermal section of ternary phase diagram Al–Cu–Si at 800 °C is presented in Fig. 8. At

this temperature, the phase CuSi_η exhibits a solubility of up to 3% Al and the phase CuSi_δ exhibits an Al-solubility up to 7.5 at.% Al. Experimental results on this particular phase are described in more detail in the “The CuSi_δ phase field” section. Similar to the sections at 600 and 700 °C, CuSi_κ exhibits a protracted homogenous phase field extending almost to the Al–Cu binary border of the diagram (see Fig. 9). The phase AlCu_β has negligible solubility of Si. This finding contradicts to the presumption of the theoretical modeling of phase diagram [22]. The phase AlCu_γ (see Fig. 10) extends far into the ternary system and shows a Si-solubility of up to 23 at.%.

The CuSi_δ phase field

One of the major goals of the current study was to describe the τ-phase reported in [39] at higher temperature. As shown in Fig. 8, this composition area

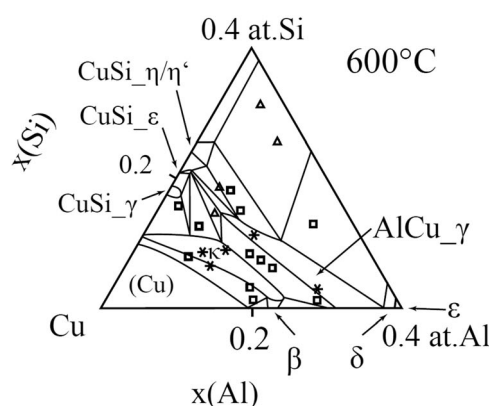
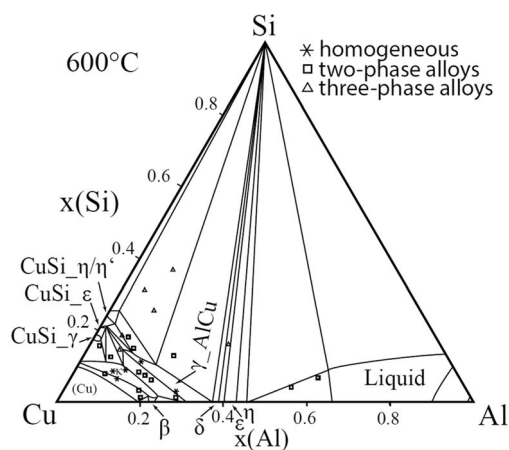


Figure 4 Isothermal section of phase diagram Al–Cu–Si at 600 °C **a** in whole concentration range and **b** Cu-rich corner. Stars represent the samples located in the single-phase field. Squares are the overall composition of the samples containing two phases in equilibrium. Triangles represent the overall composition of the samples containing three phases in equilibrium.

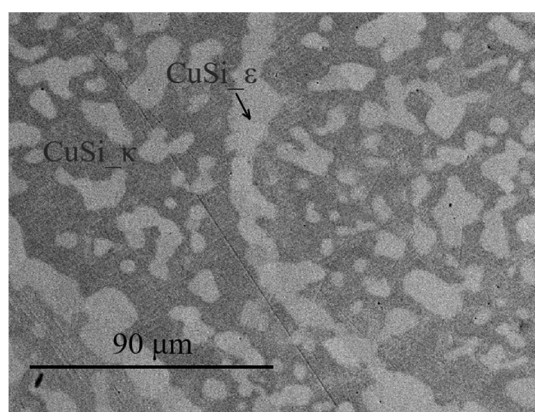


Figure 5 Microstructure of the sample 600_8 in BSE mode consisting of CuSi_ε and CuSi_κ phases.

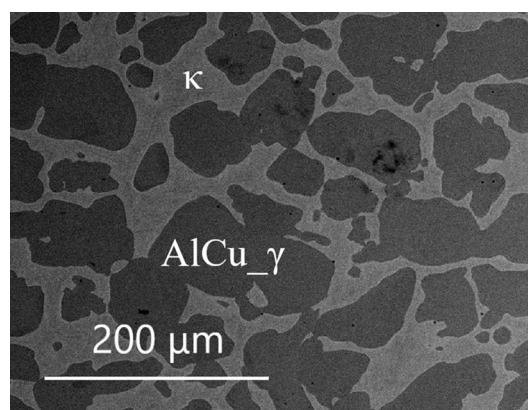


Figure 6 Microstructure of the sample 600_15 in BSE mode consisting of CuSi_κ and AlCu_γ phases.

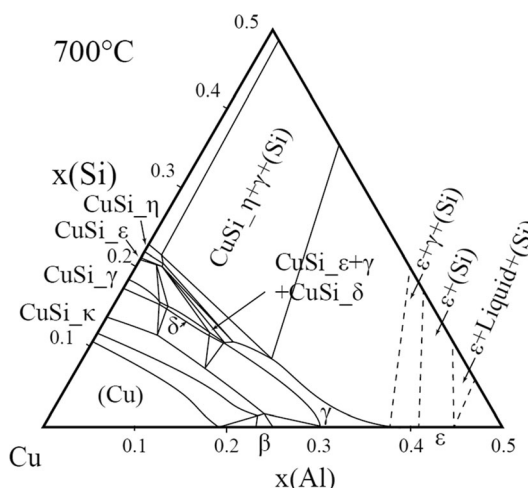


Figure 7 Redrawn and improved isothermal section of phase diagram Al–Cu–Si at 700 °C based on data from [39].

turned out to be part of the extended CuSi_δ phase-field at 800°. This implies that the ternary stability island reported at 700 °C (Fig. 7) is part of this phase field, not a true ternary phase. The shape of the homogeneous phase field of CuSi_δ was studied by a set of samples analyzed by SEM, EDX and DSC. XRD was used to confirm the proposed single-phase field. Figure 11a and Fig. 11b show the XRD patterns of single-phase samples with composition of Al between 0.7 at.% Al and 6.3 at.% Al annealed at 800 °C (800_43, 800_46, 800_45, 800_49). These patterns agree very well with each other and vary continuously with the composition, which strongly indicates continuity. The diffraction pattern is quite complex, and so it was impossible to determine the structure from the patterns. The structure of binary phase CuSi_δ is not known because it is

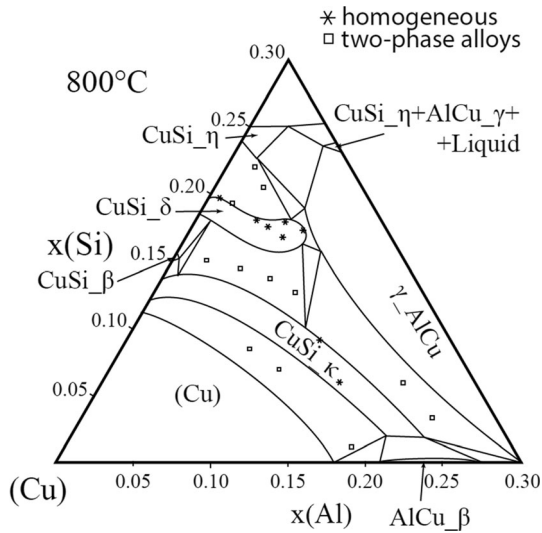


Figure 8 Isothermal section of the phase diagram Al–Cu–Si at 800 °C. Stars represent the samples located in the single-phase field. Squares are the overall composition of the samples containing two phases in equilibrium. Triangles represent the overall composition of the samples containing three phases in equilibrium.

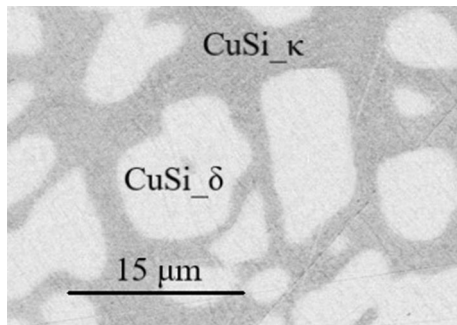


Figure 9 Microstructure of the sample 800_9 in BSE mode consist of CuSi_κ and CuSi_δ phases.

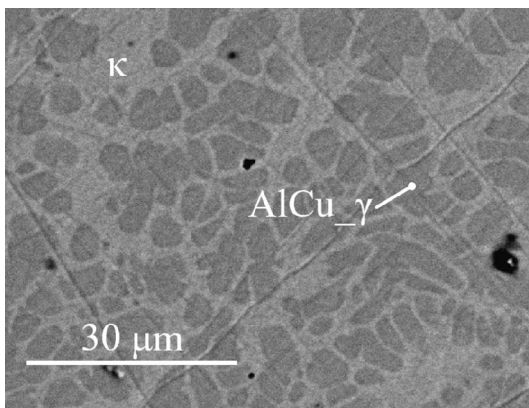


Figure 10 Microstructure of the sample 800_28 in BSE mode consist of CuSi_κ and AlCu_γ phases.

unquenchable. It is interesting, that the addition of relative small amounts of Al sufficiently stabilizes CuSi_δ to make it quenchable. This gives rise for some hope to solve the crystal structure of (ternary stabilized) CuSi_δ in future. Up to now, however, we were not able to find a single crystal of sufficient quality for structure determination.

Sample 6.3Al–Cu–16.8Si (800_49) was measured by DSC to determine the temperature stability of CuSi_δ phase (see Fig. 12). The DSC curves indicates that the CuSi_δ phase is stable in the temperature range 672–848 °C as there is no other phase transition in this interval. We therefore conclude, that the τ-phase reported at 700 °C [39] is identical with the Al-stabilized ternary CuSi_δ phase. The eutectoid decomposition of τ reported there (E2: τ → ε + γ + κ, 500 < T < 700 [39]) is consequently corrected. It is actually E2: δ → ε + γ + κ at (approximately) T = 672 °C. The CuSi_δ phase with this particular composition (6.3Al–Cu–16.8Si) was found to melt between 822 (solvus) and 850 °C (liquidus) according to Fig. 12.

Figure 13 shows the heating DSC curve of sample 0.3Al–Cu–20.2Si (800_42) annealed at 800 °C. The exothermic peak at 359 °C is the transition of CuSi_δ phase, which is metastable at this temperature, to the corresponding equilibrium phase composition. CuSi_δ phase is re-formed at 731 °C. The non-invariant effect at temperature 796 °C is most likely connected with the decomposition of CuSi_ε formed in the initial exothermal reaction. Solidus of CuSi_δ is described by onset of the last peak at 819 °C and the peak minimum at 840 °C represents the liquidus temperature. Results of the equilibrium thermal effects for six samples are listed in Table 3.

A combination of the isothermal sections (Figs. 7, 8) and the equilibrium DSC results was used for the construction of tentative vertical section of phase diagram. It is shown in Fig. 14 with superimposed experimental data. Triangles represent liquidus temperature, squares the other equilibrium phase transitions obtained by DSC measurement. Filled circles represent overall composition of long-term annealed single-phase CuSi_δ samples. Solid lines are experimentally described phase field borders, dashed line represent estimated phase field borders. Results show a remarkably constant melting point of the ternary CuSi_δ phase field in combination with a significant stabilization toward lower temperature with increasing Al content.

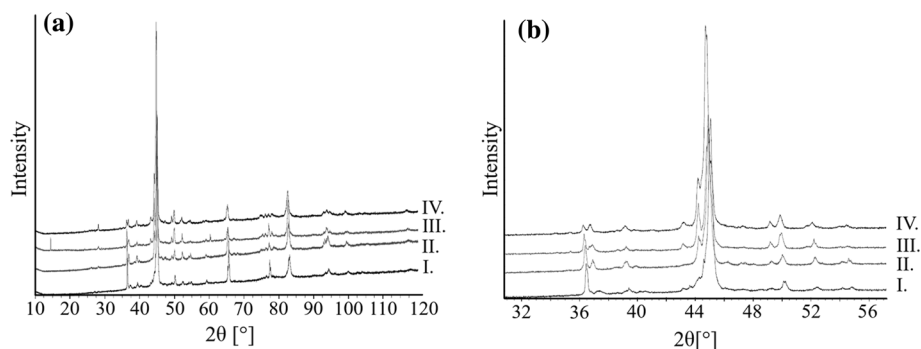


Figure 11 XRD patterns of set of homogeneous samples in phase region CuSi_δ . **a** In whole measured range, **b** in central part of pattern with the main peak. Individual patterns are shifted on Y axis for better visualization. Composition of samples are

following: I. 0.7Al-Cu-19.9Si (800_43); II. 4.0Al-Cu-18.2Si (800_46); III. 4.9Al-Cu-17.7Si (800_45); IV. 6.3Al-Cu-16.8Si (800_49).

Figure 12 Heating DSC curve of sample 6.3Al-Cu-16.8Si (800_49). Measurement condition: heating rate 10 K min^{-1} , inert atmosphere $5\text{ N Ar } 50\text{ ml min}^{-1}$, corundum crucible with the lid.

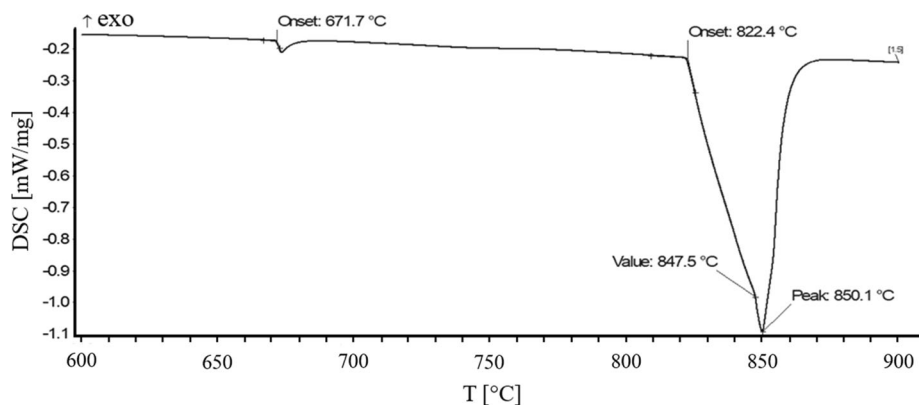
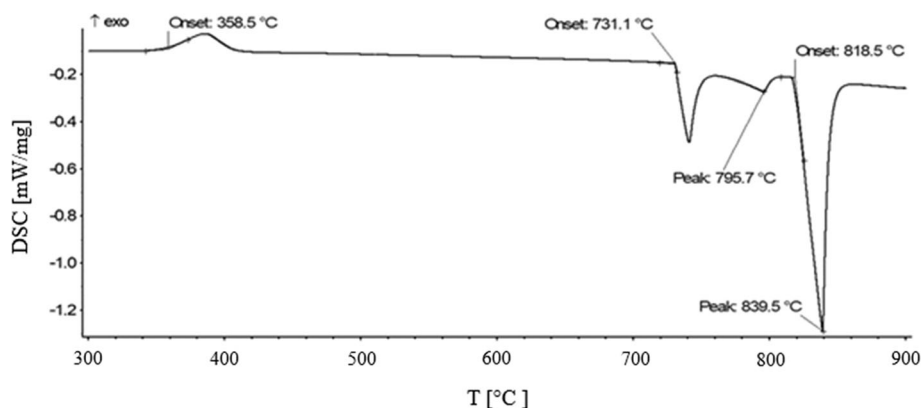


Figure 13 Heating DSC curve of sample 0.3Al-Cu-20.2Si (800_42). Measurement condition: heating rate 10 K min^{-1} , inert atmosphere $5\text{ N Ar } 50\text{ ml min}^{-1}$, corundum crucible with the lid.



Conclusion

Although literature relating to the Al-Cu-Si phase diagram is numerous, some of the phase equilibria were not well-defined. The current study was designed to contribute to the understanding of high-temperature equilibria, which were not defined satisfactorily up to now. This was achieved by a combination of standard methods: overall and phase

compositions of samples were measured using SEM-EDX, the temperature of phase transitions by DSC. The crystal structures were identified by XRD. The experimental studies were carried out at temperatures 600 and 800 °C and some additional measurements at additional temperatures were performed in the CuSi_δ region. Isothermal sections at 600 °C and 800 °C were constructed and the published phase diagram at 700 °C [39] was corrected to agree with

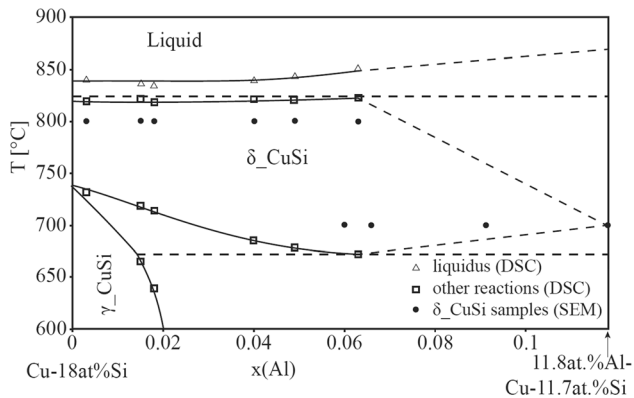


Figure 14 Tentative vertical section of Al–Cu–Si phase diagram between the points Cu-18 at.% Si and 11.8 at.% Al–Cu–11.7 at.% Si with superimposed experimental results.

the binary Al–Cu phase diagram and our new experimental results. More detailed study of CuSi_δ phase structure and its temperature stability and also more detailed investigation of liquidus surface are the most urgent tasks for future experimental studies. Nevertheless, presented data should be sufficient for a thermodynamic modelling of the Al–Cu–Si phase diagram, and the question about stability of CuSi_δ phase and primary solidification fields of the liquidus surface might be predicted.

Acknowledgements

This study was supported by the Austrian Science Fund (FWF) under the Lise-Meitner project M2293-N34.

Author contributions

OZ involved in investigation, resources, writing—original draft, visualization, project administration, funding acquisition. AK involved in methodology, writing—review and editing. KR involved in methodology, validation, writing—review and editing, supervision.

Compliance with ethical standards

Conflict of interest The authors declare that they have no conflict of interest.

References

- [1] Pan XM, Lin C, Morral JE, Brody HD (2005) An assessment of thermodynamic data for the liquid phase in the Al-rich corner of the Al–Cu–Si system and its application to the solidification of a 319 alloy. *J Phase Equilib Diffus* 26:225–233
- [2] Murray JL (1985) The aluminium–copper system. *Int Met Rev* 30:211–234
- [3] Liu XJ, Ohnuma I, Kainuma R, Ishida K (1998) Phase equilibria in the Cu-rich portion of the Cu–Al binary system. *J Alloys Compd* 264:201–208
- [4] Ponweiser N, Lengauer ChL, Richter KW (2011) Re-investigation of phase equilibria in the system Al–Cu and structural analysis of the high-temperature phase $\eta\text{-Al}_{1-\delta}\text{Cu}$. *Intermetallics* 19(11):1737–1746
- [5] Liang SM, Schmid-Fetzer R (2015) Thermodynamic assessment of the Al–Cu–Zn system, part II: Al–Cu binary system. *CALPHAD* 51:252–260
- [6] Zobac O, Kroupa A, Zemanova A, Richter KW (2019) Experimental description of the Al–Cu binary phase diagram. *Metall Mater Trans A* 50:3805–3815
- [7] Havinga EE (1972) Compounds and pseudobinary alloys with the CuAl_2 (C16)-type structure II. Theoretical discussion of crystallographic parameters. *J Less Common Metals* 27:187–193
- [8] Gulay LD, Harbrecht B (2003) The crystal structure of zeta(2)- Al_3Cu_4 -delta. *Z Anorg Allg Chem* 629:463–466
- [9] Gulay LD, Harbrecht B (2004) The crystal structure of zeta(1)- Al_3Cu_4 . *J Alloys Compd* 367:103–108
- [10] Kuwano N, Doi T, Eguchi T (1977) Period of antiphase and tetragonality in the α_2 phase of Cu–Al alloys. *Trans JIM* 18:807–815
- [11] Murray JL, McAllister AJ (1984) The Al–Si (aluminium–silicon) system. *Bull Alloy Phase Diagr* 5(74–84):89–90
- [12] Chakraborti N, Lukas HL (1992) Thermodynamic optimization of the Mg–Al–Si phase diagram. *CALPHAD* 16(1):79–86
- [13] Gröbner J, Lukas HL, Aldinger F (1996) Thermodynamic calculation of the ternary system Al–Si–C. *CALPHAD* 20(2):247–254
- [14] Ahn HJ, Kim YS, Kim WB, Sung YE, Seong TY (2006) Formation and characterization of Cu–Si nanocomposite electrodes for rechargeable Li batteries. *J Power Sources* 163(1):211–214
- [15] Parajuli O, Kumar N, Kipp D, Hahm JI (2007) Carbon nanotube cantilevers on self-aligned copper silicide nanobeams. *Appl Phys Lett* 90:173107

- [16] Liu Y, Song S, Mao D, Ling H, Li M (2004) Diffusion barrier performance of reactively sputtered Ta–W–N between Cu and Si. *Microelectron Eng* 75:309–315
- [17] Olesinskym RW, Abbaschian GJ (1986) The copper–silicon system. *Bull Alloy Phase Diagr* 7:170–178
- [18] Suffryd K, Ponweiser N, Riani P, Richter KW, Cacciamani G (2011) Experimental investigation of Cu–Si phase diagram at $x(\text{Cu}) > 0.72$. *Intermetallics* 19:1479–1488
- [19] Kaufman L (1979) Coupled phase diagrams and thermochemical data for transition metal binary systems VI. *CALPHAD* 3(1):45–76
- [20] Jacobs M (1994) COST507-thermochemical database for light metal alloys. In: Ansara I (ed) European Commission. European Commission, Brussels, p 124
- [21] Yan XY, Chang YA (2000) A thermodynamic analysis of the Cu–Si system. *J Alloys Compd* 308:221–229
- [22] Hallstedt B, Gröbner J, Hampf M, Schmid-Fetzer R (2016) Calorimetric measurements and assessment of the binary Cu–Si and ternary Al–Cu–Si phase diagrams. *CALPHAD* 53:25–38
- [23] Solberg JK (1978) Crystal structure of ϵ -Cu₃Si precipitates in silica. *Acta Crystallogr Sect A* 34:684–698
- [24] Mukherje KP, Bandyopadhyaya JP, Gupta KP (1969) Phase relationship and crystal structure of intermediate phases in Cu–Si system in composition range of 17 at pct Si to 25 at pct Si. *Trans Metall Soc AIME* 245:2335–2338
- [25] Morral FR, Westgren A (1934) The crystal structure of a complex copper-silicon compound. *Ark Kemi Miner Geol* 11B(37):1–6
- [26] Gierlotka W, Haque MA (2013) On the binary (Cu + Si) system: thermodynamic modelling of the phase diagram and atomic mobility in face centred cubic phase. *J Chem Thermodyn* 57:32–38
- [27] Arrhenius S, Westgren A (1931) X-radiation analysis of copper–silicon alloys. *Z Phys Chem* 14:66–79
- [28] Veer FE, Burgers WG (1968) Diffusion in the Cu₃Si phase of the copper silicon system. *Trans Am Inst Min Metall Pet Eng* 242:669–673
- [29] Ward WJ, Carroll KM (1982) Diffusion of copper in the copper–silicon system. *J Electrochem Soc* 129:227–229
- [30] van Loo FJJ, Vosters PJC, Becht JGM, Metselaar R (1988) The influence of impurities on the kinetics and morphology of reaction layers in diffusion couples. *Mater Sci Forum* 29:261–274
- [31] Olesinski RW, Abbaschian GJ (1994) Cu–Si (copper–silicon). In: Subramanian PR, Chakrabarti DJ, Laughlin DE (eds) *Phase diagrams of binary copper alloys*. ASM International, Materials Park, pp 398–405 (**Review, Equi. Diagram, Cryst. Struct., Thermodyn.**, 60)
- [32] Mattern N, Seyrich R, Wilde L, Baecht C, Knapp M, Acker J (2007) Phase formation of rapidly quenched Cu–Si alloys. *J Alloys Compd* 429:211–215
- [33] Matsuyama K (1934) Ternary diagram of the Al–Cu–Si system. *Kinzuko no Kenkyu* 11:461–490
- [34] Hisatsune C (1936) The constitution diagram of the copper–silicon–aluminium system. *Mem Coll Eng Kyoto Imp Univ* 9:18–47
- [35] Lukas HL, Lebrun N (2005) Al–Cu–Si (aluminium–copper–silicon), *Materials—The Landolt–Bornstein New Series IV/11A2, MSIT*, 135–147
- [36] Raghavan V (2007) Aluminum–Copper–Silicon. *J Phase Equilib Diffus* 28(2):180–182
- [37] Riani P, Suffryd K, Cacciamani G (2009) About the Al–Cu–Si isothermal section at 500 °C and the stability of the ϵ -Cu₁₅Si₄ phase. *Intermetallics* 17:154–164
- [38] He CY, Du Y, Chen HL, Xu H (2009) Experimental investigation and thermodynamic modeling of the Al–Cu–Si System. *CALPHAD* 33(2):200–210
- [39] Ponweiser N, Richter KW (2012) New investigation of phase equilibria in the system Al–Cu–Si. *J Alloys Compd* 512:252–263
- [40] Cao D, Liu Y, Su X, Wang J, Tu H, Huang J (2013) Diffusion mobilities in the fcc_A1 Cu–Si, Al–Si and Al–Cu–Si alloys. *J Alloys Compd* 551:155–163
- [41] Bruker (2009) Topas software, version 4.2. Bruker, Karlsruhe

Publisher's Note Springer Nature remains neutral with regard to jurisdictional claims in published maps and institutional affiliations.

6.5 Paper 5

- [P5] Kroupa, A., **Zobač, O.**, Richter, K.W., *The thermodynamic reassessment of the binary Al-Cu system*, Journal of Materials Science, 2021, 56, pp. 3430-3443, doi: 10.1007/s10853-020-05423-7 (IF 4.682)



The thermodynamic reassessment of the binary Al–Cu system

Aleš Kroupa^{1,*}, Ondřej Zobač^{1,2,*} , and Klaus W. Richter²

¹Academy of Science, Institute of Physics of Materials, The Czech Academy of Sciences, Žitkova 22, 616 00 Brno, Czech Republic

²Institut für Anorganische Chemie – funktionelle Materialien, Universität Wien, Währinger Straße 42, 1090 Vienna, Austria

Received: 15 May 2020

Accepted: 2 October 2020

Published online:

27 October 2020

© Springer Science+Business Media, LLC, part of Springer Nature 2020

ABSTRACT

The Al–Cu binary system has been investigated intensively in the past as key binary system for many important industrial alloys. With respect to new experimental results about phase equilibria in Al–Cu system, it was found necessary to prepare new CALPHAD-type thermodynamic description of the Al–Cu system. In course of this work, the known crystallography of several intermetallic phases and the information about site occupations in particular crystallographic positions were implemented in the new thermodynamic phase descriptions. The intermetallic phases were furthermore modelled with all their different temperature modifications. Very good agreement with the experimental results was reached both, for the Al–Cu phase diagram and for the calculated thermodynamic properties, namely the enthalpy of mixing, enthalpies of formation and thermodynamic activities.

Introduction

Phase diagrams are important for the development of new materials and the study of their properties. Detailed knowledge about the coexistence and stability of phases in stable or metastable equilibrium significantly rationalizes such design and consequent development of requested materials properties. Phase diagrams are important also for other fields of science and engineering, e.g. for the prediction of materials properties. As experimental studies of multicomponent phase diagrams are very time

consuming and the extent of experimental work might be overwhelming, the theoretical modelling of multicomponent phase diagrams is very useful tool for the materials development. Robust and reliable thermodynamic description of basic binary systems is crucial for the modelling of multicomponent system. With respect to the new experimental results about phase equilibria in Al–Cu system that were presented in our previous work [1], it was found necessary to prepare a new CALPHAD (CALculation of PHase Diagram)-type thermodynamic description of the Al–Cu system. The experimental phase diagram presented by [1] is shown in Fig. 1.

Handling Editor: P. Nash.

Address correspondence to E-mail: kroupa@ipm.cz; zobac@ipm.cz

The Al–Cu binary system has been investigated intensively as key binary system for many Al–based, Cu–based and dural alloys. The first thermodynamic description of Al–Cu system was done by Kaufman et al. [2]. Later, further work on improvement of the of Al–Cu phase diagram and the development of a more accurate thermodynamic description was based on the comprehensive work of Murray [3], who presented very detailed overview of existing experimental data and combined this with own calculations. Further progress in the field of modelling was presented by Chen et al. [4]; nevertheless, the assessment of Al–Cu system carried out by Saunders [5] and published in the public COST507 database has been most widely used and accepted in many multicomponent databases later on. The thermodynamic descriptions of the liquid and γ -brass family of phases were later reassessed by Witusiewicz et al. [6]. The most recent reassessment was carried out by Liang and Schmid–Fetzer [7], who based their work on the assessment of Murray [3] and the experimental results of Ponweiser et al. [8]. They used a new model for the γ - and γ' -phases, partially new crystal structure data and extended the description with information about the η/η' -phase transition and a thermodynamic modelling of the α' phase. Figure 2a shows the differences in the modelling of the intermetallic phases described by Witusiewicz et al. [6], in comparison with Liang and Schmid–Fetzer [7]. The comparison of the thermodynamic assessment of Liang and Schmid–Fetzer together with the experimental data from [1, 8] is shown in Fig. 2b.

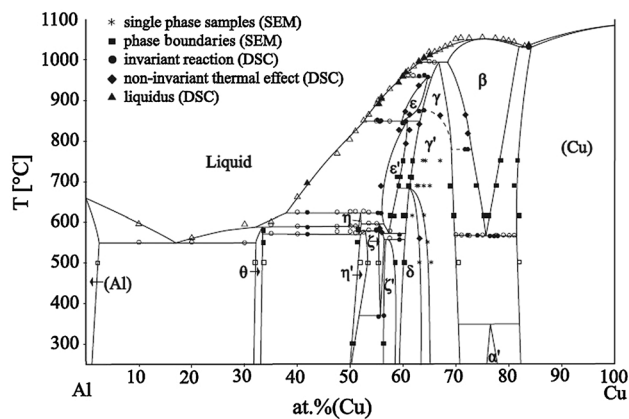


Figure 1 New experimental phase diagram from Zobac et al. [1], based on experimental results from their paper and from previous work of Ponweiser et al. [8].

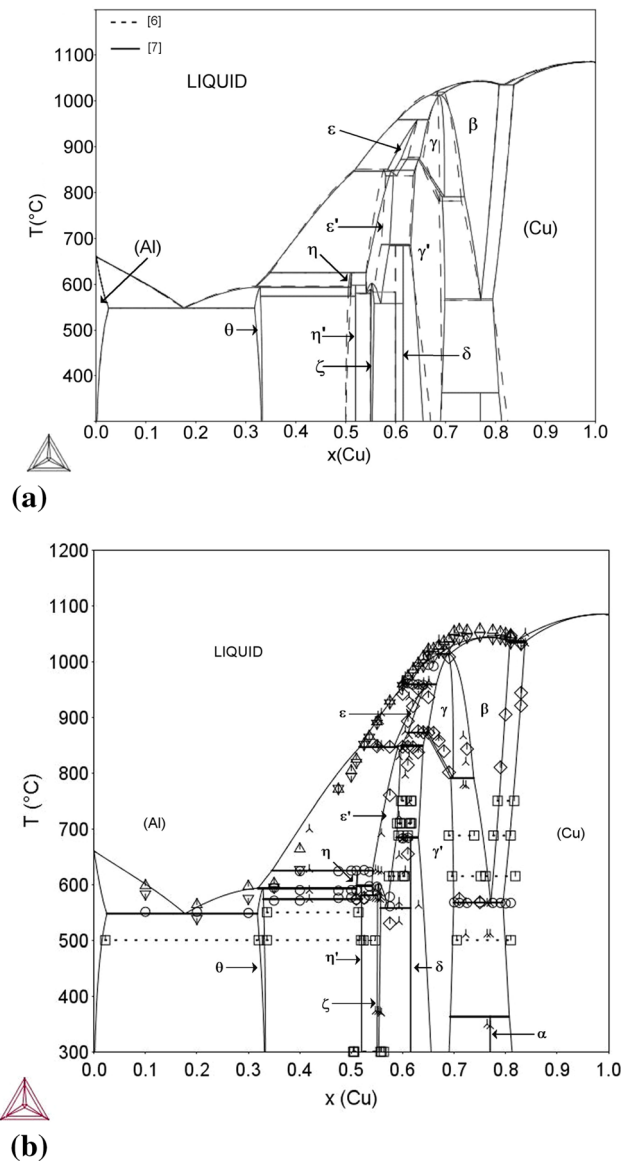


Figure 2 a Comparison of the calculated phase diagrams from Witusiewicz et al. [6] (dashed lines) and Liang and Schmid–Fetzer [7] (full lines), b comparison of the calculated phase diagram from [7] and experimental results from [1] and [8] (white up-pointing triangle, white down-pointing triangle—DSC signal for liquid on heating and cooling [1], bold circle—DSC signal for invariant reaction [1], white diamond—other DSC signals [1], black three pointed star—DSC signals [8], bold square—phase boundaries according to SEM/EDX measurements [1, 8]).

It is clear from Figs. 1 and 2a, b that the main uncertainties exist, especially in the region between 50 and 70 at% Cu, where the phase relations are very complex with many phases existing in several modifications. This part of the diagram was therefore in

details studied in the paper [1], and this results were the basis for the system reassessment.

Al–Cu thermodynamic modelling

Available experimental information

The system was studied experimentally by many teams, and the first detailed assessment of experimental results was carried out by Murray [3], who analysed the results from many papers dealing with this system. An extensive list of more than 200 papers is presented in her study. Since then, two other important experimental assessments were carried out by [8] and by the authors of this assessment [1]. The detailed study of the Al–Cu phase diagram carried out by Ponweiser et al. [8], using newer studies and their own extensive DSC/DTA (differential scanning calorimetry) and X-ray measurements, is in reasonably good agreement with the assessment of [3]. Nevertheless, the Al–Cu phase diagram is very complex containing many complex intermetallic phases, some of them with different temperature modifications and there were still several concentration and temperature regions which have not yet been solved completely. Also, the character of some of the complex phase equilibria was not well described. The recently published experimental paper [1] was designed to contribute to a better description of those parts of the phase diagram.

DSC/DTA, SEM–EDX and X-ray powder diffraction measurements were combined in [1], and main attention was given to those unsolved problems. The melting behaviour of the θ phase was studied, and the peritectic character of the relevant invariant reaction was confirmed in agreement with the results of Goedecke and Sommer [9]. A congruent solidification of the θ phase was found being metastable as proposed in [9]. Furthermore, the DSC signals at approx. 327 °C and 55% of Cu were found in the study [1]. The position of the signal corresponds quite well to the temperature where Gulay and Harbrecht observed the decomposition of the HT- ζ -phase in their study [10]. The existence of HT and LT versions of ζ -phases is the simplest explanation of this signal. Consequently, the temperature stability of the HT ζ -phase was re-evaluated and was found to lie in the range 373–587 °C and the LT ζ' -phase is supposed to exist from the room temperature to 560.5 °C. The

phase boundaries of the two-phase field $\gamma' + \epsilon'$ were experimentally defined. The difficulties in defining the γ'/δ transition were addressed by a combined EDX/XRD investigation of more than ten samples that were annealed in the temperature range 500–750 °C. Like in the previous studies, it was not possible to determine the two-phase field between the γ' - and δ -phases directly, but the shape of the ($\gamma' + \delta$) two-phase field was determined from the XRD studies of quenched samples. The temperature of the ordering reaction $\gamma \leftrightarrow \gamma'(\beta)$ was experimentally determined to be 779.6 °C. The DSC/DTA measurements confirmed very good agreement with other parts of the Al–Cu phase diagram determined in previous descriptions [3, 8]. The experimental phase diagram obtained in the scope of [1] study is shown in the Fig. 1.

Thermodynamic data were measured by many different authors. The enthalpy of mixing was measured for the temperatures between 1084 and 1317 °C by several authors [11–17], and the thermodynamic activities of Al and Cu were measured in the temperature interval 700–1200 °C in [18–24], and the enthalpies of formation were studied in [25–28]. Detailed information was presented in the paper of [7]; only the most important papers are mentioned here.

The source of key experimental information used in the theoretical assessment is summarized in the Table 1, and the basic information about crystal structures is shown in the Table 2.

Thermodynamic modelling

The CALPHAD approach [29, 30] was used for thermodynamic modelling and calculation of phase diagrams. The compositions of phases in equilibrium correspond to the minimum total Gibbs energy of a closed system at constant temperature and pressure. Calculations were done using Thermo-Calc [31] and Pandat [32] software which solve the constrained minimization problem to determine the set of non-negative amount of individual components in equilibrium phases. The Gibbs energies are considered relative to the stable element reference state (SER).

The solution phases

The Gibbs energy of the liquid was modelled using a substitutional model with one sublattice. The molar

Table 1 Experimental information included into this CALPHAD-type assessment

Complete Al–Cu phase diagram	Assessment of exp. results	Murray [3]
Complete Al–Cu phase diagram	DSC/DTA, X-ray, SEM	Ponweiser et al. [8]
Complete Al–Cu phase diagram	DSC, X-ray, SEM	Zobac et al. [1]
Al ₂ Cu phase region	Character of inv. reaction	Goedecke and Sommer [9]
ζ (Al ₃ Cu ₄), ζ' (Al ₃ Cu _{4-δ})	Cryst. structure	Gulay and Harbrecht [10, 34]
η'	Range of stability	El-Boragy et al. [38]
Enthalpy of mixing of the liquid phase	Temp. range 1084–1317 °C	Various authors [11–17]
Activity of elements	Temp. range 700–200 °C	Various authors [18–24]
Enthalpy of formation of solid phases	Temp. range 20–500 °C	Various authors [25–28]

Gibbs energy of the liquid (and solid solution generally) can be considered as the sum of different contributions:

$$G_m^\phi = \sum_{i=1}^n x_i \cdot {}^0G_i^\phi + RT \cdot \sum_{i=1}^n x_i \cdot \ln(x_i) + {}^E G_m^\phi \quad (1)$$

where first term is the molar reference Gibbs energy consisting of the weighted sum of the Gibbs energies of constituents *i* in the crystallographic structure identical to the phase φ relative to the chosen reference state.

The temperature dependence of the Gibbs energy of the pure constituent *i* is expressed by the polynomial

$$G_i^\phi = a + b \cdot T + c \cdot T \ln(T) + d_1 \cdot T^2 + d_2 \cdot T^3 + d_4 \cdot T^{-1} + \dots \quad (2)$$

where *a*, *b*, *c*, and the *d_i* are adjustable coefficients.

The second term of Eq. (1) is the contribution to the Gibbs energy from the ideal mixing of the constituents on the crystal lattice or in the liquid, where *n* is the number of constituents.

Third term, the excess Gibbs energy ^EG_m^φ, describes the influence of the non-ideal behaviour of the system on the thermodynamic properties of the phase and is given by the Redlich–Kister–Muggianu formalism [33]

$${}^E G_m^\phi = \sum_{\substack{i,j=1 \\ i \neq j}}^n x_i \cdot x_j \cdot \sum_{z=0}^m {}^z L(x_i - x_j)^z \quad (3)$$

where ^zL is the temperature dependent interaction parameters, describing the mutual interaction between constituents *i* and *j*. Their temperature dependence is defined as:

$$L(T) = a + b \cdot T + c \cdot T \ln(T) \quad (4)$$

The fcc_A1 (Al) and (Cu) and bcc_A2 (β and maybe ε phases) can be considered as substitutional solid solution phases. Nevertheless, it is more convenient to model them as an interstitial solid solution, using two sublattices (Al,Cu)₁(Va)₃, the first one being occupied by metal atoms, the second one by hypothetical interstitial atoms (where appropriate) and structural vacancies (Va). This model is used to remain consistent with assessments of other fcc_A1 and bcc_A2 containing systems where interstitials have to be included. In the present case, the second sublattice contains only vacancies, and the model behaves like the substitutional model described above. The solubility of the other elements in terminal fcc solid solution is moderate for Cu in Al and very large (almost 20 at%) for Al in Cu. There is also significant solubility region for the β-phase (bcc). The ε-phase with a solubility of several at% is also modelled with the (bcc) model.

Intermetallic phases

The Al–Cu system contains many intermetallic phases, which differ in the extent of solubility and complexity of the crystal structure (see Table 2).

The compound energy formalism is used for the modelling of intermetallic phases in the system. Only basic principles for the case of two sublattices are shown here, the details of this approach can be found, e.g. in [29].

The reference Gibbs energy equivalent to the Eq. (1) for such a model is given as:

$$G_{ref}^\phi = \sum_{i,j} y_i \cdot {}^2 y_j \cdot {}^0 G_{i,j}, \quad i, j = \text{Al, Cu, Va} \quad (5)$$

Table 2 Stable intermetallic phases in Al–Cu binary phase diagram

Phase name	Other common names	Pearson symbol	Structure type	T range (°C)	Composition and temp. range (at% Cu)			
					Min	Max	Max at T [°C]	References
(Al)	FCC_A1	<i>cF4</i>	Cu	≤ 660.5	0	2.48	548.2	[3]
θ	θ	<i>tI12</i>	Al ₂ Cu	≤ 591	32.1	32.6	549	[9]
	Al ₂ Cu				32	33.6	500	[8]
				≤ 590.5		33.6	550	[1]
η	η_1	<i>oP16/</i>	n.a.	574–625	51.5	52.9	596.3	[8]
	η_{HT}	<i>oC16</i>		573.9–624.5				[1]
η'	η_2	<i>mC20</i>	AlCu	≤ 581	51.9	54.8	500	[8]
	η_{LT}			≤ 574.5	51.4		550	[1]
ζ	ζ_2 Al ₃ Cu _{4-δ}	<i>Imm2</i>	Al ₃ Cu _{4-δ}	507–597	54.5	56.5	580/561	[8]
				ca. 425 –	55*	58*		[34]
				min. 550				
				Min.	55.2	56.7		[3]
ζ'	ζ_1 -Al ₃ Cu ₄	<i>Fmm2</i>	Al ₃ Cu ₄	373–587				[1]
				298–561	56.3	57.4	400	[8]
				Min 400–579	56.6*	57.7*		[10]
				530–590	55.2	56.3		[3]
				Min.				[1]
ε	ε_1	cubic?	n.a.	960–847	59.5	64.5	847/960	[8]
				959–846				[1]
ε'	ε_2	<i>hP4</i>	NiAs	847–578	54.5	62.5	625/847	[8]
				846–568.5				[1]
δ	δ Al ₅ Cu ₈	<i>hR52</i>	Al ₄ Cu ₉ (r)	≤ 687	60?	64?	450	[8]
				≤ 680				[1]
γ	$\gamma_0, \gamma_{CuZn}, \gamma_{brass}$	<i>cI52</i>	Cu ₅ Zn ₈	993–800	65	69	874/800	[8]
				991–779.6				[1]
γ'	$\gamma_1, \gamma_{AlCu}, \gamma_{D8_3}$	<i>cP52</i>	Al ₄ Cu ₉	≤ 874	65	70	450	[8]
				≤ 873.5	61.0	69.6	688/615	[1]
β	BCC_A2	<i>cI2</i>	W	1052–567	68	82	996/1030	[8]
				1052–566.7				[1]
α'	α_2, α_{LT}	n. a.	Superstructure based on TiAl ₃	≤ 360	76	79	–	[39]
				≤ 350			–	[1]
(Cu)	FCC_A1	<i>cF4</i>	Cu	< 1083	81	100	450	[8]

*The region of existence was not studied in details in this work

where the $^p y_i$ terms are the site fractions of each constituent in the respective sublattice p (1 or 2). The term $G_{(i;j)}$ describes the Gibbs energy of formation of the so-called “end member” $i;j$, or the Gibbs energy of pure element i in the crystallographic structure φ if both sublattices are occupied by the same component. Typically only few of the end member compounds exist, but Gibbs energy data for all end members are necessary for the theoretical modelling.

The ideal mixing term is given by

$$G_{id}^{\varphi} = \sum_{p=1}^2 f_p \cdot \sum_{i=1}^n {}^p y_i \cdot \ln({}^p y_i) \quad (6)$$

where f_p is the stoichiometric coefficient for a sublattice p and the second sum describes the effect of the ideal mixing within the sublattice p , similarly as in the Eq. (1).

The simplest model for the description of the contribution of the excess Gibbs energy for two-sublattice model is defined as:

$$G_E^\varphi = \sum^1 y_i \cdot {}^1 y_j \cdot {}^2 y_k \cdot L_{(i,j;k)} + \sum^1 y_i \cdot {}^2 y_k \cdot {}^2 y_l \cdot L_{(i;k,l)} \quad (7)$$

where

$$L_{(i,j;k)} = \sum_z {}^z L_{(i,j;k)} \cdot (y_i - y_j)^z \quad (8)$$

The parameters ${}^z L_{i,j;k}$ describe the mutual interaction of constituents i and j in the first sublattice, when the second sublattice is fully occupied by constituent k . This description can be extended to any number of sublattices.

The number of sublattices in particular intermetallic phases was selected with respect to the composition and the extent of the mutual solubility of elements in the structure and/or the complexity of the crystallographic structure. Several models were accepted from the work of Liang [7].

The composition was used as the basis for the modelling of some phases. The θ -phase (labelled THETA in the dataset) is modelled using two-sublattice model $(Al,Cu)_2(Al,Cu)_1$. It is true that the maximum content of Cu in the phase is supposed to be around 33.3 at%, but it was found that allowing slightly higher content of Cu corresponds better to the experimental results from [1]. This also leads to better results when modelling the peritectic reaction involving θ -phase and the shape of the liquidus curve in the vicinity of this phase.

The η and η' (labelled ETA and ETA_PRIME in the dataset) are both modelled as $(Al,Cu)_1(Cu)_1$. The introduction of solubility in the η' phase is based on the SEM studies of long-term annealed samples at 500 °C carried out in the original paper of Ponweiser [8], where the solubility for the η' phase was found. The additional long-term annealing experiments at 300 °C were later done in our study [1] and existence of small solubility was found as well. Identical two-sublattice model as for the η and η' phases was used for ε' phase (labelled EPS_PRIME).

The region of existence of the δ phase was studied in great details in the study [1] and is described there. The results lead us to the proposal of the model with solubility existing at higher temperatures. The δ phase (labelled as DELTA) was therefore modelled as $(Al,Cu)_5(Al,Cu)_8$. The only phase modelled as

stoichiometric is the α' phase (labelled ALPHA_PRIME) with the model $(Al)_{0.23}(Cu)_{0.77}$.

The information about crystallographic structures of the ζ' (ZETA_PRIME) and ζ (ZETA) phases is available from the works of Gullay and Harbrecht [10, 34]. The crystallography of these structures is very complicated, and the information about the existing concentration range of stability of both phases is uncertain. Therefore, these phases were modelled using two-sublattice models, defined as $(Cu)_{0.561}(Al)_{0.439}$ for ζ and $(Cu)_{0.573}(Al)_{0.427}$ for ζ' .

The information about crystallographic structures and the occupancies of concrete positions was used for the definition of sublattice models of the γ -brass family phases Al_4Cu_9 (γ' , labelled GAMMA_BRASS_ALCU) and Cu_5Zn_8 (γ , labelled GAMMA_BRASS_CUZN). They are modelled using the four-sublattice model based on the crystallographic consideration. The sublattice occupancies are defined as $(Al,Cu)_2(Cu)_2(Cu)_3(Al,Cu)_6$ for both low-temperature and high-temperature phases. This model was selected to be used in the scope of the work on the development of the SOLDERS databases in the scope of the MP0602 Actions [35, 36] as it is the most general and it should allow to cover known compositional ranges of all γ -brass family phases also in other nonrelated systems. The detailed definitions of the models used for all phases in the Al–Cu system are summarized in Table 3.

Results and discussion

The software package Thermo-Calc for the phase diagrams calculations was used for the modelling. The optimising procedure was based on the our experimental results [1] and experimental phase diagram published by Ponweiser et al. [8]. The thermodynamic data used during the assessment process are summarized in Table 1. The parameters assessed in the scope of this work are presented in Table 4. The data for pure elements are taken from the SGTE 4.4 database [37].

The calculated phase diagram using the data from Table 4 and [37] is shown in Fig. 3. The quality of the assessment can be evaluated from Figs. 4 and 5 where the agreement with the experimental data of [1, 8] is shown.

The comparison of calculated thermodynamic properties with those measured experimentally is

Table 3 Summary of phases existing in the Al–Cu system, their temperature stabilities, used in the assessment and description of thermodynamic models

Phase name (acc. to [1])	Pearson symbol	Structure type	<i>T</i> range (°C)	References	Model description
(Al)	<i>cI2</i>	Cu	≤ 660.5	[3]	(Al,Cu) ₁ (Va) ₁
θ	<i>tI12</i>	Al ₂ Cu	≤ 590.5	[1]	(Al,Cu) ₂ (Al,Cu) ₁
η	<i>oP16/oC16</i>	n.a.	573.9–624.5	[1]	(Al,Cu) ₁ (Cu) ₁
η'	<i>mC20</i>	AlCu	≤ 574.5	[1]	(Al,Cu) ₁ (Cu) ₁
ζ	<i>Imm2</i>	Al ₃ Cu ₄ ·δ	373–597	[1]	(Cu) _{0.561} (Al) _{0.439}
ζ'	<i>Fmm2</i>	Al ₃ Cu ₄	Min. 300–560.5	[1]	(Cu) _{0.573} (Al) _{0.427}
ε	cubic?	n.a.	959–846	[1]	(Al,Cu) ₁ (Va) ₃
ε'	<i>hP4</i>	NiAs	846–568.5	[1]	(Al,Cu) ₁ (Cu) ₁
δ	<i>hR52</i>	Al ₄ Cu ₉ (r)	≤ 680	[1]	(Al,Cu) ₅ (Al,Cu) ₈
γ	<i>cI52</i>	Cu ₅ Zn ₈	991–779.6	[1]	(Al,Cu) ₂ (Cu) ₂ (Cu) ₃ (Al,Cu) ₆
γ'	<i>cP52</i>	Al ₄ Cu ₉	≤ 873.5	[1]	(Al,Cu) ₂ (Cu) ₂ (Cu) ₃ (Al,Cu) ₆
β	<i>cI2</i>	W	1052–566.7	[1]	(Al,Cu) ₁ (Va) ₃
α'	n. a.	Superstructure based on TiAl ₃ [38]	≤ 360	[1]	(Al) _{0.23} (Cu) _{0.77}
(Cu)	<i>cF4</i>	Cu	< 1083	[8]	(Al,Cu) ₁ (Va) ₁

shown in Figs. 6, 7 and 8. The parameters of invariant reactions are summarised in Table 5. The description of the invariant reaction is shown in the first column, the calculated temperature is shown in column 2, the experimentally established temperatures, the temperatures modelled by Liang and Schmid-Fetzer [7] and relevant references are in columns 3 and 4, last three columns contain calculated compositions for participating phases in the order shown in column 1.

Very good agreement was obtained both, from the point of view of the phase diagram and the thermodynamic measurements.

The detail of the central part of the phase diagram is shown in Fig. 9. You can see that the peritectic reaction $\text{liq} + \eta' \rightarrow \theta$ is properly modelled and the maximum concentration of Cu in the θ -phase is 33.7 at% which corresponds very well to the experimental value approx. 33.5 at% Cu. Nevertheless, even this small deviation from the previous models for the θ -phase, which allowed the maximum concentration 33.33 at% Cu, lead to better modelling of the liquidus curve in this region of the phase diagram. There was significant deviation of calculated liquidus in comparison with experimental data towards higher temperatures in [6, 7]. This problem is significantly reduced in this assessment.

It is also clear from Fig. 9 that very good agreement was reached in the concentration interval between $\eta'(\eta)$ and δ phases with the detailed experimental

study of [1]. The agreement of the invariant temperatures with the experiments is excellent, and good agreement was reached also with the EDS measurement carried out by scanning electron microscopy by Zobac et al. [1].

The agreement between the calculated and experimentally established invariant reactions and relevant temperatures elsewhere in the phase diagram is also very good as is shown in Table 5. There is only one disagreement between the types of invariant reactions obtained theoretically and experimentally, which exists in the region shown in Fig. 9. The reaction between the ϵ' , ζ , and η' phases was deemed to be peritectoid in the work of [1, 8] but it came out in the modelling in this study as well as in [7]. The complexity of that region and existing experimental data allow for both possibilities.

A two-phase field was modelled between δ and γ' phases, as the experimentally presumed second-order phase transformation was not modelled because of complexity of both phases. Similar simplification was used for the phase transformation between γ' and γ phases. Here, again two-phase field was modelled despite the fact, that it was not observed in experimental studies.

Good agreement was also obtained for measured thermodynamic properties in Figs. 6, 7 and 8. There is only very small difference between the thermodynamic properties calculated by [7] and in this work as

Table 4 Thermodynamic parameters for liquid and optimised intermetallic phases in the Al–Cu binary system (optimised in this work)

Database name* (constituents) <i>Common Name</i>	Thermodynamic parameters (298.15 < T < 6000 K)
LIQUID (Al, Cu) ₁ <i>Liquid</i>	${}^0L_{Al,Cu}^{LIQ} = -69250.79 + 10.30229*T$ ${}^1L_{Al,Cu}^{LIQ} = +36119.82 - 10.2142*T$ ${}^2L_{Al,Cu}^{LIQ} = 11596.81 - 9.5733*T$ ${}^3L_{Al,Cu}^{LIQ} = -15246.64 + 11.53621*T$
FCC_A1 (Al, Cu) ₁ (Va) ₁ (Al), (Cu)	${}^0L_{Al,Cu:Va}^{FCC_A1} = -54220.45 + 2.0034*T$ ${}^1L_{Al,Cu:Va}^{FCC_A1} = +39015 \text{ to } 2.368*T$ ${}^2L_{Al,Cu:Va}^{FCC_A1} = 3218.23$
THETA (Al,Cu) ₂ (Al,Cu) ₁ θ	${}^0G_{Al:Al}^{THETA} = 3*G_{Al}^{BCC}$ ${}^0G_{Al:Cu}^{THETA} = -45258.14 + 4.6756*T + 2*G_{Al}^{HSER} + G_{Cu}^{HSER}$ ${}^0G_{Cu:Al}^{THETA} = 15000 + G_{Al}^{HSER} + 2*G_{Cu}^{HSER}$ ${}^0G_{Cu:Cu}^{THETA} = 15000 + 3*G_{Cu}^{HSER}$ ${}^0L_{Al:Al,Cu}^{THETA} = 1211$ ${}^1L_{Al,Cu:Cu}^{THETA} = -55350$
ZETA (Cu) _{0.561} (Al) _{0.439} ζ	${}^0G_{Cu:Al}^{ZETA} = -21426.45 + 1.085798*T + 0.439*G_{Al}^{HSER} + 0.561*G_{Cu}^{HSER}$
ZETA_PRIME (Cu) _{0.573} (Al) _{0.427} ζ'	${}^0G_{Cu:Al}^{ZETA_PRIME} = -21883.42 + 1.400093*T + 0.427*G_{Al}^{HSER} + 0.573*G_{Cu}^{HSER}$
ETA (Al,Cu) ₁ (Cu) ₁ η	${}^0G_{Al:Cu}^{ETA} = -39586.23 + 2.47353*T + G_{Al}^{HSER} + G_{Cu}^{HSER}$ ${}^0G_{Cu:Cu}^{ETA} = 4770 + 9*T + 2*G_{Cu}^{HSER}$ ${}^0L_{Al,Cu:Cu}^{ETA} = -2500$ ${}^1L_{Al,Cu:Cu}^{ETA} = -21920 \text{ to } 44.5*T$
ETA_PRIME (Al,Cu) ₁ (Cu) ₁ η'	${}^0G_{Al:Cu}^{ETA_PRIME} = -42547.08 + 6.1302*T + G_{Al}^{HSER} + G_{Cu}^{HSER}$ ${}^0G_{Cu:Cu}^{ETA_PRIME} = 10000 + 2*G_{Cu}^{HSER}$ ${}^0L_{Al,Cu:Cu}^{ETA_PRIME} = -43648.34 \text{ to } 19.7096*T$
DELTA (Al,Cu) ₅ (Al,Cu) ₈ δ	${}^0G_{Al:Al}^{DELTA} = 50000 + 13*G_{Al}^{HSER}$ ${}^0G_{Al:Cu}^{DELTA} = -288889.8 + 14.6318*T + 8*G_{Cu}^{HSER} + 5*G_{Al}^{HSER}$ ${}^0G_{Cu:Al}^{DELTA} = 20000 + 8*G_{Al}^{HSER} + 5*G_{Cu}^{HSER}$ ${}^0G_{Cu:Cu}^{DELTA} = 20000 + 13*G_{Cu}^{HSER}$
EPS_PRIME (Al,Cu) ₁ (Cu) ₁ ε'	${}^0G_{Al:Cu}^{EPS_PRIME} = -39599.52 + 3.96296*T + G_{Al}^{HSER} + G_{Cu}^{HSER}$ ${}^0G_{Cu:Cu}^{EPS_PRIME} = 9350 + 30.1*T + 2*G_{Cu}^{HSER}$ ${}^0L_{Al,Cu:Cu}^{EPS_PRIME} = -55856.4 \text{ to } 53.13*T$
GAMMA_BRASS_ALCU (Al,Cu) ₂ (Cu) ₂ (Cu) ₃ (Al,Cu) ₆ γ'	${}^0G_{Al:Cu:Cu:Al}^{GAMMA_BRASS_ALCU} = 20000 + 8*G_{Al}^{HSER} + 5*G_{Cu}^{HSER}$ ${}^0G_{Al:Cu:Cu:Cu}^{GAMMA_BRASS_ALCU} = -30000 + 2*G_{Al}^{HSER} + 11*G_{Cu}^{HSER}$ ${}^0G_{Cu:Cu:Cu:Cu}^{GAMMA_BRASS_ALCU} = +120000 + 13*G_{Cu}^{HSER}$ ${}^0G_{Cu:Cu:Cu:Al}^{GAMMA_BRASS_ALCU} = -243296.1 + 23.226*T + 6*G_{Al}^{HSER} + 7*G_{Cu}^{HSER}$ ${}^0L_{Cu:Cu:Cu:Al,Cu}^{GAMMA_BRASS_ALCU} = -450000$ ${}^1L_{Cu:Cu:Cu:Al,Cu}^{GAMMA_BRASS_ALCU} = -300000$
GAMMA_BRASS_CUZN (Al,Cu) ₂ (Cu) ₂ (Cu) ₃ (Al,Cu) ₆ γ	${}^0G_{Al:Cu:Cu:Al}^{GAMMA_BRASS_CUZN} = 20000 + 8*G_{Al}^{HSER} + 5*G_{Cu}^{HSER}$ ${}^0G_{Al:Cu:Cu:Cu}^{GAMMA_BRASS_CUZN} = -30000 + 2*G_{Al}^{HSER} + 11*G_{Cu}^{HSER}$ ${}^0G_{Cu:Cu:Cu:Cu}^{GAMMA_BRASS_CUZN} = +100000 + 13*G_{Cu}^{HSER}$ ${}^0G_{Cu:Cu:Cu:Al}^{GAMMA_BRASS_CUZN} = -142937.0 \text{ to } 59.45*T + 6*G_{Al}^{HSER} + 7*G_{Cu}^{HSER}$ ${}^0L_{Cu:Cu:Cu:Al,Cu}^{GAMMA_BRASS_CUZN} = -674456 + 185.5*T$ ${}^1L_{Cu:Cu:Cu:Al,Cu}^{GAMMA_BRASS_CUZN} = -28662 \text{ to } 218.91*T$
BCC_A2 (Al,Cu) ₁ (Va) ₃ β, ε	${}^0L_{Al,Cu:Va}^{BCC_A2} = -72619 + 3.137*T$ ${}^1L_{Al,Cu:Va}^{BCC_A2} = 56695.8 - 14.728*T$ ${}^2L_{Al,Cu:Va}^{BCC_A2} = 4774.15 - 1.4195*T$

Table 4 continued

Database name* (constituents) Common Name	Thermodynamic parameters (298.15 < T < 6000 K)
ALPHA_PRIME (Al) _{0.23} (Cu) _{0.77} α'	${}^0G_{\text{Al,Cu}}^{\text{ALPHA_PRIME}} = -15964.4 + 0.009*T + 0.23*G_{\text{Al}}^{\text{HSER}} + 0.77*G_{\text{Cu}}^{\text{HSER}}$

*The phase names used in this dataset are usually based on the common names of phases used in the literature. The exceptions are accepted when the generic name for the crystallographic structure exists to be consistent with large databases (e.g. BCC_A2, FCC_A1). The names for the γ -brass family of phases (GAMMA_BRASS_ALCU and GAMMA_BRASS_CUZN) were selected with respect to the structure prototype to ensure simple identification of corresponding data for these phases in other datasets

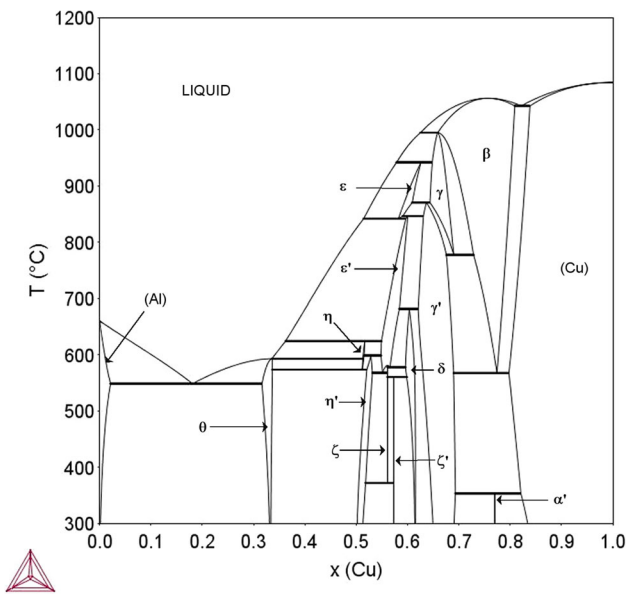


Figure 3 The assessed Al–Cu phase diagram based on the dataset in Table 4.

is seen in Figs. 6 and 8. All the features of experimentally measured concentration dependence of enthalpy of mixing, enthalpy of formation and activities are very correctly reproduced.

Conclusions

The Al–Cu binary system was newly assessed, based mainly on the experimental phase diagram evaluation done by Ponweiser et al. [8] and Zobac et al. [1]. The experimental thermodynamic data used in the work of [7] were also used during this assessment. Current work was concentrated on the newly described experimental phase equilibria from [1], and all intermetallic phases were modelled with their temperature modifications.

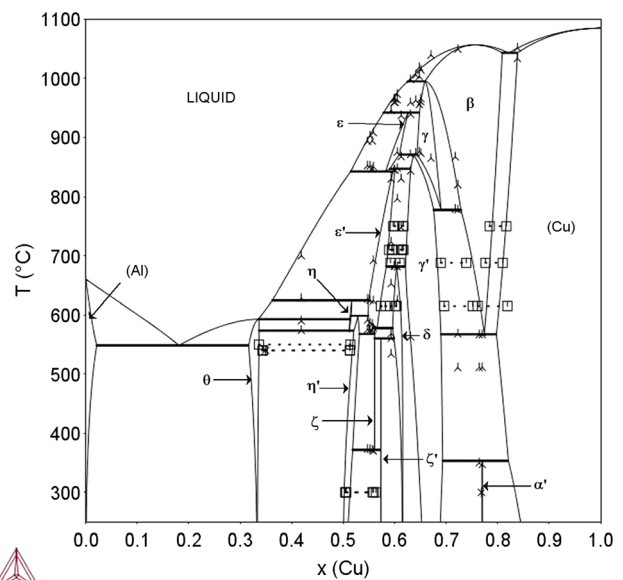


Figure 4 The assessed phase diagram in comparison with experimental data from [1] (black three pointed star—DSC signals, bold square—phase boundaries according to SEM/EDX measurements).

The HT and LT modifications of η , ζ , and γ family of phases were modelled, including their nonstoichiometricity (if the experimental data were available).

The δ phase was modelled as nonstoichiometric phase.

The four sublattice models were used for the γ -family phases.

Very good agreement with the experimental results was reached both for the Al–Cu phase diagram and for the calculated thermodynamic properties, namely the enthalpy of mixing, enthalpies of formation and activities.

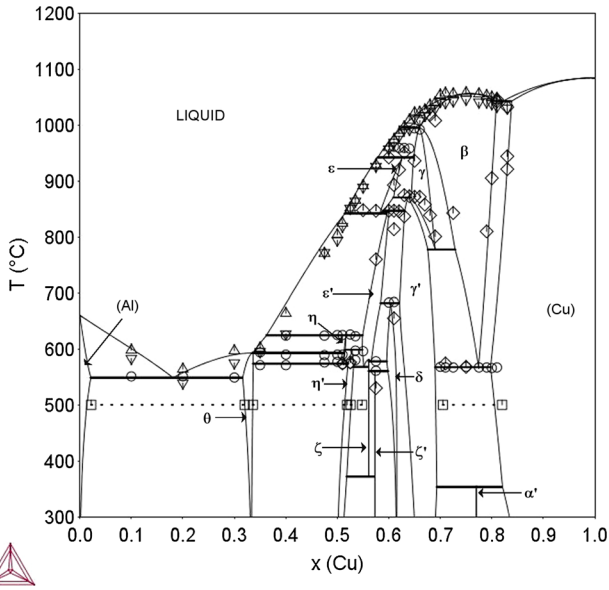


Figure 5 The assessed phase diagram in comparison with experimental data from [8] (white up-pointing triangle, white down-pointing triangle—DSC signal for liquid on heating and cooling, bold circle—DSC signal for invariant reaction, white diamond—other DSC signals, bold square—phase boundaries according to SEM/EDX measurements).

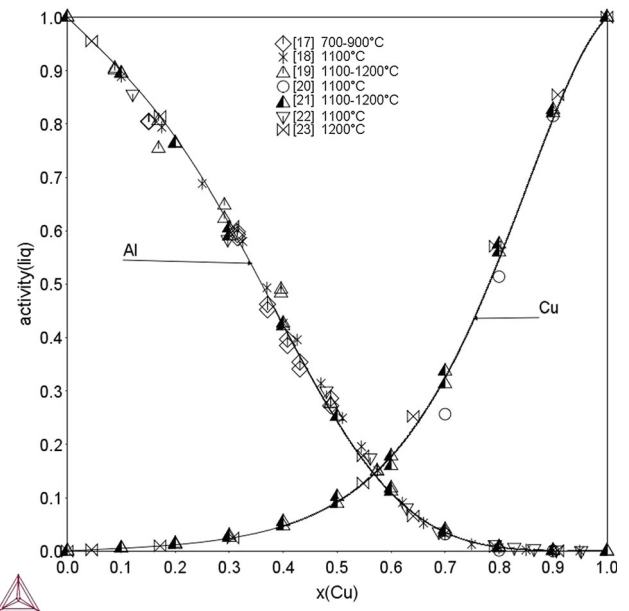


Figure 7 Calculated activities for Al and Cu in liquid phase in comparison with experimental data, standard states are Al and Cu liquids at the temperature of calculation.

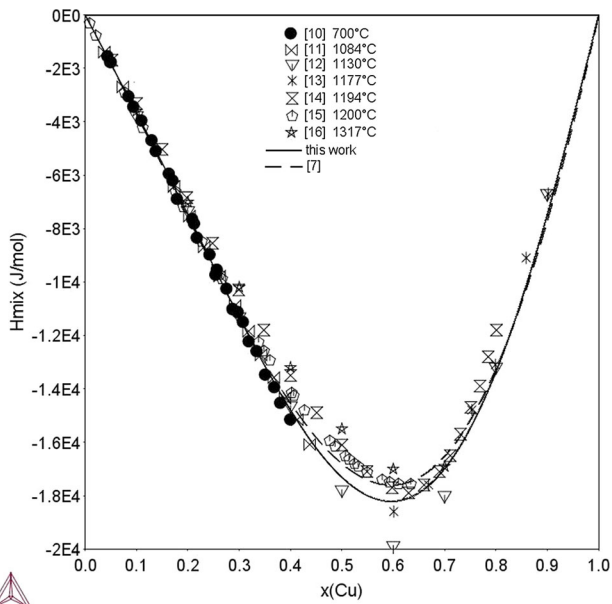


Figure 6 The enthalpy of mixing of liquid for 1300 °C in comparison with experimental data, standard states are Al and Cu liquids at the temperature of calculation.

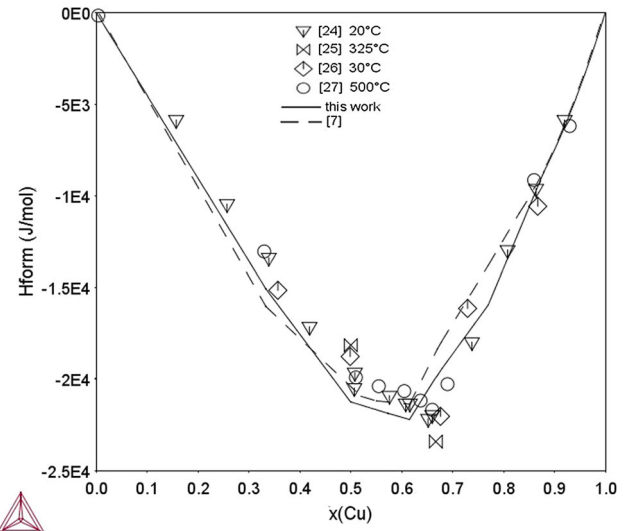


Figure 8 Calculated enthalpy of formation at room temperature in comparison with experimental data and calculation from [7], standard states are solid Cu and Al (fcc).

Table 5 Comparison of calculated (this work—column 2, and [7]) and experimentally established ([1] and [8]) characters and temperatures of invariant reactions

Invariant reaction	T (°C) [calc]	T_{exp} (°C)	References	Phase 1 $x(\text{Cu})$	Phase 2 $x(\text{Cu})$	Phase 3 $x(\text{Cu})$
liq. $\rightarrow \beta$ (congruent)	1056.3	–	[1]	0.755		
		1052	[8]			
		1043	[7]			
liq $\rightarrow \beta + (\text{Cu})$	1042.7	–	[1]	0.822	0.809	0.839
		1035	[8]			
		1035.1	[7]			
liq + $\beta \rightarrow \gamma$	995.0	991	[1]	0.625	0.659	0.658
		993	[8]			
		1013.2	[7]			
liq + $\gamma \rightarrow \varepsilon$	942.1	959	[1]	0.579	0.648	0.626
		960	[8]			
		959.3	[7]			
$\gamma + \varepsilon \rightarrow \gamma'$ (ord.)	871.0	873.5	[1]	0.644	0.609	0.637
		874	[8]			
		872.5	[7]			
$\gamma' + \varepsilon \rightarrow \varepsilon'$	846.8	846	[1]	0.631	0.591	0.600
		847	[8]			
		848.7*	[7]			
$\varepsilon \rightarrow \text{liq} + \varepsilon'$	842.3	846	[1]	0.582	0.515	0.597
		847	[8]			
		846.6	[7]			
$\gamma \rightarrow \gamma' + \beta$ (ord.)	777.6	779.6	[1]	0.690	0.676	0.729
		800	[8]			
		790.7	[7]			
$\gamma' + \varepsilon' \rightarrow \delta$	681.9	682.1	[1]	0.621	0.584	0.604
		684	[8]			
		684.6	[7]			
liq + $\varepsilon' \rightarrow \eta$	624.5	624.5	[1]	0.362	0.549	0.516
		625	[8]			
		625.0	[7]			
$\varepsilon' + \eta \rightarrow \eta'$	598.7	597	[1]	0.548	0.516	0.529
		597	[8]			
		597.9	[7]			
liq + $\eta \rightarrow \theta$	593.0	589	[1]	0.335	0.513	0.337
		591	[8]			
		593.3	[7]			
$\zeta \rightarrow \varepsilon'$ (congruent)	581.3	–		0.561		
		601.6	[7]			
$\varepsilon' \rightarrow \delta + \zeta$	578.0	575	[1]	0.566	0.596	0.561
		578	[8]			
		557.7	[7]			
$\eta \rightarrow \eta' + \theta$	573.6	573.9	[1]	0.512	0.521	0.337
		574	[8]			
		573.7	[7]			
$\beta \rightarrow (\text{Cu}) + \gamma'$	567.4	566.7	[1]	0.774	0.798	0.690
		567	[8]			
		567.5	[7]			
$\varepsilon' \rightarrow \zeta + \eta'$	568.0	–		0.551	0.561	0.532
		580.4	[7]			

Table 5 continued

Invariant reaction	T (°C) [calc]	T _{exp} (°C)	References	Phase 1 x(Cu)	Phase 2 x(Cu)	Phase 3 x(Cu)
$\eta + \zeta \rightarrow \eta'$	–	580	[1]	–	–	–
		581	[8]			
$\delta + \zeta \rightarrow \zeta'$	560.3	560.5	[1]	0.598	0.561	0.573
		563	[8]			
		–	[7]			
liq \rightarrow (Al) + θ	548.5	–	[1]	0.181	0.021	0.316
		550	[8]			
		547.7	[7]			
$\zeta \rightarrow \zeta' + \eta'$	372.1	373	[1]	0.561	0.573	0.518
		–	[8]			
		–	[7]			
(Cu) + $\gamma' \rightarrow \alpha'$	353.5	350	[1]	0.821	0.693	0.770
		–	[8]			
		363.0	[7]			

Compositions of phases are those calculated in the scope of this work

*This temperature corresponds to the reaction $\varepsilon \rightarrow \varepsilon' + \gamma'$ in [7]

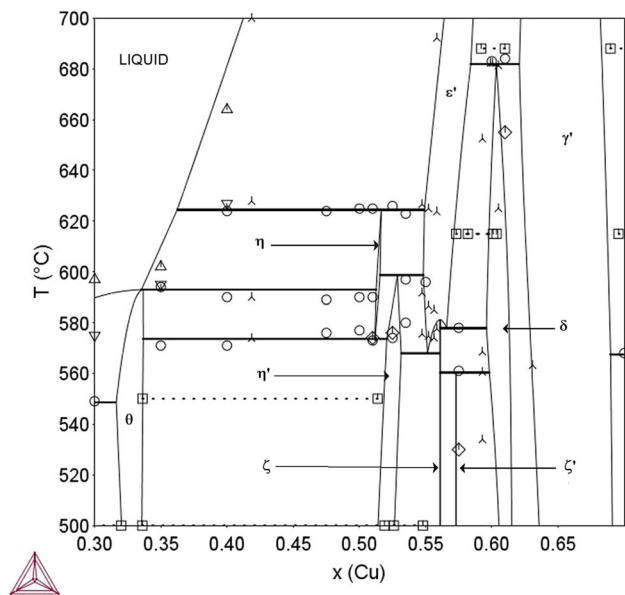


Figure 9 Central section of the assessed Al–Cu phase diagram compared with the experimental data from [1, 8] (white up-pointing triangle, white down-pointing triangle—DSC signal for liquid on heating and cooling [1], bold circle—DSC signal for invariant reaction [1], white diamond—other DSC signals [1], black three pointed star—DSC signals [8], bold square—phase boundaries according to SEM/EDX measurements [1, 8]).

Acknowledgements

This study was supported by the Austrian Science Found (FWF) under the Lisa-Meitner Project M2293-N34.

Compliance with ethical standards

Conflict of interest The authors declare that they have no conflict of interest.

References

- [1] Zobač O, Kroupa A, Zemanová A, Richter KW (2019) Experimental description of the Al–Cu binary phase diagram. *Met Mater Trans A* 50:3805–3815
- [2] Kaufman L, Nesor H (1978) Coupled phase diagrams and thermochemical data for transition metal binary systems-V. *CALPHAD* 2:325–348
- [3] Murray JL (1985) The aluminium—copper system. *Int. Met. Rev.* 30:211–234
- [4] Chen S-W, Chuang Y-Y, Austin Chang Y, Chu M (1991) Calculation of phase diagrams and solidification paths of Al-rich Al–Li–Cu alloys. *Met Trans A* 22:2837–2848
- [5] Saunders N (1998) System Al–Cu, COST 507: thermochemical database for light metal alloys, volume 2: definition of thermodynamical and thermophysical properties to provide a database for the development of new light alloys. In:

- Ansara I, Dinsdale AT, Rand MH (Eds), European Commission, Brussels
- [6] Witusiewicz VT, Hecht U, Fries SG, Rex S (2004) The Ag–Al–Cu system: Part I: reassessment of the constituent binaries on the basis of new experimental data. *J Alloy Compd* 385:133–143
- [7] Liang SM, Schmid-Fetzer R (2015) Thermodynamic assessment of the Al–Cu–Zn system, part II: Al–Cu binary system. *CALPHAD* 51:252–260
- [8] Ponweiser N, Lengauer CL, Richter KW (2011) Re-investigation of phase equilibria in the system Al–Cu and structural analysis of the high-temperature phase η_1 -Al₁₋₈Cu. *Intermetallics* 19:1737–1746
- [9] Goedecke T, Sommer F (1996) Solidification behaviour of the Al₂Cu phase. *Z Metall* 87:581–586
- [10] Gulay LD, Harbrecht B (2004) The crystal structure of ζ_1 -Al₃Cu₄. *J Alloy Compd* 367:103–108
- [11] Flandorfer H, Rechchach M, Elmahfoudi A, Bencze L, Popovič A, Ipsier H (2011) Enthalpies of mixing of liquid systems for lead free soldering: Al–Cu–Sn system. *J Chem Thermodyn* 43:1612–1622
- [12] Heyer E (1989) University of Vienna, private communication to [14]
- [13] Kawakami M (1930) A further investigation of the heat of mixture in molten metals. *Sci Rep Tohoku Imp Univ Ser* 1(19):521–549
- [14] Witusiewicz V, Stolz UK, Arpshofen I, Sommer F (1998) Thermodynamics of liquid Al–Cu–Zr alloys. *Z Metall* 89:704–713
- [15] Stolz UK, Arpshofen I, Sommer F, Predel B (1993) Determination of the enthalpy of mixing of liquid alloys using a high-temperature mixing calorimeter. *J Phase Equilib* 14:473–478
- [16] Sandakov VM, Esin YO, Geld PV, Shantarin VD (1971) Heats of formation of liquid copper–aluminium alloys. *Russ J Phys Chem* 45:1150–1152
- [17] Kanibolotsky D, Beloborodova O, Kotova N, Lisnyak V (2002) Thermodynamic properties of liquid Al–Si and Al–Cu alloys. *J Therm Anal Calorim* 70:975–983
- [18] Grube G, Hantelmann P (1942) Polarisationsmessungen bei der elektrolytischen Raffination des Aluminiums nach dem Dreischichtenverfahren, I. Mitteilung. *Z Elektrochem* 48:399–409
- [19] Wilder TC (1965) The thermodynamic properties of the liquid aluminum–copper system. *Trans Met Soc AIME* 233:1202–1208
- [20] Mitani H, Nagai H (1969) Determination of the activities of aluminum and copper in liquid Al–Cu Binary alloys by the bubbling method. *J Jpn Inst Met* 33:344–348
- [21] Batalin GI, Beloborodova EA, Vasilev VN (1972) Thermodynamic properties of molten alloys of aluminum with copper. *Ukr Khim Zh (Russ Ed)* 38:920–923
- [22] Perakis J, Chatillon C, Pattoret A (1973) High-temperature mass spectrometry. Thermodynamic properties of aluminum–copper liquid alloys. *C R Acad Sci Ser C* 276:1513–1516
- [23] Layner DI, Ostrovskaya LM, Serebryannikova OS (1976) Activities of components in liquid Cu–Al alloys. *Izv Akad Nauk SSSR Met* 15:15–18
- [24] Oyamada H, Nagasaka T, Hino M (1998) Activity measurement of the constituents in liquid Cu–Al alloy with mass-spectrometry. *Mater Trans, JIM* 39:1225–1229
- [25] W.Oelsen, W. Middel, Zur Thermochemie, I. Der Legierungen, Unmittelbare Bestimmung der Bildungswaermender Legierungsreihen Kobalt–Silizium, Eisen–Aluminium, Kobalt–Aluminium, Nickel–Aluminium, Kupfer–Aluminium und Antimon–Zink fuer den Gusszustand, *Mitt. K. W. I für Eisenforsch.*, 19(1937), 1–26
- [26] Kubaschewski O, Heymer G (1960) Heats of formation of transition-metal aluminides. *Trans Faraday Soc* 56:473–478
- [27] Sinvhal RC, Khangaonkar PR (1967) Heats of formation of some aluminum alloys by differential calorimetry. *Trans Indian Inst Met* 20:107–110
- [28] Hair J, Downie DB (1973) Thermodynamic properties of the Cu–Al system: correlation with bonding mechanisms. *Faraday Symp Chem Soc* 8:56–63
- [29] Lukas HL, Fries SG, Sundman B (2017) Computational thermodynamics: the calphad method. Cambridge University Press, New York
- [30] Saunders N, Miodownik AP (1998) *Calphad (A Comprehensive Guide)*. Pergamon Press, Oxford
- [31] Andersson J-O, Helander T, Höglund L, Shi P, Sundman S (2002) Thermo-calc and DICTRA, computational tools for materials science. *CALPHAD* 26:273–312
- [32] Cao W, Chen SL, Zhang F, Wu K, Yang Y, Chang YA, Schmid-Fetzer R, Oates WA (2009) PANDAT software with PanEngine, PanOptimizer and PanPrecipitation for multi-component phase diagram calculation and materials property simulation. *CALPHAD* 33:328–342
- [33] Redlich O, Kister A (1948) Thermodynamics of nonelectrolyte solutions—X–Y–T relations in a binary system. *Ind Eng Chem* 40:341–345
- [34] Gulay LD, Harbrecht B (2003) The crystal structure of ζ_2 -Al₃Cu₄₋₆. *Z Anorg Allg Chem* 629:463–466
- [35] Dinsdale AT, Kroupa A, Watson A, Vřešťál J, Zemanová A, Brož P (2012) The thermodynamic database COST MP0602 for materials for high-temperature lead-free soldering. *J Min Metall Sect B* 48:339–346. <https://doi.org/10.2298/JMMB120711043K>

- [36] Dinsdale AT, Kroupa A, Watson A, Vřešťál J, Zemanová A, Brož P (2012) Handbook of high-temperature lead-free solders: Vol. 1, Atlas of Phase Diagrams, COST MP0602 ACTION, COST office 2012, The Czech Republic, ISBN 978-80-905363-1-9
- [37] Dinsdale AT (2020) SGTE Unary Database, Version 4.4, www.sgte.org. Accessed 2020
- [38] El-Boragy M, Szepan R, Schubert K (1972) Kristallstruktur von $\text{Cu}_3\text{Al}_{2+}$ (h) und CuAl (r). J Less-Common Met 29:133–140
- [39] Kuwano N, Doi T, Eguchi T (1977) Period of antiphase and tetragonality in the α_2 phase of Cu-Al alloys. Trans. JIM 18:807–815

Publisher's Note Springer Nature remains neutral with regard to jurisdictional claims in published maps and institutional affiliations.

6.6 Paper 6

- [P6] **Zobač, O.**, Buchlovská, K., Pavlů, J., Kroupa, A., *A thermodynamic description of binary system nickel-selenium*, Journal of Phase Equilibria and Diffusion, 2021, 42(4), pp. 468-478, doi: 10.1007/s11669-021-00906-9 (IF 1.284)



Thermodynamic Description of Binary System Nickel-Selenium

Ondřej Zobač¹ · Kateřina Buchlovská^{1,2} · Jana Pavlů² · Aleš Kroupa¹

Submitted: 1 June 2021 / in revised form: 18 June 2021 / Accepted: 27 June 2021 / Published online: 26 July 2021
© ASM International 2021

Abstract The phase diagram of the binary Ni-Se system has been modelled by the *CALPHAD* approach for the first time. The modelled phase diagram is based on a known experimental phase diagram, enthalpy of formation of the NiSe phase and heat capacity of the NiSe₂ phase. All calculated data (the Ni-Se phase diagram, the standard enthalpy of mixing of the NiSe phase at 298 K and 1050 K and the heat capacity of NiSe₂ in the temperature range 298–1000 K) reveal very good agreement with the experimental results.

Keywords binary phase diagram · *CALPHAD* approach · Ni-Se system

1 Introduction

Knowledge of the phase equilibria, phase diagrams and thermodynamic properties of phases is crucial for the development of new materials. Detailed information about the coexistence and stability of phases in stable or metastable equilibrium significantly rationalizes the design and consequent development of materials with required properties. The semiempirical CALculation of PHase Diagram (*CALPHAD*) type modelling^[1,2] of multicomponent phase diagrams is a helpful tool for the materials

development. Furthermore, robust and reliable thermodynamic descriptions of binary systems are necessary for the modelling of ternary and higher-component systems.

As important semiconductor materials, transition metal chalcogenides find technological applications in microelectronics.^[3–5] Moreover, possible intercalation of these chalcogenides with lithium for applications in rechargeable battery electrodes has garnered a lot of attention. Metal chalcogenides are also conventionally used in several advanced technological applications, such as photovoltaics.^[3,6, 7] The investigations of the Ni-Se system were initiated as it provides a potential material for various types of electrodes.^[8] Based on these investigations, Komarek and Wessely^[9] published an experimental phase diagram shown in Fig. 1. This phase diagram was accepted in later scientific monographies/compendia.^[10,11] However, the *CALPHAD*-based thermodynamic assessment of the Ni-Se phase diagram has not been published yet.

For the reasons and motivation mentioned above, the theoretical prediction of the Ni-Se phase diagram was accomplished using the *CALPHAD* approach, which was based on published experimental phase diagram^[9] and available thermodynamic properties of the intermetallic phases, namely standard enthalpy of mixing of the NiSe phase at 298 K and 1050 K^[12] and the heat capacity of NiSe₂ in the temperature range 298–1000 K.^[13]

2 Literature Review

2.1 Available Experimental Information

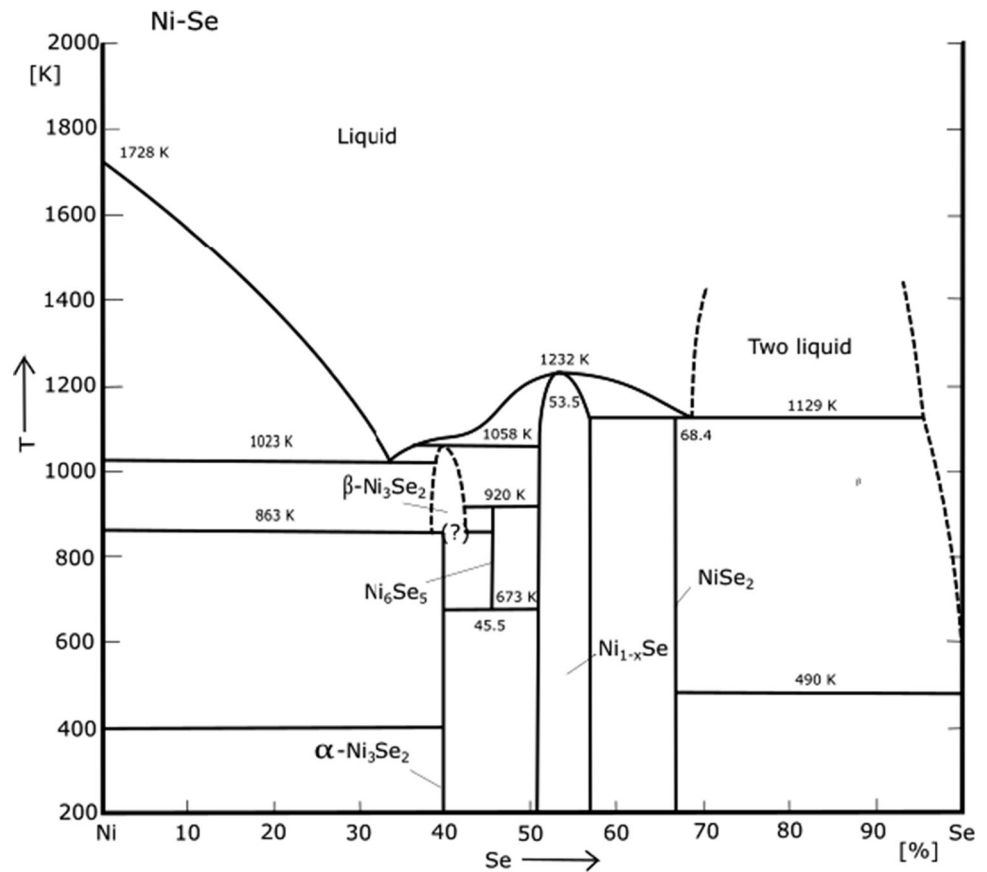
The phase equilibria in the Ni-Se system have been investigated by Grønvold et al.^[14], Hiller et al.^[15] and Kuznetsov et al.^[16] The experimental phase diagram of

✉ Ondřej Zobač
zobac@ipm.cz

¹ Czech Academy of Sciences, Institute of Physics of Materials, Žižkova 22, Brno 616 00, Czech Republic

² Faculty of Science, Department of Chemistry, Masaryk University, Kotlářská 2, Brno 611 37, Czech Republic

Fig. 1 Experimental phase diagrams proposed by Komarek and Wessely^[9]



binary system Ni-Se was constructed by Komarek and Wessely^[9] (see Fig. 1) based on the combination of results from X-ray diffraction (XRD) and thermal analysis (DTA). The results reported in Ref.^[9] have been taken as a basis for review by Lee et al.^[10] and Landolt-Börnstein^[11].

The Ni-Se system contains five intermetallic phases. The NiSe₂ intermetallic phase is stoichiometric and crystallizes in the cubic FeS₂ structure (Pearson symbol *cP12*) with space group *Pa3*.^[17] In the binary phase diagram, it is stable below 1129 K. The NiSe phase is non-stoichiometric with the solubility of selenium up to 57 at.% Se. This phase crystallizes in the hexagonal NiAs (*B81*) structure with space group *P63/mmc*^[16] and, in the binary Ni-Se phase diagram, it is stable below 1232 K. The Ni₆Se₅ intermetallic stoichiometric phase is orthorhombic and crystallizes in its own super-structure type in space group *oC48* with Pearson symbol *Cmcm*.^[18] The Ni₆Se₅ phase is stable in the temperature range between 673–920 K in the phase diagram. The intermetallic binary phase Ni₃Se₂ exists in two modifications. The hexagonal modification Ni₃Se₂_LT^[9, 15] is stable from room temperature to approx. 878 K and the cubic modification Ni₃Se₂_HT^[9] is stable at higher temperatures up to 1058 K. The high-temperature modification Ni₃Se₂_HT is proposed as a non-stoichiometric with the solubility of both Ni and Se. The character

and the temperature of the transition Ni₃Se₂_HT ↔ Ni₃Se₂_LT is not precisely known, and the temperature is estimated to be approx. 863 K.^[10] The eutectoid reaction Ni₃Se₂_HT ↔ Ni₃Se₂_LT + Ni₆Se₅ on the Se-rich part of the phase diagram occurs at 858 K.^[9] Moreover, two metastable phases α'_Ni₃Se₂ and Ni₃Se₄^[15] are described in binary system Ni-Se in literature.^[10] Table 1 summarizes the stable and metastable phases reported for the Ni-Se system, including their structure and temperature ranges of existence.

The summary of the above-discussed and other invariant reactions is presented in Table 2, comparing the invariant-reaction temperatures obtained from experimental phase diagrams^[9, 10] and calculations proposed in this work. The first column of this table lists the proposed invariant reactions; the 2nd–4th columns provide compositions of phases as mentioned in the reaction; in the 5th column are the invariant temperatures; the 7th column lists proposed reaction type, and the last column shows the references where the previous data come from. The results of this work are in bold.

Published thermodynamic data are quite sparse. Grönwold^[12] measured the enthalpy of formation of NiSe phase in the concentration range between *x*(Se)=0.5 to 0.57 and in two-phase region NiSe+NiSe₂ up to *x*(Se)=0.6667

Table 1 Crystal structure and temperature stability of stable and metastable intermetallic phases in the Ni–Se system

Phase name	Person symbol	Space group	Structure type	<i>T</i> range [K]	Ref.
Ni ₃ Se ₂ _LT	<i>hR5</i>	<i>R32</i>	Ni ₃ S ₂	< 878	[9, 15]
Ni ₃ Se ₂ _HT	<i>c**</i>	n.a.	n.a.	863–1058	[9]
Ni ₆ Se ₅	<i>oC48</i>	<i>Cmcm</i>	Ni ₆ Se ₅	673–920	[9, 18]
NiSe	<i>hP4</i>	<i>P6₃/mmc</i>	NiAs	< 1232	[16]
NiSe ₂	<i>cP12</i>	<i>Pa3</i>	FeS ₂	< 1129	[17]
Ni ₃ Se ₄	<i>mC14</i>	<i>C2/m</i>	Ni ₃ Se ₄	Metastable phase	[15]
α′_Ni ₃ Se ₂	<i>I**</i>	n.a.	n.a.	Metastable phase	[10]

n.a. stands for “not available”.

Table 2 Calculated and experimentally established invariant reactions and the reaction temperatures

Reaction	Phase composition [at.% Se]			<i>T</i> [K]	Type of reaction	Ref.
Liquid ↔ NiSe	53.5	53.5	–	1232	congruent	[9]
	53.5	53.5	–	1232		[11]
	53.2	53.2	–	1231.3		t.w.
Liquid + NiSe ↔ NiSe ₂	70.1	58	68	1129	peritectic	[9]
	68.4	56.7	66.8	1129		[11]
	67.2	54.7	66.7	1131.0		t.w.
Liquid′ ↔ NiSe ₂ + Liquid′′	n.a.	n.a.	n.a.	1126	monotectic	[9]
	n.a.	n.a.	n.a.	1129		[11]
	72.7	66.7	72.7	1128.4		t.w.
Liquid + NiSe ↔ Ni ₃ Se ₂ _HT	35.1	50.5	35.1	1058	peritectic	[9]
	36.5	50.8	40	1058		[11]
	40.5	51.4	40.5	1057.5		t.w.
Liquid ↔ FCC_A1 + Ni ₃ Se ₂ _HT	34	0	39.6	1023	eutectic	[9]
	33.7	0	39	1023		[11]
	34.4	0	40.5	1037.3		t.w.
NiSe + Ni ₃ Se ₂ _HT ↔ Ni ₆ Se ₅	50.5	42.5	45.5	920.5	peritectoid	[9]
	50.8	42.4	45.5	920		[11]
	51.3	40.5	45.5	919.9		t.w.
Ni ₃ Se ₂ _HT + FCC_A1 ↔ Ni ₃ Se ₂ _LT	42.3	0	42	873	eutectoid	[9]
	42.4	0	40	863		[11]
	40.5	0	40	865.5		t.w.
Ni ₃ Se ₂ _HT ↔ Ni ₆ Se ₅ + Ni ₃ Se ₂ _LT	42.5	45.5	42	858	eutectoid	[9]
	38.5	45.5	40	n.a.		[11]
	40.5	45.5	40	839.3		t.w.
Ni ₆ Se ₅ ↔ NiSe + Ni ₃ Se ₂ _LT	45.5	50.5	42	673	eutectoid	[9]
	45.5	50.8	40	673		[11]
	45.5	51.1	40	673.5		t.w.
Liquid ↔ NiSe ₂ + hex_A8 (Se)	<100	68	100	490	eutectic	[9]
	<100	68.4	100	490		[11]
	99.8	66.7	100	490.1		t.w.

The results of this work are in bold.

t.w. stands for “this work.”

by high-temperature reaction calorimetry at 1050 K. For three concentration variants of nickel selenide, NiSe_{0.513}, NiSe_{0.533} and NiSe_{0.566}, Grønbold^[12] derived the enthalpy of formation at room temperature. Original data on

enthalpies of formation by Fabre^[19] evaluated from the heat of solution measurement agree very well with data derived by Grønbold.^[12] Results proposed by Bichowsky and Rossini^[20] and Rossini et al.^[21] reevaluated the

experimental data from Fabre^[19]. The values do not agree well with the results published by Grønwoold^[12]. The enthalpies of formation for the single-phase region proposed by different authors are shown in Table 3. Jelinek and Komarek^[22] determined the vapor pressure of selenium in Ni-Se alloys by an isopiestic method between 723 K–1273 K. Furthermore, they also evaluated the activity of Se according to three methods, but the results from these three methods are not consistent.

3 Thermodynamic Modelling

The CALPHAD approach^[1, 2] is a theoretical approach for the thermodynamic modelling and calculations of phase diagrams. Using this approach, the phase compositions in thermodynamic equilibrium can be found as they correspond to the minimum total Gibbs energy of a closed system at constant temperature and pressure. Our calculations were done using the Pandat^[23] software, which is based on solving the constrained minimization problem to determine non-negative amounts of individual components in equilibrium phases. The Gibbs energies are considered relative to the Stable Element Reference (SER) states, which means relative to the Gibbs energies of phases of pure elements stable at $p=101325$ Pa and $T=298$ K. The data for pure elements were taken from the 24 4.4 database.^[24]

3.1 The Solution Phases

The molar Gibbs energy of the liquid (and solid solution) G_m^ϕ can be generally considered as the sum of several contributions^[11]:

Table 3 Enthalpies of formation for the single-phase regions

Phase	T [K]	ΔH_f [kJ mol ⁻¹]	Ref.
NiSe _{0.513}	298	-36.5 ± 0.2	[12]
NiSe _{0.533}	298	-37.2 ± 0.2	[12]
NiSe _{0.566}	298	-36.8 ± 0.2	[12]
NiSe	298	-38.5	[19]
NiSe	298	-29	[20]
NiSe	298	-21 ± 5	[21]
NiSe	1050	-39.97	[12]
NiSe _{0.512}	1050	-40.93	[12]
NiSe _{0.524}	1050	-41.16	[12]
NiSe _{0.535}	1050	-41.01	[12]
NiSe _{0.545}	1050	-41.14	[12]
NiSe _{0.565}	1050	-40.77	[12]

$$G_m^\phi = \sum_{i=1}^n x_i \cdot {}^0G_{m,i}^\phi + RT \cdot \sum_{i=1}^n x_i \cdot \ln(x_i) + {}^E G_m^\phi, \quad (\text{Eq 1})$$

where the first term is the molar reference Gibbs energy ${}^{ref}G_m^\phi$ consisting of the weighted sum of the Gibbs energies of constituents i in the crystallographic structure identical to the phase ϕ relative to the chosen reference state. Here, x_i is the molar fraction of constituent i and the temperature dependence of the Gibbs energy of the pure constituent i in phase ϕ ${}^0G_{m,i}^\phi$ is expressed by the polynomial^[11]:

$$G_{m,i}^\phi = a + b \cdot T + c \cdot T \ln(T) + \sum n \cdot d_i \cdot T^{n-1}, \quad (\text{Eq 2})$$

where a , b , c , and the d_i are adjustable coefficients, n represents a set of integers (typically taking the values of 2, 3 and -1), and T is temperature.

The second term of Eq 1 is the contribution to the Gibbs energy from the ideal mixing of the constituents on the crystal lattice or in the liquid ${}^{id}G_m^\phi$, where n is the number of constituents.

The third term, the excess molar Gibbs energy ${}^E G_m^\phi$, describes the influence of the non-ideal behaviour of the system on the thermodynamic properties of the phase and is given by the Redlich-Kister formalism [30]:

$${}^E G_m^\phi = \sum_{\substack{i,j=1 \\ i \neq j}}^n x_i \cdot x_j \cdot \sum_{z=0}^m {}^z L(x_i - x_j)^z, \quad (\text{Eq 3})$$

where ${}^z L$ are the temperature-dependent interaction parameters, describing the mutual interaction between constituents i and j . Their temperature dependence is defined as:

$${}^z L(T) = a + b \cdot T + c \cdot T \ln(T). \quad (\text{Eq 4})$$

Although the phase FCC_A1 (Ni) can be considered as a substitutional solid solution phase with one sublattice, it is more convenient to model it as an interstitial solid solution, using two sublattices (Ni)₁(X, Va)₁. Here the first sublattice is occupied by metal atoms and the second one by hypothetical interstitial atoms X (like carbon, nitrogen) where appropriate and structural vacancies Va. This model was used in this work to remain consistent with assessments of other FCC_A1 [30] containing systems where interstitials have to be included. In the present work, the second sublattice contains only vacancies, and the model behaves like the substitutional model described above.

The Gibbs energy of the hexagonal_A8 (Se) phase was also modelled using the above-mentioned substitutional model with one sublattice.

As only negligible solubility of selenium in nickel for FCC_A1 phase and nickel in selenium in hexagonal_A8

was proposed^[9], the model for Se was selected without any solubility of Ni atoms in its structure.

Due to the relatively high temperature of congruent melting of the NiSe phase, the liquid phase was modelled by the solution model extended to the associate model with an associated cluster with the stoichiometric composition Ni₁Se₁. The model is defined as (Ni,NiSe,Se)

3.2 Intermetallic Phases

The Ni-Se phase diagram contains five stable intermetallic phases, which differ in the solubility of constituents and complexity of the crystal structure (see Table 1). Therefore, different sublattice models were used for their description, as shown in Table 3.

The Compound Energy Formalism (CEF) was used to model intermetallic phases Ni₃Se₂-LT, Ni₃Se₂-HT, Ni₆-Se₅, NiSe and NiSe₂ employing the two-sublattice model for all of them. The ratio of positions in sublattices was defined by the stoichiometry of phases (see Table 3).

The molar reference Gibbs energy (analogous to the first term in Eq 1 in case of solution (e.g. liquid or hexagonal_A8 (Se) phase) phases) for the two-sublattice model is given as:

$${}^{ref}G_m^\phi = \sum_{i,j} {}^1y_i \cdot {}^2y_j \cdot {}^0G_{ij} \quad i,j = \text{Ni, Se}, \quad (\text{Eq 5})$$

where the ${}^p y_i$ terms are the site fractions of each constituent in the respective first or second sublattice p . The term $G_{i;j}$ describes the Gibbs energy of formation of the so-called “end-member” $i;j$. The end-members are structures with all possible exclusive occupations of sublattices by available constituents, i.e. it can also be the pure element i in the crystallographic structure ϕ if both sublattices are occupied by the same component. Typically, only a few of the end-member compounds exist, but Gibbs energy data of all of them are necessary for the theoretical modelling.

The ideal mixing term ${}^{id}G_m^\phi$ in the two-sublattice model is given by the equation:

$${}^{id}G_m^\phi = \sum_{p=1}^2 f_p \cdot \sum_{i=1}^n {}^p y_i \cdot \ln({}^p y_i), \quad (\text{Eq 6})$$

where f_p is the stoichiometric coefficient for sublattice p and the second sum describes the effect of the ideal mixing within the sublattice p , similar to Eq 1.

The simplest model for the description of the contribution of the excess Gibbs energy for the two-sublattice model is defined as:

$${}^E G_m^\phi = \sum_1 y_i \cdot {}^1 y_j \cdot {}^2 y_k \cdot L_{(i,j;k)} + \sum_1 y_i \cdot {}^2 y_k \cdot {}^2 y_l \cdot L_{(i;k,l)}, \quad (\text{Eq 7})$$

where

$$L_{(i,j;k)} = \sum_z {}^z L_{(i,j;k)} \cdot (y_i - y_j)^z \quad \text{and} \quad (\text{Eq 8a})$$

$$L_{(i;k,l)} = \sum_z {}^z L_{(i;k,l)} \cdot (y_k - y_l)^z. \quad (\text{Eq 8b})$$

Here, the parameters ${}^z L_{i,j;k}$ describe the mutual interaction of constituents i and j in the first sublattice, when the second sublattice is fully occupied by constituent k and the parameters ${}^z L_{i;k,l}$ describe the mutual interaction of constituents k and l in the second sublattice, when the first sublattice is fully occupied by constituent i . Moreover, this description can be extended to any number of sublattices.

As was mentioned above, the only thermodynamic data available for the NiSe₂ phase is the heat capacity in the temperature range of 573–1373 K^[13]. Therefore the direct modelling of heat capacity was used for the theoretical description of the NiSe₂ intermetallic phase to achieve agreement between experimental and our calculated heat capacity data.

The temperature dependence of the Gibbs energy of the pure constituent i in pure-constituent type formalism is expressed by the Eq (2). The most common polynomial form of this equation is :

$$G_m^\phi = a + b \cdot T + c \cdot T \ln(T) + d_1 \cdot T^2 + d_2 \cdot T^3 + d_4 \cdot T^{-1}, \quad (\text{Eq 9})$$

where a , b , c , and the d_i are adjustable coefficients.

This expression is usually required for a given phase to cover the whole temperature range of interest. From such expression of Gibbs energy, the other thermodynamic functions such as entropy S , enthalpy H and heat capacity C_p can be evaluated as follows^[25]:

$$S_m^\phi = -b - c - c \cdot \ln(T) - \sum n \cdot d_i \cdot T^{n-1}, \quad (\text{Eq 10})$$

$$H_m^\phi = a - c \cdot T - \sum (n-1) \cdot d_i \cdot T^n \quad (\text{Eq 11})$$

$$C_{pm}^\phi = -c \cdot T - \sum n \cdot (n-1) \cdot d_i \cdot T^{n-1}. \quad (\text{Eq 12})$$

The adjustable coefficients of equation (12) describing the temperature dependence of heat capacity of NiSe₂ phase were fitted to the experimental data and subsequently transferred in the form of Gibbs energy (Eq 9b) into the database. Parameters “ a ” and “ b^*T ” remain optimizable to achieve agreement with the phase diagram.

4 Results and Discussion

The software package for the phase diagrams calculations Pandat[29] was used for the thermodynamic modelling in this work. The optimizing procedure was mainly based on the experimental phase diagram evaluation published by Komarek^[9] and Lee^[10]. The standard enthalpy of formation of NiSe phase measured by Grønvold^[12] and heat capacity of NiSe₂ phase published later by Grønvold^[13] were also used during the assessment process.

The data for pure elements were taken from the SGTE 4.4 database.^[24] Thermodynamic parameters obtained in this work are presented in Table 3.

The phase diagram calculated using the data from Table 4 and 24 database^[24] with superimposed experimental

data from Komarek et al.^[9] and Lee^[10] is shown in Fig. 2. Experimental data are presented by various symbols: triangles represent the liquidus temperature on the heating curve, circles mark the temperatures of invariant phase reactions measured by DTA, and filled diamonds represent other thermal effects.^[9] Crosses show the eutectoid temperature of phase transition Ni₃Se₂_HT + FCC_A1 ↔ Ni₃Se₂_LT proposed by Lee.^[10]

Figure 2 shows a very good agreement between the modelled phase diagram and calculated temperatures of invariant reactions (see Table 2) with the experimental results from the work of Komarek et al.^[9] and the phase diagram published by Lee^[10]. The shape of the miscibility gap proposed by Komarek et al.^[9] is slightly different from ours (compare to Fig. 1), but Komarek et al.^[9] proposed the

Fig. 2 Assessed phase diagram in comparison with experimental data from Komarek et al.^[9] and Lee^[10] (triangles: liquidus on heating, circles: invariant phase transitions measured by DTA, diamonds: another thermal effect, crosses: temperature proposed by Lee^[10])

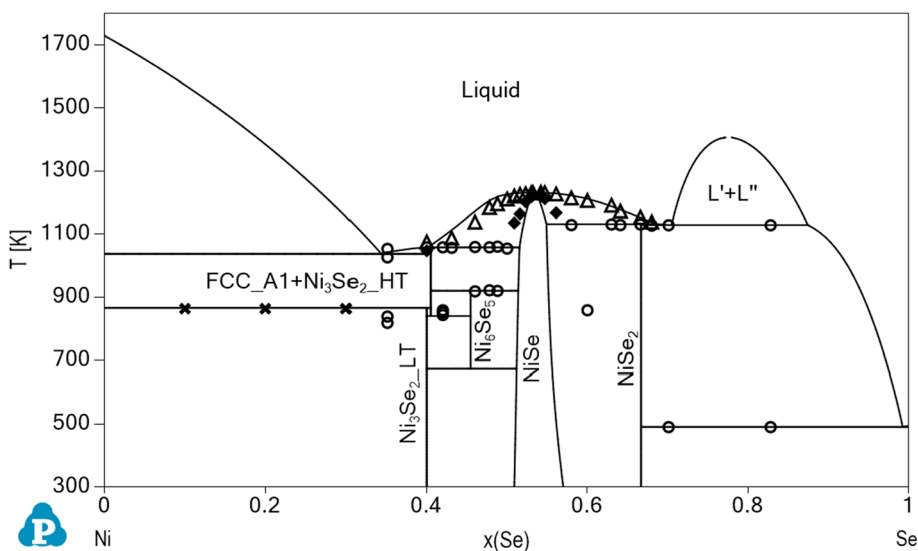
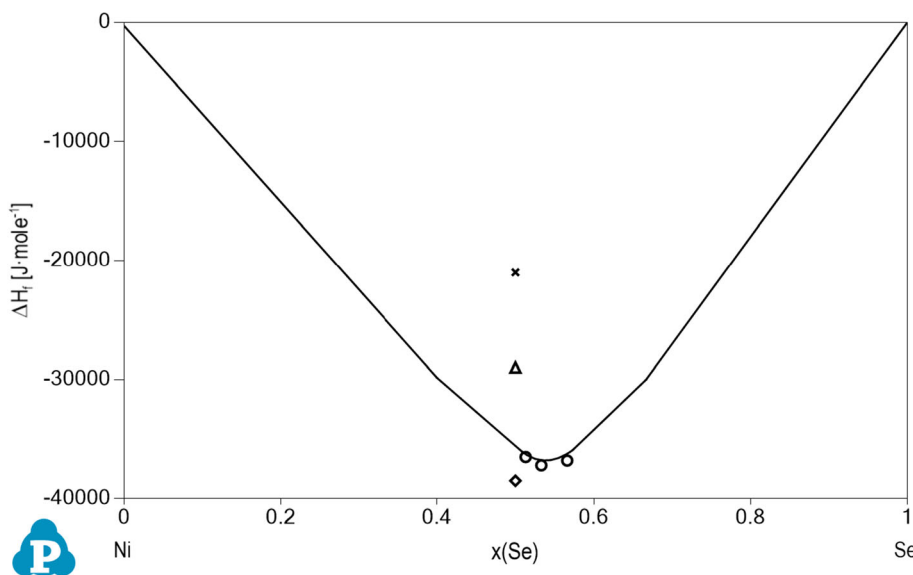


Fig. 3 Calculated enthalpy of formation of the NiSe phase at 298 K with superimposed experimental data published in different works: diamond,^[19] triangle,^[20] cross^[21] and circles.^[12] Numerical values of literature data of ΔH_f of NiSe phase are listed in Table 3. The reference states are FCC_A1 for Ni and hexagonal_A8 for Se.



description of this phenomenon without any experimental data describing the miscibility gap boundaries.

Figure 3 shows the calculated concentration dependence of the enthalpy of formation of the NiSe phase in the whole concentration range at 298 K. The reference states are FCC_A1 for Ni and hexagonal_A8 for Se. The plot is superimposed with experimental^[12, 19] and theoretically predicted values.^[20, 21] Numerical values of literature data are listed in Table 3. The agreement of our result with data proposed by Grønvold^[12] is very good.

Figure 4 shows the composition dependence of the enthalpy of formation on NiSe phase at 1050 K with superimposed experimental data published by Grønvold.^[12] The experimental results are for the single-phase region of

NiSe. The reference states of pure elements are the FCC_A1 phase for the Ni and the liquid phase for the Se, as described in the experimental work of Grønvold.^[12] The change in the slope of the curve at $x(\text{Se}) = \text{ca. } 0.515$ is caused by crossings of the solidus line in the phase diagram in our assessment. Numerical values of literature data of ΔH_f of NiSe phase are listed in Table 3. The agreement of our predicted enthalpy of formation of single-phase region NiSe with literature is very good.

The predicted heat capacity of the NiSe₂ phase with superimposed experimental data in temperature interval 300–1000 K published by Grønvold^[13] is shown in Fig. 5. The agreement between experiments and calculation is excellent up to 1000 K. However, we did not accept for our

Fig. 4 Enthalpy of formation of NiSe phase at 1050 K with superimposed experimental data published by Grønvold^[12]. Numerical values of literature data of ΔH_f of NiSe phase are listed in Table 3. The reference states are FCC_A1 for Ni and liquid for Se.

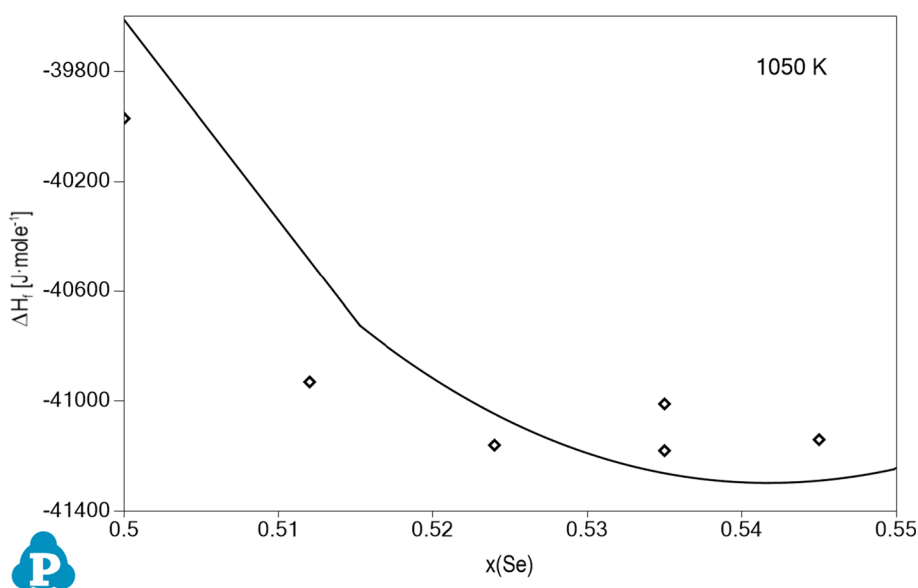
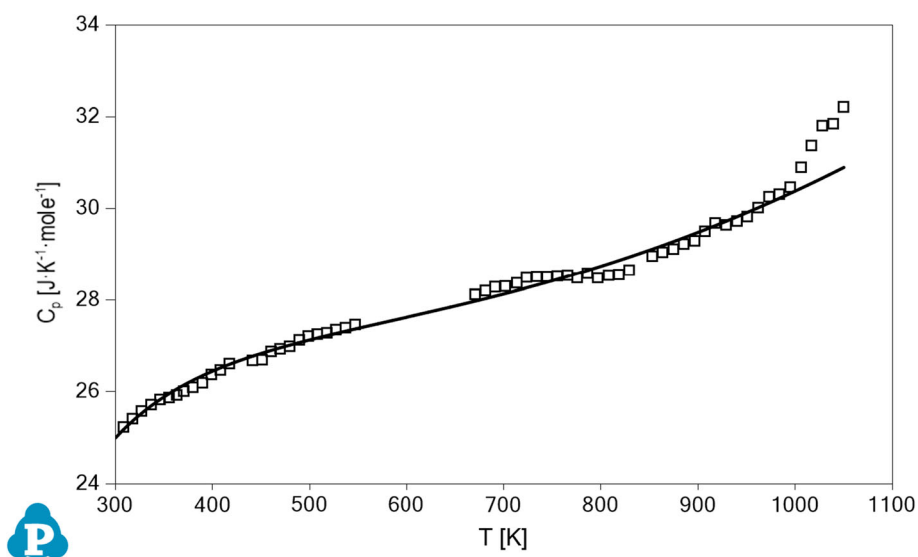


Fig. 5 Predicted heat capacity of the NiSe₂ phase with superimposed experimental data published by Grønvold^[13]



assessment the experimental heat capacity data at higher temperatures due to their rapidly increasing slope. This inconsistency might be caused by evaporating of Se above 1000 K.

5 Conclusion

This work presents the thermodynamic assessment of the Ni-Se binary phase diagram. Theoretical description of the phase diagram is based mainly on the experimental phase diagram evaluation published by Komarek et al.^[9] and by Lee and Nash^[10] and experimentally measured

thermodynamic properties, namely enthalpy of formation of NiSe phase at 298 and 1050 K and heat capacity of NiSe₂ phase. Very good agreement with the experimental results was reached for the Ni-Se phase diagram and heat capacity of the NiSe₂ phase. The calculated standard enthalpy of mixing of the NiSe phase at 298 K and $x(\text{Se})=0.5$ is equal to the $-35.4 \text{ kJ mol}^{-1}$, which corresponds reasonably with the experimental value measured by Grønvold.^[13] The enthalpy of formation of the NiSe phase at 1050 K in concentration range $x(\text{Se})=0.5-0.55$ agrees well with experimental data published by Grønvold^[13] too.

Appendix

Element	/-	ELECTRON_GAS	0	0	0 !
Element	VA	VACUUM	0	0	0 !
Element	NI	Fcc	58.693	4787	29.796 !
Element	SE	HEXAGONAL_A8	78.96	5514.5	41.966 !

SPECIES NISE NIISE1!

Function GHSERNI 298.15 -5179.159+117.854*T-22.096*T*ln(T)
 -.0048407*T**2; 1728 Y
 -27840.655+279.135*T-43.1*T*ln(T)+1.12754e+31*T**(-9); 6000 N !
 Function GBCCNI 298.15 +8715.084-3.556*T+GHSERNI; 6000 N !
 Function GCBCCN 298.15 +3556+GHSERNI; 3000 N !
 Function GCUBNI 298.15 +2092+GHSERNI; 3000 N !
 Function GHCPNI 298.15 +1046+1.2552*T+GHSERNI; 6000 N !
 Function GLIQNI 298.15
 +16414.686-9.397*T-3.82318e-021*T**7+GHSERNI; 1728 Y
 -0.0796717+18290.88-10.537*T-1.12754e+31*T**(-9)+GHSERNI; 3000 N !
 Function GHSERSE 298.15 -9376.371+174.205877*T-33.6527*T*ln(T)
 +0.02424314*T**2-1.5318461e-005*T**3+102249*T**(-1); 494 Y
 -37546.134+507.111538*T-81.2006585*T*ln(T)+0.037144892*T**2
 -5.611026e-006*T**3+2614263*T**(-1); 800 Y
 -12193.47+197.770166*T-35.1456*T*ln(T); 1000 N !
 Function GLIQSE 298.15 50533.347-1178.288242*T+194.1074389*T*ln(T)
 -0.390268991*T**2+0.000119219297*T**3-2224398*T**(-1); 494 Y
 -5228.304+183.72559*T-35.1456*T*ln(T); 1000 N !

TYPE_DEFINITION % SEQ *!
 DEFINE_SYSTEM_DEFAULT ELEMENT 2 !
 DEFAULT_COMMAND DEF_SYS_ELEMENT VA /- !

Phase Liquid % 1 1 !

Constituent Liquid :NI,NISE,SE:!

Parameter G(Liquid,NI;0) 298.15 GLIQNI; 3000 N !
 Parameter G(Liquid,SE;0) 298.15 GLIQSE; 1000 N !
 Parameter G(Liquid,NISE;0) 298.15 -45942+1*GHSERSE
 +1*GHSERNI; 1000 N !

Parameter G(Liquid,NI,SE;0) 298.15 19852; 3000 N !
 Parameter G(Liquid,NI,SE;1) 298.15 +54858; 3000 N !
 Parameter G(Liquid,NI,SE;2) 298.15 -44864; 3000 N !

Parameter G(Liquid,NI,NISE;0) 298.15 -1094; 3000 N !

Parameter G(Liquid,NISE,SE;0) 298.15 +5945; 3000 N !
 Parameter G(Liquid,NISE,SE;1) 298.15 -1140; 3000 N !
 Parameter G(Liquid,NISE,SE;2) 298.15 +12856; 3000 N !

TYPE_DEFINITION F GES AMEND_PHASE_DESCRIPTION FCC_A1 MAGNETIC -3
0.280 !

PHASE FCC_A1 %F 2 1 1 !

CONST FCC_A1 :NI:VA:!

PARAMETER G(FCC_A1,NI:VA;0) 298. GHSERNI#; 6000. N DIN91 !

PARAMETER BM(FCC_A1,NI:VA;0) 298. 0.52; 6000. N DIN91 !

PARAMETER TC(FCC_A1,NI:VA;0) 298. 633.0; 4000. N GUI89 !

Phase HEXAGONAL_A8 % 1 1 !

Constituent HEXAGONAL_A8 :SE:!

Parameter G(HEXAGONAL_A8,SE;0) 298.15 GHSERSE; 1000 N !

Phase NI3SE2_LT % 2 0.6 0.4 !

Constituent NI3SE2_LT :NI:SE:!

Parameter G(NI3SE2_LT,NI:SE;0) 298.15

-30835+10*T+0.6*GHSERNI+0.4*GHSERSE; 6000 N !

Phase NI3SE2_HT % 2 0.595 0.405 !

Constituent NI3SE2_HT :NI:SE:!

Parameter G(NI3SE2_HT,NI:SE;0) 298.15

-29900+8.6*T+0.595*GHSERNI+0.405*GHSERSE; 6000 N !

Phase NI6SE5 % 2 0.54545 0.45455 !

Constituent NI6SE5 :NI:SE:!

Parameter G(NI6SE5,NI:SE;0) 298.15

-33671.5+10.26*T+0.54545*GHSERNI+0.45455*GHSERSE; 6000 N !

Phase NISE % 2 0.5 0.5 !

Constituent NISE :NI,SE:SE:!

\$

Parameter G(NISE,NI:SE;0) 298.15

-36370+11.28*T+0.5*GHSERNI+0.5*GHSERSE; 6000 N !

Parameter G(NISE,SE:SE;0) 298.15

15000+GHSERSE; 6000 N !

Parameter G(NISE,NI,SE:SE;0) 298.15 -25000+35*T; 6000 N !

Parameter G(NISE,NI,SE:SE;1) 298.15 -35000-6*T; 6000 N !

Parameter G(NISE,NI,SE:SE;2) 298.15 -25000-6.3*T; 6000 N !

Phase NISE2 % 2 0.33333 0.66667 !

Constituent NISE2 :NI:SE:!

\$parametry c-f fit na Cp; a+b*T volne optimalizovatelne

Parameter G(NISE2,NI:SE;0) 298.15

-40218+176.7*T-31.32987*T*LN(T)+0.005135*T**2-1.616E-06*T**3

+185915.26*T**(-1); 6000 N !

Funding This research did not receive any specific grant from funding agencies in the public, commercial, or not-for-profit sectors. The raw data required to reproduce these findings are available in appendix.

References

1. N. Saunders, and A.P. Miodownik, *Calphad (A Comprehensive Guide)*. Pergamon Press, Oxford, 1998.
2. H.L. Lukas, S.G. Fries, and B. Sundman, *Computational Thermodynamics: The Calphad Method*. Cambridge University Press, New York, 2004.
3. G. Shen, D. Chen, K. Tang, C. An, Q. Yang, Y. Qian, and J. , Phase-Controlled Synthesis and Characterization of Nickel Sulfides Nanorods, *Solid State Chem.*, 2003, **173**, p 227.
4. N. Umeyama, M. Tokumoto, S. Yagi, M. Tomura, K. Tokiwa, T. Fujii, R. Toda, N. Miyakawa, and S. Ikeda, Synthesis and Magnetic Properties of NiSe, NiTe, CoSe, and CoTe, *Jpn. J. Appl. Phys.*, 2012, **51**, p 053001.
5. A. Kagkoura, T. Skaltsas, and N. Tagmatarchis, Transition-Metal Chalcogenide/ Graphene Ensembles for Light-Induced Energy Applications, *Chemistry*, 2017, **23**, p 12967.
6. N. Moloto, M.J. Moloto, N.J. Coville, and S. Sinha-Ray, Synthesis and Characterization of Nickel Selenide Nanoparticles: Size and Shape Determining Parameters, *J. Cryst. Growth*, 2011, **324**, p 41–52.
7. P.D. Matthews, P.D. McNaughten, D.J. Lewis, and P. O'Brien, Shining a Light on Transition Metal Chalcogenides for Sustainable Photovoltaics, *Chem. Sci.*, 2017, **8**, p 4177.
8. J.P. Riba, Function of Porous Selenium-Nickel Electrode, *J. Chim. Phys. Phys.- Chim. Biol.*, 1971, **68**(3), p 485.
9. K.L. Komarek, and K. Wessely, Die Systeme Nickel-Selen and Kobalt-Nickel-Selen, *Monatsh. Chem.*, 1972, **103**, p 923.
10. S.Y. Lee, P. Nash, in: "Phase Diagrams of Binary Nickel Alloys", P. Nash (ed.), ASM International, Materials Park, Ohio 1991.
11. O. Predel, O. Madelung Ni-Se (Nickel-Selenium) Landolt-Börnstein - Group IV Physical Chemistry 5I (Ni-Np - Pt-Zr) 1998.
12. F. Grønvold., Enthalpy of Formation of Iron Selenides and Nickel Selenides at 1050K, *Acta Chemica Scandinavica* 26 (1972) 2085.
13. F. Grønvold, Heat Capacities and Thermodynamic Properties of Iron Diselenide and Nickel Diselenide from 300 to 1000 K, *J. Chem. Thermodynamics*, 1975, **I**, p 645.
14. F. Grønvold, R. Mollerud, E. Rost, The High-Temperature Phases. Ni₃Se₂ and Ni₆Se₅, *Acta Chem. Scand.* 20 (1966) 1997
15. J.H. Hiller, and W. Wegener, Untersuchungen im system nickel-selen, *Neues Jahrb. Miner. Abh.*, 1960, **94**, p 1147–1159.
16. K. Kuznetsov, A. Eliseev, Z. Spak, K. Palkina, M. Sokolova, A. Dimitriev, Proc. 4th All-Union Conf. Semiconductor Materials, Moscow, USSR (1961) 159
17. F. Grønvold, and E. Jacobsen, X-Ray and Magnetic Study of Nickel Selenides in the Range NiSe and NiSe₂, *Acta Chem. Scand.*, 1956, **10**, p 1440.
18. G. Akesson, and E. Rost, A Superstructure of Ni₆Se₅, *Acta Chem. Scand. Ser. A*, 1975, **29**, p 236.
19. C. Fabre, Thermal Studies on the Selenides, *Ann. Chim. Phys.*, 1887, **10**, p 472.
20. F.R. Bichowsky, and F.D. Rossini, *The Thermochemistry of Chemical Substances*. Reinhold, New York, 1936.
21. F.D. Rossini, D.D. Wagman, W.H. Evans, S. Levine, I. Jaffe, Selected Values of Chemical Thermodynamic Properties, Natl. Bur. Std (US) Circ. No 500, 1952.
22. H. Jelinek, and K.L. Komarek, Thermodynamic Properties of Nickel-Selenium Alloys, *Monatsh. Chem.*, 1974, **105**, p 917.
23. W. Cao, S.L. Chen, F Zhang, K. Wu, Yang Y., Chang Y.A., Schmid-Fetzer R., Oates W. A., PANDAT Software with PanEngine, PanOptimizer and PanPrecipitation for Multicomponent Phase Diagram Calculation and Materials Property Simulation, 33 (2009) 328
24. SGTE Unary Database, Version 4.4.
25. A.T. Dinsdale, SGTE Data for Pure Elements, *Calphad*, 1991, **15**, p 317.

Publisher's Note Springer Nature remains neutral with regard to jurisdictional claims in published maps and institutional affiliations.

6.7 Paper 7

- [P7] **Zobač, O.**, Richter, K.W., Kroupa, A., *Experimental phase diagram of the Ag-Se-Sn system at 250, 400 and 550 °C*, Journal of Phase Equilibria and Diffusion, 2022, 43, pp. 32-42, doi: 10.1007/s11669-022-00937-w (IF 1.4)



Experimental Phase Diagram of the Ag-Se-Sn System at 250, 400 and 550 °C

Ondrej Zobac¹ · Klaus W. Richter² · Ales Kroupa¹

Submitted: 9 September 2021 / in revised form: 14 October 2021 / Accepted: 8 November 2021 / Published online: 30 January 2022
© ASM International 2022

Abstract The ternary phase diagram Ag-Se-Sn was re-investigated experimentally. The current study was designed to contribute to a better understanding of phase equilibria in isothermal sections at 250, 400 and 550 °C using long-term annealed samples. An intermediate liquid region was observed at 550 °C in agreement with older published vertical sections of the ternary phase diagram Ag-Se-Sn. A huge homogeneity range in ternary intermetallic phase Ag₈Se₆Sn at 250 °C was determined by SEM/EDX analysis of long term annealed samples and confirmed by XRD measurements. A second ternary phase AgSe₂Sn was observed at each of the studied temperatures. Complete isothermal sections at 250, 400 and 550 °C were constructed in the scope of this paper.

Keywords Ag-Se-Sn phase diagram · Ag₈Se₆Sn phase · SEM-EDX · XRD

1 Introduction and Literature Review

1.1 Introduction

The Ag-Se-Sn ternary system has been investigated in the past because of its technical importance. Ag-Se-Sn based

materials are candidates for various energy applications, whereas Ag₂Se,^[1,2] SeSn,^[3] Se₂Sn^[4] and Ag₈Se₆Sn^[5,6] compounds are used for thermoelectric applications in various temperature ranges and also for photovoltaic applications. Experimental phase diagram of Ag-Se-Sn was constructed recently.^[7] This paper was focused only partially on the phase equilibrium data and the interfacial reactions in this system were studied. Isothermal sections were constructed by combining information from the binary subsystems and ternary experimental data. The Se-rich part of the phase diagram was not studied in this work.

Yusibov et al.^[8] published several pseudo-binary phase diagrams and an isothermal section at 27 °C. It is the aim of our work to experimentally describe the isothermal sections at three temperatures using long-term annealed samples and propose the Se-rich parts of phase diagrams at 250, 400 and 550 °C.

1.2 Literature Review

Phase equilibria in the Ag-Sn-Se system were investigated in several works since the 1960's.^[7–16] Ollitrault-Fitchet et al.^[14] presented the vertical section of the phase diagram between Ag₂Se-SnSe₂ with one ternary intermetallic phase Ag₈Se₆Sn, which melts incongruently at 735 °C and undergoes a polymorphic transition at 83 °C. According to Berger and Prochukhan,^[10] the section Ag₂Se-SnSe₂ is not quasi-binary and the compound Ag₈Se₆Sn melts congruently at 754 °C. Yusibov et al.^[8] proposed the section Ag₂Se-SnSe₂ with two eutectic transitions at 495 and 722 °C based on differential thermal analysis (DTA). Pir-ela et al.^[16] reported the synthesis of the compound Ag₂SnSe₃ with monoclinic structure. The section Ag₂Se-SnSe was studied in several works.^[10,13,15] It was supposed to be quasi-binary eutectic phase diagram section

✉ Ondrej Zobac
zobac@ipm.cz

¹ Institute of Physics of Materials, The Czech Academy of Sciences, Zizkova 22, 616 00 Brno, Czech Republic

² Department of Inorganic Chemistry - Functional Materials, University of Vienna, Währinger Straße 42, 1090 Vienna, Austria

with the eutectic temperature reported at 551, 545, or 610 °C, respectively. According to Gorochov,^[12] the section $\text{Ag}_2\text{Se-SnSe}$ is not quasi-binary because the primary crystallization field of metallic silver contacts its $T-x$ plane. Berger and Prochukhan^[10] also presented the total $T-x-y$ diagram of the Ag-Sn-Se system, in which two ternary compounds $\text{Ag}_8\text{Se}_6\text{Sn}$ and AgSe_2Sn were presented. On the liquidus surface, the miscibility gap was detected.

Berger and Prochukhan^[10] published several vertical sections of the ternary Ag-Sn-Se system, along with the sections $\text{Ag}_2\text{Se-SnSe}$, $\text{Ag}_2\text{Se-Ag}_8\text{Se}_6\text{Sn}$, $\text{Ag}_8\text{Se}_6\text{Sn-SnSe}$, and $\text{Ag}_8\text{Se}_6\text{Sn-Se}$. The first two sections are of the eutectic type, and the third is characterized by a monotectic equilibrium and a degenerate eutectic equilibrium. The phase equilibria in the composition region $\text{Ag-Ag}_2\text{Se-Ag}_8\text{Se}_6\text{Sn-SnSe-Sn}$ were later presented by Gorochov^[12] and are somewhat different from Berger and Prochukhan's scheme.^[10] Gorochov^[12] indicated that there is a field in the projection of the liquidus surface that cannot be assigned to the primary crystallization of any of the phases of the system. It must be noted that Berger and Prochukhan^[10] presented only two vertical sections (one of which was constructed incompletely), whereas Gorochov^[12] did not present any vertical section, which complicates the analysis of the results of these works.

The $\text{Ag}_8\text{Se}_6\text{Sn-Se}$ section was proposed by Yusibov et al.^[8] who presented a miscibility gap in the liquid phase above a monotectic reaction at 600 °C. Yusibov et al.^[8] presented also an isothermal section at 27 °C, the liquidus surface and a 3D projection of liquidus surface and surface of separation of miscibility gap $L_1 + L_2$. Ramakrishnan et al.^[7] published partial isothermal sections of the experimental ternary phase diagram Ag-Se-Sn at 550 and 400 °C. The isothermal section at 250 °C was predicted just from the $\text{Sn/Ag}_2\text{Se}$ diffusion couple experiments with the annealing time 120 min. Two ternary phases, AgSe_2Sn and $\text{Ag}_8\text{Se}_6\text{Sn}$, were found and very limited solubility of binary intermetallics was described.

Crystallographic data on ternary compounds in the Ag-Sn-Se system are available in the literature.^[12,17–19] The high-temperature modification of $\text{Ag}_8\text{Se}_6\text{Sn}$ crystallizes in a cubic structure (space group $F4-3m$) with the lattice parameter $a = 1.112 \text{ nm}$,^[12] and the low temperature modification crystallizes in an orthorhombic system (space group $Pmn2_1$) with the unit cell parameters $a = 0.79168 \text{ nm}$, $b = 0.78219 \text{ nm}$ and $c = 1.10453 \text{ nm}$.^[19] A ternary phase AgSe_2Sn has a NaCl -type cubic structure with a lattice parameter of $a = 0.5677 \text{ nm}$ for the stoichiometric composition.^[18] Stable phases reported for Ag-Se-Sn and its subsystems are listed in Table 1. The thermodynamic properties of silver and tin selenides were determined by various electromotive force (EMF) methods^[20–22] with comparable results.

2 Experimental

The overall compositions of experimental samples were selected with the purpose to address questions in the experimental phase diagrams not clearly answered as mentioned above. Furthermore, it was our aim to determine the complete isothermal phase equilibria for selected temperatures. The prepared samples were analyzed and characterized by different static and dynamic analytical methods.

2.1 Sample Preparation

Samples were prepared from pure elements of 5N purity. The mixture of pure elements was melted at temperatures 250, 350, ... to 950 °C in steps of 100 °C in evacuated quartz glass ampoules to maximally prevent evaporation of selenium. Finally, the samples were re-melted three times in order to improve the homogeneity of the material. The long-term annealing of the samples sealed in evacuated quartz glass ampoules were performed at above defined temperatures. Conventional low-temperature muffle resistance furnace with controlled circulation of the air was used for the heat treatment. Samples were long-term annealed to achieve a state close to the thermodynamic equilibrium. Annealing time was selected with respect to annealing temperature. For the annealing temperature closer to the melting temperature shorter annealing time is sufficient. Annealing was terminated by quenching of the samples into cold water from their annealing temperatures and sample were then prepared for further investigations. Annealing times and temperatures are given in Table 2 together with experimental results.

2.2 Experimental Phase Diagram Investigation

A combination of dynamic and static methods was used for the investigation of the phase diagram. Samples were divided into several parts. The biggest part was fixed in the resin, ground and metallographically polished with using OPS suspension. Rest of the sample was powdered by mortar and pestle for the powder X-ray diffraction XRD measurement or analyzed by DTA. Phase equilibria, microstructure and chemical analyses of phases and overall compositions were performed using scanning electron microscope combined with energy dispersive X-ray spectroscopy (SEM-EDX), employing either a SEM JEOL JSM-6460 instrument equipped with an energy dispersive detector (EDX) for quantitative analysis and Tescan LYRA 3 XMH FEG/SEM equipped with X-Max80 EDX detector for X-ray microanalysis. Identification of phases present in the long-term annealed samples was achieved using X-ray

Table 1 Stable phases in Ag–Se–Sn ternary phase diagram and lower subsystems

Phase name (this work)	Common names	Pearson symbol	Space group	T range, °C phase transition	References
α (Ag)	Silver	<i>cF4</i>	<i>Fm-3m</i>	< 961.8	23
α (Se)	Selenium	<i>hP3</i>	<i>P3₁21</i>	< 220.8	24
β (Sn)	White tin	<i>tI4</i>	<i>I4₁/amd</i>	13.2–231.9	25
α (Sn)	Grey tin	<i>cF8</i>	<i>Fd-3m</i>	< 13.2	26
β -Ag ₂ Se	Ag ₂ Se-HT	<i>cI**</i>	<i>Im-3m</i>	130–910 congruent	27
α -Ag ₂ Se	Ag ₂ Se-LT	<i>o**</i>	<i>P2₁2₁2₁</i>	< 130 polymorphic	28
ζ	Ag ₄ Sn	<i>hP2</i>	<i>P6₃/mmc</i>	< 724 peritectic	29
ε	Ag ₃ Sn	<i>oP8</i>	<i>Pmnn</i>	< 480 peritectic	30
SeSn _{ht}	SeSn (β)	<i>oC8</i>	<i>Cmcm</i>	520.2–873.7 congruent	31
SeSn _{lt}	SeSn (α)	<i>oP8</i>	<i>Pnma</i>	< 526.3 polymorphic	32
Se ₂ Sn		<i>hP3</i>	<i>P-3m1</i>	< 647 congruent	33
AgSe ₂ Sn	Ag _x Se ₂ Sn _(1-x) , γ		<i>Fm-3m</i>	< 587 peritectic	8, 18
Ag ₈ Se ₆ Sn	Ag ₈ Se ₆ Sn_II		<i>F4-3m</i>	58–752 congruent	12
Ag ₈ Se ₆ Sn _{lt}	Ag ₈ Se ₆ Sn_I		<i>Pmn2₁</i>	< 58 polymorphic	19

powder diffraction. Fine sample powders were produced by powdering a representative part of the annealed sample in a WC/Co mortar (*Durit*). A Bruker D8 diffractometer using Cu K α -radiation, equipped with a high-speed position sensitive (PSD) detector (Lynxeye) was used in the $\theta/2\theta$ reflection setting. One-hour scanning time yielded high intensity data (maximum peak intensity around 20,000 counts) suitable for detailed Rietveld refinement. Refinements of selected diffraction patterns were performed with the Topas software. Annealing temperature of the sample, overall composition, coexisting phases and phase compositions of the concrete phases in the equilibrium are listed in Table 2. Annealing temperature and number of the sample are listed in column 1. Column 2 shows the annealing time, column 3 the overall composition measured by SEM-EDX area scans of as big area as experimental conditions allowed. Coexisting phases stable in the samples are listed in column 4; columns 5–7 show the composition of equilibrium phases existing in the samples measured by SEM-EDX in same order as the phases are mentioned in column 4.

Phase transition temperatures were measured using a high-temperature DTA (NETZSCH Pegasus 404 C) with samples placed in closed and evacuated quartz glass DTA ampoules. Closed ampoules were used to limit uncontrolled Se evaporation during the measurement and contamination of the inner parts of the instrument. The DTA was calibrated using a set of pure metal standards having well-defined melting temperatures (Sn, Al, Zn, Cu, Ag, Au). Calibration was carried out under the same conditions as the experimental measurements. Three heating and

cooling runs were performed for each sample. Thermal analysis results for measured samples are listed in Table 3.

3 Results and Discussion

It was possible to draw complete isothermal sections of ternary phase diagram Ag–Se–Sn at 250, 400 and 550 °C, respectively, from experimental results listed in Table 2. The results for these sections are described in detail below. The shape of the phase boundaries and phase fields not defined by our own samples were drawn based on information from binary subsystems, phase rules and data published by Ramakrishnan et al.^[7] or Yusibov et al.^[8]. Our results generally agree well with the phase diagrams published by Ramakrishnan et al.^[7] and Yusibov et al.^[8] but contain some additional clarification and improvement of areas, which were not investigated in detail in the previous studies.

3.1 Isothermal Section at 250 °C

The isothermal section of the experimental phase diagram Ag–Se–Sn at 250 °C is shown in Fig. 1. Due to the low melting point of pure tin (231.9 °C) and selenium (220.8 °C), two liquid phases, labeled as Liquid (Se) and Liquid (Sn) were observed in this section. Five binary phases, Ag₂Se, ζ -Ag₄Sn, ε -Ag₃Sn, SeSn and Se₂Sn respectively, are stable at 250 °C. All these binary phases have negligible solubility of the third element in their structures. Two ternary phases, AgSe₂Sn and Ag₈Se₆Sn, are stable at 250 °C. AgSe₂Sn is line compound which

Table 2 Chemical phase composition of the long-term annealed representative samples determined by SEM/EDX.

T, °C_No.	Annealing time, h	Overall composition, at. %			Coexisting phases	Phase 1, at. %			Phase 2, at. %			Phase 3, at. %		
		Se	Ag	Sn		Se	Ag	Sn	Se	Ag	Sn	Se	Ag	Sn
250_1	1420	6.7	38.7	54.6	$\epsilon + \text{SeSn} + \text{Liq (Sn)}$	0.4	75.4	24.2	48.7	0.1	51.2	0.1	3.6	96.3
250_2	1420	3.6	73.8	22.6	$\text{SeSn} + \zeta$	49.1	1.0	49.9	0.3	78.6	21.1			
250_3	1420	34.6	58.3	7.1	$(\text{Ag}) + \text{SeSn} + \text{Ag}_2\text{Se}$	1.2	93.4	5.4	48.9	1.2	49.9	32.9	67.1	0
250_4	1420	54.9	5.2	39.9	$\text{Se}_2\text{Sn} + \text{SeSn} + \text{AgSe}_2\text{Sn}$	66.2	0.2	33.6	49.7	0.1	50.2	50.0	21.2	28.8
250_5	1550	33.7	60.7	5.6	$\text{Ag}_2\text{Se} + \text{SeSn}$	32.8	67.2	0	49.1	1.1	49.8
250_6	1550	52.0	23.5	24.5	$\text{Ag}_8\text{Se}_6\text{Sn} + \text{Se}_2\text{Sn} + \text{AgSe}_2\text{Sn}$	53.6	33.6	12.8	64.8	3.2	32.0	48.9	26.3	24.8
250_7	1550	48.1	26.1	25.8	$\text{AgSe}_2\text{Sn} + \text{Ag}_8\text{Se}_6\text{Sn}$	48.4	25.8	25.9	40.7	50.4	9.0
250_8	1550	60.6	26.1	13.3	$\text{Ag}_8\text{Se}_6\text{Sn} + \text{Se}_2\text{Sn} + \text{Liq (Se)}$	53.7	34.1	12.2	67.0	0.2	32.8	98.3	0.6	1.1
250_9	1550	61.9	14.2	23.9	$\text{Ag}_8\text{Se}_6\text{Sn} + \text{Se}_2\text{Sn} + \text{Liq (Se)}$	50.0	38.0	12.0	65.6	0.1	34.3	n.a.	n.a.	n.a.
250_10	1550	42.9	34.9	22.2	$\text{Ag}_8\text{Se}_6\text{Sn} + \text{SeSn}$	39.9	52.4	7.7	49.6	1.2	49.2
250_11	1550	36.4	60.7	2.9	$\text{Ag}_2\text{Se} + \text{Ag}_8\text{Se}_6\text{Sn}$	33.3	66.7	0	56.3	33.2	10.5
400_1	1035	11.6	11.6	76.8	$\text{SeSn} + \text{Liq (Sn)}$	49.3	0.1	50.6	0.2	15.4	84.4
400_2	1035	3.7	76.5	19.8	$\zeta + \text{SeSn}$	0.5	81.7	17.8	49.6	0.5	49.9
400_3	1035	8.4	46.3	45.3	$\epsilon + \text{SeSn} + \text{Liq (Sn)}$	0.3	75.3	24.4	49.3	0.2	50.5	0.0	24.8	75.2
400_4	1035	55.4	4.3	40.3	$\text{Se}_2\text{Sn} + \text{SeSn} + \text{AgSe}_2\text{Sn}$	65.9	0.2	33.9	49.3	0.3	50.4	49.7	21.9	28.4
400_5	1035	33.1	64.0	2.9	$\text{Ag}_2\text{Se} + \text{SeSn} + (\text{Ag})$	32.5	67.5	0	48.6	0.7	50.7	0.6	93.4	6.0
400_6	1050	6.1	77.7	16.2	$\zeta + \text{SeSn}$	0.5	87.2	12.3	49.6	0.4	50.0	49.6	0.4	50.0
400_7	1050	48.2	25.8	26.0	$\text{AgSe}_2\text{Sn} + \text{Ag}_8\text{Se}_6\text{Sn}$	49.4	24.9	25.7	41.8	50.9	7.3
400_8	1050	43.8	25.1	31.0	$\text{Ag}_2\text{Se} + \text{SeSn} + \text{Ag}_8\text{Se}_6\text{Sn}$	33.3	66.7	0.0	49.5	0.3	50.1	39.8	53.9	6.3
400_9	1050	54.8	27.9	17.3	$\text{Liq(Se)} + \text{Ag}_8\text{Se}_6\text{Sn} + \text{Se}_2\text{Sn}$	99.3	0.0	0.7	42.8	45.6	11.7	66.2	0.2	33.6
400_10	1050	60.8	9.1	30.1	$\text{Se}_2\text{Sn} + \text{Ag}_8\text{Se}_6\text{Sn}$	66.1	0.2	33.7	43.1	45.6	11.3
400_11	1050	49.2	28.9	21.9	$\text{AgSe}_2\text{Sn} + \text{Se}_2\text{Sn} + \text{Ag}_8\text{Se}_6\text{Sn}$	49.3	25.5	25.2	65.5	0.9	33.6	42.6	44.8	12.6
550_1	900	7.2	12.1	80.7	$\text{SeSn} + \text{Liq (Sn)}$	49.7	0.0	50.3	0.5	14.3	85.2
550_2	900	4.5	73.6	21.9	$\text{SeSn} + \zeta$	49.6	0.4	50.0	0.3	80.2	19.5
550_3	900	15.5	64.8	19.7	$\text{Ag} + \text{SeSn} + \text{Liq (T)}$	0.5	87.5	12.0	37.2	48.3	14.5	48.9	0.7	50.4
550_4	900	33.6	63.3	3.1	$\text{Ag}_2\text{Se} + \text{Liq (T)}$	33.1	66.8	0.1	36.4	51.6	12.0
550_5	900	8.0	39.6	52.4	$\text{SeSn} + \text{Liq (Sn)}$	49.4	0.1	50.5	0.2	46.8	53.0
550_6	900	56.2	3.9	39.9	$\text{Se}_2\text{Sn} + \text{SeSn} + \text{AgSe}_2\text{Sn}$	66.6	0.2	33.2	49.9	0.2	49.9	50.5	16.0	33.5
550_7	1010	18.2	77.4	4.4	$\text{Ag}_2\text{Se} + (\text{Ag})$	32.6	67.4	0.0	0.6	90.5	8.9
550_8	1010	33.9	63.8	2.3	$\text{Ag}_2\text{Se} + \text{Liq(T)} + (\text{Ag})$	33.1	66.9	0.0	37.2	49.2	13.6	0.7	90.1	9.2
550_9	1010	49.3	25.0	25.7	$\text{AgSe}_2\text{Sn} + \text{Liq (T)}$	49.7	22.3	28.0	48.7	30.8	20.5
550_10	1010	56.2	22.5	21.3	$\text{Se}_2\text{Sn} + \text{Liq (T)}$	66.2	0.2	33.6	54.2	28.9	16.9
550_11	1010	62.3	19.1	18.6	$\text{Liq (Se)} + \text{Se}_2\text{Sn} + \text{Liq (T)}$	97.5	0.1	2.4	66.5	0.1	33.4
550_12	1010	54.9	35.3	9.8	$\text{Liq (Se)} + \text{Ag}_8\text{Se}_6\text{Sn} + \text{Liq (T)}$	97.1	1.6	1.3	40.0	53.3	6.7	56.5	30.8	12.7

Table 3 General results of Rietveld refinements for samples 250_10 and 250_9

Sample name	250_10	250_9
Method	Full profile Rietveld refinement	
2 θ range	10°–92°	
Phases (% of refined pattern)	$\text{Ag}_8\text{Se}_6\text{Sn}$ (49.1%) SnSe (47.3%) Ag_2Se (3.6%)	$\text{Ag}_8\text{Se}_6\text{Sn}$ (54.0%) SnSe_2 (43.2%) Se (2.8%)
Residual values (Rp/Rwp)	5.90/7.80	9.75/13.18

Fig. 1 Isothermal section of the Ag–Se–Sn experimental phase diagram at 250 °C with superimposed overall composition of two-phase samples (half-solid rectangle) and three-phase samples (solid triangle).

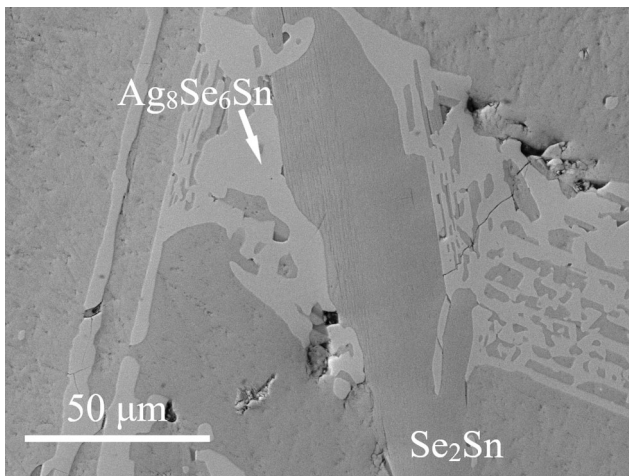
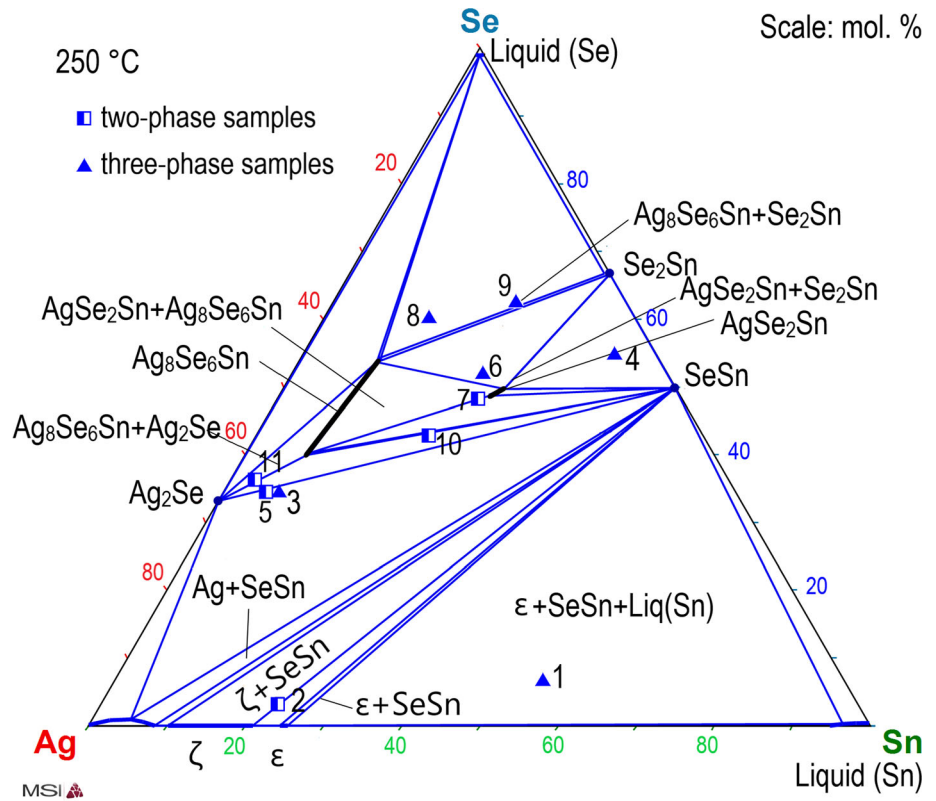


Fig. 2 Microstructure of the sample 250_9 in BSE mode, consisting of $\text{Ag}_8\text{Se}_6\text{Sn} + \text{Se}_2\text{Sn}$

contains constant amount of Se and lies between $\text{Ag}_{24}\text{Se}_{50}\text{Sn}_{26}$ and $\text{Ag}_{22}\text{Se}_{50}\text{Sn}_{28}$. The ternary phase $\text{Ag}_8\text{Se}_6\text{Sn}$ is almost a line compound with a homogeneity range between the approximate compositions $\text{Ag}_{52.5}\text{Se}_{39.3}\text{Sn}_{8.2}$ and $\text{Ag}_{35.5}\text{Se}_{54.2}\text{Sn}_{10.3}$, in contrast to the work of Ramakrishnan et al.^[7] where the $\text{Ag}_8\text{Se}_6\text{Sn}$ phase is proposed to be stoichiometric. Our results were confirmed by the X-ray and compositional analysis. Figures 2 and 3 show the micrographs of samples 250_9 and 250_10 containing $\text{Ag}_8\text{Se}_6\text{Sn}$

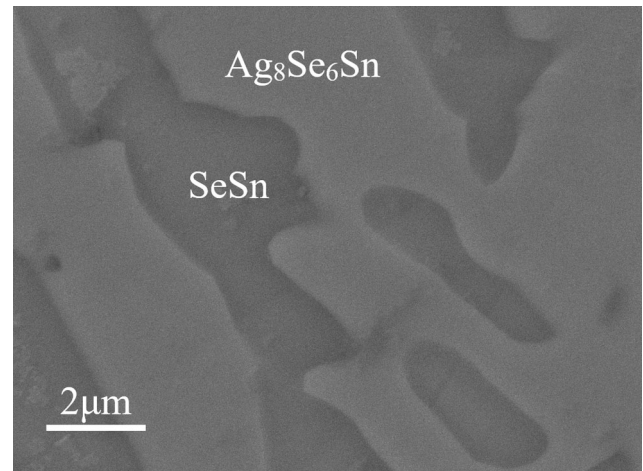


Fig. 3 Microstructure of the sample 250_10 in BSE mode, consisting of $\text{Ag}_8\text{Se}_6\text{Sn} + \text{SeSn}$

from Se-rich and Se-poor limit of the ternary intermetallic phase stability range. Figures 4 and 5 present the XRD patterns of the same samples. $\text{Ag}_8\text{Se}_6\text{Sn}$ was exclusively found in the orthorhombic low temperature form, which is in contrast to the transition temperature of 58 °C proposed in Gulay et al.^[19]

The unexpected wide homogeneity range of $\text{Ag}_8\text{Se}_6\text{Sn}$ required careful Rietveld refinement in order to crosscheck the results from SEM/EDX and XRD, and to develop a

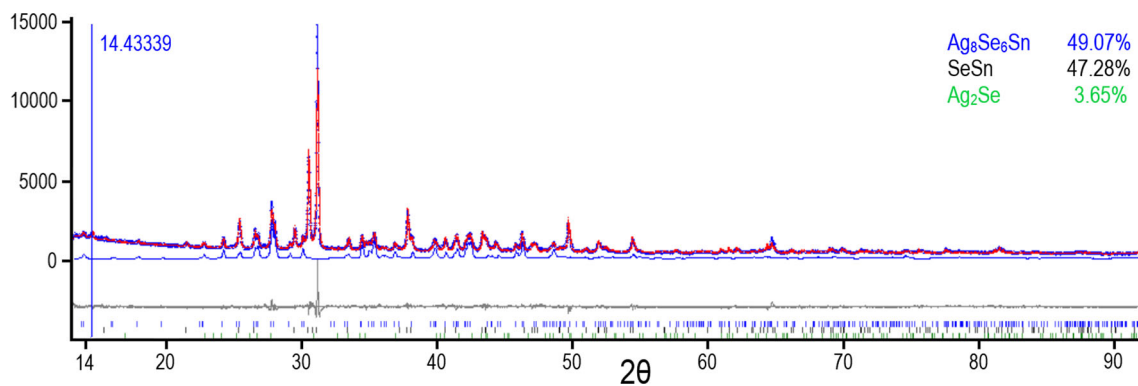


Fig. 4 XRD pattern of sample 250_10 containing SnSe, Ag-rich $\text{Ag}_8\text{Se}_6\text{Sn}$ and traces of Ag_2Se . A minor unidentified peak at 14.43° is marked by a blue line. Blue Circles: experimental data; red line: calculated pattern after Rietveld refinement, blue line: calculated

pattern of the phase $\text{Ag}_8\text{Se}_6\text{Sn}$; grey line: difference between calculated and refined pattern. The color code of the hkl -ticks below corresponds to the legend showing the percentage of calculated peak area for the different phases.

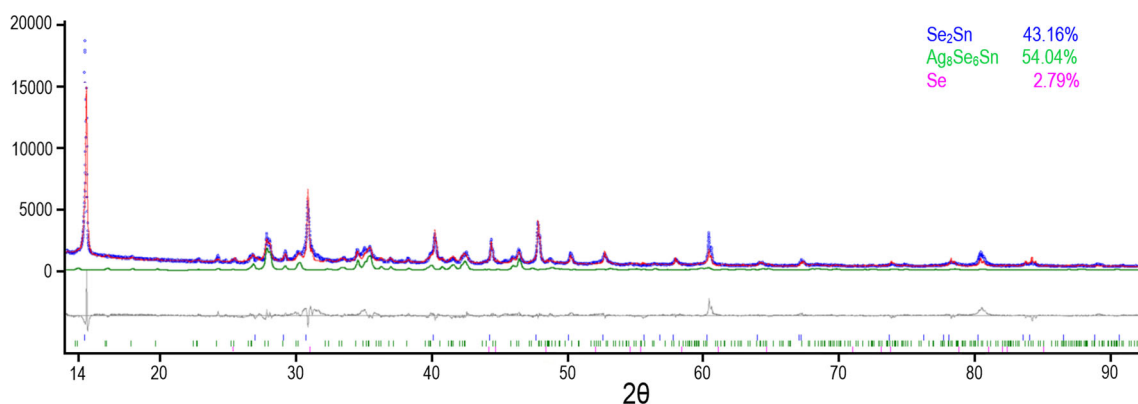


Fig. 5 XRD pattern of sample 250_9 containing SnSe_2 , Se-rich $\text{Ag}_8\text{Se}_6\text{Sn}$ and traces of Se. Blue Circles: experimental data; red line: calculated pattern after Rietveld refinement; green line: calculated pattern of the phase $\text{Ag}_8\text{Se}_6\text{Sn}$; grey line: difference between

calculated and refined pattern. The color code of the hkl -ticks below corresponds to the legend showing the percentage of calculated peak area for the different phases.

reasonable defect model for this compound. The Ag-rich side of the observed homogeneity range ($\text{Ag}_{52.5}\text{Se}_{39.3}\text{Sn}_{8.2}$) agrees very well with the values expected from the chemical formula $\text{Ag}_8\text{Se}_6\text{Sn}$ ($= \text{Ag}_{53.3}\text{Se}_{40}\text{Sn}_{6.7}$). Composition data determined from EDX show a drastic decrease of Ag and a slight increase of Sn on the Se-rich side. As a substitution of Ag by Se can be ruled out from a chemical point of view, vacancies on the metal sites are the most plausible explanation for observed homogeneity range. At the same time, some substitution of Ag by Sn is expected to explain the increase of Sn on the Se-rich side. In order to check this hypothesis, a corresponding site occupation model was tested with Rietveld refinement on the two samples 250_10 and 250_9 stemming from the Ag- and Se-rich side of the homogeneity range. General refinement data and detailed crystallographic parameters observed for the $\text{Ag}_8\text{Se}_6\text{Sn}$ phase are given in Tables 3 and 4.

Both samples contain around 50% $\text{Ag}_8\text{Se}_6\text{Sn}$ together with a tin-selenide and traces of an impurity phase. Given

the quality of the data (multiphase sample) and the complexity of the involved crystal structures, the following restrictions were chosen during refinement:

- the individual atomic positions (x,y,z) were refined in an initial step and then fixed for further refinements
- only one common thermal displacement factor (B_{eq}) was refined for all metal positions (Ag1-5 and Sn1), and another common one for all Selenium positions (Se1-5)
- Vacancies were introduced on all metal sites by refining individual occupation factors for Ag1-5 and Sn1, and the occupation factors of Se-positions were fixed to 1.
- the Ag/Sn ratio on the metal sites was not refined, because it is impossible to refine a mixture of Ag, Sn and vacancies at a single site unambiguously.

Treating both samples with this method using the exactly the same procedure yielded the results summarized in Tables 3 and 4. It is obvious, that the results support the initial hypothesis, as sample 250_10 (Ag-rich) does not

Table 4 Crystallographic parameters for the phase $\text{Ag}_8\text{Se}_6\text{Sn}$ obtained from Rietveld refinements.

Sample		Lattice parameters, nm			Crystallite size (Lorenzian), nm		
250_10 Site	Multiplicity	a = 0.7917(1)	b = 0.7824(1)	c = 1.1057(1)	93(2)		
		x	y	z	Atom	Occupation	Beq
Ag1	4	0.19814	0.53656	0.28560	Ag	0.918(18)	3.50(17)
Ag2	4	0.19800	0.10517	0.87164	Ag	0.936(20)	3.50(17)
Ag3	4	0.18199	0.14768	0.16424	Ag	0.926(18)	3.50(17)
Ag4	2	0.00000	0.61812	0.05300	Ag	0.932(22)	3.50(17)
Ag5	2	0.00000	0.72047	0.48126	Ag	0.942(23)	3.50(17)
Sn1	2	0.00000	0.25647	0.51899	Sn	0.950(25)	3.50(17)
Se1	4	0.24398	0.75737	0.89661	Se	1	0.46(20)
Se2	2	0.00000	0.00401	0.66926	Se	1	0.46(20)
Se3	2	0.00000	0.50924	0.65009	Se	1	0.46(20)
Se4	2	0.00000	0.80760	0.25508	Se	1	0.46(20)
Se5	2	0.00000	0.30083	0.99235	Se	1	0.46(20)

Sample		Lattice parameters, nm			Crystallite size (Lorenzian), nm		
250_9 Site	Multiplicity	a = 0.7918(1)	b = 0.7821(1)	c = 1.1056(1)	52(2)		
		x	y	z	Atom	Occupation	Beq
Ag1	4	0.16632	0.56346	0.29004	Ag	0.878(38)	0.92(29)
Ag2	4	0.24596	0.09890	0.89683	Ag	0.651(30)	0.92(29)
Ag3	4	0.21382	0.19858	0.18517	Ag	0.638(27)	0.92(29)
Ag4	2	0.00000	0.72770	0.08912	Ag	0.221(32)	0.92(29)
Ag5	2	0.00000	0.75388	0.55814	Ag	0.755(42)	0.92(29)
Sn1	2	0.00000	0.33051	0.55875	Sn	0.617(36)	0.92(29)
Se1	4	0.22329	0.76194	0.95161	Se	1	2.49(47)
Se2	2	0.00000	0.99301	0.70021	Se	1	2.49(47)
Se3	2	0.00000	0.52670	0.70340	Se	1	2.49(47)
Se4	2	0.00000	0.96290	0.15449	Se	1	2.49(47)
Se5	2	0.00000	0.33360	0.02921	Se	1	2.49(47)

show significant amounts of vacancies, while sample 250_9 (Se-rich) shows a drastic decrease of metal site occupations to 0.22–0.88. Calculating the refined compositions based on this model and comparing this with the phase compositions determined by SEM/EDX, we reach reasonable agreement. The SEM/EDX phase composition for sample 250_10 is $\text{Ag}_{52}\text{Sn}_8\text{Se}_{40}$, which is in good agreement with $\text{Ag}_{52}\text{Sn}_6\text{Se}_{42}$ obtained by Rietveld refinement. For sample 250_9 we obtain $\text{Ag}_{38}\text{Sn}_{12}\text{Se}_{50}$ from SEM/EDX, which is again in good agreement with $(\text{Ag},\text{Sn})_{50}\text{Se}_{50}$ obtained by Rietveld refinement. Note that in this case noticeable Ag/Sn substitution has to be assumed. Refinement was not possible for the reason explained above.

We conclude that the hypothesis of vacancies on the metal sites in combination with Ag/Sn substitution gives a reasonable explanation for the observed homogeneity range of $\text{Ag}_8\text{Se}_6\text{Sn}$. However, additional XRD investigations on single crystals or pure single-phase samples would

be helpful to further refine the mechanism of nonstoichiometry. In particular, the almost constant lattice parameters within the homogeneity range requires structural explanation.

3.2 Isothermal Section at 400 °C

The isothermal section of the experimental phase diagram Ag-Se-Sn at 400 °C is shown in Fig. 6. Two independent liquid phases, labeled as Liquid (Se) and Liquid (Sn) exist at this temperature. Five binary phases, Ag_2Se , $\zeta\text{-Ag}_4\text{Sn}$, $\varepsilon\text{-Ag}_3\text{Sn}$, SeSn and Se_2Sn respectively, are stable at 400 °C. These binary phases have again very limited solubility of the third element in their structures. The two ternary phases AgSe_2Sn and $\text{Ag}_8\text{Se}_6\text{Sn}$ are stable at 400 °C. AgSe_2Sn is a line compound with a homogeneity range between $\text{Ag}_{25.2}\text{Se}_{49.3}\text{Sn}_{25.5}$ and $\text{Ag}_{21.9}\text{Se}_{49.8}\text{Sn}_{28.3}$, a slightly larger than the homogeneity range at 250 °C. The ternary phase $\text{Ag}_8\text{Se}_6\text{Sn}$ is almost a line compound with a

Fig. 6 Isothermal section of the Ag-Se-Sn experimental phase diagram at 400 °C with superimposed overall composition of two-phase samples (half-solid rectangle) and three-phase samples (solid triangle).

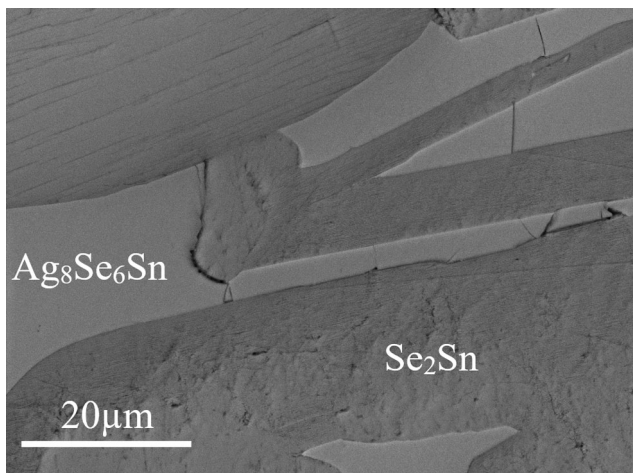
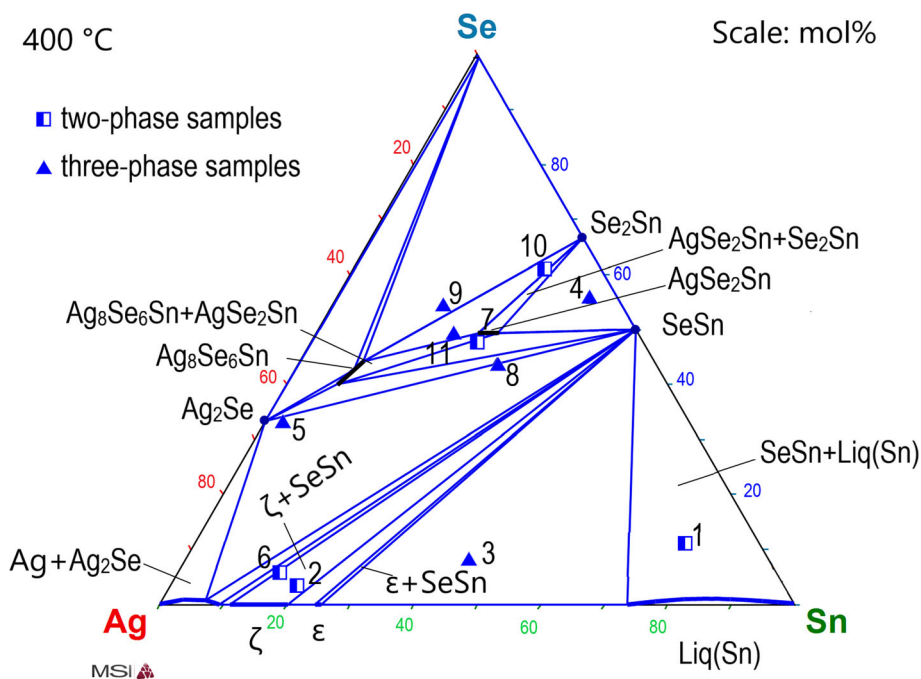


Fig. 7 Microstructure of the sample 400_10 in BSE mode, consisting of $Ag_8Se_6Sn + Se_2Sn$

homogeneity range between the approximate compositions $Ag_{52}Se_{40}Sn_8$ and $Ag_{45}Se_{45}Sn_{10}$ which is less pronounced than at 250 °C. Ramakrishnan et al.^[7] again proposed the Ag_8Se_6Sn phase without any solubility in whole temperature range of stability. Figures 7 and 8 show the micrographs containing Se-rich Ag_8Se_6Sn .

3.3 Isothermal Section at 550 °C

The proposed isothermal section of the experimental phase diagram Ag-Se-Sn at 550 °C is presented on Fig. 9. Like the sections at 250 and 400 °C two independent liquid

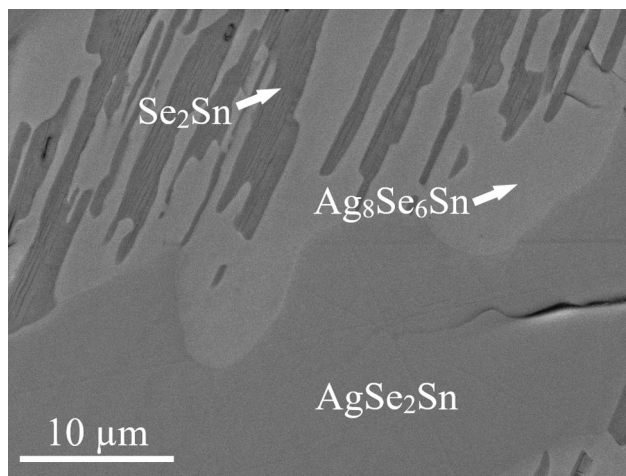


Fig. 8 Microstructure of the sample 400_11 in BSE mode, consisting of $AgSe_2Sn + Se_2Sn + Ag_8Se_6Sn$

phases, labeled as Liquid (Se) and Liquid (Sn) exist at this temperature. An additional liquid region was found in the central part of the phase diagram. Ramakrishnan et al.^[7] did not proposed this liquid phase at 550°C in their isothermal section but they had no samples and consequently experimental results in the Se-rich part of phase diagram. The existence of a stable liquid region is supported by our DTA measurements (see Table 3) and agrees well to the quasi-binary phase diagrams published by Yusibov et al.^[8]. They proposed the ternary eutectic point with a composition of $Ag_{28.5}Se_{52.5}Sn_{19}$ and the eutectic temperature equal to approximately 470 °C. Four binary phases, Ag_2Se , ζ_{Ag_4Sn} , $SeSn$ and Se_2Sn respectively are

Fig. 9 Isothermal section of the Ag–Se–Sn experimental phase diagram at 550 °C with superimposed overall composition of two-phase samples (half-solid rectangle) and three-phase samples (solid triangle).

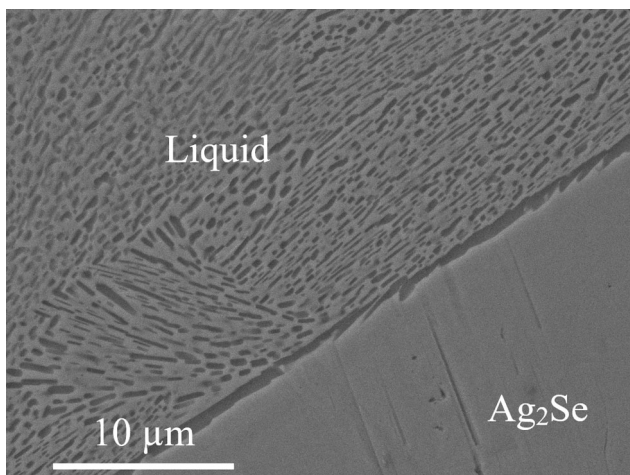
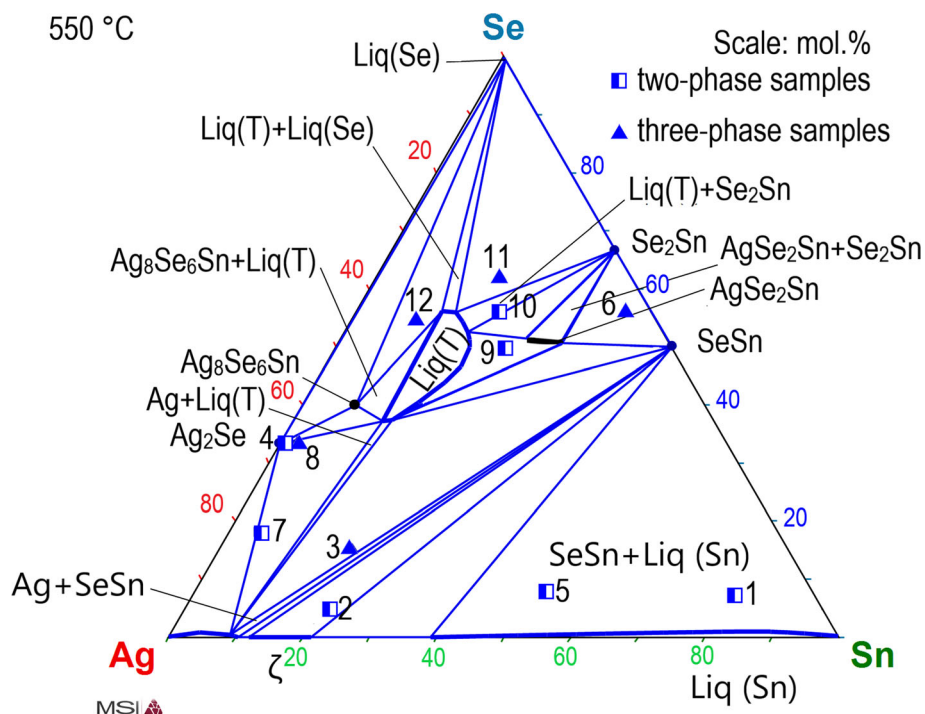


Fig. 10 Detail of the microstructure of the sample 550_8 in BSE mode consisting of phase $\text{Ag}_2\text{Se} + \text{Liq}(T)$

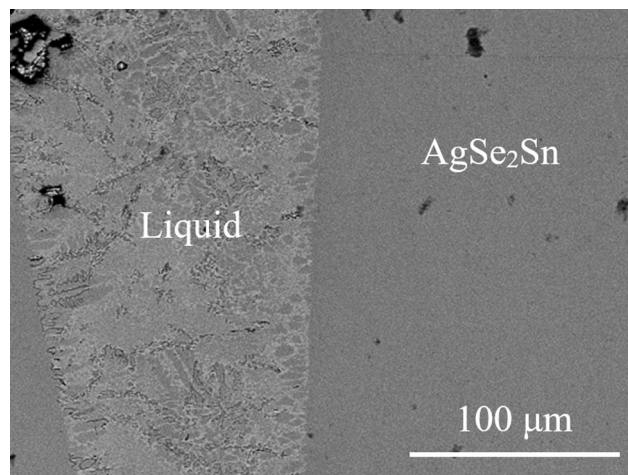


Fig. 11 Microstructure of the sample 550_13 in BSE mode consisting of $\text{AgSe}_2\text{Sn} + \text{Liq}(T)$

stable at 550 °C. These binary phases have almost no solubility of third elements in their structures. Two ternary phases, AgSe_2Sn and $\text{Ag}_8\text{Se}_6\text{Sn}$, are stable at 550 °C. AgSe_2Sn exists between $\text{Ag}_{22.2}\text{Se}_{49.6}\text{Sn}_{28.2}$ and $\text{Ag}_{15.8}\text{Se}_{50.7}\text{Sn}_{33.4}$. This homogeneity range is wider in comparison to lower temperatures. The ternary phase $\text{Ag}_8\text{Se}_6\text{Sn}$ is almost stoichiometric at 550 °C. Figures 10 and 11 show the micrographs containing the intermediate liquid region.

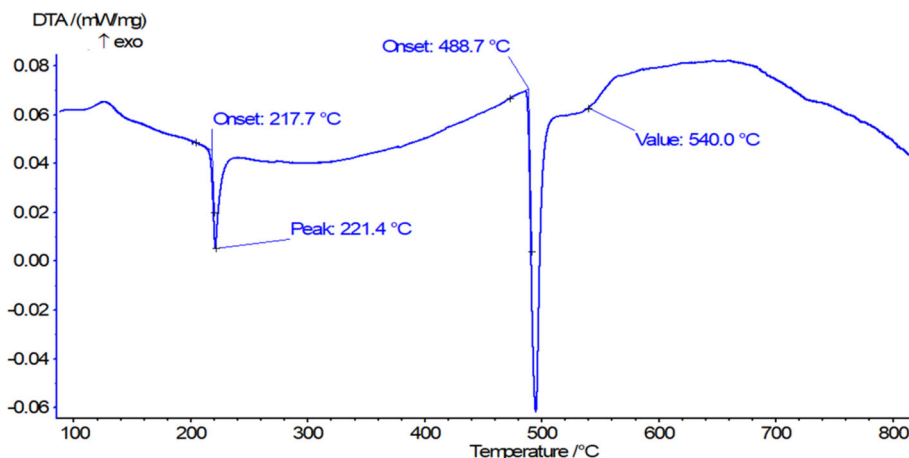
3.4 Thermal Analysis

Temperatures of phase transitions were studied experimentally by DTA in calorimeter for the simultaneous thermal analysis NETZSCH Pegasus 404 C. Measured part of sample was put in evacuated quartz glass DTA ampoule due to the possible of uncontrolled evaporation of selenium into the calorimeter. Measurement was done under an argon flow of 50 ml min^{-1} . Heating and cooling rates of each run were 5 °C min^{-1} . Three runs were performed for each sample; the thermal effects during the first heating run are listed in Table 5. Second and third heating runs did not

Table 5 Temperature of phase transitions measured by DTA

Nominal comp., at.%			Thermal effects (heating), °C			
Se	Ag	Sn	Liquidus	Solidus	Invariant transition	other transitions
6.7	38.7	54.7	762.4	756.7	219.8	474.0
2.5	72.7	24.8	758.0		660.9; 485.2	551.0; 135.7
3.6	73.8	22.6	678.0	661.0	551.5; 484.7; 131.5	
59.2	22.5	18.3		488.7	217.7, 80.6	540
7.3	34.9	57.8	785	766.4	550.0; 219.9	665.0; 468.0

Fig. 12 The 1st DTA heating curve of the 22.5Ag-59.2 at.%Se-Sn sample. Measurement conditions: sample was placed in sealed evacuated quartz-glass ampoule, measurement under inert atmosphere of 5N Ar 50 ml min⁻¹, heating rate 5 °C min⁻¹.



show any additional effect. Small differences between the first and subsequent heating and cooling curves are caused by changes in the shape of the sample following initial melting. Temperature of phase transition in solid phase was evaluated as onset of peak, liquidus was evaluated as a minimum of a peak. Results of the DTA 1st heating of the sample with composition 22.5Ag-59.2 at.%Se-Sn are presented in Fig. 12. Signals correspond to the temperature of the phase transitions: $\text{Ag}_8\text{SnSe}_6 + \text{SnSe}_2 + \text{Se} \rightarrow \text{Ag}_8\text{Se}_6\text{Sn} + \text{SnSe}_2 + \text{Liq}(\text{Se})$ (217.7 °C); $\text{Ag}_8\text{Se}_6\text{Sn} + \text{SnSe}_2 + \text{Liq}(\text{Se}) \rightarrow \text{SnSe}_2 + \text{Liq}(\text{Se}) + \text{Liq}(\text{T})$ (488.7 °C); $\text{SnSe}_2 + \text{Liq}(\text{Se}) + \text{Liq}(\text{T}) \rightarrow \text{SnSe} + \text{Liq}(\text{T})$ (540.0 °C). These temperatures correspond well to the results of DTA measurements published by Yusibov et al.^[8]. Composition of the samples was checked after DTA measurement to make certain that the sample did not react with the SiO_2 material of the ampoules and the extent of the evaporation of Se was found acceptable. Thermal analysis results are listed in Table 5.

4 Conclusions

Although the Ag-Se-Sn phase diagram was published recently, some of the complex phase equilibria were not well described. This work was designed to contribute to a better understanding of not clearly described parts of the

phase diagram that needed refinement. The experimental studies were carried out at temperatures 250, 400 and 550 °C. Isothermal sections of ternary phase diagram Ag-Se-Sn were obtained by a combination of standard methods: overall and phase compositions of samples were measured using SEM-EDX, the temperatures of phase transitions by DTA measurements in evacuated quartz-glass DTA ampoules. The crystal structures were identified by XRD. Huge solubility of selenium in the ternary intermetallic phase $\text{Ag}_8\text{Se}_6\text{Sn}$ was observed at 250 °C [$x(\text{Se}) = 0.399\text{--}0.536$]. Its solubility at 400 °C is much lower [$x(\text{Se}) = 0.40\text{--}0.442$] than at 250 °C and finally the $\text{Ag}_8\text{Se}_6\text{Sn}$ phase seems to be almost stoichiometric and close to complete melting [$x(\text{Se}) = 0.40$] at 550 °C. The ternary phase AgSe_2Sn exhibits an extending region of stability with increasing temperature. It contains constant content of Se (within experimental errors) and variable content of Sn and Ag $x(\text{Sn}) = 0.268\text{--}0.283$ at 250 °C and $x = 0.284\text{--}0.334$ for 550 °C. The polymorphic phase transition between $\text{Ag}_8\text{Se}_6\text{Sn}$ and $\text{Ag}_8\text{Se}_6\text{Sn}_{\text{It}}$ does not happen at the proposed temperature. Only the low-temperature modification of the ternary phase $\text{Ag}_8\text{Se}_6\text{Sn}$ ($Pmn2_1$) was found in whole studied temperature range.

Intermediate liquid region was found at 550 °C in contrast to the recently published isothermal sections of phase diagram at 550 °C in Ramakrishnan et al.^[7]. Nevertheless, this result agrees well with the previously

published liquidus surface and vertical sections in Yusibov et al.^[8] and Ollitrault-Fitchet et al.^[14].

Funding This study was funded by Czech Science Foundation of Czech Republic (Grant Number GA 18-25660J). Authors would like to thank Pavla Roupčova from the Institute of Physics of Materials CAS for the technical help with analysis.

Conflict of interest The authors declare that they have no conflict of interest.

References

1. A. Tubtimtae, M.-W. Lee, and G.-J. Wang, Ag₂Se Quantum-Dot Sensitized Solar Cells for Full Solar Spectrum Light Harvesting, *J. Power Sources*, 2011, **196**, p 6603–6608.
2. W. Mi, P. Qiu, T. Zhang, Y. Lv, X. Shi, and L. Chen, Thermoelectric Transport of Se Rich Ag₂Se in Normal Phases and Phase Transitions, *Appl. Phys. Lett.*, 2014, **104**, p 133903.
3. W. Shi, M. Gao, J. Wei, J. Gao, C. Fan, E. Ashalley, H. Li, and Z. Wang, Tin Selenide (SnSe): Growth, Properties, and Applications, *Adv. Sci.*, 2018, **5**, p 1–22.
4. Y. Wu, W. Li, A. Faghaninia, Z. Chen, J. Li, X. Zhang, B. Gao, S. Lin, B. Zhou, A. Jain, and Y. Pei, Promising Thermoelectric Performance in Van Der Waals Layered SnSe₂, *Mater. Today Phys.*, 2017, **3**, p 127–136.
5. W. Li, S. Lin, B. Ge, J. Yang, W. Zhang, and Y. Pei, Low Sound Velocity Contributing to the High Thermoelectric Performance of Ag₈SnSe₆, *Adv. Sci.*, 2016, **3**, p 1600196.
6. L. Li, Y. Liu, J. Dai, A. Hong, M. Zeng, Z. Yan, J. Xu, D. Zhang, D. Shan, S. Liu, Z. Ren, and J.-M. Liu, High Thermoelectric Performance of Superionic Argyrodite Compound Ag₈SnSe₆, *J. Mater. Chem. C*, 2016, **4**, p 5806–5813.
7. A. Ramakrishnan, S.W. Chen, and Y. Hutabalian, Ag-Se-Sn phase diagrams and Sn/Ag₂Se interfacial reactions, *J. Alloys Compd.*, 2020, **816**, p 152670.
8. Y.A. Yusibov, I.D. Alverdiev, L.F. Mashadieva, D.M. Babanly, A.N. Mamedov, and M.B. Babanly, Experimental Study and 3D Modeling of the Phase Diagram of the Ag-Sn-Se System, *Zh. Neorg. Khim.*, 2018, **63**(12), p 1607–1621.
9. O. Gorochov, R. Fitchet, and J. Flahaut, Diagramme de Phase et Proprietes du Systeme Ag₂Se–SnSe₂, *C. R. Acad. Sci.*, 1966, **263**, p 1422–1424.
10. L. I. Berger and V. D. Prochukhan, Ternary Diamond- Like Semiconductors Metallurgiya, Moscow, 1968.
11. O. Gorochov, C. R. Acad. Sci. 266 (1968) 1060
12. O. Gorochov, Les composés Ag₈MX₆ (M = Si, Ge, Sn et X = S, Se, Te), *Bull. Soc. Chim. Fr.*, 1968, **264**, p 2263–2275.
13. K. Dovletov, S. N. Krzhivitskaya, and K. Tashliev, Izv. Tashliev, Fazovaya diagramma Ag₂Se–SnSe, AN Turkm. SSR Ser. Fiz.-Tekh. Khim.-Geol. Nauk I (1974) 117.
14. R. Ollitrault-Fitchet, J. Rivet, and J. Flahaut, Description du systeme ternaire Ag-Sn-Se, *J. Less- Common Met.*, 1988, **138**, p 241.
15. V.M. Moroz, A.I. Shchurok, O.G. Mikolaichuk, M.V. Byalyk, V.F. Orlenko, D.I. Oleksyn, and M.B. Moroz, System Ag-Sn-Se. Structure of the T-x spacem Fiz, *Khim. Tverd. Tila*, 2003, **4**(3), p 532–535.
16. M. Pirela, A. Velásquez-Velásquez, M. Villareal, B.J. Fernandez, L. Vivas, G. Sanchez Perez, Rev. Mex. Fis. 53 (2007) 262–264.
17. D.C. Johnston, and H. Adrian, Superconducting and Normal State Properties of Ag(1 – x)Sn(1 + x)Se(2 – y), *J. Phys. Chem. Solids*, 1977, **38**, p 355–365.
18. A. Wold, and R. Brec, Structure NaCl des Phases Ag_x Sn_{1–x} X (X = S, Se, Te), *Mater. Res. Bull.*, 1976, **11**, p 761–766.
19. L.D. Gulay, I.D. Olekseyuk, and O.V. Parasyuk, Crystal Structure of β-Ag₈SnSe₆, *J. Alloys Compd.*, 2002, **339**(1–2), p 113–117.
20. M.B. Babanly, and Yu.A. Yusibov, *Electrochemical Methods in Thermodynamics of Inorganic System*. Bakin. Gos. Univ, Baku, 2011.
21. M.V. Moroz, and M.V. Prokhorenko, Measurement of the Thermodynamic Properties of Saturated Solid Solutions of Compounds in the Ag-Sn-Se System by the EMF Method, *Russ. J. Phys. Chem. A*, 2015, **89c**, p 1325–1329.
22. M.V. Moroz, M.V. Prokhorenko, PYu. Demchenko, and O.V. Reshetnyak, Thermodynamic Properties of Saturated Solid Solutions of Ag₇SnSe₅Br and Ag₈SnSe₆ Compounds in the Ag–Sn–Se–Br System Measured by the EMF Method, *J. Chem. Thermodyn.*, 2017, **106**, p 228–231.
23. J. Spreadborough, and J.W. Christian, High-Temperature X-ray Diffractometer, *J. Sci. Instrum.*, 1959, **36**, p 116–118.
24. P. Cherin, and P. Unger, The Crystal Structure of Trigonal Selenium, *Inorg. Chem.*, 1967, **6**(8), p 1589–1591.
25. J.A. Lee, and G.V. Raynor, The Lattice Spacings of Binary Tin-Rich Alloys, *Proc. Phys. Soc.*, 1954, **67**, p 737–747.
26. J. Thewlis, and A.R. Davey, Thermal Expansion of Grey Tin, *Nature (London)*, 1954, **174**, p 1011.
27. P. Rahlfs, Zeitschrift fuer Physikalische Chemie, Abteilung B: Chemie der Elementarprozesse, Aufbau der Materie, 1936, **31**, p 157–194.
28. G.A. Wiegers, The Crystal Structure of the Low-Temperature Form of Silver Selenide, *Am. Miner.*, 1971, **56**, p 1882–1888.
29. H.W. King, and T.B. Massalski, Lattice spacing relationships and the electronic structure of h.c.p. zeta-phases based on silver, *Philos. Mag.*, 1956, **8**, p 669–682.
30. C.W. Fairhurst, and J.B. Cohen, The Crystal Structure of Two Compounds Found in Dental Amalgam: Ag₂H and Ag₃Sn, *Acta Crystallogr. B*, 1972, **28**, p 371–378.
31. H.G. von Schnering, and H. Wiedemeier, The High Temperature Structure of beta-Sn S and beta-Sn Se and the B16-to-B33 Type Lambda-Transition Path, *Z. Kristallogr.*, 1981, **156**, p 143–150.
32. A.S. Avilov, R.M. Imamov, and S.N. Navasardyan, Structure of Thin Films of SnS and SnSe, *Kristallografiya*, 1979, **24**, p 874–875.
33. M.I. Karakhanova, A.S. Pashinkin, and A.V. Novoselova, *Inorg. Mater.*, 1966, **2**(7), p 1012–1014.

Publisher's Note Springer Nature remains neutral with regard to jurisdictional claims in published maps and institutional affiliations.

6.8 Paper 8

- [P8] **Zobač, O.**, Zemanová, A., Chen, S.W., Kroupa, A., *CALPHAD-type assessment of the Pb-Se-Sn system*, Journal of Phase Equilibria and Diffusion., 2022, 43, pp. 243-255, doi: 10.1007/s11669-022-00956-7 (IF 1.4)



CALPHAD-Type Assessment of the Pb-Se-Sn System

Ondrej Zobac¹ · Adela Zemanova¹ · Sinn-Wen Chen^{2,3} · Ales Kroupa¹

Submitted: 25 January 2022 / in revised form: 27 March 2022 / Accepted: 31 March 2022 / Published online: 11 May 2022
© ASM International 2022

Abstract CALPHAD-type theoretical assessment of the Pb-Se-Sn system was carried out. This assessment is part of a larger project aimed at developing an Ag-Pb-Se-Sn-Te thermodynamic database which should serve for the development of materials for thermoelectric applications. The experimental results from the literature were used but they are quite sparse and significant inconsistencies have been found between experimental data published by various authors, especially in the Se-rich regions. In general, a reasonable agreement was obtained for the theoretical and experimental sections of the phase diagram and for the enthalpies of mixing of the liquid phase in the region with low selenium content, but the agreement is rather qualitative in the Se-rich region.

Keywords CALPHAD · critical reassessment · Pb-Se-Sn phase diagram · ternary liquid phase

1 Introduction and Literature Review

Phase diagrams of thermodynamic systems are a crucial tool for the description as well as understanding of behavior and properties of both simple and

multicomponent systems. As such they are important for the development of new advanced materials and possible prediction of their materials properties. Detailed knowledge about the coexistence and stability of phases in stable or metastable equilibrium significantly rationalizes the design and preparation of complex materials with desired properties. Because experimental studies of multicomponent phase diagrams are very time consuming, and the extent of experimental work can be overwhelming, theoretical modelling of multicomponent phase diagrams is a very useful tool for materials development.

Interest in Se-based alloys has recently been renewed due to their possible importance in thermoelectric applications.^[1–5] The Pb-Se-Sn ternary system has been studied since the 1960s but there are still significant discrepancies in the results from different authors. A more detailed literature review is given below.

Wolley and Berolo^[6] proposed a pseudobinary section PbSe-SeSn in their paper based on x-ray powder analysis. Strauss^[7] experimentally studied the PbSe-SeSn section in the higher temperature range 700–1100 °C by thermal analysis and directly from as-cast samples (directly frozen ingots). Dal Corso et al.^[8] pointed to inconsistencies in previous works and published vertical sections PbSe-SnSe and PbSe-SnSe₂ respectively in the whole temperature range based on a combination of previous experimental results from thermal analysis (DTA, DSC), microstructural observations and their own experimental results. They proposed stabilization of the phase SeSn- β (high-temperature polymorph of SnSe intermetallic phase) to a lower temperature (approx. 425 °C) in the presence of lead and suggested significant solubilities of third elements in both PbSe and the SnSe family of intermetallic phases.

The experimental Pb-Se-Sn phase diagram has been published recently by Chen et al.,^[3] namely isothermal

✉ Ondrej Zobac
zobac@ipm.cz

¹ Institute of Physics of Materials, Czech Academy of Sciences, Zizkova 22, Brno, Czech Republic

² Department of Chemical Engineering, National Tsing Hua University, Hsinchu 300, Taiwan

³ High Entropy Materials Center, National Tsing Hua University, Hsinchu 300, Taiwan

sections for 350 and 500 °C. They did not observe any ternary phase in this system. The huge solubility of the third element was also observed in this work in the binary intermetallic phases PbSe and SeSn at the temperatures 350 and 500 °C in agreement with the work of Dal Corso et al.^[8] Chen et al.^[3] identified one polymorph of the binary intermetallic phase SeSn at both studied temperatures, probably low temperature SeSn- α . Nevertheless, this finding does not contradict the previous result of Dal Corso et al.^[8] Only two samples have been studied in the region where the phase change should appear, and it is not easy to distinguish between the two phases.

Partial liquidus surface was studied by Zlomanov et al.^[9] and the liquidus surface in the whole concentration range was presented by Saveliev et al.^[10] Experimentally measured enthalpies of mixing in liquid at 763, 845 and 970 °C were published by Kotchi et al.^[11]

An attempt to theoretically model a part of the Pb-Se-Sn phase diagram was made by Laugier et al.^[12] who applied a regular associated solution model to calculate the T-x ternary liquid-solid phase equilibrium of the PbSe-SnSe section of the phase diagram and the liquid surface of the Pb-Se-Sn system. Good agreement with experiments was obtained for the liquid-solid equilibrium between liquid and PbSe intermetallic phase with rocksalt structure. Full thermodynamic CALPHAD-based assessment of the ternary phase diagram has not yet been published up to now.

The phases existing in the Pb-Se-Sn system together with their crystallographic structures are listed in the Table 1.

2 Thermodynamic Modelling

The CALPHAD approach^[14,15] was used for thermodynamic modelling and calculation of phase diagrams. The compositions of phases in equilibrium correspond to the minimum total Gibbs energy of a closed system at constant temperature and pressure. Calculations were performed

using Thermo-Calc^[16] and Pandat^[17] software, which solve the constrained minimization problem to determine the set of non-negative number of individual components in equilibrium phases. The Gibbs energies are considered relative to the Standard Element Reference state (SER). The Gibbs energy data for pure elements were taken from the SGTE database for pure elements ver. 5.0.^[18]

2.1 The Solution Phases

The Gibbs energies of terminal solid solutions were mostly modelled using a substitutional model with one sublattice.

The substitutional solution model with associates was used for the thermodynamic description of the molar Gibbs energy of the liquid phase. It assumes mutual mixing of three elements Pb, Se, Sn and two associates PbSe and SeSn (in agreement with the models for liquid in the respective binary subsystems)

The molar Gibbs energy of the solution phase α is expressed as:

$$G_m^\alpha(T, x^\alpha) = {}^0 G_m^\alpha(T) + {}^{id} G_m^\alpha(T, x^\alpha) + {}^E G_m^\alpha(T, x^\alpha) \quad (\text{Eq 1})$$

where the first term is the molar reference Gibbs energy, which is the weighted sum of the Gibbs energies of the system constituents i in the crystallographic structure of the phase α or in the liquid state relative to the selected reference state.

The second term of Eq 1 is the contribution to the total Gibbs energy resulting from the ideal mixing of the constituents in the crystal lattice of the phase α or in the liquid, where n is the number of constituents Eq 2.

$${}^{id} G_m^\alpha = RT \sum_{i=1}^n x_i \cdot \ln(x_i) \quad (\text{Eq 2})$$

Third term, the excess Gibbs energy ${}^E G_m^\alpha$, describes the influence of the non-ideal behaviour of the system on the thermodynamic properties of the phase and is given by the Redlich-Kister-Muggianu formalism.^[19,20]

Table 1 The crystallographic structure of phases existing in the system

Common phase name	Phase name in database	Pearson symbol	Structure type	Ref.
(Pb)	FCC_A1	cF4	Pb	Ref 22
(Se)	HEX_A8	hP3	Se	Ref 13
(β Sn)	BCT_A5	tI4	β Sn	Ref 13
(α Sn)	DIAMOND_A4	cF8	C(diamond)	Ref 13
PbSe	PBSE	cF8	NaCl	Ref 22
Se ₂ Sn	SE2SN	hP3	CdI ₂	Ref 13
SeSn- α	SESN_ALPHA	oP8	GeS	Ref 13
SeSn- β	SESN_BETA	oC8	CrB	Ref 13

$$\begin{aligned}
 E G_m^\alpha = & \sum_{\substack{i,j=1 \\ i \neq j}}^n x_i x_j \sum_{z=0}^m {}^z L_{i,j} (x_i - x_j) + \sum_1^{n-2} \sum_{j=i+1}^{n-1} \sum_{k=j+1}^n x_i \cdot x_j \\
 & \cdot x_k \cdot L_{i,j,k}
 \end{aligned}
 \tag{Eq 3}$$

where ${}^z L_{i,j}$ are the temperature dependent binary interaction parameters describing the mutual interaction between constituent i and j , and $L_{i,j,k}$ is the interaction parameter describing the possible ternary interactions. Their temperature dependence is usually defined as:

$$L(T) = a + bT + cT \ln(T) \tag{Eq 4}$$

The substitutional solid solution phases of the elements β -Sn (bct_A5), α -Sn (diamond_A4) and Se (hexagonal_A8) were modelled by solid solution model described above. With respect to very low solubilities of other elements (especially Se) in the terminal solid solutions, the substitutional solid solution model for (β -Sn) was defined as (PB, SN)1 and no solubility of other elements were assumed for (α -Sn) and (Se).

The substitutional model with associates for liquid used in the database is labelled LIQUID and defined as (PB, PBSE, SE, SN, SNSE)1.

The Pb (fcc_A1) terminal solid solution was modelled by two-sublattice interstitial solid solution model. This model assumed that the metallic elements could substitute each other in the metal sublattice, and interstitial elements and vacancies exist in the interstitial sublattice. Because there are no interstitial elements in this system, the model corresponds from the practical point of view to the above shown substitutional model, nevertheless this model is selected to be consistent with other databases containing the fcc_A1 phase. The specific model for the solid solution fcc_A1 (Pb) in the database was therefore named FCC_A1 and defined as (PB,SN)1(VA)1.

2.2 Intermetallic Phases

The Pb-Se-Sn ternary system contains 4 intermetallic phases (PbSe, SeSn- α , SeSn- β , Se2Sn), which are stoichiometric in binary systems but exhibit the solubility of the third element in their structures in the ternary system. The Compound Energy Formalism is used to model intermetallic phases. Basic principles for the case of two sublattices are shown here, as two-sublattice models were used in this assessment. Details of this approach can be found e.g. in Ref 14,15

In the case of the PbSe phase each sublattice is occupied by one basic element and Sn substitutes Pb in the relevant

sublattice ((PB, SN)1(SE)1). The name of the phase is PBSE in the database. Similarly, Pb substitutes Sn in the SeSn family of phases and the Se2Sn phase ((SE)0.5(PB, SN)0.5 and (SE)0.66667(PB, SN)0.33333, respectively). The names of the phases are SESN_ALPHA, SESN_BETA and SE2SN in the database.

The reference Gibbs energy corresponding to the Eq 1 for constituents i and j is given as:

$$G_{ref}^\alpha = \sum y_i \cdot {}^2 y_j \cdot {}^0 G_{(ij)} \tag{Eq 5}$$

where the y_i terms are the site fractions of each constituent in the sublattice 1 or 2. The term $G(i;j)$ describes the Gibbs energy of formation of the so-called “end member” ij .

The ideal mixing term is given by

$$G_{id}^\alpha = \sum_{p=1}^2 f_p \cdot \sum_{i=1}^n {}^p y_i \cdot \ln({}^p y_i) \tag{Eq 6}$$

where f_p is the stoichiometric coefficient for a sublattice p and the second sum describes the effect of the ideal mixing within the sublattice p . The contribution of the excess Gibbs energy for the two-sublattice model with three constituents i, j, k is defined as:

$$G_E^\alpha = \sum {}^1 y_i \cdot {}^1 y_j \cdot {}^2 y_k L_{(i,j,k)} + \sum {}^1 y_i \cdot {}^2 y_k \cdot {}^2 y_l L_{(i,k,l)} \tag{Eq 7}$$

where

$$L_{(i,j,k)} = \sum_z {}^z L_{(i,j,k)} \cdot (y_i - y_j)^z \tag{Eq 8}$$

The parameters ${}^z L_{i,j;k}$ describe the mutual interaction of constituents i and j in the first sublattice when the second sublattice is fully occupied by constituent k . This description can be extended to any number of sublattices.

The individual models of intermetallic phases are listed in the Table 2. The two-sublattice model is used for all phases.

2.3 Binary Systems

Binary data of constituting subsystems are necessary for modelling the ternary system and they are used for ternary extrapolation of the Pb-Se-Sn system. The prediction provides us with basic knowledge about the phase equilibria in the system but cannot provide information about the solubility of the third element in the binary phases or the existence of a possible ternary phase. Thermodynamic descriptions of binary subsystems are known and accepted from the literature.

Se-Sn binary phase diagram was published by Feute-lais et al.^[21] It contains a family of intermetallic phases

Table 2 Thermodynamic parameters for optimized phases in the Pb-Se-Sn ternary system and binary subsystems

Phase name (Sublattice model)	Parameter	Value	Ref.
LIQUID (PB,PBSE,SE,SESN,SN)	${}^0G_{\text{PbSe}}^{\text{LIQ}}$	$-91032.45 + 29.88*T + G_{\text{Pb}}^{\text{LIQ}} + G_{\text{Se}}^{\text{LIQ}}$	Ref 22
	${}^0G_{\text{SnSe}}^{\text{LIQ}}$	$-134591.86 + 278.59972*T - 32.99*T*\ln(T) + G_{\text{Pb}}^{\text{LIQ}} + G_{\text{Se}}^{\text{LIQ}}$	Ref 21
	${}^0L_{\text{Pb,Sn}}^{\text{LIQ}}$	$+6204.5 - 0.67981*T$	Ref 23
	${}^1L_{\text{Pb,Sn}}^{\text{LIQ}}$	$+791.7 - 1.5219*T$	Ref 23
	${}^0L_{\text{Pb,PbSe}}^{\text{LIQ}}$	$+19500.32$	Ref 22
	${}^1L_{\text{Pb,PbSe}}^{\text{LIQ}}$	$-1003.26 + 0.58*T$	Ref 22
	${}^2L_{\text{Pb,PbSe}}^{\text{LIQ}}$	$+8352.21 - 5.64*T$	Ref 22
	${}^0L_{\text{PbSe,Se}}^{\text{LIQ}}$	$+17503.24 - 7.95*T$	Ref 22
	${}^1L_{\text{PbSe,Se}}^{\text{LIQ}}$	$+4201.24 - 6.42*T$	*
	${}^2L_{\text{PbSe,Se}}^{\text{LIQ}}$	$+16498.24 - 3.61*T$	Ref 22
	${}^0L_{\text{Se,SnSe}}^{\text{LIQ}}$	$+15432.8 - 19.06391*T$	Ref 22
	${}^1L_{\text{Se,SnSe}}^{\text{LIQ}}$	$+8995.55$	Ref 21
	${}^0L_{\text{Sn,SnSe}}^{\text{LIQ}}$	$+43462.43 - 21.6074*T$	Ref 21
	${}^1L_{\text{Sn,SnSe}}^{\text{LIQ}}$	-1032.5	Ref 21
	${}^0L_{\text{PbSe,Se,SnSe}}^{\text{LIQ}}$	$+1.916923E + 05 - 307.69*T$	*
	${}^1L_{\text{PbSe,Se,SnSe}}^{\text{LIQ}}$	$-1.079120E+06+420.5*T$	*
	${}^2L_{\text{PbSe,Se,SnSe}}^{\text{LIQ}}$	$-3.032750E + 05 + 175*T$	*
	${}^0L_{\text{Pb,PbSe,SnSe}}^{\text{LIQ}}$	-80000	*
	${}^1L_{\text{Pb,PbSe,SnSe}}^{\text{LIQ}}$	$-80000 - 30*T$	*
	${}^2L_{\text{Pb,PbSe,SnSe}}^{\text{LIQ}}$	0	*
	${}^0L_{\text{PbSe,SnSe}}^{\text{LIQ}}$	$-0.208615E + 04 - 33.8461*T$	*
	${}^1L_{\text{PbSe,SnSe}}^{\text{LIQ}}$	$-30.584615E + 03 + 15.3846*T$	*
	${}^2L_{\text{PbSe,SnSe}}^{\text{LIQ}}$	$+1.041846E + 04 - 21.5385*T$	*
	${}^0L_{\text{Pb,SnSe}}^{\text{LIQ}}$	$-1207.69 - 7.692*T$	*
	${}^1L_{\text{Pb,SnSe}}^{\text{LIQ}}$	0	*
	${}^2L_{\text{Pb,SnSe}}^{\text{LIQ}}$	0	*
BCT_A5 (Sn-β) (PB,SN)	${}^0L_{\text{Pb,Sn}}^{\text{BCT}_A}$	$+19700 - 15.89*T$	Ref 23
DIAMOND_A4(Sn-α) (SN) ₁	$G_{\text{Sn}}^{\text{DIA}_A4}$	$G_{\text{Sn}}^{\text{DIA}_A4}$	Ref 18
FCC_A1 (Pb) (PB,SN) ₁ (VA) ₁	${}^0L_{\text{Pb,Sn:Va}}^{\text{FCC}_A1}$	$+7145.3 - 2.30237*T$	Ref 23
HEX_A8 (Se) (SE) ₁	$G_{\text{Se}}^{\text{HEX}_A8}$	$G_{\text{Se}}^{\text{HEX}_A8}$	Ref 18
PBSE (PbSe) (PB,SN) ₁ (SE) ₁	${}^0G_{\text{PbSe}}^{\text{PbSe}}$	$-99783.25 + 22.52*T + G_{\text{Pb}}^{\text{HSER}} + G_{\text{Se}}^{\text{HSER}}$	*
	${}^0G_{\text{Sn:Se}}^{\text{PbSe}}$	$+5000 + G_{\text{Sn}}^{\text{HSER}} + G_{\text{Se}}^{\text{HSER}}$	*
	${}^0L_{\text{Pb,Sn:Se}}^{\text{PbSe}}$	$-3.125758E + 05 + 68.34*T$	*
	${}^1L_{\text{Pb,Sn:Se}}^{\text{PbSe}}$	$-92000 + 92*T$	*
	${}^2L_{\text{Pb,Sn:Se}}^{\text{PbSe}}$	$-10000 + 15*T$	*
SE2SN (Se ₂ Sn) (SE) _{0.66667} (PB,SN) _{0.33333}	${}^0G_{\text{Se:Sn}}^{\text{Se2Sn}}$	$-46104.05 + 121.16205*T$ $-24.84*T*\ln(T) - 0.00164*T^2 + 39347*T^{-1} + 1.185733E - 07*T^3$	Ref 21
	${}^0G_{\text{Se:Pb}}^{\text{Se2Sn}}$	$0.66667*G_{\text{Se}}^{\text{HSER}} + 0.33333*G_{\text{Pb}}^{\text{HSER}} + 15000$	*
	${}^0G_{\text{Se:Pb,Sn}}^{\text{Se2Sn}}$	-60000	*
SESN_ALPHA (SeSn-α) (SE) _{0.5} (PB,SN) _{0.5}	${}^0G_{\text{Se:Sn}}^{\text{SeSn_alpha}}$	$-63171.87 + 134.4964*T - 26.31*T*\ln(T) - .00182* T^2 + 61422.5* T^{-1} + 1.1076E - 07* T^3$	Ref 21
	${}^0G_{\text{Se:Pb}}^{\text{SeSn_alpha}}$	$+15000 + 0.5*G_{\text{Se}}^{\text{HSER}} + 0.5*G_{\text{Pb}}^{\text{HSER}}$	*
	${}^0L_{\text{Se:Pb,Sn}}^{\text{SeSn_alpha}}$	$-171000+65*T$	*
	${}^1L_{\text{Se:Pb,Sn}}^{\text{SeSn_alpha}}$	$-40000 - 10*T$	*
	${}^2L_{\text{Se:Pb,Sn}}^{\text{SeSn_alpha}}$	$-88850+50*T$	*
SESN_BETA (SeSn-β) (SE) _{0.5} (PB,SN) _{0.5}	${}^0G_{\text{Se:Sn}}^{\text{SeSn_beta}}$	$-62529.58 + 133.69002*T - 26.31*T*\ln(T) - .00182* T^2 + 61422.5* T^{-1} + 1.1076E - 07* T^3$	Ref 21
	${}^0G_{\text{Se:Pb}}^{\text{SeSn_beta}}$	$+15000 + 0.5*G_{\text{Se}}^{\text{HSER}} + 0.5*G_{\text{Pb}}^{\text{HSER}}$	*
	${}^0L_{\text{Se:Pb,Sn}}^{\text{SeSn_beta}}$	$-171284 + 65*T$	*

Table 2 continued

Phase name (Sublattice model)	Parameter	Value	Ref.
	${}^1L_{\text{SeSn}_{\beta}\text{Se:Pb,Sn}}$	$-40000 - 9.8 * T$	*
	${}^2L_{\text{SeSn}_{\beta}\text{Se:Pb,Sn}}$	$-88850 + 50 * T$	*

Unary data are from SGTE database^[18]

*Parameter assessed in this work

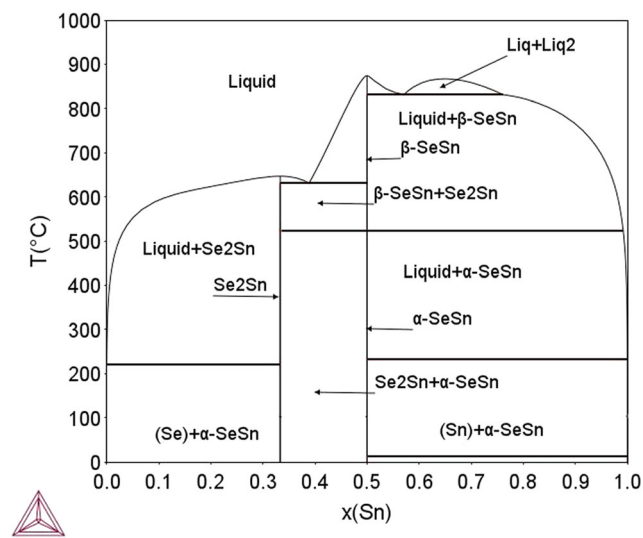


Fig. 1 The Se-Sn phase diagram calculated using the data of Feutalais et al.^[21]

SeSn, low-temperature SeSn- α and high-temperature SeSn- β modification. There is also Se2Sn intermetallic phase in the system. All three phases are modelled as stoichiometric. The liquid phase contains the SNSE associate. In the Sn-rich region, there is a small miscibility gap in liquid.

Thermodynamic assessment of the Pb-Se system was published by Liu et al.^[22] The assessment was slightly modified in the scope of this work, as there was a slight disagreement between the invariant temperature for the $L1 \rightarrow PbSe + L2$ published in Ref 22 and obtained by calculation using original dataset from the same work. The reason for this discrepancy might be caused by a typographical error. There is one intermetallic phase PbSe in the system and the liquid phase model includes the PBSE associate. The Pb-Se phase diagram also exhibits a liquid miscibility gap in the Se-rich region.

ALPHAD modelling of the Pb-Sn binary subsystem is adopted from Ohtani et al.^[23] This phase diagram is of simple eutectic type.

The calculated phase diagrams of the binary subsystems are shown in Fig. 1, 2 and 3. The thermodynamic parameters and models of the existing phases for all binary subsystems are summarized in Table 2.

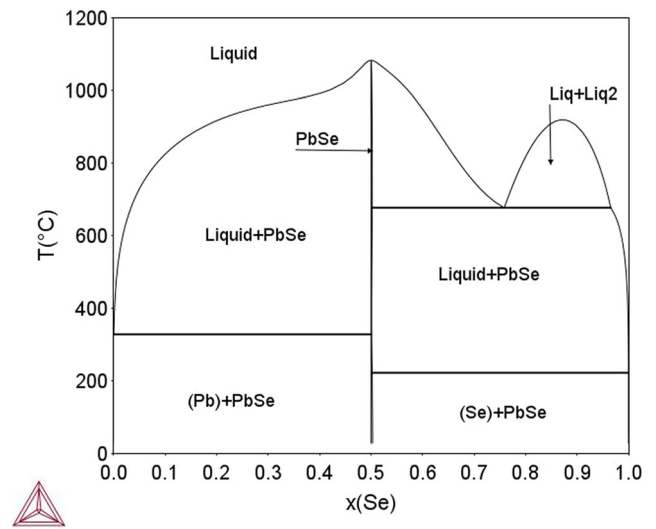


Fig. 2 The Pb-Se phase diagram calculated using the data of Liu et al.^[22]

3 Theoretical Results

The thermodynamic assessment of the ternary system was carried out using the Thermo-Calc and Pandat software packages. The above-mentioned binary assessments were used together with the experimental phase data from Ref 3,8 and 10. Experimentally measured enthalpies of mixing of liquid presented in Ref 11 were also used. As already mentioned in the Introduction, there are significant inconsistencies between the experimental data, and therefore not all data in the literature were accepted in the assessment. A more detailed discussion can be found in the relevant part of Sect. 4 (Discussion). The thermodynamic parameters for the ternary system assessed in this work and the parameters for the binary subsystems are listed in Table 2.

Two isothermal sections at 350 and 500 °C were presented in Ref 3 and a quasi-binary PbSe-SnSe section was established in Ref 8. The PbSe-Se2Sn vertical section was also studied in Ref 8 however, there is very strong inconsistency between the phase equilibria in this vertical section and the relevant phase equilibria in the isothermal sections from Ref 3. The results from Ref 3 were used for the assessment because there is a good consistency between the two experimental isothermal sections and the results obtained after long-term annealing are supported by

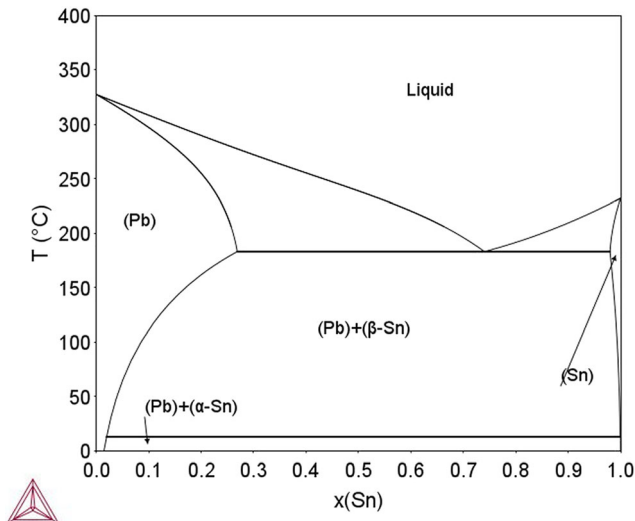


Fig. 3 The Pb-Sn phase diagram calculated using the data from Ohtani et al.^[23]

micrographs, x-ray analysis and EDX composition measurements. The quasi-binary section from Ref 8 was also used as it is consistent with results from Strauss^[7]. These sections of phase diagrams are shown in Fig. 4, 5 and 6.

In the following text, the Se-rich liquid phase is referred to as Liquid(Se), the (Pb,Sn)-rich liquid is designated as Liquid(Pb), and the liquid phase with content of about 10 at.% Pb and 10–20 at.% Sn is labelled as Liquid(ter).

The thermodynamic properties of the Pb-Se-Sn system were studied in Ref 11. The authors measured the enthalpies of mixing of liquid in the system at 763, 845 and 970 °C for different x_{Pb}/x_{Sn} and x_{Se}/x_{Pb} ratios. Unfortunately, they did not publish all the obtained experimental data, they only presented the results for selected sections with different concentration ratios and temperatures in the form of tables and figures. The comparison of the experimental results with the calculated enthalpies of mixing was performed for characteristic sections and the results are presented in Fig. 7, 8, 9, 10, 11, 12, 13 and 14.

The complete liquidus surface of the Pb-Se-Sn system was presented in Ref 10. Unfortunately, this paper is very concise, and no details are published in the paper. The authors did not provide any information on the experimental condition other than that the DTA method was used. No sample compositions and other necessary data are available. On the other hand, the liquidus surface looks reasonable for most of the concentration regions. The calculated and experimentally established liquidus surfaces are shown in Fig. 15(a), (b) and (c).

Invariant reactions containing liquid phases existing in the Pb-Se-Sn system are listed in the Table 3.

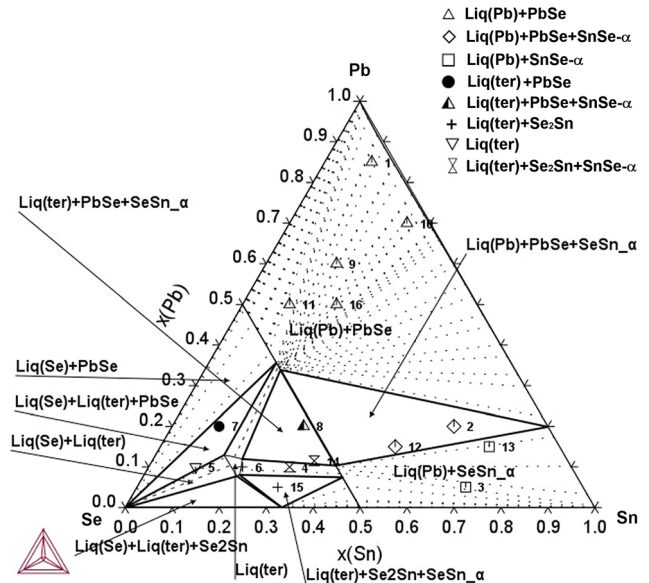


Fig. 4 Isothermal section of phase diagram Pb-Se-Sn at 350 °C with superimposed experimental data from Ref 3. The legend describes experimental equilibria. The numbers of samples correspond to the samples listed in Table 1 in Ref 3.

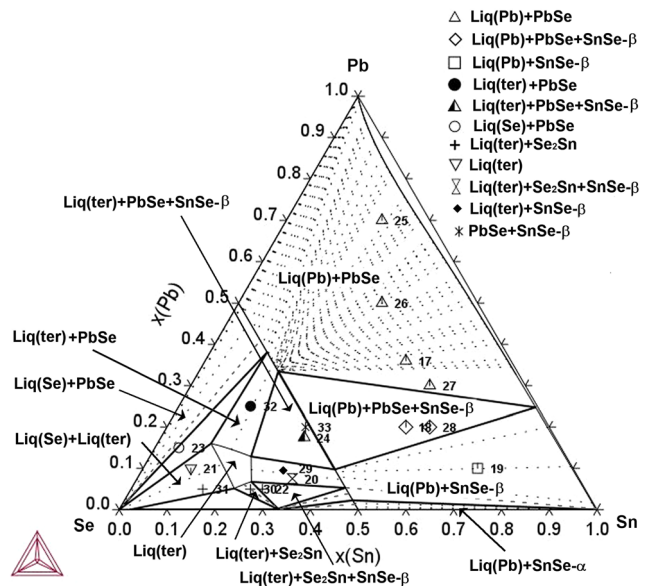


Fig. 5 Isothermal section of phase diagram Pb-Se-Sn at 500 °C with superimposed experimental data from Ref 3. The legend describes experimental equilibria. The numbers of samples correspond to the samples listed in Table 3 in Ref 3.

4 Discussion

The analysis of present results and their comparison with experiments shows only an average agreement for some calculations. One of the main reasons for the worse agreement is the inconsistency of experimental results from

Fig. 6 Pseudobinary vertical section between PbSe and SnSe. The experimental data from DTA measurements are from Ref 8

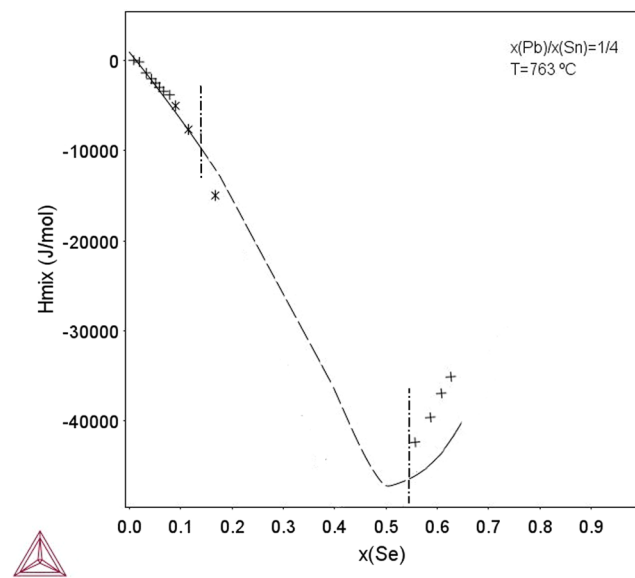
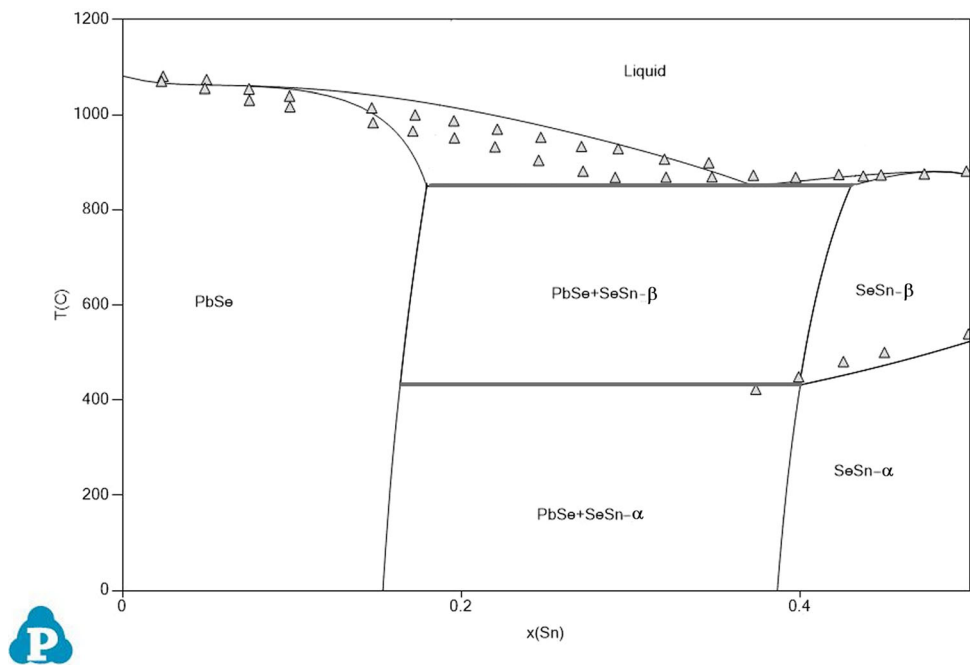


Fig. 7 Calculated enthalpy of mixing of liquid for the ratio Pb/Sn=1/4 at the temperature 763 °C in comparison with experimental data from Ref 11. Dot-dashed lines indicate the extent of pure liquid phase obtained from calculation., + indicates experimental data for single phase liquid and * indicates data for a two-phase mixture with liquid.^[11] Pure liquid elements at the temperature of measurements are selected as reference states

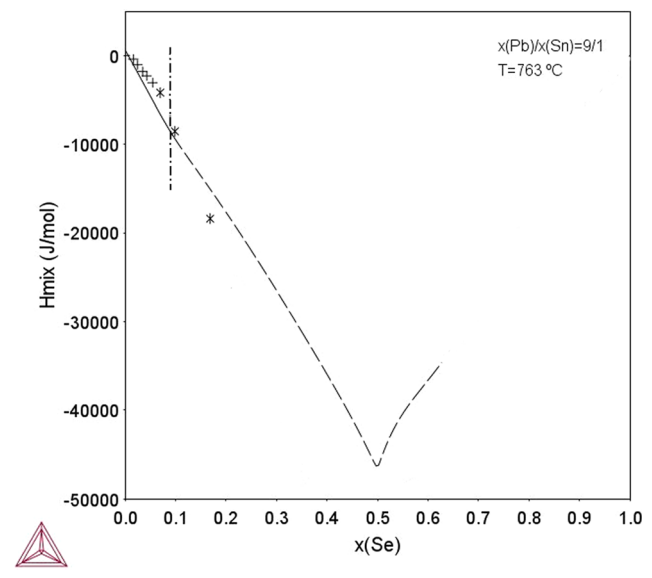


Fig. 8 Calculated enthalpy of mixing of liquid for the ratio Pb/Sn=9/1 at the temperature 763 °C in comparison with experimental data from in Ref 11. Dot-dashed line indicate the extent of pure liquid phase obtained from calculation., + indicates experimental data for single phase liquid and * indicates data for a two-phase mixture with liquid.^[11] Pure liquid elements at the temperature of measurements are selected as reference states

different authors. In general, the agreement is worse for Se-rich regions both for the phase diagram sections and the thermodynamic measurements.

The calculated isothermal sections at 350 and 500 °C from Ref 3 show a very good agreement for the region with less than 50 at.% Se. Here, all experimental results agree well with the calculated phase equilibria. There is only a

qualitative agreement in the Se-rich corner, all experimentally found phase fields are correctly modelled, but the discrepancy is in the positions of specific phase fields especially in 350 °C isothermal section.

The key discrepancy exists in the shape and size of the pure liquid region, which exists around 10 at.% Pb and 10-20 at.% Sn. Two variants for the extent and position of

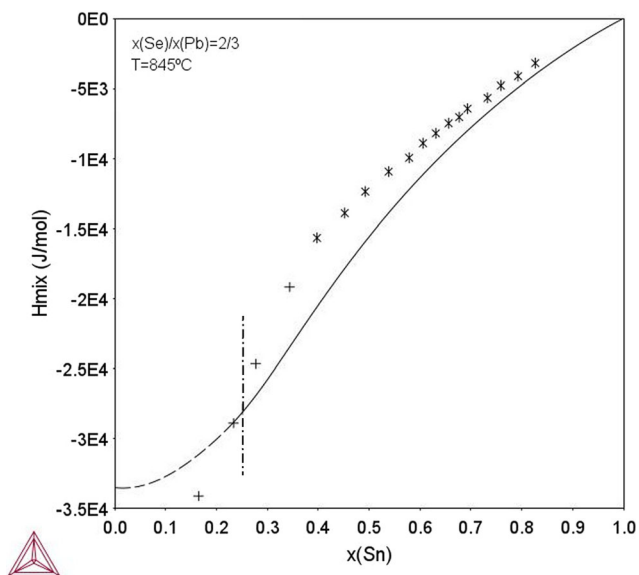


Fig. 9 Calculated enthalpy of mixing of liquid for the ratio Se/Pb=2/3 at the temperature 845 °C in comparison with experimental data from Ref 11. Dot-dashed line indicate the extent of pure liquid phase obtained from calculation., + indicates experimental data for single phase liquid and * indicates data for a two-phase mixture with liquid.^[11] Pure liquid elements at the temperature of measurements are selected as reference states

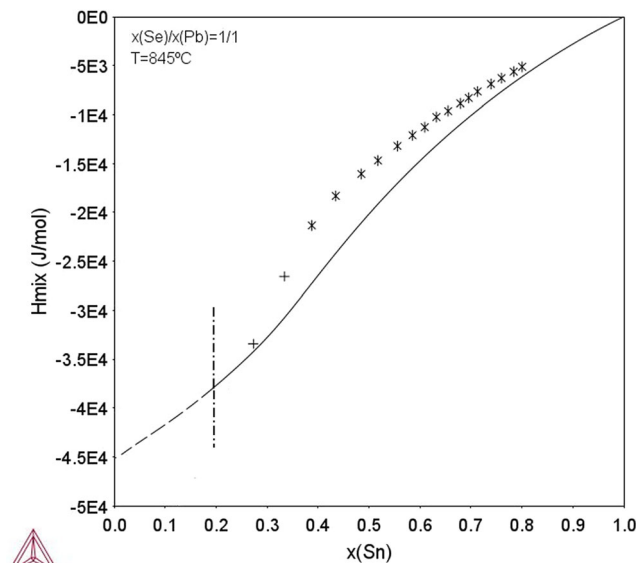


Fig. 10 Calculated enthalpy of mixing of liquid for the ratio Se/Pb=1/1 at the temperature 845 °C in comparison with experimental data from Ref 11. Dot-dashed line indicate the extent of pure liquid phase obtained from calculation., + indicates experimental data for single phase liquid and * indicates data for a two-phase mixture with liquid.^[11] Pure liquid elements at the temperature of measurements are selected as reference states.

this phase field were proposed in the work,^[3] one where a very narrow phase field connected with the pure liquid selenium exists (Fig. 1(b) in Ref 3) and second where a

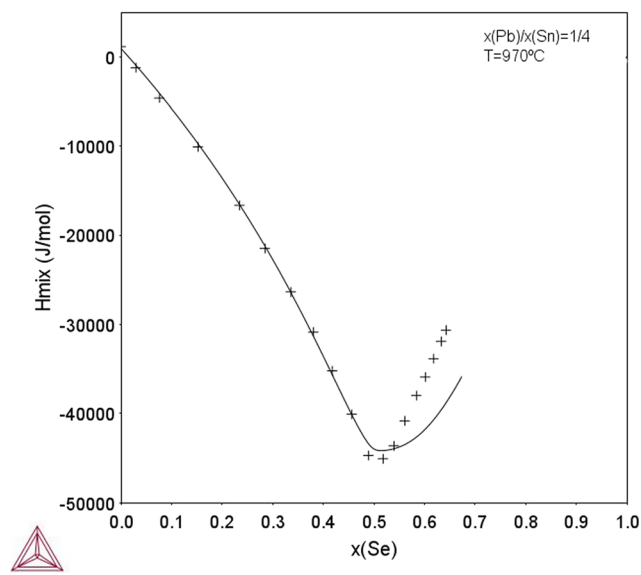


Fig. 11 Calculated enthalpy of mixing of liquid for the ratio Pb/Sn=1/4 at the temperature 970 °C; + indicates the experimental results from Ref 11. Pure liquid elements at the temperature of measurements are selected as reference states.

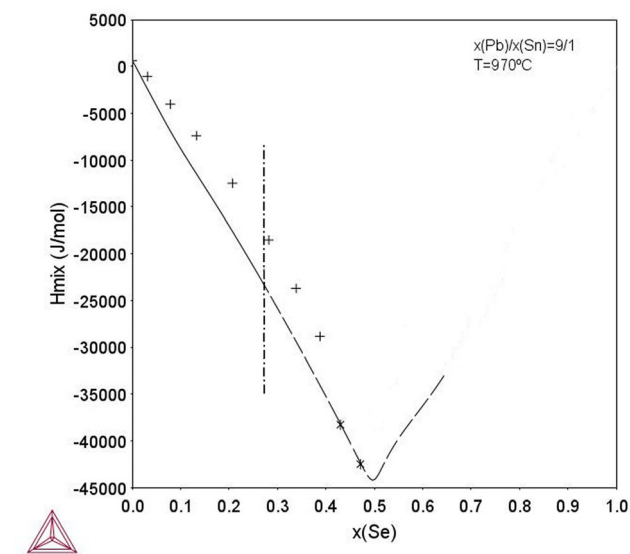


Fig. 12 Calculated enthalpy of mixing of liquid for the ratio Pb/Sn=9/1 at the temperature 970 °C in comparison with experimental data from Ref 11. Dot-dashed line indicate the extent of pure liquid phase obtained from calculation., + indicates experimental data for single phase liquid and * indicates data for a two-phase mixture with liquid.^[11] Pure liquid elements at the temperature of measurements are selected as reference states.

separate liquid phase field connected with the Se-rich liquid by two-phase field labelled (Liquid(Se) + Liquid(ter)) as shown in Fig. 1(c) in Ref 3. The selection of a more likely phase equilibrium was not done due to the lack of experimental samples in that region. Theoretical modelling strongly supported the existence of the two-phase field

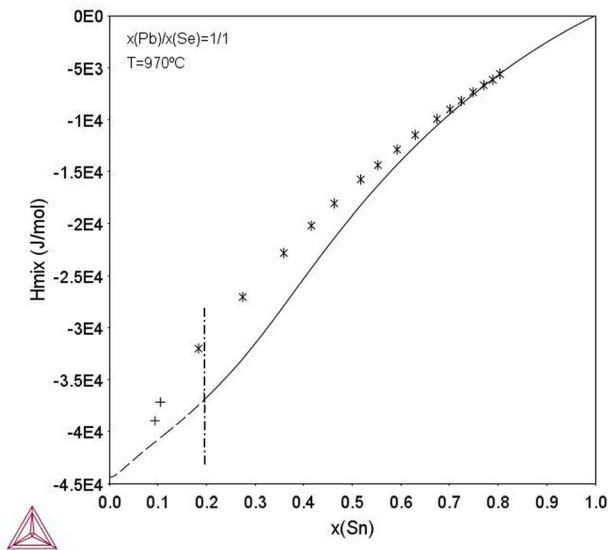


Fig. 13 Calculated enthalpy of mixing of liquid for the ratio Pb/Se=1/1 at the temperature 970 °C in comparison with experimental data from Ref 11. Dot-dashed line indicate the extent of pure liquid phase obtained from calculation., + indicates experimental data for single phase liquid and * indicates data for a two-phase mixture with liquid^[11]. Pure liquid elements at the temperature of measurements are selected as reference states

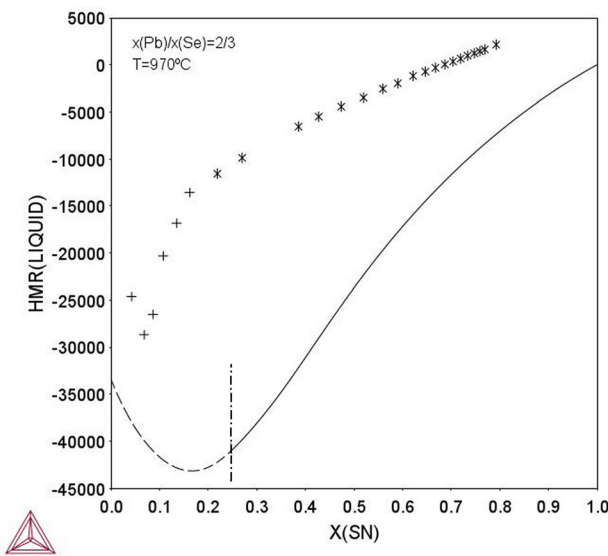


Fig. 14 Calculated enthalpy of mixing of liquid for the ratio Pb/Se=2/3 at the temperature 970 °C in comparison with experimental data from Ref 11. Dot-dashed line indicate the extent of pure liquid phase obtained from calculation., + indicates experimental data for single phase liquid and * indicates data for a two-phase mixture with liquid^[11]. Pure liquid elements at the temperature of measurements are selected as reference states

(Liquid(Se) + Liquid(ter)), nevertheless, the extent of the experimentally found Liquid(ter) phase field does not correspond to the calculated one. The calculated one is

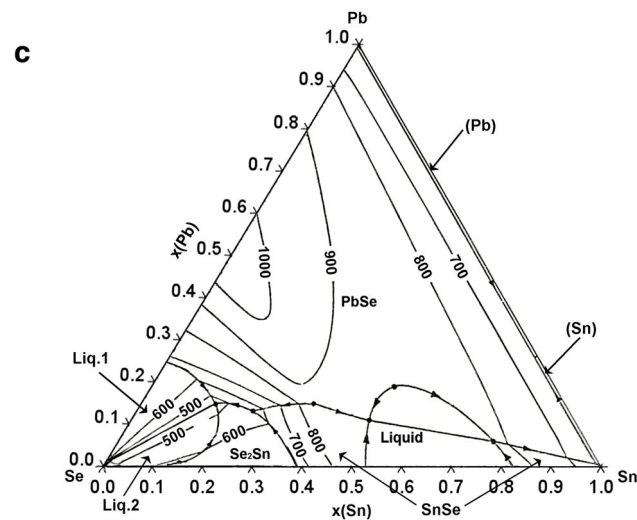
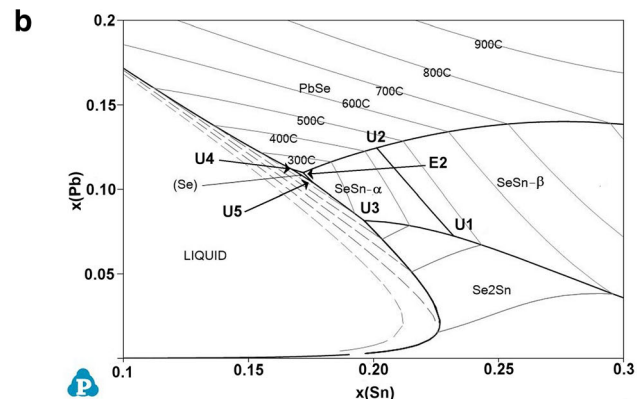
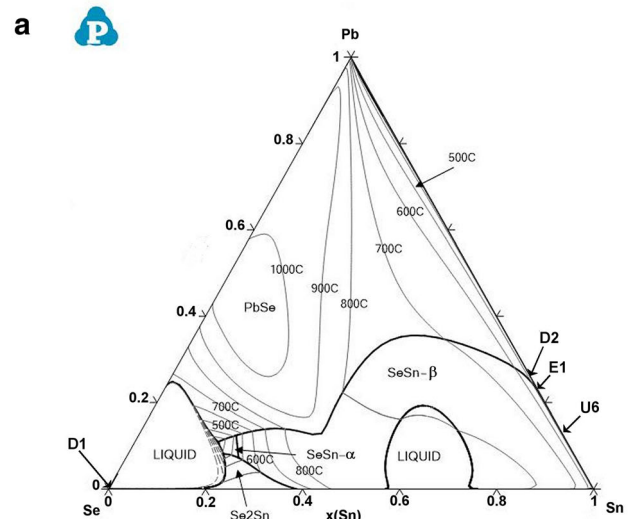


Fig. 15 (a) Calculated liquidus surface of Pb-Se-Sn phase diagram, (b) detail of the liquidus surface in the Se-rich corner, (c) the experimentally established liquidus surface from Ref 10

significantly smaller and shifted slightly towards a higher Sn content. It has been found that any attempt to model a

Table 3 The calculated invariant reactions containing liquid phases in the system Pb–Se–Sn

Type of reaction	<i>T</i> (°C)	Invariant reaction	Overall composition		
			<i>x</i> (Pb)	<i>x</i> (Se)	<i>x</i> (Sn)
U1	465.4	SeSn-β + Se ₂ Sn => Liq + SeSn-α	0.072	0.696	0.232
U2	431.9	Liq + SeSn-β => PbSe + SeSn-α	0.125	0.674	0.201
E1	431.9	SeSn-β => Liq. + PbSe + SeSn-α	0.223	0.001	0.775
U3	315.8	Liq + Se ₂ Sn => SeSn-α + Liq	0.082	0.722	0.196
U4	220.8 ₄	Liq + PbSe => Liq + (Se)	0.112	0.721	0.167
U5	220.8 ₃	Liq + Liq => SeSn-α + (Se)	0.104	0.720	0.175
D1	220.7 ₇	Liq + SeSn-α => Se ₂ Sn + (Se)	0	0.999	0.001
E2	205.3	Liq => (Se) + PbSe + SeSn-α	0.110	0.718	0.172
U6	203.6	Liq + SeSn-α => PbSe + (Sn)	0.129	0	0.871
D2	183.0	Liq => (Pb)+PbSe+(Sn)	0.260	0	0.740

Italic values indicate the amount of this element in given IR is smaller than 0.001

larger phase field, especially extended in the direction of Sn axis, leads to an expansion of the liquid phase well below 200 °C and to the existence of a very complicated multiple liquid miscibility gap structure at high temperatures not only in the Se-rich region.

Thus, the agreement is only qualitative for the section at 350 °C, all experimentally determined phase fields are present in the calculated section, however, their shape and position are to some extent different.

Rather better agreement was obtained for the isothermal section for 500 °C. Here, too, the agreement is very good for the Se-poor region, with only one exception. The SnSe-β was not identified in Ref 3 They did not consider the HT modification, probably because the transition temperature for binary SnSe-α/β intermetallics is well above 500 °C. However, according to the work,^[8] the high solubility of Pb in the SnSe family of phases leads to the stabilization of the HT modification of the SnSe intermetallic phase in the low temperature region below 500 °C.

The concentration dependence of the α/β transition temperature was modelled with respect to the data^[8] and the phase boundaries are shown for the SnSe-α + SnSe-β + Liq(Pb) phase field in Fig. 5 (the liquid phase rich in Pb and/or Sn is labeled Liquid(Pb) in the text and figures in this paper). It can be seen from Fig. 5 that the samples were only available in the assumed SnSe-β + Liq(Pb) phase field.

Better agreement was obtained for the Se-rich region of the 500 °C section compared to the 350 °C section. Especially the samples 23 and 32 agree well with the experimental results and confirmed the existence of a liquid miscibility gap in this region. The sample 23 clearly showed the existence of (Liquid(Se) + PbSe), where the liquid phase contained almost 99 at.% of Se. Sample 32 consists of PbSe phase together with Liquid(ter) with a composition of Pb-64.4 at.% Se-19.4 at.%Sn.

The PbSe–SnSe-α/β quasi-binary section is shown in Fig. 6. Here, a reasonable agreement was obtained for the liquidus line and the concentration dependence of the SnSe-α/β transition temperature with the experimental results from Ref 8. The value of eutectic temperature also agreed well with the experiment. Nevertheless, there is a significant difference for the PbSe/(PbSe + Liq) phase boundary. Thermodynamic modelling predicts much lower solubility of Sn in the PbSe intermetallic phase especially around the eutectic temperature. The values of Sn solubility in PbSe at 350 and 500 °C were accepted from Ref 3 because no other data are available for such low temperatures. The attempt to model high Sn solubility in PbSe at high temperatures led to a very strong temperature dependence for the relevant interaction parameters and consequently it was not possible to model a reasonable liquidus surface for the ternary system. Pseudo-ternary (Pb,Sn)Se phase was stabilized by tin at very high temperatures above 1500 °C and as mentioned above, all attempts to model the correct liquidus surface and the correct stability of (Pb,Sn)Se led again to multiple miscibility gaps and very unlikely shape of the liquidus surface.

The enthalpies of mixing for the three temperatures and various Pb/Sn and Pb/Se ratios were measured by Ref 11. The experimental difficulties encountered in this system were demonstrated in the published results and it can be concluded that a higher amount of Se usually meant a greater discrepancy between experiments and modelling. Some of the presented experimental results are questionable, which is also demonstrated here.

Figure 7 and 8 show a comparison between two sections with *x*(Pb)/*x*(Sn)=1/4 and 9/1, respectively, for the temperature 763 °C. Here, a single liquid phase exists in two separate concentration intervals and good agreement was obtained only for a low concentration of Se in this limited interval. Experimental data for the liquid phase in the

concentration region of approx. $x(\text{Se}) = 0.55 - 0.7$ show worse agreement. Experimental data are not available for high selenium content (approx. $x(\text{Se}) > 0.7$), where the liquid miscibility gap exists. Experimental difficulties are probably the reason for the lack of data. Dot-dashed lines indicate the calculated position of the phase boundary between the liquid and the two-phase field. The experimentally established phase boundary is in the interval between two measurements labeled by symbols + (single phase liquid) and * (two-phase with liquid). The agreement is good considering the small amount of experimental data and the uncertainty of the experimental liquidus surface (to be discussed later). Dashed line shows the calculated values of the enthalpy of mixing of liquid in the metastable region.

Figures 9 and 10 show a comparison between experimental and calculated values for two sections with $x(\text{Se})/x(\text{Pb}) = 2/3$ and $1/1$, respectively, at the temperature $845\text{ }^\circ\text{C}$. Here the tendency is well reproduced by calculations, but the differences between the experimentally and theoretically determined boundaries of the liquid phase field are worse.

The experimental results at $970\text{ }^\circ\text{C}$ were presented for several sections both for Se/Pb and Pb/Sn ratios in.^[11] The results for the $x(\text{Pb})/x(\text{Sn}) = 1/4$ and $9/1$, respectively, are shown in Fig. 11 and 12. Only a liquid phase exists for the first ratio at this temperature and the excellent agreement of the measured and calculated enthalpies of mixing was obtained for $x(\text{Se}) < 0.5$. There is also a very good agreement for the limiting enthalpy of mixing in the binary

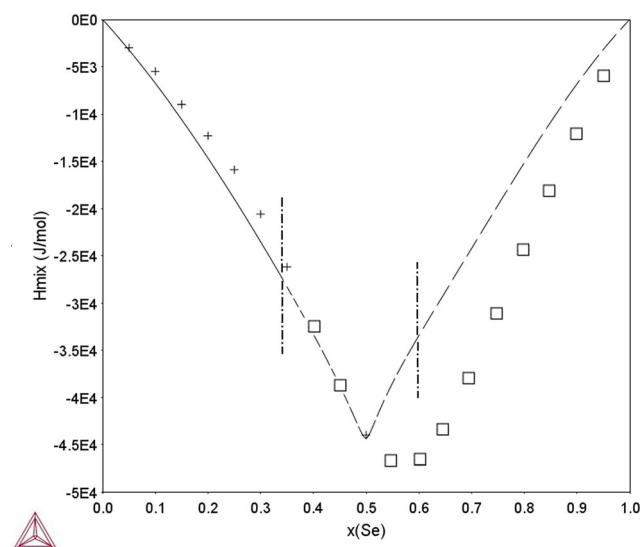


Fig. 16 Calculated enthalpy of mixing of liquid for the binary Pb-Se system at the temperature $970\text{ }^\circ\text{C}$ in comparison with experimental data from Ref 11. The dashed line marked two phase region, □—extrapolated values from Ref 11. Pure liquid elements at the temperature of measurements are selected as reference states.

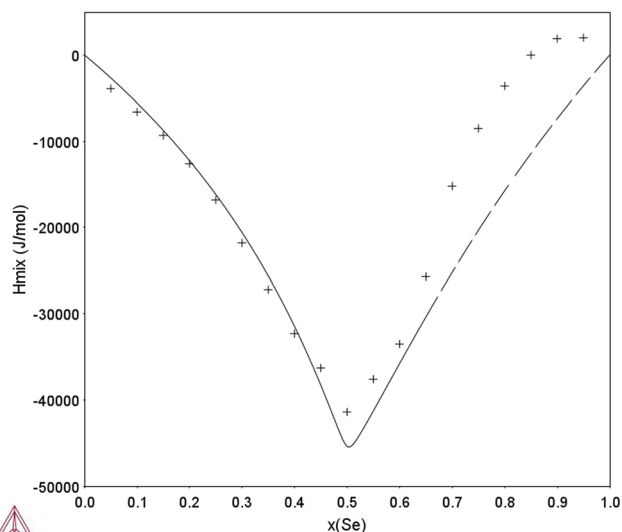


Fig. 17 Calculated enthalpy of mixing of liquid for the binary Se-Sn system at the temperature $970\text{ }^\circ\text{C}$ in comparison with experimental data from Ref 11. Pure liquid elements at the temperature of measurements are selected as reference states

Pb-Sn system. The experimental data are only available for $x(\text{Se}) < 0.643$, but in the Se-rich region, the agreement is significantly worse. A slightly worse agreement was obtained for the second ratio, but the tendency is still well reproduced. This discrepancy can be caused by significant problems in measuring the respective enthalpies of mixing in liquid for samples with a high selenium content. Such problems also occur in binary systems, where there are significant differences between the experimental enthalpies of mixing of liquid in the binary Pb-Se system measured in Ref 11 and the calculated mixing enthalpies from the accepted theoretical evaluation of binary Pb-Se.^[22] The values for $x(\text{Se}) > 0.35$ published in Ref 11 are only extrapolated. This is shown in Fig. 16. An analogical problem exists for $x(\text{Se}) > 0.5$ also in the Se-Sn binary system, a comparison between the experimental measurements for the Se-Sn system from Ref 11 and accepted theoretical assessment from Ref 21 is shown in Fig. 17.

The experimental results for $x(\text{Pb})/x(\text{Se}) = 1/1$ and $2/3$ ratios are shown in Fig. 13 and 14. The agreement between the experiments and calculations for the first Pb/Se ratio is again reasonable, considering relatively high content of selenium for small Sn contents, where the discrepancy is more pronounced. On the other hand, the experimental and theoretical boundary between the liquid and the (Liq + PbSe) two-phase field is very close. An example of a significant discrepancy between experiment and modelling is demonstrated in Fig. 14. Here the samples have a relatively high selenium content, especially in the region with a low tin content. Nevertheless, there is big difference between the experiment and the calculation in the whole region and

the experimental data are problematic even in the Sn rich region. The values of the enthalpy of mixing do not go to 0 for pure tin. Since all previously presented results in Fig. 7, 8, 9, 10, 11, 12 and 13 show good or at least reasonable agreement between the experiment and the calculation, it can be assumed that the experimental values for the $x(\text{Se})/x(\text{Pb}) = 3/2$ ratio are influenced by some systematic error. Since a less reasonable agreement between calculation and experiment in all presented figures was usually obtained for samples with high selenium content, the reason for this disagreement may be the effect of the evaporation of Se in the Se-rich samples above the boiling point of pure selenium at 685°C.

The partial liquidus surface of the Pb-Se-Sn system was studied by Zlomanov et al.^[9] and the liquidus surface in the whole concentration range was presented by Saveliev et al.^[10] Unfortunately, both papers are very brief and no detailed information is provided about the samples, the experimental method, and the evaluation of results. Saveliev et al.^[10] presented only one figure in their paper, where the liquidus surface is shown. On the other hand, their results look reasonable and presented features are broadly consistent with the calculated liquidus surface. Experimental results^[10] suggest the existence of two liquid miscibility gaps, which agrees well with the calculations. The complex structure of the calculated liquidus surface with multiple strangely shaped miscibility gaps was mentioned in the discussion of Fig. 4 and 5. This structure appeared when a better agreement was sought for the position of Liquid(ter) phase field at low temperatures and high Sn solubility in the PbSe phase around 800°C and such character of the liquidus surface is not acceptable.

A comparison of the experimental and calculated liquidus surface is shown in Fig. 15(a) and (c), the detail of the region around Liquid(ter) is presented in Fig. 15(b). It can be stated that despite the experimental uncertainties, all key features are in good qualitative agreement in both figures. Theoretical calculations suggest the existence of a miscibility gap in the Se-rich corner up to high temperatures, but the equilibria at high temperatures are metastable at ambient pressure as there will be selenium gas in equilibrium with liquid and no information is available for this region.

The invariant reactions containing the liquid phase are listed in Table 3. The two ternary invariant reactions designated as D1 and D2 are degenerate reactions in nature. They lie extremely close to the binary low-temperature invariant reactions in the Pb-Sn and Se-Sn systems and the Pandat software has not been able to describe the nature of these reactions. It only lists the phases involved, not the type of reaction. After careful analysis of many calculations of isothermal sections and isopleths, the ones listed in Table 3 were identified as the most likely, but the

designation of the reactions as degenerate was retained because there is no clear evidence to support the analysis.

5 Conclusion

The literature related to the Pb-Se-Sn phase diagram is relatively sparse and there are considerable inconsistencies between the various authors. Many phase equilibria have not been well defined. The current study presents the theoretical assessment which is based on the little experimental information considered to be reliable enough to contribute to the thermodynamic modelling of Pb-Se-Sn phase diagram in whole concentration and temperature range. This assessment is part of an effort to develop a thermodynamic database for quinary Ag-Pb-Se-Sn-Te system, which is important for the further development of materials for thermoelectric applications.

The calculated phase diagram agrees reasonably with the experimental sections at 350 and 500 °C from Ref 3 especially in the region with low selenium content and a reasonable agreement was obtained with sparse information about experimental liquidus surface. Similarly, the calculated enthalpies of mixing in liquid reasonably agree with the experimental data for lower selenium content.

Despite of this, a new experimental program for the Pb-Se-Sn system focused on significant inconsistencies between older experimental works is necessary to improve the thermodynamic assessment.

Acknowledgments The authors acknowledge the financial support of the Ministry of Science and Technology of Taiwan (MOST 107-2923-E-007-005-MY3) and the Czech Science Foundation (Project 18-25660J).

References

1. C. Chang, Q. Tan, Y. Pei, Y. Xiao, X. Zhang, Y.X. Chen, L. Zheng, S. Gong, J.F. Li, J. He, and L.D. Zhao, Raising Thermoelectric Performance of n-Type SnSe via Br Doping and Pb Alloying, *RSC Adv.*, 2016, **6**, p 98216.
2. A. Zevalkink, D.M. Sniadak, J.L. Blackburn, A.J. Ferguson, M.L. Chabinyk, O. Delaire, J. Wang, K. Kovnir, J. Martin, L.T. Schelhas, T.D. Sparks, S.D. Kang, M.T. Dylla, G.J. Snyder, B.R. Ortiz, and E.S. Toberer, A Practical Field Guide to Thermoelectrics: Fundamentals, Synthesis, and Characterization, *Appl. Phys. Rev.*, 2018, **5**, p 021303.
3. S.-W. Chen, T.-Y. Huang, Y.-H. Hsu, and A. Kroupa, Phase Diagram of the Pb-Se-Sn System, *J. Electron. Mater.*, 2020, **49**(8), p 4714-4729.
4. O. Zobac, K. Buchlovska, J. Pavlu, and A. Kroupa, Thermodynamic Description of Binary System Nickel-Selenium, *J. Phase Eq. Diffus.*, 2021, **42**, p 468-478.
5. O. Zobac, K.W. Richter, and A. Kroupa, Experimental Phase Diagram of the Ag-Se-Sn System at 250, 400 and 550 °C, *J. Phase Eq. Diffus.*, 2022. <https://doi.org/10.1007/s11669-022-00943-y>

6. J.C. Wolley, and O. Berollo, Phase Studies of the $Pb(1-x)Sn(x)Se$, *Mat. Res. Bull.*, 1968, **3**, p 445-450.
7. A.J. Strauss, Metallurgical and Electronic Properties of $Pb(1-x)Sn(x)Te$, $Pb(1-x)Sn(x)Se$ and Other IV-VI alloys, *Trans. Met. Soc. AIMIE*, 1968, **242**, p 354.
8. S. Dal Corso, B. Liautard, and J.C. Tedenac, The Pb-Sn-Se System: Phase Equilibria and Reactions in the $PbSe-SnSe-Se$ Subternary, *J. Phase Equil.*, 1995, **16**(4), p 308-313.
9. V.P. Zlomanov, V.I. Shtanov, A.K. Gapeev, A.V. Novoselova, Study of the part T-X-Y projection of the Pb-Se-Sn system (in Russian). *Doklady Akademii nauk SSSR*, 346-349 (1974)
10. V.P. Saveliev, E.M. Latypov, and V.P. Zlomanov, Study of T-X-Y liquidus surface in the diagram of the Pb-Sn-Se system (in Russian), *Zh. Neorg. Chimii*, 1975, **20**, p 2006-2008.
11. K.P. Kotchi, R. Castanet, and J.-C. Mathieu, Etude Thermodynamique des Alliages Pb-Se, Sn-Se et Pb-Se-Sn, *Z. Metallkde*, 1988, **79**(2), p 102-108.
12. A. Laugier, J. Cadoz, M. Faure, and M. Moulin, Ternary Phase Diagram and Liquid Phase Epitaxy of Pb-Sn-Se and Pb-Sn-Te, *J. Cryst. Growth*, 1974, **21**, p 235-242.
13. H. Okamoto, Se-Sn (Selenium-Tin), *J. Phase Eq. Diffus.*, 1998, **19**, p 293.
14. N. Saunders, and A.P. Miodownik, *Calphad (A Comprehensive Guide)*. Pergamon Press, Oxford, 1998.
15. H.L. Lukas, S.G. Fries, and B. Sundman, *Computational Thermodynamics: The Calphad Method*. Cambridge University Press, New York, 2007.
16. J.-O. Andersson, T. Helander, L. Höglund, P. Shi, and B. Sundman, Thermo-Calc & DICTRA, Computational Tools for Materials Science, *Calphad*, 2002, **26**, p 273-312.
17. W. Cao, S.L. Chen, F. Zhang, K. Wu, Y. Yang, Y.A. Chang, R. Schmid-Fetzer, and W.A. Oates, PANDAT Software with PanEngine, PanOptimizer and PanPrecipitation for Multicomponent Phase Diagram Calculation and Materials Property Simulation, *Calphad*, 2009, **33**, p 328.
18. SGTE Unary Database, ver. 5.0, www.sgte.net/en/free-pure-substance-database
19. O. Redlich, and A. Kister, Thermodynamics of nonelectrolyte solutions—X-Y-T relations in a binary system, *Ind. Eng. Chem.*, 1948, **40**, p 341-345.
20. Y.M. Muggianu, M. Gambino, and J.P. Bros, Enthalpies of formation of liquid alloys Bismuth-Gallium-Tin at 723 K – choice of analytical representation of integral and partial thermodynamic functions of mixing for this ternary system, *J. Chim. Phys.*, 1975, **72**, p 83-88.
21. Y. Feutelais, M. Majid, B. Legendre, and S.G. Fries, Phase Diagram Investigation and Proposition of a Thermodynamic Evaluation of the Tin-Selenium System, *J. Phase Equil*, 1996, **17**, p 40-49.
22. Y. Liu, Z. Kang, G. Sheng, L. Zhang, J. Wang, and Z. Long, Phase Equilibria and Thermodynamic Basis for the Cd-Se and Pb-Se Binary Systems, *J. Electron. Mater.*, 2012, **41**(7), p 1915-1923.
23. H. Ohtani, K. Okuda, and K. Ishida, Thermodynamic Study of Phase Equilibria in the Pb-Sn-Sb System, *J. Phase Equil*, 1995, **16**(5), p 416-429.

Publisher's Note Springer Nature remains neutral with regard to jurisdictional claims in published maps and institutional affiliations.

6.9 Paper 9

- [P9] **Zobač, O.**, Karpíšková, L., Kroupa, A., *Experimental study of the ternary phase diagram Al-Ge-Mg*, Journal of Phase Equilibria and Diffusion, 2022, 44, pp. 127-136, doi: 10.1007/s11669-023-01025-3 (IF 1.4)



Experimental Study of the Ternary Phase Diagram Al–Ge–Mg

Ondřej Zobač¹ · Lenka Karpišková^{1,2} · Aleš Kroupa¹

Submitted: 12 September 2022 / in revised form: 24 November 2022 / Accepted: 21 December 2022 / Published online: 8 February 2023
© ASM International 2023

Abstract The phase equilibria of the Al–Ge–Mg ternary phase diagram were experimentally studied at the temperatures of 250, 300, 400 and 450 °C. The ternary phase τ ($\text{Al}_2\text{Ge}_2\text{Mg}$) suggested by the earlier structural study was found to be stable at all temperatures studied. Detailed study of the phase equilibria containing the τ ($\text{Al}_2\text{Ge}_2\text{Mg}$) phase in the ternary system have been carried out. The average composition of this phase was found to be 36 at.% Al–36 at.% Ge–Mg. In contrast to the previously published binary Ge–Mg phase diagram, the solubility of Mg in Ge was found to be within a few atomic percent. It was also found that GeMg_2 intermetallic phase dissolves only small amount of Al but there is significant nonstoichiometricity with respect to the Ge/Mg ratio especially for lower annealing temperatures.

Keywords Al–Ge–Mg phase diagram · SEM · ternary phase · XRD

1 Introduction and Literature Review

The Al–Mg binary system is widely used as a basis for lightweight structural materials. The use of Germanium as an alloying element should contribute to the improvement of the properties of this alloy at higher temperatures due to

its similarity of germanium with silicon which is commonly used.^[1]

Knowledge of ternary phase equilibria in the entire concentration and temperature range is crucial for the design of new promising alloys. Unfortunately, works focused on this aspect of the Al–Ge–Mg system are quite few. Phase equilibria in the system were studied only in the works of Badaeva and Kuznetsova^[2] and Legka et al.^[3] Pukas^[4] identified one $\text{Al}_2\text{Ge}_2\text{Mg}$ ternary phase in this system and described its crystal structure, but did not present any results on its phase equilibria in the ternary system.

2 Al–Ge Binary System

The Al–Ge binary alloy is a basic eutectic system where the position of the eutectic point is approx. 72 at.% Al and 424 °C. The mutual solubility of both elements is relatively small. (see Fig. 1a). The binary system has been studied by several authors.^[5–8] Figure 1(a) represent the experimental binary phase diagram of Al–Ge subsystem proposed by McAllister and Murray^[7]

3 Al–Mg Binary System

The binary phase diagram of the Al–Mg system (see Fig. 1b) is very well described experimentally and theoretically in the literature e.g.^[9–11] In this system, there are three stable intermetallic phases with non-negligible solubility. The β -AlMg phase is stable up to 450 °C, γ -AlMg melts congruently at 457 °C, and ε -AlMg exists in the temperature range 193–417 °C. The experimental binary

✉ Ondřej Zobač
zobac@ipm.cz

¹ Institute of Physics of Materials, The Czech Academy of Sciences, Žitkova 22, 616 00 Brno, Czech Republic

² Faculty of Science, Masaryk University, Kotlarska 22, 616 00 Brno, Czech Republic

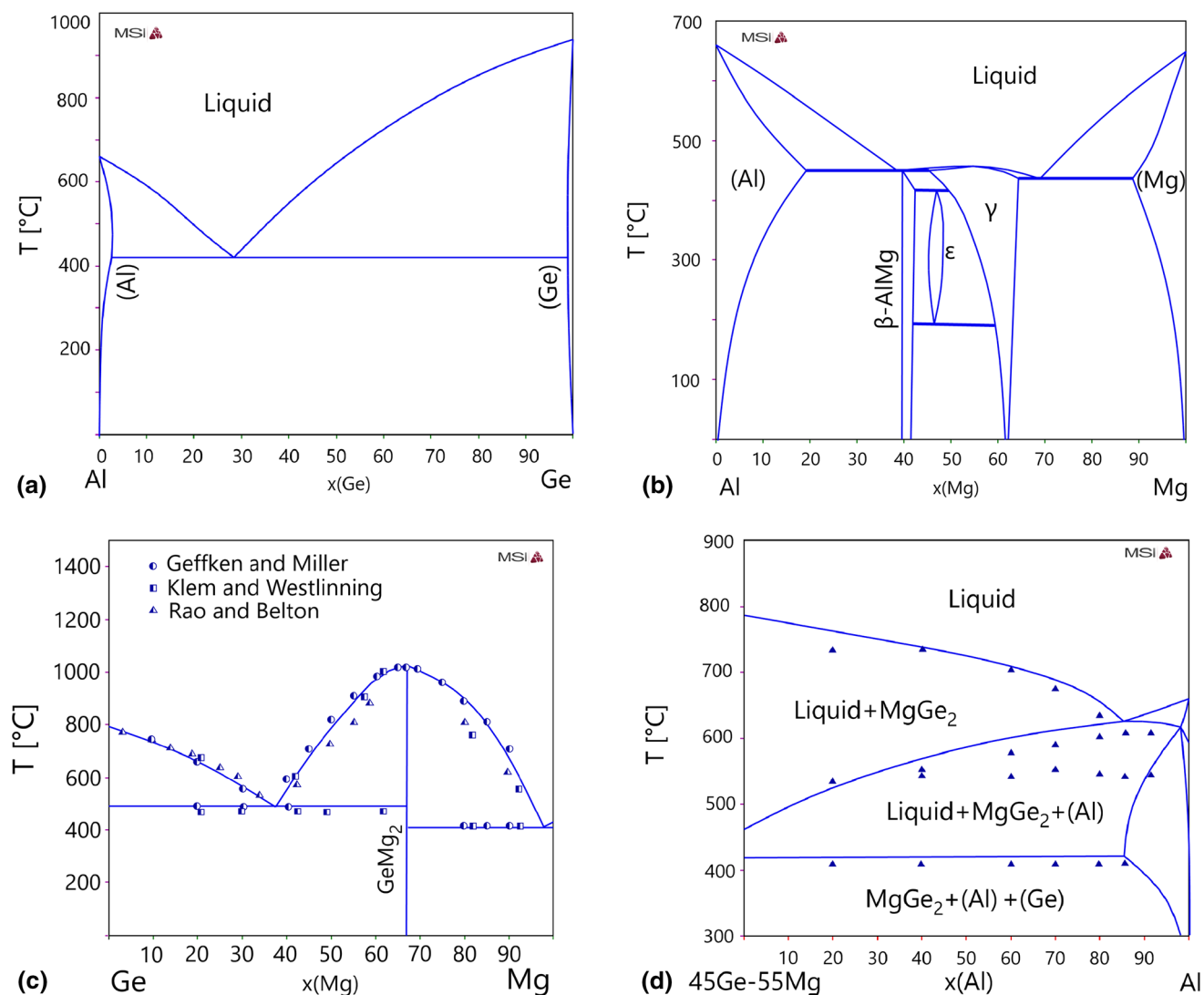


Fig. 1 Published phase diagrams of relevant systems (a) Al-Ge,^[7] (b) Al-Mg,^[10] (c) Ge-Mg,^[12] (d) Al-Ge-Mg^[8]

phase diagram of Al–Mg subsystem according to Ren et al.^[10] is shown on Fig. 1(b).

4 Ge–Mg Binary System

Klemm and Westling^[12] first established a Ge–Mg binary phase diagram using thermal analysis and microscopic observation. They found that the Ge–Mg binary system contains a single GeMg₂ intermetallic phase, supposedly with a stoichiometric composition that melts congruently, two eutectic reactions, and a negligible mutual solubility between pure Mg and Ge. These basic features of the phase diagram were subsequently confirmed in Ref 13, 14. Geffken and Miller^[13] determined the liquidus temperatures for alloys of 10 to 90 at.% Ge by thermal analysis methods. The liquidus line was later experimentally determined

by Rao and Belton^[14] from discontinuity measurements of EMF vs. temperature curve for alloys in the concentration range 10–95 at.% Ge. The liquidus transition temperatures are approximately 50 °C lower than the values proposed by Geffken and Miller^[13] and 20 °C lower than the values from Klemm and Westling^[12] in some regions. A recent thermodynamic review was published by Yan et al.^[15]. This work is based on the experimental data of Klemm and Westling^[12] and supported by an ab-initio calculation. They suggested the congruent temperature of the binary GeMg₂ phase to be 1117 °C. Two eutectic points occur in the phase diagram (see Fig. 1c), the eutectic point in the magnesium-rich part existing at 97.8 at.% Mg and 631 °C, the second eutectic point is located at 37.1 at.% Mg and 699 °C. The solubility in the GeMg₂ phase was not evaluated in any experimental work for long-term annealed samples. Figure 1(c) shows experimental binary phase

diagram of Ge-Mg subsystem with superimposed experimental data^[12–14]

5 1,4, Al–Ge–Mg Ternary System

The Al-Ge-Mg system has been studied in the past for its potential applications in the aerospace and automotive industries due to its similarity to the Al–Mg–Si system, which is already widely used in this field.^[4,16–18] B Jorge et al.^[19] experimentally studied the interface structure of precipitates in Al-0.59 at.% Mg-0.71 at.% Ge alloy. Kawai et al.^[20] investigated the age hardening of Al-rich samples at 200 °C. Karim et al.^[21] published an ab-initio study of the optoelectric and thermodynamic properties of the ternary phase τ .

The phase equilibria in the Al-Ge-Mg system were experimentally described by Badaeva^[2] using methods of thermal analysis. Various vertical sections of the phase diagram were investigated. No ternary phase was mentioned in the paper.^[2] The aluminum-rich part of the phase diagram (up to 10 at.% Al) was also experimentally studied by Legka et al.^[3] Theoretical modeling of the CALPHAD-based system was performed by Islam^[8] based on available experimental data. Some experimental points indicating phase transition temperatures were not described and explained in the published assessment. A vertical section of 45 at.% Mg-55 at.% Ge-Al is shown in Fig. 1(d). A set of DTA signals at approx. 550 °C without relevant explanation was found in the Al-rich part. No ternary phase is included in the phase diagram modeling. Recently, Pukas^[4] published information on a newly prepared ternary intermetallic phase τ (Al₂Ge₂Mg) with the structure Al₂Si₂Ca. The compound was characterized in terms of crystalline structure, thermodynamic and phase properties were not studied. A phase diagram containing the ternary phase has not yet been published. Figure 1(d) shows a vertical Sect. 45 at.% Mg-55 at.% Ge-Al of the Al-Ge-Mg system with the calculated data by Islam^[8] and superimposed experimental data of Badaeva.^[2]

6 Experimental

The nominal composition of the samples was chosen primarily with the aim to study phase equilibria containing the ternary phase τ . The isothermal sections of the ternary phase diagram in the temperature range of 250–450 °C were studied in this work. The long-term annealed samples were characterized using SEM–EDX and XRD.

6.1 Sample Preparation

Experimental samples were prepared from high purity metals (5N for Al, Mg and 6N for Ge). The samples were arc-melted on a water-cooled copper plate under a low-pressure 6N Ar atmosphere using pure titanium or magnesium as the getter. The alloys were remelted three times to achieve better sample homogeneity. The alloyed samples were sealed in quartz glass ampoules under vacuum. Vacuumed ampoules with samples were annealed for a long time in a standard muffle furnace. The samples were quenched to cold water from long-term annealing temperatures. Annealing times and temperatures were chosen in order to obtain conditions close to thermodynamic equilibrium.

6.2 Experimental Phase Diagram Investigation

The samples were prepared in the metallographic laboratory after long-term annealing. Grinding and polishing were performed under pure ethanol without water to prevent oxidation of the Mg-rich grains. Especially the GeMg₂ grains are very sensitive to oxidation. The overall and coexisting phase compositions were studied by SEM–EDX microanalysis using a JEOL JSM-6460 scanning electron microscope with an EDX Link analyzer from Oxford Instruments (Table 1).

Area analysis was used to determine the overall elemental composition from the representative surface of the sample. For the composition of the coexisting phases, point analysis was used. The grains of various phases were

Table 1 Stable phases in Al–Ge–Mg ternary system

Phase name [This work]	Other names	Pearson symbol	Structure prototype	T. range, °C	Comments, references
α -Al	FCC_A1	<i>cF4</i>	Cu	< 660	[22]
α -Ge	Diamond_A4	<i>cF8</i>	C	< 938	[22]
α -Mg	HCP_A3	<i>cI2</i>	W	< 650	[22]
β -AlMg	Al ₃ Mg ₂	<i>cF1832</i>	Al ₃ Mg ₂	< 452	[11]
γ -AlMg	Al ₁₂ Mg ₁₇	<i>cI58</i>	α -Mn	< 458	[11]
ϵ -AlMg	Al ₃₀ Mg ₂₃	<i>hR53</i>	Co ₅ Cr ₂ Mo ₃	185–410	[11]
GeMg ₂	GeMg ₂	<i>cF12</i>	CaF ₂	< 1118	[15]
τ	Al ₂ Ge ₂ Mg, Al ₇ Ge ₇ Mg ₅	<i>hP5</i>	CaAl ₂ Si ₂	≤ 450	[4, this work]

Table 2 Cell parameters of ternary phase τ with CaAl_2Si_2 structure type

Space group	a, Å	c, Å	c/a	V, Å ³	References
P-3m1	4.11693(5)	6.7873(1)	1.6486	99.627(3)	[4]
P-3m1	4.111987	6.796723	1.6497	99.52532	This work

sufficiently large and with a well-distinguishable contrast in the microscope, so a reliable analysis of the individual phases was possible. The crystallographic structure of the coexisting phases was confirmed by x-ray powder diffraction (XRPD) on an EMPYREAN diffractometer using CoK_α radiation Table 2 shows a comparison of the parameters of the ternary phase τ cells measured in the scope of this work and the results of Pukas^[4] analyzed by XRD. Compared to the work of Pukas, the “a” parameter is lower, but the “c” parameter is higher in our sample. The cell volume was lower for the ternary phase found in our work, which supports the idea that smaller magnesium atoms replace the germanium and aluminum atoms with respect to the ideal occupancy in the $\text{Al}_2\text{Ge}_2\text{Mg}$ stoichiometry.

Representative samples analyzed are listed in Table 3. Column 1 shows the annealing temperature and sample number. The annealing time is given in column 2. The overall composition of the long-term annealed samples is given in column 3. In column 4, the coexisting phases found in a state close to thermodynamic equilibrium are given. The compositions of the equilibrium phases existing in the samples measured by SEM–EDX are shown in column 5.

7 Results and Discussion

Using the experimental results of the composition of coexisting phases analyzed by SEM–EDX and listed in Table 3, experimental isotherm sections of the Al–Ge–Mg phase diagram at temperatures of 250 °C, 300 °C, 400 °C and 450 °C were constructed. The overall composition of the studied samples is represented by several symbols in the proposed phase diagrams. The square represents the total composition of samples containing two phases in equilibrium. Just few two-phase samples were found among the samples and the respective composition of each phases and the corresponding connecting tie-lines is shown by dotted line. Triangles represent the total composition of samples containing three phases in equilibrium. Phase compositions are defined by the position of the corners of the connecting triangle and indicated by empty circles. The position of the phase boundaries and the shape of the phase fields not defined by our own samples are drawn as dashed lines and are based on information from the binary subsystems and on the phase rules.

7.1 Isothermal Sections

The obtained isothermal sections of the Al–Ge–Mg phase diagram at temperatures of 250, 300, 400 and 450 °C are shown in Fig. 2. The isothermal sections look very similar in this range. The numbers given refer to the sample number annealed at the given temperature. The characteristic morphology of concrete phase structures describing the various phase fields are shown in micrographs in Fig. 3. All the micrographs are visualized in BSE mode. Figure 3(a) is a sample No 250_2 annealed at 250 °C consisting of the three phases α -Al, GeMg_2 and τ , where the ternary τ phase is a matrix. Figure 3(b) shows a sample No 250_3 annealed at 250 °C consisting of the three phases α -Al, α -Ge and τ , where the α -Ge is a matrix. Figure 3(c) shows microstructure of the sample No 300_4 annealed at 300 °C in consisting of the phases α -Al, α -Ge and τ . Figure 3(d) represents a microstructure of the sample No 300_5 annealed at 300 °C in BSE mode consisting of the phases α -Al, GeMg_2 and β -AlMg where the β -AlMg is a matrix. Figure 3(e) is the sample No 400_4 annealed at 400 °C consisting of the phases α -Al, GeMg_2 and β -AlMg, where the β -AlMg is a matrix. Figure 3(f) is a microstructure of the sample No 400_5 annealed at 400 °C in BSE mode consisting of the phases α -Al, α -Ge and τ . Figure 3(g) shows a Microstructure of the sample No 450_5 annealed at 450 °C in BSE mode consisting of the phases α -Al, GeMg_2 and τ , where the ternary τ phase is a matrix.

Aluminum (α -Al) and magnesium (α -Mg) show a very limited solubility of germanium in their structure. On the other hand, germanium shows a relatively high ternary solubility of magnesium compared to the published Ge–Mg binary phase diagram (see Fig. 1c). In the theoretically evaluated Ge–Mg binary phase diagram published by Yan et al. no solubility of magnesium in germanium was considered.^[15] As mentioned in the Sect. 1.3, no previous experimental work on Ge–Mg system has studied the mutual solubility of both elements,^[12,13] and^[14] used mainly thermal analysis and EMF measurements. We experimentally found the solubility of up to 6% Mg in Ge in the Al–Ge–Mg ternary system. The measured solubility of Mg in Ge in the ternary system is generally consistent for all isothermal section at specific temperatures and indicates a slow decrease in solubility with increasing temperature.

Table 3 Chemical composition of the long-term annealed representative sample

T, °C No	Annealed time, h	Overall composition, at.%			Coexist. phases	Phase composition, at.%		
		Al	Ge	Mg		Al	Ge	Mg
250_1	5052	23.5	43.2	33.3	α -Ge	4.0	93.8	2.2
					GeMg ₂	0.7	28.1	71.2
					τ	34.5	36.5	29.0
250_2	5052	67.1	17.7	15.2	α -Al	98.7	1.2	0.1
					GeMg ₂	1.2	27.8	71.0
					τ	36.8	34.4	28.8
250_3	5052	63.9	32.9	3.2	α -Al	98.4	1.6	0.0
					α -Ge	2.4	92.1	5.5
					τ	38.2	36.2	25.6
250_4	5052	60.4	3.5	36.1	GeMg ₂	*	*	*
					α -Al	92.0	7.5	0.5
					β -AlMg	61.1	0.5	38.4
250_5	5052	19.0	5.6	75.4	Mg	3.9	1.0	95.1
					γ -AlMg	34.0	1.1	64.9
					GeMg ₂	0.8	25.8	73.4
300_1	2304	22.0	51.9	26.1	α -Ge	3.7	91.7	4.6
					GeMg ₂	0.4	31.3	68.3
					τ	34.1	36.5	29.4
300_2	2304	67.4	17.5	15.1	α -Al	97.5	2.2	0.3
					GeMg ₂	2.3	27.5	70.2
					τ	39.7	33.6	26.7
300_3	2304	65.9	31.8	2.3	α -Al	98.2	1.8	0.0
					α -Ge	3.0	90.6	6.4
					τ	37.2	36.9	25.9
300_4	3427	54.8	32.4	12.8	α -Al	98.4	1.6	0.0
					α -Ge	3.2	93.9	2.9
					τ	34.6	37.1	28.3
300_5	3427	65.6	7.0	27.4	α -Al	88.5	10.6	0.1
					GeMg ₂	2.9	25.8	71.3
					β -AlMg	66.2	0.9	32.8
300_6	3427	58.9	3.4	37.7	α -Al	84.0	0.5	15.5
					GeMg ₂	2.2	25.8	72.0
					β -AlMg	60.8	0.4	38.8
300_7	3427	15.7	7.6	76.7	α -Mg	7.0	1.1	91.9
					GeMg ₂	1.1	26.0	72.9
					γ -AlMg	32.5	0.9	66.6
400_1	1976	85.6	14.3	0.1	α -Al	97.2	2.8	0.0
					α -Ge	2.0	92.2	5.8
					τ	37.3	38.7	24.0
400_2	1976	67.9	30.3	1.8	α -Al	97.1	2.9	0.0
					α -Ge	2.7	91.6	5.7
					τ	35.9	41.2	22.9
400_3	2567	67.0	23.1	9.9	α -Al	97.1	2.9	0.0
					α -Ge	1.5	95.0	3.5
					τ	36.6	37.4	26.0
400_4	2567	54.9	10.1	35.0	α -Al	82.4	0.8	16.8
					GeMg ₂	1.5	27.7	70.9

Table 3 continued

T, °C No	Annealed time, h	Overall composition, at. %			Coexist. phases	Phase composition, at. %		
		Al	Ge	Mg		Al	Ge	Mg
400_5	2567	58.3	29.4	12.3	β -AlMg	63.1	1.1	35.8
					α -Al	96.8	3.1	0.1
					α -Ge	3.2	91.7	5.1
400_6	2567	71.2	11.8	17.0	τ	37.0	36.7	26.3
					τ	37.3	34.5	28.2
					α -Al	98.9	1.1	0.0
400_7	2567	22.9	46.6	30.5	GeMg ₂	*	*	*
					τ	35.4	36.2	28.4
					α -Ge	5.5	86.2	8.3
400_8	2567	42.3	34.0	23.7	GeMg ₂	0.6	29.1	70.3
					τ	35.5	36.5	28.0
					α -Al	98.1	1.8	0.1
450_1	1319	23.5	46.0	30.5	α -Ge	2.2	92.1	5.7
					GeMg ₂	0.1	29.9	70.0
					τ	35.5	36.0	28.5
450_2	1319	71.9	15.6	12.5	α -Al	98.8	1.2	0.0
					GeMg ₂	0.5	28.7	70.8
					τ	38.1	32.9	29.0
450_3	1319	50.4	44.9	4.7	α -Ge	1.8	93.3	5.0
					τ	36.3	38.1	25.7
					Liquid	65.3	32.1	2.6
450_4	3288	59.2	29.1	11.7	α -Al	96.4	3.5	0.1
					τ	36.8	36.8	26.4
					Liquid	74.1	24.7	1.2
450_5	3288	77.3	8.5	14.2	α -Al	98.0	1.1	0.9
					GeMg ₂	1.9	36.8	71.3
					τ	35.8	34.9	29.3
450_6	3288	38.9	31.4	29.7	τ	35.7	36.2	28.1
					α -Al	96.0	2.9	1.1
					GeMg ₂	1.2	28.5	70.3
450_7	3288	42.3	34.0	23.7	τ	35.5	36.5	28.0
					α -Al	95.8	3.4	0.8
					GeMg ₂	1.1	23.8	75.1
450_8	3288	78.8	7.3	13.9	α -Al	99.1	0.8	0.1

*Not measurable

The solubility of Al in Ge solid solution in the Al-Ge-Mg ternary system is slightly higher than that in the Al-Ge binary system. Again, the consistency of the measured values in this work is very good. Here the increase in solubility could be attributed to the influence of the third element in the studied system. Nevertheless, a new detailed study of at least the Ge-Mg binary system is necessary.

The β -AlMg and γ -AlMg binary phases show very limited solubility of germanium. The binary phase of ϵ -AlMg was not found in our samples, since our main goal was to find phase equilibria with the ternary phase τ and we

chose the nominal compositions of studied samples accordingly. The solubility of Ge in ϵ -AlMg was estimated to be very small, consistent with measured solubility in other intermetallic phases in the Al-Mg system and the relevant phase fields were drawn by dashed lines.

We found only very limited solubility of germanium in magnesium solid solution in the relevant samples annealed at 250 and 300 °C, as shown in Fig. 2(a) and (b). Considering the limited information about the solubility in the Ge and Mg solid solutions, this result is in good agreement with the Ge-Mg binary phase diagram (Fig. 1c).

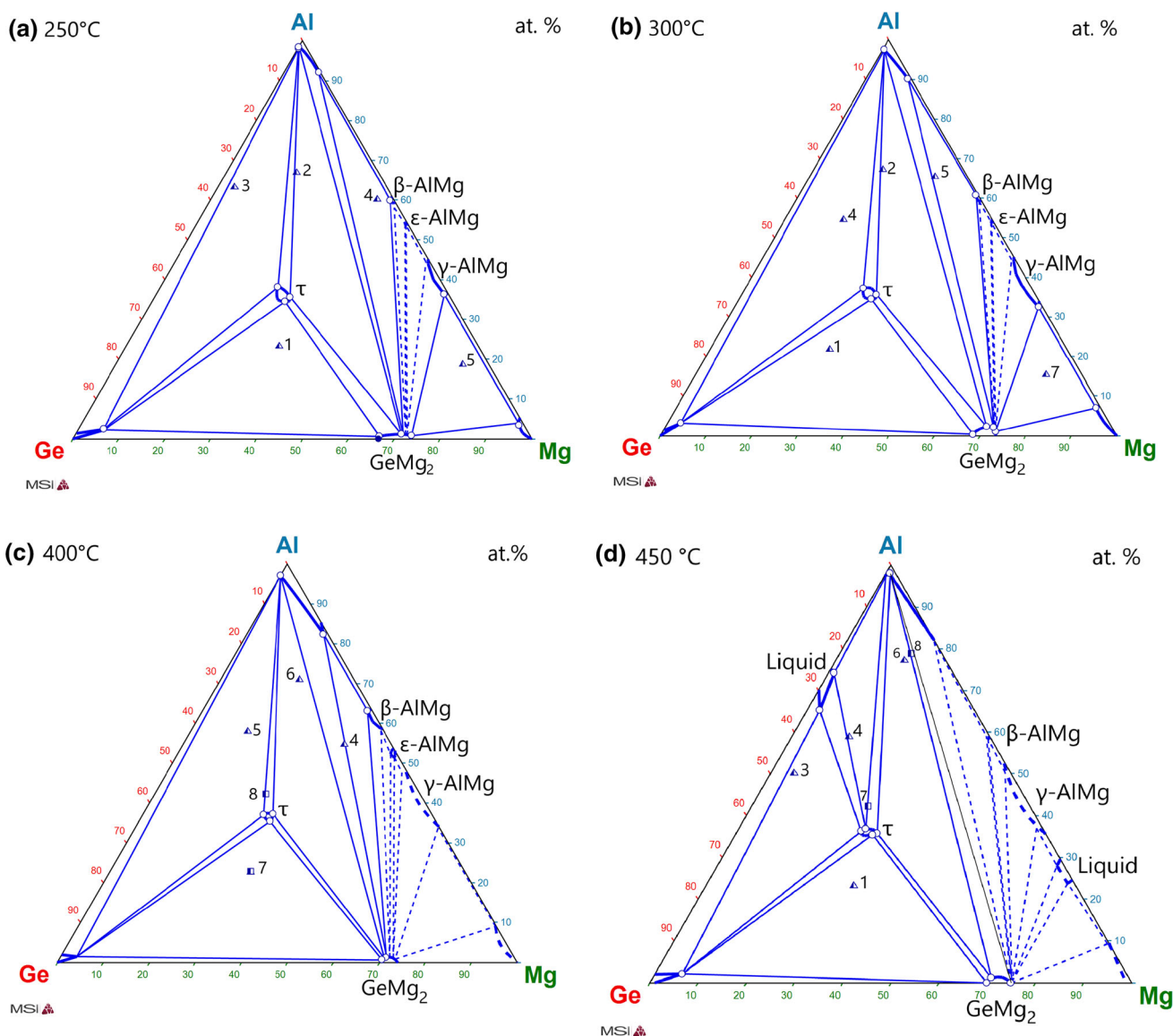


Fig. 2 Isothermal section of experimental Al-Ge-Mg ternary phase diagram at (a) 250 °C (b) 300 °C (c) 400 °C and (d) 450 °C

The GeMg_2 phase shows an extended range of composition between 66 and 73 at.% Mg at temperatures of 250 to 300 °C (Fig. 2a and b). The XRD pattern of sample No. 300_7 (15.7 at.% Al-7.6 at.% Ge-Mg) containing a reasonable amount of GeMg_2 phase is shown in Fig. 4(a), where the binary phases GeMg_2 , $\gamma\text{-AlMg}$ and magnesium coexist. At higher temperatures, the GeMg_2 phase shows only limited solubility around 72 at.% Ge (Fig. 2c and d). Again this finding contradicts the previously assessed Ge-Mg phase diagram published by Yan et al.,^[15] where the GeMg_2 phase is linear with a composition of 66.6 at.% Mg. On the other hand, the modeling performed by^[15] was based on limited experimental thermal analysis and EMF data only (^[12,13] and^[14]), the solubility of the

intermetallic phase has not been studied experimentally in any previous work to the best of our knowledge.

The ternary phase τ was found to be stable at all studied temperatures up to 450 °C and slightly nonstoichiometric with similar solubility of a few percent for all elements. In his study, Pukas^[4] described crystallographic structure of this phase as a stoichiometric one with an $hP5$ structure of the $\text{Al}_2\text{Si}_2\text{Ca}$ type. This structure for the experimentally found ternary phase τ in this study was confirmed by the XRD analysis (see Fig. 4b), but its experimentally measured composition is shifted and the center of the single-phase region is located at approx. 36 at.% Al-Ge-28 at.% Mg. This composition is consistent for all temperatures and all relevant samples containing three-phase equilibria with the τ phase (see Table 3).

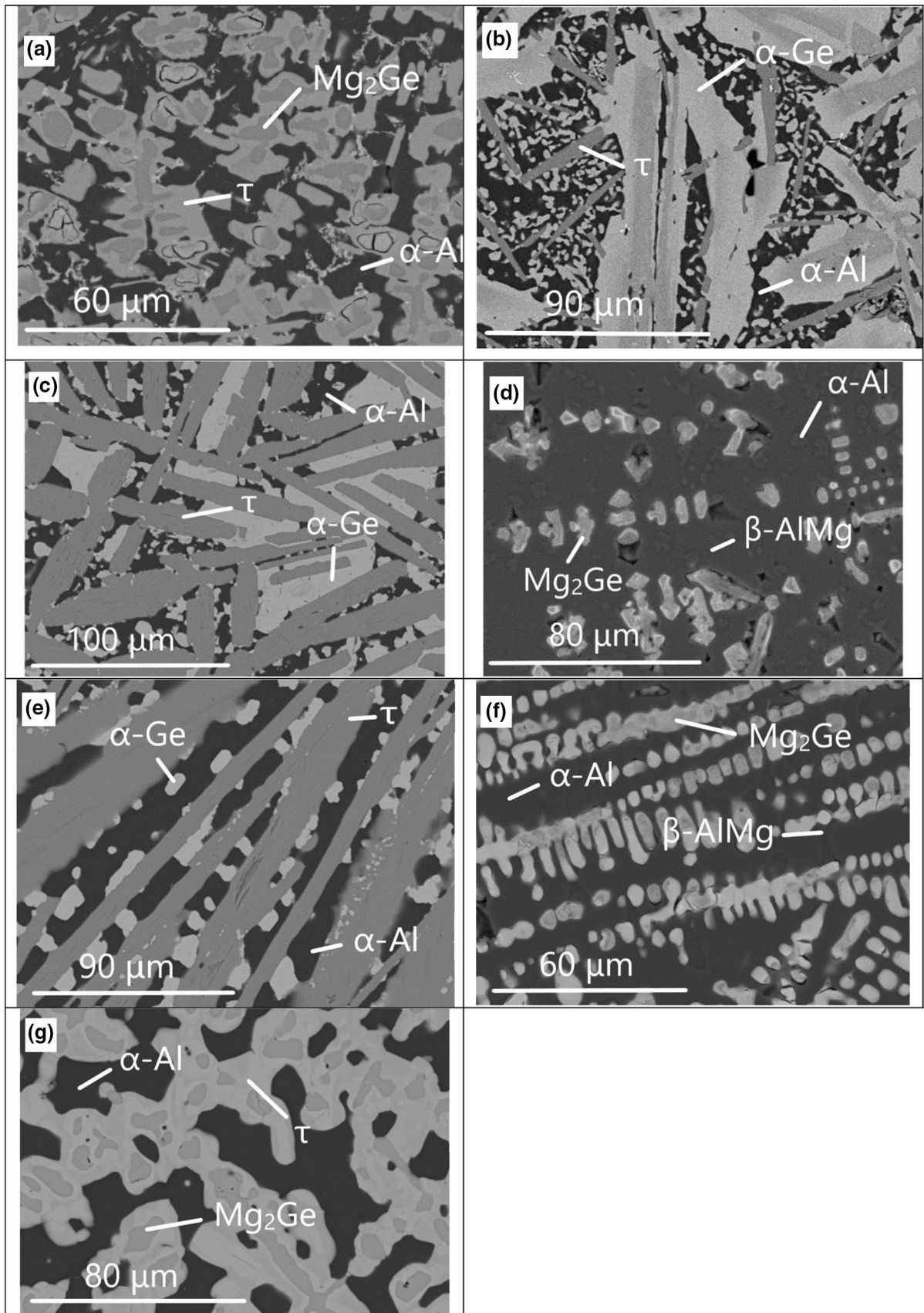


Fig. 3 Microstructures in BSE mode of long-term annealed samples (a) 250_2, (b) 250_3, (c) 300_4, (d) 300_5, (e) 400_4, (f) 400_5 and (g) 450_5

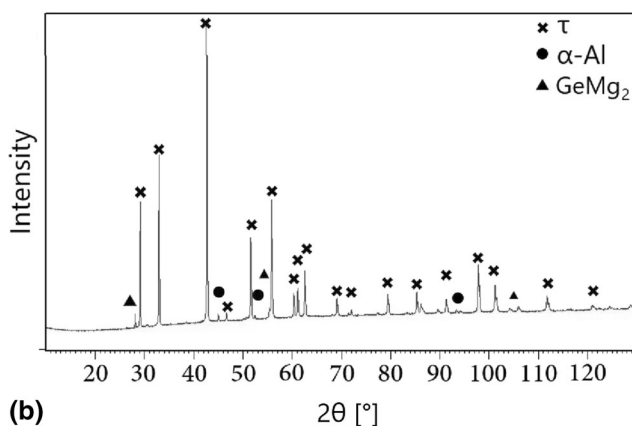
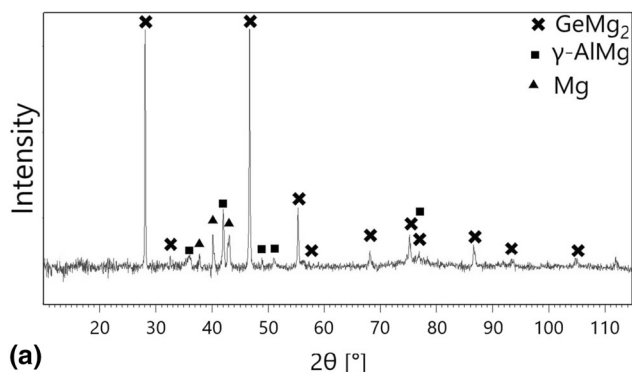


Fig. 4 XRD patterns of samples (a) 300_7 where the binary phases GeMg_2 , $\gamma\text{-AlMg}$ and magnesium coexist and (b) 400_8, where the 92.6% of ternary phase τ , 4.3 GeMg_2 phase and the 3.1% of pure aluminum coexist

8 Conclusion

Although there is literature regarding the Al-Ge-Mg phase diagram [2, 2019Leg], complex phase equilibria with recently described ternary phase^[4] have not been yet studied. This study was designed to contribute to a better understanding of the stability of the this ternary phase τ . Experimental studies were carried out at temperatures of 250 °C, 300 °C, 400 °C and 450 °C. Isothermal sections of the Al-Ge-Mg ternary phase diagram were obtained by a combination of standard methods: the overall and phase compositions of the samples were measured by SEM–EDX and the crystal structures were identified by XRD. Following key results were obtained in the scope of this work:

- Significant nonstoichiometricity of the binary intermetallic phase GeMg_2 was observed at 250 °C [$x(\text{Mg}) = 0.666\text{--}0.735$] and 300 °C [$x(\text{Mg}) =$

$0.68\text{--}0.734$]. Its position at 400 and 450 °C is close to $x(\text{Mg}) = 0.73$.

- The ternary phase τ was found to be stable at all temperatures studied.
- The composition of the τ phase was found to be close to 36 at.% Al-Ge-28 at.% Mg, which does not correspond to the published composition of 40 at.% Al-40 at.% Ge-20 at.% Mg proposed by Pukas.^[4]
- Significant differences were found for the solubility of Mg in the Ge solid solution and extent of solubility of the GeMg_2 phase with respect to the existing Mg-Ge phase diagram of Ref 12–14 With respect to the consistency of results obtained in the scope of this work, the new study of the binary system is planned.

Acknowledgments This study was funded by Czech Science Foundation of Czech Republic (Grant No. GA 22-22187S).

Funding Open access publishing supported by the National Technical Library in Prague.

Open Access This article is licensed under a Creative Commons Attribution 4.0 International License, which permits use, sharing, adaptation, distribution and reproduction in any medium or format, as long as you give appropriate credit to the original author(s) and the source, provide a link to the Creative Commons licence, and indicate if changes were made. The images or other third party material in this article are included in the article's Creative Commons licence, unless indicated otherwise in a credit line to the material. If material is not included in the article's Creative Commons licence and your intended use is not permitted by statutory regulation or exceeds the permitted use, you will need to obtain permission directly from the copyright holder. To view a copy of this licence, visit <http://creativecommons.org/licenses/by/4.0/>.

References

1. F. Ning, Z. Chunming, W. Zunije, W. Hongwei, Z. Xuejian, and C. Tao, Effect of Ge and Mg Additions on the Aging Response Behavior and Mechanical Properties of Al–Si–Cu Alloy, *Mater. Sci. Eng. A.*, 2021, **811**, 141024.
2. T. Badaeva, and R. Kuznetsova, Liquidus Surface and Aluminum Solid Solutions in the Al–Mg–Ge System, *Metalloved. Term. Obrab. Met.*, 1958, **3**, p 216–230.
3. T.M. Legka, T.M. Mika, Y.V. Milman, N.P. Korzhova, I.V. Voskoboinik, and N.M. Mordovets, Constitution of the Al Corner in the Ternary Al–Ge–Mg Phase Diagram, *Powder Metall. Met. Ceram.*, 2019, **57**(11–12), p 716–722.
4. S. Pukas, L. Pylypchak, O. Matselko, P. Demchenko, and R. Gladyshevskii, MgAl_2Ge_2 – A New Representative of the Structure Type CaAl_2Si_2 , *Chem. Met. Alloys*, 2012, **5**(1/2), p 59–65.
5. I. Ansara, J.P. Bros, and M. Gambino, Thermodynamic Analysis of the Germanium-Based Ternary Systems (Al–Ga–Ge, Al–Ge–Sn, Ga–Ge–Sn), *CALPHAD: Comput. Coupl. Phase Diagr. Thermochem.*, 1979, **3**(3), p 225–233.
6. H. Eslami, J. de Franceschi, M. Gambino, and J.P. Bros, An Electromotive-Force Study of the Activity of Aluminum in Al–

- Ga, Al-Ge and Al-Ga-Ge Systems, *Z Für Naturforschung A*, 1979, **34**(7), p 810–817.
- A.J. McAlister, and J.L. Murray, The Al-Ge (Aluminum-Germanium) System, *Bull. Alloy Phase Diagr.*, 1984, **5**(4), p 341–347.
 - F. Islam, A.K. Thykadavil, and M. Medraj, A Computational Thermodynamic Model of the Mg–Al–Ge System, *J. Alloys Compd.*, 2006, **425**(1), p 129–139.
 - P. Liang, H.L. Su, P. Donnadiou et al., Experimental Investigation and Thermodynamic Calculation of the Central Part of the Mg – Al Phase Diagram, *Int. J. Mater. Res.*, 1998, **89**(8), p 536–540.
 - Y.P. Ren, G.W. Qin, S. Li, Y. Guo, X.L. Shu, L.B. Dong, H.H. Liu, and B. Zhang, Re-Determination of $\gamma/(\gamma+\alpha\text{-Mg})$ Phase Boundary and Experimental Evidence of R Intermetallic Compound Existing at Lower Temperatures in the Mg–Al Binary System, *J. Alloys Compd.*, 2012, **540**, p 210–214.
 - R. Shi, Z. Zhu, and A.A. Luo, Assessing Phase Equilibria and Atomic Mobility of Intermetallic Compounds in Aluminum-Magnesium Alloy System, *J. Alloys Compd.*, 2020, **825**, 153962.
 - W. Klemm, and H. Westlinning, Untersuchungen über die Verbindungen des Magnesiums mit den Elementen der IV b-Gruppe, *Z. anorg. allg. Chem.*, 1941, **245**, p 365–380.
 - R. Geffken, and E. Miller, Phase Diagrams and Thermodynamic Properties of the Mg-Si and Mg-Ge Systems, *Trans. Metall. Soc. AIME*, 1968, **242**, p 2323.
 - Y.K. Rao, and G.R. Belton, Thermodynamic Properties of Mg–Ge Alloys, *Metall. Trans.*, 1971, **12**, p 2215–2219.
 - H. Yan, Y. Du, L. Zhou, H. Xu, L. Zhang, and S. Liu, Reassessment of the Mg–Ge Binary system Using CALPHAD Supported by First-Principles Calculation, *Int. J. Mater. Res.*, 2010, **101**(12), p 1489–1496.
 - K. Matsuda, S. Ikeno, and T. Munekata, HRTEM Study of Precipitates in Al-Mg-Si and Al-Mg-Ge Alloys, *Mater. Sci. Forum*, 2006, **519–521**, p 221–226.
 - K. Matsuda, T. Munekata, and S. Ikeno, Effect of Mg Content on the Precipitation in Al-Mg-Ge Alloys, *S. Mater. Sci. Forum*, 2007, **561–565**, p 2049–2052.
 - R. Bjørge, C.D. Marioara, S.J. Andersen, and R. Holmestad, Precipitation in Two Al-Mg-Ge Alloys, *Metall. Mater. Trans. A*, 2010, **41**, p 1907.
 - R. Bjørge, P.N.H. Nakashima, C.D. Marioara, S.J. Andersen, B.C. Muddle, J. Etheridge, and R. Holmestad, Precipitates in an Al–Mg–Ge Alloy Studied by Aberration-Corrected Scanning Transmission Electron Microscopy, *Acta Mater.*, 2011, **59**, p 6103–6109.
 - A. Kawai, K. Watanabe, K. Matsuda, and S. Ikeno, The Age-Precipitations Structure of Al–Mg–Ge Alloy Aged At 473K, *Arch. Metall. Mater.*, 2015, **60**(2), p 969–970.
 - A.M.M.T. Karim, M.A. Helal, M.A. Alam, M.A. Ali, I. Ara, and S.H. Naqib, Optoelectronic, Thermodynamic and Vibrational Properties of Intermetallic MgAl_2Ge_2 : A First-Principles Study, *SN Appl. Sci.*, 2021, **3**, p 229.
 - P. Villars Pearson’s handbook crystallographic data for intermetallic phases, ASM International 1997.

Publisher’s Note Springer Nature remains neutral with regard to jurisdictional claims in published maps and institutional affiliations.

6.10 Paper 10

- [P10] **Zobač, O.**, Žižka, R., Roupcová, P., Kroupa, A., *Experimental study of the Ni-Se-Sn phase diagram isothermal sections at 800 K, 1000 K and 1100 K*, Journal of Phase Equilibria and Diffusion, 2023, 44, pp. 594-605, doi: 10.1007/s11669-023-01058-8. (IF 1.4)



Experimental Study of the Ni-Se-Sn Phase Diagram Isothermal Sections at 800 K, 1000 K and 1100 K

Ondrej Zobac¹ · Rudolf Zizka¹ · Pavla Roupcová¹ · Ales Kroupa¹

Submitted: 10 May 2023 / in revised form: 7 August 2023 / Accepted: 25 August 2023 / Published online: 13 September 2023
© ASM International 2023

Abstract Three isothermal sections of the Ni-Se-Sn ternary system were experimentally investigated at 800 K, 1000 K and 1100 K in whole composition range. One stable ternary intermetallic phase, Ni_{5.62}SnSe₂, was confirmed. Solubility up to 15 at.% of tin was observed in the binary phase NiSe. Metastable binary phase Ni₃Se₄ was found at 800 K probably stabilized by third element. Complete isothermal sections at 800 K, 1000 K and 1100 K are proposed in this paper.

Keywords DTA · Ni-Se-Sn phase diagram · Ni_{5.62}SnSe₂ phase · SEM-EDX · XRD

1 Introduction and Literature Review

Knowledge of experimental phase diagrams is important for the development of new materials with specific material properties. Detailed knowledge of the coexistence and stability of phases in stable or metastable equilibrium significantly rationalizes such design and subsequent development of the required properties of new metallic materials. Phase diagrams are also important for other areas of science and technology.¹

1.1 Binary Subsystem Ni-Se

The phase diagram of the Ni-Se binary subsystem was investigated by Grønvold et al.,² Hiller and Wegener,³ and Kuznetsov et al.⁴ Later, Komarek and Wessely⁵ proposed an experimental phase diagram for the binary Ni-Se system (Fig. 1) based on a combination of x-ray diffraction (XRD) and thermal analysis (TA) experimental data. This experimental phase diagram was taken as a basis for review by Lee and Nash⁶ and Predel⁷. The latter paper was published in the Landolt-Börnstein compendium.⁷ The Ni-Se binary system consists of five stable and two known metastable intermetallic phases.

The binary intermetallic phase Ni₃Se₂ exists in two structural modifications. The low-temperature hexagonal modification Ni₃Se_{2-LT}^{3,5} is stable up to 878 K and the cubic Ni₃Se_{2-HT}⁵ is stable in temperature range 863–1058 K. The high-temperature modification Ni₃Se_{2-HT} is proposed to be non-stoichiometric with solubility extending into both Ni- and Se-rich regions, but the position of the phase boundaries is not reliably known. The Ni₆Se₅ phase is stable in the temperature range between 673 and 920 K. It crystallizes in its own orthorhombic super-structure type in space group *oC48* with Pearson symbol *Cmcm*.⁸ The NiSe (also named as Ni_(1-x)Se) phase is non-stoichiometric with the solubility of selenium between 50–57 at.% Se. The phase has hexagonal NiAs (*B81*) structure type with space group *P63/mmc*⁴ and is stable below 1232 K in the phase diagram. The stoichiometric phase NiSe₂ crystallizes in the cubic FeS₂ structure (Pearson symbol *cP12*) with space group *Pa3* and is stable below 1129 K.⁹

For the Ni-Se binary system, structural information is available for two metastable phases, α' -Ni₃Se₂⁶ and Ni₃Se₄.³ Phase equilibria in the binary Ni-Se phase diagram

✉ Ondrej Zobac
zobac@ipm.cz

¹ Institute of Physics of Materials, The Czech Academy of Sciences, Zizkova 22, Brno, Czech Republic

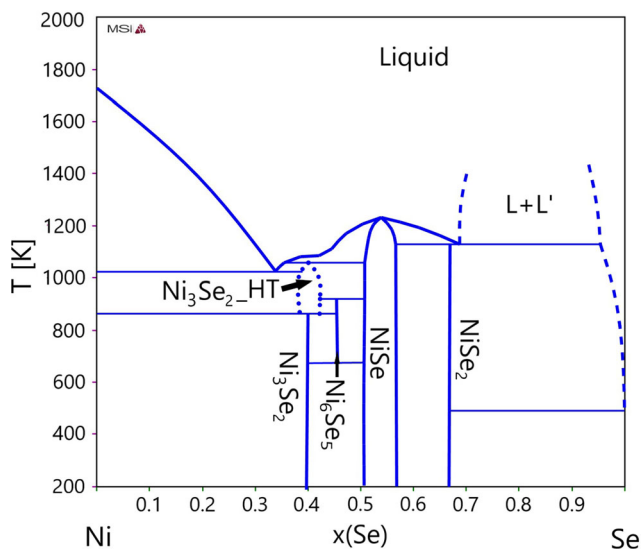


Fig. 1 Experimental Ni-Se phase diagram proposed by Komarek and Wessely⁵

were recently studied theoretically by CALPHAD method.¹⁰ Experimental phase diagram of Ni-Se system is shown in Fig. 1.

1.2 Binary Subsystem Ni-Sn

The most recent detailed experimental study of the phase equilibria in the Ni-Sn system was carried out by Schmetterer et al.¹¹ Detailed discussion of previous experimental work is presented in their paper. The Ni-Sn binary system contains seven intermetallic phases, in some cases with complex mutual interactions.

The Ni₃Sn phase exist in two structural modifications. The low-temperature Ni₃Sn_{LT} is stable up to 1221 K. Ni₃Sn_{LT} crystallizes in hexagonal Mg₃Cd structure type (space group *P6₃/mmc*). The cubic high-temperature modification Ni₃Sn_{HT} (space group *Fm-3 m*) exists in temperature range 1184–1462 K. Both phases show narrow homogeneity ranges. The intermetallic phase Ni₃Sn₂ exists in more structural modifications and exhibits almost 10 at.% homogeneity range. The hexagonal high temperature phase Ni₃Sn₂_HT (structural type Ni₂In, space group *P6₃/mmc*) is stable in temperature range 573–1553 K. Ni₃Sn₂ has very complex mutual interaction with the incommensurately modulated structures (Ni₃Sn₂_LT, Ni₃Sn₂_LT', Ni₃Sn₂_LT'') at lower temperatures. Ni₃Sn₄ crystallizes in its own structure type (*C2/m*) and it is stable up to 1071 K. The maximum solubility is about 5 at.% (Fig. 2).

1.3 Binary Subsystem Se-Sn

Binary system Se-Sn has been assessed by Feutelais et al.¹² Two intermetallic phases exist in the system, SeSn and

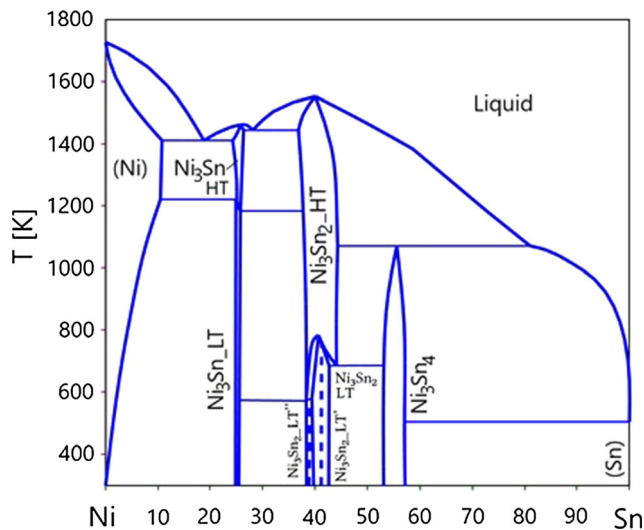


Fig. 2 Experimental Ni-Sn phase diagram proposed by Schmetterer¹¹

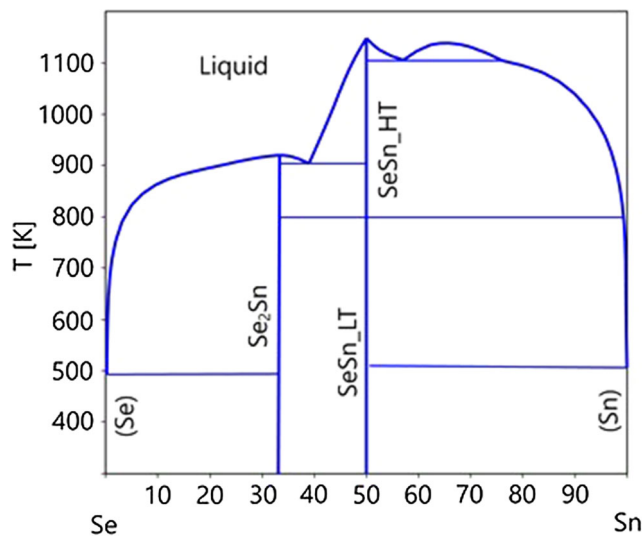


Fig. 3 Experimental Se-Sn phase diagram proposed by Feutelais et al.¹²

Se₂Sn which melt congruently at 1147 K and 930 K, respectively. The SnSe phase exists in two structural modifications, low-temperature SeSn_α phase crystallizes in GeS structural prototype (space group *Pnma*) and the high temperature SeSn_β has a CrB structural prototype with space group *Cmcm*. The polymorphic transformation temperature is 796.5 K. Se₂Sn is stoichiometric phase with CdI₂ structural prototype (space group *P-3m1*) (Fig. 3)

1.4 Ternary System Ni-Se-Sn

The Ni-Se-Sn ternary phase diagram has been investigated relatively little in the past. The existence and structure of

the ternary phase $\text{Ni}_{5.62}\text{SnSe}_2$ (space group $I4/mmm$) was described by Baranov et al.¹³ Crystal structure of the ternary phase $\text{Ni}_{5.62}\text{SnSe}_2$ was determined by single crystal XRD, detailed crystal structure parameters are listed in their paper. Musa and Chen¹⁴ have studied the interfacial reaction in the Ni/SnSe couple. They found ternary phase $\text{Ni}_{5.62}\text{SnSe}_2$ and two new ternary phases, Ni_3SnSe and NiSnSe . The Ni/SnSe couple was annealed at temperature of 573 K for 360 h. The entire reaction couple was not in thermodynamic equilibrium, but they proposed that all the interfaces could be valid because the tie-lines in the two-phase regions could be found by following the reaction path. Based on these results the isothermal section of phase diagram at 573 K was constructed.

Table 1 summarizes the stable and metastable phases reported for the Ni-Se-Sn system and its binary subsystems, including their structure and temperature ranges of existence.

2 Experimental

The overall compositions of the experimental samples were chosen with the goal to address the open questions in existing experimental datasets mentioned above. Furthermore, our aim was to determine as complete as possible the isothermal phase diagram sections for the selected

temperatures. The prepared samples were analyzed and characterized by different static and dynamic analytical methods.

2.1 Sample Preparation

Elements Se, Sn and Ni of high purity 99.999% were used for the sample preparation. Weighed pieces of pure elements, sealed in evacuated quartz glass ampoules to prevent evaporation of selenium, were heated to several temperatures ranging from 673 to 1073 K in 100 K increments. In doing so, selenium and tin were gradually mixed to raise the boiling point of the alloy (958 K). This step was necessary to decrease the amount of evaporated selenium during nickel melting. To mix nickel with selenium and tin, the samples were melted in an arc melting furnace under an argon atmosphere. Arc melting was repeated three times to achieve sample homogeneity. The prepared samples underwent long-term annealing at selected temperatures afterwards. The length of the long-term annealing was chosen with respect to the selected temperatures, with the aim to reach the state close to thermodynamic equilibrium. The precise length of annealing is shown in Table 2. Heat treatment was completed by quenching the samples in cold water.

Table 1 Intermetallic phases in the ternary system Ni-Se-Sn

Phase name	Person symbol	Space group	Structure type	<i>T</i> range, K	References
Ni_3Se_2 _LT	<i>hR5</i>	<i>R32</i>	Ni_3S_2	< 878	3, 5
Ni_3Se_2 _HT	<i>c**</i>	n.a.	n.a.	863-1058	5
Ni_6Se_5	<i>oC48</i>	<i>Cmcm</i>	Ni_6Se_5	673-920	5, 8
NiSe	<i>hP4</i>	<i>P6_3/mmc</i>	NiAs	< 1232	4
NiSe_2	<i>cP12</i>	<i>Pa3</i>	FeS_2	< 1129	9
<i>Ni₃Se₄</i>	<i>mC14</i>	<i>C2/m</i>	<i>Ni₃Se₄</i>	<i>metastable phase</i>	3
<i>α'-Ni₃Se₂</i>	<i>tI**</i>	n.a.	n.a.	<i>metastable phase</i>	6
Ni_3Sn _HT	<i>cF16</i>	<i>Fm-3 m</i>	BiF_3	1184-1462	11
Ni_3Sn _LT	<i>hP8</i>	<i>P6_3/mmc</i>	Mg_3Cd	< 1221	11
Ni_3Sn_2 _HT	<i>hP6</i>	<i>P6_3/mmc</i>	Ni_2In	573-1553	11
Ni_3Sn_2 _LT	<i>oP20</i>	<i>Pnma</i>	Ni_3Sn_2	< 781	11
Ni_3Sn_2 _LT'	n.a.	<i>Cmcm</i>	incnom.	< 753	11
Ni_3Sn_2 _LT''	n.a.	<i>Cmcm</i>	incnom.	< 573	11
Ni_3Sn_4	<i>mC14</i>	<i>C2/m</i>	Ni_3Sn_4	< 1071	11
SeSn_α	<i>oP8</i>	<i>Pnma</i>	GeS	< 796.5	15
SeSn_β	<i>oC8</i>	<i>Cmcm</i>	CrB	796.5-1147	16
Se_2Sn	<i>hP3</i>	<i>P-3m1</i>	CdI_2	< 930	11
$\text{Ni}_{5.62}\text{SnSe}_2$	n.a.	<i>I4/mmm</i>	n.a.	< 1100	[13, this work]
<i>Ni₃SnSe</i>	n.a.	n.a.	n.a.	...	14
<i>NiSnSe</i>	n.a.	n.a.	n.a.	...	14

n.a. Stands for "Not available", Metastable phases are in italics

2.2 Experimental Phase Diagram Investigation

A combination of dynamic and static methods was used to investigate the phase diagram. Samples were cut into the several pieces and adjusted for the above-mentioned experimental program. The largest piece was cast in resin and metallographically ground and polished with OPS suspension for scanning electron microscopy (SEM). A smaller piece of the samples was ground in a mortar to a fine powder and further used for x-ray diffraction (XRD). Another piece of the samples was sealed in special quartz glass ampoules for differential thermal analysis (DTA). The rest of the samples was stored for further investigation or result confirmation. The microstructure and overall chemical phase composition were studied using scanning electron microscopy with energy dispersive x-ray spectroscopy (SEM-EDX). The JEOL JSM-6460 or Tescan LYRA 3 XMH FEG/SEM devices were used for these measurements. Identification of the phases present in the samples was done by x-ray powder diffraction using XRD EMPYREAN device and $\text{CoK}\alpha$ radiation. The measured patterns were interpreted using the HighScore Plus SW and ICSD databases and Rietveld analysis.

Annealing times and temperatures for each sample, their overall composition, coexisting phases, and particular phase compositions after annealing are listed in Table 2. The first column gives the annealing temperature and identification number of the sample. The second column shows the annealing time. The overall composition measured by SEM-EDX area scan is listed in the third column. The measured area was chosen with respect to experimental conditions to obtain consistent results. The fourth column shows coexisting stable phases present in the annealed samples. The chemical compositions of the stable phases in the samples are listed in the last three columns in the same order as in the fourth column.

Differential thermal analysis (DTA) was used to determine temperatures of the phase transitions in the samples. They were placed in sealed and evacuated quartz glass DTA ampoules. Sealed ampoules were used to prevent uncontrolled evaporation of highly volatile selenium. The DTA measurements were performed by high-temperature calorimeter NETZSCH Pegasus 404 C. Calibration of the DTA analysis is based on measurement of a set of metal standards with well-defined melting temperatures (Sn, Al, Zn, Cu, Ag, Au) at the same conditions as the experimental measurements. Three heating and cooling runs were used for each sample.

3 Results and Discussion

The experimental results obtained for the long-annealed samples presented in Table 2 allow us to propose isothermal sections of the ternary Ni-Se-Sn phase diagram at 800 K, 1000 K and 1100 K. The constructed sections are discussed below. Phase boundaries which are not defined by experimental results, are estimated based on binary subsystems and thermodynamic and phase rules and are indicated by dashed lines.

3.1 Isothermal Section at 800 K

Eight binary phases were found stable in the isothermal section of the Ni-Se-Sn phase diagram at 800 K. Due to the volatility of selenium, the stability of the Se_2Sn phase was not experimentally confirmed in our samples, because the final composition of neither sample lies in the region where its existence was assumed, but we propose the shape of the relevant phase fields in accordance with the Se-Sn binary phase diagram. A metastable binary phase Ni_3Se_4 , most likely stabilized by the third element, was observed. The amount of dissolved tin in the Ni_3Se_4 phase was only about 0.5 at.% Sn, nevertheless it was enough for its stabilization. This conclusion is consistent with information in the literature.³ Hiller and Wegener³ report that the Ni_3Se_4 phase is not stable in a binary Ni-Se alloy, but even small amounts of impurities can stabilize it. This should be even more true in the case of Sn serving as the impurity, as the crystal structures of Ni_3Se_4 and Ni_3Sn_4 are identical. This pseudobinary phase is labeled $\text{Ni}_3\text{Se}_4(\text{T})$ in the following text.

Selected characteristic microstructures found at 800 K are shown in Fig. 4(a, b). Solubility of up to 10 at.% of tin was observed in binary phase NiSe and the boundary of the single-phase region was established with reasonable precision. Figure 4(a) shows a micrograph of the sample 800K_1 in back-scattered electron (BSE) mode. This sample contains two phases, NiSe and pseudobinary phase $\text{Ni}_3\text{Se}_4(\text{T})$, stabilized by tin. According the XRD analysis the phase NiSe_2 is present in this sample as well (ca. 13% of the amount of sample), but unfortunately, we did not identify this phase in section of the sample studied by SEM. The microstructure of the sample 800K_8 in BSE mode consisting of the NiSe + Ni_3Sn_2 + ternary phase $\text{Ni}_{5.62}\text{SnSe}_2$ is shown in Fig. 4(b).

Although the whole composition range of the section at 800 K was studied, only one stable ternary phase, $\text{Ni}_{5.62}\text{SnSe}_2$, was found with a small region of solubility. We have not found the other proposed ternary phases Ni_3SnSe and NiSeSn .¹⁴ The present experiments were carried out at higher temperatures than those used by Musa and Chen,¹⁴

Table 2 Phase composition of long-term annealed representative samples analyzed by SEM- EDX

T [K]_No.	Anneal. time , h	Overall composition, at.%			Proposed stable phases	Phase composition, at.%		
		Ni	Se	Sn		Ni	Se	Sn
800K_1	2784	19.1	53.8	27.1	Ni ₃ Se ₄ (T)	41.5	58.3	0.2
					SeSn_β	1.2	49.4	49.4
					NiSe ₂	*	*	*
800K_2	2784	35.7	39.2	25.1	Ni ₃ Sn ₂	57.9	0.6	41.5
					SeSn_β	2.1	48.7	49.1
					NiSe	45.8	43.9	10.3
800K_3	2784	11.2	14.2	74.5	SeSn_β	0.0	48.9	51.1
					liq. (Sn)	0.7	0.0	99.3
					Ni ₃ Sn ₄	41.9	0.1	58.0
800K_4	2784	76.7	14.8	8.5	Ni _{5.62} SnSe ₂	65.4	22.2	12.4
					Ni	97.2	0.8	2.0
					Ni ₃ Sn_LT	74.7	1.7	23.6
800K_5	2784	32.7	49.8	17.5	SeSn_β	2.7	48.3	49.0
					NiSe(sol.)	46.8	50.4	2.8
					Ni ₃ Se ₄ (T)	40.9	58.7	0.4
800K_6	2784	18.8	54.8	26.4	SeSn_β	1.4	49.6	49.0
					NiSe ₂	31.6	68.1	0.3
					Ni _{5.62} SnSe ₂	65.0	23.9	11.1
800K_7	1825	66.2	28.6	5.2	Ni ₃ Se ₂ _LT	58.7	41.1	0.2
					Ni	99.3	0.2	0.5
					Ni _{5.62} SnSe ₂	63.1	24.3	12.6
800K_8	1825	52.1	30.4	17.5	NiSe	47.4	48.0	4.6
					Ni ₃ Sn ₂	58.7	0.4	40.9
					Ni _{5.62} SnSe ₂	63.3	24.5	12.2
800K_9	1825	53.9	36.4	9.7	NiSe	48.3	46.9	4.8
					Ni ₃ Sn ₂	59.3	3.2	37.4
					Ni _{5.62} SnSe ₂	63.3	24.5	12.2
1000K_1	1775	15.4	2.6	82.0	Li _q (Sn)	0.5	0.4	99.1
					SeSn_β	0.1	44.4	55.5
					NiSn	42.9	0.4	56.7
1000K_2	1775	82.9	11.3	5.8	Ni _{5.62} SnSe ₂	65.3	23.4	11.3
					Ni	98.0	0.2	1.8
					Ni ₃ Sn ₂	58.7	0.4	40.9
1000K_3	1005	1.7	56.7	41.6	SeSn_β	0.7	51.5	47.8
					liquid	0.6	64.7	34.7
					NiSe ₂	34.1*	61.0*	4.9*
1000K_4	1005	60.6	25.4	14.0	Ni _{5.62} SnSe ₂	62.0	26.0	12.0
					Ni ₃ Sn ₂	59.6	0.3	40.1
					Ni ₃ Se ₂	57.4	42.4	0.2
1000K_5	1005	60.7	37.6	1.7	Ni _{5.62} SnSe ₂	64.6	24.3	11.1
					Ni	98.3	0.2	1.5
					Ni ₃ Sn ₂	58.1	0.0	41.9
1000K_6	1005	46.4	21.6	32.0	SeSn_β	2.0	50.0	48.0
					NiSe(sol.)	44.4	41.2	14.4
					Ni _{5.62} SnSe ₂	64.5	23.4	12.1
1000K_7	1295	62.2	26.6	11.2	Ni ₃ Sn ₂	*	*	*
					NiSe	*	*	*
					Ni _{5.62} SnSe ₂	64.5	23.4	12.1
1000K_8	1295	52.3	30.7	17.0	Ni ₃ Sn ₂	59.0	0.3	40.7
					Ni _{5.62} SnSe ₂	55.2	37.6	7.2
					Ni ₃ Se ₂	57.4	42.4	0.2

Table 2 continued

T [K]_No.	Anneal. time , h	Overall composition, at.%			Proposed stable phases	Phase composition, at.%		
		Ni	Se	Sn		Ni	Se	Sn
1000K_9	1295	49.1	39.0	11.9	NiSe	48.6	42.8	8.6
					NiSe	48.5	39.7	11.8
1000K_10	1295	26.7	60.4	12.9	Ni ₃ Sn ₂	58.2	0.5	41.3
					Liquid	31.5	68.4	0.1
					SeSn_β	0.6	50.4	49.0
1100K_1	1179	73.5	17.0	9.5	NiSe ₂	31.0	68.9	0.1
					Ni ₃ Sn_LT	74.4	0.0	25.6
					Ni	91.2	0.2	8.6
					Liquid	61.0	37.3	1.7
1100K_2	1179	58.5	25.3	16.2	Ni ₃ Sn ₂	60.9	0.4	38.7
					Ni ₃ Sn	73.8	0.0	26.2
					Liquid	58.5	34.9	6.6
1100K_3	1179	35.8	8.1	56.1	Ni ₃ Sn ₂	54.5	0.1	45.4
					Liquid	13.2	15.0	71.8
1100K_4	1179	86.4	11.5	2.1	Ni	97.4	0.1	2.5
					Liquid	59.8	38.7	1.5
1100K_5	1179	26.5	34.6	38.9	Ni ₃ Sn ₂	57.4	0.1	42.5
					Liquid	16.9	38.3	44.8
1100K_6	1222	9.1	47.1	47.1	Liquid	9.1	47.1	47.1
1100K_7	673	59.4	1.1	39.5	Ni ₃ Sn ₂	59.6	0.2	40.2
					NiSe	51.7	41.2	7.1
1100K_8	673	50.0	38.7	11.3	Ni ₃ Sn ₂	**	**	**
					NiSe	47.7	46.5	5.8

*Measurement uncertain because of morphology or size of the particle

**Not measurable

so these phases may only be stable at lower temperatures or the samples of Musa and Chen¹⁴ were not sufficiently equilibrated. Selenium and tin are already molten at 800 K. The XRD pattern of sample 800K_1 containing reasonable amount of the pseudobinary Ni₃Se₄(T) phase is shown in Fig. 5(a), where also the binary phases NiSe₂ and SeSn_α were found. XRD measurements showed the structure of the SeSn_α (*Pnma*) phase in all samples, although at a temperature of 800K and higher, the SeSn_β phase is stable according to the Se-Sn binary phase diagram (see Fig. 3). This discrepancy is probably caused by the difficulty quenching the high-temperature SeSn_β phase. The authors believe that, although the SeSn_β phase was not observed directly in the experiment, it is not possible to stabilize the SeSn_α phase by a very small presence of third element so that would it be stable instead of the HT phase even at the temperature 1100 K and, therefore, the thermodynamically stable high-temperature phase is the

SeSn_β phase in accordance with the binary phase diagram existed in the samples prior to quenching. Figure 5(b) represent the XRD pattern of sample 800K_8.

Figure 6 shows an isothermal section of the experimental Ni-Se-Sn phase diagram at 800K, the overall composition of the samples measured by SEM is indicated: Two-phase samples are marked by rectangle, three-phase samples by triangle. The assumed phase composition of the binary phases is given by a solid circle on the corresponding binary edges. Thick solid lines show the experimental phase boundaries, the dashed lines represent phase boundaries estimated from phase diagrams rules and thermodynamic laws. Thin solid lines are the tie-lines of the corresponding sample.

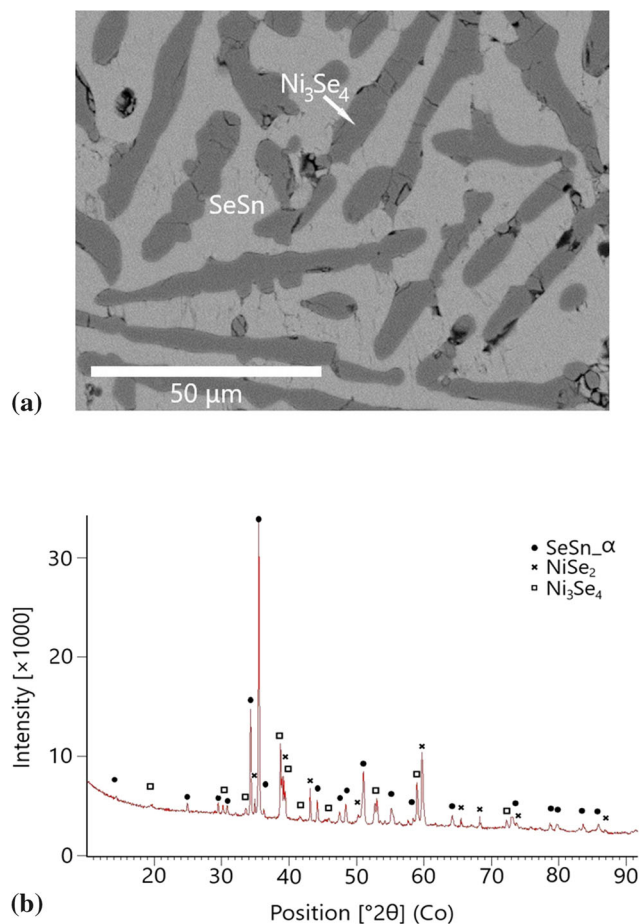


Fig. 4 Microstructure of the samples in BSE mode (a) 800K_1 (b) 800K_8

3.2 Isothermal Section at 1000 K

The Ni-Se-Sn phase diagram isothermal section at 1000 K looks like the isothermal section at 800 K described in previous chapter. Binary phase NiSe contains about 15 at.% of the tin in its structure.

The effort to prepare bulk sample that would describe the phase field containing the Ni₃Se₄(T) phase at 1000 K was not successful. Therefore, the powder prepared from sample 800K_1 containing SeSn_α, Ni₃Se₄(T) and Ni₃Se₂ phases was used and annealed again at 1000 K, nevertheless the XRD analysis showed the coexistence of too many phases (including SeSn_α, NiSe, Ni₃Sn₂, Se₂Sn and traces of Ni₃Se₄(T)) which does not satisfy the Gibbs phase rule. This sample is clearly not in thermodynamic equilibrium because each grain in the powder was stabilized in its own non-equilibrium thermodynamic state. This finding suggests that the phase equilibrium between the two temperatures has changed, and we believe that the existence of the Ni₃Se₄(T) phase cannot be confirmed at 1000 K. With respect to the small amount of the phase found it can be

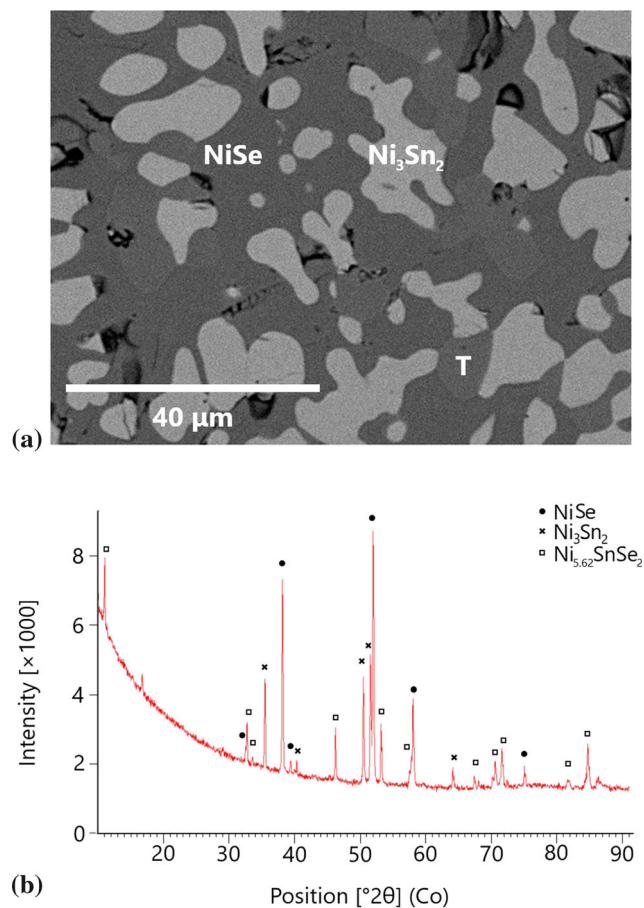


Fig. 5 XRD patterns of the samples (a) 800K_1, consists of patterns of SeSn_α, Ni₃Se₄(T) and NiSe₂ (b) 800K_8, consists of NiSe, Ni₃Sn₂ and Ni_{5.62}SnSe₂

assumed that it will eventually dissolve at this temperature in a state closer to thermodynamic equilibrium. It would be useful to re-examine the Ni-Se binary phase diagram in a follow-up study to confirm the nature of the Ni₃Se₄ binary phase.

The ternary phase Ni_{5.62}SnSe₂ is found to be stable at 1000 K with a small but not negligible homogeneity region. The microstructure of the 1000K_2 sample in BSE mode is shown on Fig. 7(a) and contains solid solution of (Ni) and ternary phase. Fig. 7(b) shows a micrograph of the sample 1000K_6 in BSE mode. This sample consists of three phases: NiSe + Ni₃Sn₂ and SeSn_β. Figure 8 XRD pattern of the sample 1000K_2, consists of Ni_{5.62}SnSe₂, Ni and one more phase which was not identified. It should be the Ni₃Se₂HT phase structure of which is not known according to the best of our knowledge. The isothermal section of the Ni-Se-Sn phase diagram at 1000K is shown in Fig. 9.

Fig. 6 Isothermal section of the experimental phase diagram Ni-Se-Sn at 800K with superimposed overall compositions of two-phase samples (rectangle) and three-phase samples (triangle)

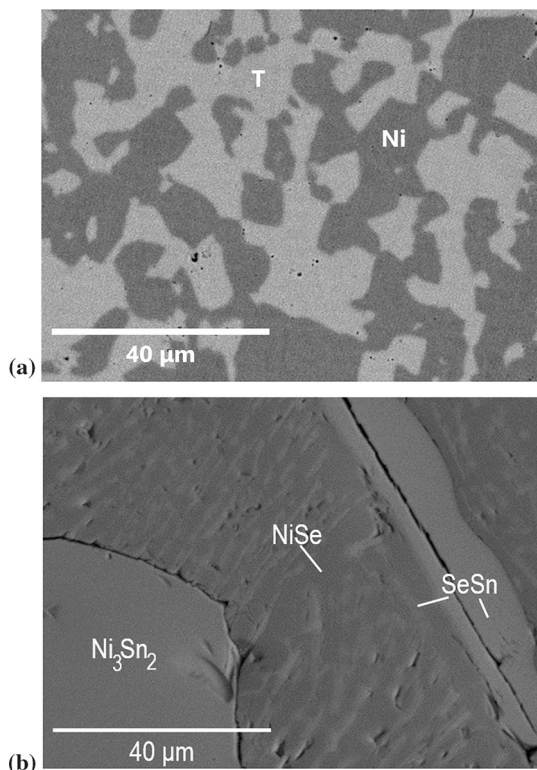
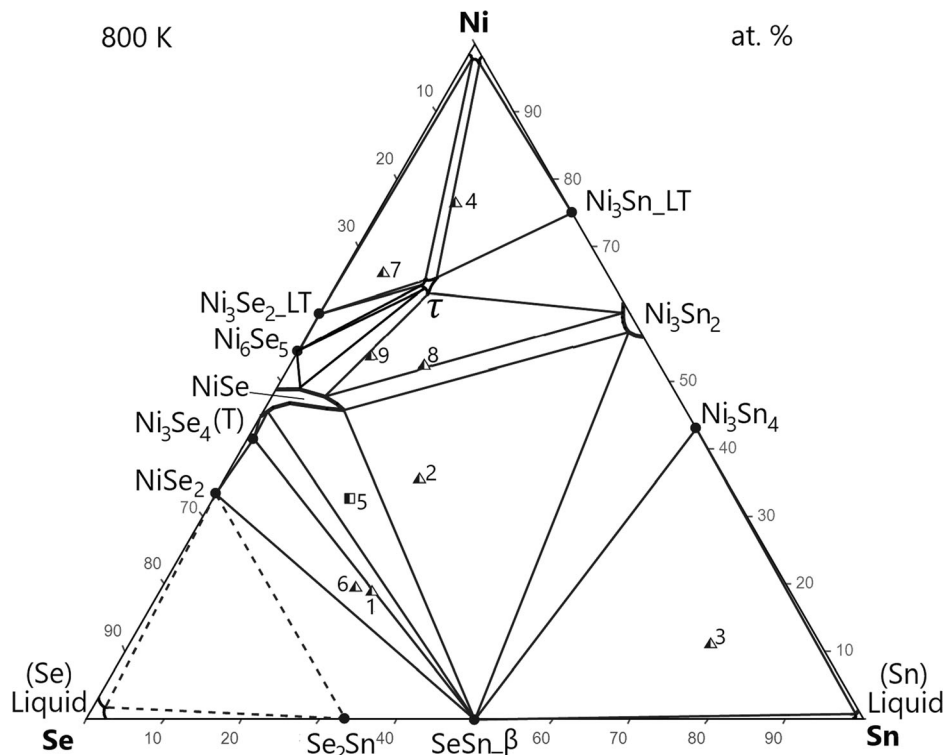


Fig. 7 Microstructure of the samples in BSE mode (a) 1000K_2 (b) 1000K_6

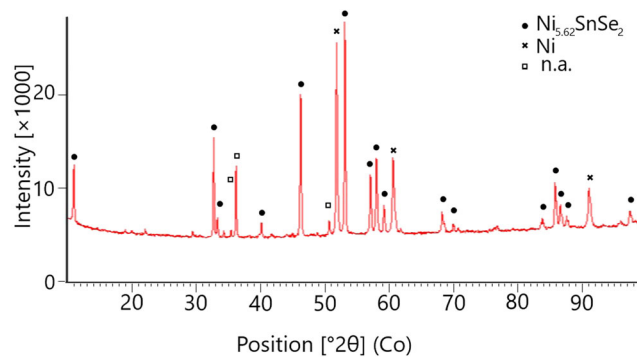
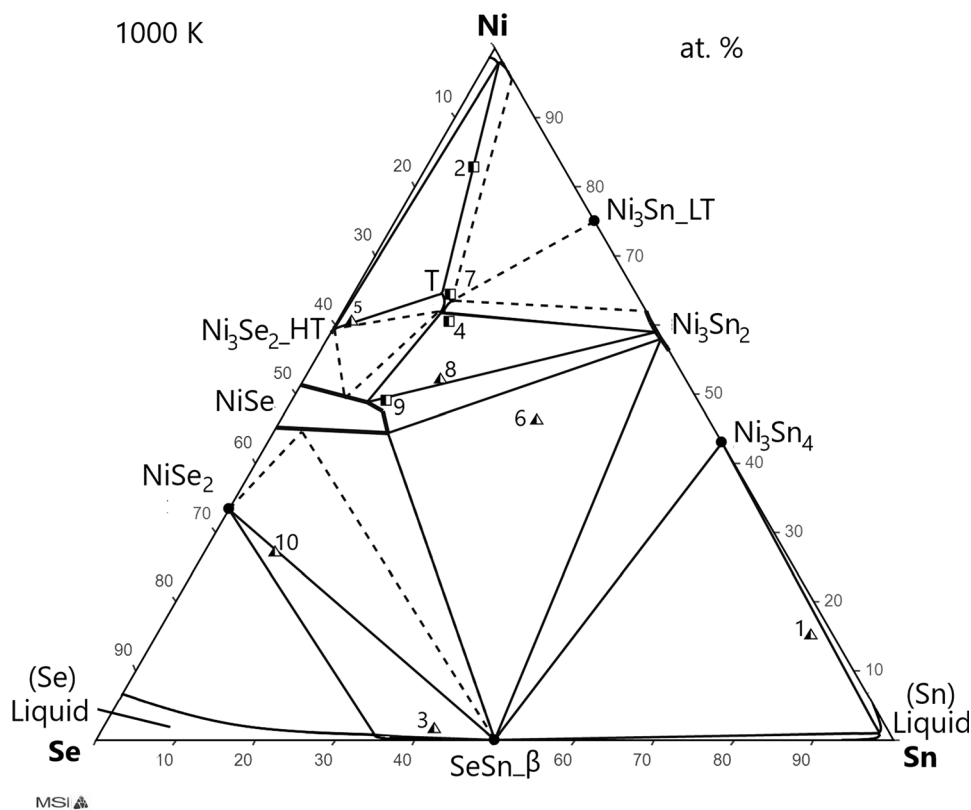


Fig. 8 XRD pattern of the sample 1000K_2, consists of Ni_{5.62}SnSe₂, Ni and one more phase which is not identified. It should be the Ni₃Se₂_HT the structure of which is not known

3.3 Isothermal Section at 1100 K

The highest temperature at which the thermodynamic equilibrium in the Ni-Se-Sn phase diagram was studied was 1100 K. The selenium-rich part of the phase diagram cannot be analyzed due to the high volatility of selenium. The Ni content is approx. 17 at.% in liquid selenium and 8 at.% in liquid tin. The latter value is better supported by the experimental results. The NiSe phase shows 8% tin solubility. The eutectic liquid at approximately 30% of Se according to the Ni-Se binary phase diagram dissolves up to 7 at.% of tin. All other binary phases have negligible solubilities for the third element and can be considered as stoichiometric. No ternary phase was found at 1100 K. The

Fig. 9 Isothermal section of the experimental phase diagram Ni-Se-Sn at 1000K with superimposed overall composition of two-phase samples (rectangle) and three-phase samples (triangle)



microstructure of sample 1100K_1 consists of Ni + Ni₃Sn + solidified liquid phase is shown in Fig. 10a. Figure 10b shows a micrograph of sample 1100K_3 in BSE mode consisting of Ni₃Sn₂ and solidified liquid phase. The solidified liquid phase is made up of SeSn_α and Sn phases, which were formed during solidification. The XRD pattern of the sample 1100K_3 consisting of Ni₃Sn₂, Sn and SeSn_α phases is presented in Fig. 11. The SeSn_α and Sn phases were formed during solidification. The constructed isothermal section of the Ni-Se-Sn phase diagram at 1100K is shown in Fig. 12.

3.4 Thermal Analysis

Differential thermal analysis (DTA) was used to experimentally determine the phase transition temperatures in the samples. The analyses were performed in a NETZSCH Pegasus 404 C DTA/DSC calorimeter. Samples to be measured were sealed in evacuated quartz glass DTA ampoule to prevent uncontrolled evaporation of volatile selenium from the sample into the calorimeter. The heating and cooling rates of each run were 5 K min⁻¹. Measurements were done under an argon flow of 50 ml min⁻¹. Three runs were performed for each sample; the thermal effects during the second and third heating run are listed in Table 3. The overall composition of the samples after the DTA measurement is given in Table 3 because of the very

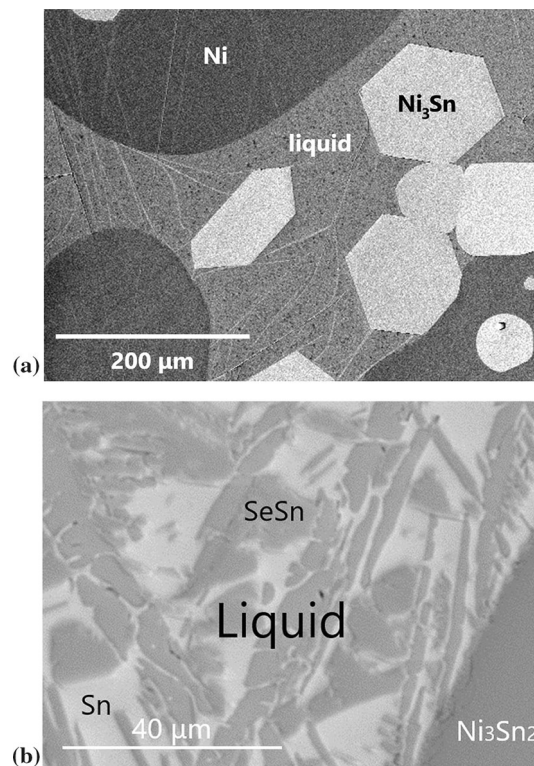


Fig. 10 Microstructure of the samples in BSE mode (a) 1100K_1 (b) 1100K_3 consist of Ni₃Sn₂ and liquid phase. The liquid phase is made up of SeSn_α and Sn phases, which were formed during solidification.

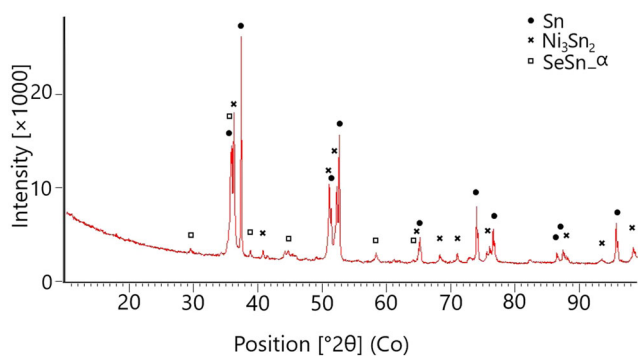


Fig. 11 XRD pattern of the sample 1100K_3, consists of Ni_3Sn_2 , Sn and SeSn_α phases. The SeSn_α and Sn phases were formed during solidification

high volatility of selenium a new equilibrium between the solid and gas phase was established during the measurement. Temperature of phase transition in solid phase was evaluated as an onset of peak, liquidus was evaluated as a minimum of a peak or the break on the curve. The DTA curves of the second and third heating run of the sample 800K_3 is presented in Fig. 13.

Fig. 12 Isothermal section of the experimental phase diagram Ni-Se-Sn at 1100K with superimposed overall composition of two-phase samples (rectangle) and three-phase samples (triangle)

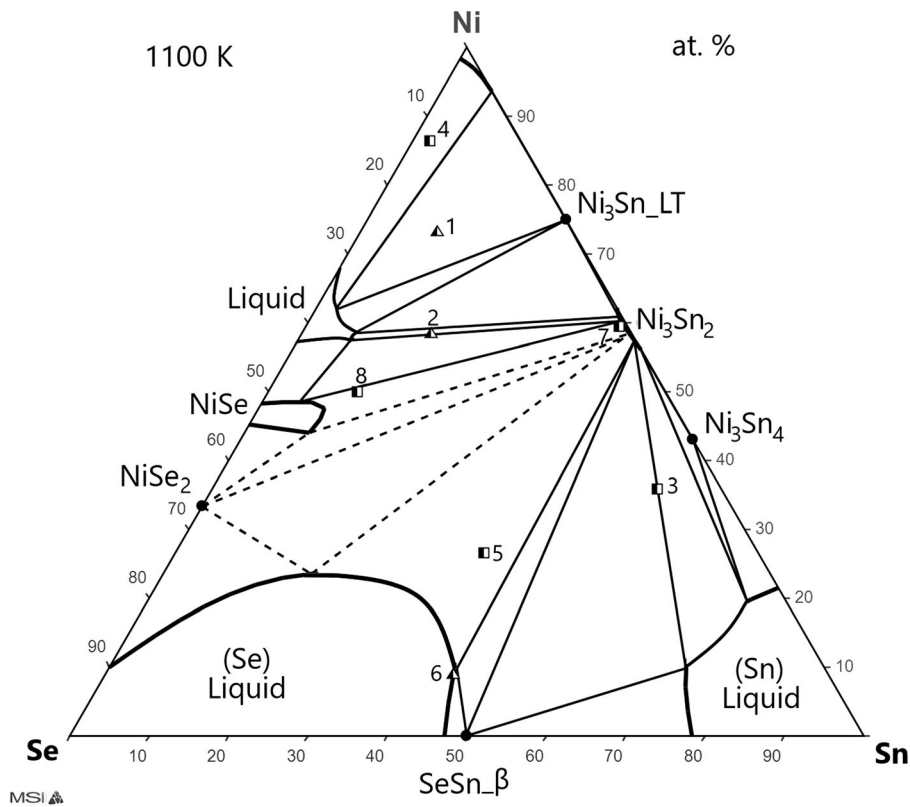
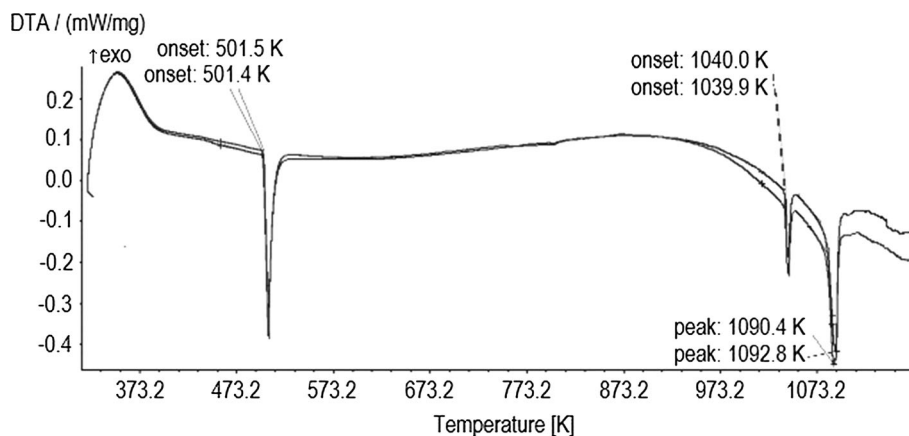


Table 3 DTA signal of selected samples

Sample	Composition after DTA measurement			Liquidus temperature, K	Invariant temperature, K	Other reaction, K
	Ni	Se	Sn			
800K_2	38.5	37.3	24.2	> 1173.2	969.8	776.2; 1000.2
800K_3	9.9	16.0	74.1	1091.6	501.5; 1040.0	
800K_4	74.4	17.4	8.2	> 1173.2	872.5; 1017.5	514.2; 853.2, 1096.7
800K_5	42.4	52.3	5.3	1109.2	966.0	1048.0
800K_6	22.5	57.8	19.7	1065.2	1040.8	564. 4; 927.6;

Fig. 13 The second and third DTA heating curve of the sample 800K_3. Measurement conditions: Sample was placed in sealed evacuated quartz-glass ampoule, measurement under argon flow atmosphere of 5N Ar 50 ml min⁻¹, heating, and cooling rate 5 K min⁻¹.



4 Conclusion

Although an isothermal section of the Ni-Se-Sn phase diagram at 573 K has recently been published,¹⁴ some complex phase equilibria have not been well described. Therefore, the aim of this work was focused on a better understanding of phase equilibria at higher temperature, especially with respect to the phase equilibria with ternary phases.

Three ternary phases were described in literature¹⁴ as stable at 573K. Our experimental studies were carried out at temperatures 800K, 1000 K and 1100 K and isothermal sections of ternary Ni-Se-Sn phase diagram were obtained by a combination of several analytical methods: Overall and phase compositions of samples were measured using SEM-EDX, the temperatures of phase transitions by DTA measurements in evacuated quartz-glass DTA ampoules and the crystal structures were identified by XRD. Following results were obtained in this work:

- Only one ternary phase (Ni_{5.62}SnSe₂) was found to be stable at temperatures 800 K and 1000 K. The phase was not found at 1100 K.
- Ternary phase Ni_{5.62}SnSe₂ exhibits small but non-negligible solubility around the ideal stoichiometric composition.
- Ternary phases Ni₃SnSe and NiSeSn were not found at studied temperatures.
- Metastable binary phase Ni₃Se₄ has been found to be stable at 800 K as pseudobinary phase, stabilized by small amount of Sn. This finding reasonably corresponds to the conclusions from Hiller and Wegener.³
- Only the SeSn_α (Pnma) phase was confirmed by XRD. It is probably caused by the difficulty to quench the SeSn_β phase. We propose SeSn_β phase as the thermodynamically stable phase in agreement with the binary phase diagram.

- Binary phase NiSe shows a relatively high solubility of Sn with the maximum of about 15 at.% Sn at 1000 K. The solubility is slightly smaller at 800 K (10.3 at.% Sn) and 1100 K (8.3 at.% Sn), respectively.
- Ni₃Sn₂ binary phase exhibits small Se solubility. All the other binary intermetallic phases show negligible solubility for the third element.

References

1. T.B. Massalski, Phase diagrams., In: *Encyclopedia of Materials: Science and Technology*, K.H.J. Buschow, R.W. Cahn, M.C. Flemings, B. Ilschner, E.J. Kramer, S. Mahajan, P. Veysière (eds), Elsevier Ltd, 2001.
2. F. Grønsvold, R. Møllerud, and E. Røst, The High-Temperature Phases Ni₃Se₂ and Ni₆Se₅, *Acta Chem. Scand.*, 1996, **20**, p 1997.
3. J.H. Hiller, and W. Wegener, Untersuchungen im System Nickel-Selen, *Neues Jahrb. Miner. Abh.*, 1960, **94**, p 1147–1159.
4. K. Kuznetsov, A. Eliseev, Z. Spak, K. Palkina, M. Sokolova, A. Dimitriev, *Proc. 4th All-Union Conf. Semiconductor Materials*, Moscow, USSR (1961) 159.
5. K.L. Komarek, and K. Wessely, Die Systeme Nickel-Selen und Kobalt-Nickel-Selen, *Monatsh. Chem.*, 1972, **103**, p 923.
6. S.Y. Lee, P. Nash, Ni-Se (nickel-selenium), in: “*Phase Diagrams of Binary Nickel Alloys*”, P. Nash (ed.), ASM International, Materials Park, Ohio (1991)
7. B. Predel, Ni-Se (Nickel-Selenium) Landolt-Börnstein - Group IV Physical Chemistry 5I (Ni-Np – Pt-Zr), O. Madelung (ed), Springer 1998
8. G. Åkesson, and E. Røst, A Superstructure of Ni₆Se₅, *Acta Chem. Scand. Ser. A*, 1975, **29**, p 236.
9. F. Grønsvold, and E. Jacobsen, X-ray and Magnetic study of Nickel Selenides in the Range NiSe and NiSe₂, *Acta Chem. Scand.*, 1956, **10**, p 1440.
10. O. Zbac, K. Buchlovska, J. Pavlu, and A. Kroupa, Thermodynamic Description of Binary System Nickel-Selenium, *J. Phase Equilib. Diffus.*, 2021, **42**, p 468–478.
11. C. Schmetterer, H. Flandorfer, K.W. Richter, U. Saeed, M. Kauffman, P. Roussel, and H. Ipsier, A New Investigation of the System Ni-Sn, *Intermetallics*, 2007, **15**, p 869–884.
12. Y. Feutelais, M. Majid, B. Legendre, and S.G. Fries, Phase Diagram Investigation and Proposition of a Thermodynamic

- Evaluation of the Tin-Selenium System, *J. Phase Equilib*, 1996, **17**, p 40–49.
13. A.I. Baranov, A.A. Isaeva, L. Kloo, V.A. Kulbachinskii, R.A. Lunin, V.N. Nikiforov, and B.A. Popovkin, 2D Metal Slabs in New Nickel–tin chalcogenides Ni₇– δ SnQ₂ (QSe, Te): Average Crystal and Electronic Structures, Chemical Bonding and Physical Properties, *J. Solid State Chem.*, 2004, **177**, p 3616–3625.
 14. A.F. Musa, and S.-W. Chen, Interfacial Reactions in Ni/Se-Sn, Ni/Se-Te, Ni/Sn-Te and Ni/Se-Sn-Te Couples, *J. Electron. Mater.*, 2021, **50**, p 4346–4357.
 15. H. Wiedemeier, and H.G. von Schnering, Refinement of the Structures of GeS, GeSe, SnS and SnSe, *Z. Kristallogr.*, 1978, **148**, p 295–303.
 16. H. Wiedemeier, and E.J. Csillag, The Thermal Expansion and High Temperature Transformation of SnS and SnSe, *Z. Kristallogr.*, 1979, **149**, p 17–29.

Publisher's Note Springer Nature remains neutral with regard to jurisdictional claims in published maps and institutional affiliations.

Springer Nature or its licensor (e.g. a society or other partner) holds exclusive rights to this article under a publishing agreement with the author(s) or other rightsholder(s); author self-archiving of the accepted manuscript version of this article is solely governed by the terms of such publishing agreement and applicable law.

6.11 Paper 11

- [P11] Kroupa A., **Zobač O.**, Zemanová A., Richter K.W., *CALPHAD-Type Reassessment of Cu-Si and Full Assessment of the Al-Cu-Si Systems*, Journal of Phase Equilibria and Diffusion, 2024, doi: 10.1007/s11669-024-01160-5. (IF 1.4)



CALPHAD-Type Reassessment of Cu-Si and Full Assessment of the Al-Cu-Si Systems

Ales Kroupa¹ · Ondrej Zobac¹ · Adela Zemanova¹ · Klaus W. Richter²

Submitted: 26 March 2024 / in revised form: 2 October 2024 / Accepted: 7 October 2024
© The Author(s) 2024

Abstract The theoretical assessment of the Al-Cu-Si was carried out in this work based on recent experimental studies (Riani et al. in *Intermetallics*, 17:154-164, 2009; He et al. in *CALPHAD*, 33:200-210, 2009. <http://dx.doi.org/10.1016/j.calphad.2008.07.015>; Ponweiser N and Richter KW in *J. of Alloys and Compd*, 512:252-263, 2012; Hallstedt et al. in *CALPHAD*, 53:25-38, 2016; Zobac et al in *J Mater Sci*, 55:5322-15333, 2020). The reassessment of the Cu-Si system was also carried out in the scope of this work, as experimental data indicates reasonable solubility of Al in all intermetallic phases in the Cu-Si binary system, and the stoichiometric models used in previous assessments of the Cu-Si binary system are not fully suitable for the extension into the ternary system. Excellent agreement was reached for the reassessment of the Cu-Si system with previous works, and new original results were obtained during the assessment of the ternary system. The high solubility of Si in the β (bcc) phase at high temperatures was modelled to explain experimental inconsistencies in the Cu-rich corner between 600 and 800 °C, and this assumption was confirmed experimentally. All main

features of the experimental Al-Cu-Si phase diagram were reproduced well by theoretical modelling.

Keywords γ -brass phase · Al-Cu-Si phase diagram · CALPHAD · Critical reassessment · Cu-Si

1 Introduction and Literature Review

Phase diagrams are important for the development of new materials and for an understanding of their properties. Detailed knowledge about the coexistence and stability of phases in stable or metastable equilibrium significantly rationalizes such design and consequent development of desired materials properties. As the experimental studies of multicomponent phase diagrams are very time consuming and the extent of experimental work might be overwhelming, the theoretical modelling of multicomponent phase diagrams is a very useful tool for materials development.

The Al-Cu-Si ternary system has been intensively studied in recent decades due to its importance in practice. Due to their low density and good material properties, Al-Cu-Si alloys are increasingly important for the automotive and aerospace industries. Despite of this industrial significance, there are not many experimental studies devoted directly to the thermodynamic equilibria and phase diagrams of this ternary system^[1-4] (see section 1.4).

Therefore, existing experimental data from literature and our recently published experimental study about phase equilibria in the Al-Cu-Si system^[5] were used to perform a new CALPHAD type thermodynamic assessment of the Cu-Si and Al-Cu-Si system. A detailed literature review of

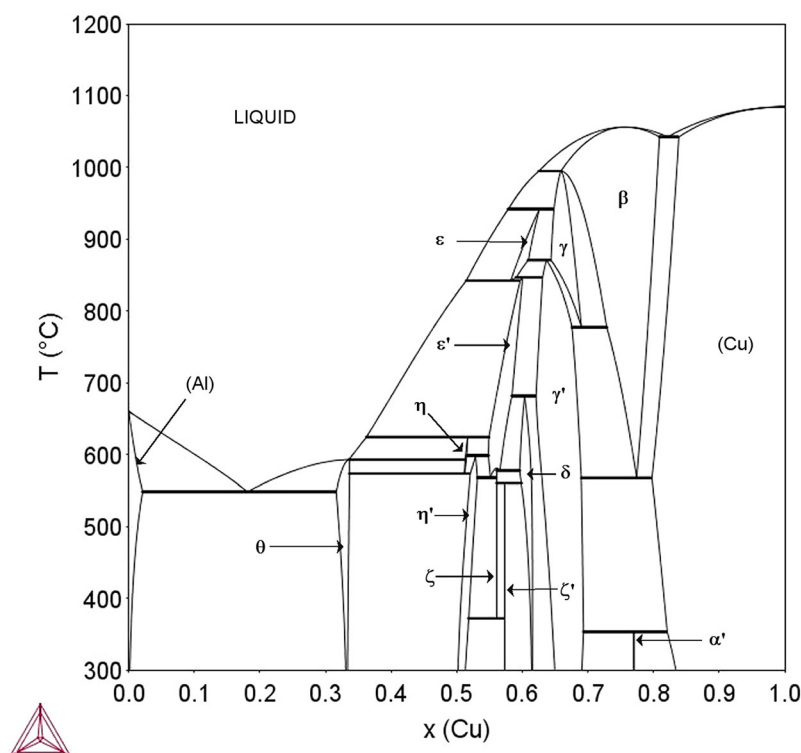
This invited article is part of a special tribute issue of the *Journal of Phase Equilibria and Diffusion* dedicated to the memory of Mats Hillert on the 100th anniversary of his birth. The issue was organized by Malin Selleby, John Ågren, and Greta Lindwall, KTH Royal Institute of Technology; Qing Chen, Thermo-Calc Software AB; Wei Xiong, University of Pittsburgh; and *JPED* Editor-in-Chief Ursula Kattner, National Institute of Standards and Technology (NIST).

✉ Ales Kroupa
kroupa@ipm.cz

¹ Institute of Physics of Materials, Czech Academy of Sciences, Žitkova 22, 616 00 Brno, Czech Republic

² Department of Functional Materials and Catalyst, University of Vienna, Währinger Straße 42, 1090 Vienna, Austria

Fig. 1 Calculated binary phase diagram of subsystem Al-Cu reprinted from our previous work^[7]



existing phase diagram information on Al-Cu-Si and its binary subsystems is given below.

1.1 Al-Cu Binary System

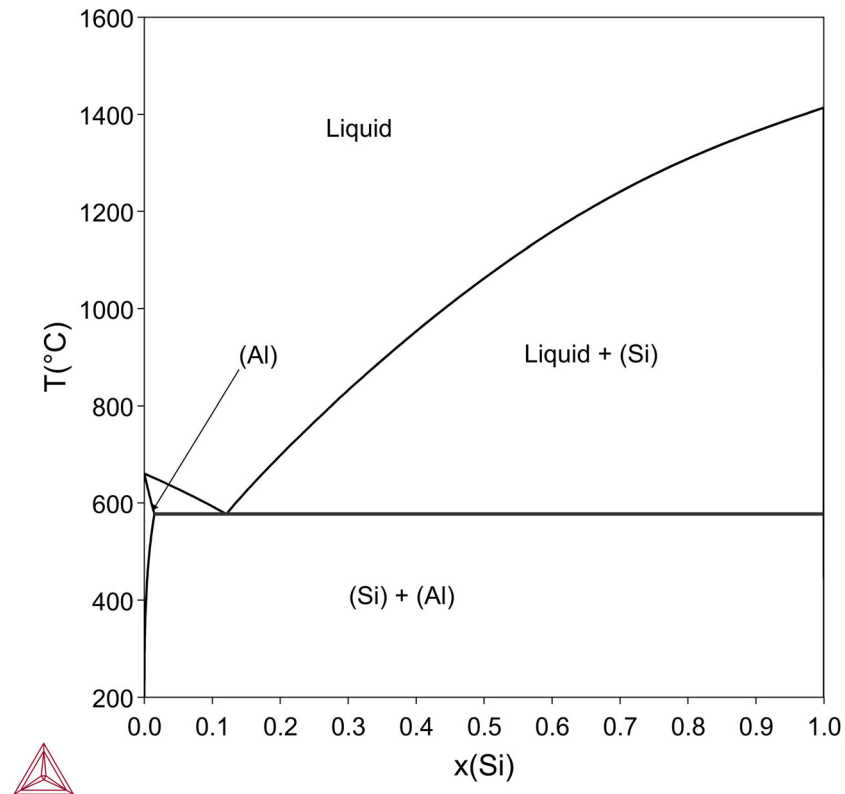
The Al-Cu phase diagram exhibits a wide range of intermetallic phases with complex mutual relationships in all regions of the phase diagram. A detailed literature review of experimental data is published in our previous works.^[6,7]

The maximal solid solubility of Cu in Al is equal to 2.5 at.% Cu at the eutectic temperature of 550 °C.^[8] The crystal structure of the θ -phase was determined as having the space group $I4/mcm$ by Havinga.^[9] Ponweiser *et al.*^[10] studied the homogeneity ranges of the η -family of phases by scanning electron microscopy with energy dispersive x-ray analysis (SEM-EDX) and x-ray diffraction (XRD) and found that the low-temperature η' -phase extends from 51.9 Cu to 54.8 at%. The orthorhombic η -phase is formed by peritectic reaction at 620 °C. Gulay and Harbrecht^[11,12] describe the structures of the ζ -family of phases with the supposed low temperature modification ζ' (Al_3Cu_4) and high temperature modification ζ ($\text{Al}_3\text{Cu}_{4-\delta}$) in detail. The ε -family of phases exists over a similar composition range as

the ζ -phases at medium and high temperatures.^[8] The γ' (AlCu) (γ - Al_4Cu_9 brass type structure, $cP52$) to δ (AlCu) transition was addressed by the combined EDX/XRD investigation and the shape of the ($\gamma' + \delta$) two-phase field was postulated from the XRD studies of quenched samples in our previous work.^[6] Liu *et al.*^[13] found that the high temperature phase labelled γ (AlCu) crystallizes in the γ - Cu_5Zn_8 brass type ($cI52$) structure and there is a second-order transition reaction between the crystallographically related phases γ' and γ . The β -phase decomposes by a eutectoid reaction to (Cu) solid solution and the γ' -phase at a temperature of 567 °C and melts congruently at 1049 °C according to.^[14] The α' phase with a composition of 77.5 at.% Cu is stable below 363 °C.^[15] The maximal solubility of Al in Cu is 18.5 at.% at the eutectoid temperature of 567 °C.^[8]

The first significantly simplified thermodynamic description of the Al-Cu system was done by Kaufman and Nesor.^[16] Later, further work on the improvement of the Al-Cu phase diagram and the development of a more accurate thermodynamic and structural description of relevant phases was based on the comprehensive work of Murray,^[8] who presented a very detailed overview of existing experimental data and combined this with own

Fig. 2 Theoretical phase diagram calculated using data from COST507^[13]



calculations. Further progress in the field of modelling was presented by Chen *et al.*^[17] Nevertheless, the assessment of the Al-Cu system carried out by Saunders and published in the public COST507^[18] database has been most widely used and accepted in many multicomponent databases later on. The thermodynamic descriptions of the liquid and γ -brass family of phases were reassessed by Witusiewicz *et al.*^[14] A further theoretical assessment was presented by Liang and Schmid-Fetzer,^[19] who based their work on the assessment of Murray^[8] and the newer experimental results of Ponweiser *et al.*^[10] The most recent theoretical reassessment was published by the authors of this study in,^[7] which is based on their own experimental results^[6] and the results of.^[10] Mainly, the less known and ambiguous parts of the Al-Cu system were studied in this work^[6] and new results on stable and metastable transition temperatures and ordering reactions were presented. The binary phase diagram assessed by Kroupa *et al.*^[7] is shown in Fig. 1.

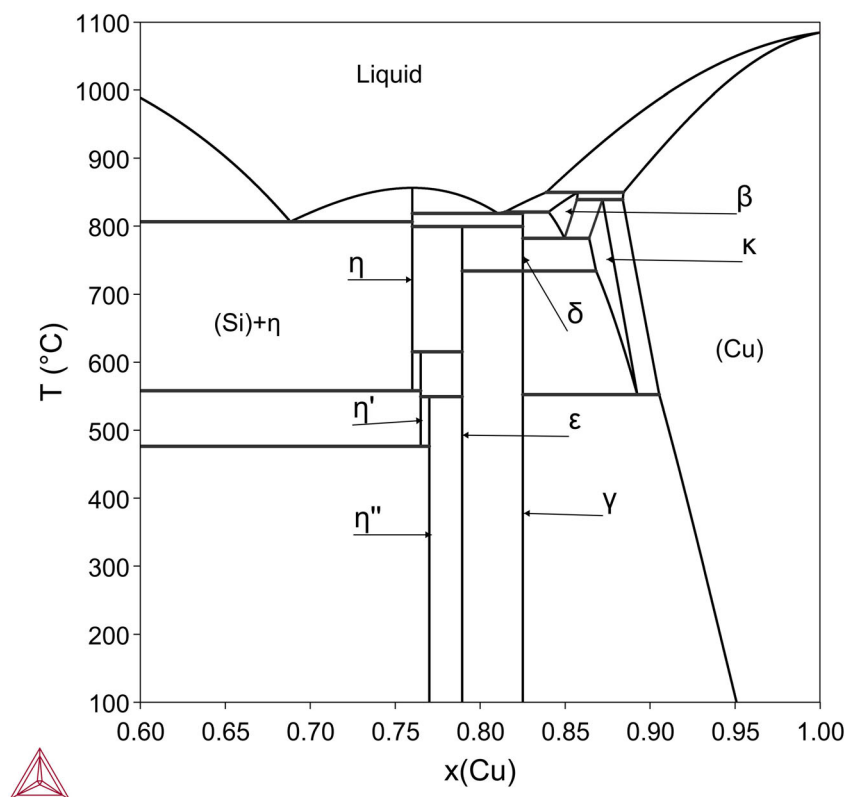
1.2 Al-Si Binary System

Dörner *et al.*^[20] and Murray and McAllister^[21] presented the early theoretical assessments of the Al-Si phase diagram. Subsequently, the phase diagram of the Al-Si system was re-adjusted using newer phase stability data and experimental results by Chakraborti and Lukas,^[22] and the resulting thermodynamic assessment was published by Gröbner *et al.*^[23] Al-Si is a simple eutectic system with two solid solution phases, fcc_A1 (Al) and diamond_A4 cubic (Si) (see Fig. 2). The composition of the eutectic point is Al-12.2 at.% Si, and the eutectic temperature is 577 °C (Fig. 3).

1.3 Cu-Si Binary System

The Cu-Si system was investigated intensively in the last decades due to the possible development of new types of

Fig. 3 Calculated binary phase diagram Cu-Si based on dataset from Hallstedt^[4]



Li-ion batteries,^[24] applications in catalysis^[25] and microelectronic research.^[26]

From the experimental point of view, Olesinski and Abbaschian^[27] gave an overview of existing experimental results and assessed the well accepted Cu-Si phase diagram in 1986. Later, Sufryd *et al.*^[28] published the most recent experimental study of the Cu-rich part of the phase diagram, where solubilities of some intermetallic phases were described, and the temperatures of phase transformations were studied.

All the intermetallic phases exist in the Cu-rich part of the phase diagram. The Cu_3Si family of phases consist of three different modifications with slightly different compositions stable over different temperature ranges. The high-temperature Cu_3Si modification is denoted as $\eta(\text{CuSi})$, an intermediate-temperature phase as $\eta'(\text{CuSi})$ and a low-temperature phase as $\eta''(\text{CuSi})$. The high-temperature η phase melts congruently at 859 °C. A first order phase transformation is supposed to occur between all Cu_3Si modifications, with two phase fields existing between 558 and 620 °C for $\eta(\text{CuSi})$ and $\eta'(\text{CuSi})$ phases, and between 467 and 570 °C for $\eta'(\text{CuSi})$ and $\eta''(\text{CuSi})$

phases. The Cu_3Si phases η and η' have a rhombohedral structure ($R\bar{3}m$ and $R\bar{3}b$ respectively). No exact information about the crystal structure of η'' exists, it was proposed to have an orthorhombic^[29] or tetragonal symmetry.^[30]

The existence of the stoichiometric intermetallic phase $\text{Cu}_{15}\text{Si}_4$ ($\epsilon(\text{CuSi})$ phase) was intensively discussed in the literature.^[31] The existence of this phase was first described by Arrhenius and Westgren.^[32] Later experimental works^[33,34] based on diffusion-couple experiments did not confirm the existence of $\epsilon(\text{CuSi})$ in the stable phase diagram. Sufryd *et al.*^[28] proposed that the formation of ϵ is kinetically inhibited, but it is thermodynamically stable in the Cu-Si system.

The $\text{Cu}_{33}\text{Si}_7$ -LT ($\gamma(\text{CuSi})$ phase) has a cubic structure ($\beta\text{-Mn}$). According to,^[28] it transforms by a congruent transformation at approximately 735 °C into the high temperature $\delta(\text{CuSi})$ phase modification, but the extent of the solubility of the low temperature phase has not yet been precisely determined. According to Shi *et al.*^[35] and Oleshinski and Abbaschian,^[36] the transition temperatures between high temperature $\text{Cu}_{33}\text{Si}_7$ -HT ($\delta(\text{CuSi})$ phase) and

Table 1 List of phases present in the Al-Cu-Si system

Names used in the paper	Phase name in database	Other common names	Pearson symbol	Structure type
(Al)	FCC_A1	(Al), fcc_A1	<i>cF4</i>	Cu
(Cu)	FCC_A1	(Cu), fcc_A1	<i>cF4</i>	Cu
(Si)	DIAMOND_A4	(Si)	<i>cF8</i>	C
θ	THETA	θ , Al ₂ Cu	<i>tI12</i>	Al ₂ Cu
η (AlCu)	ETA_ALCU	η , η_1 , η_{HT}	<i>oP16/oC16</i>	n.a.
η' (AlCu)	ETA_PRIME	η' , η_2 , η_{LT}	<i>mC20</i>	AlCu
ζ	ZETA	ζ , ζ_2 Al ₃ Cu _{4-δ}	<i>Imm2</i>	Al ₃ Cu _{4-δ}
ζ'	ZETA_PRIME	ζ' , ζ_1 -Al ₃ Cu ₄	<i>Fmm2</i>	Al ₃ Cu ₄
ε (AlCu)	BCC_A2	ε , ε_1 , ε_{HT}	<i>cubic?</i>	n.a.
ε' (AlCu)	EPS_PRIME	ε' , ε_2 , ε_{LT}	<i>hP4</i>	NiAs
δ (AlCu)	DELTA_ALCU	δ , Al ₅ Cu ₈	<i>hR52</i>	Al ₄ Cu ₉ (r)
γ (AlCu)	GAMMA_CUZn	γ , γ_0 , γ_{CuZn} , γ_{D8_2}	<i>cI52</i>	Cu ₅ Zn ₈
γ' (AlCu)	GAMMA_ALCU	γ' , γ_1 , γ_{AlCu} , γ_{D8_3}	<i>cP52</i>	Al ₄ Cu ₉
β (AlCu)	BCC_A2	β , bcc_A2	<i>cI2</i>	W
α' (AlCu)	ALPHA2_ALCU	α' , α_2 , α_{LT}	n. a.	Super structure based on TiAl ₃
γ (CuSi)	CU33SI7_A13	γ_{CuSi} , CuSi_ γ Cu ₃₃ Si ₇	<i>cP20</i>	β -Mn
δ (CuSi)	CU33SI7_HT	CuSi_ δ $\delta_{Cu_{33}Si_7}$	<i>tP*</i>	n.a.
ε (CuSi)	CU15SI4_D86	CuSi_ ε Cu ₁₅ Si ₄	<i>cI76</i>	Cu ₁₅ Si ₄
η (CuSi)	CU3SI_HT	CuSi_ η Cu ₃ Si	<i>hR*</i>	Cu ₃ Si
η' (CuSi)	CU3SI_MT	CuSi_ η' Cu ₃ Si_ η'	<i>hR9</i>	η' -Cu ₃ Si
η'' (CuSi)	CU3SI_LT	CuSi_ η'' Cu ₃ Si_ η''	<i>oC*</i>	n.a.
κ (hcp)	HCP_A3	CuSi_ κ	<i>hP2</i>	Mg
β (bcc)	BCC_A2	CuSi_ β	<i>cI2</i>	W

n.a. not available.

the Cu₃₃Si₇-LT (γ (CuSi) phase) phases are 724 and 735 °C, respectively.

The β (bcc) and κ (hcp) are intermediate solution phases stable at high temperatures. The β (bcc) phase forms by the peritectic reaction from (Cu) solid solution and liquid at 852 °C and decomposes by eutectoid reaction at 785 °C. The κ (hcp) phase is formed by a peritectoid reaction from β (bcc) and (Cu) at 842 °C and decomposes at 552 °C.^[37] The δ (CuSi) phase is formed by a peritectic reaction from β (bcc) and liquid at 824 °C and transforms at 735 °C into γ (CuSi) phase).

In the theoretical field, Kaufman^[38] computed the first simplified version of the phase diagram of the Cu-Si system. A more complex description of the Cu-Si phase

diagram was produced by Bühler *et al.* and published in the COST507 database.^[39] This assessment was later improved by Yan and Chang.^[40] Gierlotka and Haque, in their theoretical assessment,^[41] modelled the γ (CuSi) phase as stoichiometric, being formed at 732 °C by peritectoid reaction $\delta + \kappa \rightarrow \gamma$. Hallstedt *et al.*^[4] made the most recent critical theoretical reassessment based on his own and previously published experimental results. Both Gierlotka and Haque^[41] and Hallstedt *et al.*^[4] accepted the conclusion made by Sufryd *et al.*^[28] about the stability of the ε (CuSi) phase and it was included in the theoretical assessment of the Cu-Si phase diagram.

Table 2 Invariant reactions (IR) in the Cu-Si system compared with theoretical and experimental data

Inv. reaction	Type of reaction	T (°C)	Composition (at.%Si)				Reference
L → η-Cu ₃ Si	congruent	856.3	24.0	24.0	[4]
		[28]
		852.7	24.1	24.1	this work
(Cu) + L → β(CuSi)	peritectic 1	849 ± 2	...	16.0	14.2	...	[28]
		849.6	11.6	16.1	14.3	...	[4]
		848.6	11.5	16.0	14.2	...	this work
		839 ± 2	...	14.5	12.5	...	[28]
(Cu) + β(CuSi) → κ(CuSi)	peritectic 2	839.1	11.6	14.3	12.8	...	[4]
		839.4	11.6	14.2	12.8	...	this work
		821 ± 2	16.5	19.2	17.5	...	[28]
β(CuSi) + L → δ	peritectic 3	820.6	16.0	18.5	17.5	...	[4]
		818.8	16.0	18.6	17.8	...	this work
L + δ → η	eutectic 1	818 ± 3	19.8	17.7	23.2	...	[28]
		818.7	19.0	17.5	24.0	...	[4]
		818.1	18.8	18.0	23.8	...	this work
L + η → (Si)	eutectic 2	807 ± 2	[28]
		806.4	31.2	24.0	100	...	[4]
		812.7	31.4	25.0	100	...	this work
δ + η → ε	peritectoid 1	800 ± 2	18.5	23.5	21.1	...	[28]
		799.2	17.5	24.0	21.1	...	[4]
		798.9	17.9	23.8	21.1	...	this work
β(CuSi) → δ + κ	eutectoid 1	781 ± 2	16.2	17.0	14.2	...	[28]
		782.0	15.0	17.5	13.6	...	[4]
		780.7	15.0	17.3	13.5	...	this work
δ + ε → κ	<i>peritectoid 2</i>	[28]
		[4]
		<i>733.8</i>	<i>17.4</i>	<i>21.1</i>	<i>17.6</i>	...	<i>this work</i>
δ → ε + γ		<i>735 ± 2</i>	<i>17.9</i>	<i>21.1</i>	<i>17.8</i>	...	[28]
		[4]
		<i>this work</i>
δ → γ		[28]
		<i>734.2</i>	<i>17.5</i>	<i>17.5</i>	[4]
		<i>this work</i>
δ → γ + κ	eutectoid 2	734 ± 2	16.9	17.5	13.2	...	[28]
		[4]
		731.9	17.2	17.5	13.1	...	this work
ε + η → η'	peritectoid 3	618 ± 3	21.1	24.2	24.2	...	[28]
		615.0	21.1	24.0	23.5	...	[4]
		613.8	21.1	23.9	23.6	...	this work
η → η' + (Si)	eutectoid 3	555 ± 3	26.0	26.0	100	...	[28]
		557.9	24.0	23.5	100	...	[4]
		558.4	24.9	24.5	100	...	this work
ε + η' → η''	peritectoid 4	570 ^a	21.1	24.4	24.4	...	[28]
		549.1	21.1	23.5	23.0	...	[4]
		548.9	21.1	23.6	23.6	...	this work
κ → γ + (Cu)	eutectoid 4	552 ^a	[28]
		552.3	10.8	17.5	9.5	...	[4]
		555.9	10.5	17.2	9.3	...	this work
η' → η'' + (Si)	eutectoid 5	467 ^a	[28]
		476.3	23.5	23.0	100	...	[4]
		469.2	24.5	24.4	100	...	this work

^aExperimental value from literature

IRs written in italics are different in different literature

1.4 Al-Cu-Si Ternary System

The ternary system Al-Cu-Si was first studied by Matsuyama^[42] and Hisatsune^[43] in the 1930s. Both authors used the thermal analysis and studied the thermal arrest signals to identify the phase transformations. Matsuyama^[42] also used the electrical resistance method and microscopical examination. Hisatsune^[43] measured the overall composition of all samples “by analysis”, no other details were given in his paper. They described the phases present in the binaries and information on invariant ternary equilibria including the liquidus surface projection. Several isopleths of in Al-Cu-Si were studied by Phillips.^[44] Lukas and Lebrun^[45] collected all relevant phase diagram information up to the year 2005 and carried out an assessment of the phase diagram information. They identified no ternary intermetallic phases at that time. These works were summarized in the review paper by Raghavan^[46] in 2007.

Later, Riani *et al.*^[1] determined the isothermal section at 500 °C for the whole composition range, with special attention to Cu-rich alloys and He *et al.*^[2] experimentally studied the isotherms at 500 and 600 °C.

More recently, Ponweiser and Richter^[3] studied isothermal phase equilibria at 500 and 700 °C. A ternary high-temperature phase τ was found to exist in the 700 °C section. The β (bcc) phase, which was reported in the Al-Cu subsystem, was omitted in their isothermal section. It was clearly an error when drawing the isothermal section as negligible solubility of Si in this phase at this temperature was expected. They studied the isopleths for 40 and 10 at.% Si and presented a full isopleth for 40 at.% Si. The isopleth for 10 at.% Si shows significant inconsistency in the Cu-rich region, where the authors failed to describe the phase equilibria at temperatures between 500 and 800 °C consistently with the phase equilibria result for the isotherms at 500 and 700 °C. They also assessed the reaction sequences in the Cu-rich part of the ternary Al-Cu-Si system.

The most recent results of the Al-Cu-Si phase diagram experimental study focused mostly on the equilibria in the Cu-rich corner, were presented in our previous paper.^[5] Here the isothermal sections at 600 and 800 °C were studied and several distinctive features not identified in previous works were described. Significant solubility of Al was found in the high temperature δ (CuSi) phase which reaches approximately 6–8 at.%. Also the η , η' -Cu₃Si phases exhibit solubility of Al at a level of several at.%. The presumed ternary τ phase described by Ponweiser and Richter^[3] at 700 °C was identified as the high temperature δ (CuSi) phase in this paper.^[5] It is stabilized by the Al content at lower temperatures where it exists in equilibrium with low temperature modification γ (CuSi). Also, a significantly higher solubility of Al was found in the κ (hcp)

phase at both studied temperatures. Except of these two findings, the rest of the Cu-rich corner phase diagram is consistent with the results presented by Ponweiser and Richter,^[3] Riani *et al.*^[1] and He *et al.*^[2] for isothermal sections at various temperatures.

Only one study reports thermodynamic data for the Al-Cu-Si system, namely enthalpies of mixing at 1575K for three different sections (Al_xSi_{1-x} - Cu, x = 0.2, 0.5, 0.8) which were measured by Witusiewicz *et al.*^[47]

The first attempt of a theoretical assessment was carried by Pan *et al.*,^[48] who focused on an optimization of the experimental thermodynamic data in the Al-rich liquid phase. They computed a liquidus projection and vertical sections depicting the liquid-solid equilibria and compared these results with the experimental data. This work was also included in the paper of Raghavan.^[46]

The first full thermodynamic assessment of the Al-Cu-Si system was presented by He *et al.*^[2] supported by their own experimental results. Nevertheless, they used simplified models for the family of γ -brass phases in their theoretical assessment, and these models do not allow to model Cu-rich γ' (AlCu) phase, which was confirmed by above mentioned experimental works, including their own.

Hallstedt *et al.*^[4] published the most recent theoretical description of the Al-Cu-Si system, but they specified that they did not carry out a complete assessment but just a preliminary study which reasonably describes the main features of the available experimental isothermal and iso-composition sections. Their work also contains a very detailed description of the experimental results available at the time of its publication.

A list of all phases present in the ternary system is given in Table 1. There is a significant number of phases in this ternary system stemming from the Al-Cu and Cu-Si binary subsystems with similar crystal structures, compositions and common names. Therefore, their unambiguous names used in the scope of this paper are presented in the column 1 of Table 1. Other common names, the names used in the thermodynamic database and their crystallographic characterizations are in adjacent columns.

2 Thermodynamic Modelling

The semiempirical CALPHAD approach^[49,50] was used for thermodynamic modelling and calculation of the phase diagram. This approach is based on the theoretical modelling of thermodynamic equilibria starting with binary systems using reliable and consistent phase and thermodynamic experimental data to obtain a consistent set of thermodynamic parameters. These thermodynamic datasets of relevant binary systems are then combined to model ternary and higher order systems, using again available

experimental data. Additional ternary and higher order (if necessary) thermodynamic parameters are used to describe the difference between the phase diagrams calculated using just the parameters from binary systems and the experimental data.

The compositions of phases in equilibrium correspond to the total minimum Gibbs energy of a closed system at constant temperature and pressure. Calculations were done using Thermo-Calc^[51] and Pandat^[52] software which solve the constrained minimization problem to determine the set of non-negative number of individual components in equilibrium phases. The Gibbs energies are considered relative to the Standard Element Reference state (SER) at 298.15 K and 1 bar. The Gibbs energy data for the pure elements were taken from the SGTE database for pure elements ver. 5.0.^[53]

2.1 Solution Phases

The Gibbs energy of the substitutional solid solution is mostly modelled by a substitution model with one sublattice, which assumes the mixing of three elements Al, Cu and Si. For the thermodynamic description of the molar Gibbs energy of the liquid phase, the substitution solution model is also used.

The Gibbs energy of the solution phase α is expressed as follows

$$G_m^\alpha(T, x^\alpha) = {}^0G_m^\alpha(T) + {}^{id}G_m^\alpha(T, x^\alpha) + {}^E G_m^\alpha(T, x^\alpha) \quad (\text{Eq 1})$$

where the first term is the reference molar Gibbs energy, ${}^0G_m^\alpha(T)$, which is calculated as the weighted sum of the Gibbs energies of the constituent i of the system in the crystal or liquid phase α with respect to the above-mentioned reference state.

The second term in (Eq. 1) is the contribution to the total Gibbs energy resulting from the ideal mixing of the components in the lattice, where n is the number of components (Eq. 2).

$${}^{id}G_m^\alpha = RT \sum_{i=1}^n x_i \cdot \ln(x_i) \quad (\text{Eq 2})$$

The third term, the Gibbs excess energy, ${}^E G_m^\alpha$, describes the effect of the non-ideal behaviour of the system on the thermodynamic properties of the phase and is given by the Redlich-Kister-Muggianu formalism.^[54,55]

$${}^E G_m^\alpha = \sum_{\substack{i,j=1 \\ i \neq j}}^n x_i x_j \sum_{z=0}^m {}^z L_{i,j}(x_i - x_j) + \sum_1^{n-2} \sum_{j=i+1}^{n-1} \sum_{k=j+1}^n x_i \cdot x_j \cdot x_k \cdot L_{i,j,k} \quad (\text{Eq 3})$$

where ${}^z L_{i,j}$ is a temperature-dependent binary interaction parameter describing the interaction between components i and j and $L_{i,j,k}$ is an interaction parameter describing the possible ternary interactions. This temperature dependence is usually defined as follows:

$$L(T) = a + bT + cT \ln(T) \quad (\text{Eq 4})$$

This substitutional model was used to model the **LIQUID** phase in this work in the form **(Al,Cu,Si)₁**.

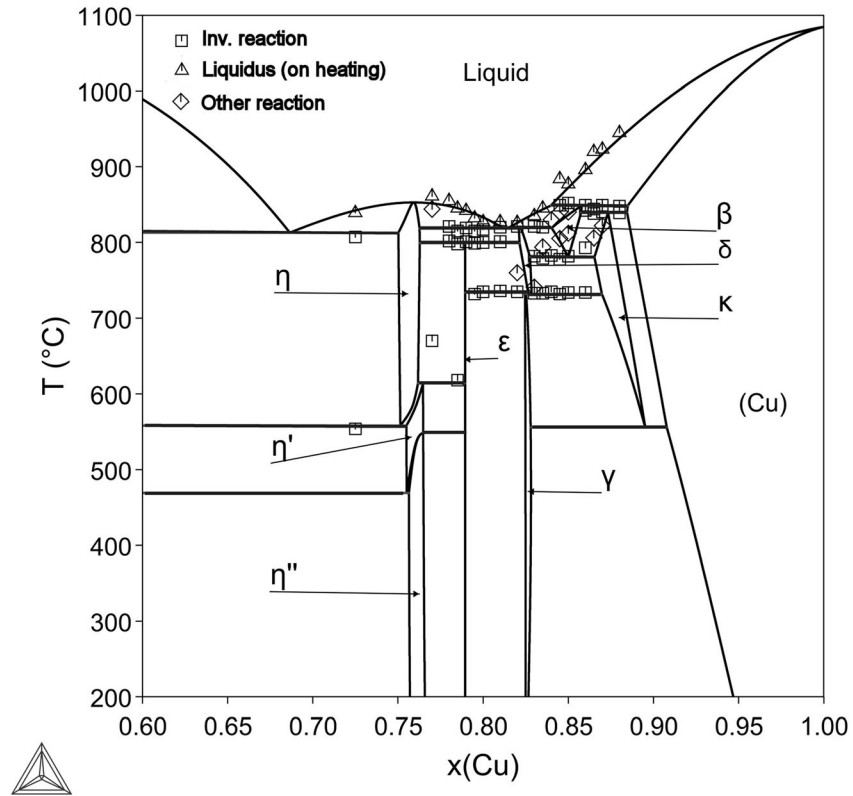
The terminal solid solution phases, existing in the system as (Al), (Cu) with fcc_A1 structure, can be modelled with the substitutional solid solution model described above. Nevertheless, to keep the consistency with other thermodynamic datasets and multicomponent databases, this solid solution is modelled using two-sublattice model, used mainly for interstitial solid solutions. Here first sublattice of the model is identical with above described model and is occupied by elements located in substitutional positions in the crystal structure. The second lattice is usually partly occupied by elements like C or N located in interstitial positions, the rest of the sublattice is empty (occupied by vacancies Va). As there are no interstitial elements in this system, the second sublattice is empty, and the model corresponds to the one sublattice solid solution model. More details about the interstitial solid solution model can be found in.^[49,50] Therefore, the specific model for the fcc_A1 phases (Al) and (Cu) is named **FCC_A1** and defined as **(Al,Cu,Si)₁(Va)₁**.

Silicon crystallizes in diamond_A4 structure, where the solubility of other elements is negligible. In this work, the model proposed in the work of Hallstedt et al^[4] was used in the form **(Al,Si)₁(Cu,Va)₁**. The name of this phase is **DIAMOND_A4**.

In addition to the terminal solid solutions, some intermetallic phases also crystallize in the hcp_A3 and bcc_A2 structures. Here, the substitutional model can be used as described above, but again, for consistency reasons, the two-sublattice model for interstitial solid solutions is used for these phases. Therefore, the ϵ (AlCu), β (AlCu), β (CuSi) are modelled as **(Al,Cu,Si)₁(Va)₃** using the name **BCC_A2**.

The crystal structure of the κ (hcp) phase was identified as hcp_A3, and the two-sublattice model named **HCP_A3** was used with the model **(Al,Cu,Si)₁(Va)_{0.5}**.

Fig. 4 Reassessed Cu-Si phase diagram compared with experimental data from DTA measurements from Sufryd et al.^[28]



2.2 Intermetallic Phases

The ternary Al-Cu-Si system contains many intermetallic phases with complex mutual relations and often with complex crystal structures. The Compound Energy Formalism is used to model such phases in the CALPHAD method, which is based on the existence of several sublattices with various occupancies by elements and various sizes of the sublattice. The sublattices are defined either with respect to the crystallography of the phase or the composition of the phase if the structures are unknown or too complex. The number of sublattices in a model for a given intermetallic compound is chosen taking into account the complexity of the crystal structure, the composition of the phase and the extent of mutual dissolution of the elements in the structure.

Here we present the basic principles for the case of two sublattices in the phase; details of this approach can be found for example in.^[48,49]

The reference Gibbs energy equivalent to the Eq. (1) for the two-sublattice model is given as

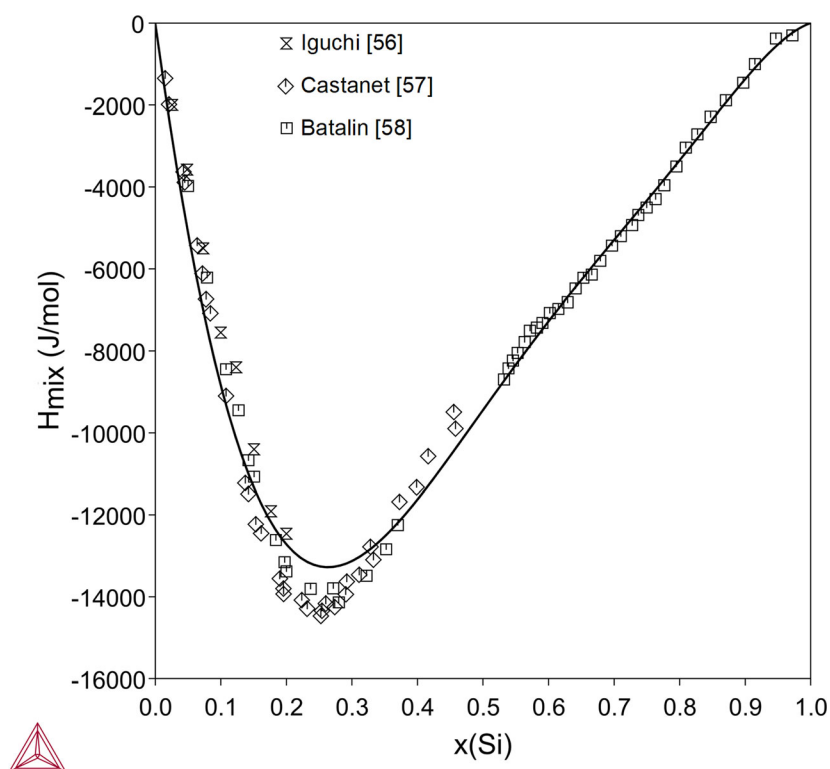
$$G_{ref}^{\phi} = \sum_{i,j}^1 y_i \cdot {}^2 y_j \cdot {}^0 G_{ij} \quad i, j = \text{Al, Cu, Si, Va} \quad (\text{Eq } 5)$$

where the term ${}^p y_i$ is the site fraction of each constituent in given sublattice p (1 or 2); $G_{(i,j)}$ is the Gibbs formation energy of 'end-member' $i:j$ or of pure element i in the crystal structure ϕ when both sublattices are occupied by the same component. Usually only a few end-member compounds exist, but reasonable Gibbs energy data for all end-members are required for theoretical modelling.

The ideal mixture term is given by

$$G_{id}^{\phi} = \sum_{p=1}^2 f_p \cdot \sum_{i=1}^n {}^p y_i \cdot \ln({}^p y_i) \quad (\text{Eq } 6)$$

Fig. 5 Enthalpy of mixing for liquid phase at 1008 °C compared with experimental data from Iguchi^[56], Castanet^[57] and Batalin.^[58] The reference states are pure liquid Cu and Si. The difference between our calculation and the calculation from Hallstedt^[4] cannot be distinguished



where f_p is the stoichiometric coefficient for sublattice p , and the second summation describes the effect of the ideal mixture in the sublattice p as in equation (2).

The simplest model to describe the contribution of excess Gibbs energy in a two-lattice model is defined as follows:

$$G_E^{\phi} = \sum^1 y_i \cdot^1 y_j \cdot^2 y_k \cdot L_{(i,j;k)} + \sum^1 y_i \cdot^2 y_k \cdot^2 y_l \cdot L_{(i;k,l)} \quad (\text{Eq 7})$$

where

$$L_{(i,j;k)} = \sum_0^z z L_{(i,j;k)} \cdot (y_i - y_j)^z \quad (\text{Eq 8})$$

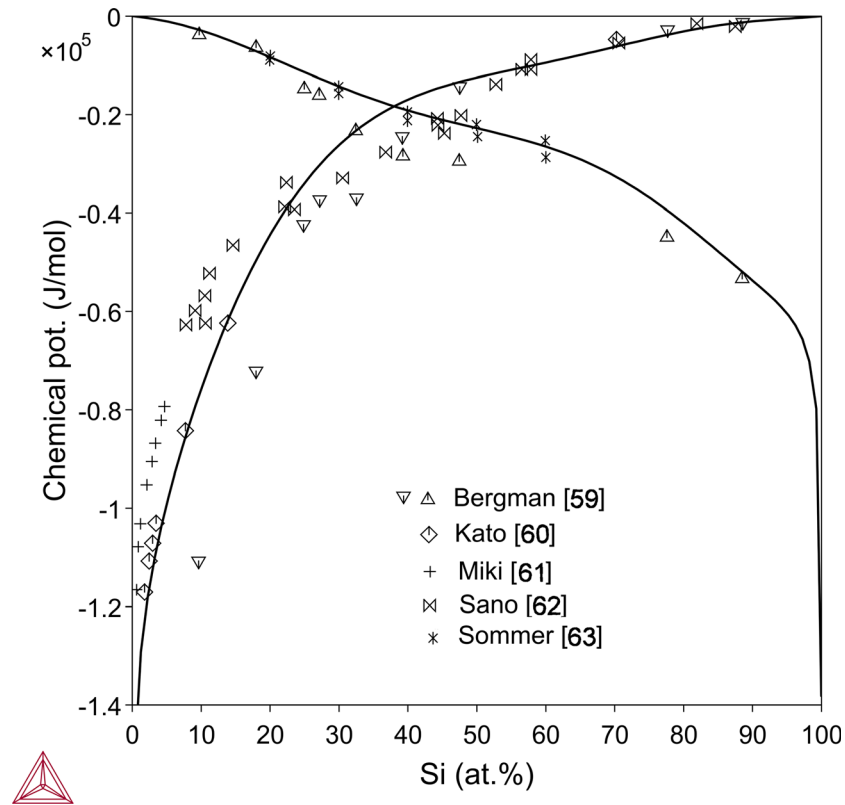
The parameter ${}^z L_{i,j;k}$ describes the interaction of components i and j in the first sublattice when the second sublattice is completely occupied by component k . This definition can be extended to any number of sublattices.

2.2.1 Models for Intermetallic Phases

The two sublattice models were used for most of intermetallic phases in the Al-Cu and Cu-Si systems. As mentioned above, there are no intermetallic phases in the Al-Si system. The solubility of third element is very small or unknown in many binary phases, especially in the Al-Cu system, therefore, the models defined in the work of Kroupa *et al.*^[7] with no assumed solubility of Si were used in such case. Limited experimental information about the $\epsilon(\text{AlCu})$ and $\delta(\text{AlCu})$ phases were obtained from the papers^[5] and^[2] where a small solubility of Si was introduced to reproduce the phase equilibrium observed there.

The only phase which exhibits great solubility of Si in the ternary system studied is $\gamma'(\text{AlCu})$. Here again the model from^[7] was used and the presence of Si was assumed in the same sublattices as Al. The information about crystal structures and the occupancies of specific positions was used for the definition of sublattice models of

Fig. 6 Calculated chemical potentials for Cu and Si in liquid phase at 1400°C compared with experimental data from.^[59-63] The reference states are pure liquid Cu and Si

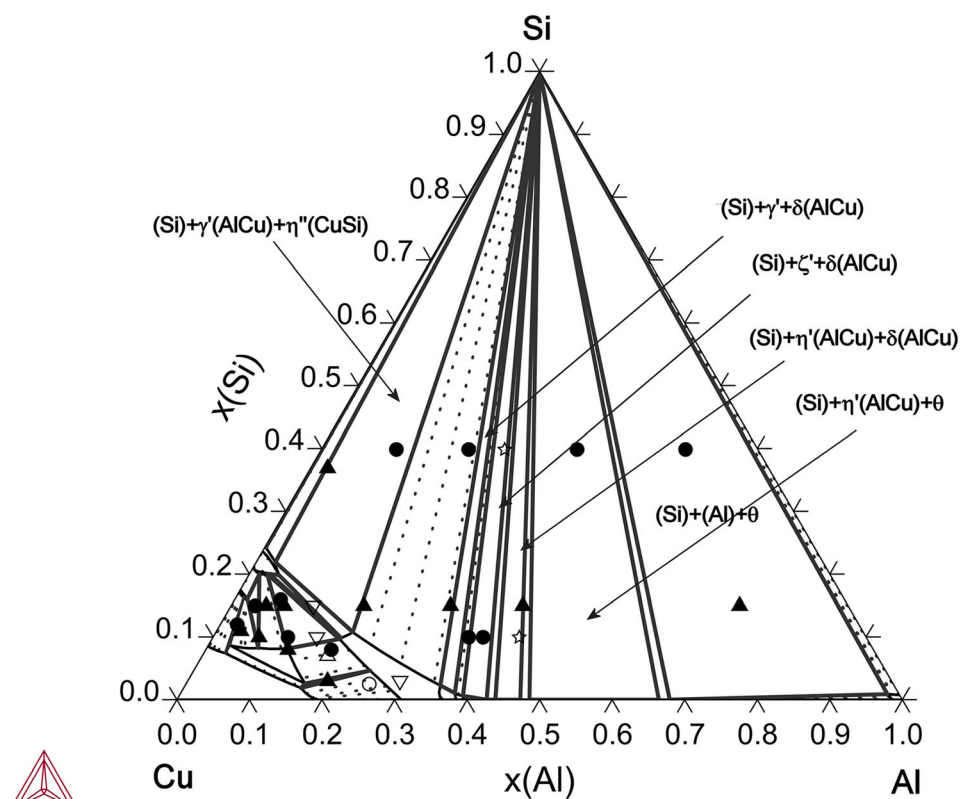


the γ -brass family phases D8₃ (γ' (AlCu), labelled **GAM-MA_ALCU**) and D8₂ (γ (AlCu), labelled **GAMMA-CUZN**). They are modelled using a four sublattice model based on their crystallography. The sublattice occupancies are defined as $(\text{Al,Cu,Si})_2(\text{Cu})_2(\text{Cu})_3(\text{Al,Cu,Si})_6$ for both low-temperature and high-temperature phases. This model was selected within the scope of the development of material specific databases as it is the most general, and it should allow to cover the known compositional ranges of all γ -brass family phases also in other nonrelated systems. The models of the binary phases for the Al-Cu subsystem (adjusted from ^[7]) are shown in Table 3.

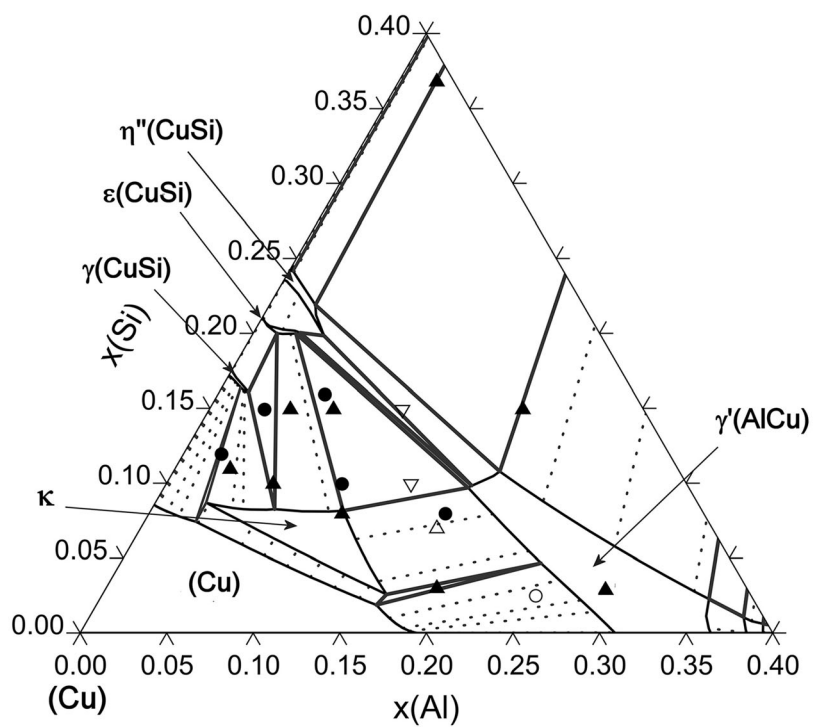
The intermetallic phases found in the binary Cu-Si system mostly exhibit small to moderate solubility of aluminium, and therefore, the models had to be adjusted to cover the experimental findings. Also, the experimental

data from^[5] indicate the need for the change of some models for binary Cu-Si phases, as the stoichiometric models used in previous Cu-Si assessments,^[4,14] especially δ (CuSi) and the family of η (Cu₃Si) phases, would be difficult to extend to ternary assessment. Therefore, the reassessment of the Cu-Si binary system was carried out, with the dataset of Hallstedt *et al.*^[4] being used as the basis when possible. This reassessment is presented in the following chapter, and the selection of models is described there in detail.

Fig. 7 Calculated isothermal section of the Al-Cu-Si system at 500°C (a) and detail of the Cu-rich corner (b) with experimental data from He *et al.*^[2] (up and down pointing triangles) and Ponweiser and Richter^[3] (circles and stars) superimposed (solid circles or up pointing triangles - correct equilibrium, empty circles or up pointing triangles - wrong equilibrium, stars or down pointing triangles - close to correct equilibrium)



(a)



(b)

Fig. 8 Calculated Cu-rich corner of isothermal section of the Al-Cu-Si system at 600°C with experimental data from He *et al.*^[2] (up and down pointing triangles) and Zobac *et al.*^[5] (circles and stars) superimposed (solid circles or up pointing triangles - correct equilibrium, empty circles or up pointing triangles - wrong equilibrium, stars or down pointing triangles - close to correct equilibrium)

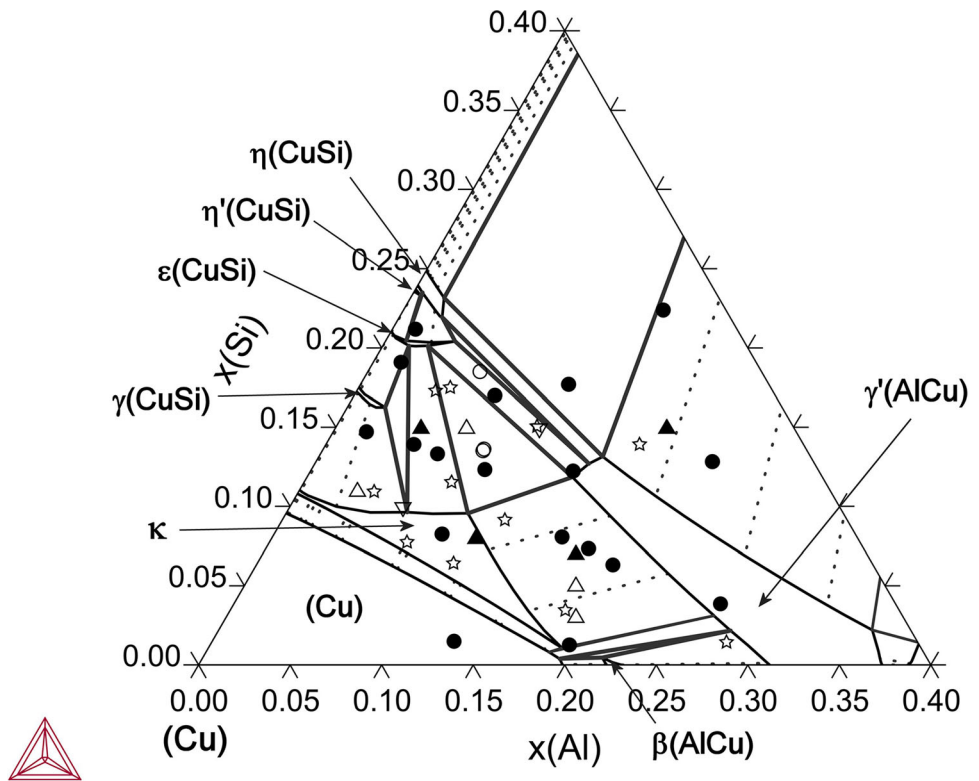


Fig. 9 Calculated Cu-rich corner of isothermal section of the Al-Cu-Si system at 700 °C with experimental data from Ponweiser and Richter^[3] (circles and stars) superimposed (solid circle - correct equilibrium, empty circle - wrong equilibrium, empty star - close to correct equilibrium). Squares indicate samples, where the experiment showed equilibrium with κ(hcp), but the calculations predicted equilibrium with β(bcc)

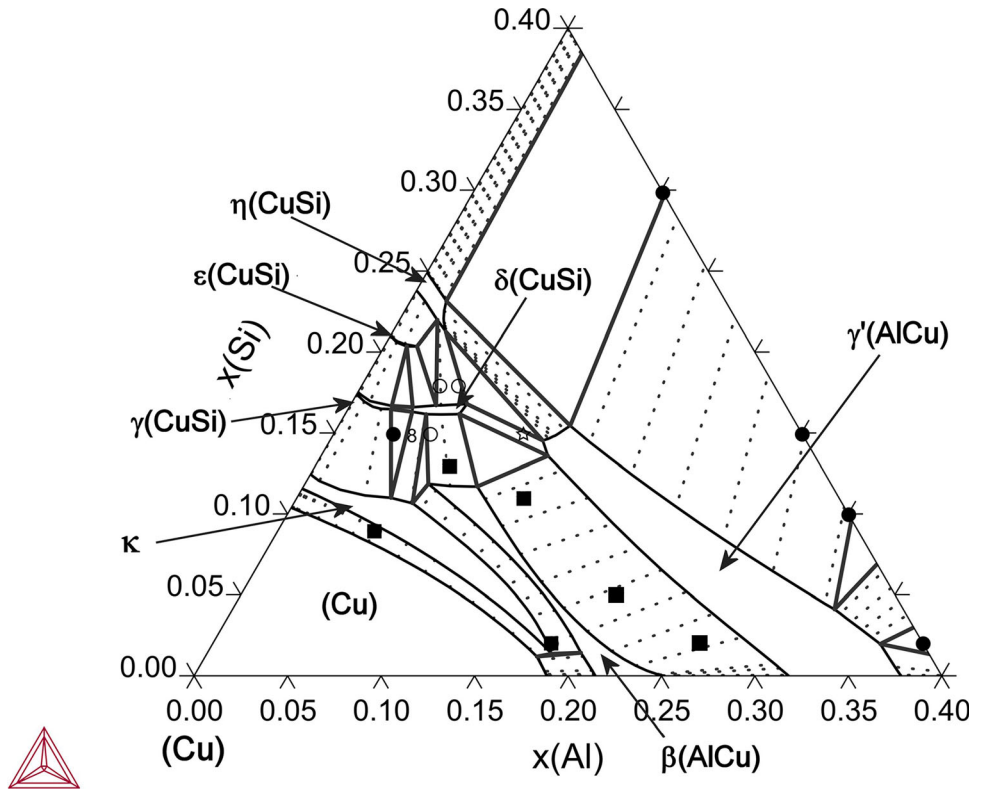
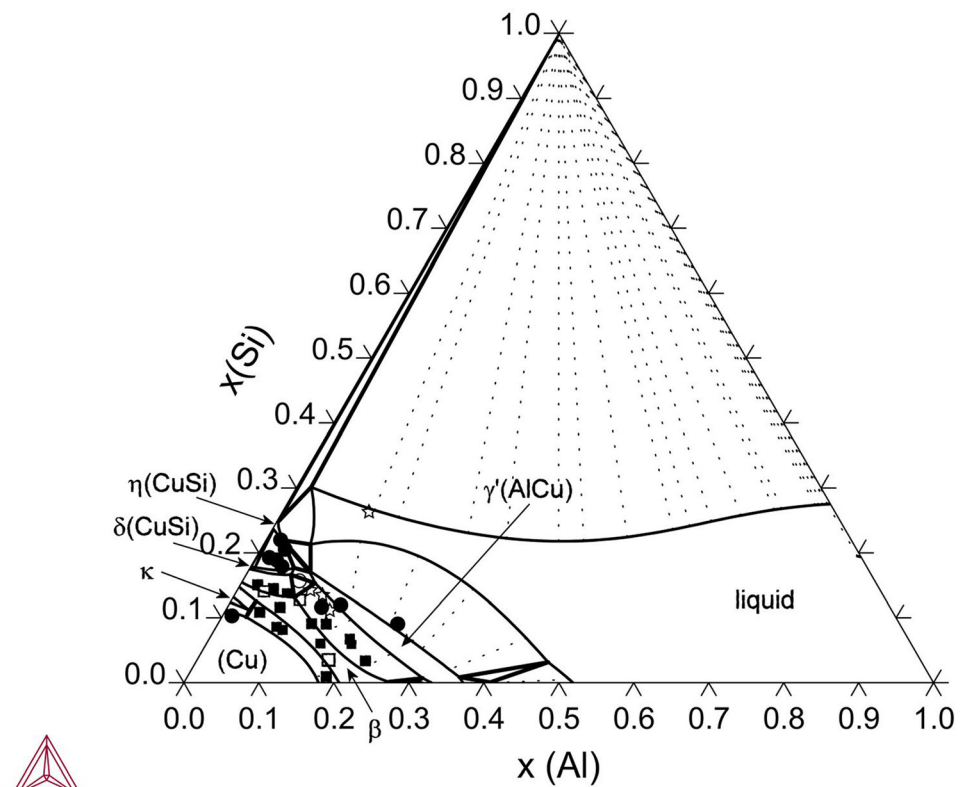
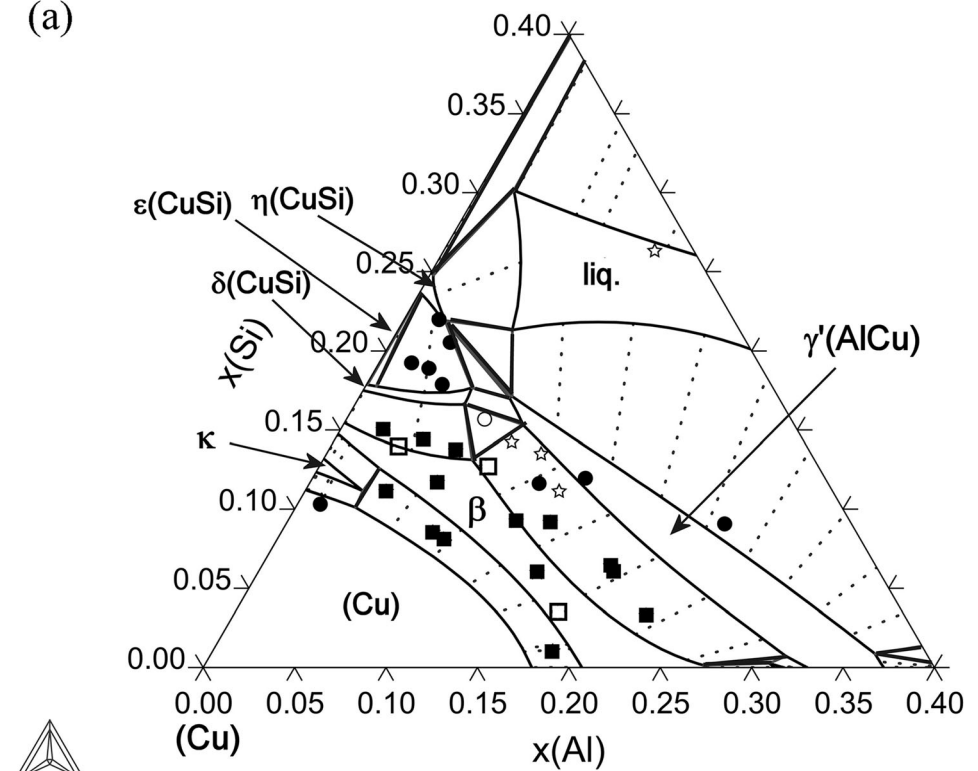


Fig. 10 Calculated isothermal section of the Al-Cu-Si system at 800°C (a) and detail of the Cu-rich corner (b) superimposed with experimental data from Zobac *et al.*^[5] (solid circle - correct equilibrium, empty circle - wrong equilibrium, empty star - close to correct equilibrium). Squares indicate samples, where the experiment showed equilibrium with κ (hcp), but the calculations predicted equilibrium with β (bcc)

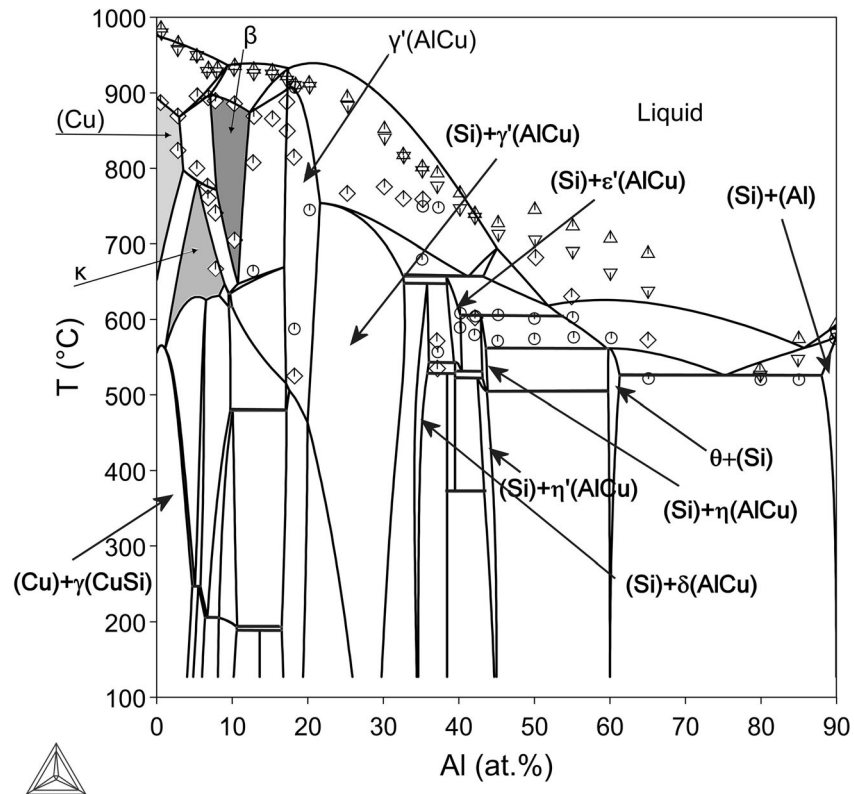


(a)



(b)

Fig. 11 Calculated isopleth section of the Al-Cu-Si system for 10 at.% Si with experimental data from Ponweiser and Richter^[3] (circles - invariant reactions, triangles - liquidus temperatures during heating and cooling, diamonds - other signals). The single phase fields for (Cu), β (bcc) and κ (hcp) are highlighted by various shades of grey and only relevant phase fields are identified due to complexity of the vertical section



3 Results

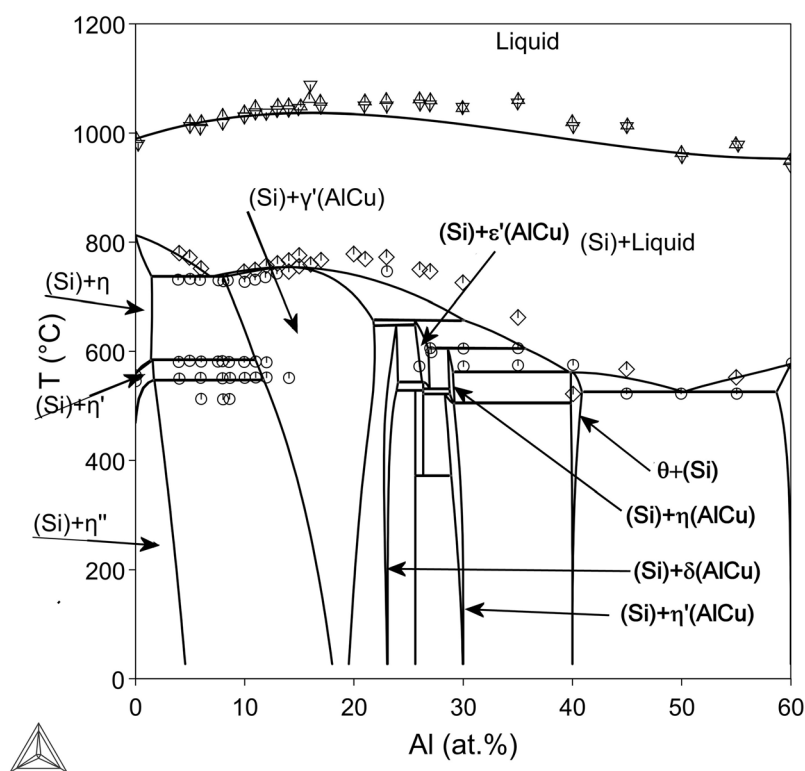
3.1 The Reassessment of the Cu-Si System

The most recent assessment of the Cu-Si system was published by Hallstedt *et al.*^[4] and this work was originally accepted as a basis for the assessment of the ternary system. The liquidus curve and the invariant reactions and temperatures were correctly described with respect to their own and literature thermodynamic and phase experimental data, mainly the work of Sufryd *et al.*^[28] With respect to the small extent of experimental data all intermetallic phases were modelled as stoichiometric with exception to κ (hcp) and β (bcc) where enough experimental data was available to model the solubility.

The stoichiometric models for the rest of intermetallic phases were nevertheless found not being suitable for the assessment of the Al-Cu-Si ternary system with respect to the experimental phase data from^[3] and^[5]. The reason for the reassessment only became apparent when the work on the optimization of the ternary system started and we had to take into account the solubilities of Al in these phases.

The main feature of Hallstedt *et al.*'s assessment of the Al-Cu-Si ternary system is the constant content of Cu in all Cu-Si stoichiometric intermetallic phases. The experimental results published by Ponweiser and Richter^[3] and Zobac *et al.*^[5] indicate that the situation is more complicated, and the phase composition data presented in the tables in^[3] and^[5] showed that some intermetallic phases do not behave this way, e.g., the content of Si in the ϵ (CuSi) phase seems to be constant, even if the experimental errors are taken into account. In the case of the γ (CuSi) phase,

Fig. 12 Calculated isopleth section of the Al-Cu-Si system for 40 at.% Si with experimental data from Ponweiser and Richter^[3] (circles - invariant reactions, triangles - liquidus temperatures during heating and cooling, diamonds - other signals). Only relevant phase fields are identified due to complexity of the vertical section



neither Cu nor Si seem to be constant with increasing amounts of Al in the phase. Similarly, the $\delta(\text{CuSi})$ phase exhibits significant solubility of Al, and both the content of Cu and Si is not constant according to Table 2 in the paper,^[5] the Cu content varies between 77 and 80.5 at.% depending on the Al content in the ternary alloy. A similar situation is also true for Si. These results indicate that the Al atoms do not simply occupy only Si positions in the crystallographic structures of these phases.

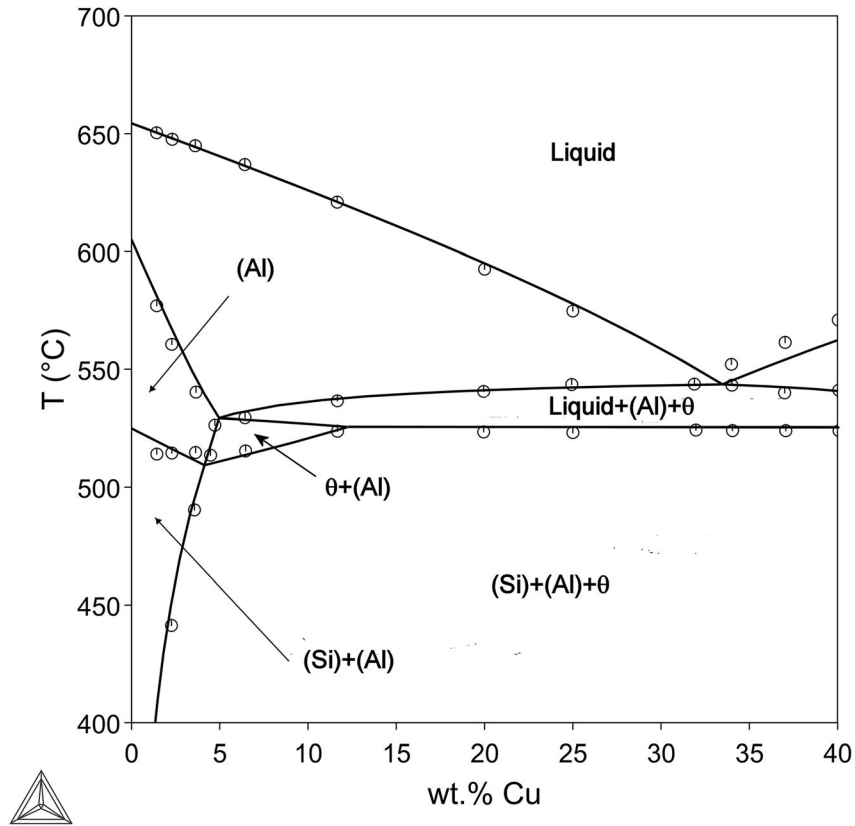
Extending Hallstedt's models for intermetallic phases by adding the Al to both sublattices does not allow to satisfactorily model the experimental data from^[3] and^[5] in the ternary system. Therefore, it was necessary to return to the binary Cu-Si subsystem and change some of the models. The main aim was not modelling some solubility in the binary system, as more significant solubility presented in the work of Sufryd *et al.*^[28] exists only for the $\eta(\text{CuSi})$ family of phases and it is less than 1% for the rest of phases modelled by Hallstedt *et al.*^[4] as stoichiometric. We reassessed the Cu-Si system to obtain the flexibility needed to model the phase behaviour and solubility of Al in the assessment of the ternary system.

We considered the nonstoichiometric character of the $\eta(\text{CuSi})$ -family of phases and $\delta(\text{CuSi})$ and $\gamma(\text{CuSi})$ phases proposed in the work by Sufryd *et al.*^[28] They studied the samples after long term equilibration by high temperature x-ray diffraction, electron probe microanalysis and x-ray diffraction at room temperature after cooling and did extensive differential thermal analysis (DTA) measurements in the Cu-rich region.

The binary Cu-Si reassessment is still based on the data published by Hallstedt *et al.*^[4] The models for liquid phase, (Cu) and (Si) solid solutions, $\kappa(\text{hcp})$ and $\beta(\text{bcc})$ were taken from their work^[4] and the parameters were used as starting point for the reassessment of the system.

The models for the $\eta(\text{Cu}_3\text{Si})$ family of phases were selected as $(\text{Cu},\text{Si})_{0.76}(\text{Cu},\text{Si})_{0.24}$. The phase names are **CU3SI_HT** for $\eta(\text{CuSi})$, **CU3SI_MT** for $\eta'(\text{CuSi})$ and **CU3SI_LT** for $\eta''(\text{CuSi})$. Similar two sublattice models were selected for the low and high temperature modifications of the $\gamma(\text{CuSi})$ and $\delta(\text{CuSi})$ in the form $(\text{Cu},\text{Si})_{0.825}(\text{Cu},\text{Si})_{0.175}$ with the names **CU33SI7_A13** and **CU33SI7_HT**. The $\varepsilon(\text{CuSi})$ phase was still modelled as stoichiometric phase $(\text{Al})_{15}(\text{Si})_4$ according to^[4] as there is no information about solubility in this phase.^[28]

Fig. 13 Calculated isopleth of the Al-Cu-Si system at 1 wt% Si compared with experimental data from.^[44] The experimental points were redrawn from the work from.^[2]



In the first step of the re-assessment, the thermodynamic descriptions of the Gibbs energy of the liquid phase and the other phases, whose models have remained unchanged from Hallstedt *et al.*,^[4] were adopted. The remaining intermetallic phases were assessed afterwards, taking into account the character and temperatures of invariant reactions. Less weight was given to the solubilities of these phases with respect to uncertainties indicated in the work of Sufryd *et al.*^[28] Also, less weight was given to the transition temperatures between the η' (CuSi) and η'' (CuSi), as there is no experimental data.^[28] The values identical with the work of Hallstedt *et al.*^[4] were set as a target for the assessment. Parameters for all phases were readjusted in the final step of the reassessment to obtain the best possible agreement between the experiments and calculations. No parameter changes for the (Cu) and (Si) solid solutions were necessary, and only a very small change in

one interaction parameter for liquid phases was made in this final step.

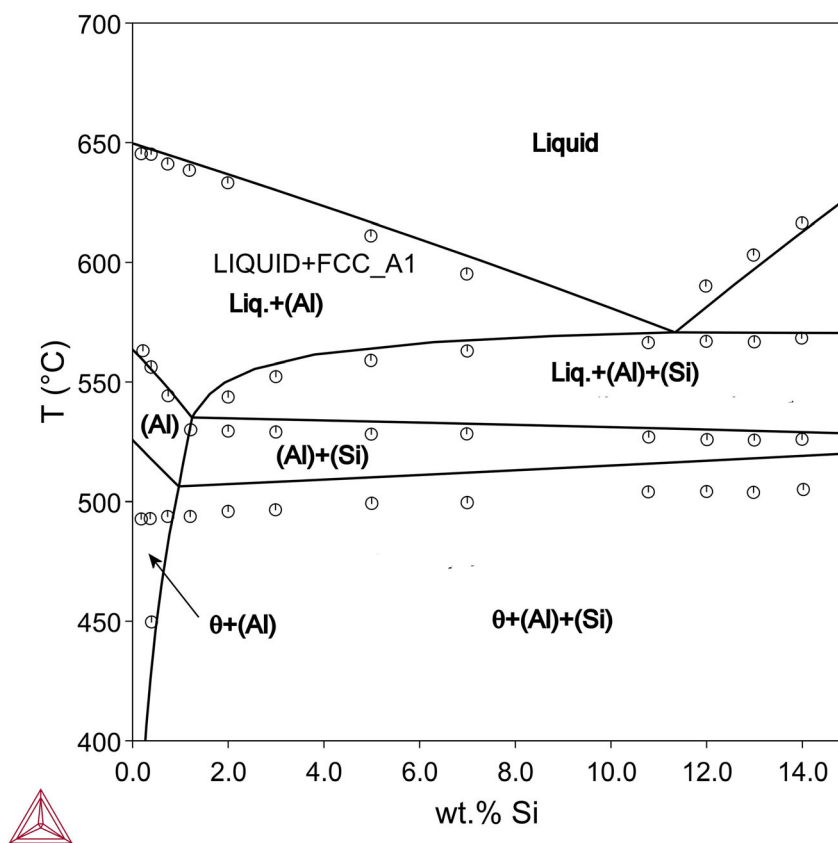
The Cu-Si phase diagram, together with experimental data, is shown in Fig. 4. The data for the invariant reactions compared to other experimental and calculated literature results are shown in Table 2.

The comparison of thermodynamic calculations with selected thermodynamic experimental data are shown in Fig. 5 and 6. The enthalpy of mixing in liquid phase at the temperature 1008 °C is presented in Fig. 5, calculated chemical potentials of Cu and Si in liquid phase of the Cu-Si system at 1400 °C are shown in Fig. 6.

3.2 The Assessment of the Al-Cu-Si System

The assessment of the Al-Cu-Si system was carried out because of the lack of proper theoretical description of this industrially important system. As mentioned above, only a

Fig. 14 Calculated isopleth of the Al-Cu-Si system at 4 wt% Cu compared with experimental data from.^[44] The experimental points were redrawn from the work from.^[2]



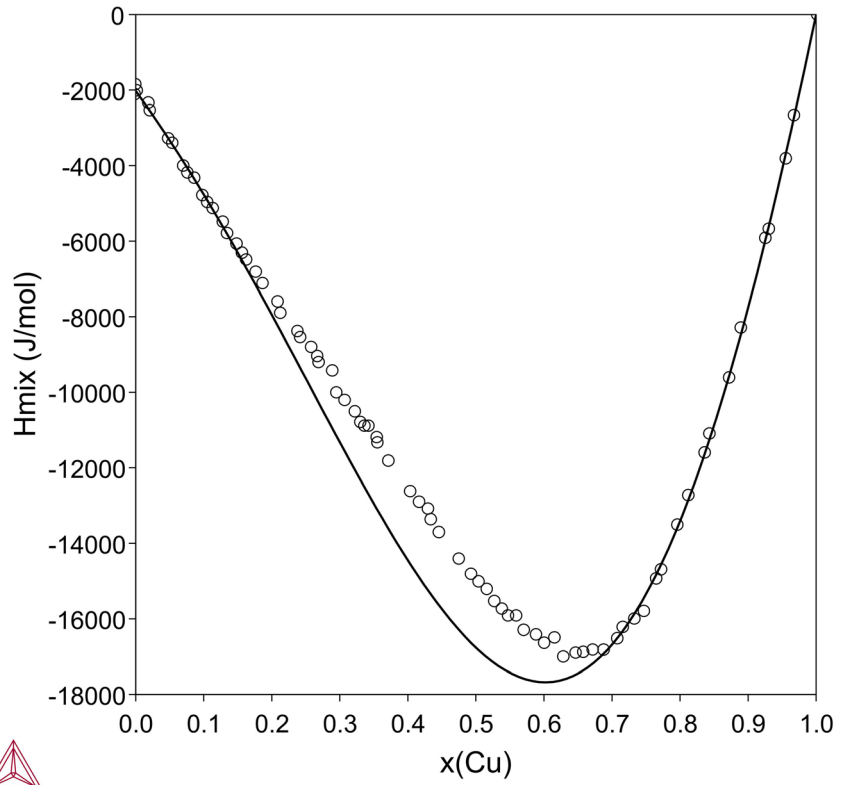
complete theoretical assessment was carried out by,^[2] where the three sublattice model $(Al,Si)_4(Al,Cu)_1(Cu)_8$ was accepted from^[18] for the $\gamma'(AlCu)$ and $\gamma(AlCu)$ phases. This model limits the maximum content of Cu to approx. 70 at.%. This limitation does not allow a correct description of the experimentally found behaviour of the above mentioned $\gamma(AlCu)$ and $\gamma'(AlCu)$ phases, where the Cu content exceeds this value with increasing content of Si. All experimental results describing the Al-Cu-Si isotherms^[1-3,5] show this behaviour.

The theoretical assessment carried out by Hallstedt *et al.*^[4] used 3 sublattice model $(Cu)_4(Cu)_6(Al,Cu,Si)_{16}$ which covers experimentally observed compositions, but their work focused on the experimental and theoretical study of the Cu-Si system and the assessment of the ternary system was only preliminary and proved the applicability of the above mentioned 3 sublattice model for the

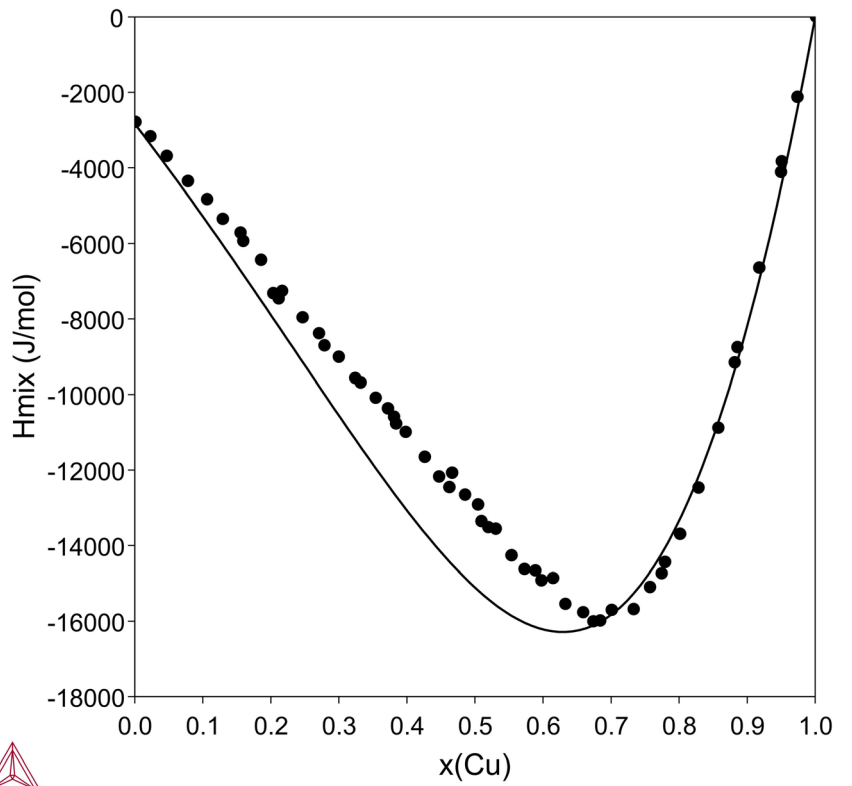
description of the behaviour of $\gamma(AlCu)$ and $\gamma'(AlCu)$ phases.

The assessment was carried out using the Thermo-Calc and Pandat software packages in this work. The experimental phase equilibria data were used from Riani *et al.* (experimental isotherm at 500 °C),^[1] He *et al.*^[2] (experimental isotherm at 500 and 600 °C), Ponweiser and Richter^[3] (experimental isotherm at 500 and 700 °C, isopleths for 40 and 10 at.% Si), Zobac *et al.*^[5] (experimental isotherm at 600 and 800 °C, DSC measurements) and Phillips^[44] (isopleths for 4 Cu and 1 wt.% Si). The older experimental results from Matsuyama^[42] and Hisatsune^[43] were used for later verification of the obtained results. The only thermodynamic data, the enthalpies of mixing at 1575K for three different sections $(Al_xSi_{1-x} - Cu)$, $x = 0.2, 0.5, 0.8$ published by Witusiewicz *et al.*^[47] were used as well.

Fig. 15 Calculated enthalpies of mixing of liquid at 1575 K along the sections, (a) Al_{0.8}Si_{0.2}-Cu; (b) Al_{0.5}Si_{0.5}-Cu; (c) Al_{0.2}Si_{0.8}-Cu, compared with experimental data from^[47]

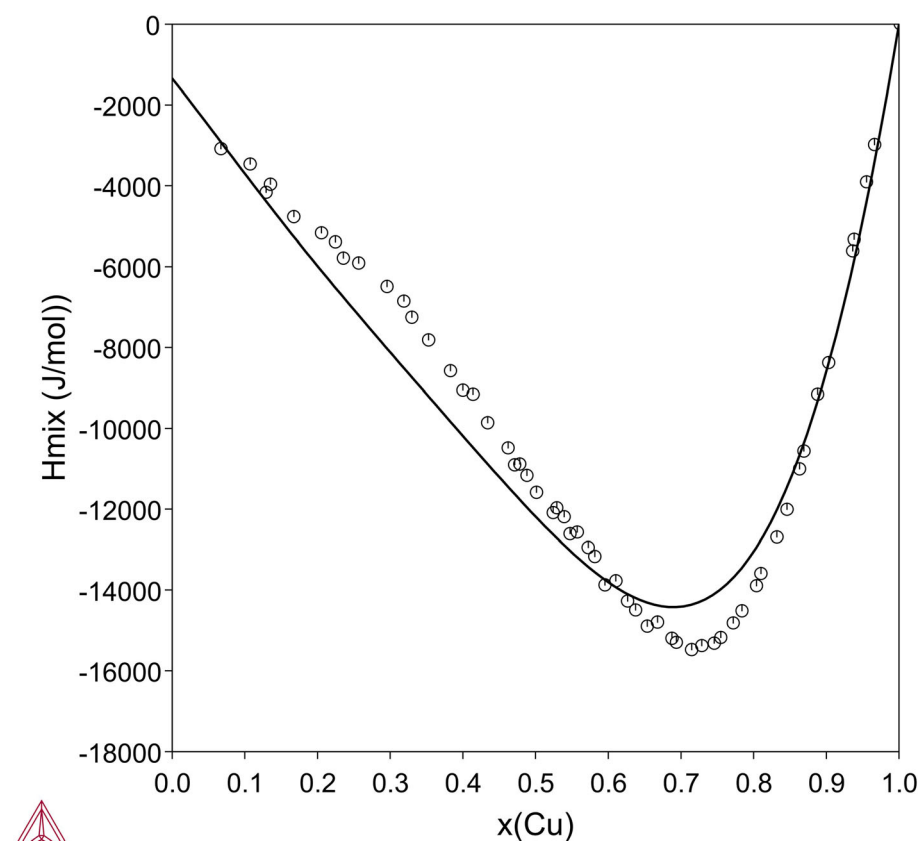


(a)



(b)

Fig. 15 continued



(c)

The results of the assessment using the above mentioned experimental results are presented in Fig. 7, 8, 9, 10, 11, 12, 13, and 14, where the isothermal sections at 500, 600, 700 and 800 °C are shown, together with the isopleths for 10 and 40 Si and for 4 wt.% Cu and 1 wt.% Si.

The agreement between the experiment and modelling is good for most of the results except for limited parts of the isothermal sections of the ternary phase diagram at 600, 700 and 800 °C. Here the equilibria between (Cu) solid solution and κ (hcp) phase (dissolving large amount of Al) and only negligible solubility of Si in β (bcc) phase was found in all used experimental data from,^[1-3,5] but there was significant inconsistency with other experimental data, especially for the 800 °C isotherm and the isopleth for 10 at.% of Si.^[3]

All these results and problems are discussed in detail in the following Section 4. Significant inconsistencies between experimental results and modelling are described and the solution used to resolve the discrepancies during the assessment is described.

The only available thermodynamic data were measured by,^[47] who published the enthalpies of mixing for three sections with a constant Al/Si ratio at 1302°C. The results of the modelling are presented in Fig. 15, 16 and 17.

There are no systematic experimental studies of the liquidus surface of the ternary system. Small DTA study was carried out by Zöbäck *et al.*^[5] They prepared samples in the section where single γ' (AlCu) phase should exist at temperatures studied in that work and measured the temperatures of liquidus, solidus and a few other phase transformations in the high temperature region. Selected samples belong to the section between the binary (80Cu20Si) and (35Al65Cu) compositions (at.%).

The prediction of the liquidus surface of the system is shown in Fig. 16. The invariant reactions which include liquid phase are shown in Table 4. The isopleth for compositions mentioned in previous paragraph is presented in Fig. 17. The complete liquidus surface looks very reasonable and there is excellent agreement between the calculations and the DTA measurements from the work.^[5]

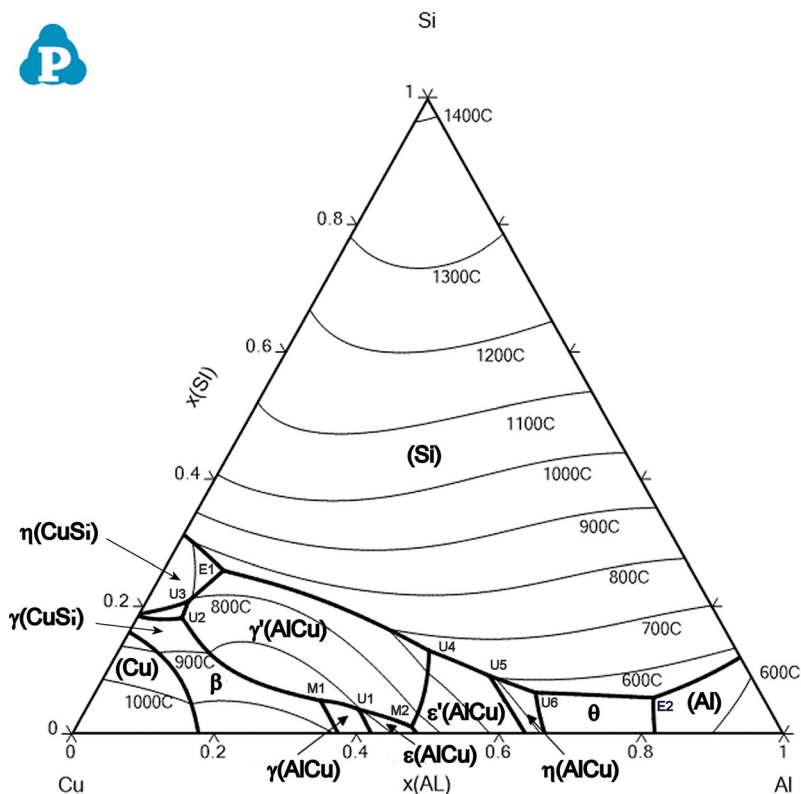


Fig. 16 Calculated liquidus surface prediction of the Al-Cu-Si system

The theoretical dataset of the Al-Cu-Si system is presented in Table 3 together with the data for the Cu-Si binary system.

4 Discussion

4.1 The Reassessment of the Cu-Si System

The results presented in the Fig. 4, 5 and 6 show very good agreement not only with the experimental data but also agree well with the results published earlier by Hallstedt *et al.*^[4] As the reassessment was based on their work, it

indicates that the changes in the description of the key intermetallic phases were properly introduced into the new dataset. The thermodynamic parameters used for the calculation are presented in Table 3.

4.2 The Assessment of the Al-Cu-Si System

4.2.1 Disagreement Between Experiments and Calculations

Characteristic features of all isotherms, based on the experimental data in the literature [1, 2, 3, 5), are extensive solubility of Si in γ' (AlCu) phase and similarly high solubility of Al in κ (hcp) phase as is shown in Fig. 18. On the

other hand, the β (bcc) phases existing in the Al-Cu and Cu-Si systems both show very low solubility for the third element.

Therefore, great attention was paid to the proper representation of these features in the first part of the theoretical assessment and the version 1 of the thermodynamic database was created. The results obtained in this first stage of the assessment work were in good agreement with experiments mentioned in the section 3.2 and also with the final results presented in Fig 7, 8 and 12, 13, 14 and 15 for 500 and 600 °C and for all but one of the presented vertical sections. Only negligible differences were found for almost all calculations using version 1 of the database in comparison with the final one (Table 3) for the same sections. The only significant differences were found for the isotherm at 800°C and the isopleth for 10 at.% of Si. The results of these two calculations obtained using version 1 of the database are shown in Fig. 19, 20.

Serious problems can be seen in Fig. 19 and 20. There is clear disagreement of experiments and calculations between 600 and 800 °C up to 10 at.% of Al in Fig. 19, where set of DTA signals was observed for compositions that belong to κ (hcp) single phase field and cannot be attributed to any phase boundary. This area was not interpreted by Ponweiser and Richter in their experimental

work (Fig. 7 in^[3]) and no phase boundaries were drawn in their work for this region.

In the case of isotherm shown in Fig. 20, most samples fit well with calculated phase fields, except of the (Cu) + κ (hcp) two phase field. Here, the (Cu)/(κ + (Cu)) phase boundary is reasonably presented, but serious disagreement exists for the (κ + (Cu))/ κ phase boundary. Generally, it is near to impossible to model such a much wider two phase field with respect to the model used for the κ (hcp) phase and its solubility in the Cu-Si binary subsystem (Table 4).

Checking Fig. 19 and 20, it is clear that a solution to this problem must be found (the simpler, the better) with respect to other experimental results, which seem to be mutually consistent (except of Fig. 19). It is difficult to reason that intermetallic phases or a possible ternary phase identified in^[3] can at the same time explain the existence of undescribed signals in Fig. 19 and the disagreement at 800 °C. Hallstedt *et al.*^[4] proposed that β (bcc) phase can play a certain role in it, as there are complex relations between phases with A2 structure in both binary systems of interest. Two A2 phases exist in the Al-Cu system: the β (AlCu) phase in the Cu-rich region, where the A2 structure was reliably confirmed and the ε (AlCu) phase, where the structure is just proposed and not definitely known. The

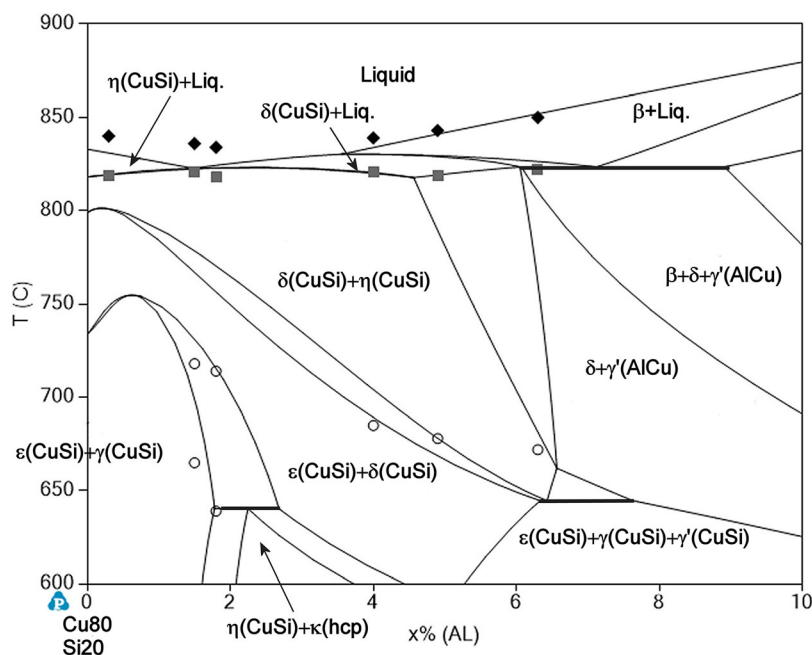


Fig. 17 Calculated isopleth Cu80Si20-Al35Cu65 (at.%) in comparison with experimental DSC data from^[5] (solid diamonds – liquidus, solid squares – solidus, circles – other reactions)

Table 3 Thermodynamic parameters for liquid and optimised intermetallic phases in the Cu-Si binary and Al-Cu-Si ternary system (* optimised in this work)

Database name (constituents) <i>Name used in the text</i>	Thermodynamic parameters (298.15 < T < 6000 K)	Ref	
LIQUID (Al, Cu, Si) ₁ Liquid	Al-Cu		
	${}^0L_{Al,Cu}^{LIQ} = - 69250.79 + 10.30229*T$	[7]	
	${}^1L_{Al,Cu}^{LIQ} = + 36119.82 - 10.2142*T$	[7]	
	${}^2L_{Al,Cu}^{LIQ} = 11596.81 - 9.5733*T$	[7]	
	${}^3L_{Al,Cu}^{LIQ} = - 15246.64 + 11.53621*T$	[7]	
	Al-Si		
	${}^0L_{Al,Si}^{LIQ} = - 11340.1 - 1.23394*T$	[23]	
	${}^1L_{Al,Si}^{LIQ} = - 3530.93 + 1.35993*T$	[23]	
	${}^2L_{Al,Si}^{LIQ} = + 2265.39$	[23]	
	Cu-Si		
	${}^0L_{Cu,Si}^{LIQ} = - 37776 + 3.47*T$	[4]	
	${}^1L_{Cu,Si}^{LIQ} = - 44866 + 14.53*T$	[4]	
	${}^2L_{Cu,Si}^{LIQ} = - 40866 + 8.62*T$	[4]	
	${}^3L_{Cu,Si}^{LIQ} = - 10960 + 0.4*T$	[*]	
	${}^4L_{Cu,Si}^{LIQ} = + 17550$	[4]	
	Al-Cu-Si		
	${}^0L_{Al,Cu,Si}^{LIQ} = 80309 - 30.08*T$	[*]	
	${}^1L_{Al,Cu,Si}^{LIQ} = 79986.5 - 89.322*T$	[*]	
	${}^2L_{Al,Cu,Si}^{LIQ} = - 20224.8 - 29.985*T$	[*]	
	BCC_A2 (Al,Cu,Si) ₁ (Va) ₃ β(CuSi), β(AlCu), ε(Al,Cu)	Al-Cu	
${}^0L_{Al,Cu:Va}^{BCC_A2} = - 72619 + 3.137*T$		[7]	
${}^1L_{Al,Cu:Va}^{BCC_A2} = 56695.8 - 14.728*T$		[7]	
${}^2L_{Al,Cu:Va}^{BCC_A2} = 4774.15 - 1.4195*T$		[7]	
Al-Si			
${}^0L_{Al,Si:Va}^{BCC_A2} = - 3143.78 + 0.39297*T$		[23]	
Cu-Si			
${}^0L_{Cu,Si:Va}^{BCC_A2} = - 19600 + 10.95*T$		[*]	
${}^1L_{Cu,Si:Va}^{BCC_A2} = - 88400 - 9.23*T$		[*]	
Al-Cu-Si			
${}^0L_{Al,Cu,Si:Va}^{BCC_A2} = 25010$		[*]	
${}^1L_{Al,Cu,Si:Va}^{BCC_A2} = 24093$		[*]	
${}^2L_{Al,Cu,Si:Va}^{BCC_A2} = 22981$		[*]	
CU15SI4_D86 (Al,Cu) ₁₅ (Al,Si) ₄ ε(CuSi)		Cu-Si	
		${}^0G_{Cu:Si}^{CU15SI4_D86} = 15* G_{Cu}^{HSER} + 4* G_{Si}^{HSER} - 93468.23 - 73.51*T$	
		Al-Cu-Si	
		${}^0G_{Al:Al}^{CU15SI4_D86} = + 19* G_{Al}^{HSER} + 600000$	
		${}^0G_{Al:Si}^{CU15SI4_D86} = + 15* G_{Al}^{HSER} + 4* G_{Si}^{HSER} + 200000$	
	${}^0G_{Cu:Al}^{CU15SI4_D86} = + 15* G_{Cu}^{HSER} + 4* G_{Al}^{HSER} + 200000$		
	${}^0G_{Al:Al}^{CU15SI4_D86} = + 19* G_{Al}^{HSER} + 600000$		
	${}^0L_{Al,Cu:Si}^{CU15SI4_D86} = - 253080 - 40.8*T$		
	${}^1L_{Al,Cu:Si}^{CU15SI4_D86} = 717309 - 101.3*T$		
	${}^0L_{Cu:Al,Si}^{CU15SI4_D86} = - 233533.4 + 66.67*T$		
	${}^1L_{Cu:Al,Si}^{CU15SI4_D86} = 502300 - 99.15*T$		
	CU33SI7_A13 (Al,Cu,Si) _{0.825} (Al,Cu,Si) _{0.175} γ(CuSi)	Cu-Si	
${}^0G_{Cu:Cu}^{CU33SI7_A13} = G_{Cu}^{HSER} + 2500$		[*]	
${}^0G_{Cu:Si}^{CU33SI7_A13} = 0.825* G_{Cu}^{HSER} + 0.175* G_{Si}^{HSER} - 4464 - 3.5*T$			

Table 3 continued

Database name (constituents) <i>Name used in the text</i>	Thermodynamic parameters (298.15 < T < 6000 K)	Ref
	${}^0G_{\text{Si:Cu}}^{\text{CU33SI7_A13}} = 0.825 * G_{\text{Si}}^{\text{HSER}} + 0.175 * G_{\text{Cu}}^{\text{HSER}} + 3000$ ${}^0G_{\text{Si:Si}}^{\text{CU33SI7_A13}} = G_{\text{Si}}^{\text{HSER}} + 15000$ ${}^0L_{\text{Cu,Si:Si}}^{\text{CU33SI7_A13}} = -11000 + 10 * T$	
	Al-Cu-Si ${}^0G_{\text{Al:Cu}}^{\text{CU33SI7_A13}} = 0.825 * G_{\text{Al}}^{\text{HSER}} + 0.175 * G_{\text{Cu}}^{\text{HSER}} + 5000$ ${}^0G_{\text{Al:Si}}^{\text{CU33SI7_A13}} = 0.825 * G_{\text{Al}}^{\text{HSER}} + 0.175 * G_{\text{Cu}}^{\text{HSER}} + 4400$ ${}^0G_{\text{Al:Al}}^{\text{CU33SI7_A13}} = G_{\text{Al}}^{\text{HSER}} + 15000$ ${}^0G_{\text{Cu:Al}}^{\text{CU33SI7_A13}} = 0.825 * G_{\text{Cu}}^{\text{HSER}} + 0.175 * G_{\text{HSERAL}} + 5000$ ${}^0G_{\text{Si:Al}}^{\text{CU33SI7_A13}} = 0.825 * G_{\text{Cu}}^{\text{HSER}} + 0.175 * G_{\text{HSERAL}} + 4400$ ${}^0L_{\text{Al,Cu:Si}}^{\text{CU33SI7_A13}} = -46018.02 + 26.74 * T$ ${}^1L_{\text{Al,Cu:Si}}^{\text{CU33SI7_A13}} = -46840 + 80 * T$ ${}^0L_{\text{Cu:Al,Si}}^{\text{CU33SI7_A13}} = -17585 - 5.004 * T$	
CU33SI7_HT (Al,Cu,Si) _{0.825} (Al,Cu,Si) _{0.175} δ(CuSi)	Cu-Si ${}^0G_{\text{Cu:Cu}}^{\text{CU33SI7_HT}} = G_{\text{Cu}}^{\text{HSER}} + 600$ ${}^0G_{\text{Cu:Si}}^{\text{CU33SI7_HT}} = 0.825 * G_{\text{Cu}}^{\text{HSER}} + 0.175 * G_{\text{Si}}^{\text{HSER}} - 2425 - 5.45 * T$ ${}^0G_{\text{Si:Cu}}^{\text{CU33SI7_HT}} = 0.825 * G_{\text{Si}}^{\text{HSER}} + 0.175 * G_{\text{Cu}}^{\text{HSER}} + 12000$ ${}^0G_{\text{Si:Si}}^{\text{CU33SI7_HT}} = G_{\text{Si}}^{\text{HSER}} + 19000$ ${}^0L_{\text{Cu,Si:Si}}^{\text{CU33SI7_HT}} = -14960 + 13 * T$ ${}^1L_{\text{Cu,Si:Si}}^{\text{CU33SI7_HT}} = -20100 + 10.2 * T$	[*]
	Al-Cu-Si ${}^0G_{\text{Al:Cu}}^{\text{CU33SI7_HT}} = 0.825 * G_{\text{Al}}^{\text{HSER}} + 0.175 * G_{\text{Cu}}^{\text{HSER}} + 10000$ ${}^0G_{\text{Al:Si}}^{\text{CU33SI7_HT}} = 0.825 * G_{\text{Al}}^{\text{HSER}} + 0.175 * G_{\text{Cu}}^{\text{HSER}} + 20000$ ${}^0G_{\text{Al:Al}}^{\text{CU33SI7_HT}} = G_{\text{Al}}^{\text{HSER}} + 15000$ ${}^0G_{\text{Cu:Al}}^{\text{CU33SI7_HT}} = +0.825 * G_{\text{Cu}}^{\text{HSER}} + 0.175 * G_{\text{Al}}^{\text{HSER}} - 16949 + 13 * T$ ${}^0G_{\text{Si:Al}}^{\text{CU33SI7_HT}} = 0.825 * G_{\text{Cu}}^{\text{HSER}} + 0.175 * G_{\text{Al}}^{\text{HSER}} + 28000$ ${}^0L_{\text{Al,Cu:Al,Si}}^{\text{CU33SI7_HT}} = -84312 + 44 * T$ ${}^1L_{\text{Al,Cu:Al,Si}}^{\text{CU33SI7_HT}} = 94650 - 45 * T$ ${}^0L_{\text{Al,Cu:Si}}^{\text{CU33SI7_HT}} = -7015.5 - 26.5 * T$ ${}^1L_{\text{Al,Cu:Si}}^{\text{CU33SI7_HT}} = 40719 - 3 * T$ ${}^0L_{\text{Cu:Al,Si}}^{\text{CU33SI7_HT}} = 4229.75 - 15.75 * T$ ${}^1L_{\text{Cu:Al,Si}}^{\text{CU33SI7_HT}} = 500$	
CU3SI_HT (Cu,Si) _{0.76} (Al,Cu,Si) _{0.24} η(CuSi)	Cu-Si ${}^0G_{\text{Cu:Cu}}^{\text{CU3SI_HT}} = G_{\text{Cu}}^{\text{HSER}} + 17500 + 7 * T$ ${}^0G_{\text{Cu:Si}}^{\text{CU3SI_HT}} = 0.76 * G_{\text{Cu}}^{\text{HSER}} + 0.24 * G_{\text{Si}}^{\text{HSER}} - 4410 - 4.8308 * T$ ${}^0G_{\text{Si:Cu}}^{\text{CU3SI_HT}} = 0.76 * G_{\text{Si}}^{\text{HSER}} + 0.24 * G_{\text{Cu}}^{\text{HSER}} + 35000$ ${}^0G_{\text{Si:Si}}^{\text{CU3SI_HT}} = G_{\text{Si}}^{\text{HSER}} + 46000 + 4 * T$	[*]

Table 3 continued

Database name (constituents) <i>Name used in the text</i>	Thermodynamic parameters (298.15 < T < 6000 K)	Ref
CU3SI_MT (Cu,Si) _{0.76} (Al,Cu,Si) _{0.24} η ⁺ (CuSi)	${}^0L_{Cu,Si:Si}^{CU3SI_HT} = -45850 + 18 * T$	
	${}^1L_{Cu,Si:Si}^{CU3SI_HT} = 2000 + 3.2 * T$	
	${}^0L_{Cu:Cu,Si}^{CU3SI_HT} = -26401 + 15 * T$	
	${}^1L_{Cu:Cu,Si}^{CU3SI_HT} = -5345.3 + 15.81 * T$	
	Al-Cu-Si	
	${}^0G_{Cu:Al}^{CU3SI_HT} = 0.76 * G_{Cu}^{HSER} + 0.24 * G_{Al}^{HSER} - 8000 - 7 * T$	
	${}^0G_{Si:Al}^{CU3SI_HT} = 0.76 * G_{Si}^{HSER} + 0.24 * G_{Al}^{HSER} + 10000$	
	${}^0L_{Cu:Al,Si}^{CU3SI_HT} = -2745$	
	Cu-Si	[*]
	${}^0G_{Cu:Cu}^{CU3SI_MT} = G_{Cu}^{HSER} + 20500 + 6 * T$	
	${}^0G_{Cu:Si}^{CU3SI_MT} = 0.76 * G_{Cu}^{HSER}$ $+ 0.24 * G_{Si}^{HSER} - 5300 - 3.788 * T$	
	${}^0G_{Si:Cu}^{CU3SI_MT} = + 0.76 * G_{Si}^{HSER}$ $+ 0.24 * G_{Cu}^{HSER} + 35000$	
	${}^0G_{Si:Si}^{CU3SI_MT} = G_{Si}^{HSER} + 36000 + 6.5 * T$	
	${}^0L_{Cu,Si:Si}^{CU3SI_MT} = -42850 + 18 * T$	
	${}^1L_{Cu,Si:Si}^{CU3SI_MT} = 8650 + 4.66 * T$	
${}^0L_{Cu:Cu,Si}^{CU3SI_MT} = -28801 + 12.4 * T$		
${}^1L_{Cu:Cu,Si}^{CU3SI_MT} = -5645.3 + 16.11 * T$		
Al-Cu-Si		
${}^0G_{Cu:Al}^{CU3SI_MT} = 0.76 * G_{Cu}^{HSER} + 0.24 * G_{Al}^{HSER} - 13000$		
${}^0G_{Si:Al}^{CU3SI_MT} = 0.76 * G_{Si}^{HSER} + 0.24 * G_{Al}^{HSER} + 2000$		
${}^0L_{Cu:Al,Si}^{CU3SI_MT} = -4169$		
Cu-Si	[*]	
${}^0G_{Cu:Cu}^{CU3SI_LT} = G_{Cu}^{HSER} + 17500 + 7 * T$		
${}^0G_{Cu:Si}^{CU3SI_LT} = 0.76 * G_{Cu}^{HSER}$ $+ 0.24 * G_{Si}^{HSER} - 5374.2 - 3.698 * T$		
${}^0G_{Si:Cu}^{CU3SI_LT} = 0.76 * G_{Si}^{HSER}$ $+ 0.24 * G_{Cu}^{HSER} + 35000$		
${}^0G_{Si:Si}^{CU3SI_LT} = G_{Si}^{HSER} + 45000 + 4 * T$		
${}^0L_{Cu,Si:Si}^{CU3SI_LT} = -38630 + 18 * T$		
${}^1L_{Cu,Si:Si}^{CU3SI_LT} = -4653 + 8.72 * T$		
${}^0L_{Cu:Cu,Si}^{CU3SI_LT} = -27541 + 15 * T$		
${}^1L_{Cu:Cu,Si}^{CU3SI_LT} = -7495.3 + 19.851 * T$		
Al-Cu-Si		
${}^0G_{Cu:Al}^{CU3SI_LT} = 0.76 * G_{Cu}^{HSER} + 0.24 * G_{Al}^{HSER} - 13000$		
${}^0G_{Si:Al}^{CU3SI_LT} = 0.76 * G_{Si}^{HSER} + 0.24 * G_{Al}^{HSER} + 5000$		
${}^0L_{Cu:Al,Si}^{CU3SI_LT} = -8460 + 5.04 * T$		
DIAMOND_A4 (Al, Si) ₁ (Cu, Va) ₁ (Si)		
Al		
${}^0G_{Al:Va}^{Diamond_A4} = GHSERAL + 30 * T$	[23]	
Al-Cu		
${}^0G_{Al:Cu}^{Diamond_A4} = 0$	[*]	
Al-Si		
${}^0L_{Al,Si:Va}^{Diamond_A4} = + 113246.16 - 47.55509 * T$	[23]	
Cu-Si		
${}^0G_{Si:Cu}^{Diamond_A4} = G_{Si}^{HSER} + G_{Cu}^{HSER} + 100000$	[4]	
${}^0G_{Si:Va}^{Diamond_A4} = G_{Si}^{HSER}$	[53]	

Table 3 continued

Database name (constituents) <i>Name used in the text</i>	Thermodynamic parameters (298.15 < T < 6000 K)	Ref
	${}^0L_{\text{Si:Cu,Va}}^{\text{Diamond_A4}} = + 47230 - 30.23 * T$	[4]
	Al-Cu-Si no ternary parameters	
FCC_A1 (Al, Cu, Si) ₁ (Va) ₁ (Al), (Cu)	Al-Cu ${}^0L_{\text{Al,Cu:Va}}^{\text{FCC_A1}} = - 54220.45 + 2.0034 * T$	[7]
	${}^1L_{\text{Al,Cu:Va}}^{\text{FCC_A1}} = + 39015 - 2.368 * T$	[7]
	${}^2L_{\text{Al,Cu:Va}}^{\text{FCC_A1}} = + 3218.23$	[7]
	Al-Si ${}^0L_{\text{Al,Si:Va}}^{\text{FCC_A1}} = - 3143.78 + 0.39297 * T$	[23]
	Cu-Si ${}^0L_{\text{Cu,Si:Va}}^{\text{FCC_A1}} = - 32244 + 20 * T$	[4]
	${}^1L_{\text{Cu,Si:Va}}^{\text{FCC_A1}} = - 43581 - 28.5 * T$	[4]
	Al-Cu-Si ${}^0L_{\text{Al,Cu,Si:Va}}^{\text{FCC_A1}} = - 24000$	[*]
	${}^1L_{\text{Al,Cu,Si:Va}}^{\text{FCC_A1}} = - 30000$	[*]
	${}^2L_{\text{Al,Cu,Si:Va}}^{\text{FCC_A1}} = 70000$	[*]
HCP_A3 (Al, Cu, Si) ₁ (Va) _{0.5} κ(CuSi)	Al-Cu ${}^0L_{\text{Al,Cu:Va}}^{\text{HCP_A3}} = - 63990 + 2 * T$	[7]
	${}^1L_{\text{Al,Cu:Va}}^{\text{HCP_A3}} = + 35590 - 2 * T$	[7]
	${}^2L_{\text{Al,Cu:Va}}^{\text{HCP_A3}} = + 1170$	[7]
	Al-Si ${}^0L_{\text{Al,Si:Va}}^{\text{HCP_A3}} = 15000$	[23]
	Cu-Si ${}^0L_{\text{Cu,Si:Va}}^{\text{HCP_A3}} = - 25735 + 11.686 * T$	[*]
	${}^1L_{\text{Cu,Si:Va}}^{\text{HCP_A3}} = - 61800 - 16 * T$	[*]
	Al-Cu-Si ${}^0L_{\text{Al,Cu,Si:Va}}^{\text{HCP_A3}} = - 123650 + 50.3 * T$	[*]
	${}^1L_{\text{Al,Cu,Si:Va}}^{\text{HCP_A3}} = - 88191.9 + 60.757 * T$	[*]
	${}^2L_{\text{Al,Cu,Si:Va}}^{\text{HCP_A3}} = 10000$	[*]
ETA_ALCU (Al,Cu,Si) ₁ (Cu) ₁ η(AICu)	Al-Cu-Si ${}^0G_{\text{Si:Cu}}^{\text{ETA_ALCU}} = G_{\text{Si}}^{\text{HSER}} + G_{\text{Cu}}^{\text{HSER}} + 5000 + 9 * T$	[*]
	${}^0L_{\text{Al,Si:Cu}}^{\text{ETA_ALCU}} = - 26450$	[*]
DELTA (Al,Cu,Si) ₅ (Al,Cu) ₈ δ(AICu)	Al-Cu ${}^0G_{\text{Al:Cu}}^{\text{DELTA}} = 5 * G_{\text{Al}}^{\text{HSER}} + 8 * G_{\text{Cu}}^{\text{HSER}} - 288889.8 + 14.6318 * T$	[*]
	${}^0G_{\text{Cu:Al}}^{\text{DELTA}} = 8 * G_{\text{Al}}^{\text{HSER}} + 5 * G_{\text{Cu}}^{\text{HSER}} + 20000$	[*]
	Al-Si ${}^0G_{\text{Si:Al}}^{\text{DELTA}} = 5 * G_{\text{Si}}^{\text{HSER}} + 8 * G_{\text{Al}}^{\text{HSER}} + 60000$	[*]
	Cu-Si ${}^0G_{\text{Si:Cu}}^{\text{DELTA}} = 5 * G_{\text{Si}}^{\text{HSER}} + 8 * G_{\text{Cu}}^{\text{HSER}} + 60000$	[*]
	Al-Cu-Si ${}^0L_{\text{Al,Si:Cu}}^{\text{DELTA}} = - 69005.8 - 103.93 * T$	[*]
EPS_PRIME (Al,Cu,Si) ₁ (Cu) ₁ ε'(AICu)	${}^0G_{\text{Si:Cu}}^{\text{EPS_PRIME}} = G_{\text{Si}}^{\text{HSER}} + G_{\text{Cu}}^{\text{HSER}} + 10000$	[*]
	${}^0L_{\text{Al,Si:Cu}}^{\text{EPS_PRIME}} = - 25856.4$	[*]
GAMMA_ALCU (Al,Cu,Si) ₂ (Cu) ₂ (Cu) ₃ (Al,Cu,Si) ₆ γ'(AICu)	Cu-Si ${}^0G_{\text{Si:Cu:Cu:Si}}^{\text{GAMMA_AICU}} = 8 * G_{\text{Si}}^{\text{HSER}} + 5 * G_{\text{Cu}}^{\text{HSER}} + 220000$	[*]
	${}^0G_{\text{Si:Cu:Cu:Cu}}^{\text{GAMMA_AICU}} = 2 * G_{\text{Si}}^{\text{HSER}} + 11 * G_{\text{Cu}}^{\text{HSER}} + 200000$	[*]

Table 3 continued

Database name (constituents) <i>Name used in the text</i>	Thermodynamic parameters (298.15 < T < 6000 K)	Ref
	${}^0\text{G}_{\text{GAMMA_AlCu}} \text{Cu:Cu:Cu:Cu} = 13 * \text{G}_{\text{Cu}}^{\text{HSER}} + 120000$ ${}^0\text{G}_{\text{GAMMA_AlCu}} \text{Cu:Cu:Cu:Si} = 6 * \text{G}_{\text{Si}}^{\text{HSER}} + 7 * \text{G}_{\text{Cu}}^{\text{HSER}} + 150000$ ${}^0\text{L}_{\text{GAMMA_AlCu}} \text{Cu:Cu:Cu:Cu,Si} = - 592700 - 250 * \text{T}$ ${}^1\text{L}_{\text{GAMMA_AlCu}} \text{Cu:Cu:Cu:Cu,Si} = 80000$ ${}^2\text{L}_{\text{GAMMA_AlCu}} \text{Cu:Cu:Cu:Cu,Si} = 600000$	
	Al-Cu-Si ${}^0\text{G}_{\text{GAMMA_AlCu}} \text{Al:Cu:Cu:Si} = 2 * \text{G}_{\text{Al}}^{\text{HSER}} + 6 * \text{G}_{\text{Si}}^{\text{HSER}} + 5 * \text{G}_{\text{Cu}}^{\text{HSER}} + 50000$ ${}^0\text{G}_{\text{GAMMA_AlCu}} \text{Si:Cu:Cu:Al} = 2 * \text{G}_{\text{Si}}^{\text{HSER}} + 6 * \text{G}_{\text{Al}}^{\text{HSER}} + 5 * \text{G}_{\text{Cu}}^{\text{HSER}} + 30000$ ${}^0\text{L}_{\text{GAMMA_AlCu}} \text{Cu:Cu:Cu:Al,Cu,Si} = - 1063408 - 400.6 * \text{T}$ ${}^1\text{L}_{\text{GAMMA_AlCu}} \text{Cu:Cu:Cu:Al,Cu,Si} = - 1353587 - 398.5 * \text{T}$ ${}^0\text{L}_{\text{GAMMA_AlCu}} \text{Cu:Cu:Cu:Al,Si} = 288250 - 250 * \text{T}$ ${}^1\text{L}_{\text{GAMMA_AlCu}} \text{Cu:Cu:Cu:Al,Si} = - 506500 + 420 * \text{T}$	
GAMMA_CUZN (Al,Cu,Si) ₂ (Cu) ₂ (Cu) ₃ (Al,Cu,Si) ₆ γ(AlCu)	Cu-Si ${}^0\text{G}_{\text{GAMMA_CuZn}} \text{Si:Cu:Cu:Si} = 8 * \text{G}_{\text{Si}}^{\text{HSER}} + 5 * \text{G}_{\text{Cu}}^{\text{HSER}} + 220000$ ${}^0\text{G}_{\text{GAMMA_CuZn}} \text{Si:Cu:Cu:Cu} = 2 * \text{G}_{\text{Si}}^{\text{HSER}} + 11 * \text{G}_{\text{Cu}}^{\text{HSER}} + 200000$ ${}^0\text{G}_{\text{GAMMA_CuZn}} \text{Cu:Cu:Cu:Cu} = 13 * \text{G}_{\text{Cu}}^{\text{HSER}} + 120000$ ${}^0\text{G}_{\text{GAMMA_CuZn}} \text{Cu:Cu:Cu:Si} = 6 * \text{G}_{\text{Si}}^{\text{HSER}} + 7 * \text{G}_{\text{Cu}}^{\text{HSER}} + 150000$ ${}^0\text{L}_{\text{GAMMA_CuZn}} \text{Cu:Cu:Cu:Cu,Si} = - 600000$ ${}^1\text{L}_{\text{GAMMA_CuZn}} \text{Cu:Cu:Cu:Cu,Si} = 80000$ ${}^2\text{L}_{\text{GAMMA_CuZn}} \text{Cu:Cu:Cu:Cu,Si} = 600000$	[*]
	Al-Cu-Si ${}^0\text{G}_{\text{GAMMA_CuZn}} \text{Al:Cu:Cu:Si} = 2 * \text{G}_{\text{Al}}^{\text{HSER}} + 6 * \text{G}_{\text{Si}}^{\text{HSER}} + 5 * \text{G}_{\text{Cu}}^{\text{HSER}} + 50000$ ${}^0\text{G}_{\text{GAMMA_CuZn}} \text{Si:Cu:Cu:Al} = 2 * \text{G}_{\text{Si}}^{\text{HSER}} + 6 * \text{G}_{\text{Al}}^{\text{HSER}} + 5 * \text{G}_{\text{Cu}}^{\text{HSER}} + 30000$ ${}^0\text{L}_{\text{GAMMA_CuZn}} \text{Cu:Cu:Cu:Al,Cu,Si} = - 963500 - 500 * \text{T}$ ${}^1\text{L}_{\text{GAMMA_CuZn}} \text{Cu:Cu:Cu:Al,Cu,Si} = - 1463500 - 500 * \text{T}$ ${}^0\text{L}_{\text{GAMMA_CuZn}} \text{Cu:Cu:Cu:Al,Si} = 268250 - 250 * \text{T}$ ${}^1\text{L}_{\text{GAMMA_CuZn}} \text{Cu:Cu:Cu:Al,Si} = - 496500 + 500 * \text{T}$	

The phase names used in this dataset are usually based on the common names of phases used in the literature. Exceptions are accepted when the generic name for the crystallographic structure exists to be consistent with large databases (e.g. BCC_A2, FCC_A1). The names for the γ-brass family of phases (GAMMA_ALCU and GAMMA_CUZN) were selected with respect to the structure prototype to ensure simple identification of corresponding data for these phases in other datasets.

No silicon was introduced into the models for ζ, ζ', θ and η'(AlCu) phases because of a lack of experimental information.

β(CuSi) phase also exists in a small region around 800C in the Cu-rich region of the Cu-Si binary phase diagram.

On the other hand, negligible solubility was found in β(bcc) phase in all experimentally measured isotherms, and only κ(hcp) was identified when the samples were studied by x-ray diffraction after quenching. Small solubility of Si in β(AlCu) at 600°C was proposed by He *et al.*,^[2] but no substantial evidence was found in their work.

After analysing above mentioned arguments, the authors decided to consider a significantly larger solubility of Si for the standard model for the β(bcc) family of phases, and it was found that this assumption can very well explain above mentioned problems. By assessing extensive solubility of

Si mainly in the β(AlCu) phase, starting at 600 °C which even reaches complete solubility at 800 °C between Al-Cu and Cu-Si binaries, excellent agreement is reached. The agreement between the experiment and modelling at 800 °C is now very good, as presented in Fig. 21, where the two phase field region is now represented by the (Cu) + β(bcc) equilibrium instead of the (Cu) + κ(hcp) as it was in previous calculations (Fig. 20). Here the experimental tie lines representing the (Cu) + β(bcc) phase equilibrium fit very well the calculated phase boundaries and there is very good agreement for the rest of the experimental samples.

The detail of the high temperature Cu-rich corner of the 10 at.% Si isopleth is shown in Fig. 22. There is very good

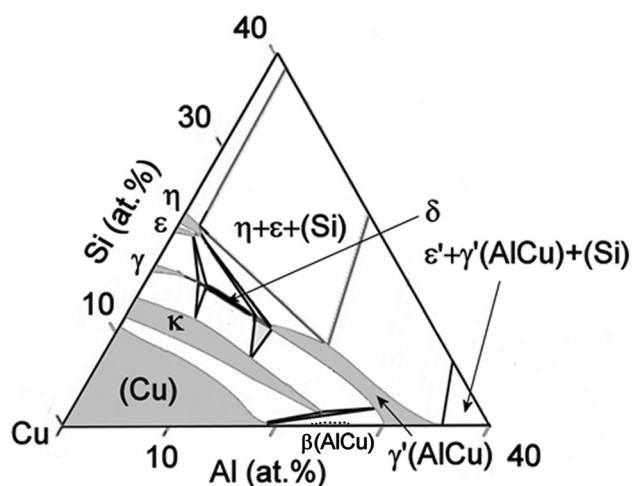


Fig. 18 The experimental isotherm at 700 °C redrawn according to.^[3] The projection of δ (CuSi) high temperature phase was observed at this temperature (originally identified as ternary phase), the β – AlCu (bcc) phase with very low Si solubility was omitted as it was not observed in the experiment, nevertheless it exists in the vicinity of binary Al-Cu diagram around 25 at.% of Al

agreement between the experimental signals from the thermal analysis^[3] and calculated phase boundaries. This agreement defines the solubility of Si in β (bcc) phase starting from relatively low value at 600 °C, significant solubility at 700 °C and complete solubility at 800 °C (Fig 8, 9 and 10, and 22). All calculated isothermal sections show now very good agreement with experimental data.

The very good agreement of calculated and experimental phase boundaries alone cannot be accepted as a fully conclusive proof of the assumption of Si solubility in the bcc phases, as long as the problem with the difference in the experimentally confirmed crystal structures (hcp versus bcc) is not solved. Therefore, an additional experiment was carried out by authors of this paper. The samples used for the experiments at 600 and 800 °C in the work

of^[5] were still available and two of them were selected. The compositions of samples were measured by SEM JEOL JSM-6460 equipped with EDX and the compositions were found to be (7.8Al-11.6Si-Cu) for sample 1 and (12.2Al-8.9Si-Cu) for sample 2 (in at.%).

Both samples should exhibit either single phase κ (hcp) or two phase structure with a very high content of κ (hcp) phase according to experiments. At the same time, they should contain the κ (hcp) phase at 600 °C and the β (bcc) phase at 800 °C according to the modelling. High temperature (HT) x-ray diffraction was employed, using an x-ray powder diffractometer Empyrean (PanAnalytical) with Bragg-Brentano geometry with HTK-16 high-temperature chamber. A full Rietveld refinement of the obtained patterns at different temperatures was carried out at the University of Vienna. The measurements were carried out at RT, 400, 600 and 800 °C and the results for sample 1 are shown in Fig. 23a,b. The existence of the κ (hcp) phase was clearly confirmed at 600 °C for both samples. The existence of the β (bcc) phase at 800 °C was confirmed for sample 2, two phase structure with β (bcc) and a negligible amount of fcc phase was found for sample 1.

These results of the x-ray experiments sufficiently confirm the validity of our assumption about the existing large solubility of the third element in the β (bcc) family of phases at elevated temperatures. Silicon tends to dissolve extensively in the β (AlCu) at temperatures between 600 and 800 °C and this behaviour can successfully explain the disagreements and inconsistencies found by current authors and by Ponweiser and Richter.^[3]

The reason for the disagreement with the experimental results from^[1-3,5] is probably the property of the high-temperature β (bcc) phase, which cannot be quenched under standard conditions. Consequently, the XRD analysis performed at room temperature showed the κ (hcp) phase instead of β (bcc).

Fig. 19 (a) The isopleth for 10 at.% of Si calculated using Version 1 of the database compared with experimental results from,^[3] (b) detail of this calculation in HT region (triangles are for liquidus curve, circles for invariant reactions and diamonds for other type of reactions)

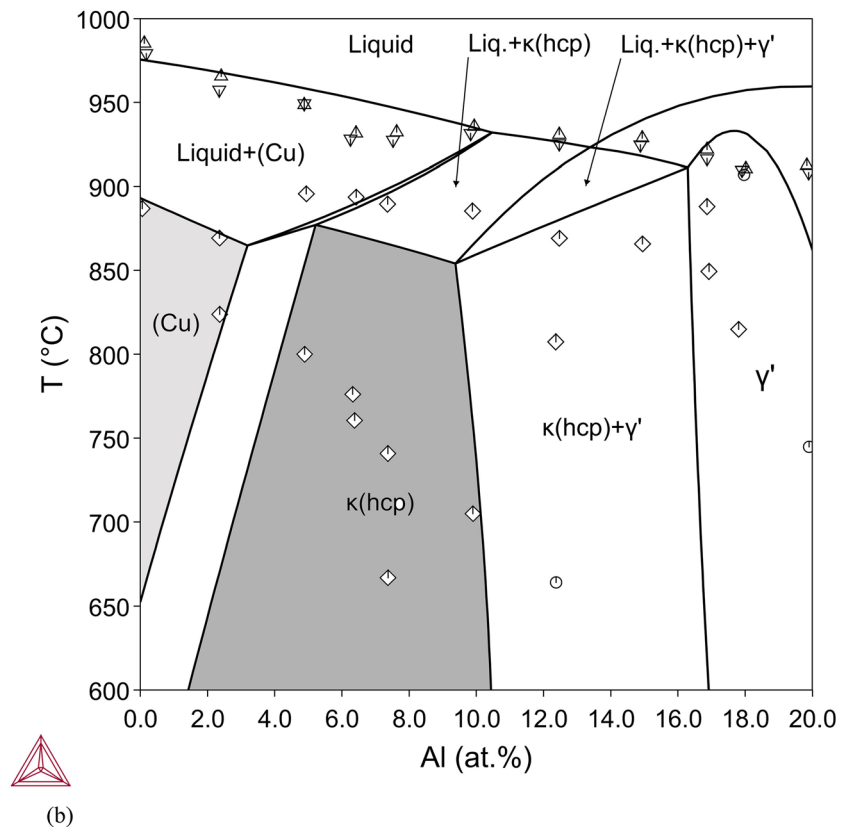
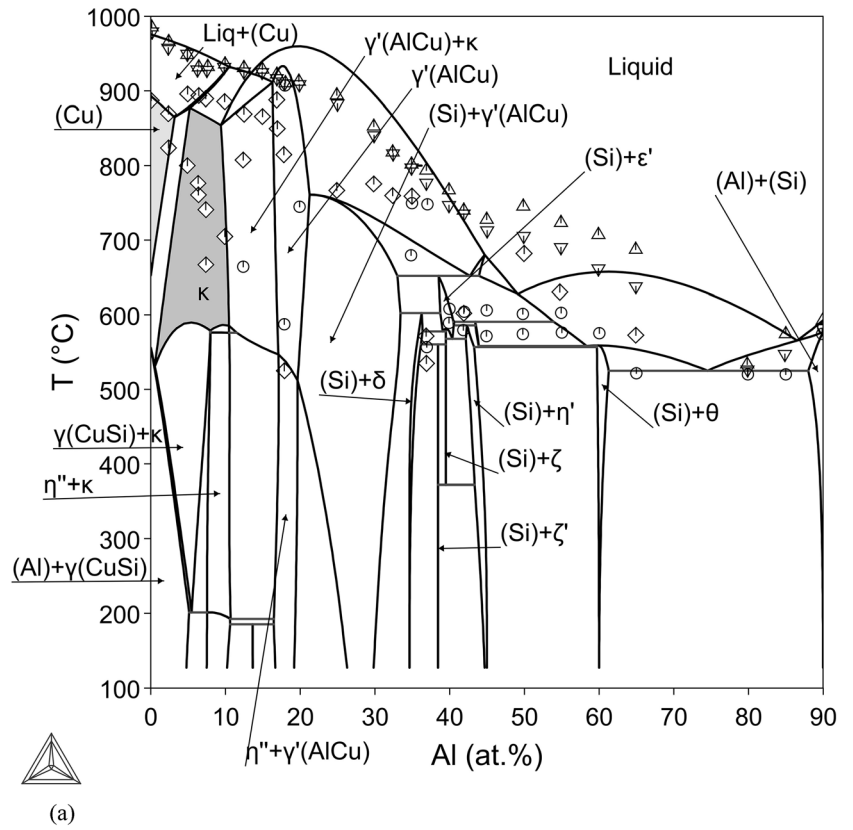
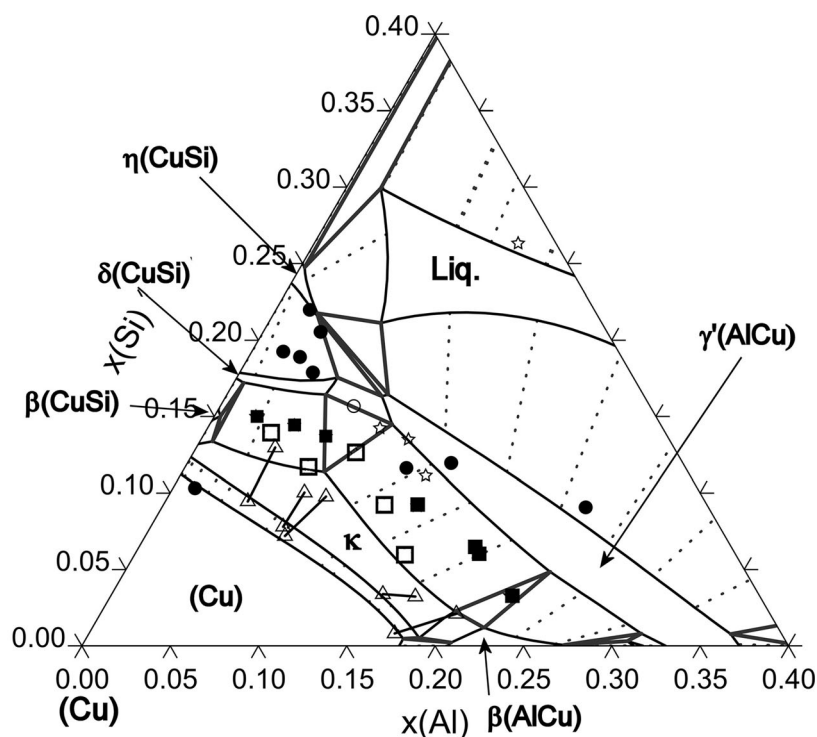


Fig. 20 Calculated isotherm for 800 °C using version 1 of the database compared with experimental data from Zobac *et al.*^[5] superimposed. The experimental tie-lines for the (Cu) + κ (hcp) two phase field are shown here as black lines connecting triangles, circles and stars indicate positions of other samples, squares indicate samples, where the experiment showed equilibrium with κ (hcp), but the calculations predicted equilibrium with β (bcc) (solid symbol - correct equilibrium, empty star, squares - close to correct equilibrium, empty circles - wrong equilibrium) (Color figure online)



4.2.2 Comparison of Al-Cu-Si Assessment with Other Literature Sources

As mentioned in Section 3.2., older works of Matsuyama^[42] and Hisatsune^[43] were not used for the full assessment in this study, but results obtained in the scope of this work were compared with their results. He *et al.*^[2] did use these works for their assessment as the newer studies,^[1,3] and^[5] were published later, so these experimental measurements were the only isopleths available for them. The works^[42] and^[43] are very extensive studies where the authors used thermal analysis and electric resistivity measurements to establish iso-composition sections of the Al-Cu-Si system. They generally studied various sections with constant silicon or aluminium content or their ratio, with the maximum Si content being 20 wt.% or less. Unfortunately, the experimental details given in their works were generally very brief. For example,

Hisatsune^[43] did not describe the process of sample preparation or the possible heat treatment in his work. For the method employed for the thermal analysis, he mentioned his earlier works without any concrete reference.

He *et al.*^[2] presented several sections for constant content of Si and constant Cu/Al ratios. The agreement is reasonably good, but a significant difference was found when the dataset from^[2] was used to calculate the isopleth for 40 at.% of Si published by Ponweiser and Richter.^[3] Here, the calculated solidus line is almost 90 °C higher than the experimental one. All attempts to assess the thermodynamic parameters in our dataset to describe better both the data from^[3] and^[42,43] were unsuccessful. These discrepancies tend to appear in all calculations where there is significant content of all elements. As the data presented by Ponweiser and Richter^[3] are based on very careful experimental work using advanced equipment, it was decided to use their results for the assessment, and the

Table 4 Invariant reactions containing liquid for the Al-Cu-Si system

Reaction type	Temp, (°C)	Invariant reaction	Phase comp.	x(Al)	x(Cu)	x(Si)
M1	937.54	$\beta = > L + \gamma'(AlCu) + \gamma(AlCu)$	L	0.324	0.624	0.052
			$\gamma'(AlCu)$	0.299	0.669	0.032
			$\gamma(AlCu)$	0.321	0.666	0.013
			β	0.315	0.664	0.021
U1	902.24	$L + \gamma(AlCu) = > \gamma'(AlCu) + \varepsilon(AlCu)$	L	0.384	0.578	0.038
			$\gamma'(AlCu)$	0.331	0.651	0.018
			$\varepsilon(AlCu)$	0.358	0.628	0.014
			$\gamma(AlCu)$	0.341	0.653	0.006
M2	836.67	$\varepsilon(AlCu) = > L + \varepsilon'(AlCu) + \gamma'(AlCu)$	L	0.472	0.517	0.011
			$\varepsilon'(AlCu)$	0.402	0.597	0.001
			$\gamma'(AlCu)$	0.366	0.630	0.004
			$\varepsilon(AlCu)$	0.412	0.584	0.004
U2	823.46	$L + \beta = > \gamma'(AlCu) + \delta(CuSi)$	L	0.064	0.754	0.182
			$\gamma'(AlCu)$	0.094	0.749	0.157
			$\varepsilon(AlCu)\eta$	0.079	0.787	0.134
			$\delta(CuSi)$	0.060	0.774	0.166
U3	803.52	$L + \delta(CuSi) = > \gamma'(AlCu) + \eta(CuSi)$	L	0.060	0.731	0.209
			$\gamma'(AlCu)$	0.081	0.748	0.171
			$\delta(CuSi)$	0.059	0.765	0.176
			$\eta(CuSi)$	0.023	0.758	0.219
E1	736.64	$L = > \gamma'(AlCu) + \eta(CuSi) + (Si)$	L	0.085	0.658	0.257
			$\gamma'(AlCu)$	0.112	0.725	0.163
			$\eta(CuSi)$	0.019	0.749	0.232
			(Si)	~ 0	~ 0	1.0
U4	656.66	$L + \gamma'(AlCu) = > (Si) + \varepsilon'(AlCu)$	L	0.436	0.433	0.131
			(Si)	~ 0	~ 0	1.0
			$\varepsilon'(AlCu)$	0.420	0.566	0.014
			$\gamma'(AlCu)$	0.354	0.622	0.024
U5	604.95	$L + \varepsilon' = > (Si) + \eta(AlCu)$	L	0.541	0.368	0.091
			(Si)	~ 0	~ 0	1.0
			$\eta(AlCu)$	0.467	0.513	0.020
			ε'	0.442	0.547	0.011
U6	561.72	$L + \eta(AlCu) = > (Si) + \theta$	L	0.620	0.316	0.064
			(Si)	~ 0	~ 0	1.0
			θ	0.664	0.336	0.0
			$\eta(AlCu)$	0.478	0.508	0.016
E2	525.58	$L = > (Si) + (Al) + \theta$	L	0.789	0.155	0.056
			(Si)	~ 0	~ 0	1.0
			(Al)	0.967	0.021	0.012
			θ	0.681	0.319	0.0

Fig. 21 Calculated isotherm for 800 °C using final version of the database compared with experimental data from Zobac *et al.*^[5] The experimental tie-lines for the (Cu) + κ (hcp) two phase field are shown here as black lines connecting triangles, circles and stars indicate positions of other samples, squares indicate samples, where the experiment showed equilibrium with κ (hcp), but the calculations predicted equilibrium with β (bcc) (solid symbol - correct equilibrium, empty star, squares - close to correct equilibrium, empty circles - wrong equilibrium) (Color figure online)

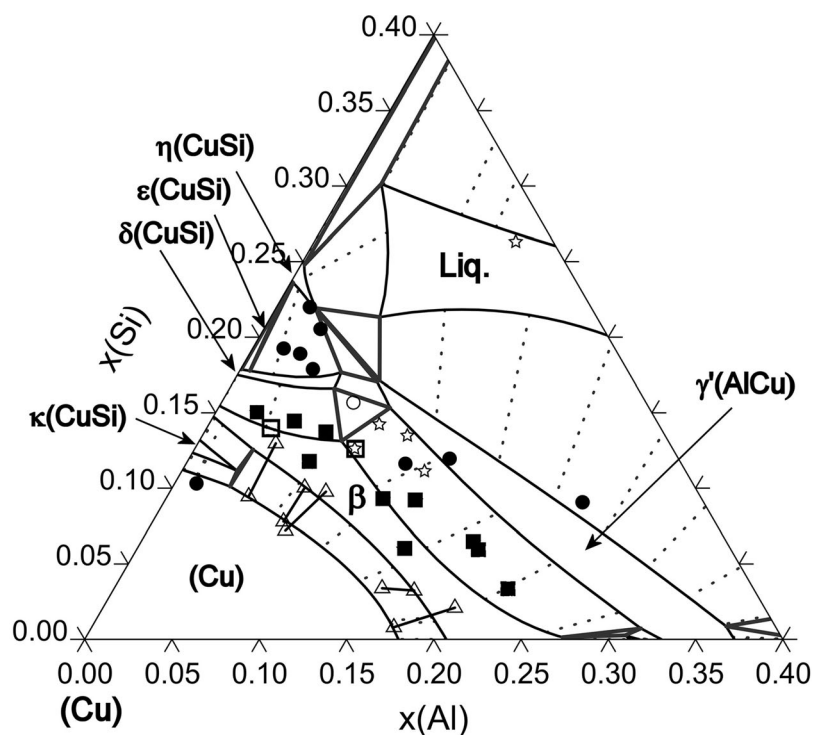
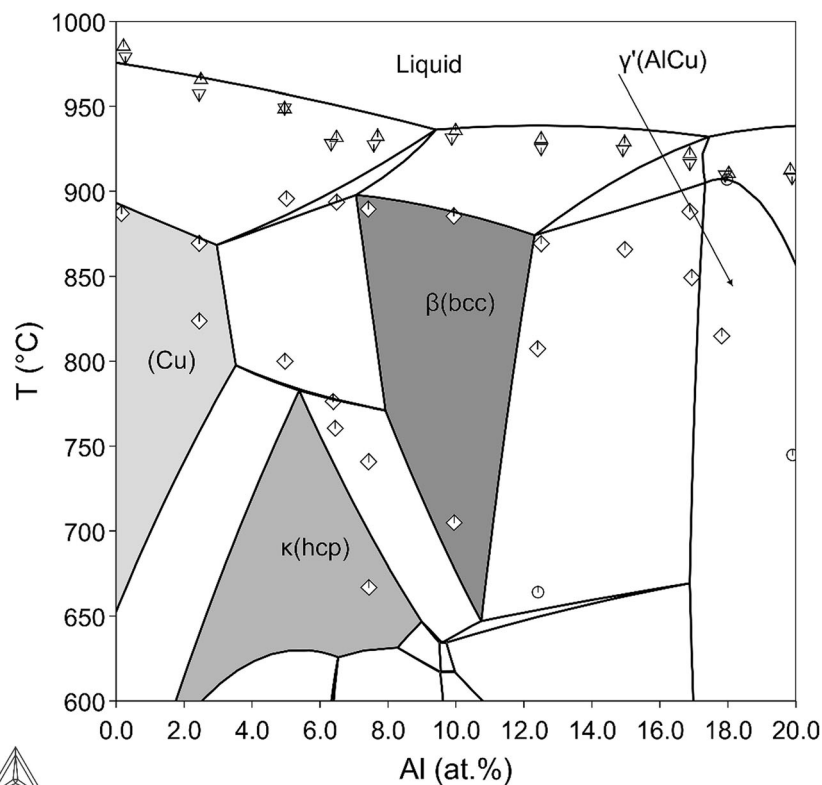


Fig. 22 Detail of the high temperature and Cu-rich corner of the isopleth for 10 at.% Si calculated using final version of the database with significant solubility of Si in bcc family of phases compared with experimental data from.^[3] (circles - invariant reactions, triangles - liquidus temperatures during heating and cooling, diamonds - other signals). The single phase fields for (Cu), β (bcc) and κ (hcp) are highlighted by various shades of grey



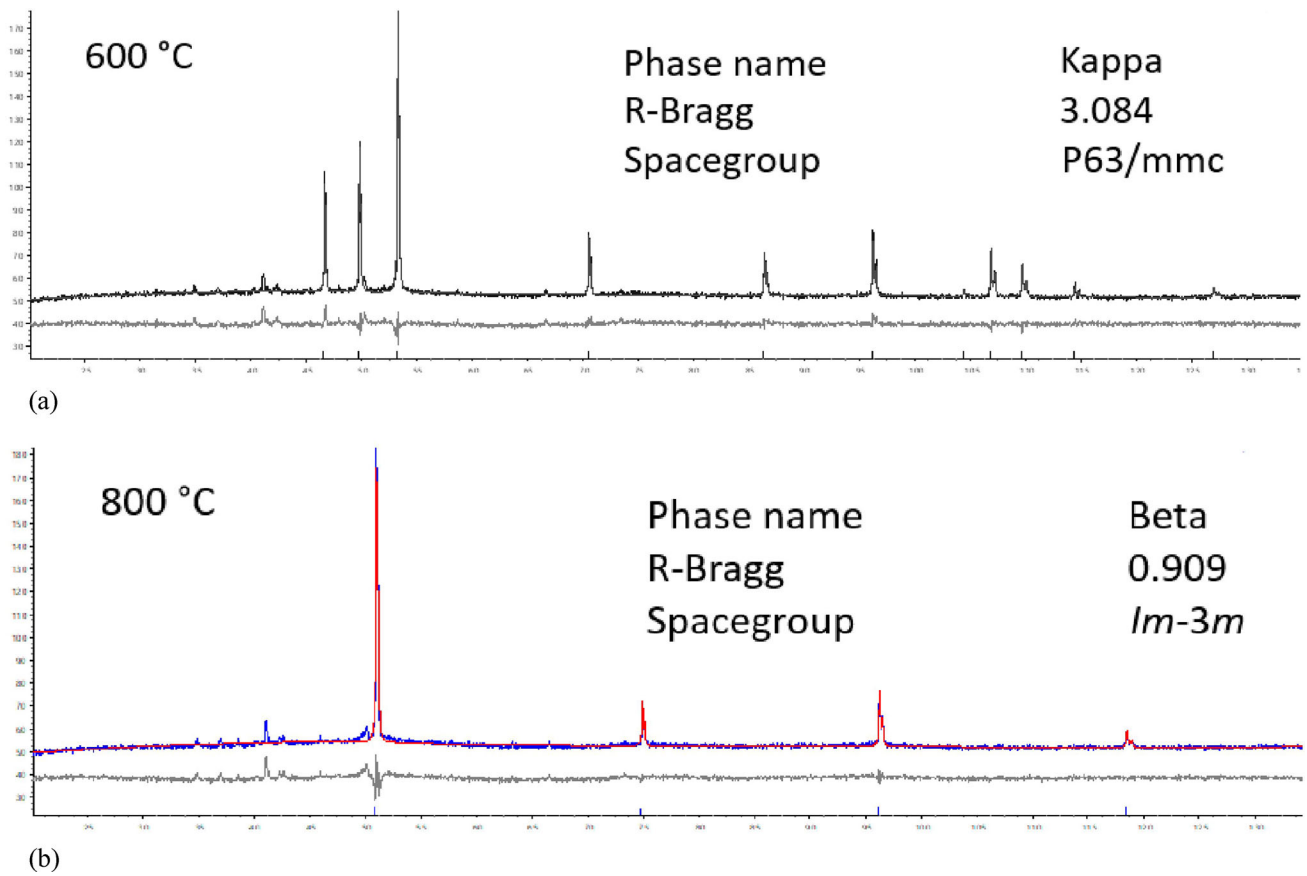


Fig. 23 HT x-ray diffractograms of sample 1 at 600 °C (a) and at 800 °C (b). Blue curve: measured XRD pattern, red curve: calculated pattern after Rietveld refinement. Grey curve: difference between experiment and refinement. Colour codes refer to the online version only

Fig. 24 Calculated isopleth for Cu_{0.95}Al_{0.05}-Si section (in weight fraction) compared with experimental data of Matsuyama^[42]

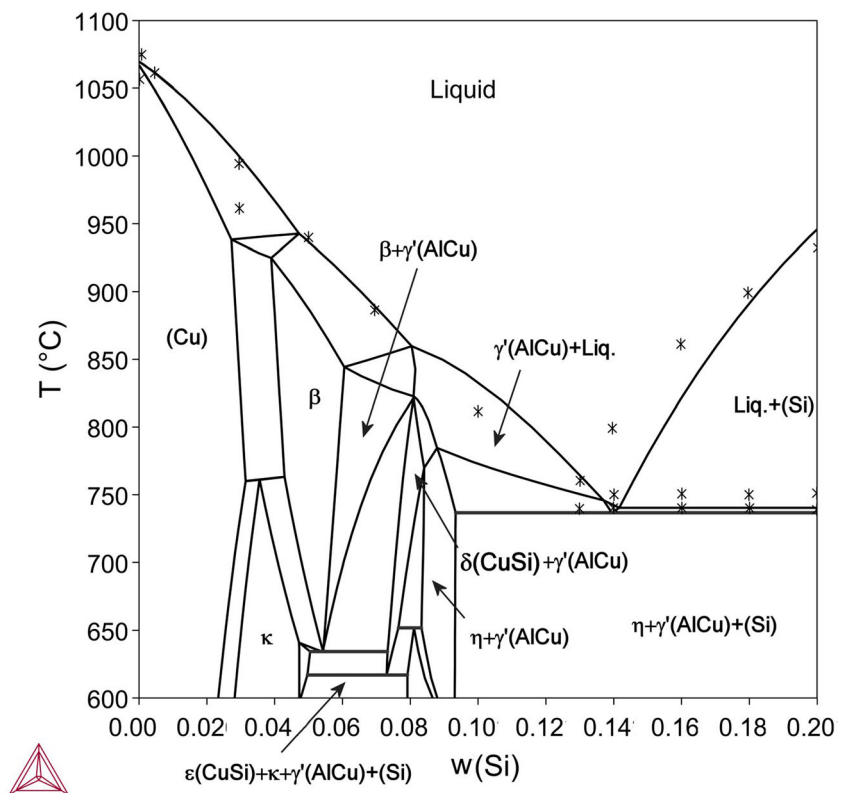


Fig. 25 Calculated isopleth for $\text{Cu}_{0.30}\text{Al}_{0.70}\text{-Si}$ section (in weight fraction) compared with experimental data of Matsuyama^[42]

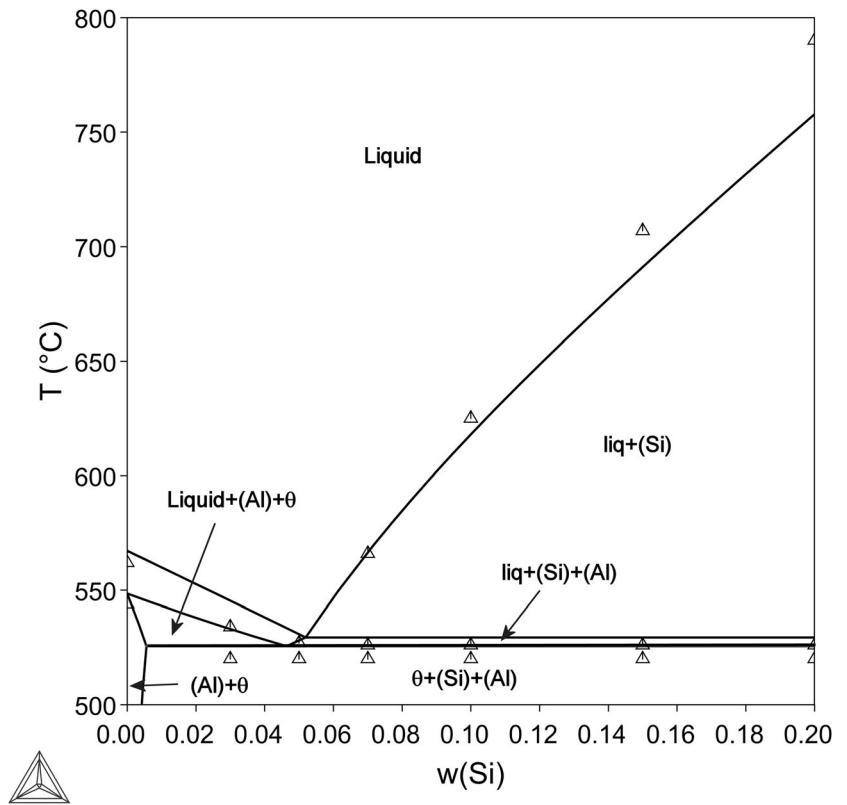


Fig. 26 Calculated isopleth for $\text{Cu}_{0.60}\text{Al}_{0.40}\text{-Si}$ section (in weight fraction) compared with experimental data of Matsuyama^[42]

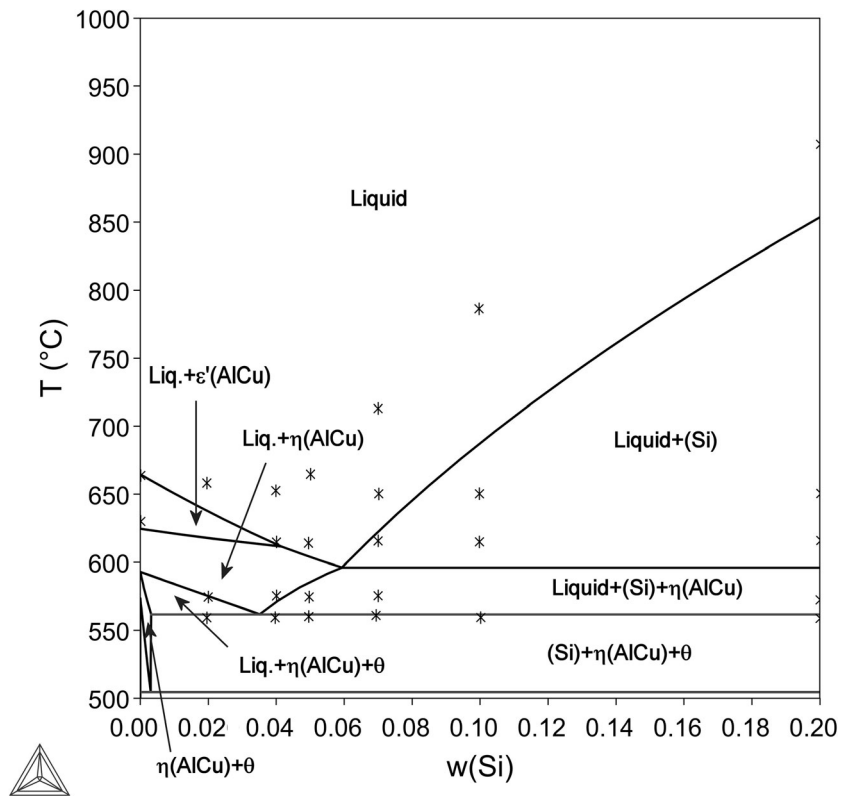


Fig. 27 Calculated isopleth for 2 wt.% of Si section (in weight fraction) compared with experimental data of Hitsasune^[43]

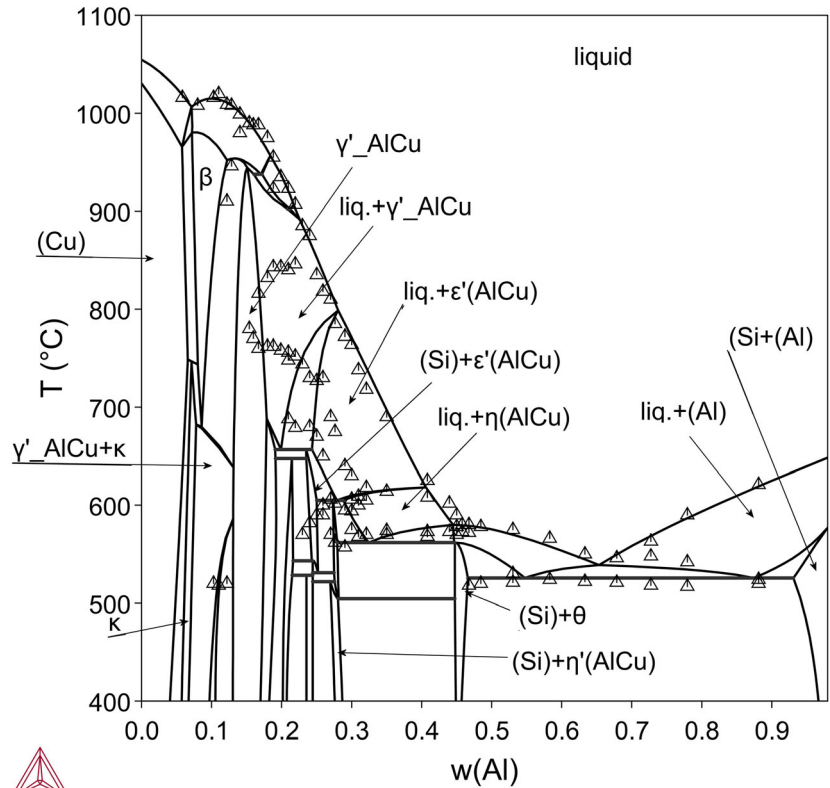


Fig. 28 Calculated isopleth for 20 wt.% of Si section (in weight fraction) compared with experimental data of Hitsasune^[43]

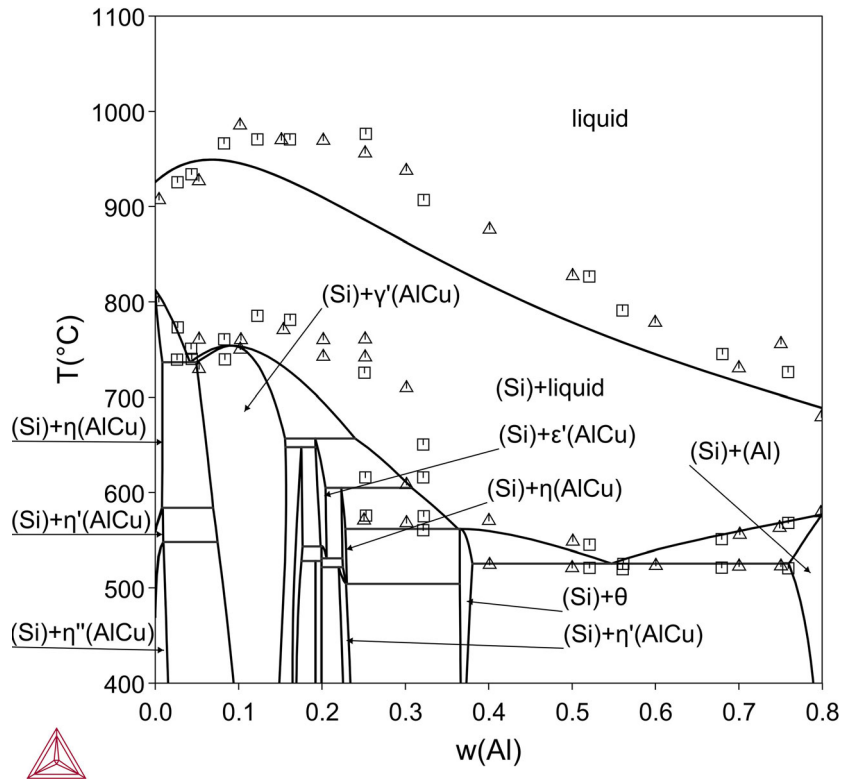
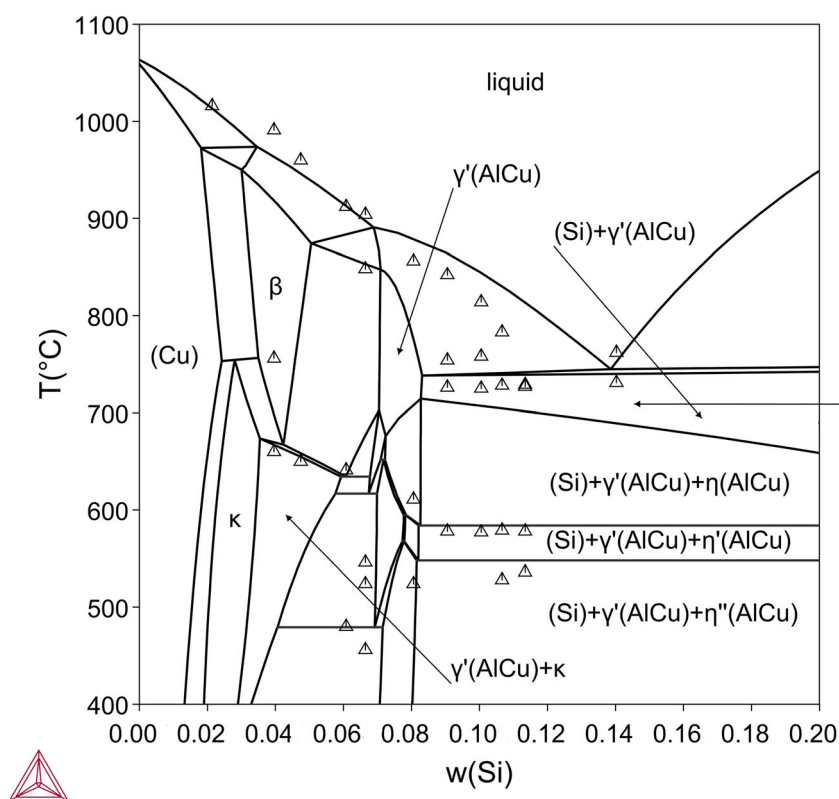


Fig. 29 Calculated isopleth for 6 wt.% of Al section (in weight fraction) compared with experimental data of Hitsasune^[43]



results from papers^[42,43] (taken from the original studies) only for comparison with the dataset assessed in this work.

The calculations for selected compositions are presented in Fig. 24, 25, 26, 27, 28 and 29. Examples were chosen to cover all types of experimental data, which were published in.^[42,43] Generally, it can be seen that there is very good or even excellent agreement between these experimental data and our calculations for smaller amounts of any third element, both for constant content of an element^[43] or constant ratio of elements.^[42] There is more pronounced disagreement in the central part of the diagrams, where the experimental values of the liquidus line are generally higher than the calculated ones. A similar discrepancy in the opposite direction exists between the calculations obtained using the database of He *et al.*^[2] for 40 at.% Si.

5 Conclusion

Although the literature on the properties of the Al-Cu-Si system is abundant, the phase equilibria and phase diagrams of this system are not well defined. The current study was designed to create a full assessment of the Al-Cu-Si system (and necessary reassessment of the Cu-Si system) based on the newest experimental results obtained mainly during the last 15 years. Good agreement was obtained

with experimental results, and the following key conclusions should be pointed out.

- The reassessment of the Cu-Si system was carried out, where solubility was introduced into most of the Cu-rich intermetallic phases, needed to better model the generally significant solubility of Al in these phases.
 - The agreement with the experimental data of Sufryd *et al.*^[28] and the previous theoretical assessment of Hallstedt *et al.*^[4] is excellent.
- The existence of the β (bcc) phase with extensive solubility of Al (and even complete solubility between binary Al-Cu and Cu-Si systems) at high temperatures (700–800 °C) was confirmed theoretically and experimentally. This phase is not quenchable under standard conditions but is confirmed in high-temperature XRD studies.
- The discrepancies between experiments and modelling were fully explained by this finding.
- Very good agreement was consequently obtained with the experimental results of^[1–3] and^[5] for isotherms at 500, 600, 700 and 800 °C.
- Good agreement was obtained for the vertical sections from^[3] and thermodynamic measurements from.^[47]
- The calculations were compared with old experimental works,^[42,43] which mainly studied isopleths in the Cu-

rich corner and close to the Cu-Al binary system, which were not directly used during the assessment work. Reasonable agreement was obtained especially for lower amounts of Al and Si. Disagreement was observed mainly for liquidus lines for higher content of Si.

Acknowledgment The authors would like to express their thanks to Dr. Pavla Roupčová for valuable help with the x-ray measurements, to Dr. Andrew Watson for valuable discussions, and Katerina Dockalová for the help during the preparation of the paper.

Funding Open access publishing supported by the National Technical Library in Prague.

Open Access This article is licensed under a Creative Commons Attribution 4.0 International License, which permits use, sharing, adaptation, distribution and reproduction in any medium or format, as long as you give appropriate credit to the original author(s) and the source, provide a link to the Creative Commons licence, and indicate if changes were made. The images or other third party material in this article are included in the article's Creative Commons licence, unless indicated otherwise in a credit line to the material. If material is not included in the article's Creative Commons licence and your intended use is not permitted by statutory regulation or exceeds the permitted use, you will need to obtain permission directly from the copyright holder. To view a copy of this licence, visit <http://creativecommons.org/licenses/by/4.0/>.

References

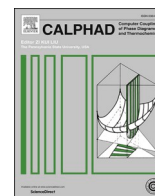
- P. Riani, K. Sufryd, and G. Cacciamani, About the Al-Cu-Si Isothermal Section at 500 °C and the Stability of the ϵ -Cu₁₅Si₄ Phase, *Intermetallics*, 2009, **17**, p 154-164.
- C.-Y. He, Y. Du, H.-L. Chen, and H. Xu, Experimental Investigation and Thermodynamic Modeling of the Al-Cu-Si System, *Calphad*, 2009, **33**, p 200-210. <https://doi.org/10.1016/j.calphad.2008.07.015>
- N. Ponweiser and K.W. Richter, New Investigation of Phase Equilibria in the System Al-Cu-Si, *J. of Alloys and Compd.*, 2012, **512**, p 252-263.
- B. Hallstedt, J. Gröbner, M. Hampl, and R. Schmid-Fetzer, Calorimetric Measurements and Assessment of the Binary Cu-Si and Ternary Al-Cu-Si Phase Diagrams, *Calphad*, 2016, **53**, p 25-38.
- O. Zobac, A. Kroupa, and K.W. Richter, Experimental Isothermal Sections of the Ternary Phase Diagram Al-Cu-Si at 600 °C and 800 °C, *J. Mater. Sci.*, 2020, **55**, p 15322-15333.
- O. Zobac, A. Kroupa, A. Zemanova, and K.W. Richter, Experimental Description of the Al-Cu Binary Phase Diagram, *Met. Mater. Trans. A*, 2019, **50A**, p 3805-3815. <https://doi.org/10.1007/s11661-019-05286-x>
- A. Kroupa, O. Zobac, and K.W. Richter, The Thermodynamic Reassessment of the Binary Al-Cu System, *J. Mater. Sci.*, 2021, **56**, p 3430-3443. <https://doi.org/10.1007/s10853-020-05423-7>
- J.L. Murray, The Aluminium-Copper System, *Int. Met. Rev.*, 1985, **30**, p 211-234.
- E.E. Havinga, Compounds and Pseudobinary Alloys with the CuAl₂ (C16)-Type Structure. II. Theoretical Discussion of Crystallographic Parameters, *J. Less-Common Met.*, 1972, **27**, p 187-193.
- N. Ponweiser, Ch.L. Lengauer, and K.W. Richter, Re-Investigation of Phase Equilibria in the System Al-Cu And Structural Analysis of the High-Temperature Phase η -Al₁₋₈Cu", *Intermetallics*, 2011, **19**, p 1737-1746.
- L.D. Gulay and B. Harbrecht, The Crystal Structure of ζ_2 -Al₃Cu₄, *Z. Anorg. Allg. Chem.*, 2003, **629**, p 463-466.
- L.D. Gulay and B. Harbrecht, The Crystal Structure of ζ_1 -Al₃Cu₄, *J. Alloys Compd.*, 2004, **367**, p 103-108.
- X.J. Liu, I. Ohnuma, R. Kainuma, and K. Ishida, Phase Equilibria in the Cu-Rich Portion of the Cu-Al Binary System, *J. Alloys Compd.*, 1998, **264**, p 201-208.
- V.T. Witusiewicz, U. Hecht, S.G. Fries, and S. Rex, The Ag-Al-Cu System: Part I: Reassessment of the Constituent Binaries on the Basis of New Experimental Data, *J. Alloy. Compd.*, 2004, **385**, p 133-143.
- N. Kuwano, T. Doi, and T. Eguchi, Period of ANTIPHASE and Tetragonality in the Alpha₂ Phase of Cu-Al Alloys, *Trans JIM*, 1977, **18**, p 807-815.
- L. Kaufman and H. Nesor, Coupled Phase Diagrams and Thermochemical Data for Transition Metal Binary Systems-V, *Calphad*, 1978, **2**, p 325-348.
- S.-W. Chen, Y.-Y. Chuang, Y.A. Chang, and M. Chu, Calculation of Phase Diagrams and Solidification Paths of Al-Rich Al-Li-Cu Alloys, *Met. Trans. A*, 1991, **22**, p 2837-2848.
- N. Saunders, System Al-Cu, COST 507: thermochemical database for light metal alloys, Volume 2: definition of thermodynamical and thermophysical properties to provide a database for the development of new light alloys, In: I. Ansara, A.T. Dinsdale, M.H. Rand (Eds.), European Commission, 1998.
- S.M. Liang and R. Schmid-Fetzer, Thermodynamic Assessment of the Al-Cu-Zn System, Part II: Al-Cu Binary System, *Calphad*, 2015, **51**, p 252-260.
- P. Dörner, E.-T. Henig, H. Krieg, H.L. Lukas, and G. Petzow, Optimization and Calculation of the Binary System Al-Si, *Calphad*, 1980, **4**, p 241-254.
- J.L. Murray and A.J. McAllister, The Al-Si (Aluminium-Silicon) System, *Bull. Alloy Phase Diagr.*, 1984, **5**, p 74-84.
- N. Chakraborti and H.L. Lukas, Thermodynamic Optimization of the Mg-Al-Si Phase Diagram, *Calphad*, 1992, **16**, p 79-86.
- J. Gröbner, H.L. Lukas, and F. Aldinger, Thermodynamic Calculation of the Ternary System Al-Si-C, *Calphad*, 1996, **20**, p 247-254.
- H.J. Ahn, Y.S. Kim, W.B. Kim, Y.E. Sung, and T.Y. Seong, Formation and Characterization of Cu-Si Nanocomposite Electrodes for Rechargeable Li Batteries, *J. Power. Sources*, 2006, **163**, p 211-214.
- O. Parajuli, N. Kumar, D. Kipp, and J.I. Hahn, Carbon Nanotube Cantilevers on Self-Aligned Copper Silicide Nanobeams, *Appl. Phys. Lett.*, 2007, **90**, 173107.
- Y. Liu, S. Song, D. Mao, H. Ling, and M. Li, Diffusion Barrier Performance of Reactively Sputtered Ta-W-N Between Cu and Si, *Microelectron. Eng.*, 2004, **75**, p 309-315.
- R.W. Olesinskym and G.J. Abbaschian, The Copper-Silicon System, *Bull. Alloy Phase Diagr*, 1986, **7**, p 170-178.
- K. Sufryd, N. Ponweiser, P. Riani, K.W. Richter, and G. Cacciamani, Experimental Investigation of Cu-Si Phase Diagram at $x(\text{Cu}) > 0.72$, *Intermetallics*, 2011, **19**, p 1479-1488.
- J.K. Solberg, Crystal-Structure of η -Cu₃Si Precipitates in Silica, *Acta Crystallogr. section A: Found. Crystallogr.*, 1978, **34**, p 684-698.
- K.P. Mukherje, J.P. Bandyopadhyaya, and K.P. Gupta, Phase Relationship and Crystal Structure of Intermediate Phases in Cu-Si System in Composition Range of 17 at. Pct. Si to 25 at. Pct. Si, *Trans. Metall. Soc. AIME*, 1969, **245**, p 2335-2338.

31. F.R. Morral and A. Westgren, The Crystal Structure of a Complex Copper–Silicon Compound, *Ark. Kemi. Miner. Geol.*, 1934, **11B**, p 1-6.
32. S. Arrhenius and A. Westgren, X-Radiation Analysis of Copper–Silicon Alloys, *Z. Phys. Chem.*, 1931, **14**, p 66-79.
33. F.E. Veer and W.G. Burgers, Diffusion in the Cu₃Si Phase of the Copper Silicon System, *Trans. Am. Inst. Min. Metall. Pet. Eng.*, 1968, **242**, p 669-673.
34. W.J. Ward and K.M. Carroll, Diffusion of Copper in the Copper–Silicon System, *J. Electrochem. Soc.*, 1982, **129**, p 227-229.
35. D. Shin, J.E. Saal, and Z.-K. Liu, Thermodynamic Modelling of the Cu–Si System, *Calphad*, 2008, **32**, p 520-526. <https://doi.org/10.1016/j.calphad.2008.05.003>
36. R.W. Olesinski, G.J. Abbaschian, Cu–Si (Copper–Silicon), in *Phase Diagrams of Binary Copper Alloys*. P.R. Subramanian, D.J. Chakrabarti, D.E. Laughlin, Eds., ASM International, Materials Park, OH, 1994, p 398–405
37. N. Matern, R. Seyrich, L. Wilde, C. Baetz, M. Knapp, and J. Acker, Phase Formation of Rapidly Quenched Cu–Si Alloys, *J. Alloys Compd.*, 2007, **429**, p 211-215.
38. L. Kaufman, Coupled Phase Diagrams and Thermochemical Data for Transition Metal Binary Systems VI, *Calphad*, 1979, **3**, p 45-76.
39. T. Bühler et al., in COST507-Thermochemical database for light metal alloys, I. Ansara, A.T. Dinsdale, M.H. Rand (eds.), European Commission, 124 (1994).
40. X.Y. Yan, and Y.A. Chang, A thermodynamic Analysis of the Cu–Si System, *J. Alloys Compd.*, 2000, **308**, p 221-229.
41. W. Gierlotka and M.A. Haque, On the Binary (Cu+Si) System: Thermodynamic Modelling of the Phase Diagram and Atomic Mobility in Face Centred Cubic Phase, *J. Chem. Thermodyn.*, 2013, **57**, p 32-38.
42. K. Matsuyama, Ternary Diagram of the Al–Cu–Si system, *Kinzuko no Kenkyu*, 1934, **11**, p 461-490.
43. C. Hisatsune, The Constitution Diagram of the Copper–Silicon–Aluminium System, *Mem. Coll. Eng. Kyoto Imp. Univ.*, 1935, **9**, p 18-47.
44. H.W.L. Phillips, The Constitution of Aluminium–Copper–Silicon Alloys, *J. Inst. Met.*, 1953, **82**, p 9-15.
45. H.L. Lukas, N. Lebrun, Al–Cu–Si (aluminium–copper–silicon), *Materials–The Landolt–Börnstein New Series IV/11A2*, MSIT, 2005, p. 135-147.
46. V. Raghavan, Aluminium–Copper–Silicon, *J. Phase Equilib. Diffus.*, 2007, **28**, p 180-182.
47. V.T. Witusiewicz, I. Arpshofen, H.-J. Seifert, and F. Aldinger, Enthalpy of Mixing of Liquid Al–Cu–Si Alloys, *J. Alloys Compd.*, 2000, **297**, p 176-184.
48. X.M. Pan, C. Lin, J.E. Morral, and H.D. Brody, An Assessment of Thermodynamic Data for the Liquid Phase in the Al-Rich Corner of the Al–Cu–Si System and its Application to the Solidification of a 319 Alloy, *J. Phase Equilib. Diffus.*, 2005, **26**, p 225-233.
49. H.L. Lukas, S.G. Fries, and B. Sundman, *Computational thermodynamics: the CALPHAD method*. Cambridge University Press, New York, 2017.
50. N. Saunders and A.P. Miodownik, *CALPHAD (A comprehensive guide)*. Pergamon Press, Oxford, 1998.
51. J.-O. Andersson, T. Helander, L. Höglund, P. Shi, and B. Sundman, Thermo-Calc and DICTRA, computational tools for materials science, *Calphad*, 2002, **26**, p 273-312.
52. W. Cao, S.L. Chen, F. Zhang, K. Wu, Y. Yang, Y.A. Chang, R. Schmid-Fetzer, and W.A. Oates, PANDAT software with PanEngine PanOptimizer and PanPrecipitation for multicomponent phase diagram calculation and materials property simulation, *Calphad*, 2009, **33**, p 28-342.
53. A. Dinsdale, SGTE Data for Pure Elements, *CALPHAD*, **15**, p. 317-425, (1991), version 5.0, <https://www.sgte.net/en/free-pure-substance-database>.
54. O. Redlich and A.T. Kister, Thermodynamics of Nonelectrolyte Solutions: X–Y–T Relations in a Binary System, *Ind. Eng. Chem.*, 1948, **40**, p 341-345.
55. Y.-M. Muggianu, M. Gambino, and J.-P. Bros, Enthalpies de Formation des Alliages Liquides Bismuth–Étain–Gallium à 723 K. *Choix d'une Représentation Analytique des Grandeurs d'excès Intégrales et Partielles de Mélange*, *J Chim Phys*, 1975, **72**, p 83-88. <https://doi.org/10.1051/jcp/1975720083>
56. Y. Iguchi, H. Shimoji, S. Ban-ya, and T. Fuwa, Calorimetric Study of Heat of Mixing of Copper Alloys at 1120 °C, *J. Iron Steel Inst. Jpn.*, 1977, **63**, p 275-284.
57. R. Castanet, Thermodynamic Investigation of Copper–Silicon Melts, *J. Chem. Thermodyn.*, 1979, **11**, p 787-791. [https://doi.org/10.1016/0021-9614\(79\)90010-7](https://doi.org/10.1016/0021-9614(79)90010-7)
58. G.I. Batalin and V.S. Sudavtsova, Thermodynamic Properties of Liquid Alloys of the Copper–Silicon System, *Inorg. Mater.*, 1982, **18**, p 133-135.
59. C. Bergman, R. Chastel, and J.-C. Mathieu, Determination of the Thermodynamic Properties of (Copper+Silicon) Melts by Knudsen - Cell Mass Spectrometry, *J. Chem. Thermodyn.*, 1986, **18**, p 835-845. [https://doi.org/10.1016/0021-9614\(86\)90118-7](https://doi.org/10.1016/0021-9614(86)90118-7)
60. Y. Kato, T. Yoshikawa, Y. Kagawa, and K. Morita, Effect of Fe Addition on the Activity Coefficient of Si in Cu–Fe–Si Melt at 1623K, *ISIJ Int.*, 2013, **53**, p 1320-1324. <https://doi.org/10.2355/isijinternational.53.1320>
61. T. Miki, N. Ogawa, T. Nagasaka, and M. Hino, Activity Measurement of Silicon in Molten Cu–Si Binary Alloy, *ISIJ Int.*, 2002, **42**, p 1071-1074. <https://doi.org/10.2355/isijinternational.42.1071>
62. K. Sano, K. Okajima, and N. Okuda, Thermodynamic Studies on the Formation of Molten Silicon Alloys Using the Galvanic Cells. 1: The System Copper–Silicon, *Mem. Fac. Eng. Nagoya Univ.*, 1956, **8**, p 127-130.
63. F. Sommer, D.K. Choi, and B. Predel, Bestimmung der Aktivitäten flüssiger Kupfer–Silicium - Legierungen nach der Effusionsmethode, *Z. Metallkd.*, 1989, **80**, p 366-369.

Publisher's Note Springer Nature remains neutral with regard to jurisdictional claims in published maps and institutional affiliations.

6.12 Paper 12

- [P12] **Zobač O.**, Kroupa A., Dinsdale A., Use of third generation data for the pure elements to model the thermodynamics of binary alloy systems: Part 3 – The theoretical prediction of the Al–Si–Zn system, CALPHAD, 2024, 87, 102742. doi: 10.1007/s11669-024-01160-5. (IF 1.947)



Use of third generation data for the pure elements to model the thermodynamics of binary alloy systems: Part 3 – The theoretical prediction of the Al–Si–Zn system

Ondrej Zobac^{a,*}, Ales Kroupa^a, Alan Dinsdale^b

^a Institute of Physics of Materials, The Czech Academy of Sciences, Zizkova 22, 616 00, Brno, Czech Republic

^b Hampton Thermodynamics Limited, UK

ARTICLE INFO

Handling Editor: Z.K. Liu

Keywords:

CALPHAD assessment
Al–Si and Si–Zn binary systems
Al–Si–Zn ternary system
3rd generation unary data

ABSTRACT

In a previous paper a method was developed to define Einstein temperatures for metastable phases of the elements and their relation to the so-called lattice stabilities used in the past, and also the variation of the Einstein temperature with composition to account for the composition dependence of the excess entropy. This approach was demonstrated successfully for the Al–Zn system. In this paper this approach is extended to cover the Al–Si and Si–Zn binary systems. The phase diagram for the Al–Si–Zn ternary system was then predicted from the thermodynamic description of the binary subsystems only without any ternary interaction parameters. Agreement with the experimental data is shown to be very good.

1. Introduction

Over the last few years, many developments have been made exploring the possibility of representing the thermodynamic properties of elements and binary alloy systems using more physically based models than used hitherto. In the first Ringberg meeting [1–3] the Debye and Einstein models were proposed as potential bases to represent the thermodynamic properties of crystalline phases over the whole temperature range. The Einstein model is simpler to work with while the Debye model is capable of giving a more accurate description at very low temperatures close to 0 K. The approach has been used with some success for a number of elements [4–13]. A simplified approach had been applied by Refs. [14,15] using the Einstein model for the description of the thermodynamic behaviour of pure elements below 298.15 K linked to existing SGTE pure element data. A limited number of attempts have been made to extend these physically based models to describe the thermodynamic properties and phase diagrams of binary systems [16–23]. Our previous work on the Al–Zn system [21] attempted to express the variation of the Einstein or Debye temperature of the solution phases as a function of composition and to represent data for metastable phases of the pure components (lattice stabilities). The aim of this work is to extend the data for the Al–Zn system through the addition of the recently assessed data for Si [12] and reassessments of

the data for the corresponding binary and ternary systems.

2. Application of third generation unary data to binary and ternary systems

2.1. Thermodynamic model for crystalline phases

The contribution to the heat capacity is given by Eq. (1) according to the Einstein model with additional contribution and correction terms [2]. It is necessary to account for magnetic contributions, anharmonic and electronic effects and the conversion from C_v to C_p . Without the magnetic contribution C_p should be given as follows

$$C_p = 3R \left(\frac{\theta_E}{T} \right)^2 \frac{e^{\theta_E/T}}{(e^{\theta_E/T} - 1)^2} + aT + bT^2 + cT^3 + dT^4 \quad (1)$$

Where R ($\text{J}\cdot\text{mol}^{-1}\text{K}^{-1}$) is the gas constant, T (K) the temperature and θ_E (K) the Einstein temperature.

The Gibbs energy, which is necessary for phase diagram calculations, can also be expressed as follows:

$$G = E_0 + \frac{3}{2}R\theta_E + 3RT \ln \left(\frac{e^{\theta_E/T} - 1}{e^{\theta_E/T}} \right) - \frac{a}{2} T^2 - \frac{b}{6} T^3 - \frac{c}{12} T^4 - \frac{d}{20} T^5 \quad (2)$$

During the critical assessment of data for the elements the aim is to

* Corresponding author.

E-mail address: zobac@ipm.cz (O. Zobac).

<https://doi.org/10.1016/j.calphad.2024.102742>

Received 7 May 2024; Received in revised form 2 September 2024; Accepted 7 September 2024

Available online 11 September 2024

0364-5916/© 2024 Elsevier Ltd. All rights are reserved, including those for text and data mining, AI training, and similar technologies.

define the parameters a , b , c , d and θ_E to reproduce the known value for S_{298} and the heat capacity from 298.15 K to the temperature of melting.

At higher temperatures, it is important to constrain any extrapolation to prevent the entropy of the crystalline phase becoming higher than that of the liquid [5]. An extra temperature range is included for temperatures above the melting point as follows:

$$C_p = 3R \left(\frac{\theta_E}{T} \right)^2 \frac{e^{\theta_E/T}}{(e^{\theta_E/T} - 1)^2} + a' + b'T^{-6} + c'T^{-12} \quad (3)$$

The parameters a' , b' and c' are selected such that the heat capacity and its derivative are continuous at the melting point and merges with that of the liquid phase at some high temperature eg. 6000 K.

2.2. Thermodynamic model for the liquid phase

The two-state model proposed by Agren [24] was adopted by the Ringberg workshops [1] as the basis for future representation of the thermodynamic data for the liquid phase. According to this model the liquid can be thought of as consisting of two types of atoms existing in thermodynamic equilibrium: *solid like atoms* and *liquid like atoms* with more translational freedom.

The Gibbs energy of the *solid like atoms* can be thought of as representing the amorphous solid and will take a similar form to that for the crystalline phase.

$$G_{am} = E_0 + \frac{3}{2}R\theta_E + 3RT \ln \frac{(e^{\theta_E/T} - 1)}{e^{\theta_E/T}} + A + aT^2 + bT^3 \quad (4)$$

The Einstein temperature of the amorphous phase could be expected to be similar to the Einstein temperature of the stable crystalline phase. Only a few correction terms may be necessary.

The difference in Gibbs energy between the *liquid like* and *solid like* atoms, ΔG_d can be expressed as:

$$G_{liq} - G_{am} = \Delta G_d = B + CT + DT \ln(T) \dots \quad (5)$$

The parameters θ_E , A , a , b , B , C and D may in principle be used in order to get best agreement with the experimental data. In practice the number of parameters used may be limited by the quantity of reliable experimental thermodynamic data available for the liquid phase.

2.3. Modelling of lattice stabilities using the einstein model

Lattice stabilities, ie. differences in Gibbs energy between two phases, are the key pieces of information required in order to model phase diagrams and thermodynamic data for systems. A lattice stability could be a constant value independent of temperature, to reflect the difference in crystal structure and strength of bonds in the two phases. However the two phases could also have different Einstein temperatures leading to a difference in entropy between the two phases.

Using the Einstein model without any correction terms, the entropy S is given by

$$S = 3R \left[\frac{\theta_E/T}{(e^{\theta_E/T} - 1)} - \ln \frac{(e^{\theta_E/T} - 1)}{e^{\theta_E/T}} \right] = 3R \left[\frac{\theta_E/T}{(e^{\theta_E/T} - 1)} - \ln(1 - e^{-\theta_E/T}) \right] \quad (6)$$

For high temperatures, this can be simplified to

$$S = 3R (1 - \ln(\theta_E/T)) \quad (7)$$

The entropy difference between two phases, α and β , at high temperatures can then be expressed as:

$$S^\alpha - S^\beta = 3R \ln \left(\frac{\theta_E^\beta}{\theta_E^\alpha} \right) \quad (8)$$

This means that the difference in entropy between the two phases will become constant at high temperatures. A more detailed derivation is given in the [21] paper.

2.4. Composition dependence of the thermodynamic properties

In our previous work [21] the extension of the description of the thermodynamic properties of the elements into the Al–Zn binary system was published in a logical and consistent manner such that there are no excess entropy terms. This implies that there are no non-configurational contributions to the entropy of mixing of a solution phase at 0 K. This involves some extension of the equations developed earlier to derive the Einstein temperatures of metastable phases of the elements.

From equation (7), the excess entropy for a solution phase between components A and B can be written as

$$S^{ex} = -3R(\ln \theta_M - x_A \ln \theta_A - x_B \ln \theta_B) \quad (9)$$

The mixing properties of a solution phase are commonly expressed in terms of a Redlich-Kister power series eg.

$$G^{ex} = x_A x_B (L_0 + L_1(x_A - x_B) + L_2(x_A - x_B)^2 + \dots) \quad (10)$$

$$S^{ex} = x_A x_B (S_0 + S_1(x_A - x_B) + S_2(x_A - x_B)^2 + \dots) \quad (11)$$

$\ln \theta^{ex}$ can also be expressed in terms of a Redlich-Kister power series

$$\ln \theta^{ex} = x_A x_B (\ln \theta_0 + \ln \theta_1(x_A - x_B) + \ln \theta_2(x_A - x_B)^2 + \dots) \quad (12)$$

and $\ln \theta$ by

$$\ln \theta = x_A \ln \theta_A + x_B \ln \theta_B + x_A x_B (\ln \theta_0 + \ln \theta_1(x_A - x_B) + \ln \theta_2(x_A - x_B)^2 + \dots) \quad (13)$$

A comparison of equation (13) and equations (9) and (11) shows that the coefficients for the excess entropy, S_0 , S_1 , S_2 , etc can be related directly to the coefficients for the variation of $\ln \theta$ with composition:

$$\ln \theta_0 = -S_0/3R, \ln \theta_1 = -S_1/3R, \ln \theta_2 = -S_2/3R, \text{ etc} \quad (14)$$

3. Review of literature data

In previous work [21], we focussed on modelling the thermodynamic and phase diagram data for the Al–Zn system. This present work concerns the application of the third generation unary data to the thermodynamic properties and phase diagram of the Al–Si–Zn ternary system and its associated binary subsystems Al–Si and Si–Zn. The Al–Si system is a eutectic system with negligible solubility of aluminium in crystalline silicon. The Si–Zn system is also a simple eutectic system, in this case with the eutectic point very close to pure Zn. The solubility of Si in crystalline Zn, and Zn in crystalline Si is negligible.

3.1. Pure elements

The 3rd generation thermodynamic modelling of data for Al and Zn is described in detail in our previous work [21]. The data for fcc Al, including the Einstein temperature, were based on Bigdeli [8] who assessed a value of 294.414 K for the Einstein temperature. It was felt that the assessment of Bigdeli for the liquid phase of Al did not correspond to the spirit of the two state model in that the *liquid like* atoms were not predicted to be predominant at high temperatures. As a result new data were derived for the liquid phase. Fig. 1 shows the experimental heat capacity data for crystalline and liquid phases. Most of the assessments of data for liquid Al assumed a constant heat capacity obtained from enthalpy drop measurements and the aim of the [21] assessment was to reproduce these data. The calculated heat capacity data for Al with superimposed experimental data are shown in Fig. 1.

The data for diamond_A4 and liquid phases of Si have recently been assessed by Bajenova et al. [12]. A combination of 2 Einstein temperatures was necessary for the diamond_A4 phase in order to provide a satisfactory fit to the experimental data with the first Einstein

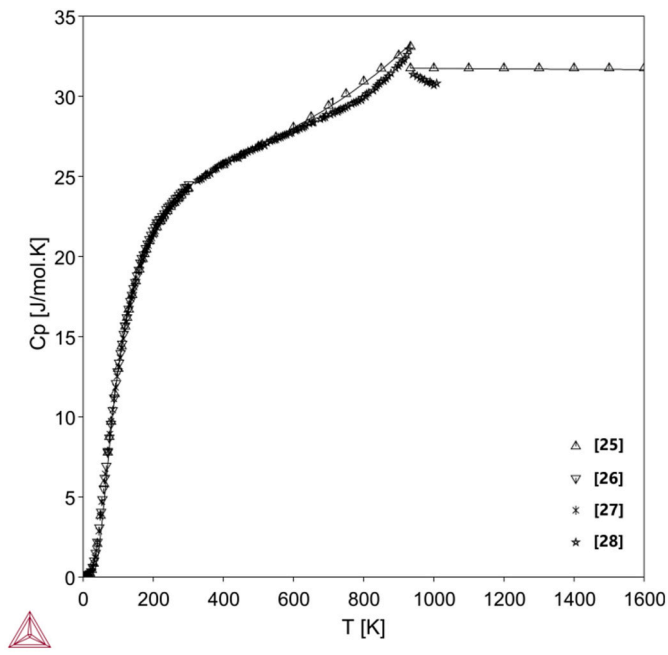


Fig. 1. Calculated heat capacity data for Al with superimposed representative experimental data [25–28].

temperature equal to 615.43 K with the weight factor of 0.674 and the second Einstein temperature of 207 K with weight factor 0.326. For the liquid phase Bajenova et al. [9] used in addition, experimental data for the amorphous phase and this also required the use of 2 Einstein temperatures. For simplicity in modelling data for binary and multicomponent systems Bajenova et al. also provided data for the liquid phase using just 1 Einstein temperature based on the experimental high temperature data only, and these were the data used in the current work. The calculated heat capacity based on this assessment with superimposed experimental data [29–34] is shown in Fig. 2.

The data for the hcp and liquid phases of Zn have recently been assessed by Dinsdale and Khvan [35]. A value of 162.2 K was derived for

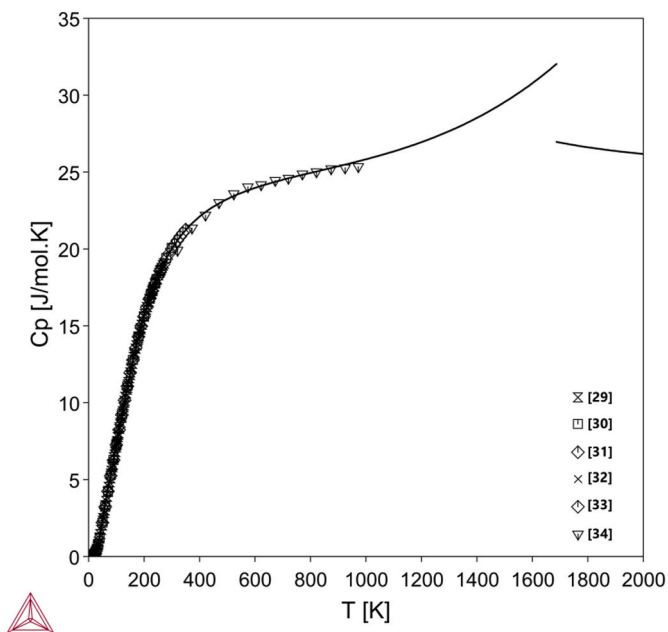


Fig. 2. Calculated heat capacity data for Si with superimposed experimental data [29–34].

the Einstein temperature for the hcp phase. The calculated heat capacity based on the assessment of Dinsdale and Khvan [35] is shown in Fig. 3.

3.2. Al–Si

The phase diagram for the Al–Si system is a simple eutectic with two crystalline phases fcc_A1 (Al) and diamond_A4 (Si). There is appreciable solubility of Si in fcc_A1 (Al) and therefore the phase has been modelled as a solid solution. In contrast there is negligible solubility of Al in diamond_A4 (Si) and this phase has been modelled as stoichiometric. The eutectic temperature of 577 °C has been determined rather precisely and the eutectic point lies at 12.2 at.% Si. The solubility of Si in fcc Al reaches a maximum of 1.5 at.% at the eutectic temperature. Feufel et al. [36] presented a critically assessed phase diagram using SGTE unaries [37] based on several experimental studies [38–45]. The phase diagram proposed by Feufel et al. [36] is shown in Fig. 4.

The enthalpy of mixing of liquid Al–Si alloys has been determined calorimetrically by Körber et al., Mathieu et al., Bros et al. and Batalin et al. [46–49]. The most reliable results seem to be the data published by Bros et al. [48] which were, on the whole, accepted by Murray et al. [50]. The enthalpies of mixing published by Batalin et al. [49] are, at 50 at% Si, more negative by a factor of two than those measured by Bros et al. [48].

Thermodynamic activities of the components in liquid Al–Si alloys have been measured by different methods. The activities using electrochemical cells have been obtained by Schaefer et al. [51] and Schaefer [52] at 1100 K, Berthon et al. [39] from 853 to 1253 K and Batalin et al. [45] between 950 and 1650 K. Mitani and Nagai determined activities by equilibrating liquid Al–Si alloys with AlCl_3 [53]. Chatillon et al. calculated the activities from vapour pressures they measured by a mass-spectrometry method (1473–1700 K) [54], and Loseva et al. from vapour pressures using a fluorescence technique [55].

3.3. Al–Zn

Several critical assessments of data for the Al–Zn system have been carried out either experimental in Ref. [56], or using the CALPHAD approach [57–62]. The thermodynamic data critically assessed by

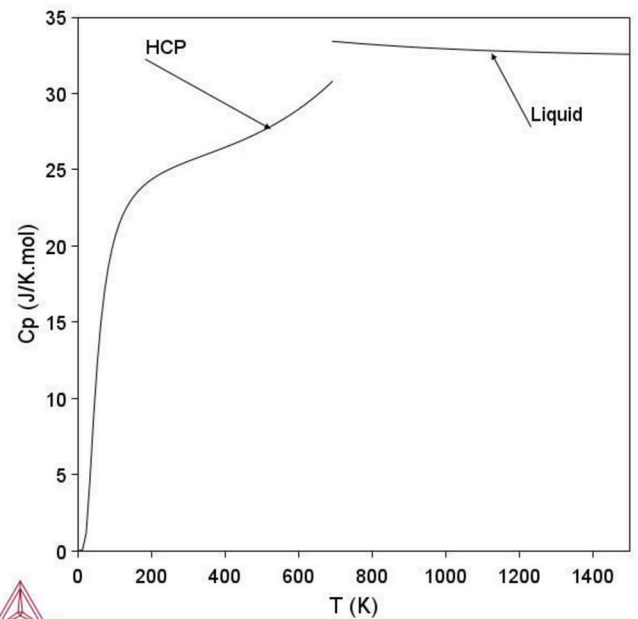


Fig. 3. Calculated heat capacity data for Zn based on assessment of Dinsdale and Khvan [35], used also in the work of [21].

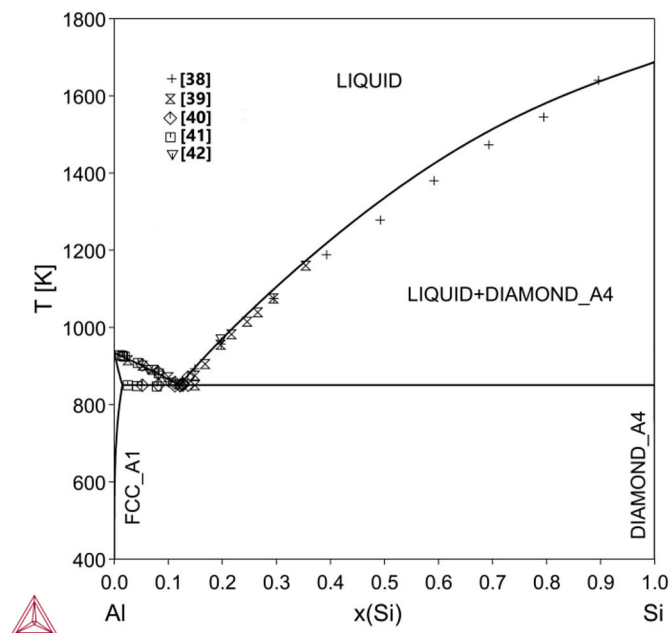


Fig. 4. Calculated phase diagram for the Al-Si system using the critically assessed data by Feufel et al. [36] with superimposed experimental data [38–42].

Mathon et al. [61] were used in our previous work [21] as being the most reliable critical assessment and used the Redlich-Kister model to represent the variation of thermodynamic properties with composition. Fig. 5 shows the calculated phase diagram for the Al-Zn system using the critically assessed data of Mathon et al. [61].

3.4. Si-Zn

The Si-Zn system is a eutectic system characterised by complete mixing of the components in the liquid phase and negligible solubility of the other element in either the diamond form of Si or the hcp form of Zn. The shape of the liquidus surface indicates positive enthalpies of mixing

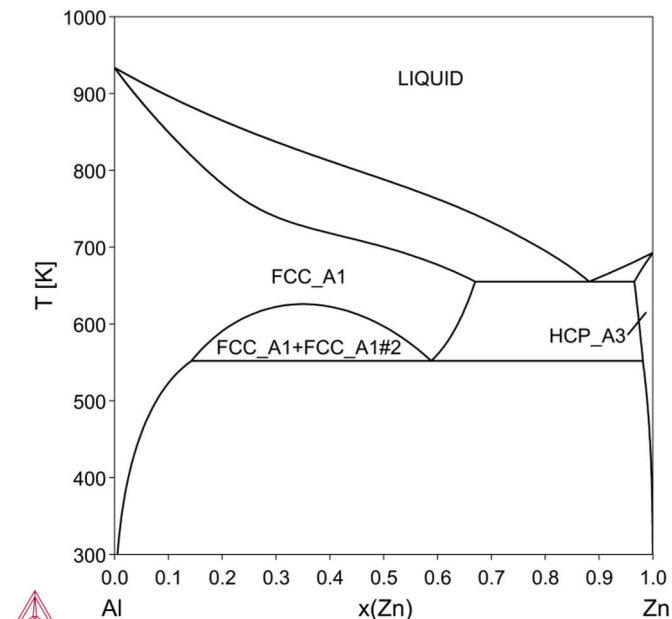


Fig. 5. Calculated phase diagram for the Al-Zn system using the critically assessed data of Mathon et al. [61].

and the possibility of a metastable miscibility gap. The liquidus data were studied experimentally by several authors, Girault [63], Thurmond and Kowalchik [64], John et al. [65] and Schneider and Krumnacker [66]. The critically assessed data for this system have been taken from the work of Jacobs and Spencer [67]. The calculated phase diagram using the data of Jacobs and Spencer [67] with superimposed experimental data is shown on Fig. 6. This was based entirely on measurements of the liquidus temperatures. The system has also been assessed by an Mey and Hack [57] and by Olesinski and Abbaschian [68].

3.5. Al-Si-Zn

Differential thermal analysis (DTA) was used for the evaluation of the liquidus curve by several authors, Padeshnova et al. [70], Dimova et al. [71], Planchamp [72] and Ibe and Holtz [73]. Nishimura and Tamura [74] determined the liquidus temperatures and Axon et al. [75] determined the solidus temperatures by the use of thermal analysis. Girault [63] reported solubility data for Si in liquid $\text{Al}_{10}\text{Zn}_{90}$ mixtures. The ternary eutectic point has been reported by Mondolfo [76], Hanemann and Schrader [77], Spengler [78] and Phillips [79]. Solidus temperatures at low Si contents (<12 at.%) have been measured by Nishimura and Tamura [74] (using dilatometry), Dimova et al. [71] (using DTA) and Planchamp [72] (using DTA). Ibe and Holtz [73] measured transition data for alloys with higher Si contents (<60 at.%) using DTA. In addition, the latter authors measured transitions involving the vapour phase. All authors mentioned above have determined parts of the liquidus and/or solidus surface, no isothermal sections based solely on the experimental data have been published up to now. A thermodynamic assessment of the ternary Al-Si-Zn system was published by Jacobs and Spencer [67]. They [67] predicted several isopleths of the Al-Si-Zn phase diagram and compared them with the experimental data. Vertical sections of phase diagram Al-Si-Zn with a constant amount of silicon $x(\text{Si}) = 0.047$ is shown in Fig. 7 as an example.

The only thermodynamic properties experimentally measured and presented in the literature were the activity data in the liquid phase measured by Sebkova et al. They measured the activity of Zn [80,81] using a transportation method. They also measured the activity of Al

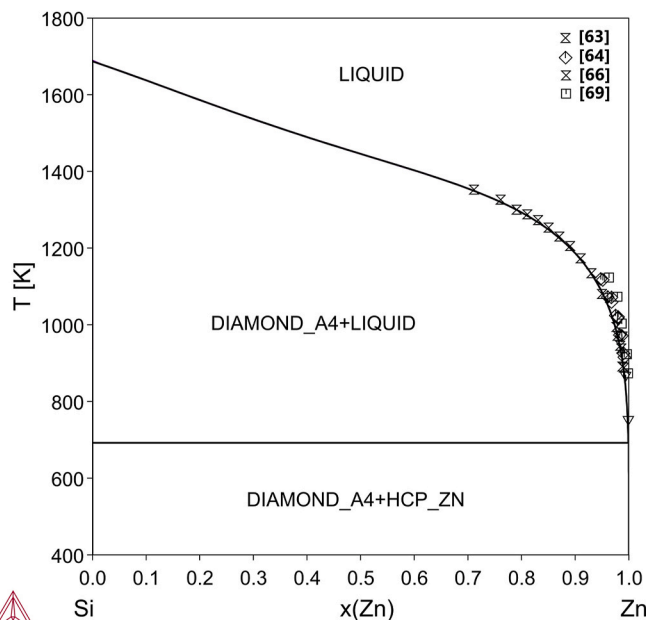


Fig. 6. Calculated phase diagram for the Si-Zn system using the critically assessed data of Jacobs and Spencer [67] with experimental data from literature superimposed [63,64,66,69].

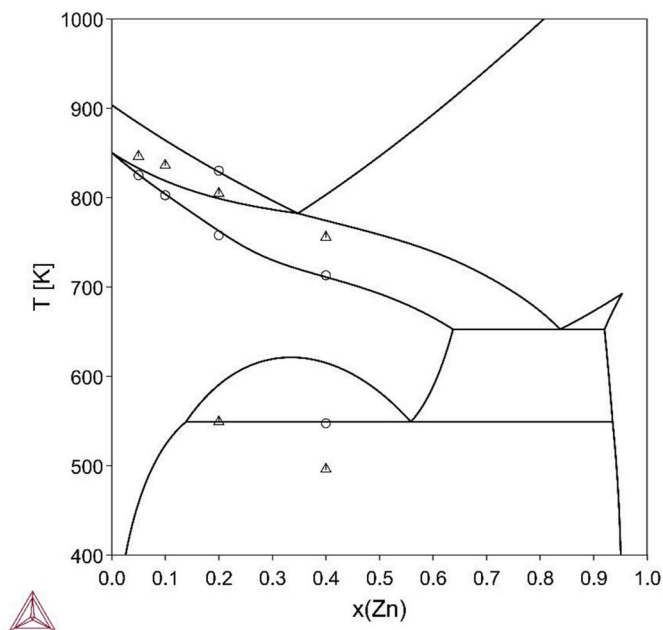


Fig. 7. Calculated isopleth [67] through the Al-Si-Zn phase diagram at $x(\text{Si}) = 0.047$ with superimposed experimental data of Ibe and Holtz [73] where the triangles represent cooling and the circles heating experiments.

[82] using an EMF technique. All activity measurements were carried out for alloys with Al contents greater than 67 at.%.

4. Results and discussion

4.1. Al-Si

Bajenova et al. [12] derived data for the diamond_A4 and liquid forms of Si. It was also necessary to define a single Einstein temperature for Si in the fcc_A1 phase to model data for the solution of Si in crystalline Al. For this the procedure used successfully by Khvan et al. [23] for the Pb-Sn system was used. The resulting value for the Einstein temperature of fcc_A1 Si is 182.6 K with the enthalpy of fcc_A1 Si equal to 51000 relative to the diamond_A4 phase.

The assessed data of Feufel et al. [36] were adopted to form the starting point for the current assessment.

The conversion relations developed in Ref. [21] were then used to calculate the values of interaction parameters i.e. to represent the enthalpy of mixing and the variation of the Einstein temperature with composition for the liquid and fcc_A1 phases of the Al-Si system. These were consequently used as the starting points for the reassessment of the thermodynamic data for the system. The temperature independent coefficients of the SGTE interaction parameters L0, L1 and L2 were retained and the entropic term (temperature dependent terms of the SGTE L0, L1 and L2 parameters), expressing the temperature dependence, were recalculated according to Eq. (14).

Fig. 8 shows the calculated phase diagram of binary system Al-Si with superimposed experimental data [39–45]. The details of the phase diagram in the Al-rich corner are shown in Figs. 9 and 10. Agreement with the experimental data is excellent. When comparing the results with the thermodynamic assessment of Feufel et al. [36] (Fig. 4), the agreement with the experimental data is even slightly better.

Fig. 11 shows the calculated enthalpy of mixing of the liquid phase at 1377 K with the experimental data from Bros superimposed [48]. Fig. 12 shows the calculated activity of Al and Si in the liquid phase at 1700 K with experimental data superimposed [53,54]. The agreement between the calculated thermodynamic functions for the liquid phase and the

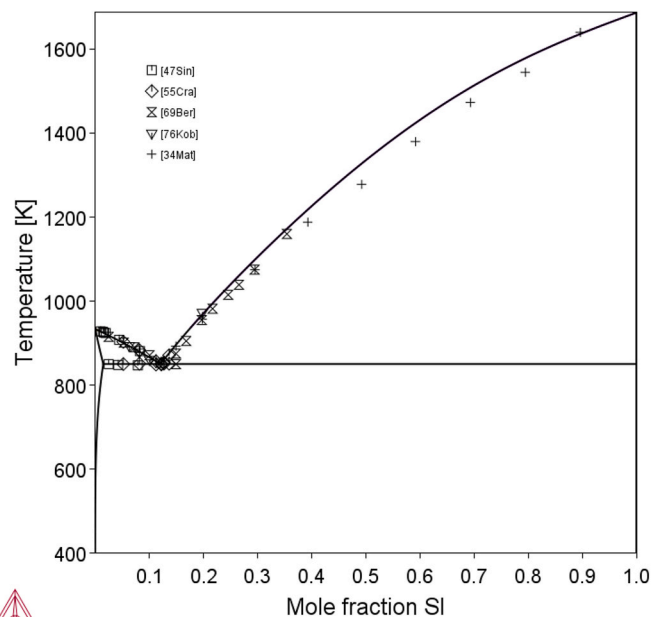


Fig. 8. Theoretical phase diagram of the Al-Si system based on 3rd generation of unaries assessed in this work with superimposed experimental data [38–45].

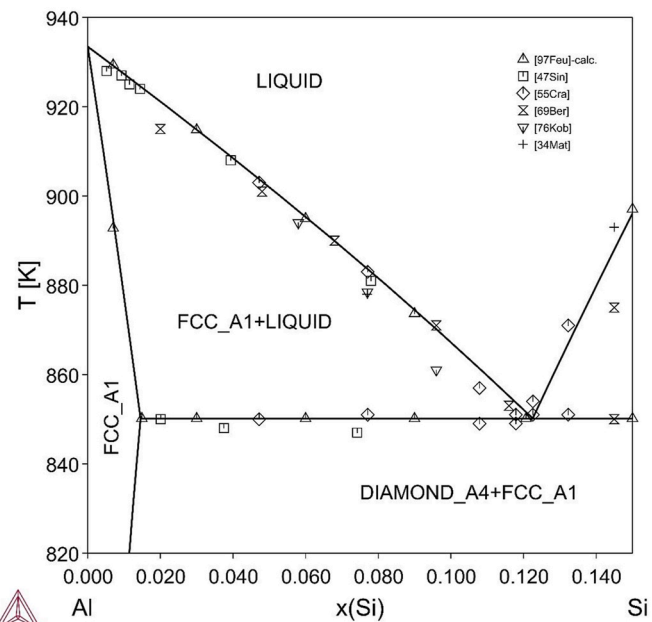


Fig. 9. Detail of the theoretical phase diagram of the Al-Si system based on 3rd generation of unaries assessed in this work with superimposed experimental data [38–45].

experimental data is very good. Table 1 lists the reassessed interaction parameters for the binary Al-Si system.

The calculated phase diagram of the Al-Si binary system is in very good agreement with the experimental data. The liquidus line slightly disagrees with the experimental data from Ref. [38] in the central part of the phase diagram. Nevertheless, a very similar disagreement (even slightly worse) was observed in the Al-Si phase diagram assessed by Ref. [36] using SGTE unary data. Here the reason might be caused by the experimental data which are very old.

The thermodynamic properties of liquid phase fits reasonably well to the experimental data. The experimental data for the enthalpy of mixing

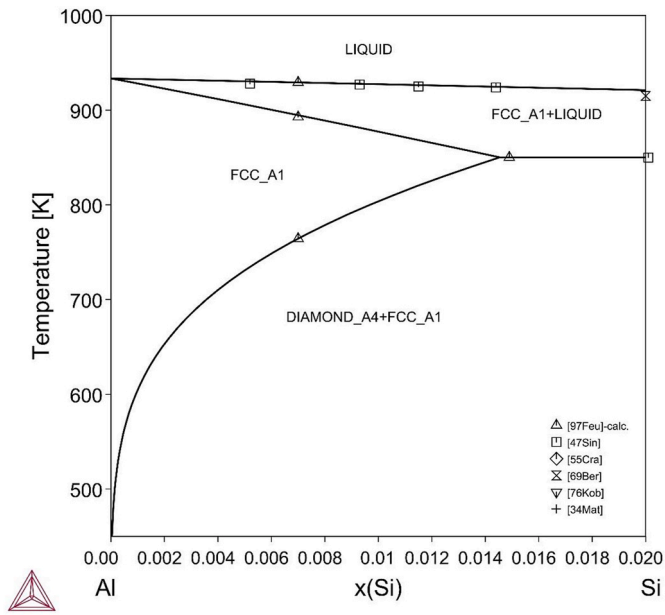


Fig. 10. Detail of the theoretical phase diagram of the Al-Si system based on 3rd generation of unaries assessed in this work with superimposed experimental data [38–45].

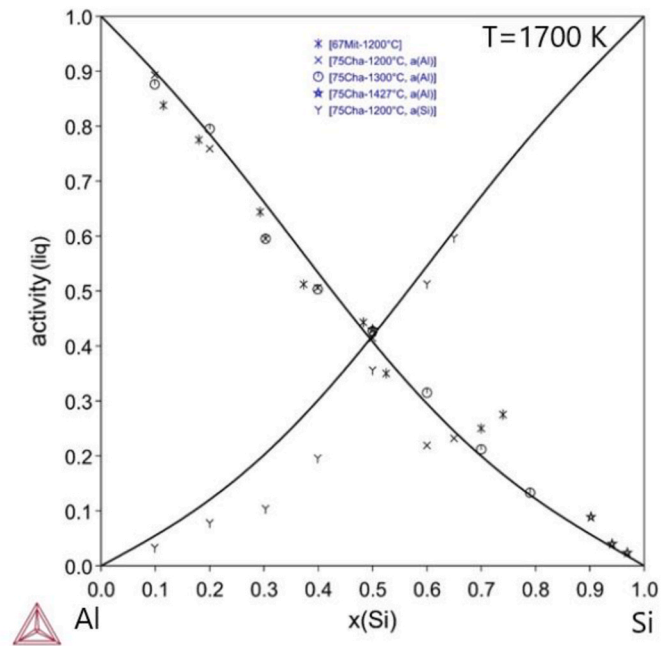


Fig. 12. Calculated activity of Al and Si in liquid phase at 1700 K with superimposed experimental data [53,54].

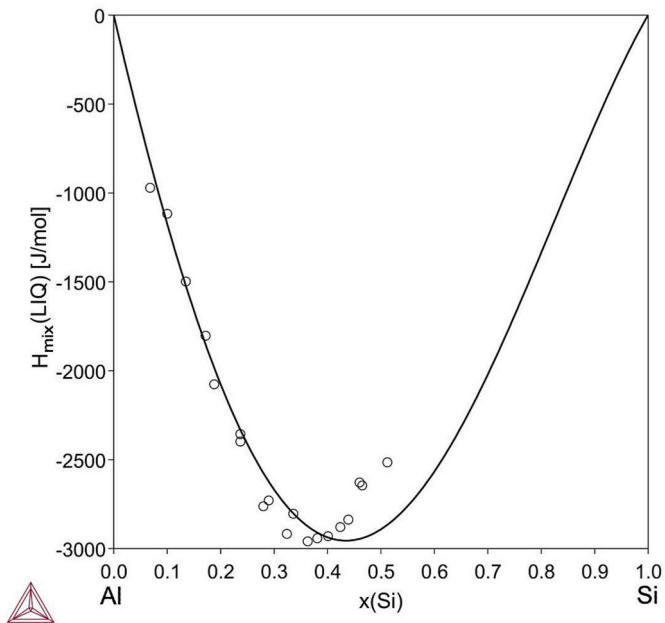


Fig. 11. Calculated mixing enthalpy of liquid phase at 1377K with superimposed experimental data [48].

published by different authors [46–48] exhibit significant differences as shown in Fig. 12. The data from Ref. [48] were used for the assessment, as also used by Ref. [50] and the discrepancies are comparable to those in Ref. [36].

Generally the agreement between experimental phase diagram, thermodynamic properties and theoretically calculated values resulting from this work is very good and this reassessment is suitable for the modelling of higher-ordered systems.

Table 1

The unary and binary assessed parameters for the Al-Si system developed in the scope of this work.

Phase	Parameter	Value
Liquid	$E_T-1(\text{Al})$	294.414
	$G_0^{\text{liq}}(\text{Al})$	-967.4973
	$G_D^{\text{liq}}(\text{Al})$	$2475.62 + 37.10227 \cdot T$
	$E_T-1(\text{Si})$	323.9
	$G_0^{\text{liq}}(\text{Si})$	26584.22
	$G_D^{\text{liq}}(\text{Si})$	$18880.66 - 24.5753 \cdot T$
	$G_0^{\text{liq}}(\text{Al,Si})$	-11495.93
	$G_1^{\text{liq}}(\text{Al,Si})$	-3873.45
	$G_2^{\text{liq}}(\text{Al,Si})$	2520.0
	$\ln \theta_1^{\text{liq}}(\text{Al,Si})$	0.01602
	$\ln \theta_1^{\text{liq}}(\text{Al,Si})$	0.07401
	$\ln \theta_{1/2}^{\text{liq}}(\text{Al,Si})$	0.0
	$\Delta G_{a,b}^{\text{liq}}(\text{Al,Si})$	0.0
Diamond	$E_T-1(\text{Si})$	615.45
	$E_T-2(\text{Si})$	206.96
	Theta F1	0.67401
	Theta F2	0.32599
	$G_0^{\text{diam}}(\text{Si})$	$-9229 + \text{GCORSI}$
fcc_A1	$E_T^{\text{fcc}}(\text{Al})$	294.414
	$E_T^{\text{fcc}}(\text{Si})$	182.6
	$G_0^{\text{fcc}}(\text{Al})$	GCORAL
	$G_0^{\text{fcc}}(\text{Si})$	$51000 + \text{GCORSI}$
	$G_0^{\text{fcc}}(\text{Al,Si})$	-12038.205
	$\ln \theta_0^{\text{fcc}}(\text{Al,Si})$	-0.0038425

4.2. Al-Zn

The thermodynamic parameters published in Ref. [21] gave essentially nearly identical result in comparison with the assessment of Mathon et al. [61]. The data for the liquid phase, based now on the two state model, could differ from the previous assessment. Fig. 13 shows the

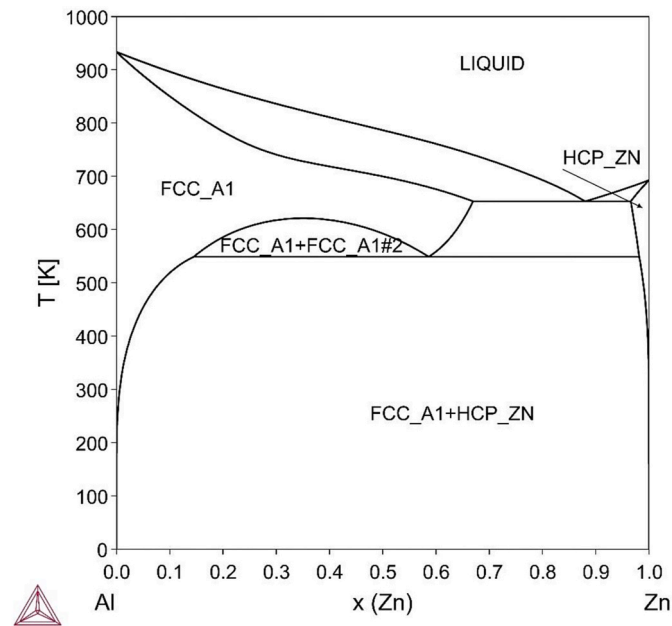


Fig. 13. Calculated phase diagram for the Al-Zn system using the coefficients derived in the paper [21].

Table 2

The assessed parameters for the Al-Zn developed in the scope of our previous work [21].

Phase	Parameter	Value
Liquid	$E_{T1}(\text{Al})$	294.414
	$G_0^{\text{liq}}(\text{Al})$	-967.4973
	$G_D^{\text{liq}}(\text{Al})$	$2475.62 + 37.10227 * T$
	$E_{T1}(\text{Zn})$	162.2
	$G_0^{\text{liq}}(\text{Zn})$	-4088.202
	$G_D^{\text{liq}}(\text{Zn})$	$3442.37 + 41.34521 * T - 7.35647 * T * \ln(T)$
	$G_0^{\text{liq}}(\text{Al,Zn})$	10466.6
	$\ln \theta_1^{\text{liq}}(\text{Al,Zn})$	-0.136049
	$\Delta G_{d,b}^{\text{liq}}(\text{Al,Zn})$	0.0
	Hcp_Zn	$E_T^{\text{hcp,Zn}}(\text{Zn})$
$G_0^{\text{hcp,Zn}}(\text{Zn})$		GCORZN
$E_T^{\text{hcp,Zn}}(\text{Al})$		273.9166706
$G_0^{\text{hcp,Zn}}(\text{Al})$		5481+GCORAL
$G_0^{\text{hcp,Zn}}(\text{Al,Zn})$		18824.72
$\ln \theta_1^{\text{hcp,Zn}}(\text{Al,Zn})$		-0.35891271
fcc_A1		$E_T^{\text{fcc}}(\text{Al})$
	$E_T^{\text{fcc}}(\text{Zn})$	152.30739
	$G_0^{\text{fcc}}(\text{Al})$	GCORAL
	$G_0^{\text{fcc}}(\text{Zn})$	$2969.82 + \text{GCORZN}$
	$G_0^{\text{fcc}}(\text{Al,Zn})$	7298.94
	$G_1^{\text{fcc}}(\text{Al,Zn})$	6612.875
	$G_2^{\text{fcc}}(\text{Al,Zn})$	-3097.93
	$\ln \theta_0^{\text{fcc}}(\text{Al,Zn})$	0.01905544
	$\ln \theta_1^{\text{fcc}}(\text{Al,Zn})$	-0.18409584
	$\ln \theta_2^{\text{fcc}}(\text{Al,Zn})$	0.13255341

calculated phase diagram which is in very good agreement with almost all the experimental data. The obtained results are described in more detail in Ref. [21].

The assessed parameters are listed in Table 2. The parameters were recalculated using the conversion relations developed in the paper [21] and no other reassessment of these parameters was necessary.

4.3. Si-Zn

The interaction parameters for the Si-Zn binary system optimized in this work give a calculated phase diagram in very good agreement with the published experimental data and previous theoretical CALPHAD-type assessments. Table 3 lists the assessed thermodynamic parameters of the CALPHAD approach to the Si-Zn system used within the scope of this project. Fig. 14 shows the calculated phase diagram for the Si-Zn system based on the 3rd generation of unaries assessed in this work with experimental data [63,64,66,69] superimposed. Agreement with the results of Jacobs and Spencer [67] calculated using the SGTE unary data and with the experimental data is very good. There are no experimental thermodynamic data available for this system.

Table 3 lists the interaction parameters for the Si-Zn system, which were reassessed and which give good agreement with experimental phase diagram data. As in the case of the reassessment of the Al-Si system the interaction parameters were initially recalculated from original paper of [67] converted using the approach described in Ref. [21] and then used as the starting point for the reassessment.

4.4. Al-Si-Zn

Prior to this work, the only published thermodynamic description of the thermodynamic properties of the ternary Al-Si-Zn system had been the assessment of by Jacobs and Spencer [67], which is in good agreement with the quite sparse published experimental data. Their ternary phase diagram had been calculated from the datasets for the Al-Si, Al-Zn and Si-Zn binary subsystems without using any ternary interaction parameters.

The same approach was adopted in this work. The relevant phase diagram sections and thermodynamic properties were calculated without introducing any ternary parameters. No isothermal sections or information about the solubility of third elements in binary terminal solution phases had been published. Also, no ternary phases had been observed in the Al-Si-Zn system. Several isopleths have been published by Ibe and Holtz [73] and Nishimura and Tamura [74]. Activities have been measured by Refs. [80–82]. Our assessment agrees well with the

Table 3

The interaction parameters for the Si-Zn reassessed in the scope of this work.

Phase	Parameter	Value
Liquid	$E_{T1}(\text{Si})$	323.9
	$G_0^{\text{liq}}(\text{Si})$	26584.22
	$G_D^{\text{liq}}(\text{Si})$	$18880.66 - 24.5753 * T$
	$E_{T1}(\text{Zn})$	162.2
	$G_0^{\text{liq}}(\text{Zn})$	-4088.202
	$G_D^{\text{liq}}(\text{Zn})$	$3442.37 + 41.34521 * T - 7.35647 * T * \ln(T)$
	$G_0^{\text{liq}}(\text{Si,Zn})$	7229,25
	$G_1^{\text{liq}}(\text{Si,Zn})$	-4038.18
	$G_2^{\text{liq}}(\text{Si,Zn})$	-891.33
	$\ln \theta_1^{\text{liq}}(\text{Si,Zn})$	0
Diamond	$E_{T1}(\text{Si})$	615.45
	$E_{T2}(\text{Si})$	206.96
	Theta F1	0.67401
	Theta F2	0.32599
	$G_0^{\text{diam}}(\text{Si})$	$-9229 + \text{GCORSI}$
Hcp_Zn	$E_T^{\text{hcp,Zn}}(\text{Zn})$	162.2
	$G_0^{\text{hcp,Zn}}(\text{Zn})$	GCORZN
	$E_T^{\text{hcp,Zn}}(\text{Si})$	173.7347
	$G_0^{\text{hcp,Zn}}(\text{Si})$	$49200 + \text{GCORSI}$

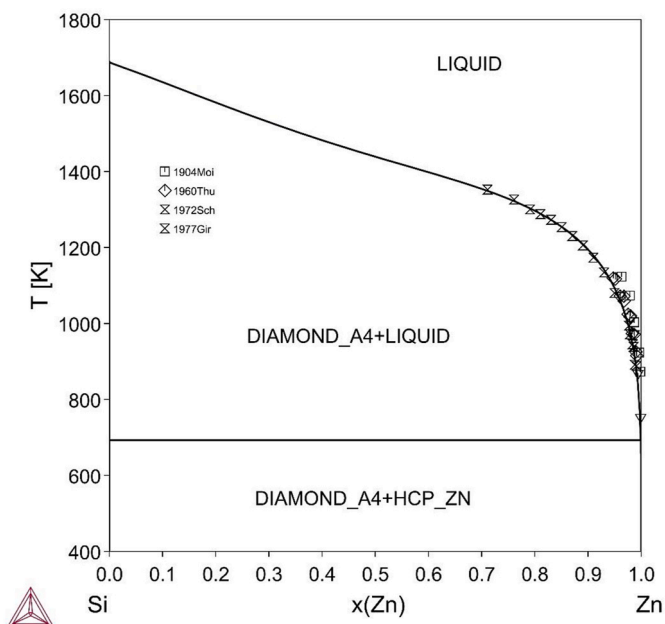


Fig. 14. Assessed phase diagram for the Si-Zn system based on 3rd generation of unaries calculated in this work with the experimental data superimposed [63, 64,66,69].

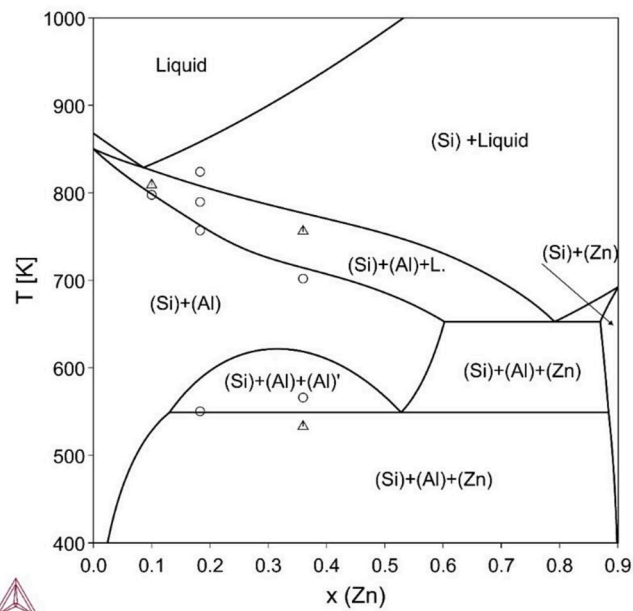


Fig. 16. Calculated isopleth through the Al-Si-Zn phase diagram at $x(\text{Si}) = 0.099$ with the experimental data of Ibe and Holtz [73] superimposed where the triangles represent cooling and the circles heating.

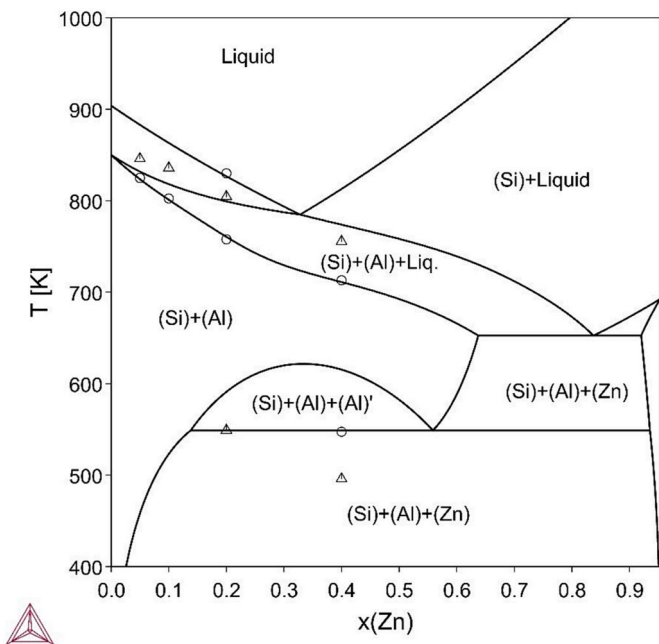


Fig. 15. Calculated isopleth through the Al-Si-Zn phase diagram at $x(\text{Si}) = 0.047$ with the experimental data of Ibe and Holtz [73] superimposed where the triangles represent cooling and the circles heating.

experimental data and with the thermodynamic modelling by Jacobs and Spencer [67].

Vertical sections of the Al-Si-Zn phase diagram calculated from our new parameters with constant amounts of silicon $x(\text{Si}) = 0.047$ and $x(\text{Si}) = 0.099$ are shown on Figs. 15 and 16 respectively. Fig. 17 shows the isopleth at $x(\text{Zn}) = 0.4$. These isopleths also show, superimposed, the experimental data of Ibe and Holtz [73], where the triangles represent cooling and the circles represent heating experiments. A comparison of the theoretical calculation of the concentration section between $(x_{\text{Si}}, x_{\text{Zn}})$

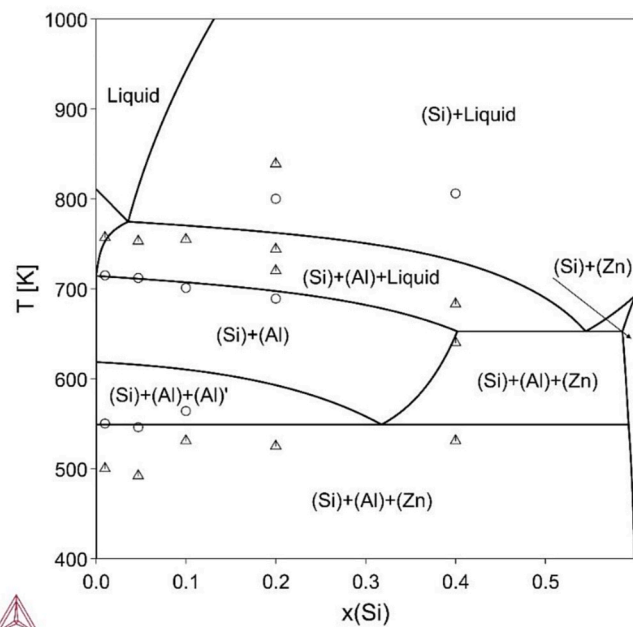


Fig. 17. Calculated isopleth through the Al-Si-Zn phase diagram at $x(\text{Zn}) = 0.4$ with the experimental data of Ibe and Holtz [73] superimposed where the triangles represent cooling and the circles represent heating.

$= (0.0530, 0)$ and $(0.1193, 0.8807)$ with the experimental data from Ref. [71] is shown in Fig. 18. The activity calculations are shown in Figs. 19 and 20 compared with experimental data from Refs. [80–82]. The agreement between the calculated and experimental data is very good for all the results shown, and they are also very similar to those calculated by Ref. [67] (see Fig. 7).

A theoretically predicted liquidus surface of the Al-Si-Zn phase diagram is shown in Fig. 21. There has been no systematic experimental study of the liquidus surface, but this prediction is very reasonable and almost identical to the calculation shown in Ref. [67]. A univariant

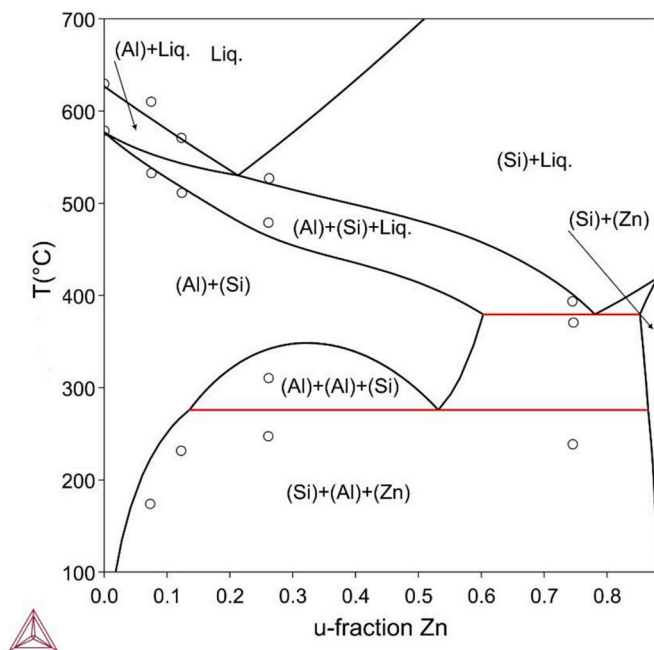


Fig. 18. Calculated isopleth along the section $(x_{Si}, x_{Zn}) = (0.0530, 0)$ to $(0.1193, 0.8807)$ with the experimental data of Dimova et al. [71] superimposed.

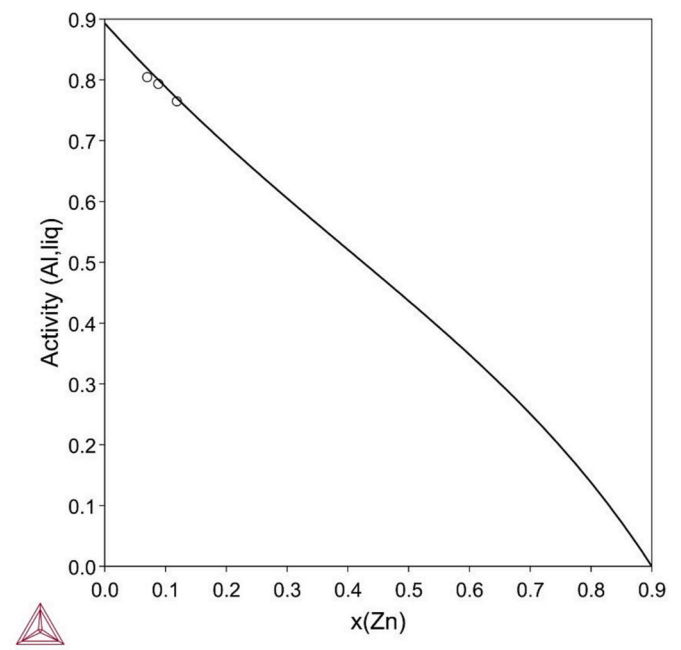


Fig. 20. Calculated activity of Al in liquid for $x_{Si} = 0.1$ at 1073 K with the experimental data of Sebkova et al. [82] superimposed.

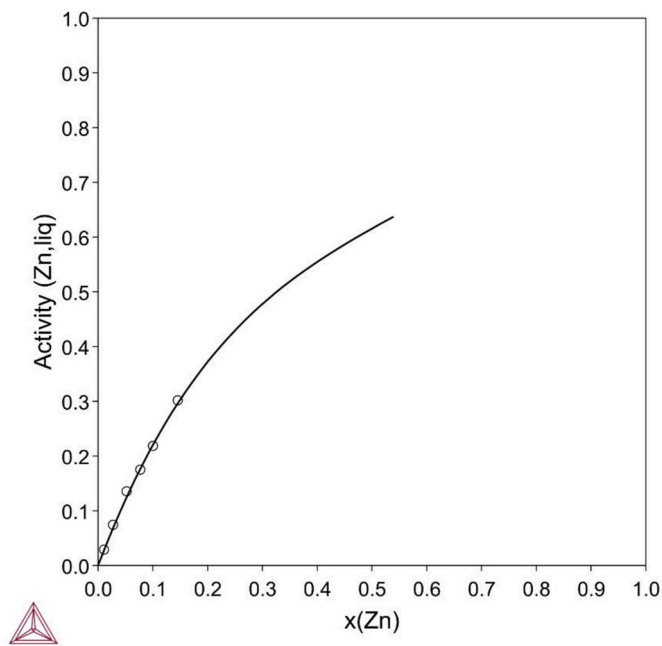


Fig. 19. Calculated activity of Zn in liquid at 1053 K along the section $(x_{Si}, x_{Zn}) = (0.1699, 0)$ to $(0, 0.5382)$ with the experimental data of Sebkova et al. [80, 81] superimposed.

reaction $(Si) + Liq. \rightarrow (Al)+(Zn)$ at the temperature 649.6 K is predicted in the system.

5. Conclusions

Thermodynamic reassessments of the binary Al–Si and Si–Zn systems and the ternary Al–Si–Zn system were carried out using the 3rd generation unary data for Al, Si and Zn. One Einstein temperature model was used to model the heat capacity of liquid Si based on the work of [12].

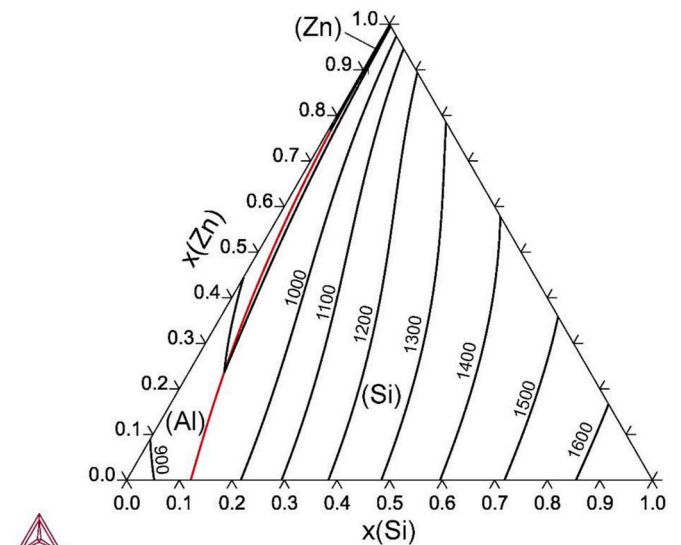


Fig. 21. Calculated liquidus surface of the Al–Si–Zn system. Temperature is given in K.

The relations for the composition dependence of the thermodynamic properties for the liquid phase and solid solution phases developed in our previous work [21] were applied to binary systems Al–Si and Si–Zn. Very good agreement was found between the calculated results using the new 3rd generation unary data models and data from previous assessments based on SGTE or experimental data, respectively. This approach has been extended to the ternary system Al–Si–Zn, where no interaction parameters were needed to give very good agreement with experimental data. The existence of a univariant reaction $(Liq. + Si \rightarrow Al + Zn)$ at the temperature 649.6 K was predicted, and the agreement with experimental value 654 K [77,83] is reasonable.

CRedit authorship contribution statement

Ondrej Zobac: Writing – review & editing, Writing – original draft, Validation, Supervision, Investigation, Conceptualization. **Ales Kroupa:** Writing – original draft, Investigation, Conceptualization. **Alan Dinsdale:** Writing – review & editing, Supervision, Methodology, Investigation, Conceptualization.

Declaration of competing interest

The authors declare that they have no known competing financial interests or personal relationships that could have appeared to influence the work reported in this paper.

Data availability

No new experimental data was used for the research described in the article.

Acknowledgement

This study was supported by the Austrian Science Fund (FWF) under the Lisa-Meitner project M2293–N34 and by the Czech Science Foundation project No 22–22187S.

Appendix A. Supplementary data

Supplementary data to this article can be found online at <https://doi.org/10.1016/j.calphad.2024.102742>.

References

- J. Ågren, B. Cheynet, M.T. Clavaguera-Mora, J. Hertz, F. Sommer, U. Kattner, Group 2: extrapolation of the heat capacity in liquid and amorphous phases, *Calphad* 19/4 (1995) 449–480.
- M.W. Chase, I. Ansara, A.T. Dinsdale, G. Grimvall, L. Hoglund, H. Yokokawa, Group 1: heat capacity models for crystalline phases from 0 K to 6000 K, *Calphad* 19 (1995) 437.
- B. Sundman, F. Aldinger, The Ringberg workshop 1995 on unary data for elements and other end-members of solutions, *Calphad* 19/4 (1995) 433–436.
- O. Tolochko, J. Ågren, Thermodynamic properties of supercooled Fe–B liquids—A theoretical and experimental study, *J. Phase Equil.* 21/1 (2000) 20–24.
- Q. Chen, B. Sundman, Modeling of thermodynamic properties for BCC, FCC, liquid and amorphous iron, *J. Phase Equil.* 22/6 (2001) 631–644.
- C.A. Becker, J. Ågren, M. Baricco, Q. Chen, S.A. Decterov, U.R. Kattner, J. H. Perepezko, G.R. Pottlacher, M. Selleby, Thermodynamic modelling of liquids: CALPHAD approaches and contributions from statistical physics, *Phys. Status Solidi B* 251/1 (2014) 33–52.
- S. Bigdeli, H. Mao, M. Selleby, On the third-generation Calphad databases: an updated description of Mn, *Phys. Status Solidi B* 252/10 (2015) 2199–2208.
- S. Bigdeli, PhD Thesis, KTH Royal Institute of Technology, Stockholm Sweden, 2017.
- A.V. Khvan, A.T. Dinsdale, I.A. Uspenskaya, M. Zhilin, T. Babkina, A.M. Phiri, A thermodynamic description of data for pure Pb from 0 K using the expanded Einstein model for the solid and the two state model for the liquid phase, *Calphad* 60 (2018) 144–155.
- A.V. Khvan, T. Babkina, A.T. Dinsdale, I.A. Uspenskaya I.V. Fartushna, A. I. Druzhinina, A.B. Syzdykova, M.P. Belov, I.A. Abrikosov, Thermodynamic properties of tin: Part I Experimental investigation, ab-initio modelling of α -, β -phase and a thermodynamic description for pure metal in solid and liquid state from 0 K, *Calphad* 65 (2019) 50–72.
- A.V. Khvan, N. Konstantinova, I.A. Uspenskaya, A.T. Dinsdale, A.I. Druzhinina, A. Ivanov, I. Bajenova, A description of the thermodynamic properties of pure indium in the solid and liquid states from 0 K, *Calphad* 79 (2022) 102484.
- I.A. Bajenova, A.S. Ivanov, N.M. Konstantinova, I.A. Uspenskaya, A.V. Khvan, A. T. Dinsdale, A. Kondratiev, A new thermodynamic description of pure silicon from 0 K at 1 bar, *Calphad* 81 (2023) 102554.
- A.V. Khvan, I.A. Uspenskaya, N.M. Aristova, Critical assessment of the data for Pure Cu from 0 K, using two-state model for the description of the liquid phase, *Calphad* 84 (2024) 102637.
- J. Vřešťál, J. Štrof, J. Pavlů, Extension of SGTE data for pure elements to zero kelvin temperature—A case study, *Calphad* 37 (2012) 37–48.
- J. Pavlů, P. Rehák, J. Vřešťál, M. Sob, Combined quantum-mechanical and calphad approach to description of heat capacity of pure elements below room temperature, *Calphad* 51 (2015) 161–171.
- J. Vřešťál, J. Pavlů, U.D. Wdowik, M. Sob, Modelling of phase equilibria in the Hf–V system, *J. Min. Metall. B Metall.* 53/3 (2017) 239–247.
- Y. Jiang, S. Zomorodpoosh, I. Roslyakova, L. Zhang, Thermodynamic re-assessment of binary Cr–Nb system down to 0 K, *Calphad* 62 (2018) 109–118.
- S. Bigdeli, M. Selleby, A thermodynamic assessment of the binary Fe–Mn system for the third generation of Calphad databases, *Calphad* 64 (2019) 185–195.
- Y. Jiang, S. Zomorodpoosh, I. Roslyakova, L. Zhang, Thermodynamic re-assessment of the binary Cr–Ta system down to 0 K, *Int. J. Mater. Res.* 110/9 (2019) 797–807.
- M.H.G. Jacobs, R. Schmid-Fetzer, A.P. van den Berg, Phase diagrams, thermodynamic properties and sound velocities derived from a multiple Einstein method using vibrational densities of states: an application to MgO–SiO₂, *Phys. Chem. Miner.* 44 (2017) 43–62.
- A. Dinsdale, O. Zobac, A. Kroupa, A. Khvan, Use of third generation data for the elements to model the thermodynamics of binary alloy systems: Part 1 – the critical assessment of data for the Al–Zn system, *Calphad* 68 (2020) 101723.
- Z. He, M. Selleby, A third generation Calphad description of W–C including a revision of liquid C, *Calphad* 78 (2022) 102449.
- A.V. Khvan, A.T. Dinsdale, Q. Chen, Use of third generation data for the elements to model the thermodynamics of binary alloy systems: Part 2 – the critical assessment of data for the Pb–Sn system, *Calphad* 76 (2022) 102396.
- J. Agren, Thermodynamics of supercooled liquids and their glass transition, *Phys. Chem. Liq. Intl J.* 18/2 (1988) 123–139.
- P.D. Desai, Thermodynamic properties of selected binary aluminum alloy systems, *Phys. Chem. Ref. Data* 16/1 (1987) 91.
- W.F. Giauque, P.F. Meads, The heat capacities and entropies of aluminum and copper from 15 to 300° K, *J. Am. Chem. Soc.* 63 (1941) 1897–1901.
- D.B. Downie, J.F. Martin, An adiabatic calorimeter for heat-capacity measurements between 6 and 300 K. The molar heat capacity of aluminium, *J. Chem. Therm.* 12 (1980) 779.
- W. Kramer, J. Nörling, Anomale spezifische Wärmen und Fehlordnung der Metalle Indium, Zinn, Blei, Zink, Antimon und Aluminium, *Acta Metall.* 20/12 (1972) 1353–1359.
- O.V. Timofeev, The heat capacity of extra-pure silicon, Institute of Chemistry of High-Purity Substances of the Russian Academy of Sciences (ICHPS RAS) (1999). PhD thesis, Nizhni Novgorod.
- P. Flubacher, A.J. Leadbetter, J.A. Morrison, The heat capacity of pure silicon and germanium and properties of their vibrational frequency spectra, *Phil. Mag.* 39/4 (1959) 273–294.
- H. Abe, National standard and new reference material for specific heat capacity measurements, *Anal. Sci.* 37/1 (2021) 201–210.
- H. Abe, Development of low temperature specific heat capacity standard, *J. Cryo. Super. Soc. Jpn.* 50 (2015) 314–321, 6.
- B. North, K.E. Gilchrist, Effect of impurity doping on a reaction-bonded silicon carbide, *Am. Ceram. Soc. Bull.* 60 (1981) 549–554, 5.
- Y.S. Sung, H. Takeya, K. Hirata, K. Togano, Specific heat capacity and hemispherical total emissivity of liquid Si measured in electrostatic levitation, *Appl. Phys. Lett.* 83 (6) (2003) 1122–1124.
- A. Dinsdale, A. Khvan, A. Aristova, A new generation of data for the elements: critical assessment of data for Zn and Cd, Presented at CALPHAD XLIV, May 31–June 5 2015, Loano, Italy, Book of Abstract P. 42.
- H. Feufel, T. Goedecke, H.L. Lukas, F. Sommer, Investigation of the Al–Mg–Si system by experiments and thermodynamic calculations, *J. Alloys Compd.* 247 (1997) 31–42.
- A.T. Dinsdale, SGTE data for pure elements, *Calphad* 15/3 (1991) 317–425.
- K. Matsuyama, Ternary diagram of Al–Cu–Si system, *Kinzoku No Kenkyu* 11 (1934) 461–490.
- O. Berthon, G. Petot-Ervas, C. Petot, P. Desre, Thermodynamics of ai–Si alloys containing from 2 to 35 at.% Si, *C. R. Acad. Sci. Paris* 268 (1969) C1939–C1942.
- C.M. Craighead, E.W. Cawthorne, R.I. Jaffee, Solution rate of solid aluminum in molten Al–Si alloy, *Trans. AIME* 203 (1955) 81–87.
- A.R.E. Singer, S.A. Cottrell, Hot-shortness of the aluminium–silicon alloys of commercial purity, *J. Inst. Met.* 73 (1947) 33.
- K. Kobayashi, R.H. Shingu, R. Ozaki, Shift of aluminium liquidus in Al Si system due to the sodium addition, *Scripta Metall.* 10 (1976) 525.
- W. Fraenkel, Silicon–aluminum alloys, *Z. Anorg. Chem.* 58 (1908) 154.
- W. Broniewski, Smialovski, on the Al–Si alloys, *Rev. Métall.* 29 (1932) 542.
- G.I. Batalin, E.A. Beloborodova, V.A. Stukalo, Study of the thermodynamic properties of Al–Si melts, *Izv. Akad. Nauk. SSSR, Met. (2)* (1971) 44. *Metally No. 2* 1971, 69; *Russ. Met. (English Transl.)*.
- F. Körber, W. Oelsen, H. Lichtenberg, On the thermochemistry of alloys. II. Direct determination of the heat of formation of ternary alloys of the system iron–nickel–aluminium–silicon, *Mitt. KWI Eisenforsch. Düsseldorf* 19 (1937) 156.
- J.C. Mathieu, B. Journel, P. Desré, E. Bonnier, Heats of dissolution of tin, silver, silicon and iron in liquid aluminum, *Thermodyn. Nucl. Mater. Symp.* Vienna (1967) 767, publ. 1968.
- J.P. Bros, H. Eslami, P. Gaune, Ber. Bunsenges. Thermodynamics of Al – Si and Al – Ge – Si liquid alloys: enthalpies of formation by high temperature calorimetry, *Phys. Chem.* 85 (1981) 333.
- G.I. Batalin, E.A. Beloborodova, A.N. Schlapak, I.V. Nikolaenko, V.P. Kurach, Zh Fiz Khim, *Russ. J. Phys. Chem.* 55 (1981) 1580, 55 (1981) 888.
- J.L. Murray, A.J. McAlister, The Al–Si (Aluminum–Silicon) system, *Bull. Alloy Phase Diagrams* 5 (1984) 74–84.
- S.C. Schaefer, N.A. Gokcen, Thermodynamic properties of liquid Al–Ni and Al–Si systems, *High. Temp. - High. Press.* 11 (1979) 31.

- [52] S.C. Schaefer, Thermodynamics of the Al–Si system, U.S. Dept. Of interior, bur. Of mines, Rept. of Investigations (1974) 7895.
- [53] H. Mitani, H. Nagai, Determination of equilibrium constant of $2\text{Al(l)} + \text{Al(g)}\text{Cl}_3\text{(g)} = 3\text{AlCl(g)}$ reaction and activities of Al and Si in Al–Si binary alloys, *J. Jpn. Inst. Metals* 31 (1967) 1296.
- [54] C. Chaiton, M. Allibert, A. Pattoret, Thermodynamic study by mass spectrometry of aluminum–silicon alloys from 1000 to 1700 K, *High. Temp. - High. Press.* 7 (1975) 583–594.
- [55] A.F. Loseva, A.I. Almkulemedov, V.N. Tyumentsev, M.A. Luzhova, Thermodynamic properties of molten aluminum– silicon alloys, *Zh. Fiz. Khim.* 51 (1977) 495. *Russ. J. Phys. Chem. (English Transl.)* 51 (1977) 290.
- [56] D. Hanson, M.L. Gayler, Further study of the alloys of aluminium and zinc, *J. Inst. Met.* 27 (1922) 267–294.
- [57] S. an Mey, K. Hack, A thermodynamic evaluation of the Si–Zn, Al–Si and Al–Si–Zn systems, *Z. Metallkd.* 77/7 (1986) 454–459.
- [58] S.L. Chen, Y.A. Chang, A thermodynamic analysis of the Al–Zn system and phase diagram calculation, *Calphad* 17/2 (1993) 113–124.
- [59] S. Mey, Reevaluation of the Al–Zn system, *Z. Metallkd.* 84/7 (1993) 451–455.
- [60] H. Adachi, K. Osamura, H. Okuda, Metastable phases in Al–Zn–Mg ternary based alloys, *J. of the Japan Institute of Metals and Materials* 63/6 (1999) 733–740.
- [61] M. Mathon, K. Jardet, E. Aragon, P. Satre, A. Sebaoun, Al–Ga–Zn system: reassessments of the three binary systems and discussion on possible estimations and on optimisation of the ternary system, *Calphad* 24/3 (2000) 253–284.
- [62] S. Wasiur–Rahman, M. Medraj, A thermodynamic description of the Al–Ca–Zn ternary system, *Calphad* 33/3 (2009) 584–598.
- [63] B. Girault, Liquidus curves of various silicon–metal systems, *Compt. Rend. Acad. Sci., Ser. B*, t. 284 (1977) 1–4.
- [64] C.D. Thurmond, M. Kowalchik, Germanium and silicon liquidus curves, *Bell Sys. Tech. J.* 39 (1960) 169–204.
- [65] M. John, K. Hein, E. Buhrig, Investigation of II–IV–V systems by the method of differential thermal analysis, *Cryst. Res. Technol.* 14 (1979) 841–848.
- [66] M. Schneider, M. Krumnacker, Study of the zinc–silicon phase diagram, *Neue Hutte* 17 (1972) 519–521.
- [67] M.H.G. Jacobs, P.J. Spencer, A critical thermodynamic evaluation of the systems Si–Zn and Al–Si–Zn, *Calphad* 20/3 (1996) 307–320.
- [68] R.W. Olesinski, G.J. Abbaschian, Alloy phase diagrams, *Bull. Alloy Phase Diagrams* 6 (1985) 589–590.
- [69] H. Moissan, F. Siemens, On the solubility of silicon in zinc and in lead, *C.R. Acad. Sci. Paris* 138 (1904) 657–661.
- [70] E.M. Padeshnova, V.V. Cherkasov, T.V. Dobotkina, Nature of phase equilibria in Al–Si–Cu–Zn alloys, *Izv. Akad. Nauk. SSSR, Met.* 1 (1974) 234–236.
- [71] V. Dimova, T. Markov, D. Danilov, V. Momkhillova, Vertical section of the Al–Zn–Si diagram at 5.5% Si, *tekhnicheska misul, Sofia* 2Q (1983) 109–111.
- [72] C. Planchamp, Study of the Aluminium–Rich Corner of the Ternary System Al–Si–Zn and Mechanical Properties of These Alloys, *Universite Claude Bernard – Lyon I, France*, 1974, pp. 1–131. Thesis.
- [73] G. Ibe, S. Holtz, **Noted in [67] as to Be Published.**
- [74] H. Nishimura, K. Tamura, *Nippon kinzoku gakkai–Si*, *Trans. Inst. Metals, Japan* 4 (1949) 116–119.
- [75] H.J. Axon, E. Butchers, W. Hume–Rothery, *J. Inst. Metals* 24 (1980) 330–344.
- [76] L.F. Mondolfo, *Metallography of Aluminium Alloys*, John Wiley & Sons, New York, 1943, pp. 121–122.
- [77] H. Hanemann, A. Schrader, *Atlas Metallographicus*, Vol. III, Verlag Stahleisen M.B. H, Düsseldorf, 1952, p. 150.
- [78] H. Spengler, The importance of research on eutectics and its application to ternary eutectic aluminium alloys, *Metall* 14 (3) (1960) 201–206.
- [79] H.W.L. Phillips, *Equilibrium diagrams of aluminium alloy systems*, Inf. Bull. 25 (1960) 36. Aluminium Development Association, London.
- [80] J. Sebkova, M. Beranek, J. Koritta, Activity of zinc in liquid aluminum–zinc–silicon alloys, *Kovove Mater.* 10 (1972) 385–391.
- [81] J. Sebkova, M. Beranek, Thermodynamické vlastnosti kapalné slitiny Al–Mg–Si–Zn, *Kovove Mater.* 3 (21) (1983) 228–229.
- [82] J. Sebkova, M. Beranek, Thermodynamic properties of Al–Zn–Si alloys measured by the EMF method, *Kovove Mater.* 15 (1977) 14–23.
- [83] H. Spengler, Die Bedeutung der Eutektikumforschung in Anwendung auf ternäre eutektische Aluminiumlegierungen, *Metall* 14 (3) (1960) 201–206.